MEASUREMENT OF PARTICLE TEMPERATURES DURING COAL PYROLYSIS AND COMBUSTION

Guangwei Huang, Francis J. Vastola and Alan W. Scaroni

Combustion Laboratory
The Pennsylvania State University
404 Academic Activities Building
University Park, PA 16802

Introduction

The surface temperature of pyrolyzing and/or burning coal particles has been the subject of intensive investigation (1-6) because it is important in the estimation of the rate of devolatilization and/or carbon oxidation. A number of models have been established in order to predict the surface temperature of pulverized coal particles smaller than 200 μm diameter. However, few convincing models for millimeter size coal particles have emerged because of the complication of temperature gradients within the particle.

The ignition mechanism of coal particles in a hot oxidizing atmosphere is another subject of debate (5-8). Further experimental work is needed to determine whether initial ignition occurs homogeneously in the gas phase or heterogeneously at the particle surface.

The work presented here had three objectives: firstly, to develop a technique to monitor the transient temperature variations in the gas phase around a single particle during pyrolysis and/or combustion; secondly, to extrapolate the data to estimate the particle surface temperature; and thirdly, to analyze the ignition mechanism of coal and char particles.

Experimental Equipment

A schematic diagram of the equipment is shown in Figure 1. For pyrolysis studies, a flow of prepurified nitrogen was passed over copper at 673 K to remove oxygen, then through a drierite column to remove water. Dry air was used to study combustion. The reactor, a horizontal vycor tube of 8 mm internal diameter, is heated by two enclosing furnaces. The first furnace acts to preheat the in-coming gas while the second maintains the reactor at the desired temperature.

Details of the sample injection and temperature measurement systems are given in Figure 2. A single coal particle was introduced by gravity through an electromagnetically controlled injector. An electrotrigger was used to energize a 24 volt (DC) solenoid which injects the particle into the reactor.

A new approach was used to measure the transient temperature variations around the coal particle. A group of extra-fine Chromel-Alumel thermocouples with 0.05 mm diameter was employed to provide precise temperature measurement with rapid response. The thermocouples were protected by two-hole ceramic tubes. Four thermocouples were bound together using high temperature cement to form a thermocouple array (Figure 2). In order to simplify the calculation of the temperature gradient, the distance between adjacent thermocouples in the array was always the same. In this study, 0.5 and 1.0 mm spacings were used. The voltage signals generated by the thermocouple array were amplified then converted into digital signals in the data acquisition system before being sent to the microcomputer. When the particle injector was triggered, the computer was

automatically initialized to record the output of the thermocouples at 2 millisecond intervals and the data stored on disk for later analysis.

Procedure

The characteristics of the Texas subbituminous coal used are shown in Table 1. For each run a 1 mm diameter coal particle was injected into the reactor containing either preheated nitrogen or air. The bulk gas temperature was held constant at 873 K for all the experiments reported here. Before particle injection, the gas flow was stopped so that the experiments were carried out essentially in a static system. Char particles were prepared by injecting coal particles into the reactor swept by nitrogen at 873 K for 30 minutes.

Results and Discussion

The temperatures measured by the thermocouple array as a function of time, and the extrapolated surface temperatures of the single coal and char particles, are presented in Figures 3, 4 and 5 for coal pyrolysis, coal combustion and char combustion, respectively. A pyrolysis run illustrated by Figure 3 shows the temperature variations caused by the transient heat transfer between the hot gas environment and the colder coal particle. The temperature profiles illustrate the practical thermal boundary layer in the vicinity of a pyrolyzing coal particle. A rapid drop followed by a rapid increase in temperature occurred in the spherical layer 1 mm away from the particle surface while almost no temperature variation was detected 4 mm away from the particle surface.

Data for the combustion of coal and char particles are shown in Figures 4 and 5, respectively. A significant aspect of coal combustion in Figure 4 is the sudden temperature rise in the gas phase about 1.5 mm from the surface of the coal particle, compared with the much smoother curve for char combustion shown in Figure 5. Point A in Figure 4 is significant because it represents a transition from net heat loss to net heat gain by the gas. The gaseous layer surrounding the particle experienced a rapid temperature drop prior to point A and a rapid increase after this point, in contrast with the relatively smooth increase in the particle surface temperature. This implies that homogeneous ignition occurred in gas phase rather than heterogeneous ignition at the particle surface. For the experimental conditions used, the homogeneous ignition temperature was around 830 K with approximately 800 ms induction time, as represented by point A in Figure 4. This is in general agreement with the calculated results of Annamalai and Durbetaki (5). The temperture in the homogeneous combustion layer increased rapidly as the volatile matter was combusted until there was not sufficient volatile matter evolving from the particle to sustain homogeneous combustion (point B in Figure 4). The remaining and subsequently-evolved volatile matter then experienced slower oxidation with a lower heat release rate. Consequently, there was a drop in the temperature in the surrounding gas layer. Because of the need to exceed both the ignition temperature and volatile matter concentration, homogeneous combustion was observed only in the thin spherical layer about 1.5 mm from the particle surface. No rapid gas temperature rise was detected by the thermocouples closer to, or farther from, the particle surface.

Particle surface temperature and heating rate versus time are given in Figures 6 and 7, respectively. The heating rate is of interest because it is related to the rate of devolatilization and char combustion. The significance of devolatilization on combustion is seen clearly in Figures 6 and 7 which indicate that during pyrolysis the coal particle heating rate was slow and the particle temperature never exceeded the reactor temperature. In the case of devolatilized char particles a higher heating rate was observed up to the equilibrium burning

temperature of 1075 K, about 200 K higher than the reactor temperature. Figure 7 shows that coal particles had the same heating rate initially during pyrolysis and combustion until divergence at point C. This point corresponds to that of homogeneous ignition in Figure 4. After point C the heating rate was higher for combustion than pyrolysis because the heat from the homogeneous combustion reactions was transferred to the particle surface.

Two major differences existed between the char and coal during combustion. Firstly, no temperature rise in the gas was detected at any distance from the char surface (Figure 5). Secondly, the surface temperature of the char particle increased at a higher rate than that of the coal particle (Figure 6). This supports the concept of heterogeneous ignition of the char particles.

Conclusions

A fast response thermocouple array was employed to provide information on the transient heating processes associated with pyrolysis and combustion of 1 mm diameter coal and char particles at a furnace temperature of 873 K. The measured temperature variations implied that ignition occurred at the surface of the char particles but in the gas phase surrounding pyrolyzing coal particles. Homogeneous ignition occurred at 830 K causing a temperature rise in the gas in a narrow spherical layer about 1.5 mm from the surface of the coal particle.

Acknowledgements

Financial support for this work was provided by the Penn State Coal Cooperative Program. The coal was supplied by the Penn State/DOE Sample Bank and Data Base.

References

1. Field, M. A., Gill, D. W., Morgan, B. B., and Hawksley, P. G. W., Combustion of Pulverized Coal, The British Coal Utilization Research Association, Leatherhead, England (1967), p. 191.

2. Bandyopadhyay, S., and Bhaduri, D., Combustion and Flame 18, 411 (1972).

3. Howard, J. B., and Wall, T. F., Combustion and Flame 9, 377 (1965).

4. Juniper, L. A., and Durbetaki, P., Combustion and Flame 39, 69 (1980).

5. Annamalai, K., and Durbetaki, Combustion and Flame 29, 193 (1977).

6. Thomas, G. R., Stevenson, A. J., and Evans, D. G., Combustion and Flame 21, 133 (1973).

7. Gomez, C. O., and Vastola, F. J., Fuel 64, 558 (1985).

8. Stevenson, A. J., Thomas, G. R., and Evans, D. G., Fuel 52, 281 (1973).

Table 1
Characteristics of Texas Subbituminous B Coal, PSOC-423

Proximate Analysis (wt%)	As Received	Dry Basis
Moisture	24.11	
Ash	10.31	13.59
Volatile Matter	38.31	54.48
Fixed Carbon	27.27	35.93
Ultimate Analysis (wt%)		
C	47.58	62.69
H	4.01	5.29
N	0.71	0.93
S (total)	1.34	1.76
O (diff.)	11.95	15.74
Calorific Value Btu/lb (mm-Free Basis)	9836	13540

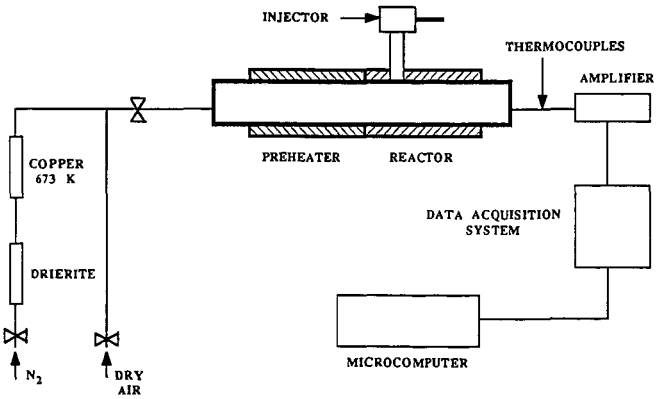

FIG. 1 SCHEMATIC DIAGRAM OF THE EQUIPMENT

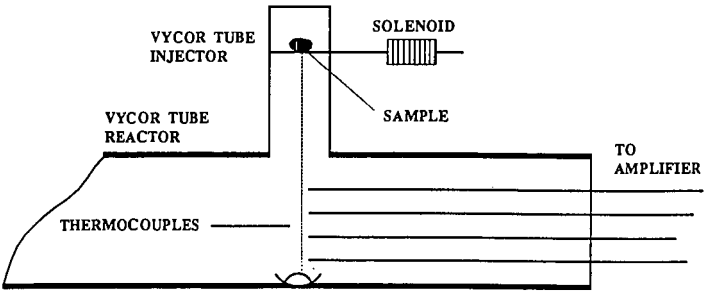

FIG. 2 INJECTION AND TEMPERATURE MEASUREMENT SYSTEM

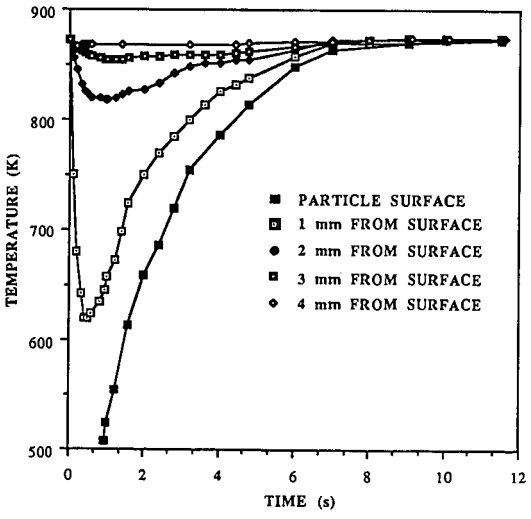

FIG. 3 TEMPERATURE HISTORY OF COAL PARTICLE SURFACE DURING PYROLYSIS

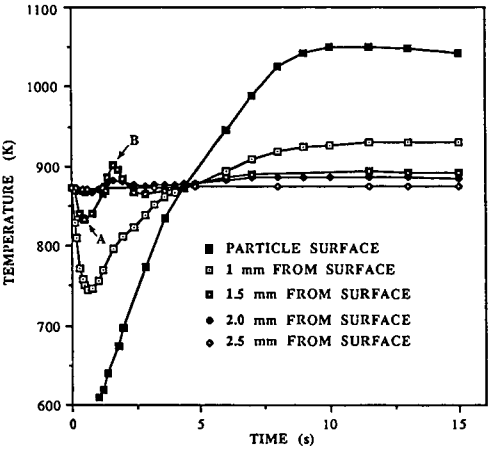

FIG. 4 TEMPERATURE HISTORY OF COAL PARTICLE SURFACE DURING COMBUSTION

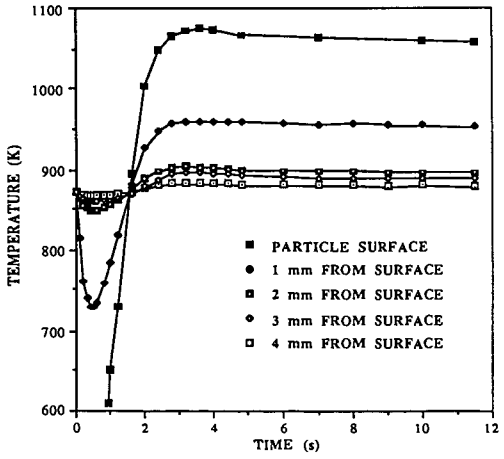

FIG. 5 TEMPERATURE HISTORY OF CHAR PARTICLE SURFACE DURING COMBUSTION

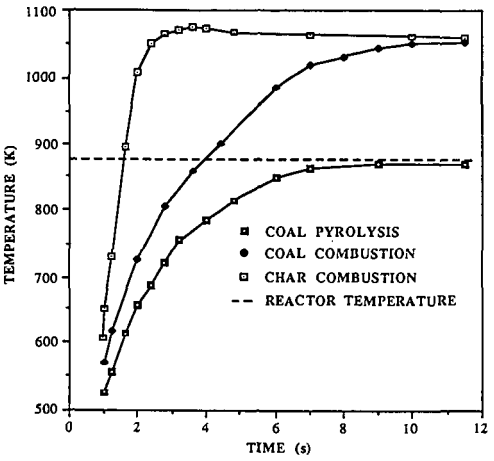

FIG. 6 TEMPERATURE HISTORY OF THE PARTICLE SURFACE

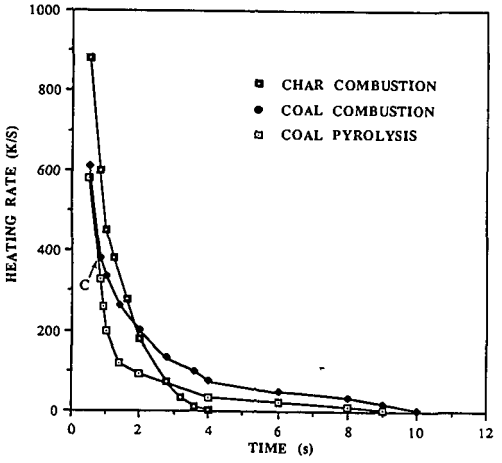

FIG. 7 HEATING RATE VERSUS TIME

INTRA-PARTICLE HEAT TRANSFER EFFECTS IN COAL PYROLYSIS

Mohammed R. Hajaligol, William A. Peters, and Jack B. Howard
Energy Laboratory and Department of Chemical Engineering,
M.I.T., Cambridge, MA 02139

May, 1987

Abstract

Time and spatial temperature gradients within pyrolyzing coal particles can exert strong effects on devolatilization behavior including apparent pyrolysis kinetics. This paper mathematically models transient spatial non-isothermalities within an isolated, spherical coal particle pyrolyzing by a single first-order reaction. The analysis provides three distinct indices of heat transfer effects by quantitatively predicting the extent of agreement between: (a) centerline and surface temperature; (b) volume averaged pyrolysis rate [or (c) volume averaged pyrolysis weight loss] and the corresponding quantity calculated using the particle surface temperature for the entire particle volume. Regimes of particle size, surface heating rate, and reaction time where particle "isothermality" according to each of criteria (a) through (c) is met to within prescribed extents, are computed for conditions of interest in entrained gasification and pulverized coal combustion, including pyrolysis under non-thermally neutral conditions.

Introduction. Many coal combustion and gasification processes involve particle sizes and surface heating rates producing temporal and spatial temperature gradients within the coal particles during pyrolysis. These gradients may strongly influence volatiles yields, compositions, and release rates, and can confound attempts to model coal pyrolysis kinetics with purely chemical rate expressions. Mathematical modelling of particle non-isothermalities is needed to predict reaction conditions (viz. particle dimension, surface heating rate, final temperature, and reaction time) for which intra-particle heat transfer limitations do not significantly influence pyrolysis kinetics, and to predict pyrolysis behavior when they do. When pyrolysis is not thermal-neutral, the analysis is non-trivial since local temperature fields are coupled non-linearly to corresponding local heat release (or absorption) rates and hence to local pyrolysis kinetics.

Much of the pertinent literature has addressed pseudo steady-state models for spatial temperature gradients within catalyst particles playing host to endo- or exothermic reactions, including, for some cases, mathematical treatment of the attendant limitations on intra-particle mass transfer of reactants or products [See Ref. (1) and references cited therein]. There appear to have been few analyses of non-isothermalities within a condensed phase material simultaneously undergoing non-thermally neutral chemical reaction(s). Previous work includes rather empirical approaches to fitting coal weight loss kinetics [see reviews by Howard (2) and Gavalas (3)], and more refined analyses of spatial non-isothermalities within exploding solids (4,5). Gavalas (2) calculated regimes of coal particle size where pyrolysis kinetics should be free of heat transfer effects, and Simmons (6) provided similar information for cellulose pyrolysis. Valuable contributions are also

emanating from the laboratories of Essenhigh (7), and Freihaut and Seery (8).

There is need for a generic, quantitative formalism to reliably predict transient intra-particle non-isothermalities and their effects on pyrolysis, as a function of operating conditions of interest in modern fuels utilization technologies. To this end the present paper presents, for an isolated spherical coal particle pyrolyzing by a single first-order reaction, quantitative predictions of three distinct indices of particle non-isothermality - namely the extent of agreement between: (1) temperatures at the particle surface and centerline; (2) the pyrolysis rate [or (3) the pyrolysis weight loss] averaged over the particle volume and the corresponding quantity calculated using the particle surface temperature for the entire particle volume. Each index is explicitly dependent on time and thus accounts for the temporal as well as the spatial non-idealities in particle "isothermality".

Method of Analysis. Spatial limitations allow only a brief summary of the theoretical approach, which is described in more detail with broader applications, by Hajaligol et al. (9). For an isolated spherical coal particle with temperature invarient thermal physical properties, pyrolyzing by a single first-order endo or exo-thermic reaction with an Arrhenius temperature dependency, heated at its surface, and transmitting heat internally only by conduction, (or by processes well-described by an apparent isotropic thermal conductivity) a standard heat balance gives the following partial differential equation for the time and spatial dependence of the intra-particle temperature field

$$\frac{1}{\alpha}\left(\frac{\partial T}{\partial t}\right) = \frac{1}{r^2}\frac{\partial}{\partial r}\left(r^2\frac{\partial T}{\partial r}\right) + \frac{(-\Delta H_{py})\,\rho\, k_0\, e^{-E/RT}}{\lambda} \qquad (1)$$

Following Boddington et al. (1982) and others, this may be rewritten in dimensionless form as

$$\left(\frac{\partial \theta}{\partial \tau}\right) = \frac{1}{\xi^2}\frac{\partial}{\partial \xi}\left(\xi^2\frac{\partial \theta}{\partial \xi}\right) + \delta \exp\left[\frac{\theta}{\beta + \varepsilon\theta}\right] \qquad (2)$$

Symbols are defined in the nomenclature section at the end of the paper. Solution of Equation (1) or (2) requires specification of one initial condition and two spatial boundary conditions. The initial condition prescribes the temperature field throughout the coal particle at the instant heating begins

$$T(r,0) = T_o \qquad (3)$$

or

$$\theta(\xi,0) = 1 \qquad (4)$$

One boundary condition is the mathematical expression for centerline symmetry of the particle temperature field at all pyrolysis times

$$\left(\frac{\partial T}{\partial r}\right)_{r=0} = 0 \tag{5}$$

or

$$\left(\frac{\partial \theta}{\partial \xi}\right)_{\xi=0} = 0 \tag{6}$$

Four cases are of interest for the second boundary condition in the present analysis:

(1) A finite rate of heat transmission to the particle surface describable in terms of an apparent heat transfer coefficient

$$-\lambda\left(\frac{\partial T}{\partial r}\right)_{r=R_0} = h_{eff}\left(T - T_\infty\right) \tag{7}$$

or

$$\left(\frac{\partial \theta}{\partial \xi}\right)_{\xi=1} = -N_{Bi}\left(\theta - \theta_\infty\right) \tag{8}$$

This case would be applicable to heating of coal particles in a fluidized bed or by molecular conduction from a high temperature gas. It also automatically accommodates cases where the overall rate of heat transfer to the particle is influenced by extra-particle resistance [i.e. cases of non-infinite Biot number].

(2) A prescribed constant rate of increase in the particle surface temperature:

$$T_s(t) = T_0 + \dot{m}\, t \tag{9}$$

or

$$\theta_s(\tau) = 1 - \gamma\, \tau \tag{10}$$

This case is applicable to screen heater reactors or other apparatus where surface heating rates are maintained essentially constant.

(3) A known, constant surface heat flux density:

$$-\lambda\left(\frac{\partial T}{\partial r}\right)_{r=R_0} = \dot{q}_0/4\pi R_0^2 \tag{11}$$

or

$$\left(\frac{\partial \theta}{\partial \xi}\right)_{\xi=1} = -\Phi \tag{12}$$

This case is especially applicable to fires and furnaces under conditions where the particle surface temperature remains well below the temperature of the surroundings, and sample heating is dominated by radiation.

(4) A special limiting case of (1) through (3) above is an infinitely rapid surface heating rate:

$$T_s(t) = T_s(\infty) \quad , \qquad r = R_o \tag{13}$$

or

$$\theta_s(\tau) = 0 \quad , \qquad \xi = 1 \tag{14}$$

This case would approximate the heat transfer characteristics of systems providing very rapid surface heating of the coal particles, for example shock tubes, laser and flash lamp reactors, and coal dust explosions, where surface heating rates are estimated to exceed 10^5 - 10^7 C/s.

Equations (1) and (2) were solved numerically for each of the above four cases of boundary condition, using a procedure based on the method of lines and on Gear's method. Only our results for constant surface heating rate, Case (2) above, will be presented here. Results for other cases are presented by Hajaligol et al. (9).

The solutions to these two equations are predictions of the spatial variation of the intra-particle temperature field with pyrolysis time. This information was used to compute three distinct indices of particle non-isothermality:

(1) The extent of agreement between the surface and centerline temperature of the particle:

$$\eta_T(t) = \left[T_s(t) - T_{cL}(t) \right] / T_s(t) \tag{15}$$

or

$$\hat{\eta}_T(\tau) = \theta_{cL}(\tau) - \theta_s(\tau) \tag{16}$$

(2) A time dependent effectiveness factor for pyrolysis rate, defined as the ratio of: the local pyrolysis rate averaged over the particle volume, to the pyrolysis rate calculated using the particle surface temperature for the entire particle volume:

$$\eta_r(t) = \frac{\frac{1}{V}\int_V k_o e^{-E/RT(r,t)}\, dV}{k_o e^{-E/RT_s(t)}} \tag{17}$$

or

$$\hat{\eta}_r(\tau) = \frac{3\int_0^1 k_o e^{-\frac{\beta}{\beta\varepsilon+\varepsilon^2\theta}(\xi,\tau)}\, \xi^2 d\xi}{k_o e^{-\beta/(\beta\varepsilon+\varepsilon^2\theta_s(\tau))}} \tag{18}$$

(3) A time-dependent effectiveness factor for overall pyrolytic conversion (i.e. weight loss or total volatiles yield) defined as the ratio of: the volume averaged weight loss, to the weight loss calculated using the particle surface temperature for the entire particle volume:

$$\eta_c(t') = \frac{1 - \frac{1}{V}\int_V \left\{ \exp\left[-\int_0^{t'} k_0 e^{-E/RT(V,t)} dt \right] \right\} dV}{1 - \left\{ \exp\left[-\int_0^{t'} k_0 e^{-E/RT_s(t)} dt \right] \right\}} \qquad (19)$$

or

$$\hat{\eta}_c(\hat{\tau}) = \frac{1 - 3\int_0^1 \left\{ \exp\left[-\int_0^{t'} \phi e^{-\beta/[\varepsilon\beta + \varepsilon^2 \theta(\xi,\tau)} d\tau \right] \right\} d\xi}{1 - \left\{ \exp\left[-\int_0^{t'} \phi e^{-\beta/[\varepsilon\beta + \varepsilon^2 \theta_s(\tau)} d\tau \right] \right\}} \qquad (20)$$

Results and Discussion. The above analysis was used with boundary condition (2) [constant surface heating rate] to predict effects of various pyrolysis parameters on $\eta_T(t)$, $\eta_r(t)$, and $\eta_c(t)$ as a function of pyrolysis time. Unless otherwise stated the following values of thermal physical and chemical properties of the coal were employed: ρ = 1.3 g/cm³, λ = 0.0006 cal/cm-s-C, C_p = 0.4 cal/g-C, ΔH_{py} = 0 cal/g, k_o = 10^{13} s^{-1}, and E = 50 kcal/g-mole. Effects of non-zero heats of pyrolysis are discussed later in the paper.

Figures 1 - 3 respectively show the effects of particle size on $\eta_T(t)$, $\eta_r(t)$, and $\eta_c(t)$, for a surface heating rate and final temperature of 10^4 C/s and 1000 C. For particle sizes > 50 μm, the time to relax internal temperature gradients [i.e. for $\eta_T(t)$ to decline from its maximum value to about zero] increases with roughly the square of particle diameter as expected. Initially the spatial non-idealities in temperature (Fig. 1) increased with increasing pyrolysis time, because the time for the surface to reach the final temperature [$T_{s,f}$/m] is much less than the particle thermal response time, and the intra-particle temperature field is unable to keep pace with the rapidly rising surface temperature. The magnitude and duration of this initial temperature transient increases with particle diameter, because the particle thermal response time increases with particle size.

The rate index of non-isothermality, $\eta_r(t)$ (Figure 2) tracks the non-idealities in particle temperature. For a given particle size and thermally neutral reactions $\eta_r(t)$ indicates spatially non-isothermal kinetic behavior [i.e. $\eta_r(t) < 1$] over a broader range of pyrolysis times than does $\eta_T(t)$ [i.e. for which $\eta_T(t) > 0$, Fig. 1]. The rate index expresses the influence of the temperature non-idealities on the predicted volume averaged pyrolysis rates via an exponential function. Thus an amplification of the magnitude and duration of the temperature non-idealities is not surprising. Furthermore, when volatiles release rates are of interest, $\eta_r(t)$ is clearly a more reliable index of particle non-isothermality than is $\eta_T(t)$.

The conversion index of non-isothermality, $\eta_c(t)$ (Fig. 3), reflects the non-idealities in rate, and the exponential increase in conversion with total pyrolysis time. The latter effect attenuates the former at short and long pyrolysis times by respectively, denying and supplying the reaction adequate time to attain completion at the imposed heating rate. Thus for each particle size there is an intermediate range of reactions times throughout which the strong non-idealities in pyrolysis rate (Fig. 2) contribute major non-idealit-

ies in conversion (Fig. 3). The exponential dependencies of conversion on rate and reaction time, also cause the magnitude of $\eta_x(t)$ to change rapidly with pyrolysis time, resulting in the sharp variations in this index depicted in Fig. 3. Clearly, in light of the differences in Figures 1 through 3, when total volatiles yield is of interest, $\eta_x(t)$ is the preferred index of non-isothermality over either $\eta_T(t)$ or $\eta_r(t)$.

Figure 4 shows that at a fixed particle size, increasing the surface heating rate increases the magnitude but decreases the duration of the initial non-idealities in the particle temperature field. The first effect arises because, with increasing surface heating rate, the surface temperature increases so rapidly during a time equal to the thermal response time of the particle, that the intra-particle temperature field lags further and further behind the surface temperature. The shorter relaxation time arises because the higher initial temperature gradients generated at higher surface heating rates cause a more rapid attenuation of the initial disturbance. With increasing heating rate, these sharp initial intra-particle temperature gradients translate into strong non-idealities in the local pyrolysis rates and hence into significant departures of $\eta_r(t)$ from unity (Fig. 5). With declining heating rates (Fig. 5) the magnitude of these non-idealities is attenuated but they remain significant over increasing ranges of pyrolysis time. These effects respectively arise because decreasing the surface heating rate reduces the differences between the surface and internal temperatures (Fig. 4), and because the resulting intra-particle temperature gradients are lower, and thus provide less driving force for temperature relaxation, thereby extending the time over which the intra-sample pyrolysis rates exhibit significant non-idealities. Increasing particle size at a fixed heating rate exacerbates each of the above effects (Fig. 2).

The impacts of these intra-sample rate variations on the conversion index of non-isothermality $\eta_x(t)$, are attenuated strongly in both magnitude and duration (Fig. 6), due to the interplay of rate and cumulative pyrolysis time discussed above. The magnitude of the non-idealities in $\eta_x(t)$ are worsened with increasing heating rate, because surface temperature and surface pyrolysis rate more and more rapidly outpace the corresponding quantities within the particle, thus expanding the differences between the extents of conversion predicted for these two regions at smaller and smaller reaction times. Conversely, the non-idealities in $\eta_x(t)$ decrease when heating rate decreases, because the particle temperature field (Fig. 4), and average pyrolysis rate (Fig. 5), track the surface temperature more and more closely, and because the greater time required for the surface temperature to attain its final value, allows intra-particle conversion to proceed further to completion.

For a thermally neutral reaction, a change in the activation energy for pyrolysis has no effect on intra-particle temperature gradients [and hence on $\eta_T(t)$], but Figure 7 shows that increasing E increases the magnitude of the non-idealities in $\eta_r(t)$, as would be expected since larger E's imply stronger dependencies of rate on temperature. Since $\eta_T(t)$ is unaffected by changing E, any effect of E on $\eta_x(t)$ will reflect only E-induced changes in $\eta_r(t)$. Such effects should be small since at this heating rate (10^3 C/s) quite large changes in $\eta_r(t)$ at an E of 50 kcal/g-mole (Fig. 5), are strongly attenuated in $\eta_x(t)$ (Fig. 6), and the E-induced variations in $\eta_r(t)$ (Fig. 7) are by comparison, rather small.

Figure 8 shows that for constant ρ and C_p, decreasing either the thermal conductivity or thermal diffusivity of the coal increases the magnitude and duration of non-idealities in $\eta_T(t)$ and $\eta_\xi(t)$. For an endothermic reaction the values of $\eta_T(t)$ and $\eta_T(t)$ at long pyrolysis times would increase with increasing values of either of these thermal parameters. For example, for $\Delta H_{py} \simeq +50$ cal/g coal, these two indices would increase by a factor of 10, for 10 to 15% increases in α or λ (Hajaligol et al. 1987).

Figure 9 shows the effects of pyrolysis time on $\eta_T(t)$, $\eta_T(t)$, and n(t) for cases where pyrolysis is not thermal neutral. The discussion is simplified by expressing the results in terms of a dimensionless parameter δ, which reflects the interaction of chemical kinetic and thermal physical parameters in determining the impact of chemical enthalpy on particle non-isothermality. Delta is derived by non-dimensionalizing Eq. (1), see Eq. (2), and physically can be thought of as the ratio of the average rate of heat generation (or depletion) at the particle surface from pyrolysis, to the average rate of conductive transfer of heat into the particle from its surface. Figure 9 shows that for reasonable exo- or endo-thermicities, $\eta_T(t)$ and $\eta_T(t)$ do not approach perfect ideality, even at long pyrolysis times, while $\eta_\xi(t)$ goes virtually to unity (isothermal behavior) in reasonable times. The magnitude and duration of the non-idealities expressed by $\eta_\xi(t)$ depend on the ratio of the pyrolysis time to the particle heat-up time (Hajaligol et al. 1987). At long pyrolysis times $\eta_T(t)$ and $\eta_T(t)$ attain δ-specific plateaus that are independent of heating rate or particle size, although both parameters affect the magnitude and duration of the transients in these two indices.

Figure 10 shows, for thermally neutral pyrolysis, domains of particle size and surface heating rate where the particle is at least 95% "isothermal" according to each of the above indices [$\eta_T(t)$, $\eta_T(t)$, and $\eta_\xi(t)$]. The temperature index provides a broader range of compliant particle sizes and heating rates, because it is uninfluenced by devolatilization kinetics. For a non-thermally-neutral reaction it is much more difficult to define domains of particle size and heating rate where $\eta_T(t)$ meets the 95% ideality criterion - note the very small δ values required for $\eta_T(t)$ to approach 0 in Fig. 9.

The rate index [$\eta_T(t)$] obviously enfolds kinetic effects, and consequently presents a more narrow domain of isothermality (Fig. 10). Clearly this index, rather than $\eta_T(t)$ alone, should be considered in evaluating the role of heat transfer effects in devolatization kinetic data and in designing experiments to probe intrinsic chemical rates. The conversion index, $\eta_\xi(t)$, provides a somewhat broader isothermality domain, due to the damping effect of pyrolysis time discussed above.

Effects of activation energy and thermal physical properties on the isothermality domains can be inferred from Fig.'s 7 and 8 respectively. Increasing or decreasing E as in Fig. 7, has no effect on the regions prescribed by $\eta_T(t)$ and $\eta_\xi(t)$, but respectively decreases and increases the domains defined by $\eta_T(t)$ (dashed lines of Fig. 10).

When pyrolysis is not thermally neutral, the domains of particle isothermality may, depending on the magnitude of ΔH_{py}, shrink from the boundaries defined in Fig. 10. Regimes of D_p and $\dot{m}$ meeting each of the above criteria can still be prescribed by calculating compliant families of curves in Fig. 10, using ΔH_{py} as a parameter. Alternatively, the parameter δ can be used to

advantage in a more efficient computation procedure that accounts explicitly for all parameters contributing to heat of pyrolysis effects. The rate index, $\eta_r(t)$ shows the greatest effect of ΔH_{py} (Fig. 9). Figure 11 shows how $\eta_r(t)$ varies with $|\delta|$, where the upper and lower branches [$\eta_r(t) > 1$, and < 1], reflect exo- and endo-thermic pyrolysis, respectively. This figure is used to obtain values of δ such that $\eta_r(t)$ indicates a desired extent of isothermality, say 95%. With δ fixed, and fixed thermal-physical properties, the particle diameter, D_p, final surface temperature T_s, and surface heating rate, m, become the only adjustable parameters of the system. For preselected particle diameters, Fig. 10 is then used to define the allowed maximum surface heating rates for any of the isothermality indices, and the value from Fig. 11 sets the corresponding maximum allowed surface temperature. Alternatively a desired surface heating rate can be pre-selected with the corresponding maximum allowed particle diameter and surface temperature being obtained from Figs. 10 and 11 (via δ) respectively, or a maximum surface temperature can be pre-chosen with the compliant δ value (Fig 11) prescribing the maximum allowed D_p, and Fig. 10 the corresponding maximum acceptable surface heating rate. This protocol is conservative in that it is valid for all pyrolysis times, and utilizes the most stringent of the above isothermality indices, $\eta_r(t)$.

Conclusions

1. The extent of coal particle non-isothermality at any stage of pyrolysis can be quantitatively depicted in terms of numerical indices reflecting not only spatial non-uniformities of the intra-particle temperature field, but also non-idealities in the rate and extent of pyrolysis.

2. Mathematical modeling of coupled rates of intra-particle pyrolysis and heat transmission, relates each index to operating conditions of interest in coal combustion and gasification including surface heating rate, particle diameter, final temperature, and pyrolysis time.

3. Domains of surface heating rate and particle diameter where each isothermality criterion is met to within 5% at all pyrolysis times are plotted for a base case of zero heat of pyrolysis.

4. Data and procedures for using these same isothermality maps when pyrolysis is not thermal neutral are also provided.

5. The analysis shows that diagnosing a pyrolyzing coal particle as "isothermal" based upon close agreement between its surface and centerline temperature, can lead to serious errors in estimates of corresponding volatiles release rates and total volatiles yields.

6. Each isothermality index exhibits significant temporal variations, showing that pyrolysis time, and hence extent of conversion must be considered in assessing particle non-isothermality and its impact on pyrolysis behavior.

Nomenclature

d_p	Particle Diameter, Cm
E	Activation Energy, Cal/g-mole
h_{eff}	Effective Heat Transfer Coefficient, Cal/(Cm²-Sec-C)
k_o	Reaction Frequency Factor, sec^{-1}
$\dot{m}$	Surface Heating Rate, °K/sec
N_{Bi}	Biot Number; $h_{eff}\, d_p / 2\lambda$
$\dot{q}$	Surface Heat Flux Density, Cal/sec
R	Gas Constant; 1.987 Cal/gmole°K
r	Radius, Cm
R_o	Partice Radius, Cm
T	Temperature, °K
T_o	Initial Temperature, °K
T_s	Surface Temperature, °K
$T_{s,f}$	Final Surface Temperature, °K
T_∞	Ambient Temperature, °K
t	Time, Sec
V	Particle Volume, Cm^3
ρ	Particle Density, g/cm^3
λ	Particle Thermal Conductivity, Cal/(Cm-Sec-C)
α	Particle Thermal Diffusivity, Cm^2/Sec
ΔH_{py}	Heat of Pyrolysis, Cal/g
θ	Dimensionless Temperature; $\frac{T - T_{s,f}}{T_o - T_{s,f}}$
θ_s	Dimensionless Surface Temperature; $\frac{T_{s(t)} - T_{s,f}}{T_o - T_{s,f}}$
θ_{CL}	Dimensionless Center Temperature; $\frac{T_{CL(t)} - T_{s,f}}{T_o - T_{s,f}}$
θ_∞	Dimensionless Ambient Temperature; $\frac{T_\infty - T_{s,f}}{T_o - T_{s,f}}$
τ	Dimensionless Time; $\alpha t / R_o^2$
ξ	Dimensionless Length; r/R_o

$\eta_T, \hat{\eta}_T$ Dimensionless Temperature Index

$\eta_r, \hat{\eta}_r$ Dimensionless Rate Index

$\eta_c, \hat{\eta}_c$ Dimensionless Conversion Index

ε Dimensionless Parameter; $R T_{s,f} / E$

β Dimensionless Parameter; $R T_{s,f}^2 / E (T_o - T_{s,f})$

δ Dimensionless Parameter; $(-\Delta H_{py}) \rho d_p^2 k_o e^{-E/R T_{s,f}} / [4 \lambda (T_o - T_{s,f})]$

γ Dimensionless Heating Rate; $\dot{m} d_p^2 / [4 \alpha (T_o - T_{s,f})]$

Φ Dimensionless Heat Flux Density; $\dot{q}_s / [2\pi \lambda d_p (T_o - T_{s,f})]$

Acknowledgements

Prime U.S.D.O.E. support for this work was provided via Contract No. DE-AC22-84PC70768, from the AR & TD Combustion Program of the Pittsburgh Energy Technology Center. Additional U.S.D.O.E. support was provided under Contract No. DE-AC21-85MC222049, from the Advanced Gasification Program of the Morgantown Energy Technology Center.

References

1. Froment, G. F., and K. B. Bischoff, Chemical Reactor Analysis & Design, John Wiley and Sons, 1979.

2. Howard, J. B., Fundamentals of Coal Pyrolysis and Hydropyrolysis, in Chemistry of Coal Utilization, 2nd Suppl. Vol., Wiley NY 1981.

3. Gavalas, G. R., Coal Pyrolysis, Elsevier Scientific Pub., 1982.

4. Boddington, T., P. Gray, and S. K. Scott, J. Chem. Soc., Faraday Trans. 2, 78, 1721-1730, 1982.

5. Scott, S. K., T. Boddington, and P. Gray, Chem. Eng. Science, Vol. 39, No. 6, 1079-1085, 1984.

6. Simmons, G.M., Am. Chem. Soc., Div. of Fuel Chem. Preprints, April 1984.

7. Essenhigh, R.H., Dept. of Mechanical Eng., Ohio State University, Work in Progress, 1987.

8. Seery, D. J., J. D. Freihaut, and W. M. Proscia, Technical Progress Reports for DOE, 1985-1986, United Technologies Research Center, E. Hartford, CT.

9. Hajaligol, M. R., J. B. Howard, and W. A. Peters, Predicting Temporal and Spatial Non-Isothermalities within Reacting Condensed Phase Media, To be Submitted to the AIChE journal, 1987.

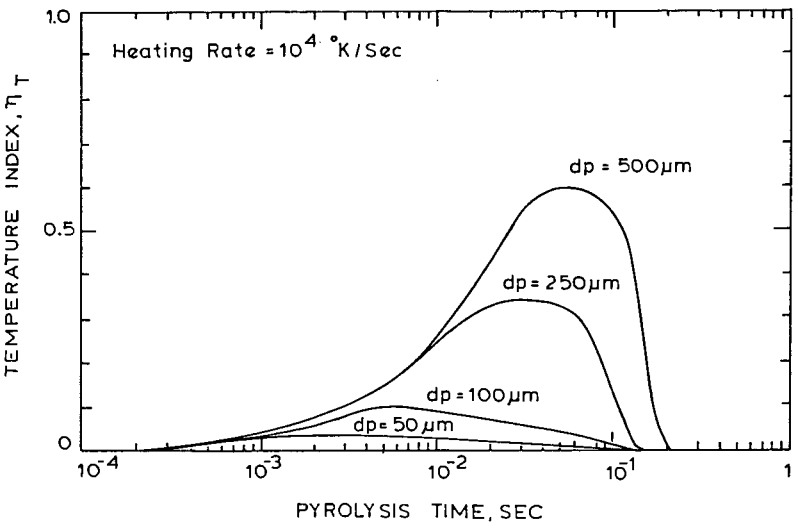

Figure 1. Effects of Particle Diameter on the Temperature Index at 10^4 K/sec Heating Rate.

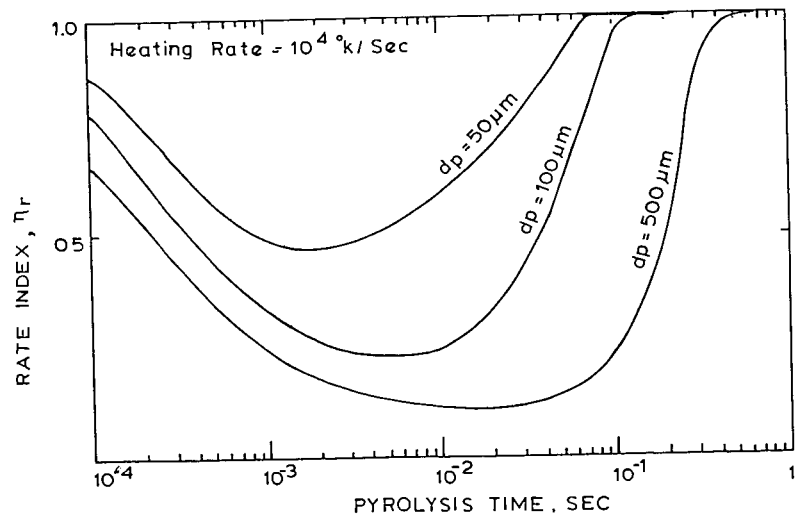

Figure 2. Effects of Particle Diameter on the Rate Index at 10^4 K/sec Heating Rate.

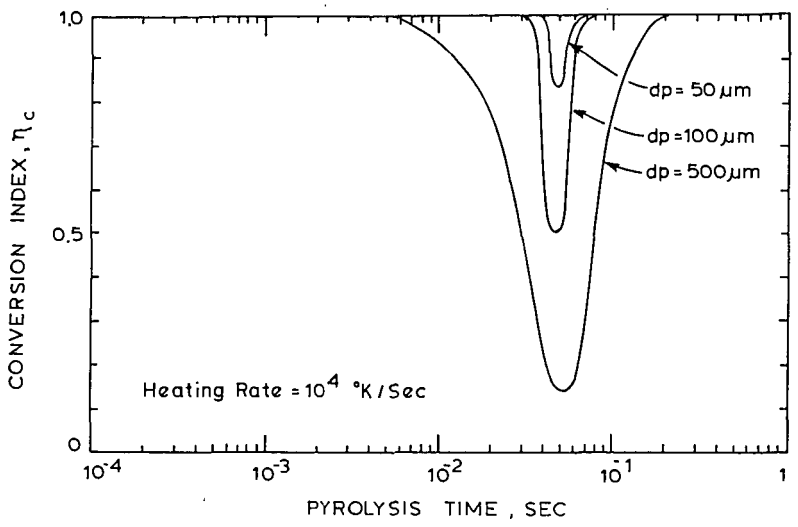

Figure 3. Effects of Particle Diameter on the Conversion Index at 10^4 K/sec Heating Rate.

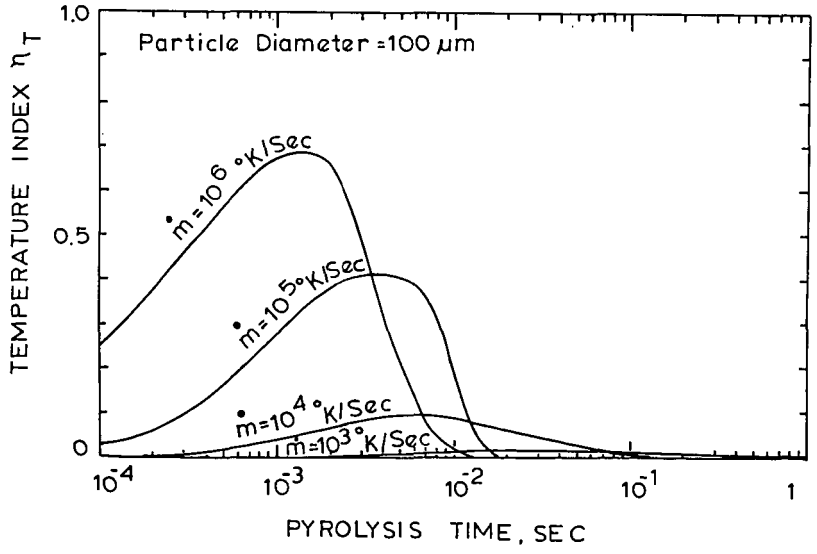

Figure 4. Effects of Heating Rate on the Temperature Index for 100 mm Particle Diameter.

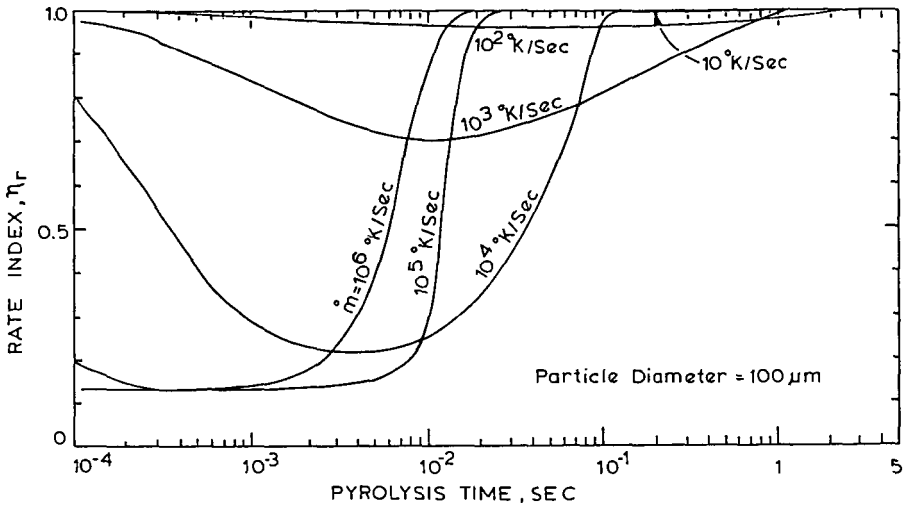

Figure 5. Effects of Heating Rate on the Rate Index for 100 mm Particle Diameter.

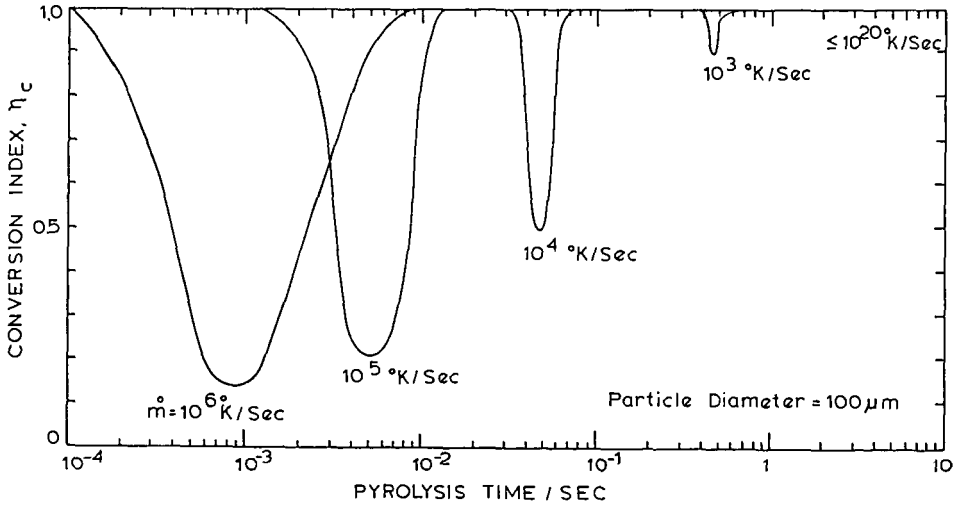

Figure 6. Effects of Heating Rate on the Conversion Index for 100 mm Particle Diameter.

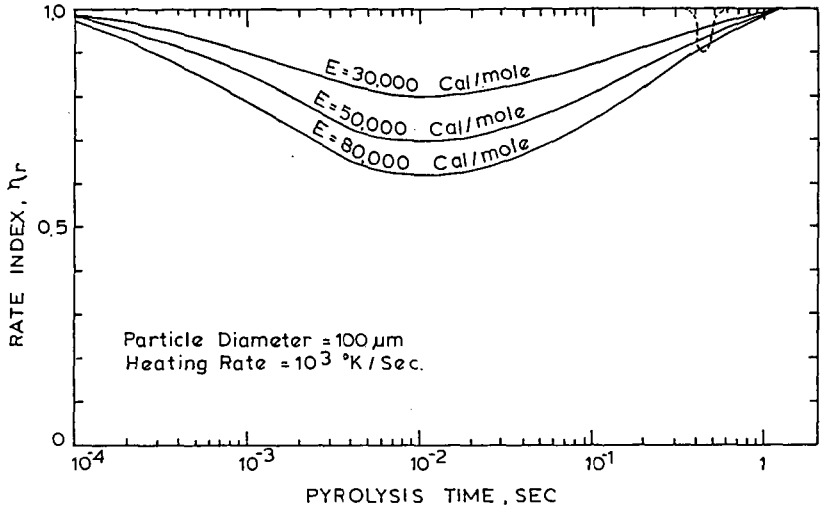

Figure 7. Effects of Activation Energy on the Rate and Conversion Indices.

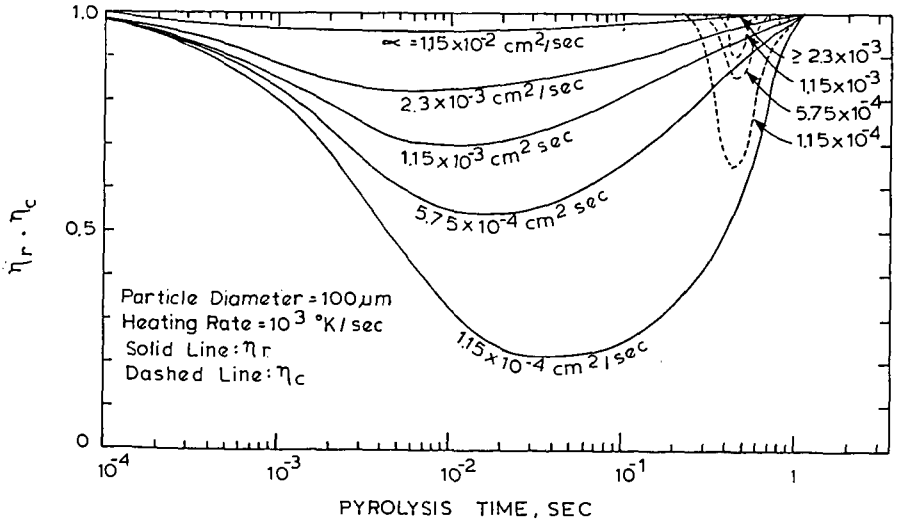

Figure 8. Effects of Thermal Diffusivity on Rate and Conversion Indices.

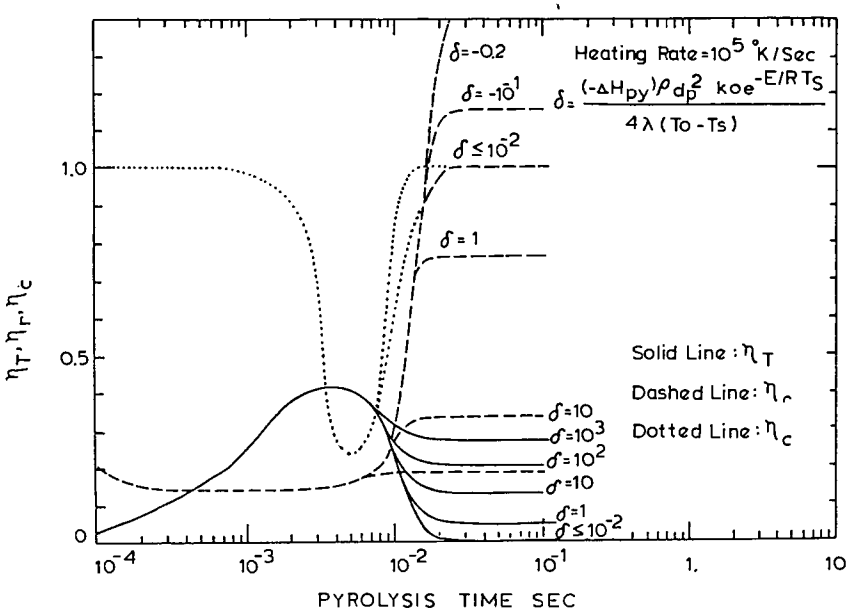

Figure 9. Effects of Heat of Pyrolysis on Indices.

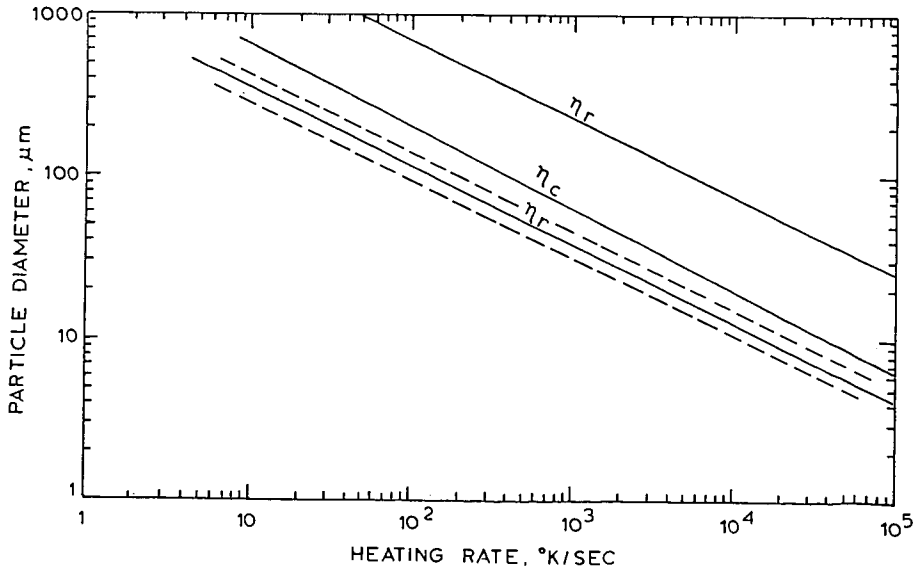

Figure 10. Isothermal Regions Defined by Different Indices.

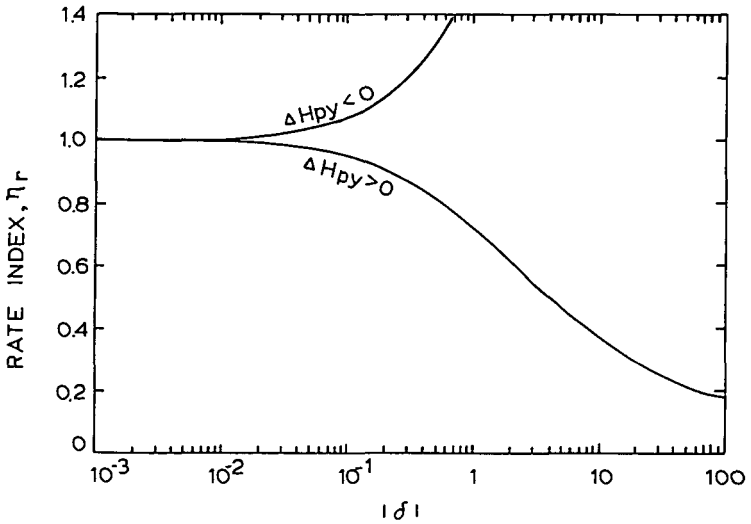

Figure 11. Effects of Heat of Pyrolysis on the Spatial Value of Rate Index.

THERMOKINETIC TRANSPORT CONTROL AND STRUCTURAL MICROSCOPIC REALITIES IN COAL AND POLYMER PYROLYSIS AND DEVOLATILIZATION: THEIR DOMINANT ROLE IN DUST EXPLOSIONS

By M. Hertzberg, I. A. Zlochower, R. S. Conti, and K. L. Cashdollar

U. S. Bureau of Mines
Pittsburgh Research Center
P.O. Box 18070
Cochrans Mill Road
Pittsburgh, PA 15236

ABSTRACT

The reaction mechanism for coal pyrolysis and devolatilization involves the inward progression from the exposed surface of a decomposition wave, whose speed of propagation determines the pyrolysis rate. The speed is controlled by the heat flux driving the wave and by thermodynamic transport constraints within the particle. Microscopic data are presented that reveal the structure of that wave front for unidirectional laser exposure of both macroscopic coal samples and microscopic dust particles. At burner-level heat fluxes of 100 to 125 W/cm^2, the wave front thickness is less than 50 μm.

New data are also presented for polymethylmethacrylate (PMMA) at flux levels of 12-115 W/cm^2 that give a pyrolysis and devolatilization "rate coefficient" of,

$$k_t = \{\int_{T_o}^{T_s} C(T)dT + \Delta H_v\}^{-1} ,$$

whose value is predictable from thermodynamic transport constraints alone. Except for the complication of the coal's char-layer residue and its increasing thickness, which insulates the wave front from the heat source flux that drives it, both coal and PMMA behave similarly. For PMMA, the decomposition temperature, T_s, is 350-400° C; for coal it is 450-600° C.

There is no substantive evidence to support the traditional viewpoint that the reaction processes occur isothermally under chemical rate control and that they are describable by unimolecular, Arrhenius functions of the source temperature.

The volatility yield of a dust and its rate of devolatilization play dominant roles in the overall mechanism of flame propagation in dust-air mixtures. Data for the particle size dependences of the lean limits of flammability for coals and polymers reveal those roles. The above measured rate coefficient for PMMA gives a reasonable prediction of the coarse size at which the particle devolatilization process becomes rate limiting in a PMMA dust explosion.

INTRODUCTION

Two theories or models have been used to describe the process of coal particle pyrolysis and devolatilization. The first is the traditional viewpoint, which considers the reaction process to be under chemical rate control (1, 2, 3); the second is a newer viewpoint that considers the reaction process to be under heat transport control (4, 5, 6, 7). In the traditional model the reaction or reactions are viewed as occurring isothermally throughout the particle and are described by classical, unimolecular, Arrhenius functions of the particle temperature, T. The reaction rate is given by

$$\frac{d\,V(t)}{dt} = k_o\,[e^{-E_a/RT}]\,[V(\infty) - V(t)], \qquad 1)$$

where V(t) is the volatile yield (in pct) after an exposure time, t; $V(\infty)$ is the maximum volatile yield as $t \to \infty$; k_o is the preexponential factor; E_a is the activation energy; R is the universal gas constant; and T is the temperature of the pyrolyzing particle. Considerable effort has gone into the development of complex, parallel or sequential reaction schemes to predict the overall rate of pyrolysis and the yields of volatile products. Surprisingly, however, little effort has been devoted to a realistic analysis of the heat transport processes by which particle temperatures, initially at T_o, are elevated to the reaction temperature T after

their exposure to some high temperature source at T_h. Early researchers generally assumed that the exposed coal particles rapidly reached the high temperatures of the furnace walls, or the hot gases, or the electrically-heated screens to which they were exposed. The temperature used in Equation 1 was generally the source temperature, T_h. A major exception was Zielinski (7), whose independent analysis of the data of many investigators led to the conclusion that the rate of the heat transfer from the high-temperature source to the coal particles exerted the dominant influence on the rate of volatiles evolution. He noted that coal particle temperature measurements were "very rare indeed," and cautioned researchers against assigning "the temperature of the heat carrier or the container walls" to the temperature of "the coal particles themselves." Zielinski's analysis was generally ignored until the more recent studies of Freihaut and Vastola (8), and the reanalysis of particle pyrolysis data by Solomon and coworkers (9, 10). Using direct optical measurements of particle temperatures, Solomon et al. (10) showed clearly that, during pyrolysis, T was generally much lower than T_h. For example, in an entrained flow reaction at a source temperature of T_h = 1300° C, coal particles of 45-75 μm diameter were completely devolatilized by the time they had reached temperatures of only 700-800° C. Their analysis is nevertheless limited to the problem of heat transfer to the particle; the particle itself is still treated as reacting isothermally, and uniformly throughout its extent. Internal variations in temperature and reaction rate are ignored. Since, however, the particle is not isothermal, one must go even further in the reanalysis. For coal, especially, there is inevitably a hotter, opaque char layer at the surface of the particle that surrounds and conceals the lower temperature region of active pyrolysis further within the particle.

Accordingly, not only must one consider heat transport limitations to the particle from the external heat source, but also heat transport limitations within or through the particle; that is, from its surface to its interior. Attempts to address that limitation lead to the newer viewpoint or model. The situation in its simplest form is depicted in Figure 1, and the newer theory simply applies the First Law of Thermodynamics to the system. A planar coal surface is depicted, pyrolyzing and devolatilizing at a steady-state rate, $\dot{x}_o$, in an incident radiative source flux of intensity, I. The system depicted is coal, which is complicated by a char residue above the pyrolysis reaction zone. Initially, it will be simpler to assume that the reactant is one that devolatilizes completely so that the incident flux is absorbed directly at the devolatilizing surface. Polymethylmethacrylate (PMMA) is an example of such a substance. A fraction of the incident flux, rI, is reflected, and another portion, I_ℓ, is lost to the colder surroundings by conduction, convection, and reradiation. For the steady-state propagation of the pyrolysis wave, at the liner rate, $\dot{x}_o$, the First Law requires that the net absorbed flux, $I_{abs} = I(1-r)-I_\ell$, first supply the power necessary to bring each element of the solid reactant with its heat capacity C(T) to the reaction zone or decomposition temperature, T_s, from its initial temperature, T_o; and second, supply the heat of devolatilization. Thus,

$$I_{abs} = I(1 - r) - I_\ell = \dot{x}_o \rho [\int_{T_o}^{T_s} C(T)dT + \Delta H_v]. \qquad 2)$$

Solving for the mass devolatilization rate per unit area gives

$$\dot{m} = \dot{x}_o \rho = k_t I_{abs} = [\int_{T_o}^{T_s} C(T)\, dT + \Delta H_v]^{-1} I_{abs}, \qquad 3)$$

where the rate coefficient, k_t, is given by the reciprocal of the net enthalpy change for the overall heating and devolatilization process.

This newer viewpoint should be contrasted with the traditional one. In this flux-driven, heat-transport-limited model (Equations 2 and 3), once the input flux level exceeds some critical value for the onset of reaction, which is the loss flux, the predicted rate is not particularly sensitive to the reaction zone temperature of the pyrolyzing surface. That temperature, T_s, is only the upper bound of a heat capacity integral. The rate coefficient, k_t, is much more sensitive to the heat of devolatilization or vaporization, ΔH_v. By contrast, in the traditional viewpoint (Equation 1), the reaction temperature T is the only variable determining the rate. In the flux-driven model, the system is nonisothermal and the exact temperature of

the reacting surface becomes virtually irrelevant once it reaches some threshold value. The traditional viewpoint, by contrast, focuses on that one intensive thermodynamic variable, T, and it does so only in one region of the system, the reaction zone. The newer viewpoint emphasizes extensive thermodynamic variables: The absorbing flux, I_{abs}, and the overall enthalpy change for the pyrolysis and devolatilization process, quite independent of the temperature of any one region of the nonisothermal system. In the newer model, the driving force for the reaction is the net energy flux density being absorbed by the reactant. The "barrier" to reaction is not some obscure activation energy, E_a, which must be overcome by raising the temperature of one particular region to a high enough level; rather it is the "resistance" or thermal inertia of the entire system that must be overcome. The thermal inertia is $\int_{T_o}^{T_s} C(T)\, dT + \Delta H_v$, and the reciprocal of that resistance is the "conductivity" of the reaction wave, which is its rate coefficient, k_t.

PYROLYSIS RATES AND STRUCTURAL MICROSCOPIC REALITIES FOR COAL

Kinetic data for the devolatilization rates of microscopic coal particles of varying diameter, heated in a CO_2 laser beam were reported previously (4, 5). The data at a constant input laser flux of 300 W/cm^2 for particles of 51-, 105-, and 310-μm average diameter are shown in Figure 2. The data show clearly that the time required for complete devolatilization increases monotonically with increasing particle diameter, as would be predicted by the flux-driven model of Figure 1. The effect of varying the incident laser flux for a given particle size was also studied.

For a more careful analysis of the data, it should be noted that the percentage mass loss versus time curves in Figure 2 have characteristic s-shapes. Since final volatility yields, $V(\infty)$, are approached only asymptotically as $t \to \infty$, it is most realistic to express the rate of the devolatilization reaction in terms of the time required for the particle to devolatilize to half its maximum value. That half life or $t_{1/2}$-value corresponds to the inflection point of the s-shaped curve. All the data are summarized in Figure 3, where the measured $t_{1/2}$ data points are plotted as a function of the incident laser flux for the three particle sizes studied. For the cubic particle with sides of width a_o, as depicted in Figure 1,

$$t_{1/2} = \frac{a_o}{2\dot{x}_o} = \frac{a_o\, \rho}{2k_t I_{abs}} = \frac{k' D_p}{(I - I_\ell')} \quad , \qquad 4)$$

where I_ℓ' is an effective loss flux and k' is a constant of proportionality which is linearly proportional to the thermal inertia of the devolatilization reaction, but which is also related to the shape of the particle and its orientation in the beam. The average particle diameter is D_p. The predictions of Equation 4 are also shown in Figure 3 as the dashed lines. The effective loss fluxes, I_ℓ', were taken as 50 W/cm^2 for the 51-μm particles, 25 W/cm^2 for the 105-μm particles, and 10 W/cm^2 for the 310-μm particles. These losses are mainly associated with conduction-convection to the cold surroundings, and their choice is discussed in detail elsewhere (5, 6). A constant k'-value of 1.46 kJ/cm^3 for all sizes gives the best fit to the data. The reasonable agreement between the data points and the theory curves predicted by Equation 4 tends to confirm the reasonableness of its derivation. It suggests that even on the microscopic level of particles as small as 50 μm, the pyrolysis process proceeds at a rate determined by the heat-transport-limited speed with which the devolatilization wave is driven through the particle by the heat source flux. The pyrolysis "rate constant" is determined by the thermodynamic properties of the medium, and no further assumption regarding a reaction kinetic mechanism appears to be necessary.

In terms of the actual thermal structure of the pyrolysis wave front, the data containing the most detailed spatial resolution were reported by Lee, Singer, and Chaiken (11) for large coal cylinders 1.8 cm in diameter and 5 cm high. Temperatures were measured every 3 mm. Their temperature profiles, obtained with the same laser but at much lower fire-level heat fluxes, are summarized in Figure 4.

They also obtained x-ray density profiles which showed that the reaction zone of active pyrolysis and devolatilization is characterized by a minimum density of 0.2 g/cm^3. These minimum density points are shown in Figure 4 superimposed on their measured temperature profiles. That reaction zone of minimum density is bounded on the cold side by unreacted coal (ρ = 1.33 g/cm^3) and on the hot side by a consolidated char residue (ρ = 0.85 g/cm^3). The reaction zone temperature corresponding to these minimum density points is 440-475° C.

The minimum density zone may be viewed as a "fizz zone" of active devolatilization composed of "frothing" liquid bitumen. The liquid bitumen consists of high-molecular-weight pyrolysis products, and it is frothing because lower molecular weight gases and tar vapors are bubbling through it. The bubbling "fizz zone" is also physically transporting the frothing mass of charifying liquid bitumen into the mass of previously formed char above it. The consolidated char of higher density is thus a compacted residue of the frothing mass of charifying liquid. Some secondary char-forming reactions are also occurring in the char layer above the fizz zone, as pyrolysis vapors diffuse through that cap of higher temperature char.

The data of Lee, Singer, and Chaiken also show clearly that the pyrolysis wave front propagates inward at a velocity that is proportional to the radiant flux; however, as the insulating char layer at the surface thickens in time, the surface temperature increases and flux losses to the cold surroundings increase markedly. It is not surprising, therefore, that the velocity of their pyrolysis wave front diminishes in time. Note also that the reaction zone temperature, however, remains essentially constant at 440-475° C, quite independent of the magnitude of the source flux that drives it, or the resultant velocity of the pyrolysis wave front. At their highest laser flux, the maximum temperature of the char layer at the surface was 760-800C. Because of the char layer expansion and swelling, the final surface is at a negative displacement relative to the original surface position at 0.0 cm.

That surface temperature may be considered to be the "source temperature" in such experiments since it is the char layer at the surface that directly absorbs the laser flux as time proceeds. Heat is then conducted through that char layer to the reaction zone below. Thus, although the source temperature is as high as 760-800° C for the higher flux data, the real temperature of the coal mass that is pyrolyzing and devolatilizing is only 440-475° C, and it would be incorrect to assign that char layer temperature to the reacting coal. It should also be noted that if the temperature of the coal sample or "particle" were measured optically from the surface spectral radiance, one would, of course, obtain only the surface temperature of the char residue and not the temperature of the reacting coal.

Structural data will now be presented that reveal the morphological changes in the coal structure that result from the propagation of such a pyrolysis wave front. The microscopic data will be presented for fine coal particles such as those used to obtain the data in Figures 2 and 3, and also for large coal samples comparable in size to those for which the data in Figure 4 were obtained. Scanning electron microscope (SEM) photographs of a coal particle exposed for 100 ms to a laser flux of 100 W/cm^2 are shown in Figure 5. The same particle is shown at two magnifications. The measured weight loss was only about 1 pct, and it can thus be inferred that the exposure time barely exceeded the induction time required for the surface of the particle to reach the decomposition temperature. There is, nevertheless, clear evidence that liquid bitumen was formed near the surface of the particle. That bitumen was oozing out from between the bedding planes while the particle was being heated, but after the beam was turned off, the surface cooled and the bitumen resolidified in the form of ridges. Those ridges are clearly seen to be oriented parallel to the bedding planes. A few blow holes are visible in those ridges of resolidified bitumen, but there are many more unbroken bubbles containing volatiles that were probably never emitted from the heated surface. Most of those volatiles have recondensed as liquid tars that are probably still contained within the bubble enclosures. Clearly, although devolatilization may have occurred within those bubbles, the process was not yet registered as a weight loss since the volatiles never broke through the bubble walls. The SEM photographs in Figure 5 suggest that the extent of thermal pyrolysis in a particle may be more extensive

than that obtained from the devolatilization weight loss. In order to be more precise, one should therefore distinguish between those two sequential processes. Pyrolysis or decomposition occurs first, and volatile emission occurs later. The photographs clearly illustrate the nature of the mass transport limitation involved in the transition between the generation of volatiles by thermochemical pyrolysis and their subsequent emission by bubble transport and rupture. It is only after the latter process is complete that a finite weight loss is registered.

The SEM photograph shown in Figure 6 is a later stage in the same process. It is a particle exposed for a time of 400 ms at a laser flux of about 125 W/cm^2. Based on its mass loss, the particle is somewhat more than half devolatilized, and it has clearly not reacted uniformly throughout its extent. Only the upper half of the particle (seen in Figure 6 as its right side) has devolatilized. The lower half of the particle (on the left) is essentially unreacted. It is the original coal structure. The laser beam was incident on the upper surface of the particle, and only the upper portion was devolatilized during the exposure time. It devolatilized into a dome or bubble, and after the volatiles contained within that dome were vented through blowholes, the whole structure seems to have started to collapse under its own weight. But, as it was collapsing, the higher molecular weight pyrolysis products that comprise the dome wall were simultaneously solidifying into a char. When they did solidify, a wrinkled skin residue was left.

The devolatilization wave thus appears to have traversed more than half way through the particle by the time the laser beam was turned off. The particle then cooled, and the devolatilization process was quenched with the pyrolysis wave "frozen" in place. Clearly the thickness of the wave front is substantially smaller than the particle diameter, and one can infer a wave front thickness of no more than 50 μm from the SEM photograph. Similar examples of such partially devolatilized particles are shown in Figure 7. Those particles are somewhat smaller in diameter and were exposed to a laser flux of about 100 W/cm^2 for about 1 s. Based on their average weight loss, the particles were about two-thirds devolatilized. In all four instances, the particles are viewed from the top, which was the surface on which the laser beam was incident. Blowholes and char residues are seen on the top portions of the particles. Unreacted coal residues with their cleaved edges and ledges are clearly visible at the bottoms of the particles. Again, the pyrolysis waves are frozen in place after having transversed only part of the way into the particles.

Experiments were also conducted with macroscopic coal samples of Pittsburgh seam bituminous coal, and those results are shown in Figure 8. The dimensions of the sample studied in Figure 8 and its orientation during laser exposure are sketched at the top of the figure. The face to be inspected by the SEM was deliberately cleaved some 20-30° beyond the vertical so that it would be "in the shadow" of the upper, irradiated surface. Exposure of the samples to a laser flux of 100-125 W/cm^2 for 2 s resulted in coking of the surface and its upward expansion as the char layer built up in thickness. Only the edge of the pyrolysis wave front moves down the cleaved face during that exposure time, and it is the edge that is viewed by the SEM, as illustrated in the sketch. The SEM photographs of the transition zone between the coal below and the char above are shown at three magnifications, with the largest magnification on the right. The transition region appears to be quite sharp. Despite the complications associated with the viewing angle, the swelling and frothing of the char layer, and the waviness of the pyrolysis front, one can estimate a reaction zone thickness for the quenched pyrolysis wave that is no larger than about 50 μm.

One must also realize that there is some thermal inertia in such a wave front so that its progression does not stop instantaneously after the laser source is turned off, especially if the wave front is being driven by the temperature gradient and thermal inertia of a char layer above it. The wave will inevitably progress to some extent during the decay time, and thermal diffusion during that same period may also thicken the wave front. The quenched "dead" wave seen in Figure 8 may therefore be somewhat broader than an active "live" wave. Such thermal inertia effects are even more significant for particles that are heated omnidirectionally in a furnace or a flow reactor than for the unidirectionally-heated particles described here.

A macroscopic sample of a Wyoming coal with a low-free swelling index (Hannah seam) was also studied by the same technique, and those results are reproduced in Figure 9. There was substantial cracking of the sample caused by the mechanical stresses induced by the high temperature gradient laser exposure (100-125 W/cm^2 for 2 seconds). Those fractures provide a revealing, three-dimensional view of the structure of the transition zone between the char above and the coal below. The position of the pyrolysis wave front is indicated in Figures 9A-F by the arrows at the edges of the SEM photographs. A detailed analysis of the structure is given elsewhere (6), but again the data give an intrinsic width of the wave front that is less than 50 μm.

These SEM photographs in Figures 5, 6, 7, 8, and 9 clearly reveal the existence of the pyrolysis wave front and its structural reality on the microscopic scale. They strongly support the newer viewpoint that the process occurs in the form of the inward progression of a pyrolysis wave front from the exposed surface. Even for small particles, these microscopic realities directly contradict the traditional viewpoint that the reaction process occurs isothermally throughout the particle.

PYROLYSIS AND DEVOLATILIZATION OF PMMA

Long cylinders of polymethylmethacrylate (PMMA) with diameters of 0.45 cm were oriented on end, and exposed to the same CO_2 laser beam. The pyrolyzing upper surface of the rod maintained its circular cross section as the surface regressed downward along the axis of the cylinder. The weight or mass loss per unit area, Δm, was measured as a function of exposure time in a given laser flux. The data are summarized in Figure 10. The good linearity of the Δm versus time curves indicate that steady-state conditions were obtained. Lines are drawn in Figure 10 for the least squares fits to the data points at each flux level. The lines are well represented by the equation

$$\Delta m = \dot{m} (t - \tau). \qquad 5)$$

The slope of each line thus represents the steady-state devolatilization rate, $\dot{m}$, at each flux, and the horizontal intercept is the induction time, τ, at that flux. Clearly, the induction time is simply the time required for the surface of the sample to be heated to the devolatilization temperature. The steady-state rates are plotted in Figure 11 as a function of the net incident flux $I(1 - r) = 0.93\ I$, where the reflectance, r, is taken as 7 pct. A least squares fit to the five sets of data points in Figure 11 gives

$$\dot{m}\ (mg/cm^2 s) = 0.72\ (mg/J)\ [0.93\ I - 9.8]\ (W/cm^2). \qquad 6)$$

The inferred steady-state loss flux is therefore $I_\ell = 9.8$ W/cm^2, and the rate coefficient for the pyrolysis and devolatilization of PMMA is therefore k_t (PMMA) = 0.72 mg/J = 3.01 g/kcal. Its reciprocal, $1/k_t = 332$ cal/g, is the thermal inertia of the pyrolysis wave. According to Equation 3, the thermal inertia is given by $\int_{T_o}^{T_s} C(T)dT + \Delta H_v$. Taking the decomposition temperature for PMMA as 400 °C (12), the heat capacity data reported by Bares and Wunderlich (13) give $\int_{25}^{400} C(T)\ dT = 196$ cal/g. The calorimetrically measured value for the heat of depolymerization of PMMA (corrected to 400° C) is 126 cal/g (14). The sum, 322 cal/g, is therefore the calculated thermal inertia of the system. The thermodynamically predicted rate constant obtained from Equation 3 for the pyrolysis and devolatilization of PMMA is thus in excellent agreement with the measured value obtained from Figure 11. Furthermore, the measured slope from Figure 11 for data obtained at radiant fluxes of 12-115 W/cm^2 is in quite good agreement with the slopes measured independently by Vovelle, Akrich, and Delfau (15) and by Kashiwagi and Ohlemiller (12). Their data were obtained at radiant fluxes in a much lower range of 1.4-4.0 W/cm^2. A detailed analysis of both their data is presented elsewhere (6). Their data were for vertically oriented slabs of PMMA with much larger cross-sectional areas of 10 x 10 cm^2 and 4 x 4 cm^2, respectively. Accordingly, their loss fluxes were only about 1.0 and 1.5 W/cm^2, respectively, but their plotted slopes were essentially the same as those in Figure 11.

The coal data presented earlier can also be used to obtain estimates for the coal's k_t-value. The macroscopic $\dot{m}$ versus I curves reported by Lee, Singer, and Chaiken (11) have also been analyzed in detail elsewhere (6), and their measured slope gives k_t = 0.75 g/kcal for coal. The microscopic particle data shown in Figure 3 can also be used to infer a rate coefficient for coal of $k_t = \rho/2k' =$ 1.91 g/kcal, which is a factor of 2-3 higher. Clearly those data for coal are substantially less accurate than the PMMA data. A difference of a factor of 2 or 3 for independently-measured rate coefficients for coal is probably the best one can expect considering the complexities associated with the coal's insulating char layer, the uncertainties in the shape factors for the fine particles, the in-depth absorption of the laser beam which is significant for particle dimensions but trivial for large samples, the two orders of magnitude range in incident fluxes, and the three orders of magnitude differences in sample size. Thus there is considerable uncertainty in the k_t-value for coal, but the available data suggest that it is somewhat lower than the value for PMMA. Clearly, except for the complication of the coal's char layer residue and its more complex devolatilization thermodynamics, there appear to be no other extraordinary differences in the pyrolysis and devolatilization behavior for the two substances. Both pyrolysis rates are describable in terms of the progression of a decomposition wave whose speed of propagation is controlled by thermodynamic transport constraints.

Returning to the PMMA data, Kashiwagi and Ohlemiller (12) and Kashiwagi (16), also measured surface temperatures during devolatilization, and those data are shown in Figure 12. Their data, obtained at two flux levels show that $\dot{m}$-values are insignificant until some threshold temperature is approached, at which point the rate becomes exceedingly rapid as the $\dot{m}$ versus T curve turns vertically upward. Above the threshold temperature, the rate of pyrolysis and devolatilization becomes virtually insensitive to the surface temperature. For the exposed surface to reach the decomposition temperature of 350-400° C, a minimum threshold heating flux is required in order to overcome the loss flux, I_ℓ. A theory curve is shown in Figure 12 which is a simple step function at T_s, and it represents the assumption implicit in the derivation of Equations 2 and 3.

According to the assumption used for the new model, there is no devolatilization in the horizontal portion of the curve ($\dot{m} = 0$) until the surface temperature of the sample reaches the decomposition temperature, T_s. Once the surface reaches the decomposition temperature T_s, the rate becomes finite and one is in the vertical portion of the step function. The rate is then controlled entirely by the source flux intensity, and the temperature of the reacting surface becomes both invariant and virtually irrelevant.

The model represented by Equations 2 and 3 thus uses a step function to approximate the finite curvature of the transition depicted in Figure 12. In the horizontal portion of the step, the surface is heating up in the input flux, but there is no devolatilization occurring because the temperature is too low. Once the temperature reaches T_s and significant pyrolysis and devolatilization begin, one transits into the vertical portion of the step, and the system is under heat transport control.

It is also interesting to compare the measured induction times for the onset of the pyrolysis and devolatilization process for the PMMA samples with those predicted on the basis of the measured T_s value of 400° C and the exact solution to the time-dependent heat transport equation. For a semi-infinite solid whose surface is heated by a constant source flux, Carslaw and Jaeger (17) give:

$$\tau = \frac{\pi}{4} C \rho \lambda (T_s - T_o)^2/[I(1-r)-I_\ell]^2. \qquad 7)$$

The time required for the surface to reach the temperature T_s is the induction time, τ. The system is initially isothermal at T_o = 25° C. The heat capacity, C, is taken as the average value for the temperature range between T_o and T_s, which is 0.52 cal/g °C (13). The density ρ is 1.18 g/cm^3, and the thermal conductivity λ is taken as 4.5 x 10^{-4} cal/cm s °C (14). The source flux is taken as $I_{abs} = I(1-r)-I_\ell$.

The comparison between the measured τ-values from Figure 10 and those calculated from Equation 7 is shown in Table 1. The comparison is made for two cases: one with the measured steady state loss flux of $I_\ell = 9.8$ W/cm^2; the other for $I_\ell = 0$. Initially at $t = 0$, the entire sample is at ambient temperature and $I_\ell = 0$; however, as $t \to \tau$, $I_\ell \to 9.8$ W/cm^2. Clearly during the non-steady-state induction period as the surface temperature increases from $T_o = 25°$ C to $T_s = 400°$ C, the loss flux, which is due mainly to conduction and convection to the cold surroundings, increases from 0 to 9.8 W/cm^2. The loss flux is clearly time-dependent, but its average value should vary between those two limiting cases. The table clearly shows that the measured τ-values fall between the two predicted limiting cases. The only exception is the measured τ-value at the highest flux which is about a factor of two higher than the calculated value. That difference is attributed to the finite absorption depth of the laser beam. At low fluxes that absorption depth is trivial compared to the characteristic width of the subsurface temperature profile; however, at the highest flux, the two may be of comparable dimensions. Such in-depth absorption is significant at the the highest flux, and a larger mass near the surface is actually heated by the flux than is calculated from the simple theory from which Equation 7 was derived. As a result, the actual induction time required for the surface to reach T_s for in-depth absorption is longer than that calculated on the assumption that the flux is deposited entirely at the surface.

Table 1. - Comparison of Measured Induction Times for the Laser Pyrolysis of PMMA with Theoretical Calculations of Equation 7

Laser Flux, W/cm^2		Induction Time, τ, s		
Incident	Net		Calculated, Equation 7	
I	$I_{abs}=I(1-r)-I_\ell$	Measured	$I_\ell = 9.8$ W/cm^2	$I_\ell = 0$
115.0	97.2	0.101	0.057	0.047
71.0	56.2	0.160	0.169	0.123
42.5	29.7	0.50	0.605	0.342
23.2	11.8	1.83	3.84	1.16
12.4	1.73	6.70	178	4.04

It should also be noted that the theory curves in Figure 3 for coal particles are based on the steady state condition and are uncorrected for such induction time delays. At the higher fluxes, especially for the larger particles, the τ-corrections are small in comparison to the steady-state $t_{1/2}$-values. The corrections are however significant at the lower fluxes for the smaller particles. Nevertheless, there is also a decay time correction required, as discussed earlier. The pyrolysis wave's thermal inertia results in some continuing propagation even after the source flux is turned off. These non-steady-state corrections for induction time and decay time would tend to counteract one another.

PYROLYSIS AND DEVOLATILIZATION IN DUST FLAME PROPAGATION

The flame propagation processes in pulverized coal-fired burners or in accidental dust explosions (18) are examples of combustion processes in which the pyrolysis and devolatilization of the solid fuel particles play a key role. Flame propagation in dust-air mixtures involves three sequential processes (19): heating and devolatilization of the dispersed dust particles; mixing of the emitted volatiles with air in the space between particles; and gas phase combustion of the premixed fuel-air mixture. Each sequential process has its characteristic time constant: τ_{dv}, τ_{mx}, and τ_{pm}. The resultant burning velocity of the dust-air flame, S_u, will be given by $S_u = (\alpha/\tau_e)^{1/2}$ where α is the effective diffusivity for heat and/or free radical mass transfer across the flame front, and τ_e is the effective time constant for the completion of the above sequence of processes. The slowest of those processes will be the rate-limiting process, and accordingly, the resultant τ_e will be controlled by the slowest of those τ-values.

For very fine dust particles at low, lean-limit concentrations, the first two processes are so rapid that the propagation rate is controlled by the last process:

gas-phase combustion. Since that is essentially the same process that controls homogeneous, premixed, gaseous flames, dust flame behavior in those limits is virtually identical to that of an equivalent homogeneous gas-air mixture of the dust's volatiles (20, 21). Thus for very fine dust particles at lean-limit concentrations, each particle is completely devolatilized within the flame front, and the lean limit concentration of the dust-air mixture is determined by the total combustible volatile content of the dust. For example, the lean-limit mass concentration for fine polyethylene, CH_3-$(CH_2)_n$-CH_3, a dust that devolatilizes completely in its lean-limit flame, is identical to that of homogeneous gas-air mixtures of the saturated alkanes (20, 21).

For homogeneous gas flames, there exists a minimum burning velocity for natural convective quenching of about 3 cm/s, below which normal flame propagation is impossible (22, 23). For dust flames, the limit burning velocity appears to be somewhat higher for a variety of reasons (24). For a homogeneous gas flame of burning velocity S_u, the characteristic width of the flame front is $\delta=\alpha/S_u$ and the characteristic time for the completion of the homogeneous gas phase reactions is $\tau_{pm} = \delta/S_u = \alpha/S_u^2$. Setting $\alpha = 0.55$ cm/s and $S_u = 3$ cm/s for the limit burning velocity gives $\tau_{pm} = 60$ ms. That 60 ms is the characteristic time required for the completion of the gas-phase reactions, and if the rate processes are slower than that, the normal high-temperature flame propagation process is quenched by natural convection (23). For heterogeneous dust-air flames the situation appears to be somewhat more complicated. The limit velocities appear to be about a factor of 2 higher, but at the same time the flame zone thicknesses appear to be broader (24). A higher S_u would, for homogeneous flames, normally be associated with thinner flame fronts according to the previous equation, $\delta= \alpha/S_u$. A higher burning velocity and a thicker flame front for dusts suggest that the dust flame is always somewhat accelerated by turbulent vortices which enhance the diffusivity factor, α, increasing it to a value that is higher than the normal laminar one (24). Those vortices are associated with the dust fuel concentration, which is intrinsically inhomogeneous on the scale of either the particle diameter or the distance between particles. In any case, that complication for dust flames leaves one with an uncertainty in the proper choice for τ_e for the heterogeneous flame. It will be here assumed that for heterogeneous flames, the higher S_u at the limit and the wider flame zone thickness (24) give a τ_e that is about a factor of 2 longer than for homogeneous flames, so that 120 ms is chosen for τ_e. That value is thus the maximum time available for pyrolysis and devolatilization. If the process takes any longer, the volatiles are emitted in the burned gases, which is too late for them to contribute to the propagation process within the flame front.

As dust concentrations increase above their lean limit values, or as the dust particles become coarser, the heating and devolatilization process will begin to become rate limiting. In the former case, as stoichiometric concentrations (with respect to the volatiles) are approached, S_u for hydrocarbon-like dusts approaches its maximum value of about 40 cm/s (25). Since τ_e varies as $(S_u)^{-2}$, that order of magnitude increase in S_u reduces τ_e by two orders of magnitude: from 120 ms to only about 1 ms. For such rapidly propagating dust flames, only the surface regions of the dust particles can contribute volatiles to the flame. The flame "rides the crest" of a near-stoichiometric concentration of volatiles regardless of the initial dust loading. That devolatilization rate limitation is responsible for the absence of a "normal" rich limit of flammability for dusts. Although excess fuel volatiles may continue to be emitted in the burned gases at high dust loadings, they are emitted too late to dilute the flame front with excess fuel vapor (18, 20, 21).

Data for the particle size dependence of the lean limits of flammability for coal and PMMA, as measured in a 20-L chamber (26), are shown in Figure 13. They show clearly how the pyrolysis and devolatilization rate process becomes rate limiting as the dust particles become coarser. The curves for coal and PMMA have similar shapes. The initially flat region demonstrates a lean limit that is independent of particle size as long as the particle diameter is small enough. The smaller particles can all totally devolatilize in the time available, and the system behaves as an equivalent homogeneous premixed gas. As diameters increase, the

curves turn upward at some characteristic diameter because of the devolatilization rate limitation, and a size dependence begins to appear. As shown earlier in Figures 2 and 3, for a given heating flux the devolatilization time increases linearly with particle diameter. Thus the pyrolysis and devolatilization rate limitation appears to adequately explain the shapes of the curves. For a fixed flame flux, the time required for devolatilization τ_{dv} will vary linearly with the particle diameter D_p. Below some characteristic diameter, $\tau_{dv} << \tau_{pm}$, the particles can devolatilize completely in the time available, and τ_e is controlled by the gas phase combustion reactions. In that range of fine particle sizes there is no size dependence. However, as $\tau_{dv} \rightarrow \tau_{pm}$, the devolatilization rate process becomes significant in the overall flame propagation process and a particle size dependence begins to appear. For still coarser sizes, $\tau_{dv} >> \tau_{pm}$, and the rate of devolatilization becomes rate controlling. Only the surface regions of the coarser dust particles can then devolatilize in the 120 ms that is available for flame propagation, and hence, a higher dust loading is required to generate a lean limit concentration of combustible volatiles. The curves must therefore turn upward. Eventually, when the particles are so coarse that an excessive dust loading is required, then other thermal quenching processes become significant, and the critical diameter is reached above which propagation is impossible even at the highest dust concentrations. Those critical diameters are the vertical asymptotes of the curves in Figure 13.

A more quantitative analysis is possible using the pyrolysis and devolatilization rate constants reported here for coal and PMMA. The coal value was uncertain by a large factor, but it was nevertheless lower than the k_t-value for PMMA, which was 3.01 g/kcal. According to Equation 3, when exposed for a time t to a net flux I_{abs}, a devolatilization wave front will travel a distance $x = \dot{x}_o t = k_t I_{abs} t/\rho$. For dust flames at their limits of flammability, the I_{abs} and t values are comparable for the two dusts. For PMMA, the rate constant is higher than for coal, and its density is only slightly lower. Thus, Equation 3 predicts that the characteristic diameter for PMMA should be somewhat larger than the value for coal. The data curves in Figure 13 support that expectation.

A prediction of the absolute magnitude of the characteristic diameter is also possible. As indicated earlier, the time available for devolatilization within a heterogeneous flame front propagating at the limit velocity is t = 120 ms. But what value is one to use for I_{abs} when the particle is being heated in a flame front? The major uncertainty in predicting the characteristic diameter is the uncertainty in estimating, I_{abs}, the effective or net heating flux to which the particles are exposed as they approach, enter, and traverse through the flame front. For homogeneous gas flames, radiation from the burned gases to the unburned fuel is usually not significant because the unburned gaseous mixture has a trivial absorptivity. That is not the case for dust particles, so that well before the particles actually enter the flame front, they will absorb the radiance emitted from the hot combustion products, which consist of burned gases, soot, and char. Typically, hydrocarbon flames exhibit a fairly constant limit flame temperature of 1400 to 1500 K, and the Planck radiance at those temperatures is 5-7 cal/cm^{2}s. But for a spherical particle approaching a flame front, that radiance is seen only by its forward-facing hemisphere. That radiance will however be seen for a considerably longer time period than the particle's 120-ms residence time in the flame front. As the particle heats up in that radiance, it will, however, lose an increasing fraction of that radiance by conduction and convection to the surrounding cold air. It is difficult to estimate the effects of that radiant heat transport process, but it is clear from the previous estimate of the particle loss fluxes, which were as high as 50 W/cm^2 for 50-μm particles at T_s = 450-600° C, that the particle temperatures will remain well below the decomposition temperature during that approach period. The particle could nevertheless be preheated significantly above ambient temperature as it enters the flame front. Upon entering the flame front, there is an additional conductive-convective heat flux from the hot gases within the flame front. That heating flux increases in magnitude as the particle penetrates into the burned gases. As it begins to devolatilize in that

conductive-convective flux, the heat transport process becomes exceedingly complex, and the "blowing effect" of the emitted volatiles markedly reduces the Nusselt number. Realistic estimates are difficult to make; however, in (25) it is estimated that the average power density across a homogeneous, laminar, flame-front is given by S_u C ρ (T_b-T_u). For the dust flames under limit conditions S_u = 6 cm/s, C = 0.35 cal/g K, ρ=1.5 x 10^{-3} g/cm^3, and T_b-T_u = 1500-300 = 1200 K. The resultant is an average conductive-convective flux of about 4 cal/cm^{2}s. If one adds to that flux about half of the previously estimated radiant flux (since only the forward hemisphere of the particle sees the flame), one obtains I_{abs} = 7 cal/cm^{2}s. For PMMA, the travel distance of the devolatilization wave into the particle during its exposure within the flame front thus becomes $x = k_t I_{abs} \tau_e/\rho$ = 21 μm. Thus for PMMA the depth of penetration of the devolatilization wave front in the time available for flame front passage under near limit-conditions is about 21 μm. For a square particle heated from two opposing faces, the predicted characteristic diameter would therefore be $\overline{42}$ μm. For a spherical particle in an omnidirectional source flux, the devolatilization of an outer shell 21-μm in depth would actually represent the devolatilization of some 90 pct of the mass of a 75-μm-diameter particle. One should also realize that such omnidirectional heating generates a converging wave front which will accelerate as heat accumulates within the particle. Equation 3 was derived for a planar, steady-state wave front. The converging wave will penetrate farther into the particle during the same exposure time. Accordingly, one estimates that the measured rate coefficient for PMMA should correspond to a characteristic diameter of about 80-100 μm for spherical particles. That estimate is also in fair agreement with the data in Figure 13.

CONCLUSIONS

On the basis of a detailed analysis and evaluation of a diverse set of experimental observations reported by many independent investigators, and on the basis of the data reported here for pyrolysis rates and microscopic structure, it is concluded that there is no substantive evidence to support the traditional viewpoint that the coal particle pyrolysis process proceeds isothermally, under chemical rate control, or that it is describable by a unimolecular, Arrhenius function of the source temperature, T_h, to which the coal particles are exposed. The overwhelming weight of evidence shows that the process occurs in the form of a non-isothermal decomposition wave whose propagation velocity is linearly proportional to the net absorbed heat flux intensity and inversely proportional to the overall enthalpy change for the reaction.

The pyrolysis and devolatilization "rate coefficient" is the reciprocal of that overall enthalpy requirement for heating and devolatilization. Although the rate coefficient for Pittsburgh seam bituminous coal is smaller than that for the simple polymer, PMMA, the pyrolysis and devolatilization behavior of the coal is not markedly different from that of PMMA, except for the complications associated with the coal's char layer residue.

At fire and burner level heat fluxes of 10-100 W/cm^2 and above, the pyrolysis and devolatilization behavior of coals and polymers is realistically describable by the thermodynamic transport-controlled model in which the intrinsic rate of decomposition is described as a simple step-function at the decomposition temperature, T_s. Below T_s the intrinsic rate is near zero. At T_s, the intrinsic rate is so rapid that the system is heat transport controlled. There is no substantive evidence that the temperature of the reactant during pyrolysis and devolatilization can significantly exceed T_s, regardless of the source temperature, T_h, to which it is exposed. For PMMA, T_s is 350-400 °C; for the coal it is 450-600 °C.

REFERENCES

1. Van Krevelen, D.W. Coal Typology-Chemistry-Physics-Constitution, Elsevier, 1961, 514 pp.
2. Badsiock S. and P. G. W. Hawksley. Industrial Engineering Chemistry, Process Des. Develop. 9 (1970), p. 521
3. Anthony, D. B. and J. B. Howard. AIChE Journal, 22 (1976), p 625.
4. Ng, D. L., M. Hertzberg, and J. C. Edwards. A Microscopic and Kinetic Study of Coal Particle Devolatilization in a Laser Beam. Poster Session Paper No. 83, 20th Combustion Symposium, 1984.
5. Hertzberg, M. and D. L. Ng. NATO Advanced Research Workshop on Fundamentals of Physical Chemistry of Coal Combustion, ed. by J. Lahaye, NATO Series Catalogue, Martinus Nijhoff, to be published 1987.
6. Hertzberg, M., I. A. Zlochower, and J. C. Edwards. Coal Particle Pyrolysis Mechanisms and Temperatures. Bureau of Mines Report of Investigation, to be published 1987.
7. Zielinski, E. Fuel 46 (1967), p 329.
8. Freihaut, J. D. and F. J. Vastola. Eastern Section - Combustion Institute, Fall Technical Mtg., Miami Beach, Florida, Nov. 29-Dec. 1, 1978, p 32-1.
9. Solomon, P. R., R. M. Corangelo, P. E. Best, J. R. Markham, and D. G. Hamblen. The Spectral Emittance of Pulverized Coals and Char. 21st Symposium (Int.) on Combustion, to be published 1987.
10. Solomon, P. R., and M. A. Serio. Evaluation of Coal Pyrolysis Kinetics. NATO Advanced Research Workshop on Fundamentals of Physical Chemistry of Coal Combustion, ed. by J. Lahaye, NATO Series Catalogue, Martinus Nijhoff, to be published 1987.
11. Lee, C. K., J. M. Singer, and R. Chaiken. Comb. Sci. and Techn., 16 (1977), p 205.
12. Kashiwagi, T. and T. J. Ohlemiller. 19th Symposium (Int.) on Combustion, Combustion Institute, 1982, p 815.
13. Bares, V. and B. Wunderlich. J. Polymer Sci, Polymer Phys Edition, 11 (1973), p 861.
14. Brandrup, J. and E. H. Immergut. Polymer Handbook, 2nd ed, J. Wiley and Sons (1975), pp II-425 and V-56.
15. Vovelle, C. R. Akrich, and J. L. Delfau. Comb. Sci. and Techn., 36 (1984), p 1.
16. Kashiwagi, T. Combustion and Flame, 34 (1979), p 231.
17. Carslaw, H. S. and J. C. Jaeger. Conduction of Heat in Solids, 2nd ed., Oxford, p 75.
18. Hertzberg, M. and K. L. Cashdollar. Introduction to Dust Explosions, in STP 958, Industrial Dust Explosions, American Society for Testing and Materials, Philadelphia, PA 1987, to be published.
19. Hertzberg, M., K. L. Cashdollar, D. L. Ng, and R. S. Conti. 19th Symposium (Int.) on Combustion, Combustion Institute, 1982, p 1169.
20. Hertzberg, M., K. L. Cashdollar, and I. A. Zlochower. Flammability Limit Measurements for Dusts and Gases: Ignition Energy Requirements and Pressure Dependencies, 21st Symposium (Int.) on Combustion, Combustion Institute, to be published 1987.
21. Hertzberg, M., I. A. Zlochower, and K. L. Cashdollar. Volatility Model for Coal Dust Flame Propagation and Extinguishment, 21st Symposium (Int.) on Combustion, Combustion Institute, to be published, 1987.
22. Hertzberg, M. Bureau of Mines RI 8127, (1976).
23. Hertzberg, M. 20th Symposium (Int.) on Combustion, Combustion Institute (1984), p 1967.
24. Klemens R. and P. Wolanski. Flame Structure in Dust and Hybrid Mixtures Near the Lean Flammability Limit. Poster Session Paper No. 100, 20th Combustion Symposium, 1984.
25. Hertzberg, M. Bureau of Mines RI 8469, (1980).
26. Cashdollar, K. L. and M. Hertzberg, Rev. Sci Instrum., 56 (1985) p. 596.

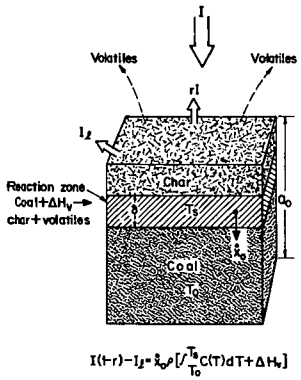

Figure 1. - A schematic idealization of the propagation of a planar steady-state pyrolysis and devolatilization wave front in coal as it is being driven by a plane-wave radiant source flux of intensity, I.

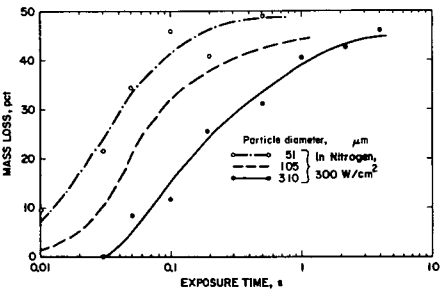

Figure 2. - The devolatilization mass loss for coal particles of 51, 105, and 310μm diameter as a function of exposure time at a constant laser source intensity of 300 W/cm^2, from reference 5.

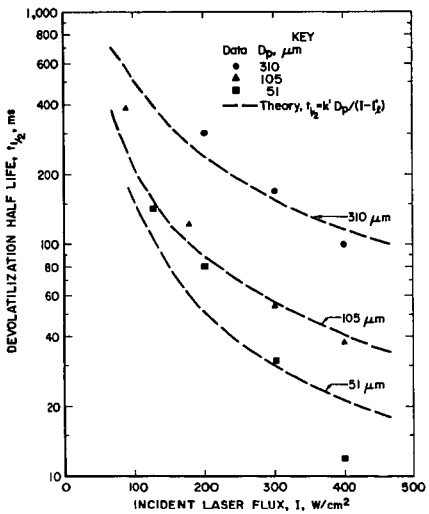

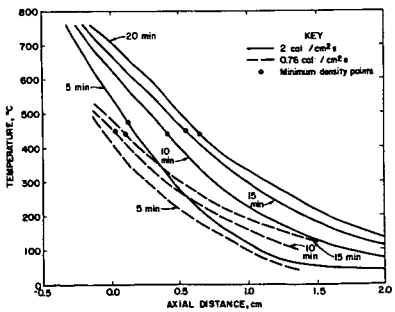

Figure 4. - Measured temperature profiles for coal during pyrolysis and devolatilization as a function of time for two laser intensities, as measured by Lee, Singer, and Chaiken(11).

Figure 3. - Summary of the measured half lives for coal particles as a function of laser source intensity for the three coal particle sizes from reference 5. The data points are compared with the theory based on heat transport limitations according to the First Law of Thermodynamics.

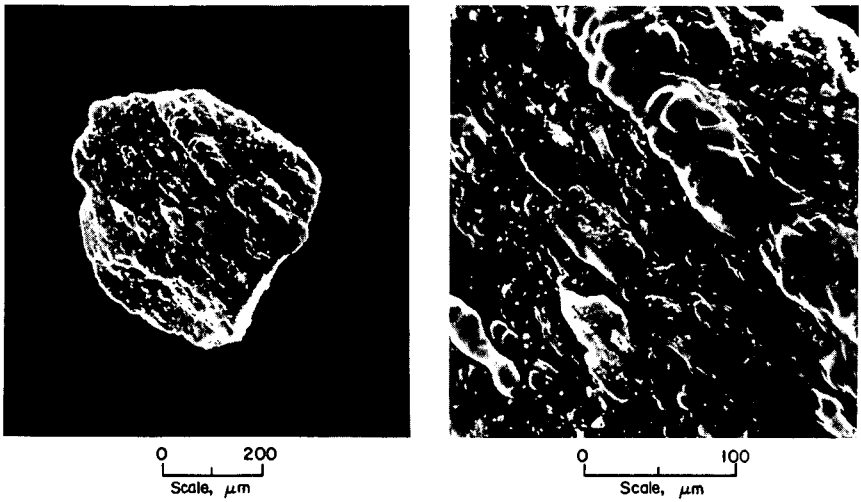

Figure 5. - Scanning Electron Microscope (SEM) photographs of the exposed surface of a coal particle exposed for 100 ms to a laser flux of about 100 W/cm^2, seen at two magnifications.

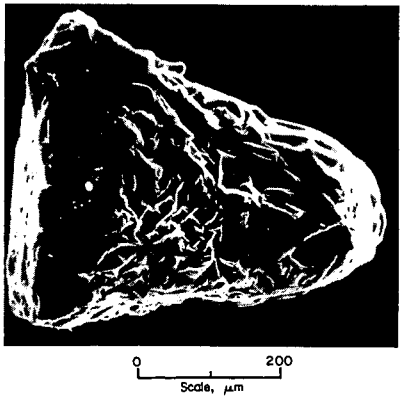

Figure 6. - SEM photograph of a coal particle, which is about two-thirds devolatilized after exposure for 400 ms to a laser flux of about 125 W/cm^2.

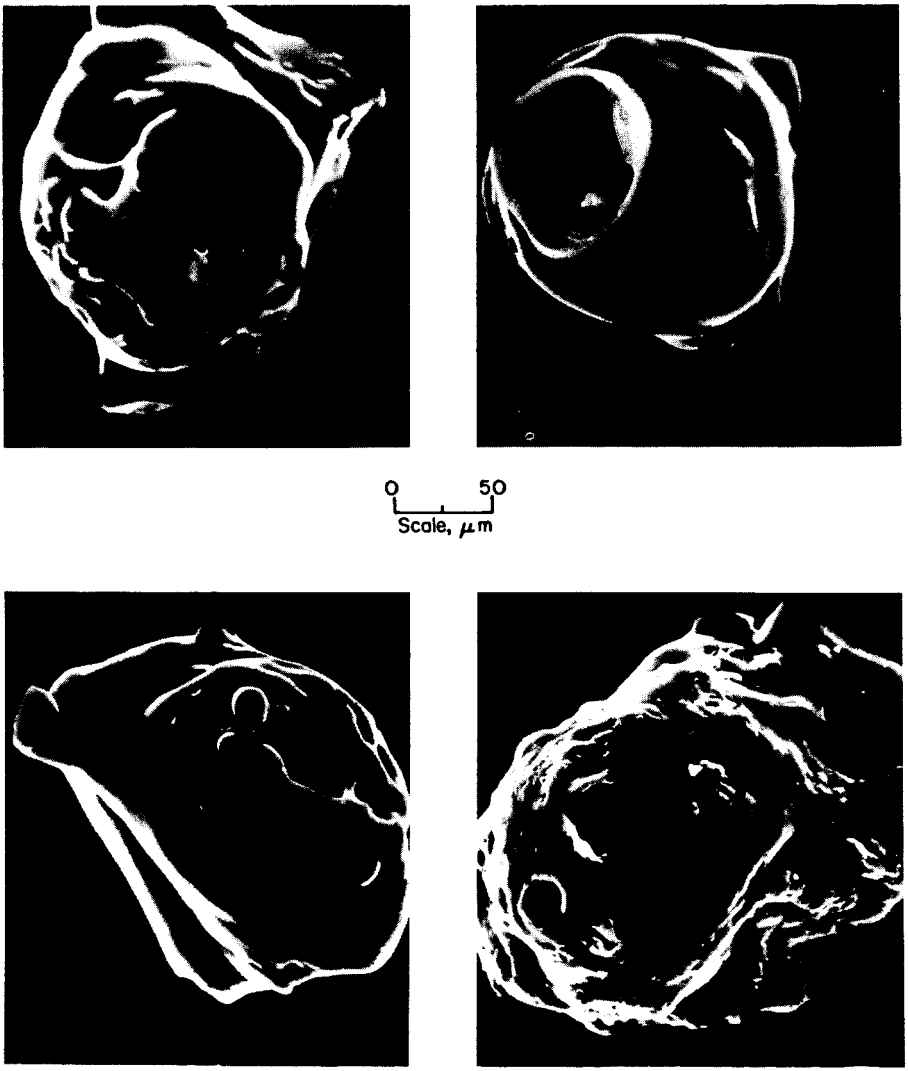

Figure 7. - SEM photographs of four different particles exposed to a laser flux of about 100 W/cm^2 for 1 s. The particles are all about two-thirds devolatilized by the laser flux incident from above.

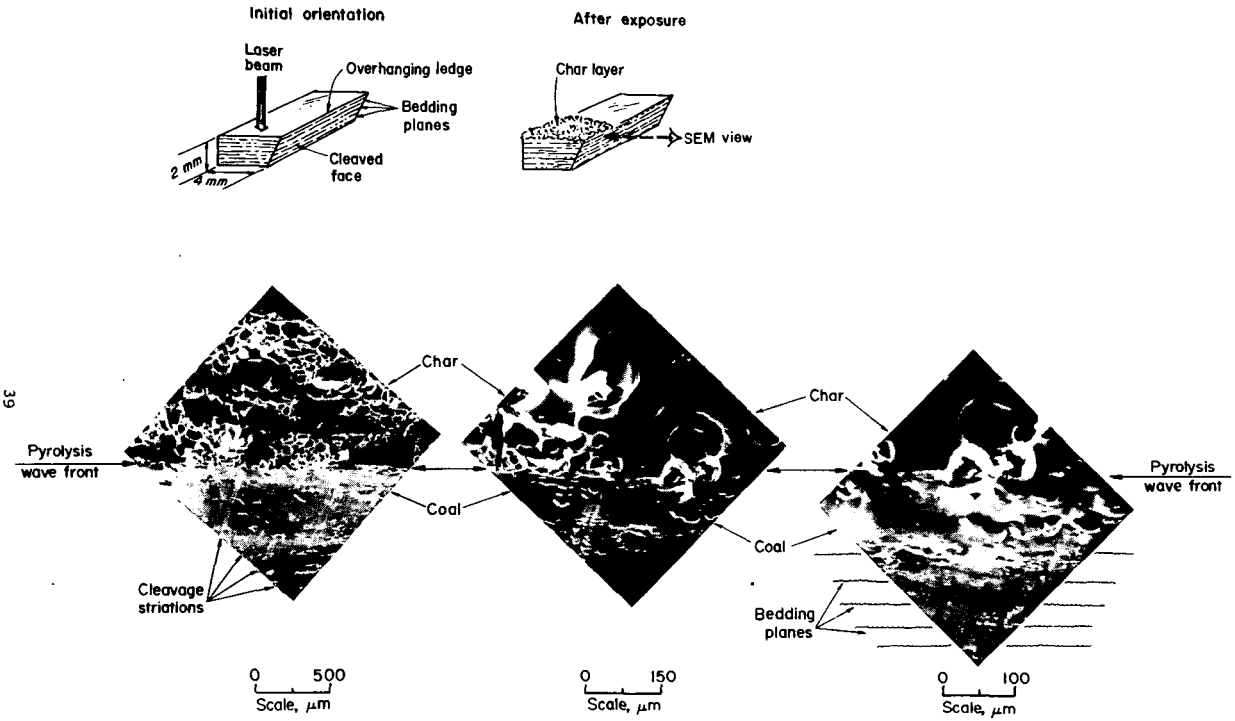

Figure 8. - SEM photographs viewed from the side of a shadowed, cleaved face of a macroscopic sample of Pittsburgh seam bituminous coal exposed for 2 s to a laser flux of 100-125 W/cm^3. The pyrolysis and devolatilization wave front is viewed at three magnifications.

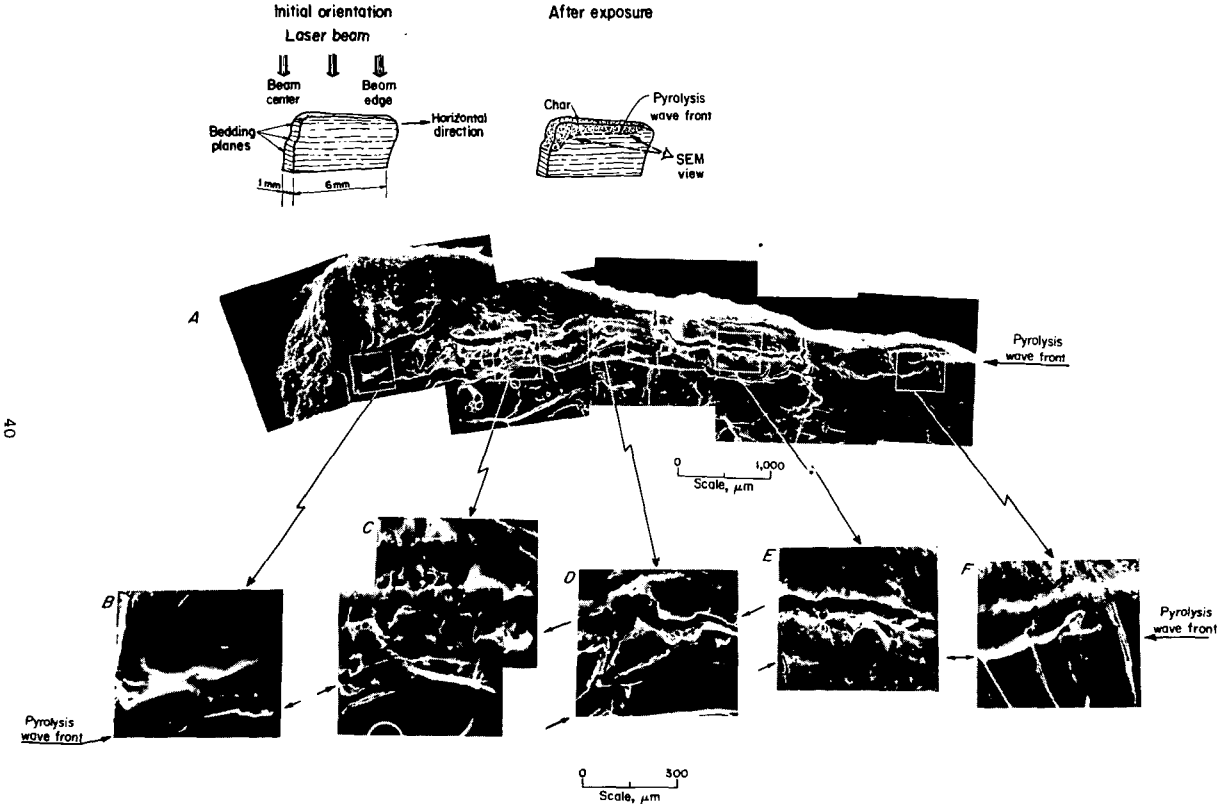

Figure 9. - SEM photographs of a macroscopic sample of the Hannah-seam coal exposed to a maximum laser flux of 100-125 W/cm^2 for 2 s, as viewed from the side. Lower magnification montage in A; higher magnification views of the pyrolysis and devolatilization wave front in B, C, D, E, and F.

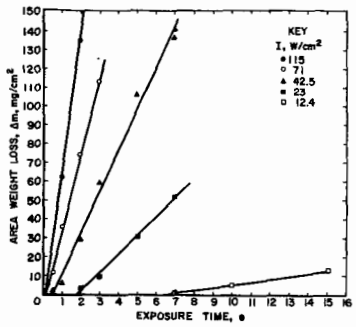

Figure 10. - The measured pyrolysis and devolatilization weight (or mass) losses for 0.45 cm diameter, PMMA cylinders as a function of exposure time for different input laser flux intensities in the range 12 to 115 W/cm^2.

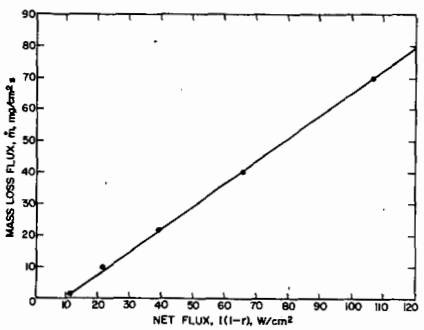

Figure 11. - The measured, steady-state rates of pyrolysis and devolatilization for 0.45 cm diameter PMMA cylinders, as a function of input laser flux corrected for surface reflectance, r.

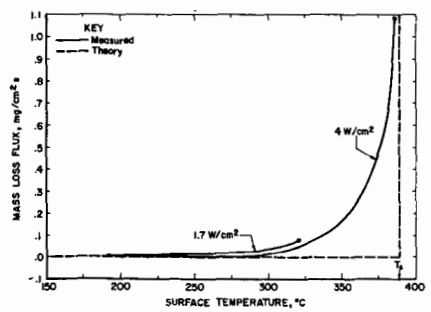

Figure 12. - The measured surface temperatures at various mass loss rates during the pyrolysis and devolatilization of PMMA at two radiant fluxes as reported by Kashiwagi and Ohlemiller. Measured values compared with simplified, step-function theory using a discrete, decomposition temperature, T_s.

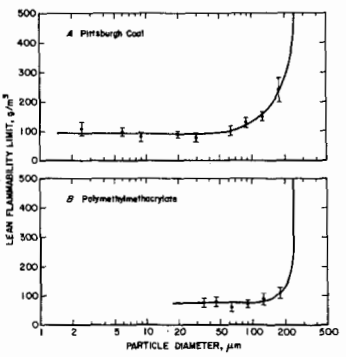

Figure 13. - Lean flammability limit as a function of particle diameter for Pittsburgh seam bituminous coal and polymethacrylate.

SPECTRAL EMISSION CHARACTERISTICS OF SIZE-GRADED COAL PARTICLES*

Thomas H. Fletcher, Larry L. Baxter and David K. Ottesen

Sandia National Laboratories, Livermore, CA 94550

The spectral emission characteristics of coal are examined using Fourier transform infrared emission spectroscopy. The data were collected from a single layer of stationary, narrowly size-classified samples of coal and graphite placed on a heated NaCl window. Sample temperatures ranged from 120 to 200°C. FTIR data were collected at wavelengths between 2.2 and 17 μm (between 4500 and 580 cm^{-1}). Particle sizes ranged from 40 to 120 μm and coal rank ranged from lignite to bituminous.

The focus of this work is to evaluate the effects of the nongray emission characteristics of coal on heat transfer calculations and pyrometry measurements. Chemical functional groups responsible for the features of the spectral emission are identified but not discussed. Well characterized spectral features from coal samples are observed and discussed. The intensity of spectral peaks due to chemical functional groups in coal are analyzed as a function of particle size and extent of reaction. The impact of spectral irregularities on pyrometry measurements and heat transfer calculations is evaluated. Featureless regions of the infrared emission spectra of coal are also analyzed and compared to graybody behavior. Reliability of pyrometry measurements in these regions and effective emissivities of coal particles for heat transfer calculations are discussed.

INTRODUCTION

Spectral and total emission characteristics of coal have been reported in the past, with emissivities ranging from 0.1 to near unity. Several investigators (1-3) have published results indicating that coal is not a strong absorber of radiation at infrared wavelengths. Values of the imaginary part of the complex index of refraction on the order of 0.05 are reported by these authors. Other authors report much larger imaginary coefficients, of the order of 0.3 (4-6), indicative of higher abosrbance and emittance of radiation.

A strong and irregular dependence of emissivity on wavelength would be expected of an organic compound containing a variety of chemical functional groups, such as coal, if the material is either generally transparent or very thin. Such results are reported by Solomon and coworkers (3) for particles less than 40 μm in diameter, although the size of the particles is not always well defined in their work. Commonly available infrared absorption and diffuse reflectance spectra of coal samples are consistent with the spectral features reported by Solomon. However, these features should become indistinguishable from the diffuse background absorption as the particle size increases. Solomon noted this trend, but did not define a particle size where the spectral features of the emission become insignificant compared to the diffuse background radiation. Large or highly absorbing particles should show less variation of emissivity with wavelength; they should become approximate gray-bodies.

* Research conducted at the Combustion Research Facility, Sandia National Laboratories, Livermore, California, and sponsored by the U.S. Department of Energy through the Pittsburgh Energy Technology Center's Direct Utilization Advanced Research and Technology Development Program.

The overall emissivity of coal includes diffuse, broadband absorption in addition to peaks associated with specific functional groups. The broadband absorption of coal probably arises from electronic excitations of π electrons in the graphitic, aromatic bonds in the coal matrix (7-9). These electrons are loosely bound by the nuclei, and can absorb radiation over a continuous wavelength region which extends far into the infrared. However, the electrons are not entirely free from nuclear attractions, and their emission spectra would not necessarily be expected to follow Planck's law. Therefore, even the radiation from coal at wavelengths void of any identifiable functional groups may not be gray in its characteristics.

The literature cited above indicates that the spectral emission of coal particles at sizes of importance to pulverized coal combustors (50-150 μm) is potentially nongray and could depend in complicated ways on particle size, coal rank, temperature and extent of reaction. However, the emission would be expected to behave more like a graybody with increasing particle size, coal rank, temperature, and extent of reaction. Although all of the literature suggests that there is some size at which the coal particle emission is nongray, no study has been sufficiently definitive to quantify such a size for coals of various rank.

IMPACT OF NONGRAY COAL EMISSION ON COMBUSTION

The potentially nongray emission of coal particles impacts combustion in the areas of overall heat transfer and in the calculation of particle temperature from pyrometer measurements. An abnormally low emissivity due to nongray behavior could impact radiative heat transfer effects and either increase or decrease the rate of particle heat up, depending on the wall and particle temperatures and the optical depth of the combustion gases. Data collected in experimental and industrial combustors in which radiation is a signficiant contributor to the overall heat transfer to the particle may be subject to misinterpretation or error if an inappropriate emission spectrum is assumed. A particle emissivity which depends on particle size, coal type, and extent of burnout may be required to accurately calculate radiation heat transfer.

The sensitivity of two-color pyrometry to nongray emissions is illustrated in Figure 1 for three sets of wavelengths. The effective emissivities of the coal were assumed to be 0.9 and 0.8 at λ_1 and λ_2, respectively. The same results would apply for any emissivities with a ratio of 9:8. Pyrometry measurements at longer wavelengths are more sensitive to nongray emissivities. For example, if the ratios of emissivities are 9:8, a pyrometer operating at 5 and 6 μm would indicate the temperature of a 1500 K particle is over 3000 K and that a 2000 K particle would be measured as over 9000 K. This sensitivity provides practical motivation for determining the spectral emissivities of coal.

The experimental work reported in this paper analyzes spectral emissivities of various sizes and ranks of coal particles using emission FTIR techniques. Discussions of the experiment, the functional groups found in the spectra, and the size, burnout, and rank dependence of the findings follow.

EXPERIMENTAL PROCEDURE

Figure 2 is an illustration of the experimental equipment and optical layout employed in this study. A single layer of sized particles of coal and graphite were placed on a horizontal window of NaCl mounted in an aluminum ring. An electric strip heater was wrapped around the mount. The NaCl window was used because it can withstand higher temperatures without degradation and has a higher thermal conductivity than other windows that are transparent throughout the infrared spectrum. Temperatures as high as 400°C are possible

with this arrangement, although the temperatures used to obtain the spectra presented in this report seldom exceeded 200°C. The heated sample, optics, interferometer, and detector were enclosed in a nitrogen-purged container.

All coal samples were obtained from the Pennsylvania State University Coal Bank. The coal samples were ground in a nitrogen atmosphere, size classified by sieve trays, and some were dried in a nearly inert atmosphere at 305°C. Graphite samples were prepared similarly. All samples were visually examined and some were photographed after they were placed on the window to ensure they were well size-classified and formed a single layer.

The heated sample disc was movable in the horizontal plane, allowing the FTIR instrument to measure emission from the coal and from the graphite through the heated window, and from the heated window itself. The field of view of the system, calculated from geometric optics, was 6 mm in diameter at the sample plane. In practice, a portion of the signal from the edge of the collecting lens was lost, probably due to overfilling the detector.

The spectra in this paper were produced by averaging 800 interferograms, each with a resolution of 4 cm^{-1}. Approximately 5 minutes were required to obtain one spectrum under these condtiions. The large number of scans produced a high signal-to-noise ratio over most of the infrared region; peaks were observed with sufficient resolution to allow comparison with literature results. The emissivity of the coal (ϵ_s) was determined at each wavelength from the following equation:

$$\epsilon_s = \left(\frac{R_s/A_s - R_w/A_w}{R_g/A_g - R_w/A_w} \right) \epsilon_g \qquad 1)$$

where R is the measured intensity (radiance and system response), A is the emitting area, ϵ is emissivity, and subscripts s, g, and w refer to sample (coal), graphite, and window, respectively. The numerator in Equation 1 represents the energy flux emitted by the sample, accounting for background emission from the window. The quantity in parenthesis represents the emissivity of the sample relative to the emissivity of the graphite, and hence the right-hand side is multiplied by ϵ_g. This approach assumes that ϵ_g is constant over the wavelength spectrum. The spectral emissivity of the graphite particles was determined by correcting the measured intensity (R_g) for the system responsivity; the graphite particles exhibit nearly graybody behavior with a total emissivity of 0.92.

Emission FTIR is subject to interference from atmospheric absorption and emission. This effect was minimized in this experiment by measuring the emissivity of a reference body (graphite) of the same size and under the same conditions as the coal. This experimental procedure is roughly equivalent to individually calibrating the system responsivity for each measurement. Our experience was that this technique, combined with Equation 1, yielded spectra of superior quality to the more common approach of determining a single fixed system responsivity for several or all of the spectra.

The emitting areas of the graphite and coal and the transmissivity of the window were determined by measuring the extinction of a HeNe laser beam as it passed through a sample. The HeNe beam was expanded, and a central portion of the beam with the same diameter as the diagnostic area (6 mm) was used to minimize

errors from gradients in beam intensity. A power meter with a large detection area was used to measure the beam intensities and minimize errors due to scattered light.

The particle temperatures were assumed to be close to the window temperature, which were measured with a type K thermocouple placed on the window itself in the vicinity of the sample. The temperature at the center of the window was typically 5-10 Kelvins lower than that at the edge. However, the samples were located equidistant from the window edge to minimize errors due to temperature gradients. The data analysis can be completed without specifying the actual temperature so long as the window, coal, and graphite temperatures are equal.

The estimated accuracy of the measured emissivities is $\pm$ 5 relative percent. The major source of uncertainty in the emissivity was the determination of the actual emitting surface area. Although the HeNe laser could accurately measure the cross-sectional area of the samples within the nominal 6 mm sample, there were indications that a fraction of the signal from this area was not transmitted to the detector.

FEATURES OF THE COAL SPECTRA

Figure 3 is typical of the spectra collected in this study, showing the spectral emissivity of 40 μm diameter particles of a hvA bituminous coal (Pittsburgh #8, PSOC 1451). Peaks from various functional groups are identified in the figure. One small peak, at about 1850 cm^{-1}, is not typical of coal and has not yet been identified. The remaining peaks agree precisely with published spectra collected with a variety of instruments and techniques and validate the experimental procedure described above. Similar spectral features were found in the coals of other ranks. The spectra show maximum emissivities close to unity in regions of functional group absorption. The absorption of these peaks is typically high for submicron particles (8) and should not decrease with increasing particle diameter.

Some reaction of the coal was observed when the temperature was held above 150°C for 3 hours or longer. For example, the evolution of a peak at 1850 cm^{-1} is observed over a 2.0 hour period. Other coal reactions which were indicated by reductions in peak size include loss of hydrogen-bound hydroxyl and a small decrease in the aliphatic carbon. However, consecutive spectra taken within one hour of each other showed no losses and were reproducible at temperatures below 170°C. In any case, there was no evidence that a spectrum changed during the 5 minutes required to collect it.

DEPENDENCE OF EMISSIVITY ON SIZE, BURNOUT AND RANK

The spectral emissivity for 115 μm particles of a Pittsburgh seam (high-volatile A) bituminous coal is shown in Figure 4. A comparison of Figures 3-4 shows the dependence of spectral emissivity on coal particle size. The peaks are broader, the valleys are higher, and the emissivity in the featureless regions has increased for the larger particles, as anticipated. The emissivity of 115 μm particles of this bituminous coal varies from 0.7 to 1.0 over the range of 500 to 4100 cm^{-1}.

The spectral emissivities for 115 μm particles of a subbituminous coal and a lignite are shown in Figures 6 and 7. The subbituminous sample (PSOC-1445d) is a Western coal from the Blue #1 seam, and the lignite sample (PSOC-1507d) is a lignite from the Beulah Zap seam. These coal samples were sieved and aerodynamically classified under nitrogen to enhance size classification. These particular samples were not dried prior to analysis.

The dependence of emissivity on coal rank can be seen by comparing Figures 5-7. The nongray behavior of the lignite is more pronounced than in either of the higher rank coals, with emissivity varying from 0.57 to 1 0 in the region of the infrared indicated. However, little indication of aromatic spectral features is present in either of these samples. Interference from water in these undried samples is evident in the spectra.

A spectrum of partially devolatilized bituminous (PSOC 1451) coal appears in Figure 8. This sample was prepared by entraining the coal in a 1000 K inert gas stream in a down-fired, laminar flow reactor. The proximate volatile content of the parent coal is 40 % on a dry, ash-free basis. The weight loss of these samples has not yet been measured, but it is estimated that devolatilization was nearly completed when the sample was collected. The unreacted coal particles used in this analysis were those used to generate Figure 5. The dependence of particle emissivity on coal burnout can be seen by comparing Figures 5 and 8.

The emissivity of these particles is quite constant at 0.8 at wavenumbers above 1900 cm^{-1}. The aliphatic and hydroxyl groups, which were emitting strongly in the unreacting coal, appear to have either volatilized or reacted to form other compounds. However, a weak aromatic peak persists at 3000 cm^{-1}. The emissivity of the aromatic peaks between 500 cm^{-1} and 1900 cm^{-1} slightly exceeds that of the parent coal, possibly due to the formation of tar. Finally, the emissivity in featureless regions of the spectrum did not change appreciably from the parent coal.

IMPLICATIONS ON PYROMETRY AND RADIATIVE HEAT TRANSFER

The spectral emissivity shown in Figure 5 can be used to evaluate the potential impact of nongray emissions on pyrometry measurements. For example, a two-color pyrometer operating at 3333 and 2500 cm^{-1} (3 and 4 μm) would overestimate the temperature of a 1500 K particle by 200 K. A similar error would occur if the pyrometer operates at 3333 and 2000 cm^{-1} (3 and 5 μm). If the pyrometer were operating at 2000 and 1667 cm^{-1} (5 and 6 μm), it would underestimate the particle temperature by 700 K. Errors in pyrometry measurements due to nongray emissivities can be minimized by making one measurement at a short wavelength (around 1 μm) or increasing the separation between wavelengths, the former strategy being more effective than the latter. These trends are shown in Figure 1. However, signal strengths at typical combustion temperatures decrease sharply with decreasing wavelength in the near infrared and visible regions, requiring a judicious choice between acceptable signal-to-noise ratios and sensitivity to this type of error.

Total emissivities for use in radiative heat transfer calculation will depend in a complicated way on coal rank and on particle size, temperature, and degree of burnout. For high rank coals above 40 μm in size, the total emissivity could vary between 0 65 and near 1.0. Lignites have a wider variation in emissivity. The importance of these variations and the effect they have on heating rate depend primarily on the combustor configuration and flow field. In many instances, devolatilization may be completed before the particle reaches a high temperature, and only the optical properties of the residual char affect combustion behavior.

CONCLUSIONS

An emission FTIR experimental technique is used to study emission characteristics of coal particles. Coal particles in the size ranges between 40 and 115 μm show nongray behavior at wavelengths between 2.2 and 17 μm Spectral emissivities of high rank coals vary from 0.7 to 0.98. Spectral emissivities of lignites may be as low as 0 5 at some wavelengths. The particles generally are more gray as particle size, rank and extent

of burnout increase. The emissivity generally increases with increasing rank and particle size. As burnout increases, the particle emissivity can either increase, decrease, or remain constant, depending on the region of the spectrum being considered.

Pyrometry measurements in the 2.2 to 17 μm wavelength interval are subject to errors due to nongray effects. The errors in temperature measurement vary from a few hundred degrees to many thousands, depending on the wavelengths chosen. Operating one channel of the pyrometer at a short wavelength reduces the chance for error.

The effect of nongray emissions on heat transfer calculations will depend on the particular combustor and flow field being used. Total particle emissivities range from about 0.6 to 0.95 for 115 μm diameter particles, depending on particle temperature and coal rank. Smaller particles from low rank coals have lower emissivities. Partially devolatilized samples of bituminous coal emit as gray bodies over a large portion of the infrared spectrum, with emissivities of about 0.8.

REFERENCES

1. Brewster, M. Q., and Kunitomo, T. "The Optical Constants of Coal, Char, and Limestone," *ASME Transactions, 106, (1984).*
2. *Huntjens, F. J., and van Krevelen, D. W., Fuel, 33, (1954).*
3. *Solomon, P. R., Carangelo, R. M., Best, P. E., Markham, J. R. and Hamblen, D. G., "The Spectral Emittance of Pulverized Coal and Char," Twenty-first Symposium (International) on Combustion, Munich, West Germany, 1986.*
4. *Foster, P. J. and Howarth, C. R., "Optical Constants of Carbons and Coals in the Infrared," Carbon, 6 (1968).*
5. *Blokh, A., The Problem of Flame as a Disperse System, Halsted Press, (1974).*
6. *Cannon, C. G. and George, W. H., Proc. Conf. Ultrafine Structure of Coals and Cokes, BCURA, London, 1944.*
7. *Berry, R. S., Rice, S. A. and Ross, J. Physical Chemistry, Wiley, New York 1980.*
8. *van Krevelen, D. W., Coal, Elsevier, 1981.*
9. *Berkowitz, N., The Chemistry of Coal, Elsevier, 1985.*

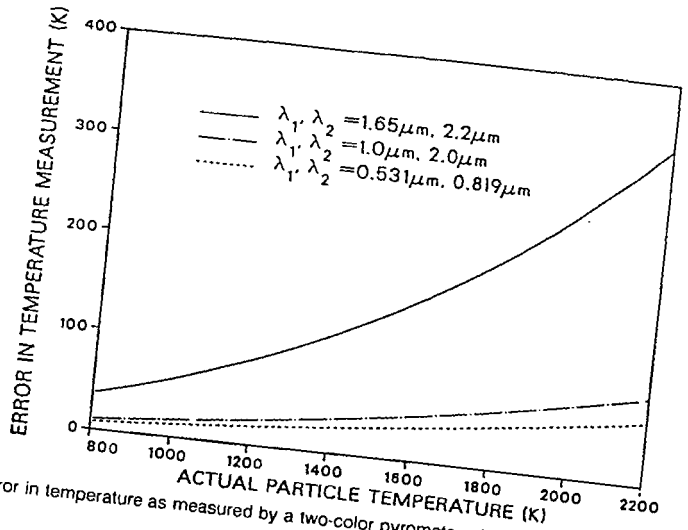

Figure 1. Error in temperature as measured by a two-color pyrometer when the emissivity ratio at λ_1 and λ_2 is 9·8.

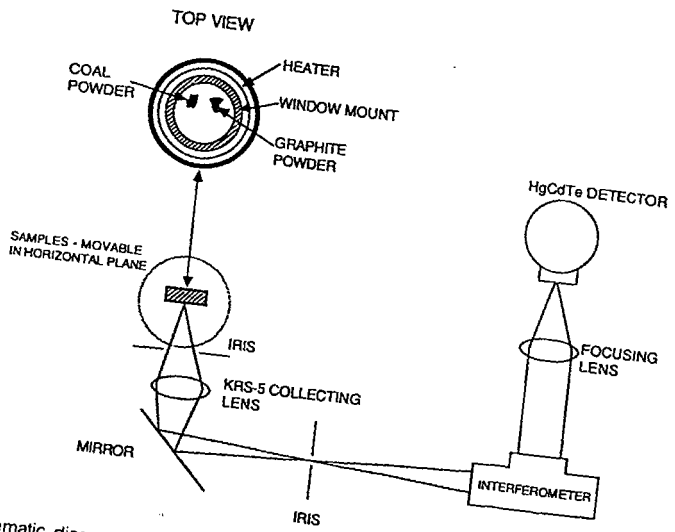

Figure 2. Schematic diagram of experimental facility for measurements of the spectral emissivity of coal particles.

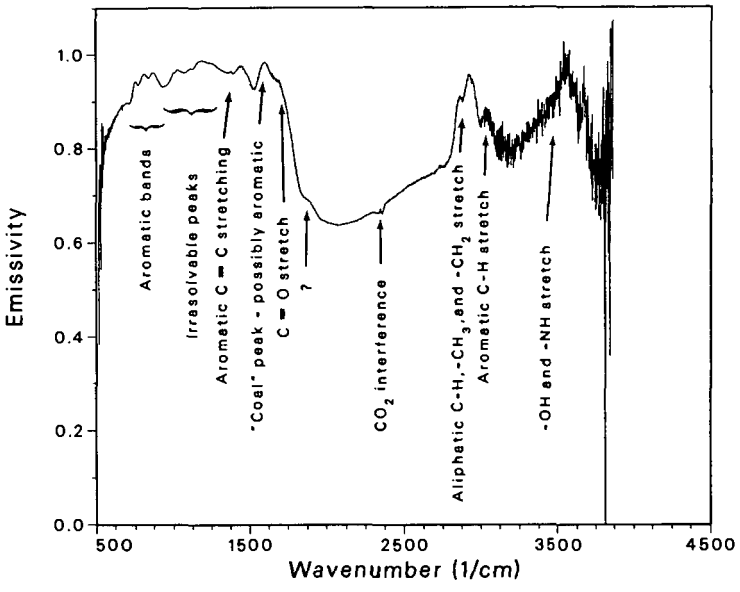

Figure 3. Spectral emissivity of 40 μm hvA bituminous coal (PSOC 1451) at 171°C, identifying peaks associated with various coal functional groups.

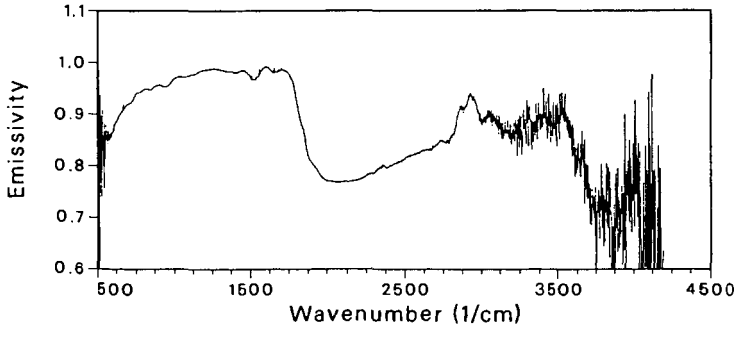

Figure 4. Spectral emissivity of 115 μm diameter hvA bituminous coal particles (PSOC 1451) at 182°C.

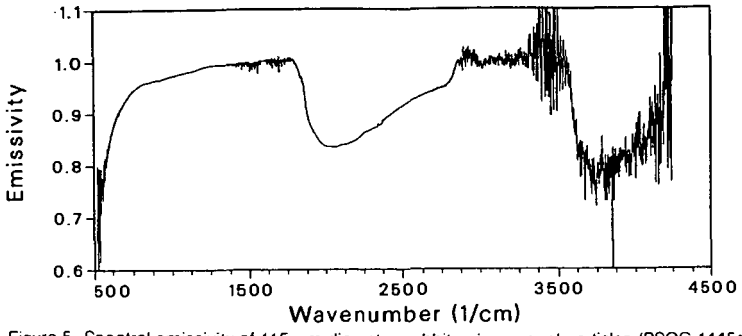

Figure 5. Spectral emissivity of 115 μm diameter subbituminous coal particles (PSOC 1445d) at 180°C.

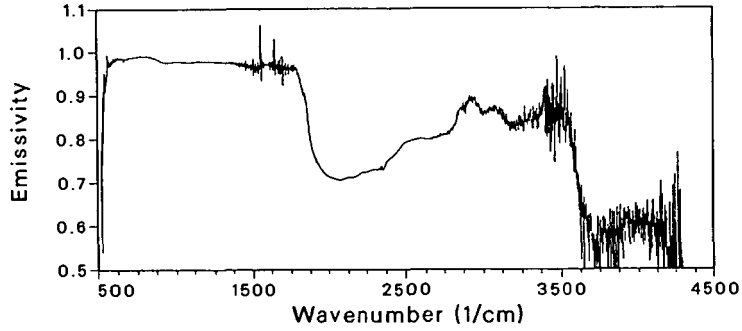

Figure 6. Spectral emissivity of 115 μm diameter lignite particles (PSOC 1507d) at 190°C.

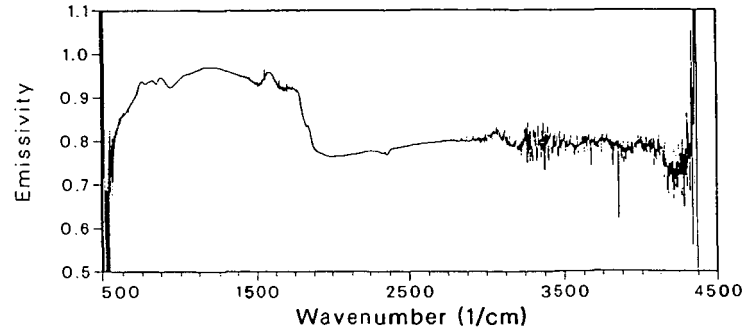

Figure 7. Spectral emissivity of 115 μm diameter hvA bituminous coal particles (PSOC 1451) at 182°C after partial devolatilization at 1000 K.

The Significance of Transport Effects in Determining Coal Pyrolysis Rates and Yields

Eric M. Suuberg
Division of Engineering
Brown University
Providence, R.I. 02912

INTRODUCTION

The recent search for robust but mathematically simple models of coal pyrolysis has led to many significant advances in the area of modeling the wide range of chemical reactions responsible for many key phenomena (gas release, tar formation). It has also become clear that transport phenomena cannot be disregarded in such models. There has emerged a debate concerning the role of heat transfer and various mass transfer processes in determining both the overall timescales of pyrolysis, and the compositions of products from these processes. Many of the earlier theories concerning the role of transport processes in coal pyrolysis were reviewed in various recent publications (Howard, 1981; Gavalas,1982; Suuberg,1985). It seems appropriate in the context of this symposium to review some recent developments and conclusions.

THE ROLE OF HEAT TRANSFER

THE HEAT OF PYROLYSIS

It is instructive to consider exactly what is meant by the term "heat of pyrolysis". This term has been used in many different ways by many different workers, and as a result there is some confusion about the magnitude of the term and whether it even warrants inclusion in any particular analysis. The various possible components of the heat of pyrolysis are:

1. The sensible enthalpy of heating the coal and its decomposition products to a particular temperature.
2. The enthalpy of the actual decomposition reactions.
3. The heat of vaporization of any condensed phase decomposition products that ultimately escape the particle by evaporation (i.e. not all tar molecules evaporate immediately when formed in the coal- they must diffuse first to a surface at which they can evaporate).

Some species essentially evaporate as they are formed (e.g. CO_2), and it is customary to lump the heat of evaporation and heat of reaction into a single term (the enthalpy of reaction) in those cases. Under the conditions of relevance in coal pyrolysis, only in the case of formation of the heavy tars will the distinction between steps 2 and 3 above be important.

Most, though not all workers in the field, have sought to distinguish between the contributions of items 1 and 2 to the heat of pyrolysis. Few workers have tried to distinguish between all three effects. Many of the experiments upon which estimates of the heat of pyrolysis are based simply are not designed so as to permit the distinctions to be drawn. for example, a calorimetric experiment in which a sample is pyrolyzed in the interior of a calorimeter (Davis,1924) will not take into account the heat effect due to item 3 above-in addition to the recondensation of tars inside the calorimeter, one will also have to generally contend with condensation of water and lighter oils as well. The corrections due to such condensation effects (which are

generally unlikely in actual pulverized gasification or combustion processes) may be difficult to make, even if the composition of the products is known. Other types of experimental systems have not lent themselves well to separation of sensible enthalpy and reaction enthalpy effects.Much of the difficulty derives from the fact that the enthalpy effects due to reaction and evaporation processes are small, and of the same order of magnitude as sensible enthalpy effects.

The work of Davis and Place(1924) is often cited as evidence that the heat of pyrolysis is small enough to neglect. These workers however pointed out several important facts:

1. The net heat of pyrolysis varies quite a bit with rank
2. The heat of pyrolysis that will be reported from any experiment depends upon the conditions under which pyrolysis is performed.
3. Related to the above, the heat effects of pyrolysis involve a series of endo- and exotherms which sum to the total heat of pyrolysis.

Davis and Place reviewed some earlier relevant literature that suggested many of the same uncertainties that are cited today--the variabilty of apparent heats of pyrolysis was large, with values ranging from 1060J/g endothermic to 837J/g exothermic.In their own calorimetric work, Davis and Place found apparent enthalpies of reaction that were in all cases less than 400J/g endothermic. The lower ranks of coal were observed to exhibit the largest endothermic reaction enthalpies, when a correction was applied to take into account the latent heat of condensation of water. Higher temperatures seemed to promote the occurrence of more endothermic processes, as did the addition of hydrogen to the gaseous environment (Davis, 1924). It is important to note that this work involved slowly heated samples, pyrolyzed at low temperatures. No corrections were included for the latent heat of evaporation of tars. It is not clear how reliably these results can be extrapolated to the higher temperature and heating rate conditions of pulverized coal processing.

Some years later, Mahajan et al.(1975) studied the same problem using differential scanning calorimetric techniques (DSC). They obtained qualitatively similar results to those of Davis and Place, in that their enthaplies of pyrolysis ranged from about 80J/g exothermic to 250J/g endothermic.

Burke and Parry (1927) provided a different viewpoint to the study of this problem. They distilled coals to 870K in an open retort, such that all the tar that was evolved from the bed could escape in the vapor state, and thus at least some contribution of a latent heat of tar evaporation was included. Also, they did not separate out sensible enthalpy effects from reaction enthalpy and latent heat effects in their experiments. The net heat consumed by a Colorado subbituminous coal was 1109J/g, while a Pittsburgh high volatile bituminous coal consumed 946J/g. An attempt was made by the authors to factor out the contribution of sensible enthalpy, and they concluded that the values of 16J/g (Pitt. coal) and 198J/g (Colo. coal), both exothermic, were in reasonable agreement with the results of Davis and Place (not including latent heat corrections). These values demonstrate very well the difficulty that will be encountered in any attempt to factor out sensible enthalpies by calculation--the values are sufficiently large compared to the reaction enthalpy terms that the calculations cannot be considered reliable, except to provide an order of magnitude estimate.

A number of subsequent attempts have been made to estimate the heats of pyrolysis, including the sensible enthalpy terms. The work of Kirov (1965) has led to a correlation for the heat of coking:

$$Q(J/g)=343+1.20T$$

where T is the temperature of coking in centigrade (see also Sharkey and McCartney,1981). The work of Lee (1968) suggests a similar correlation:

$$Q(J/g) = [0.728 + 8.28 \times 10^{-4} T + (1.38 + 2.30 \times 10^{-3} T) V](T-21)$$

where V is the volatile matter content of the coal. Using either method yields fair agreement with the earlier cited data of Burke and Parry, though obviously the first correlation's use is restricted to coking coals. The success of such simple correlations must again be ascribed to the fact that sensible enthalpy terms dominate the estimates.

The above viewpoint is apparently at odds with that of Baum and Street (1971), who imply that there is a distinct heat of vaporization which has to be supplied in order for volatiles to escape. The value cited in that work is 627.9J/g of coal, and is based upon the authors' own experiments. This value is considerably higher than most estimates of the heat of reaction, and most estimates of the latent heat of tar volatiles evaporation. It is difficult to obtain data on the latent heats of vaporization of the heavy tars of interest in coal pyrolysis. Briggs and Popper (1957) proposed a correlation for the latent heat of vaporization of "tar oils" which has the form:

$$\Delta H_v(J/g) = S_{20}(485.8 - 0.598 T_b)$$

where S_{20} is the specific gravity of the tar at 20°C and T_b is its boiling point in K. The difficulty in using this correlation for coal tars is that their boiling points are not well known. To address the need for estimates of tar vapor pressures, Unger and Suuberg (1983) developed a crude correlation as a function of molecular weight alone, based on limited data on the vapor pressure of ring compounds with sidechains:

$$P^o(atm) = 5756 \exp(-255 M^{.586}/T)$$

where M is the molecular weight of the tar, T is the temperature in K.A "typical" tar molecular weight of 600 (see Unger and Suuberg,1984) would be estimated to have T_b=1250K. This is clearly outside the range of applicability of the above correlation. Instead, applying the Clausius-Clapeyron equation to the vapor pressure equation itself yields

$$\Delta H_v(J/g) \approx 2120 M^{-0.414}$$

Another similar analysis by Homann(1976) yields:

$$\Delta H_v(J/g) \approx 1960 M^{-0.346}$$

These correlations give estimates for a typical tar species of 600 molecular weight of ΔH_v=150 to 215J/g.To compare this value to earlier cited estimates of heats of pyrolysis, one can note that tar yields represent typically no more than 1/4 to 1/3 the mass of a particle; thus the latent heat of tar evaporation is a sink of order 70J/g coal if all tar had M=600. A lower assumed molecular weight does not change the conclusion much--e.g. M=200 gives a latent heat requirement of about 100J/g coal. Thus, the latent heat term is of the same order of magnitude as the measured heats of pyrolysis reported earlier.

Estimation of the reaction enthalpy term is also quite difficult, because there are so many possible contributing processes. Attempts at estimation of this term by measurement of pyrolysis products, and then comparing heats of combustion of starting material and final products have been difficult (one such attempt is described in Suuberg et al.,1978). All that can be said as a result of these efforts is that at high heating rates (1000K/s), the general conclusion of near-thermoneutrality seems to still apply. Recent experiments in which the temperature response of a coal-loaded, electrically heated wire grid is carefully examined seem, upon rough calculation, to support the earlier estimates of the magnitude of the heat of pyrolysis as well (Freihaut and Seery,1983).

HEAT TRANSFER CONTROL

It appears, then, that the weight of evidence still favors the viewpoint that the heat of pyrolysis is dominated by sensible enthalpy requirements for heating the particle to reaction temperature, and that the reaction enthalpy requirements and

latent heat requirements are both modest (not more than 1/4 to 1/2 of the total). This means that the classical analysis of heat conduction in a solid, in which the reaction enthalpy and latent heat effects are neglected, still appears reasonable. Under these circumstances, the characteristic time for diffusion of heat in the absence of reaction heat effects is:

$$t_H = O\ (r^2/\alpha)$$

where r is the particle radius and α the thermal diffusivity of the particle; the latter is temperature dependent, but of order $1x10^{-3}cm^2/s$ at low temperatures (Badzioch et al.,1964). The timescale for pyrolysis reaction may be defined:

$$t_R = O\ [A\ \exp(-E/RT)]^{-1}$$

Naturally, the absence of heat transfer limitations during reaction is assured by $t_R >> t_H$, or, approximately:

$$r < [0.1\alpha\ \exp(E/RT)/A]^{-1}$$

This is similar to the criterion suggested by Gavalas(1982). The selection of A and E has a significant effect on the conclusions, however. A conservative approach might involve selection of these parameters for the fastest reaction of interest. This might be, for example, the initial CO_2 evolution reactions in pyrolysis of lignites, for which $A=2.1x10^{11}s^{-1}$, E=151kJ/mol (Suuberg et al., 1978). Selecting as an arbitrary ambient temperature 1650K, heat transfer limitations are apparently not important only if r<0.05μm! For a temperature of 1200K, r<0.4μm. These radii are considerably smaller than those calculated by Gavalas, and serve to illustrate the importance of the choice of kinetic constants in such analyses. Recognizing that coal pyrolysis involves a broad spectrum of reactions, each with its own kinetic parameters, the so-called distributed activation energy models have been developed. If one uses a mean activation energy to obtain a characteristic timescale for <u>all</u> pyrolysis reactions, the conclusions change markedly. For example, Anthony et al. (1975) report that for pyrolysis of a lignite, the mean value of E is 204kJ/mol, $A=1.07x10^{10}s^{-1}$. With these kinetic parameters, such a timescale analysis suggests that at 1200K, r<30μm is sufficient to assure the absence of heat transfer limitations. It is also apparent that the choice of temperature has an effect on the conclusions reached above. It may legitimately be asked if the use of the ambient temperature as the characteristic temperature may not be too conservative, since the particle may be well below this temperature during much of the process. This aspect will be clarified below.

Another analysis that has been suggested as a method of determining whether heat transfer limitations are significant is that due to Field et al.(1967). In this analysis, the magnitude of the temperature gradient in a particle is examined (generally the center of the particle is cooler than the ambient). The magnitude of the surface to center temperature gradient is, conservatively:

$$\Delta T = rq/2k$$

where q is the surface heat flux and k the thermal conductivity of the particle. For a 100μm particle being radiatively heated in a 1650K environment, the maximum value of q is roughly $40W/cm^2$. Taking a typical $k=2.5x10^{-3}W/cm\text{-}K$ (Badzioch et al.,1964), the maximum ΔT is calculated to be roughly 40K. Field et al. cite this as evidence that pulverized fuel particles, which are generally less than 100μm in diameter, may be taken as essentially spacially isothermal. For any particle that does have an internal temperature gradient, the relative rates of pyrolysis at its surface and center may be estimated from:

$$k_s/k_c = \exp[(1/T_c - 1/T_s)E/R] \approx \exp[\Delta TE/RT_s^2]$$

where the k's are rate constants and the subscripts c and s refer to center and surface, respectively. For E=151kJ/mol and the above ΔT=40K, apparently the ratio is 1.65 at

T_s=1200K or 1.3 at 1650K. Thus the rates throughout the particle are reasonably constant. The ratio increases with increasing E and decreasing T_s, but even if E=204kJ/mol and T_s=1200K, the ratio is but 2. Thus the rates at the surface and center of the particle are both of the same order of magnitude in such a case.

The two different methods of analysis apparently yield contradictory conclusions about the importance of internal heat transfer limitations for particles in the 30-100μm size range. This is symptomatic of the confusion that exists concerning the role of heat transfer in pyrolysis. The resolution of the apparent conflict comes in closer examination of the criteria for heat transfer control.It was noted above that the use of the ambient temperature in the calculation of characteristic times for reaction was unduly conservative. The more reasonable approach involves examining the timescales for pyrolysis of both the center and the surface of the particle, given an estimate of the actual ΔT in the particle. Only if the latter quantities differ significantly is there an important internal heat transfer limitation.

There has also been some confusion caused by imprecise discussion of the role of external heat transfer limitations. For the purposes of illustration, assume that pyrolysis can be modeled as a simple first order process with a rate:

$$dM/dt=-A\ M\ \exp(-E/RT)$$

where M is the mass of unpyrolyzed material remaining at time t. Further, assume that the particle heats up at a linear rate dT/dt=B, then it has been shown numerous times that it is possible to approximately integrate the rate expression above to obtain conversion ($1-M/M_0$) as a function of maximum temperature achieved (T_m):

$$(1-M/M_0) \approx \exp[-A\ \exp(-E/RT_m)[t_i+RT_m^2/EB]] \qquad \text{(Eqn. A)}$$

where t_i is the time of any isothermal period during which the particle is held at T_m. Since the conversion as a function of time is determined by B, which in turn is a function of external heat transfer rate, this has in some cases been interpreted as an example of an "external heat transfer limitation". But it should be noted that chemical kinetics do indeed play a role in determining the time necessary to achieve complete conversion. Also, the case in which B is infinite can be recognized as the familiar case of complete chemical rate control.

RELEVANCE FOR PULVERIZED COAL DEVOLATILIZATION

From a simple heat balance, the surface heat flux to particles being uniformly heated at a constant rate B(K/s) must be given by:

$$q = d\rho c_p B/6 = dkB/6\alpha$$

where d is the particle diameter. Assuming B=1000K/s, d=75μm, and previously cited values, q=3.1W/cm^2, which implies that ΔT=2.4K. Thus the particles are essentially uniform in temperature and the many experiments on pulverized particles heated at these rates (common for heated grids) would be expected to be governed by the nonisothermal kinetic expressions of the form of eqn. A. These experiments then do indeed yield information on true kinetics. If particles of 1mm are examined under the same conditions, ΔT ≈ 430K, and the interpretation of the results in the same terms is questionable at best.

At a nominal average heating rate of B=10^{4}K/s, 75μm particles would support a temperature gradient of about 24K, given the present assumptions. At a surface temperature of 1000K, the rate of a pyrolysis reaction with 210kJ/mol activation energy would be 1.8 times as high on the surface as in the center of the particle. However, it should be noted that about 60% of the mass of the particle is within 10μm of its surface. At a depth of 10μm, the temperature will lag that of the surface by only 12K, and the reaction rate will be only 35% lower. Such small differences in rate would normally not be apparent within the uncertainty of measurements in such high heating

rate experiments.

Only at particle average heating rates of 10^5K/s and above do internal heat transfer limitations become important for typical pulverized-size particles. The surface heat fluxes implied by such heating rates are 300W/cm^2 for 75 μm particles, and temperature gradients of order 240K may be expected, based on the above analysis. It is then not surprising that at such fluxes (produced by laser radiation), Hertzberg and Ng (1987) observed a particle diameter effect on devolatilization half-life, with particles in the range 51-105μm. At 100W/cm^2 irradiation, the effect of particle size was seen to be very small. The implication is that for typical pulverized coal particles heated at ordinary rates (<10^4K/s or <100W/cm^2 flux), pyrolysis can be well described by a standard Arrhenius rate expression that accounts for the temporal nonisothermality of the process (e.g. equations of the form of A), without specifically accounting for internal heat transport limitations.

At higher fluxes, pyrolysis is expected to exhibit the observed "wave" character, in which the onset of reaction coincides with penetration of the thermal wave into the coal. The temperature of the wavefront is easily predicted from equation A, setting t_i=0 and assuming for example that the appearance of the wavefront coincides with about 50% conversion for the most facile reaction (kinetic parameters cited earlier for such a reaction were A=2.11x10^{11}s^{-1}, E=151kJ/mol). For a heating rate B=10^5K/s, the calculated T_m=960K is the apparent wavefront temperature. For B=10^4K/s, which would yield pyrolysis wave behavior only in "large" particles according to the above analysis, the apparent wavefront temperature is calculated to be about 870K, in good agreement with the observations of Hertzberg and Ng.

It may be concluded further that for high fluxes or large particles, that the standard Arrhenius kinetic expressions, combined with standard heat transfer analysis, are sufficient to describe the rate of pyrolysis, without the need to resort to the concept of a "decomposition temperature". As shown above, such a temperature would be a function of heating rate and reaction kinetics, and thus not a fundamental quantity.

More detailed analyses of the combined heat transfer-reaction processes in coal are still hampered by the lack of good thermodynamic and transport data on these systems. Even if the data on heats of reaction and latent heats were available, construction of a robust heat transfer model would have to wait for simultaneous development of a mass transfer model, since the location of evaporative tar loss (and thus the associated heat sink) would not necessarily coincide with the location of the reaction front in the coal.

THE ROLE OF MASS TRANSFER

There has recently appeared an extensive review on modeling of mass transfer limitations in coal pyrolysis (Suuberg,1985), and this material will not be repeated here. Since the publication of that review, there have been a number of developments in understanding the processes involved, and these will be briefly summarized. As usual, a distinction is drawn between processes that are mainly of relevance in softening coals, and those that occur in the porous structure of non-softened coals.

Mass Transfer in Softening Coals

A major unresolved issue is that concerning the handling of bubble transport of volatiles, and whether it plays the dominant role in determining tar yields during pyrolysis. It has been shown that models which involve transport of volatiles out of the coal through bubbling-type behavior can indeed capture many essential features of the process (Lewellen,1975;Oh et al.,1983,1984). However, it has also been shown that a simple model in which liquid phase diffusion controls the rate of escape of tars might also explain the tar yield data equally well for pulverized particles (Suuberg and

Sezen, 1985). Thus it is not yet clear what role the bubbles must play in transporting tars. Further work on this latter model has, not surprisingly, revealed that liquid phase diffusion is most likely not fast enough to explain tar yields from particles much larger than about 100μm, under high heating rate conditions. Consequently, the evidence favors at least some role of bubbles in helping remove the tar from the particles, since no other convective mechanism is evident. A new, semi-empirical model of bubble transport has recently been proposed.

This new model of bubble transport of tar volatiles proposes that the tars are carried out in small bubbles that are nucleated by light gaseous species and oils. Solomon (1987) proposes an analogy of cups on a conveyor belt-each cup can carry out a certain amount of tar, as determined by the saturation vapor pressure of the tar. The effect of pressure on tar yields is seen through the effect on the size of the cups-the higher the pressure, the smaller the cup, and the less tar it transports. The smaller the rate of tar transport out via the cups, naturally the longer the residence time of tars in the particle, and the greater the opportunity for yield reducing cracking/coking reactions. More formally, each bubble is assumed saturated with respect to all tar species present in the surrounding liquid. Assuming ideal vapors and liquid solutions, the total number of moles of a tar species of molecular weight M_i in a bubble is:

$$n_i = P_i v_b/RT = P_i^0 x_i (v_g+\Sigma v_j)/RT$$

where v is a volume, with the subscript b referring to the whole bubble, g referring to the fixed gases in the bubble, and j to the volume contribution of the tars themselves. The quantity x_i is a liquid phase fraction of species i and P_i^0 is its vapor pressure.

The rate of escape of the tar species i is governed by the rate of escape of bubbles from the particle, which is given, at constant pressure, by the total volumetric rate of escape of bubbles:

$$dN_i/dt = (P_i^0 x_i/RT)dV_t/dt = (p_i^0 x_i/P_{tot})dN_t/dt$$

where N_i is the same as n_i multiplied by the total number of bubbles that escape, and V_t is the total volume of all volatiles, which is related by the ideal gas law to the total number of moles of volatiles, N_t. The pressure P_{tot} is the prevailing ambient pressure.

The implied inverse pressure dependence of the rate of tar escape is the same as was previously noted based on another model-one in which film diffusion controls the rate of tar escape (Suuberg et al.,1979,1985; Unger and Suuberg,1981). In that model, the rate of tar escape was given for a particle of radius R by:

$$dN_i/dt = 4\pi RDx_i P_i^0/RT$$

where the inverse pressure dependence is implicit in the vapor phase diffusion coefficient of tar in the gas film around the particle (D).Either model will predict a variation of molecular weight distribution with pressure (see Suuberg et al.1985).

Solomon (1987) has noted that the rate of escape of the bubbles from the coal should be linked to the size of the particle, the viscosity of the coal melt (μ), and the pressure difference between bubble and ambient (ΔP). The latter effect is proportional to dN_t/dt, leading to the following suggested empirical form for the rate of tar escape:

$$dN_i/dt = (c_1 P_i^0 x_i/RP_{tot}\mu)(dN_t/dt)[1/(P_{tot}+\Delta P)]$$
$$= (c_1 P_i^0 x_i/RP_{tot}\mu)(dN_t/dt)\{1/[P_{tot}+c_2(dN_t/dt)]\}$$

As of this writing, equations of this form are being tested.

Porous Transport

There has been relatively little new work in this area since it was last reviewed, except that the standard pore transport analysis has been extended to account for temporal nonisothermality (Bliek et al.,1985). This area awaits further work on the question of how pressures affect yields of tar volatiles in non-softening coals. It

seems clear that pressure affects the rate of convection and diffusion. But is this in turn affecting tar yields by virtue of an impact on the residence times of vapor phase species in pores (affecting the residence time for vapor phase cracking/coking) or by virtue of an impact on evaporation rate of tar species (affecting the residence time for condensed phase cracking/coking)? It also appears necessary to clarify what role if any, is being played by microporous transport, under reactive conditions. The distinction between micropore transport and bulk diffusion remains hazy.

ACKNOWLEDGEMENT

The support of the USDOE through grant DE-FG22-85PC80527 is gratefully acknowledged.

REFERENCES

Anthony,D.B., J.B.Howard,H.C.Hottel, and H.P.Meissner, 15th Symp.(Int.)on Comb.,p1303 The Combustion Institute,1975.

Badzioch,S., D.R.Gregory,M.A. Field, Fuel,43,267 (1964).

Baum,M.M. and P.J. Street,Comb. Sci. and Tech.,3,231 (1971).

Bliek,A.,W.M.vanPoelje,W.P.vanSwaaij,and F.P.van Beckum, AIChEJ,31,1666 (1985).

Briggs,D.K. and F.Popper,Trans.Inst.Chem.Engr.(London),35,369 (1957).

Burke,S.P.and V.F. Barry, I&EC,19, 15 (1927).

Davis,J.D., I&EC,16(7),726 (1924).

Davis,J.D. and Place,P.B.,I&EC,16(6),589 (1924); Fuel,3,434 (1924).

Field,M.A.,D. Gill,B.Morgan, and P. Hawksley, BCURA Monthly Bulletin,31(3),81 (1967).

Freihaut, J.D., and D.J.Seery, ACS Division of Fuel Chem. Prepr., 28(4), 265 (1983)

Gavalas,G.R.,Coal Pyrolysis,Elsevier, New York,1982.

Homann,K.H., 16th Symp.(Int.) on Comb.,p717,The Combustion Institute, 1977.

Hertzberg,M. and D.Ng, paper presented at NATO Advanced Research Workshop on Fundamentals of Physical Chemistry of Coal Comb., Les Arcs, France,1986.

Kirov,N.Y., BCURA Monthly Bulletin,29(2),33 (1965).

Lee,A.L.,ACS Div.Fuel Chem. Prepr.,12(3),19 (1968).

Lewellen,P.C., M.S. Thesis, Dept. of Chem. Eng., M.I.T., Cambridge, Mass., 1975.

Mahajan,O.P., A. Tomita, J.R. Nelson, and P.L. Walker, Jr.,ACS Div. Fuel Chem. Prepr.,20(3),19 (1975).

Oh,M.,W.A. Peters, and J.B. Howard, Proc.Int. Conf. on Coal Sci.,p483, IEA (1983).

Oh,M.,J.B.Howard,and W.A.Peters,"Modeling Volatiles Transport in Softening Coal Particles, paper presented at the AIChE annual meeting, November,1984.

Sharkey,A.G.,Jr. and J.T. McCartney,in Chem. of Coal Utilization, Second Suppl.Vol. M.A. Elliott,Ed.,p198,Wiley, New York,1981.

Solomon, P.R., AFR,Inc., personal communication (1987).

Suuberg,E.M., in Chemistry of Coal Conversion,R.Schlosberg,Ed., p67,Plenum, 1985.

Suuberg,E.M.,W.A.Peters, and J.B.Howard,17th Symp.(Int.)on Comb.,p117, The Comb. Inst., 1979.

Suuberg,E.M.,W.A. Peters, and J.B. Howard,I&EC Proc. Des. and Dev.,17,37 (1978).

Suuberg,E.M. and Y. Sezen, Proc.Int. Conf. on Coal Sci.,p913, Pergamon (1985).

Suuberg,E.M., P.E. Unger and W.D.Lilly, Fuel,64,956 (1985).

Unger,P.E. and E.M.Suuberg,18th Symp.(Int)on Comb.,p1203,The Comb. Inst.,1981.

Unger,P.E. and E.M.Suuberg,Fuel,63,606 (1984).

Unger,P.E. and E.M.Suuberg,ACS Div.FuelChem.Prepr.,28(4),278 (1983).

DIFFUSIONAL CONTRIBUTIONS TO VOLATILE RELEASE IN PYROLYZING COAL PARTICLES

Mahendra K. Misra and **Robert H. Essenhigh**

The Ohio State University
Department of Mechanical Engineering
206 West 18th Avenue
Columbus, Ohio 43210

SUMMARY

Unsteady state calculations of pyrolyzing coal particles under slow and rapid heating have been compared with experimental data for particles in the size range 20 microns to 4 mm; and the comparison has shown, contrary to common assumption, that the diffusional escape is an important factor in determining the pyrolysis times for all particle sizes. Pyrolysis times for particles greater than 500 microns range from 0.1 to 10 sec; and for particles less than 100 microns range from 0.05 to 0.5 sec with an unexpected overlap in times. This overlap is accounted for by assuming that the diffusion coefficients for the escaping volatiles are about 100 times greater (order of 10^{-1} cm^2/sec) for the larger particles than for the smaller particles (order of 10^{-3} cm^2/sec). This result raises the questions regarding purely kinetic interpretations of pyrolysis rate data for small particles.

1. INTRODUCTION

In this paper we present comparison between calculated and experimental values of pyrolysis times in the particle size range 20 microns to 4 millimeter. The experimental data were taken from the literature [1-17]. The calculations are based on an unsteady state heat transfer model, with escape of volatiles after chemical release inside the particle controlled, we assume, by diffusional or convective escape. The model and a number of other results, notably temperature-time distribution through a particle and profiles of pyrolysis release rates, have been described earlier [18,19]. In this paper, we summarize the elements of the model, the equations and computational procedures; focus here is on the contribution of the diffusional escape.

In past evaluation of pyrolysis studies, it has generally been concluded that escape of pyrolysis products from particles below about 100 microns is so fast as to be effectively "instantaneous". This conclusion, however, is not in fact supported by values of pyrolysis times in the larger data base now available; and, as we shall show in this paper, we have only been able to obtain good agreement between the experimental values and our predictions for the times, and their variations with diameter, when a significant diffusional escape factor is included in the calculations, even for particles as small as 20 microns. This result clearly raises questions regarding the purely kinetic interpretations of pyrolysis rate data for small particles presented in the past.

2. EXPERIMENTAL DATA BASE

A data base consisting of total pyrolysis times under different conditions from the literature was compiled for comparison with our predicted values of times and their variation with particle size. The experimental methods used included (mostly) Drop-tube and or Heated-grid experiments, carried out in inert atmospheres; and from experiments performed in the presence of oxidizing atmospheres (mostly flame experiments). A summary of the data along with the investigators and the nature of experimentation is given in Tables 1 and 2 and in Figure 1.

In the majority of the measurements on captive particles [1] (650 values) coal particles were cemented to silica fibers and burnt between two electrically heated, flat spiral coils. The burning times of the volatiles were determined using a PE

cell, and these times were assumed to be equal to the pyrolysis times. The experiment was carried out for 10 different coals with particle sizes in each case ranging from about 700 microns to 4 millimeters. For each coal type, the pyrolysis time and the particle size could be related by the expression

$$t_v = K_v d_o^n \qquad (1)$$

The values of K_v and n are listed in Table 2; it can be seen that the values of K_v are about 100 c.g.s units, and the index n is about 2. A similar result was obtained by Kallend and Nettleton [2] in a similar experiment, but with the particles mounted on thermocouples. Figure 1 shows that the results of the two experiments are in close agreement. Other data are for particles smaller than 200 microns and have been taken mostly from some of the Drop-tube, Heated-grid,and flame experiments. The pyrolysis times in these cases have been defined as the time period between the 1% and 99% loss by weight of the ultimate yield of Volatile Matter. The data collected are for heating rates ranging from 10^3 to 10^5 deg.K/sec.

Figure 1 shows an unexpected overlap in the pyrolysis times between the larger particles below 100 microns, and the smaller of the captive particles above 700 microns. A continuous curve from a single equation passing approximately through all data sets would be a dog-leg, which is unexpected. Also unexpected is the apparently strong dependence of pyrolysis times on diameter below 100 microns, contrary to the common belief. It is these two aspects of behavior, in particular, that we are addressing in this paper.

3. PHYSICAL MODEL

The model is that of a particle plunged into an enclosure whose temperature is rising. Heat transfer can be jointly by conduction (convection) and by radiation. The calculations show that, in the case of the captive particles, radiation only dominated over conduction for particles greater than 2 millimeters. The behavior is an unsteady state so that temperature non-uniformities can exist through the particles, resulting in variable rates of pyrolysis at different points. Escape of the products is treated phenomenologically as a diffusional process, either actual, and dependent on concentration differences, or effective, where the actual driving force may be pressure differences. One objective here is to establish the actual or apparent diffusion coefficients required to account for the experimental results as targets for further mechanistic analysis using approximate pore and pore-tree models.

4. MATHEMATICAL MODEL

4.1 Governing Equations:

Heat Transfer: For a particle in a thermal enclosure, the dimensionless equations for heat transfer inside and outside the particle, describing the change in temperature, θ, as a function of radial distance, η, and time, τ, is

$$R_c \, \partial\theta/\partial\tau = (1/\eta^2)\,\partial[\eta^2 \, \partial\theta/\partial\eta]/\partial\eta - C \exp(-1/\theta)\delta \qquad (2)$$

where the dimensionless groups are defined as

$$\theta = RT/E \qquad (3)$$

$$\tau = (\alpha_p / r_o^2)t \quad ; \qquad \eta = (r/r_o) \qquad (4)$$

$R_c = 1$ for $\eta < 1$; $R_c = \alpha_p / \alpha_a$ for $\eta > 1$.

and $\delta = 1$ for $\eta < 1$; $\delta = 0$ for $\eta > 1$

The quantity C is

$$C = \sigma k_o r_o^2 \Delta H(V_o - V)/\lambda_p \qquad (5)$$

The initial conditions are (for $\tau = 0$):

for $0 < \eta < 1$, $\theta = 1$ and for $1 < \eta < \infty$, $\theta = \theta_o$

and the boundary conditions are

$$[\partial\theta/\partial\eta]_{\eta=0} = 0 \quad ; \quad [\theta]_{\eta=\infty} = 0 \qquad (6)$$

At the particle surface, the temperatures of the particle and the gas are equal, and the heat flux to the particle is the sum of heat flux from the gas and the net radiative heat flux from the enclosure. This shows that the radiation appears as a boundary condition at the particle surface.

Pyrolysis is assumed to be a first-order, one-step reaction; and the heat absorbed in pyrolysis is

$$h = \sigma k_o \exp(-E/RT)(\Delta H)(V_o - V) \qquad (7)$$

Mass Transfer: The governing equations for the diffusion of volatiles through the coal matrix are of the same form as the heat transfer equations and can be written as

$$\partial m/\partial t = (1/r^2)\partial(r^2 D_i \partial m/\partial r)/\partial r + \delta m_g \qquad (8)$$

where

$$m_g = \sigma_p k_o \exp(-E/RT)(V_o - V) \qquad (9)$$

and

$\delta = 1$, $D_i = D_p$ for $r < r_o$; $\delta = 0$, $D_i = D_a$ for $r > r_o$.

The boundary conditions are

$$[\partial m/\partial r]_{r=0} = 0$$
$$[D_p \partial m/\partial r]_{r=r_o} = [D_a \partial m/\partial r]_{r=r_o} \text{ and } m_{part} = m_{air} \qquad (10)$$
$$\partial m/\partial r = 0 \text{ at } r = \infty.$$

Mass Loss: At any instant of time, the flow rate of volatiles out of the particle surface is

$$m_t = 4\pi r_o^2 D_p [\partial m/\partial r]_{r=r_o} \qquad (11)$$

and the total mass loss over a period t is given by

$$M_t = \int_0^t m_t dt \qquad (12)$$

4.2 Solution Procedures Eqn.(2) is transformed into appropriate difference forms for solution using a Central difference approximation on the spatial coordinate, and a backward difference approximation on the time co-ordinate. Equations 2 and 8 can be written in the common dimensionless, difference form

$$-\eta_{i-1/2}^2 \theta_{i-1}^{n+1}/\Delta\eta^2 + [R_c \eta_i^2/\Delta\tau + (\eta_{i+1/2}^2 + \eta_{i-1/2}^2)/\Delta\eta^2]\theta_i^{n+1} -$$
$$\eta_{i+1/2}^2 \theta_{i+1}^{n+1}/\Delta\eta^2 = \delta C \eta_i^2 \exp(-1/\theta_i^n) + \eta_i^2 R_c \theta_i^n/\Delta\tau \qquad (13)$$

The relevant difference equations were then solved numerically using a fully implicit backward-difference scheme and iterating at each time step for the non-linear terms.

5. RESULTS

5.1 Pyrolysis Times: Instantaneous Escape of Volatile Matter: The results of earlier attempts to predict pyrolysis times and their variation with particle size with only chemical kinetics in the model and diffusional escape omitted, are presented in Fig. 2, with the experimental data of Fig. 1 included for comparison. These results are obtained by selecting $D_i = \infty$.

It can be seen in Figure 2 that the predicted curve is sigmoid shaped -- largely under-predicting times for large particles (greater than 2000 microns) and over-predicting times for small particles. The shape of the curve also indicates that pyrolysis times are insensitive to the variation of particle size in the small size range. The predictions are good for a small intermediate range (1000 microns to 2000 microns) but this agreement would now appear to be fortuitous. Increasing the kinetic rate by decreasing the activation energy from 30 kcal/mole to 25 kcal/mole did not improve the predictions. Though the pyrolysis times were reduced, the calculations still over-predicted times for small particles and under-predicted for large particles.

Examination of the calculated temperatures of the small particles during pyrolysis showed that the particles would heat up to a final temperature of about 950 K without significant pyrolysis, and that they then pyrolyzed at constant temperature; it was also found that the temperature gradients within the small particles (less than 500 microns) were insignificant. At constant temperature, pyrolysis is a volumetric process; the pyrolysis time then depends on the temperatures of the particles, and is independent of the particle size. The final temperatures attained by the small particles were about the same. This is the source of the flattening of the predicted curve in the small particle range. Although this supports the common belief that pyrolysis being independent of particle size below 100 microns, it is clearly contrary to the facts. It also emphasizes the inadequacies of the assumptions, and the need to re-examine them (following).

The under-prediction of pyrolysis times for large particles indicated by Fig. 2 suggests that escape time is important for such particles. When this assumption was incorporated in the model equations, it was then found to be applicable to all particle sizes.

5.2 Pyrolysis Times: Diffusion of Pyrolysis Products: With diffusional escape included in the model, the results illustrated in Fig. 3 were obtained. Figure 3 shows 3 diffusional escape times, using diffusion coefficients of 10^{-3}, 10^{-4}, 10^{-5} cm^2/sec. To obtain the lines shown, an adjustment to the velocity constant coefficients was necessary; otherwise, the calculated times were high by one or two orders of magnitude. The fit was obtained by reducing the activation energy from 30 to 12 kcal/mole. This is substantially below the values quoted for individual reactions in a multiple pyrolysis model, but it is of the typical magnitude found by fitting a single step to multiple reactions [3].

The fit then shows that the separate trends of the large and the small diameters can be accounted for by attributing the major differences to the different diffusion rates. Second order variations, to the extent that these can be identified, can be attributed to differences in the actual kinetics.

6. DISCUSSION

The principal problem then remaining is to account for the very different diffusion coefficients (by two orders of magnitude) between the "large" and the "small" particles. It is not a matter of oxidizing or non-oxidizing ambient atmospheres since the small particle group include some values obtained in flames. Two possible explanations can be advanced. One factor that can be significant is the extent of swelling. It is now generally agreed that (small) particles heating rapidly swell only marginally or not at all [19]. With the large particles, swelling was very evident -- with the exception of the anthracite -- with measured swelling

factors average 1.5 for all the coals (except for the anthracite) [20]. This explanation, however, does not account for the behavior of the non-swelling anthracite whose large-particle pyrolysis times do not differ significantly from those of the bituminous coal.

If swelling is not responsible for the differences we must postulate, it would seem, some unidentified differences in the mechanical properties of the coals that are solely particle size dependent, and which include anthracite. One such property could be microcracks in all particles greater than about 100 microns so that the VM escape rate in smaller particles can be diffusion-dominated, generating the left-hand data set of Fig. 3. If the VM escape through the microcracks of larger particles was then instantaneous, all pyrolysis times of particles about 100 microns would level off at about 0.5 sec.,and the line would become horizontal in the right-hand segment of the graph. If escape through the microcracks is not instantaneous, and is governed by some form of diffusion mechanism, the line to the right would then rise with particle size, as it does in fact.

The same qualitative result is obtained if we assume, alternatively, an array of microcracks at all particle sizes, and with microcrack size diminishing with particle size.

This is all hypothetical at this time but it does indicate the line of thinking that would appear to be necessary at this time to account for the observed results.

7. CONCLUSIONS

1. The experimental data on the variation of pyrolysis times with diameter clearly show influence of particle size over the size range 20 to 4000 microns.
2. The dependence of pyrolysis times on diameter is interpreted at this time as being due to the influence of (diffusional) escape in the pyrolysis mechanism. This is in agreement with conventional views of pyrolysis greater than 100 microns; but it contrary to those views for particles less than 100 microns.
3. A single line or band drawn (empirically) through all the data has a sigmoid (dog-leg) shape that cannot at this time be accounted for, theoretically, by any model that excludes diameter-dependent parameter coefficients.
4. The two extreme segments of the sigmoid curve can be predicted by arbitrarily assuming that values of a diffusion coefficient governing VM escape differ by two orders of magnitude.
5. Mechanistic reasons for any such difference in diffusion coefficients are not clear at this time. Some factors, such as the influence of the composition of the ambient atmosphere (oxidizing or non-oxidizing) can apparently be ruled out. A tentative explanation in terms of microcracks is suggested but this needs to be tested by approximate analytical developments and physical examinations.

ACKNOWLEDGEMENTS

We would like to acknowledge the support of Mr. J. Hickerson, Department of Energy (contract # DE-AC22-84PC-70768) and Dr. D. Seery, United Technologies Research Center (contract # 101404) in funding this project.

NOMENCLATURE

D_a : diffusion coeff. in air (cm^2/s)
D_p : diff. coeff. in particle (cm^2/s)
E^a : activation energy (kcal/mole)
k^p : rate constant (s^{-1})
k_o : preexponential factor (s^{-1})
m : mass conc. of VM (g/cc)
m_g^o : volatile generation rate ($g/cm^3 s$)
q_r : radiative heat flux ($cal/cm^2 s$)

r	: radial distance (cm)	r_o	: radius of a particle (cm)
R	: gas constant (cal/mole deg.K)	t	: time (s)
T	: Temperature (deg.K)		
T_o	: Initial Temperature (deg.K)	V	: volatile yield (%)
V^c	: ultimate volatile yield (%)	α_a	: thermal diffusivity in air
α^p	: thermal diffusivity in particle	ΔH	: heat of reaction (cal/gram)
r^p	: dimensionless radial distance	λ_a	: thermal conductivity of air
λ_p	: thermal conductivity of coal	σ_a	: density of air (gram/cc)
σ^p	: density of coal (gram/cc)	τ	: dimensionless time
θ^p	: dimensionless temperature		

REFERENCES

1. Essenhigh, R.H. The Influence of Coal Rank on the Burning Times of Single Coal Particles. Journal of Eng. for Power. 1963. pp.183-190.

2. Kallend, A.S and Nettleton, M.A. Burning of Volatile Matter from Single Coal Particles. Sonderdruck aus >> Erdol und Kohle. Erdgas. Petrochemie <<. 19. 1966. pp.354-356.

3. Anthony, D.B; Howard, J.B; Hottel, H.C and Meissner, H.P. Rapid Devolatilization of Pulverized Coal. Fifteenth Symp. (Int.) on Combustion. 1975. pp. 1303-1317.

4. Desypris, J; Murdoch, P and Williams, A. Investigation of the Flash Pyrolysis of some Coals. Fuel. 61. 1982. pp.807-816.

5. Howard, J.B and Essenhigh, R.H. Pyrolysis of Coal Particles in Pulverized Fuel Flames. I & EC Process Design and Development. 6. 1967. pp.74-84.

6. Kobayashi, H; Howard, J.B and Sarofim, A.F. Coal Devolatilization at High Temperatures. Sixteenth Symposium (Int.) on Combustion. 1977. pp.411-425.

7. Maloney, D.J and Jenkins, R.G. Coupled Heat and Mass Transport and Chemical Kinetic Rate Limitations during Coal Rapid Pyrolysis. Twentieth Symposium (International) on Combustion. 1984. p.1435-1443.

8. Niksa, S; Heyd, L.E; Russel, W.B and Saville, D.A. On the Role of Heating Rate in Rapid Coal Devolatilization. Twentieth Symp. (Int.) on Comb. 1984. pp.1445-1453.

9. Nsakala, N.Y; Essenhigh, R.H and Walker, P.L. Studies on Coal Reactivity: Kinetics of Lignite Pyrolysis in Nitrogen at 808 deg.C. Combustion Science and Technology. 1977. pp.153-163.

10. Peters, W and Bertling, H. Kinetics of the rapid Degasification of Coals. Fuel. 44. 1965. pp.317-331.

11. Scaroni, A.W; Walker, P.L and Essenhigh, R.H. Kinetics of Lignite Pyrolysis in an Entrained-Flow, Isothermal Furnace. Fuel. 60. 1981. pp.71-76.

12. Seeker, W.R; Samuelsen, G.S; Heap, M.P and Trolinger, J.D. The Thermal Decomposition of Pulverized Coal Particles. Eighteenth Symposium (International) on Combustion. 1981. pp.1213-1226.

13. Smoot, L.D; Horton, M.D and Williams, G.A. Propagation of Laminar Pulverized Coal-Air Flames. Sixteenth Symposium (Int.) on Combustion. 1977. pp.375-387.

14. Solomon, P.R; Serio, M.A; Carangelo, R.M and Markham, J.R. Very Rapid Coal Pyrolysis. Fuel. 65. 1986. pp.182-193.

15. Thring, M.W and Hubbard, E. H. Radiation from Pulverized-Fuel Flames. Paper#4 . Second conference on Pulverized Fuel, Nov.,1957. Inst. Fuel, London. 1957.

16. Ubhayakar, S. K; Stickler, D. B; Von Rosenberg, C. W and Gannon, R. E. Rapid Devolatilization of Pulverized Coal in Hot Combustion Gases. Sixteenth Symposium (International) on Combustion. 1977. pp.427-436.

17. Misra, M. K, M.S Thesis, Department of Mechanical Engineering, The Ohio State University, Columbus, Ohio. 1987.

18. Misra, M. K and Essenhigh, R. H, Pyrolytic Behavior of Coal Particle: Effect of Unsteady State Heating and Temperature Gradients. Paper# 10 presented at the Spring Technical Meeting, Central States Section, The Combustion Institute, Chicago, IL. May, 1987.

19. Discussion at the Workshop on "Fundamentals of Physical-Chemistry of Pulverized-coal combustion" held at Les Arcs (Bourg-Saint Maurice), France. July-August, 1986.

20. Essenhigh, R. H and Yorke, G. C, Reaction Rates of Single Coal Particles: Influence of Swelling, Shape, and Other Factors. Fuel. vol 44, May, 1965. pp.177-189.

Table 1: Pyrolysis Times from Drop-tube (DT) Heated -grid (HG), and Flame (F) Experiments.

Investigators	Particle Size (microns)	Heating Rate (deg.K/sec)	Pyrolysis Time (sec)	
Anthony [3]	53-83	10^4	0.1	HG
		3×10^3	0.3	
Nsakala [9]	64	9×10^3	0.2	DT
Niksa [8]	125	10^2-10^4	0.5	HG
Kobayashi [6]	37-44	$> 10^4$	0.1	DT
Howard [5]	< 200	10^4	0.2	F
Smoot [13]	21	10^4	0.05	F
Thring [15]	< 100	-	0.1	F
Ubhayakar [16]	< 74	$> 10^5$	0.011	DT
Seeker [12]	80	10^5	0.08	Shock Tube
Peter [10]	1200	200	3.5	-
Desypris [4]	126	-	0.5	HG
	44	-	0.5	
Maloney [7]	62	-	0.17	DT
Solomon [14]	53-74	10^4	0.064	DT
	44-74	3×10^4	0.02	
	44-74	4×10^4	0.023	

Table 2: Values of the volatile combustion constants (K_v and n).
(Source: Ref. 1)
(The errors in K_v are between 2 and 5% , the errors given against n are in percentage.)

COAL	VM% (d.a.f)	K_v (c.g.s units)	n
1. Stanllyd	9.9	44.6	1.82 ± 4.18%
2. Five ft.	14.9	80.0	2.32 ± 4.37%
3. Two ft. Nine	28.8	120.0	2.63 ± 3.33%
4. Red Vein	23.3	86.6	2.19 ± 4.22%
5. Garw	30.6	96.8	2.06 ± 2.14%
6. Silkstone	41.5	91.6	2.19 ± 3.86%
7. Winter	39.3	93.6	2.24 ± 3.18%
8. Cowpen	40.2	91.4	2.15 ± 3.28%
9. High Hazel	40.7	134.0	2.28 ± 2.79%
10. Lorraine	40.2	98.9	2.14 ± 2.55%

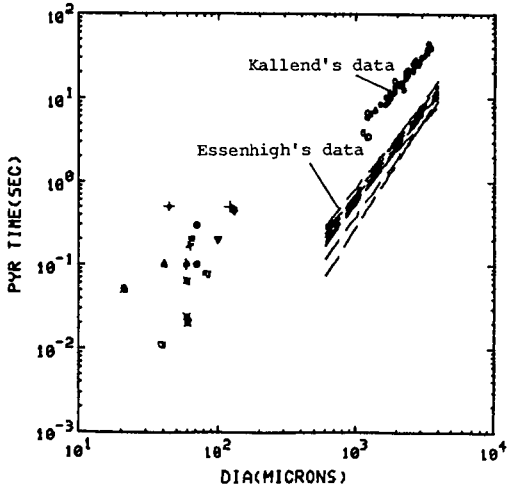

Figure 1. Experimental values of variation of total pyrolysis times with particle size. Values are listed in Tables 1 and 2.

● Anthony. ■ Nsakala. ♦ Niksa. ▼ Howard. ▲ Kobayashi. ✱ Smoot. ♦ Thring. ▼ Solomon. ✱ Maloney. + Desypris. ○ Ubhayakar. ○ Peters. ▽ Seeker.

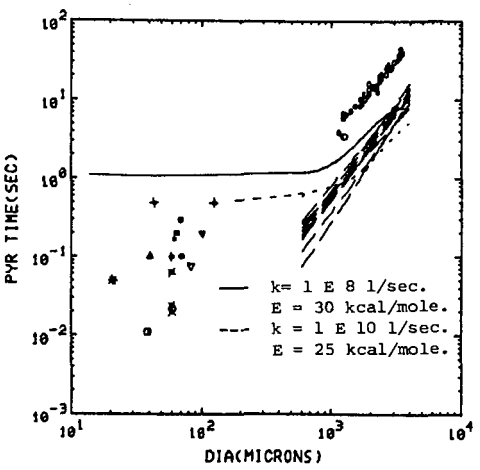

Figure 2. Comparison of the calculated and experimental variation of pyrolysis times with particle size. The calculations do not include the diffusional escape of VM.

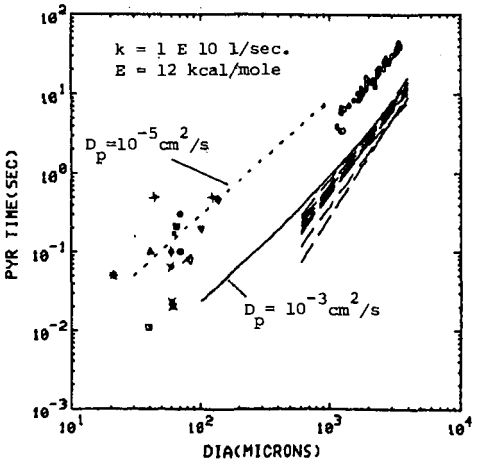

Figure 3. Comparison of calculated and experimental variation of pyrolysis times with particle size. The calculations include the diffusional escape of VM.

A MATHEMATICAL SIMULATION OF THE PYROLYSIS OF A MODEL ASPHALTENE

PHILLIP E. SAVAGE[1] AND MICHAEL T. KLEIN

DEPARTMENT OF CHEMICAL ENGINEERING
AND
CENTER FOR CATALYTIC SCIENCE AND TECHNOLOGY
UNIVERSITY OF DELAWARE
NEWARK, DE 19716

[1] PRESENT ADDRESS: UNIVERSITY OF MICHIGAN
DEPARTMENT OF CHEMICAL ENGINEERING
ANN ARBOR, MI 48109

INTRODUCTION

Reaction engineering experiments with coal or heavy oil fractions typically allow observation of only global kinetics and the yields of lumped product fractions; the controlling reaction fundamentals are obscured by the complexity of the reactant and its product spectra. This limitation has motivated experiments with model compounds to help resolve the fundamental reaction pathways, kinetics, and mechanisms involved. These fundamentals are of the model compound reactions, however, and their relation to the reactions of the moieties they mimic in a complex reactant can be vague. Model compound results are often used in the analysis of the reactions of coal or asphaltenes in a qualitative fashion. The object of this paper is to report on a mathematical model of asphaltene pyrolysis which serves as a quantitative bridge between model compounds and actual asphaltenes by combining model-compound deduced reaction pathways and kinetics with aspects of asphaltene structure.

BACKGROUND

Asphaltenes are operationally defined as a response to a solvent extraction protocol. However, the functional groups and chemical moieties they comprise have been probed by numerous spectroscopic and pyrolytic investigations (1-5), and structural scenarios typically include condensed aromatic and heteroaromatic cores to which are attached peripheral alkyl, naphthenic, and heteroatomic substituents. Several of these substituted aromatic cores, referred to as unit sheets, can be bonded together in macromolecular fashion to form an asphaltene particle.

Of the covalent bonds in asphaltene, those in heteroatomic peripheral substituents are the most thermally labile; they are also present in relatively low proportions. C-C bonds in aromatic rings, on the other hand, constitute a large fraction of asphaltene bonds, but they are stable even at very high temperatures. Aliphatic C-C bonds in alkylaromatic, alkylhydroaromatic, and alkylnaphthenic positions are both abundant and reactive and thus constitute the most prevalent thermally scissile groups in asphaltene. Therefore, the reactions (6-10) of the model compounds n-pentadecylbenzene, n-dodecylbenzene, n-butylbenzene, 2-ethylnaphthalene, n-tridecylcyclohexane, and 2-ethyltetralin, mimics of these scissile moieties, seemed a relevant probe of the thermal reactions of the basic hydrocarbon framework of asphaltenes. These model compound data were combined with asphaltene structural information to simulate the pyrolysis of a generic, hypothetical, fully hydrocarbon asphaltene. Structural data used in the model were selected from an overall understanding of asphaltene composition and constitution (8) and were not obtained from spectroscopic characterization of any particular asphaltene. Note however, that the model can readily incorporate structural data from any asphaltene of interest and simulate its pyrolysis specifically.

MODEL DEVELOPMENT

Reactant Asphaltene.

The simulated asphaltene is illustrated schematically in Figure 1. Asphaltenes were regarded (8) as a blend of hydrocarbon particles, defined as covalently bonded oligomers of unit sheets with a degree of polymerization ranging from 1 to 5. The unit sheets comprised between 2 and 30 six-membered rings which could, in turn, be either aromatic or saturated. The maximum number of aromatic rings in a unit sheet was 15, and the number of

saturated rings never exceeded the number of aromatic rings. Peripheral aromatic and saturated carbon atoms in a unit sheet were, respectively, 45% and 25% substituted by aliphatic chains containing from 1 to 25 carbon atoms. A fraction of these chains served as the covalent links which bonded unit sheets into particles, and the balance were terminal substituents.

Four probability distributions describing, respectively, the alkyl substituent chain lengths, the number of aromatic and the number of saturated rings in a unit sheet, and the degree of polymerization of asphaltene particles are displayed in Figure 2. These data were selected such that the average structural parameters for the reactant asphaltene were consistent with values reported in the literature.

In the simulations, the reactant asphaltene consisted of a collection of particles containing the model's basis of 10,000 unit sheets, assembled in a stochastic process. The first step of this assembly was to determine the number of unit sheets in each particle by comparing a random number between 0 and 1 with the integrated probability distribution describing the particle's degree of polymerization (i.e. Fig 2d). The numbers of aromatic and saturated rings in each of the unit sheets in the particle were then determined by comparing independent random numbers with the integrated probability distributions in Figures 2b and 2c. Each saturated ring in the unit sheet was then individually categorized as either hydroaromatic or naphthenic based on whether it was fused to an aromatic ring or exclusively to other saturated rings, respectively. This was accomplished by comparing a random number with the probability, P_H, of a saturated ring being fused to an aromatic ring. P_H was estimated from Equation 1 on the basis that the type of ring (saturated or aromatic) to which a saturated ring was fused was directly proportional to the number of aromatic, N_{ar}, or saturated, N_{nr}, rings in the unit sheet.

$$P_H = \frac{N_{ar}}{N_{ar} + N_{nr} - 1} \tag{1}$$

The numbers of internal and peripheral aromatic and saturated carbon atoms in the unit sheet, defined respectively as those bonded to 3 and to 2 other cyclic carbon atoms, were calculated according to the method of Hirsch and Altgelt (11,12). The number of peripheral atoms of each type was then multiplied by their appropriate degrees of substitution (0.45 and 0.25 for aromatic and saturated carbons, respectively) to calculate the number of peripheral positions containing substituents. The number of peripheral aromatic carbon atoms bearing alkyl chains was then calculated as the total number of substituted aromatic carbon atoms minus the number of peripheral aromatic carbon atoms in hydroaromatic rings. Assembly of the unit sheets was finally completed by comparing a random number with the integrated probability distribution in Figure 2a to determine the number of carbon atoms in each aliphatic substituent. The steps outlined above were repeated for each unit sheet until an entire particle had been constructed. Additional particles were then assembled until 10,000 unit sheets had been included.

Pyrolysis Simulation.

The model compound pyrolyses (8) revealed that ring-opening reactions were of minor consequence for even the saturated rings. Therefore, the polycyclic portion of the unit sheet was modeled as being thermally stable and, hence, conserved during pyrolysis. The only effect of pyrolysis was then to break C-C bonds in the peripheral alkyl substituents and the inter-unit sheet links.

Asphaltene pyrolysis therefore amounted to accounting for the temporal variation of the distribution functions of Figure 2. This was accomplished by 1.) developing differential rate equations for the three reactive moieties (i.e. alkylaromatic, alkylnaphthenic, and alkylhydroaromatic), 2.) integrating these equations numerically with model-compound-deduced rate constants as parameters, 3.) updating the integrated probability distributions to reflect the effects of pyrolysis, and 4.) using the updated distributions to stochastically assemble 10,000 unit sheets which represented the reaction products.

The rate of reaction of an alkylaromatic chain, A_i, of length i in a constant-volume batch reactor was given as Equation 2 where k_{A_i} is the first-order rate constant.

$$\frac{dA_i}{dt} = -k_{A_i} A_i + \sum_{j=1}^{25-i} \nu_{A_{i+j,i}} k_{A_{i+j}} A_{i+j} \tag{2}$$

The two terms on the right hand side account for, respectively, the cleavage of alkylaromatic substituents with i carbon atoms, and the formation of alkylaromatics with i carbons from alkylaromatics containing i+j carbon

atoms where $\nu_{A_{i+j,j}}$ is the stoichiometric coefficient. Completely analogous equations described the rate of reaction of the alkylnaphthenic, N_i, and alkylhydroaromatic, H_i, moieties.

The rate of formation of aliphatic products, AP_i, with i carbon atoms is given by Equation 3, where k and ν are rate constants and stoichiometric coefficients, respectively. Note that secondary reactions of the primary aliphatic products were neglected.

$$\frac{dAP_i}{dt} = \sum_{j=1}^{25-i} (\nu_{A_{i+j,j}} k_{A_{i+j}} A_{i+j} + \nu_{H_{i+j,j}} k_{H_{i+j}} H_{i+j} + \nu_{N_{i+j,j}} k_{N_{i+j}} N_{i+j}) \tag{3}$$

Finally, cleavage of the inter-unit sheet links in the oligomeric particles was described by Equation 4. In modeling the depolymerisation kinetics, all inter-unit sheet linkages were treated as alkylaromatic chains. That is, the rate constant for breaking an inter-unit link was the same as that for cleaving an alkylaromatic substituent.

$$\frac{dP_i}{dt} = -k_{A_i} P_i (i-1) + \sum_{j=1}^{5-i} 2k_{A_{i+j}} P_{i+j} \tag{4}$$

The two terms on the right hand side account for the depolymerization of particles containing i unit sheets, P_i, and the formation of such particles from those with more than i unit sheets, P_{i+j}, respectively.

The rate constants and stoichiometric coefficients required for numerical solution of Equations 2-4 were obtained from the model compound pyrolyses (6-9). For example, the initial product selectivities in pentadecylbenzene (PDB) pyrolysis (6,9) showed that bond scission occurred at the β position about 35% of the time, at the γ position 15% of the time, and at each of the other 12 bonds roughly 4% of the time. These relative proportions for cleavage of each aliphatic bond were modelled to apply to all other alkylaromatics. Similarly, the initial selectivities observed for tridecylcyclohexane (TDC) and 2-ethyltetralin (2ET) pyrolyses (8) provided the stoichiometric coefficients for the alkylnaphthenic and alkylhydroaromatic moieties, respectively.

A unique rate constant for each of the 3 reactive moieties containing from 1 to 25 aliphatic carbons was calculated from the rate constant for the relevant model compound scaled by the square root of the carbon number, as suggested by the apparent first-order rate constant for a Rice-Herzfeld (13) chain. For example, all 15 carbon atom alkylaromatic chains were assumed to follow the pyrolysis kinetics of PDB, and rate constants for alkylaromatic chains with i carbon atoms were calculated as

$$k_{A_i} = k_{PDB} (\frac{i}{15})^{1/2} \tag{5}$$

Although only approximate, Equation 5 correlated available experimental data quite well (8).

To summarise, this mathematical model simulated asphaltene pyrolysis by simultaneously solving 105 differential rate equations; 25 each for cleavage of alkylaromatic, alkylnaphthenic, and alkylhydroaromatic moieties, 25 for the formation of aliphatic products, and 5 for depolymerisation of asphaltene particles. The kinetic parameters in these equations were deduced through model compound pyrolyses. The structural data in the probability distributions, shown in Figure 2 for the reactant asphaltene, were then updated to reflect the effects of pyrolysis, and 10,000 unit sheets were assembled as reaction products.

Reaction Products.

The simulated pyrolyses produced aliphatics, via scission of peripheral moieties on the asphaltenic unit sheet, and product particles containing at least one unit sheet. The product particles were stochastically assembled using the procedure described previously for the reactant asphaltene particles, and they differed from their precursors only in their degree of polymerization and in the length and number of their terminal aliphatic constituents. The polycyclic portion of the unit sheet was thermally stable and hence unaltered by pyrolysis.

To allow comparison with experimentally observed (9,10) temporal variations of solubility-based product fractions from asphaltene pyrolysis, each reaction product from the simulated pyrolyses was assigned to either a gas, maltene, asphaltene, or coke product fraction. Aliphatic products were assigned to the gas fraction if they contained 4 or fewer carbon atoms and to the maltene fraction if they contained more than 4 carbon atoms. The product particles were assigned to one of the solubility-based product fractions on the basis of combinations

of molecular weight and H/C atomic ratio as shown in Table 1. These two parameters provided a physically significant yet convenient means of correlating particle solubility with chemical composition and structure in this model.

MODEL RESULTS

The simulations were of the constant-volume, isothermal, batch pyrolyses of a generic asphaltene and not the particular off-shore California asphaltene used in the experiments. Quantitative agreement between the model and experimental results should not be expected in all cases and treated as a coincidence when found. Note that detailed spectroscopic analysis of any one asphaltene could permit prediction of its reactions, however. Model predictions are presented in terms of the temporal variation of average structural parameters and solubility-based product fractions.

Structural Parameters.

The model monitored the number of each type of aliphatic, aromatic, and naphthenic carbon and hydrogen atoms in the 10,000 unit sheets so that average structural parameters could be determined for the collection of asphaltene particles. The values of selected structural parameters for the reactant asphaltene are reported in Table 2 and are clearly consistent with the ranges of these parameters typically reported in the literature (2,3,14-19) for petroleum asphaltenes.

Figure 3 presents the temporal variation of the particle and unit sheet number average molecular weights, whereas Figure 4 displays the particle molecular weight distribution parameteric in time for simulated asphaltene pyrolysis at 425°C. The particle molecular weight decreased very rapidly and approached the unit sheet average molecular weight, suggesting essentially complete asphaltene depolymerization. Figure 4 shows that the molecular weight distribution for the reactant asphaltene was broad and possessed a high average value and that a significant reduction in average molecular weight and a narrowing of the distribution occurred for asphaltene pyrolysis even at short reaction times.

Experimental data are lacking for a direct quantitative comparison of the model results in Figures 3 and 4, but previous experiments (8) do allow limited scrutiny as follows. Asphaltene pyrolyses at 400°C for 30 min significantly reduced the average molecular weight of the sulfur- and vanadium-containing compounds in asphaltene and shifted the molecular weight distribution to lower values. These results, if generally true for all of the asphaltenic constituents, are in qualitative accord with the model's predictions.

The temporal variation of the H/C atomic ratio and the fraction of carbon atoms being aromatic, f_a, from simulated asphaltene pyrolyses at 425°C are portrayed on Figure 5. The H/C atomic ratio decreased from 1.20 initially to 0.85 at 120 min. The value of f_a, on the other hand, increased from an initial value of 0.42 to 0.61 at 120 min. The predicted variation of the H/C ratio is in good accord with the experimental results from asphaltene pyrolysis at 400°C shown in Figure 6. No experimental data were available for comparison with the temporal variation of f_a.

Product Fractions.

Figure 7 presents the temporal variations of the yields of the gas, maltene, asphaltene, and coke product fractions from simulated asphaltene pyrolyses at 400, 425, and 450°C. Experimental data are provided in Figure 8 for comparison. The simulations at 400°C predicted the experimentally observed induction period for coke production, and maltene and gas yields of the correct order. No experiments were performed at 425°C, but the results of simulated pyrolyses at this temperature closely resembled the experimental results at 400°C. This corroborates the qualitative trends predicted by the model, and further suggests that the model of a generic asphaltene underpredicted the reactivity of the off-shore California asphaltene used in the experiments. The agreement between the model predictions and the experimental temporal variations of the product fractions at 450°C was almost quantitative. Essentially complete asphaltene conversion at 30 minutes, an ultimate coke yield of about 60% that decreased with time, and an ultimate yield of maltenes and gases of about 40% are all common features.

DISCUSSION

The model predictions were consistent with the available experimental data on a qualitative basis without exception, and on a quantitative basis in several instances. This agreement between model and experimental

results is striking because the model deals with a simplified asphaltene structure, includes only model-compound-deduced reaction pathways and kinetics, and contains no kinetics parameters regressed from experiments with actual asphaltenes. The overall consistency of the experimental and simulated asphaltene pyrolyses suggest that the model included many key features of asphaltene structure and its thermal reactivity, and that the pyrolysis kinetics of the model compounds mimicked those of the related moieties in asphaltene.

The model results showed that dealkylation of the asphaltene unit sheets caused the particles to become increasingly hydrogen deficient and more aromatic thereby suggesting an attendant change in their toluene-solubility. Thus as reactant asphaltenes, toluene soluble because of their aliphaticity, were cleaved of their peripheral substituents their toluene solubility diminished, and they eventually appeared as coke in the pyrolysis simulation. The modeling results thus demonstrate that severe overreaction of primary products is not necessary to predict high yields of coke. This corroborates our previous interpretation (10) of the coke fraction as, mainly, a primary pyrolysis product containing the polycyclic cores of asphaltenic unit sheets.

Finally, the model results also permit speculation into the role of pyrolysis in nominally catalytic asphaltene hydroprocessing reactions. The simulations showed that asphaltene depolymerization occurred even at short reaction times and that many particles existed as single unit sheets rather than covalently bonded oligomers thereof. These individual asphaltene unit sheets, which are much smaller than the macromolecular particles, will be major participants in catalytic reactions because they can more readily diffuse within the porous catalyst. This suggests that catalytic hydroprocessing at high temperatures will be of thermally derived asphaltene fragments and not the asphaltene particle itself.

LITERATURE CITED

1 Yen, T. F. in Chemistry of Asphaltenes, ACS Adv. Chem. Ser. No. 195 **1981**, 39.

2 Yen, T. F., Wu, W. H., Chilingar, G. V. *Energy Sources* **1984**, 7, 203.

3 Yen, T. F., Wu, W. H., Chilingar, G. V. *Energy Sources* **1984**, 7, 275.

4 Speight, J. G., Moschopedis, S. E. in Chemistry of Asphaltenes, ACS Adv. Chem. Ser. No. 195 **1981**, 1.

5 Koots, J. A., Speight, J. G. *Fuel* **1975**, 54, 179.

6 Savage, P. E., Klein, M. T. *Ind. Eng. Chem. Research* **1987**, in press.

7 Savage, P. E., Klein, M. T. *Ind. Eng. Chem. Research* **1987**, 26, 374.

8 Savage, P. E. *Ph.D. Dissertation* University of Delaware **1986**

9 Savage, P. E., Klein, M. T., Kukes, S. G. *ACS Div. Fuel Chem. Prepr.* **1985** 30, 408.

10 Savage, P. E., Klein, M. T., Kukes, S. G. *Ind. Eng. Chem. Process Des. Dev.* **1985**, 24, 1169.

11 Hirsch, E., Altgelt, K. H. *Anal. Chem.* **1970**, 42, 1330.

12 Hirsch, E. *Anal. Chem.* **1970**, 42, 1326.

13 Rice, F. O., Herzfeld, K. F. *J. Am. Chem. Soc.* **1934**, 56, 284.

14 Ali, L. H., Al-Ghannam, K. A. *Fuel* **1981**, 60, 1043.

15 Boduszynski, M. M., Chadha, B. R., Szkuta-Pochopien, T. *Fuel* **1977**, 56, 443.

16 Speight, J. G. *Fuel* **1970**, 49, 134.

17 Speight, J. G. *Fuel* **1971**, 50, 102.

18 Suzuki, T., Itoh, M., Takegami, Y., Watanabe, Y. *Fuel* **1982**, 61, 402.

19 Yen, T. F. *Energy Sources* **1974**, 1, 447.

TABLE ONE

CRITERIA FOR ASSIGNING PARTICLES TO PRODUCT FRACTIONS

Criteria	Product Fraction	Operational Definition
MW < 300 and H/C > 1.0	Maltene	heptane - soluble
MW > 300 and H/C > 1.0	Asphaltene	heptane - insoluble
MW < 300 and H/C < 1.0		toluene - soluble
MW > 300 and H/C < 1.0	Coke	toluene - insoluble

TABLE TWO

AVERAGE STRUCTURAL PARAMETERS FOR PETROLEUM ASPHALTENE

Parameter	Significance	Model	Literature (1-5, 14-19)
H/C	atomic ratio	1.20	1.09 - 1.29
f_a	fraction of C atoms in aromatic rings	0.42	0.30 - 0.61
f_n	fraction of C atoms in saturated rings	0.13	0.06 - 0.24
H_a	fraction of H atoms in aromatic rings	0.09	0.04 - 0.11
H_n	fraction of H atoms in saturated rings	0.16	0.16 - 0.19
C_p/C_a	peripheral aromatic carbons / total aromatic carbons (shape of aromatic core)	0.48	0.31 - 0.55
C_s/C_{sa}	total saturated carbons / saturated carbons α to ring (average alkyl chain length)	4.93	3.1 - 8.4
C_{sa}/C_p	saturated carbons α to ring / peripheral aromatic carbons (degree of substitution of aromatics in unit sheet)	0.45	0.39 - 0.65

Figure 1: Structural Hierarchy in Pyrolysis Model

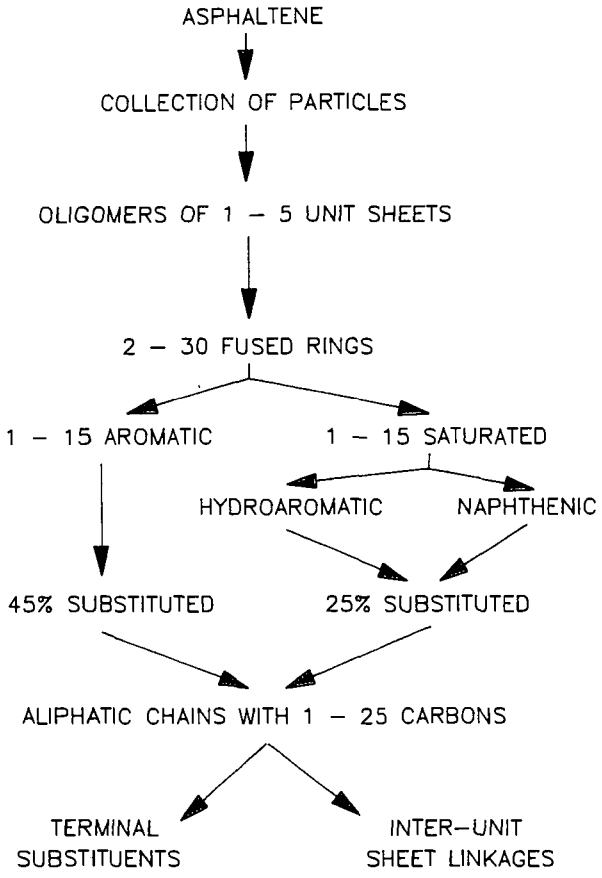

Figure 2: Integrated Distributions for Elements of Asphaltene Structure

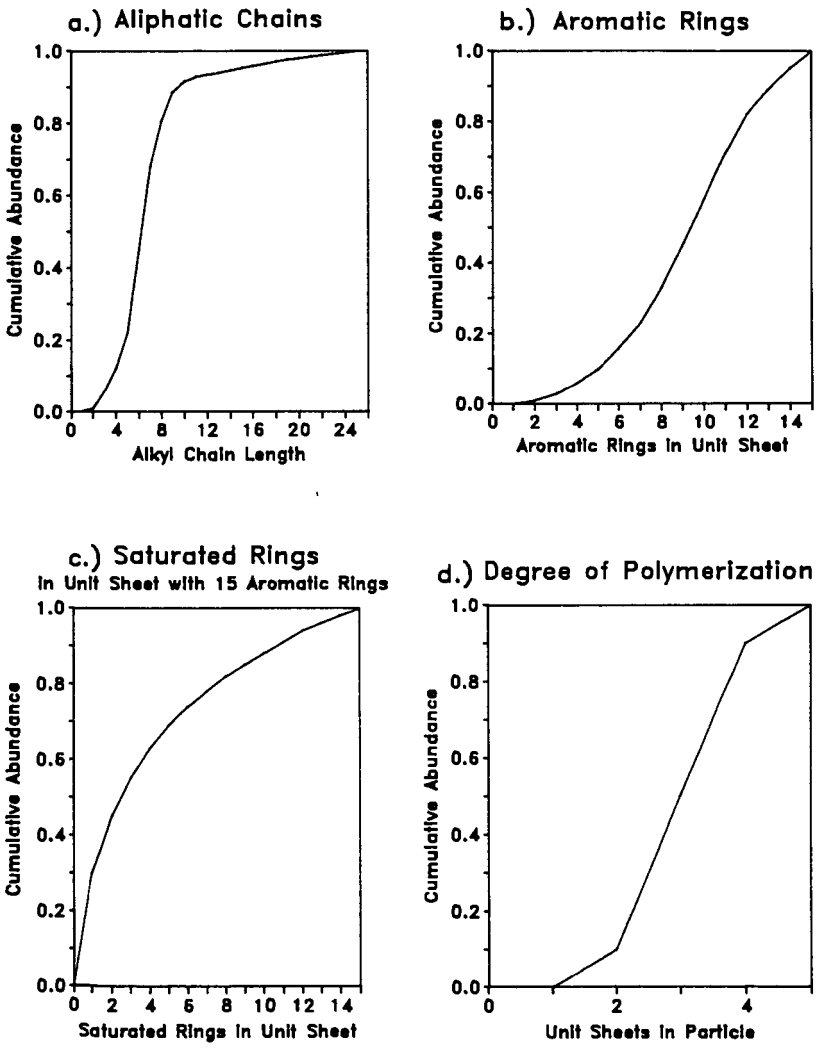

Figure 3: Temporal Variation of MW

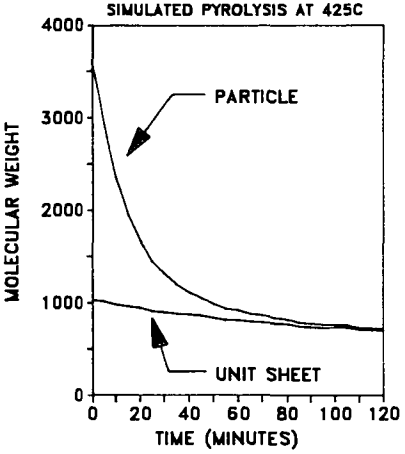

Figure 4: Molecular Weight Distributions

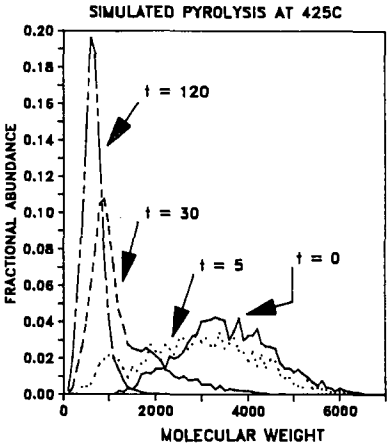

Figure 5: Temporal Variation of H/C and f_a

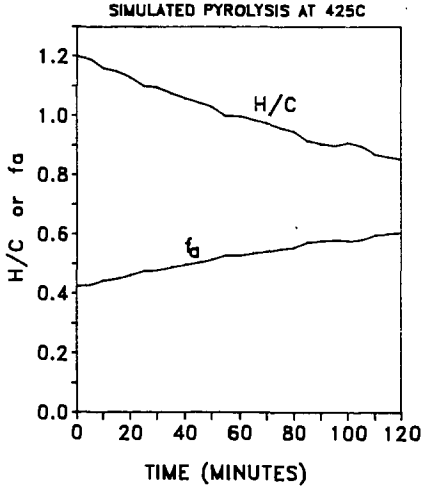

Figure 6: Temporal Variation of H/C

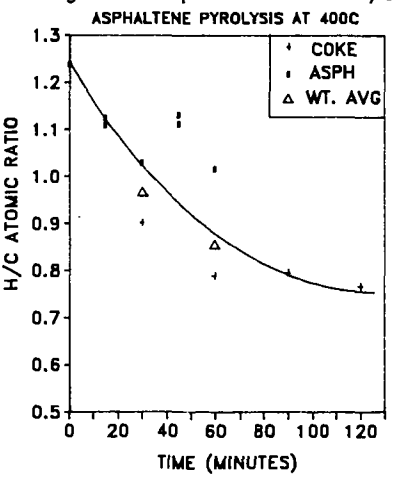

Figure 7: Temporal Variation of Product Fractions
from Simulated Asphaltene Pyrolysis

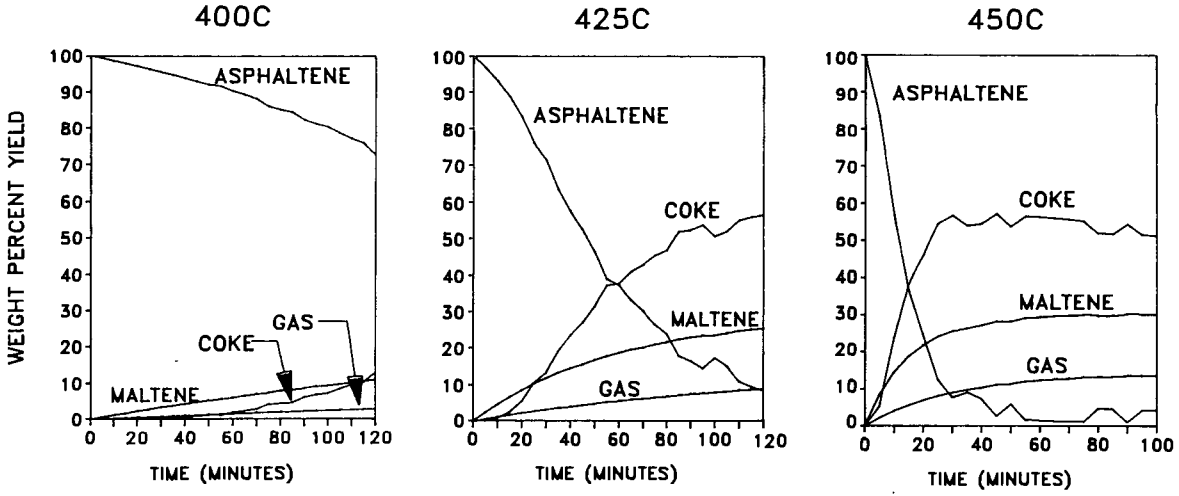

Figure 8: Temporal Variation of Product Fractions from Asphaltene Pyrolysis

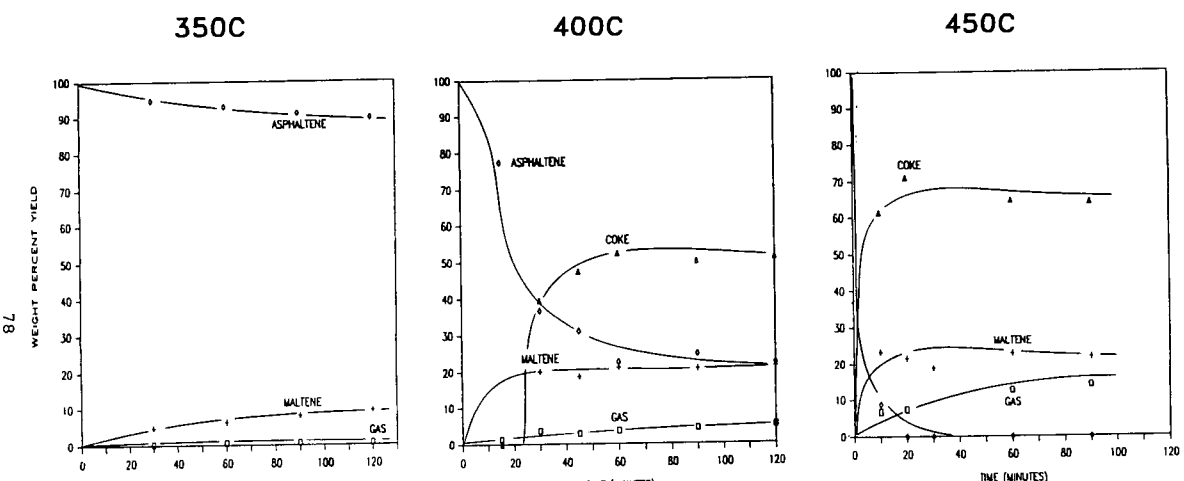

INTERPRETING RAPID COAL DEVOLATILIZATION AS AN EQUILIBRIUM FLASH DISTILLATION DRIVEN BY COMPETITIVE CHEMICAL KINETICS

Stephen Niksa

High Temperature Gasdynamics Laboratory
Mechanical Engineering Department
Stanford University
Stanford, CA 94305

Introduction

As the ambient pressure for a coal devolatilization process is reduced, ultimate yields of tar increase substantially. For high volatile bituminous coals, tar yields from vacuum pyrolysis can be fifty percent greater than from high-pressure pyrolysis. This behavior has long been attributed to competitive secondary chemistry in the gas phase occurring on a time scale dictated by transport of volatile matter through the particle surface. Among the escape mechanisms compatible with coal's complex physical structure, bulk and Knudsen pore diffusion, external film diffusion, continuum flow, and bubble growth in viscous melts have been treated, as reviewed recently by Suuberg (1).

These models correlate the reduced ultimate yield for increased ambient pressures, but important features of pyrolysis over a range of pressure remain unexplained. First, the measured rate of weight loss for identical thermal histories is the same for pressures between vacuum and 3.45 M Pa (2). Second, tar deposition exerts a negligible influence on both yields and evolution rates throughout all pressures of practical interest, based on the scaling from an independently-measured tar cracking rate and a measured volatiles escape rate (3). Third, the molecular weight distributions (MWD) of tar shift toward lower molecular weights as the ambient pressure is increased (1,4,5).

The reaction model introduced here (FLASHKIN) correlates the reduced ultimate yields, predicts evolution rates which are independent of pressure, and explains the observed shifts in tar MWD for varied ambient pressures. It interprets coal devolatilization as a single-stage equilibrium flash distillation driven by competitive chemical kinetics. While the mathematical formulation accommodates rate-limiting mass transport resistances, homogeneous chemistry is excluded and mass transport resistances are deemed negligible for the particle sizes considered in the comparisons with data. In this respect, FLASHKIN advances a minority viewpoint rooted in the parallels between pyrolysis and evaporative drying drawn by Peters and Bertling (6), and the aspects of phase equilibrium included in the models of James and Mills (7) and Niksa (8).

Reaction Mechanisms

The reaction mechanisms in FLASHKIN develop an analogy between coal pyrolysis and a single-stage equilibrium flash distillation. In any flash distillation, an equilibrium relation (such as Raoult's law in the simplest case) describes the partitioning of chemical species into the vapor and condensed phases at fixed pressure and temperature. The portion of the feedstream which evaporates is determined by a mole balance among the feed and product streams. Usually the composition and throughput of the feedstream and the temperature and pressure of the flash chamber are known, so that the composition and efflux of the vapor and liquid streams can be determined.

In the coal pyrolysis reaction system, there is no feedstream per se; rather, the coal macromolecule disintegrates into fragments which range in size from hydrocarbon gases having an average molecular weight of 25 g/mole to polymeric pieces of coal of molecular weight to, perhaps, 10^4-10^6 g/mole. The rate at which theses species are introduced into the system is determined by the primary thermal reactions.

The flash chamber is, of course, the porous fuel particle. In softening coals, the vapor is fully dispersed throughout the melt as bubbles in a viscous liquid; otherwise, the vapor is dispersed throughout a pore system which delineates solid subunits of a few hundred angstroms in size (the size of mesopores). Regardless of the form of the condensed phase, we assume that their composition is uniform throughout the particle, because the characteristic dimension of the subunits of condensed matter is so small. The temperature of the system is externally imposed and, under the restriction of negligible internal heat transfer resistances, the particle is isothermal. But the internal pressure reflects the reaction dynamics. In actuality, the internal pressure reaches a level compatible with the generation rate of gases and the resistance to escape. Despite the modeling discussed earlier, the internal pressure remains ambiguous because coal's physical structure admits several plausible transport mechanisms, and also because the transport coefficients are uncertain. We assert that the time scale for mass transport is much shorter than the primary decomposition time, as applicable to continuum flow driven by a pressure gradient, and deduce that the internal and ambient pressures are nearly equivalent.

Since the primary decomposition fragments encompass light gases and high polymers, the vapor is regarded as a binary mixture of (a) noncondensibles, restricted to molecular weights below 100 to represent light gases, and (b) a continuous mixture of vapor fragments of molecular weight from 100 to infinity, to represent tar. The tar vapor is represented by a continuous MWD. The condensed phase is envisioned as a binary mixture of nonvolatile char and a continuous mixture of evaporating com-

pounds of molecular weight greater than 100; again, the condensed-phase continuous mixture is represented by a continuous MWD.

Equilibrium is asserted between the vapor and condensed continuous mixtures on the basis of scaling the molar concentrations in the vapor and condensed phases. Since the densities of gaseous and condensed species differ by three to four orders of magnitude, the accumulation of vapor within the particle is entirely negligible. In other words, the vapor composition is in quasi-steady equilibrium with the changing condensed phase composition. The time scale on which the phase equilibrium is established is the shortest in the system.

The compositions of the continuous mixtures in the vapor and condensed phases are related by a generalization of Raoult's law. This simple form is in keeping with the lack of data on high molecular weight coal products such as tar. Nevertheless, the formulation in FLASHKIN is more advanced than previous renderings of Raoult's law in pyrolysis modeling (7-9).

Until very recently, multi-component phase equilibrium was analyzed in terms of discrete pseudo-components presuming that basic thermodynamic relations expressed in terms of the mole fractions of the species apply, computational burdens notwithstanding. Their obvious limitation is that discrete mole fractions for mixtures as complex as coal tar are impossible to measure. "Continuous thermodynamics" circumvents this deficiency by recasting the conditions for phase equilibria in terms of continuous distributions of macroscopic characteristics such as aromaticity, carbon number, normal boiling point and, most pertinent to this model, molecular weight. Recent publications by Prausnitz and coworkers (10,11) and Ratzsch and Kehlen (12) develop the results used in FLASHKIN and access the literature on the general theory.

Finally, to complete the analogy between pyrolysis and a flash distillation, the efflux of vapor and liquid "products" must be specified. The efflux of vapor species is simply the sum of the evolution rates of gas and tar. Within the constraints of negligible mass transport restrictions and negligible vapor accumulation noted above, the escape rate of light gases must match the generation rate of gases from the primary thermal reactions; i. e., gases escape at their rate of production by chemical reaction. The tar evolution rate is also specified by this rate, with the additional constraints that mole fractions for the binary vapor sum to unity, and that phase equilibrium is maintained.

Of course, no condensed phase species leave the particle. But their efflux rate is analogous to the rate at which the condensed continuous mixture forms an involatile char. Lacking guidance from experiment, we assume that the char formation rate is independent of the molecular weight of the components in the mixture.

The basic structure of coal pyrolysis, especially tar evolution, shares many similarities with a single stage equilibrium flash distillation. The amount of tar in the vapor phase within the fuel particle is in equilibrium with a continuous mixture of high molecular weight fragments in either the solid subunits or viscous melt. Generation rates and the efflux of intermediates and products are established by chemical reaction rates. As elaborated in the full paper, the evolution rates of tar and light gases, and the tar MWD are completely specified by closing the mole balance among the reaction species.

References

1. Suuberg, E. M., in "Chemistry of Coal Conversion" (Ed. R. H. Schlosberg), Plenum Press, NY, 1985, pp. 67-120.

2. Niksa, S., Russel, W. B., and Saville, D. A., Nineteenth Symp. (Int.) on Comb., The Combustion Institute, Pittsburgh, 1982, p. 1151.

3. Niksa, S., Combust. Flame 66, 111 (1986).

4. Unger, P. E. and Suuberg, E. M., Fuel 63, 606 (1984).

5. Suuberg, E. M., Unger, P. E., and Lilly, W. D., Fuel 64, 966 (1985).

6. Peters, W. and Bertling, H., Fuel 44, 317 (1965).

7. James, R. K. and Mills, A. F., Lett. Heat Mass Transf. 5, 1 (1976).

8. Niksa, S. "Time Resolved Kinetics of Rapid Coal Devolatilization," Ph. D. Thesis, Department of Chemical Engineering, Princeton University, Princeton, NJ, 1982.

9. Unger, P. E. and Suuberg, E. M., Eighteenth Symp. (Int.) on Comb., The Combustion Institute, Pittsburgh, 1981, p. 1203.

10. Cotterman, R. L., Bender, R., and Prausnitz, J. M., Ind. Eng. Chem. Process Des. Dev. 24, 194 (1985).

11. Cotterman, R. L. and Prausnitz, J. M., Ind. Eng. Chem. Process Des. Dev. 24, 434 (1985).

12. Ratzsch, M. T. and Kehlen, H., Fluid Phase Equil. 14, 225 (1983).

A GENERAL MODEL OF COAL DEVOLATILIZATION

P.R. Solomon, D.G. Hamblen, R.M. Carangelo, M.A. Serio and G.V. Deshpande

Advanced Fuel Research, Inc., 87 Church St., East Hartford, CT 06108 USA

INTRODUCTION

Coal devolatilization is a process in which coal is transformed at elevated temperatures to produce gases, tar* and char. Gas formation can be related to the thermal decomposition of specific functional groups in the coal. Tar and char formation is more complicated. It is generally agreed that the tar formation includes the following steps which have been considered by a number of investigators.

1. The rupture of weaker bridges in the coal macromolecule to release smaller fragments called metaplasts (1).

2. Possible repolymerization (crosslinking) of metaplast molecules (2-14).

3. Transport of lighter molecules to the surface of the coal particles by diffusion in the pores of non-softening coals (5,8,15,16) and liquid phase or bubble transport in softening coals (17-19).

4. Transport of lighter molecules away from the surface of the coal particles by combined vaporization and diffusion (4,14).

Char is formed from the unreleased or recondensed fragments. Varying amounts of loosely bound "guest" molecules, usually associated with the extractable material, are also released in devolatilization.

The combined chemical and physical processes in devolatilization were recently reviewed by Gavalas (20) and Suuberg (21). While gas formation can be accurately simulated by models employing first order reactions with ultimate yields (3,22-29), success in mechanistic modeling of tar formation has been more limited. Predicting tar formation is important for many reasons. Tar is a major volatile product (up to 40% of the coal's weight for some bituminous coals). In combustion or gasification, tar is often the volatile product of highest initial yield and thus controls ignition and flame stability. It is a precursor to soot which is important to radiative heat transfer. The process of tar formation is linked to the char viscosity (9,17,30,31) and subsequent physical and chemical structure of the char and so is important to char swelling and reactivity. Also, because they are minimally disturbed coal molecule fragments, primary tars provide important clues to the structure of the parent coal (27,28,32).

This paper presents a general model for coal devolatilization which considers the evolution of gas, tar, char and guest molecules. The general model combines two previously developed models, a Functional Group (FG) model (25-29) and a Devolatilization-Vaporization-Crosslinking (DVC) model (12,13,33-36). The FG model considers the parallel independent evolution of the light gas species formed by the decomposition of functional groups. Alternatively, functional groups can be released from the coal molecule attached to molecular fragments which evolve as

*Tar is defined as the room temperature condensibles formed during coal devolatilization.

tar. The kinetic rates for the decomposition of each functional group and for tar formation have been determined by comparison to a wide variety of data (25-29). To a first approximation, these rates are insensitive to coal rank. The FG model uses an adjustable parameter to fit the total amount of tar evolution. This parameter depends strongly on the details of the time-temperature history of the sample, the external pressure, and the coal concentration and, therefore, varies with the type of experiment performed.

The variation in tar yield with the above mentioned parameters can be predicted by the DVC model (12,13,33-36). In the DVC model, tar formation is viewed as a combined depolymerization and surface evaporation process in which the pyrolytic depolymerization continually reduces the weight of the coal molecular fragments through bond breaking and stabilization of free radicals, until the fragments are small enough to evaporate and diffuse away from the surface. This process continues until the donatable hydrogens are consumed. Simultaneously, crosslinking can occur. The model employs a Monte Carlo technique to perform a computer simulation of the combined depolymerization, vaporization and crosslinking events. Until now, internal mass transport limitations have not been included. However, current research shows that considering the transport limitations of surface evaporation and film diffusion alone are not sufficient to predict the reduced tar yields when devolatilization occurs at low temperatures. An empirical expression for internal transport has, therefore, been added to the DVC model.

These two models have been combined to eliminate their respective deficiencies. The DVC model is employed to determine the yield of tar and molecular weight distribution in the tar and char. The FG model is used to describe the gas evolution, and the functional group compositions of the tar and char. The crosslinking is predicted by assuming that this event can be correlated with gas evolution.

The paper describes the two models and how they have been combined. The predictions of the FG-DVC model are compared to published data for product yields, extract yields, volumetric swelling ratio (determined by crosslink density) and molecular weight distributions for the devolatilizations of Pittsburgh Seam coal (2,3,9,12,28). The predictions are in good agreement with the data.

MODELS

General Description of Coal Devolatilization

The general outline of devolatilization employed in this work was recently presented by Solomon and Hamblen (27) and Serio et al. (28). Fig. 1 from Ref. 28 presents a hypothetical picture of the coal's or char's organic structure at successive stages of devolatilization. The figure represents: a) the raw coal, b) the formation of tar and light hydrocarbons during primary pyrolysis, and c) char condensation and crosslinking during secondary pyrolysis. The hypothetical structure in Fig. 1a represents the chemical and functional group compositions for a Pittsburgh Seam bituminous coal as discussed by Solomon (32). It consists of aromatic and hydroaromatic clusters linked by aliphatic bridges. During pyrolysis, the weakest bridges, labeled 1 and 2 in Fig. 1a, can break producing molecular fragments (depolymerization). The fragments abstract hydrogen from the hydroaromatics or aliphatics, thus increasing the aromatic hydrogen concentration. These fragments will be released as tar if they can get to a surface and vaporize, since they are small enough to vaporize under typical pyrolysis conditions, assuming the vaporization law proposed by Suuberg et al. (14) is correct. The

other two fragments are not small enough to vaporize.

The other events during primary pyrolysis are the decomposition of functional groups to release CO_2, light aliphatic gases and some CH_4 and H_2O. The release of CH_4, CO_2, and H_2O may produce crosslinking, CH_4 by a substitution reaction in which the attachment of a larger molecule releases the methyl group, CO_2 by condensation after a radical is formed on the ring when the carboxyl is removed and H_2O by the condensation of two OH groups to produce an ether link (labeled 3 in Fig. 1b). The crosslinking is important to determine the release of tar and the visco-elastic properties of the char.

The end of primary pyrolysis occurs when the donatable hydrogen from hydroaromatics or aliphatics is depleted. During secondary pyrolysis (Fig. 1c) there is additional methane evolution (from methyl groups), HCN from ring nitrogen compounds, CO from ether links, and H_2 from ring condensation.

Functional Group Model

The Functional Group (FG) model developed in this laboratory has been described in a number of publications (25-29). It permits the detailed prediction of volatile species concentrations (gas yield, tar yield and tar functional group and elemental composition) and the chemical and functional group composition of the char. It employs coal independent rates for the decomposition of individual assumed functional groups in the coal and char to produce gas species. The ultimate yield of each gas species is related to the coal's functional group composition. Tar evolution is a parallel process which competes for all the functional groups in the coal. In the FG model, the ultimate tar yield is an input parameter which is adjusted for each type of experiment since the model does not include the mass transfer effects or char forming reactions which lead to tar yield variations.

FG Model Development - The FG model development was initiated by Solomon and Colket (25). A series of heated grid experiments were performed on a variety of coals in which individual products (gas species and tar) were monitored. It was noticed that while the ultimate yields of species varied from coal to coal and could be related to the coal's composition, the evolution rates for individual species were, to a good first approximation, independent of coal rank. Solomon and Hamblen examined a variety of literature data and found the insensitivity of individual species evolution rates to coal rank to be a general phenomenon (37). A similar conclusion was reached in a recent study by Xu and Tomita (38).

In subsequent work using entrained flow reactors (26-28) and a heated tube reactor (29), it was found that the general assumptions of the FG model were good, but that the original single activation energy rates derived from the heated grid experiments (25) were inaccurate. The use of a distributed activation energy rate expression, a wide variety of heating rates, and particle temperature measurements has provided more accurate and reactor independent kinetic rates for the present model (26-29). The general rates and specific composition parameters for Pittsburgh Seam coal are presented in Table I.

FG Model Formulation - The mathematical description of the functional group pyrolysis model has been presented previously (25-29). The evolution of tar and light gas species provides two competing mechanisms for removal of a functional group from the coal: evolution as a part of a tar molecule and evolution as a distinct gas species. Each process assumes a first order reaction,

$$dW_i(gas)/dt = k_i W_i(char), \quad (1)$$

where, $dW_i(gas)/dt$ is the rate of evolution of species i into the gas phase, k_i is its rate constant and $W_i(char)$ is the functional group source remaining in the char. Note that $W_i(char)$ also is decreased by evolution of the source with the tar, according to,

$$dW_i(tar)/dt = k_{tar} W_i(char). \quad (2)$$

The reduction of $W_i(char)$ is thus,

$$-dW_i(char)/dt = dW_i(gas)/dt + dW_i(tar)/dt \quad (3)$$

The kinetic rates, k_i and k_{tar}, for each functional group employs a distributed activation energy of the form used by Anthony et al. (2).

The Depolymerization-Vaporization-Crosslinking (DVC) Model

The Depolymerization-Vaporization-Crosslinking model has been described in a number of publications (12,13,33-36). It predicts the tar yield, the tar molecular weight distribution, the char yield, the char molecular weight distribution, the extract yield and the crosslink density.

DVC Model Development - The model had its beginning in a study of polymers representative of structural features found in coal (33). The objective of that study was to develop an understanding of coal pyrolysis by studying a simpler, more easily interpretable system. The polymers were studied in a series of pyrolysis experiments in which tar amounts and molecular weights were measured. A theory was developed to describe the combined effects of: i) random bond cleavage in long polymer chains (similar to Gavalas et al. (39)), ii) molecular weight dependent vaporization of the fragments to produce tar (similar to Unger and Suuberg (4)), and iii) a limitation on the number of breakable bonds which depended on the availability of donatable hydrogens to cap the free radicals formed by the cleavage.

The model was subsequently improved by Squire et al. (35,36) by adding the chemistry for the consumption of donatable hydrogens to cap free radicals along with corresponding carbon-carbon double bond formation at the donor site. In the polymers which were studied, the ethylene bridges were identified as a source of donatable hydrogen with the formation of a double bond between the bridge carbons (35,36). The double bond formation was assumed to remove a breakable bond. This improvement in the model removed the donatable hydrogen as an adjustable parameter. It should be noted that hydroaromatic groups are also a source of donatable hydrogen with aromatization of the ring, however, for simplicity, the DVC model assumes all donatable hydrogens are in bridges. The model was further improved by the implementation of a Monte Carlo method for performing the statistical analysis of the bond breaking, the hydrogen consumption and the vaporization processes. A single kinetic rate described the random bond breaking. This kinetic rate (35) employs an activation energy which is in agreement with resonance stabilization calculations (40,41) and an overall rate which agrees with previous measurements on model compounds (42). The rate determined for the breaking of ethylene bridges between naphthalene rings is in good agreement with the rate for tar formation from coal (28,29). The model predicted the observed molecular weight distribution and dependence of yield with the availability of donatable hydrogen. The results for model polymers compared favorably with many of the details of tar formation in softening coals. However, in the version of the model reported in Ref. 35, there

was no explicit char forming reaction. Char consisted of molecular fragments which were too heavy to vaporize and thus remained after the donatable hydrogen had been consumed.

Crosslinking Reactions - The next improvement in the model to be reported (12,13,35) was the addition of char forming repolymerization (crosslinking) reactions. These reactions are important in describing the rank and heating rate dependence of the tar molecular weight distributions and yields. Work has been performed to define the reactions which cause crosslinking (43-45). Under the assumption that the crosslinking reactions may also release gas species, the molecular weight between crosslinks or crosslink density (estimated using the volumetric swelling technique developed by Larsen and co-workers (46-48)) was correlated with the observed evolution of certain gas species during pyrolysis. Likely candidates were CO_2 formation from carboxyl groups or methane formation from methyl groups. Suuberg at al. (48) also noted that crosslinking in low rank coals is correlated with CO_2 evolution. Both reactions may leave behind free radicals which can be stabilized by crosslinking. Condensation of hydroxyl groups to form water and an ether link is also a possible reaction.

For a series of chars, the loss of volumetric swelling ratio in pyridine was compared with CO_2 evolution for a Zap, North Dakota lignite and CH_4 evolution for a Pittsburgh Seam bituminous coal (44). The lignite reaches maximum crosslinking before the start of methane evolution and the Pittsburgh Seam bituminous evolves little CO_2. On a molar basis, the evolution of CO_2 from the lignite and CH_4 from the bituminous coal appear to have similar effects on the volumetric swelling ratio. The results suggest that one crosslink is formed for each CO_2 or CH_4 molecule evolved. No correlation was observed between the volumetric swelling ratio and tar yield for either coal. A correlation with water yield appears valid for the Zap, North Dakota lignite, but not for the Pittsburgh Seam bituminous coal.

DVC Model Description - In the current DVC model, the parent coal is represented as a two-dimensional network of monomers linked by strong and weak bridges as shown in Fig. 2a. It consists of condensed ring clusters (monomers) linked to form an oligomer of length "n" by breakable and non-breakable bridges. The clusters are represented by circles with molecular weights shown in each circle. The breakable bridges (assumed to be ethylene) are represented by single lines, the unbreakable bridges by double lines. "m" crosslinks are added so that the molecular weight between crosslinks corresponds to the value reported in the literature (49) for coals of similar rank. Unconnected "guest" molecules (the extract yield) are obtained by choosing the value of n. The ratio of ethylene bridges (two donatable hydrogens per bridge) to non-breakable bridges (no donatable hydrogens) is chosen to obtain the appropriate value for total donatable hydrogen. The parameters for a Pittsburgh Seam coal are presented in Table II.

Figure 2b shows the molecule during pyrolysis. Some bonds have broken, other bonds have been converted to unbreakable bonds by the abstraction of hydrogen to stabilize the free radicals and new crosslinks have been formed. Char formation in the DVC model can occur by crosslinking at any monomer to produce a two dimensional crosslinked network.

Figure 2c shows the final char which is highly crosslinked with unbreakable bonds and has no remaining donatable hydrogen.

The Combined FG-DVC Model

A detailed description of the pyrolysis behavior of coal is obtained by

combining the DVC model with the FG model. The FG model predicts the gas yields, and using the correlation developed for crosslinking with gas yields, it also determines the rate and number of crosslinks formed, assuming one crosslink is formed per CO_2 or CH_4 molecule evolved, for the DVC model. The DVC model supplies the tar yield to the FG model, replacing what was previously an adjustable parameter. It also supplies the number of new methyl groups formed and the concentration of C_2H_4 and C_2H_2 bridges.

FG-DVC Model Description - The model is initiated by specifying the Functional Group composition and the parameters (number of breakable bridges, starting oligomer length n, number of added crosslinkings, m, and the monomer molecular weight distribution). The starting DVC molecule is represented in Fig. 2a. The monomers are assumed to have the average elemental and functional group composition given by the FG model. Each computer simulation considers a coal molecule consisting of 2400 monomers. The model has been programmed in Fortran 77 and run on an Apollo DN580 computer.

Once the starting coal molecule is established, it is then subjected to a time-temperature history made up of a series of isothermal time steps. During each step, the gas yields, elemental composition and functional group compositions are computed using the FG model. To determine the change of state of the computer molecule during a time step, the number of crosslinks formed is determined using the FG model, and then input to the DVC model. These crosslinks are distributed randomly throughout the char, assuming that crosslinking probability is proportional to the molecular weight of the monomer. Then the DVC model breaks the appropriate number of bridging bonds (assuming a distribution of activation energies for the bond breaking rates) and calculates the quantity of tar evolved for this time step using the vaporization law. The modified expression of Suuberg et al. (14) is now employed for the vaporization law rather than that of Unger and Suuberg (4). A fraction of the abstractable hydrogen is used to stabilize the free radicals formed by bridge breaking and the appropriate fraction of breakable bridges is converted into (unbreakable) double-bonds. Tar formation is complete when all the donatable hydrogen is consumed. A typical simulation for a complete time temperature history takes about ten minutes.

Internal Transport Limitations - When comparing the predictions of the model to available data it was found that tar yields were overpredicted when devolatilization occurred at low temperatures. This was observed for either low heating rate experiments (28) or experiments with rapid heating to relatively low temperatures (9). As discussed in the Results Section, it appears that the lower yields were the result of the additional transport limitations within the particle. This limitation can be: i) the transit of bubbles containing tar from the interior of the particle to the surface; ii) the transport of tars within the liquid to the bubble; iii) the stirring action of the bubble. In the absence of sufficient information to accurately model these processes, the simple assumption was made that tars are carried out of the particle at their equilibrium vapor pressure in the light devolatilization products.

Then,

$$(dn_i/dt)_{tr} = P_{si}\, X_i \sum_{\substack{\text{light}\\ \text{products}}} (dn_i/dt)_{chem} \quad \frac{1}{P_o + \Delta P} \qquad (4)$$

where $(dn_i/dt)_{tr}$ is the transport rate for tar component i, of number in the particle n_i. $(dn_i/dt)_{chem}$ is the rate of production of component i. P_o is the

ambient pressure, P_{gi} is the equilibrium vapor pressure for component i (given by Suuberg et al. (14)) and ΔP is the average pressure difference in the particle which drives the transport. X_i is the mole fraction of component i in the metaplast. For the highly fluid Pittsburgh Seam bituminous coal, we have considered the upper limit to this rate where $P_o \gg \Delta P$. Then all the terms in Eq. 1 can be determined by the combined FG-DVC model.

The net rate for tar transport is calculated by assuming that the resistance to internal and external transport occur in series. For melting coals ΔP is proportional to the coal's viscosity and so, will become important for less fluid coals. It is also important when P_o is small.

Summary of FG-DVC Model Assumption - Assumptions a-c are made for the FG model and d-n for the DVC model.

(a) Light gas species are formed from the decomposition of specific functional groups with rate coefficients which depend on the functional group but are insensitive to coal rank. The evolution rate is first order in the remaining functional group concentrations in the char. The rates follow an Arrhenius expression with a Gaussian distribution of activation energies (2,26,27).

(b) Simultaneous with the production of light gas species, is the thermal cleavage of bridge structures in the coal to release molecular fragments of the coal (tar) which consist of a representative sampling of the functional group ensemble. The instantaneous tar yield is given by the DVC model.

(c) Under conditions where pyrolysis products remain hot (such as an entrained flow reactor), pyrolysis of the functional groups in the tar continues at the same rates used for functional groups in the char, (e.g., the rate for methane formation from methyl groups in tar is the same as from methyl groups in the char).

(d) The oligomer length, n, the number of crosslinks, m, and the number of unbreakable bonds are chosen to be consistent with the coal's measured extract yield, crosslink density and donatable hydrogen concentration.

(e) The molecular weight distribution is adjusted to best fit the observed molecular weight distribution for that coal, measured by pyrolysis of the coal (in vacuum at 3°C/min to 450°C) in a FIMS apparatus (50). Molecular weights 106, 156, 206, 256, 306, 356 and 406 (which are 1,2,3,4,5,6 and 7 aromatic ring compounds with two methyl substituents) are considered as representative of typical monomer molecular weights.

(f) During pyrolysis, the breakable bonds are assumed to rupture randomly at a rate k, described by an Arrhenius expression with a Gaussian distribution of activation energies. Each rupture creates two free radicals which consume two donatable hydrogens to stabilize and form two new methyl groups.

(g) Two donatable hydrogens (to cap free radicals) are available at each breakable bridge. The consumption of the donatable hydrogen converts the bridge into an unbreakable bridge by the formation of a double bond.

(h) Tar formation continues until all the donatable hydrogens are consumed.

(i) During pyrolysis, additional unbreakable crosslinks are added at a rate determined by the evolution of CH_4 and CO_2. One crosslink is created for each evolved molecule. The rate of CH_4 and CO_2 evolution is given by the FG model.

(j) The crosslinks are distributed randomly, with the probability of attachment on any one monomer being proportional to the molecular weight of the monomer.

(k) Tar molecules are assumed to evaporate from the surface of the coal particle at a molecular weight dependent rate controlled by evaporation and gas phase diffusion away from the particle surface. The expressions derived by Suuberg et al. (14) are employed.

(l) Internal transport resistance is assumed to add to the surface transport resistance. A simple empirical expression (Eq. 4) was used to describe bubble transport resistance in softening coals. This appears to be the step most in need of further work.

(m) Extractable material (in boiling pyridine) in the char is assumed to consist of all molecules less than 3000 AMU. This can be adjusted depending on the solvent and extract conditions.

(n) The molecular weight between crosslinks, M_c is computed to be the total molecular weight in the computer molecule divided by the total number of crosslinks. This assumption will underestimate M_c since broken bridges are not considered.

RESULTS

The model predictions have been compared to the results obtained from a number of experiments on the pyrolysis of a Pittsburgh Seam coal at AFR and MIT (2,3,9,28). The coal composition parameters are presented in Tables I and II. It should be noted that different samples of Pittsburgh seam coal from different sources were employed. While the elemental compositions were similar, extract yields varied substantially depending on the sample source. The oligomer length was chosen to fit an extract yield of 30%. It is expected that yields may vary slightly from predictions for other samples, but the predicted rates should be sample independent. Comparisons are considered for gas yields, tar yields, tar molecular weight distributions, extract yields and volumetric swelling ratio.

Volatile and Extract Yields

Extensive comparisons of the FG model with gas yields have been presented previously (27-29) and won't be repeated here. The Functional Group parameters and the kinetic rates for the Pittsburgh Seam coal are those published in Ref. 28. The methane parameters for the Pittsburgh Seam coal were adjusted (methane X-L = 0.0, methane-L = 0.02, methane-T = 0.015, unchanged) to better match yield of Refs. 2, 27 and 28 (see Fig. 20c in Ref. 28). A second modification is that the CH_x-aliphatic rate in Ref. 28 applies to the observed gas species (paraffins, olefins, C_2H_6, C_2H_4) only. The aliphatic material in the CH_x-aliphatic group is assumed to be made up of bridges which volatilize only when attached to a tar molecule (i.e., $k_{bridge} = 0$). Results for methane are considered because the methane is associated with crosslinking. The CO_2 yields are not considered in this paper since they are too low in the Pittsburgh Seam coal to cause significant crosslinking.

Figure 3 compares the FG-DVC predictions to the data of Fong et al. (9) on total volatile yield and extract yield as a function of temperature in pyrolysis at 0.85 ATM. The experiments were performed in a heated grid at heating rates of approximately 500°C/sec, variable holding times and rapid cool down. The predictions at the two higher temperatures (3c and 3d) are in excellent agreement

with the data. Having fixed all the rates and functional group compositions based on previous work, the only adjustable parameters were the number of labile bridges (which fixes the donatable hydrogen concentration) and the monomer distribution, assumed to be Gaussian. The predictions for the two lower temperatures were not good when internal transport limitations were neglected. The dashed line in Fig. 3a shows the predicted yield in the absence of internal transport limitations. The predicted ultimate yield is clearly too high. The data suggest that the low yields are not a result of unbroken bonds (which would result from a lower bond breaking rate), since the extract yields at low temperatures are equivalent to those at the higher temperatures. The low yields thus appear to be a result of an additional transport limitation.

Equation 4 was employed for the internal transport resistance and the number of labile bridges were readjusted for the 1018°K case. The predictions are the solid lines in Fig. 3. The internal transport limitation is important when pyrolysis occurs at low temperatures and $\sum_{light} dn_i/dt$ is small. It is much less important for the 1018K and 992K cases, making only a small difference in the predicted yields.

There still is a discrepancy between the prediction and the data at early times for the two lower temperatures (Figs. 3a and b). While it is possible that the rate k for bond breaking is too high, adjustment of this rate alone significantly lowers the extractable yield, since the lower depolymerization rate is closer to the methane crosslinking rate. In addition, both the methane and depolymerization rates appear to be in good agreement with the data at even lower temperatures, as shown in Fig. 4 (discussed below). Another possibility is that the coal particles heat more slowly than the nominal temperatures given by Fong et al. (9). Such an effect could be caused by having some clumps of particle which would heat more slowly than isolated particles, by reduction in the convective heat transfer due to the volatile evolution (blowing effect), or by endothermic tar forming reactions. A firm conclusion as to the source of the discrepancy cannot be drawn without further investigation.

It is also seen in Figs. 3a and b that the crosslinking rate is higher than predicted. This can be due to additional methane from methyl groups created during tar formation, which is not yet counted in the model, or to other crosslinking events not considered. These possibilities are currently under investigation.

Figure 4 presents comparisons of devolatilization yields at slow (30°C/min), heating rates in a thermogravimetric analyzer with Fourier transform infrared analysis of evolved products (TG-FTIR). This reactor has been previously described (51). The model predictions and experimental results are in excellent agreement. The agreement validates the assumed rates for depolymerization and crosslinking produced by CH_4 at low temperatures. Also, the use of Eq. 4 appears to predict the appropriate drop in tar yield (maximum value 17%) compared to 30% when devolatilization occurs at high temperature.

Pressure Effects

The predicted effect of pressure on the tar molecular weight distribution is illustrated in Figs. 5a and b. The average molecular weight and the vaporization "cut-off" decrease with increasing pressure. The trends are in agreement with observed tar molecular weight distributions shown in Figs. 5c and d. The spectra are for previously formed tar which has been collected and analyzed in a FIMS apparatus (50). The low values of intensity between 100 and 200 mass units is due

to loss of these components in collection and handling due to their high volatility.

Pressure effects on yields have been examined. Figure 6 compares the predicted and measured pressure dependence on yield. Figure 6a compares to the total volatile yield data of Anthony et al. (2) while Fig. 6b compares to the tar plus liquids data of Suuberg et al. (3). The agreement between theory and experiment is good at one atmosphere and above, but of overpredicts the yields at low pressure. Below one atmosphere, it is expected that ΔP within the particle will become important compared to the ambient pressure, P_o.

CONCLUSIONS

A general model for coal devolatilization which combines a functional group model for gas evolution and a statistical model for tar formation has been presented. The tar formation model includes depolymerization, vaporization, crosslinking and internal transport resistance. The crosslinking is related to the formations of CO_2 and CH_4 species evolution, with one crosalink formed per molecule evolved. The predictions of the tar formation model are made using Monte Carlo methods.

The general model predictions compare favorably with a variety of data for the devolatilization of Pittsburgh Seam coal, including volatile yields, extract yields, and tar molecular weight distributions. The variations with pressure and devolatilization temperature were accurately predicted. While film diffusion appears to limit surface evaporation and the transport of tar when devolatilization occurs at high temperatures, internal transport appears to become dominate when devolatilization occurs at low temperatures.

ACKNOWLEDGMENT

This work was supported under DOE Contracts DEAC21-85MC22050, DEAC21-84MC21004 and DE-AC21-86MC23075. The authors wish to express their thanks to Professor Eric Suuberg for many helpful discussions on transport properties.

REFERENCES

1. van Krevelen, D.W. and Schuyer, J., Coal Science, Elsevier, Amsterdam, (1957).
2. Anthony, D.B., Howard, J.B., Hottel, H.C., and Meissner, H.P., 15th Symp. (Int) on Combustion, The Combustion Institute, Pittsburgh, PA, pg. 1303, (1974).
3. Suuberg, E.M., Peters, W.A., and Howard, J.B., 17th Symp. (Int) on Combustion, The Combustion Institute, Pittsburgh, PA, pg. 117, (1979).
4. Unger, P.E. and Suuberg, E.M., 18th Symp. (Int) on Combustion, The Combustion Institute, Pittsburgh, PA, pg. 1203, (1981).
5. Russel, W.B., Saville, D.A., and Greene, M.I., AIChE J., **25**, 65, (1979).
6. James, R.K. and Mills, A.F., Letters in Heat and Mass Transfer, **3**, 1, (1976).
7. Lewellen, P.C., S.M. Thesis, Department of Chemical Engineering, MIT, (1975).
8. Chen, L.W. and Wen, C.Y., ACS Div. of Fuel Chem. Preprints, **24**, (3), p141, (1979).
9. Fong, W.S., Peters, W.A., and Howard, J.B., Fuel, **65**, 251, (1986).
10. Niksa, S. and Keratein, A.R., Combustion and Flame, **66**, #2, 95, (1986).
11. Niksa, S. Combustion and Flame, **66**, #2, 111, (1986).
12. Solomon, P.R., Squire, K.R., Carangelo, R.M., proceedings of the International Conference on Coal Science, Sydney, Australia, pg. 945, (1985).
13. Solomon, P.R. and Squire, K.R., ACS Div. of Fuel Chem. Preprints, **30**, #4, 347,

(1985).
14. Suuberg, E.M., Unger, P.E., and Lilly, W.D., Fuel, **64**, 956, (1985).
15. Gavalas, G.R. and Wilks, K.A., AIChE, **26**, 201, (1980).
16. Simons, G.A., Prog. Energy Combust. Sci., **9**, 269, (1983).
17. Oh, M., Peters, W.A., and Howard, J.B., Proc. of the 1983 Int. Conf. on Coal Sci., p 483, International Energy Agency, (1983).
18. Suuberg, E.M. and Sezen, Y., Proc. of the 1985 Int. Conf. on Coal Sci., p913, Pergamon Press, (1985).
19. Melia, P.F. and Bowman, C.T., Combust. Sci. Technol. **31**, 195 (1983); also An analytical model for coal particle pyrolysis and swelling, paper presented at the Western States Section of the Combustion Institute, Salt Lake City, 1982.
20. Gavalas, G.R., Coal Pyrolysis, Elsevier (1982).
21. Suuberg, E.M., in Chemistry of Coal Conversion, (R.H. Schlosberg, Ed.), Chapter 4, Plenum Press, NY (1985).
22. Juntgen, H. and van Heek, K.H., Fuel Processing Technology, **2**, 261, (1979).
23. Weimer, R.F. and Ngan, D.Y., ACS Div. of Fuel Chem. Preprints, **24**, #3, 129, (1979).
24. Campbell, J.H., Fuel, **57**, 217, (1978).
25. Solomon, P.R. and Colket, M.B., 17th Symposium (Int) on Combustion, The Combustion Institute, Pittsburgh, PA, 131, (1979).
26. Solomon, P.R., Hamblen, D.G., Carangelo, R.M., and Krsuse, J.L., 19th Symposium (Int) on Combustion, The Combustion Institute, Pittsburgh, PA, 1139, (1982).
27. Solomon, P.R. and Hamblen, D.G., in Chemistry of Coal Conversion, (R.H. Schlosberg, Editor), Plenum Press, NY, Chapter 5, pg. 121, (1985).
28. Serio, M.A., Hamblen, D.G., Markham, J.R., and Solomon, P.R., Energy and Fuels, **1**, (2), 138, (1987).
29. Solomon, P.R., Serio, M.A., Carangelo, R.M., and Markham, J.R., Fuel, **65**, 182, (1986).
30. Fong, W.S., Khalil, Y.F., Peters, W.A. and Howard, J.B., Fuel, **65**, 195 (1986).
31. van Krevelen, D.W., Properties of Polymers, Elsevier, Amsterdam (1976).
32. Solomon, P.R., New Approaches in Coal Chemistry, ACS Symposium Series **169**, American Chemical Society, Washington, DC, pp 61-71, (1981).
33. Solomon, P.R. and King, H.H., Fuel, **63**, 1302, (1984).
34. Solomon, P.R., Squire, K.R., and Carangelo, R.M., ACS Div. of Fuel Chem. Preprints, **29**, #2, 84, (1984).
35. Squire, K.R., Solomon, P.R., Carangelo, R.M., and DiTaranto, M.B., Fuel, **65**, 833, (1986).
36. Squire, K.R., Solomon, P.R., DiTaranto, M.B., and Carangelo, R.M., ACS Div. of Fuel Chem. Preprints, **30**, #1, 386, (1985).
37. Solomon, P.R. and Hamblen, D.G., Prog. Energy Comb. Sci., **9**, 323, (1983).
38. Xu, W.-C., and Tomita, A., Fuel, **66**, 632 (1987).
39. Gavalas, G.R., Cheong, P.H., and Jain, R., Ind. Eng. Chem. Fundam. **20**, 113, and 122, (1981).
40. Stein, S.E., New Approaches in Coal Chemistry, (B.D. Blaustein, B.C. Bockrath, and S. Friedman, Editors), ACS Symposium Series, **169**, 208, Am. Chem. Soc. Washington, DC, (1981).
41. Stein, S.E., "Multistep Bond Breaking and Making Processes of Relevance to Thermal Coal Chemistry", Annual Report for GRI Contract No. 5081-261-0556. Accession No. GRI-81/0147, (1983).
42. Stein, S.E., Robaugh, D.A., Alfieri, A.D., and Miller, R.E., "Bond Homolysis in High Temperature Fluids", Journal of Amer. Chem. Society, **104**, 6567, (1982).
43. Solomon, P.R., Serio, M.A., and Deshpande, G.V., "Crosslinking Reactions in Coal Liquefaction", presented at the DOE Contractor's Review Conference, Monroeville, PA, (1986).

44. Solomon, P.R., Hamblen, D.G., Carangelo, R.M., Serio, M.A., and Deshpande, G.V., "Models of Tar Formation During Coal Devolatilization", submitted to Combustion and Flame, (1987).
45. Solomon, P.R., Hamblen, D.G., Deshpande, G.V. and Serio, M.A., A General Model of Coal Devolatilization, International Coal Science Conference, The Netherlands, October 1987.
46. Green, T.K., Kovac, J., and Larsen, J.W., Fuel, **63**, #7, 935, (1984).
47. Green, T.K., Kovac, J., and Larsen, J.W., in Coal Structure, (R.A. Meyers, Editor), Academic Press, NY, (1982).
48. Suuberg, E.M., Lee, D., and Larsen, J.W., Fuel, **64**, 1668, (1985).
49. Nelson, J.R., Fuel, **62**, 112, (1983).
50. St. John, G.A., Burrill, Jr., S.E. and Anbar, M., ACS Symposium Series, **71**, p. 223 (1978).
51. Carangelo, R.M. and Solomon, P.R., Fuel, **66**, (1987), accepted for publication.

Table I. Kinetic Rate Coefficients and Species Compositions for Pittsburgh Seam Coal

composition parameters	gas	primary functional group source	rate equation[a]	Pittsburgh No. 8 bituminous coal
C		———	———	0.821
H		———	———	0.056
N		———	———	0.017
S(organic)		———	———	0.024
O		———	———	0.082
total		———	———	1.000
Y_1^*	CO_2 extra loose	carboxyl	$k_1 = 0.56E+18 \exp(-(30000\pm2000)/T)$	0.000
Y_2^*	CO_2 loose	carboxyl	$k_2 = 0.65E+17 \exp(-(33850\pm1500)/T)$	0.006
Y_3^*	CO_2 tight	———	$k_3 = 0.11E+16 \exp(-(38315\pm2000)/T)$	0.005
Y_4^*	H_2O loose	hydroxyl	$k_4 = 0.22E+19 \exp(-(30000\pm1500)/T)$	0.011
Y_5^*	H_2O tight	hydroxyl	$k_5 = 0.17E+14 \exp(-(32700\pm1500)/T)$	0.011
Y_6^*	CO ether loose	———	$k_6 = 0.14E+19 \exp(-(40000\pm6000)/T)$	0.050
Y_7^*	CO ether tight	ether O	$k_7 = 0.15E+16 \exp(-(40500\pm1500)/T)$	0.022
Y_8^*	HCN loose	———	$k_8 = 0.17E+14 \exp(-(30000\pm1500)/T)$	0.009
Y_9^*	HCN tight	———	$k_9 = 0.69E+13 \exp(-(42500\pm4750)/T)$	0.022
Y_{10}^*	NH_3	———	$k_{10} = 0.12E+13 \exp(-(27300\pm3000)/T)$	0.000
Y_{11}^*	CH_4 aliphatic	H(al)	$k_{11} = 0.84E+15 \exp(-(30000\pm1500)/T)$	0.190
Y_{12}^*	methane extra loose	methoxy	$k_{12} = 0.84E+15 \exp(-(30000\pm1500)/T)$	0.000
Y_{13}^*	methane loose	methyl	$k_{13} = 0.75E+14 \exp(-(30000\pm2000)/T)$	0.020
Y_{14}^*	methane tight	methyl	$k_{14} = 0.34E+12 \exp(-(30000\pm2000)/T)$	0.015
Y_{15}^*	H aromatic	H(ar)	$k_{15} = 0.10E+15 \exp(-(40500\pm6000)/T)$	0.012
Y_{16}^*	methanol	———	$k_{16} = 0.00E+00 \exp(-(30000\pm0)/T)$	0.000
Y_{17}^*	CO extra tight	ether O	$k_{17} = 0.20E+14 \exp(-(45500\pm1500)/T)$	0.020
Y_{18}^*	C nonvolatile	C(ar)	$k_{18} = 0$	0.583
Y_{19}^*	S organic	———	———	0.024
total				1.000
Y^*	tar	———	$k_T = 0.86E+15 \exp(-(27700\pm1500)/T)$	

a. The Rate Equation is of the Form $k_i = k_0 \exp(-(E/R \pm \sigma)/T)$, with k_0 in s^{-1}, E/R in K, and σ/R in K.

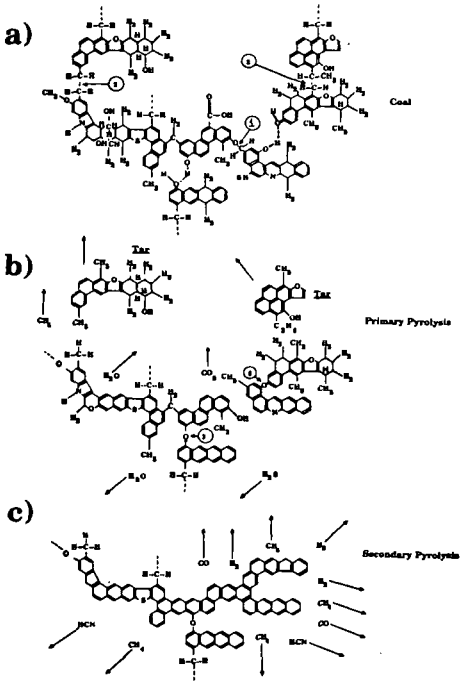

Figure 1. Hypothetical Coal Molecule During Stages of Pyrolysis. (reprinted from Ref. 28).

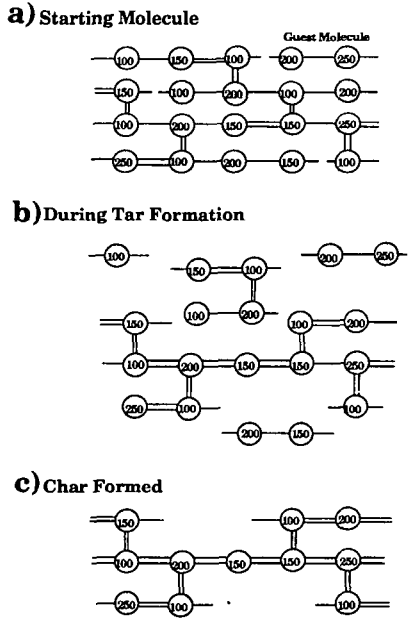

Figure 2. Representation of Coal Molecule in the DVC Simulation. The Circles Represent the Monomers (ring clusters and peripheral groups). The Molecular Weight Shown by the Numbers is the Molecular Weight of the Monomer Including the Attached Bridges. The Single Line Bridges are Breakable and can Donate Hydrogen. The Double Line Bridges are Unbreakable and do not Donate Hydrogen.

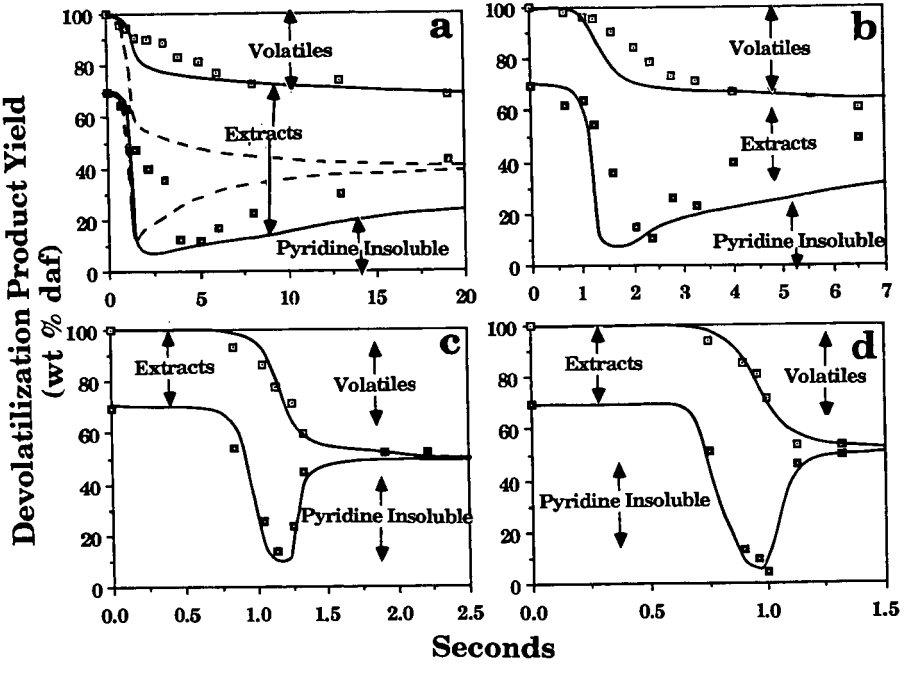

Figure 3. Comparison of FG-DVC Model Predictions (lines) with the Data of Fong et al (9) (symbols) for Pittsburgh Seam Coal. a) 813K @ 470 k/s, b) 858K @ 446k/s, c) 992K @ 514k/s and d) 1018K @ 640k/s. P=0.85 atm. The Dashed Line in a Shows the Predicted Yield in the Absence of Internal Transport Limitations.

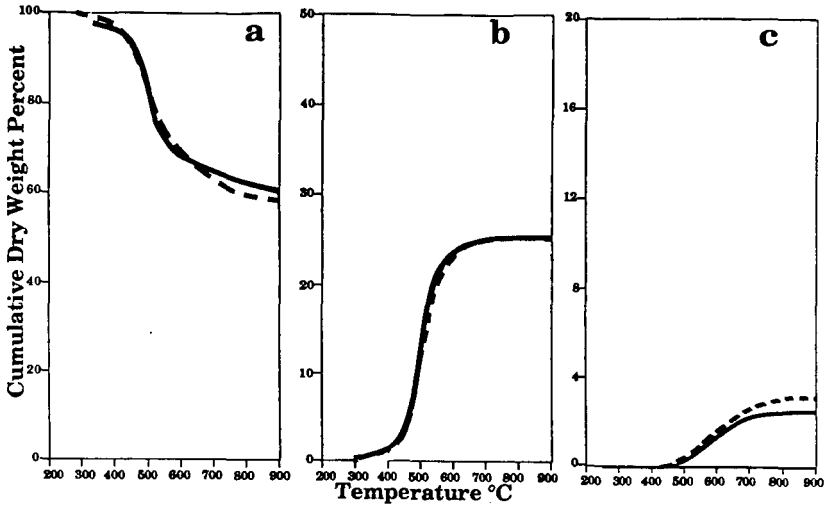

Figure 4. Comparison of Measured (solid line) and Predicted (dashed line) Volatile Yields for Pittsburgh Seam Coal Heated in Helium in a TG-FTIR at 0.5°C/sec to 900°C. a) Weight Loss, b) Tar Plus Aliphatics, and c) Methane.

TABLE II

PARAMETERS FOR DVC MODEL

		PITTSBURGH BITUMINOUS
Labile bridges	W_1 (wt.%)	9.6
Nuclei (ring clusters)	W_2* from FG model (wt.%)	56.2
Peripheral groups	W_3 from FG model (wt.%)	34.2
Donatable hydrogens	(2/28)W_1	0.68
No. of crosslinks in coal	m #/monomer	0.095
Oligomer length	n #/oligomer	8
No. of potential crosslink sites (CO_2)	a #/monomer	0.07
No. of potential crosslink sites (CH_4)	b #/monomer	0.42
	MOLECULAR WEIGHTS	
Labile bridges	Fixed at 28	28
Monomers	Distribution+ M_{avg}, (σ)	256,(250)
Gas	From FG model	
Tar	Predicted in model from vaporization law	
Non-labile bridges	Fixed at 26	26

* Carbon in aromatic rings plus non-labile bridges

\+ Gaussian Distribution

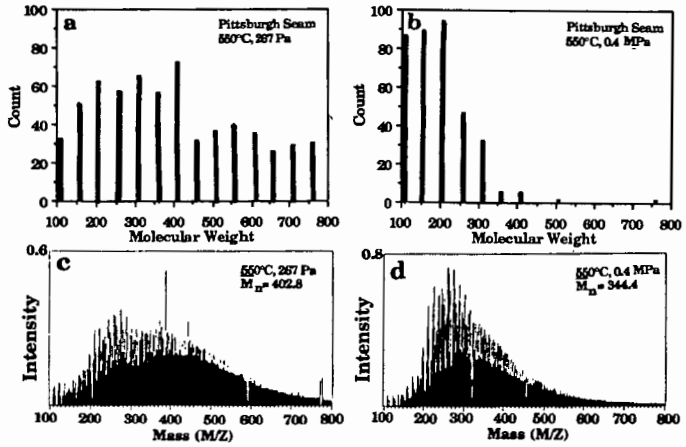

Figure 5. Comparison of Predicted (a and b) and Measured (c and d) Tar Molecular Weight Distribution for Pyrolysis of a Pittsburgh Seam Coal in a Heated Grid Apparatus at a Heating Rate of 500°C/sec to 550°C. Figure a and c Compare the Prediction and the Measurement at 267 Pa. Figure b and d Compare the Prediction and Measurement at 0.4 MPa.

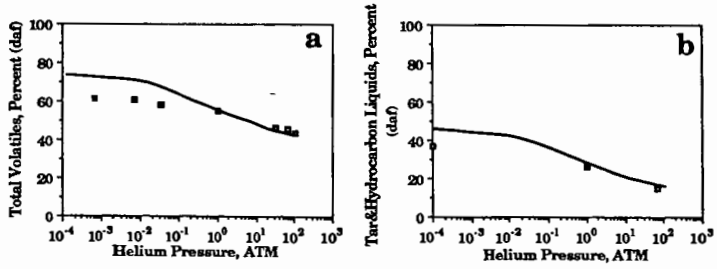

Figure 6. Comparison of Measurement and Prediction of Product Yields as a Function of Pressure. a) Volatile vs. Pressure (data form Anthony et al.(2)) and b) Tar Plus Liquids vs. Pressure Data from Suuberg et al. (3).

KINETIC MODELING OF COAL PYROLYSIS IN A LAMINAR-FLOW REACTOR SYSTEM

William S. O'Brien, Juh Wah Chen, Asadollah Moslehi and Rong-Chein Richard Wu

Mechanical Engineering and Energy Processes Department
Southern Illinois University at Carbondale
Carbondale, Illinois 62901-6603

INTRODUCTION

There will soon be an intense competition in the energy marketplace among oil, natural gas, coal, nuclear fission and the newly developing alternatives of solar, wind and waste utilization. The charge to the energy-entrepreneurs is to intensify their search to recognize and exploit the most economical and technically expedient manner of converting these raw energy sources into acceptable forms for the public's use.

Coal will certainly play a leading role in supplying the future energy needs of this nation's industrial and commercial ventures. But coal is an extremely complex heterogeneous material, composed of a number of distinct organic entities, called macerals, and inorganic minerals. Coals from different coal seams and even from separated points in the same seam often behave quite differently in a gasification reactor because of the unique associations of the maceral and mineral species in the coal matrix.

When the coal particle is first injected into the hot gasifier, the associated water is rapidly evolved. This drying mechanism is usually modeled as being independent of the other subsequent reactions; however, intuition says that a severe drying action could alter the particle's surface characteristics which in turn would significantly alter the later devolatilization and gasification reactions. As the dry coal particle is then rapidly heated, bound water, carbon oxides and hydrocarbon fragments are thermally cleaved from the coal's organic matrix and evolves into the surrounding gas phase. The amount and composition of this "volatile matter" are significantly controlled by the heat and mass transfer conditions in that pyrolysis/devolatilization zone. The physical severity of those devolatilization reactions, sometimes resembling mini-explosions, drastically affects the rate of the subsequent char-gasification reactions.

Today's most commercially-successful coal gasification processes completely shatter the coal's organic structure into blends of carbon monoxide and hydrogen, syngas mixtures that can be reassembled into a variety of desired gaseous and liquid products (1). Although proven to be technically and economically feasible in the present energy-market atmosphere, that destruction and reconstruction method of converting coal to useful energy and feedstock forms may not have the highest thermodynamic efficiency compared to other yet-to-be commercialized coal^{2}conversion mechanisms. In a return to the controlled destructive distillation of the old coke-making era, research emphasis is now re-examining low-temperature, "mild gasification" methods which can skillfully carve a suite of desirable products from the coal-structure, such as specific specie blends of gaseous feedstocks and/or highly aromatic condensibles, along with specially-formed chars (2).

In order to recognize the most expedient paths to perform these selective coal-radical slicing, one must understand fully the individual pyrolysis/devolatilization reactions of that particular coal. A laminar flow reactor has some advantages in studying coal devolatilization, such as precise control of experimental conditions like the flow rate and composition of the carrier-reactant gas. Also, both the reactor temperature and particle residence time can be easily

varied to evaluate the effects of changes of the heating rate of the coal-particle. There are also disadvantages to analyzing the data from such a laminar-flow reactor system, mainly associated with the need to mathematically compute the particle temperature and then to isolate the chemical reactivity from the mass transfer resistances. Many of the original studies using laminar-flow reactors used rather high temperatures where the particle heatup time was negligible. This permitted the particles to be considered at steady-state temperature for the entire particle residence time in the reactor. However, studies of the coal devolatilization in the 650° to 1100°K range in inert or non-igniting atmospheres reveal significant time-lags before devolatilization weight-loss starts.

In this presentation, experimental weight-loss data from the devolatilization treatment of a Herrin (Illinois) No. 6 coal in a laminar-flow laboratory reactor are examined and the observed reaction behavior are used to outline criteria for a coal-pyrolysis kinetic model.

EXPERIMENTAL REACTOR SYSTEM

The concept of the laminar-flow reactor design derives from those used by Badzioch and Hawksley (3), Kobayashi (4), Nsakala et al. (5) and Agreda et al. (6). Modifications were made in the design of the coal-feed inlet and the exiting-solids collector tube to permit a smooth 0.46 gm/min flow of coal solids, to expose the solids to reactor temperatures up to 1073°K with particle residence times up about 400-500 msec, and to collect and quickly quench-cool the coal-char solids immediately as they leave the hot-zone of the reactor. This reactor system, described in detail by Wu (7) and Moslehi (8), is illustrated in Figure 1.

In this reactor system, the hot nitrogen-gas stream enters the top head of the reactor into the shell-annulus surrounding the coal-feeder tip. This gas is then directed down into the main reactor tube chamber through a flow-straightener formed from a 3.8 cm (1.5-inch) thick disk of Corning "Macor" machineable glass-ceramic through which 2.2 mm diameter holes were drilled to form a 38% voidage ratio across the primary gas flow region. The vertical reactor chamber body was formed of a nominal two-inch, Schedule 40, Type 316 stainless-steel tube twenty inches long surrounded by a tube furnace. After passing through the heated reactor zone, the solids enter the throat of the char-solids collector where a cool-flush of nitrogen flowing inward through a permeable sintered stainless-steel tube at the collector tip quickly quench-cools the solid-particle and dilutes the surrounding reactive gases. The solids are separated in mini-cyclones and the condensible and permanent gases collected for quantification and analysis. The collector assembly tube was designed with a slip-joint around its outside diameter so that the uppermost tip of the collector could be positioned at any desired distance below the coal-inlet feeder tip. Thus, the coal particle reaction path-length, which determines the particle residence time, can be varied from almost zero to more than 50 cm.

The Herrin (Illinois) No. 6 coal used in the experiments was extracted from a west-central Illinois underground mine and had a dry-analysis of 43.3% volatile matter, 9.8% ash and 46.9% fixed carbon, along with a 4.2% total sulfur content. The coal was vacuum-dried and ground to an average particle diameter of about 75 micrometers before being fed to the reactor. The operating conditions of the reactor during the processing of this coal are listed in Table 1.

EXPERIMENTAL RESULTS AND DISCUSSION

The pyrolysis reactions were examined at three reactor temperatures; 450°, 600° and 800°C; and at three particle flow path lengths; 10, 20 and 30 cm. The

total residence times of the coal-particles, computed using the reactor operating conditions existing at these nine temperature-length combinations, are listed in Table 1, the values ranging from 137 to 473 msec. The overall weight-loss data from these experiments, computed by an ash-content balance and expressed on a dry ash-free basis, are shown in Figure 2. The reasoning and procedures of all the computational analyses have been detailed by Wu (7) and Moslehi (8).

It can be seen in Figure 2 that for a given temperature, the weight loss increases with time almost exponentially, approaching a maximum value. This maximum weight loss value is definitely a function of temperature, with a value in the upper 40% (daf weight loss) approached at 600°C, while the maximum weight loss at 800°C is in the upper 50% range.

Although the five-stage succession of devolatilization reactions detailed by Suuberg et al. (9) is probably the most chemically realistic, the single-reaction first order decomposition model discussed by Howard (10) can be utilized in approximating the coal's devolatilization behavior for quick comparison with those described in previous literature-reported studies. This model is stated as;

$$dW/dt = k (W^* - W) \qquad 1).$$

where W represents the weight-loss of the coal-particle (expressed on a dry ash-free basis) and W^* is the weight loss after an infinite exposure time at the reaction temperature, gas flow rate and other operating conditions. Badzioch and Hawksley (3) and other investigators realized that there was negligible weight loss until the dry coal particle was heated to about the 300°-to-500°C temperature range where the weight loss reactions became significant. They incorporated a particle heating time into their model;

$$\text{Total Time} = \text{Heatup Time} + \text{Reaction Time}. \qquad 2).$$

In order to simplify the mathematics, they assumed there to be no reactions taking place during this heatup time, even though the particle would be heating slowly through the entire devolatilization temperature range up to the steady-state temperature of the reactor.

Using the relationships derived by Kobayashi (4) in a mathematical analysis of the temperature and velocity flow in a similar laminar-flow reactor, which were modified and used by Agreda et al. (6) and Felder and coworkers (11) in their studies, particle heatup times were computed to be in the range of 24 to 27 msec for the three experimental reactor temperatures. The values of the pseudo rate constant, k , yielded a reasonably straight line on an Arhennius plot. This experimental data correlates by the expression;

$$k = k_0 \exp(-E/RT) \qquad 3).$$

with the pre-exponential factor, k_0 , being equal to 16035 sec^{-1} and the apparent activation energy, E, being equal to 68.12 KJ/mole (16.27 kcal/mole). This activation energy value compares quite well with the results found by Felder et al. (11) who, when devolatilizing a western Kentucky No. 11 coal in a similar reactor system, found the value of the apparent activation energy to be 80 KJ/mole (19.12 kcal/mole).

For use as a comparison with the experimental results of this study as shown in Figure 2, the devolatilization weight loss data reported by Felder et al. (11) for the western Kentucky Seam No. 11 coal is plotted in Figure 3. It

should be noted that the western Kentucky coal Seam No. 11 is believed to have been deposited in the same geological time-period aa the Herrin (Illinois) No. 6 seam. The lines sketched in both Figures 2 and 3 are merely to depict a trend-connection of the points, not to suggest a specifically derived model path.

The 450°C and the 600° weight-loss lines of Figure 2, along with the 600° line of Figure 3, demonstrate that there is a definite effect of reactor temperature on the heating time of the particle. The mathematical analysis of Kobayashi (4) used to approximate the particle heatup time in this study was originally derived for coal devolatilization at much higher reactor temperatures than those of these experiments. Both the 800° lines in Figure 2 and 3 could approach zero reaction within the 20-30 msec range predicted by the Kobayashi relationship. At the lower temperatures, however, the onset of devolatilization is much affected by reactor temperature as well as by other reactor operating conditions. The Felder et al. data for the 600° experiments in Figure 3 indicate that no weight loss occurred for almost 200 msec, while at 600° in this study, the reactions seem to have started before 100 msec.

Note also that reactor operating conditions, other then the temperature effect, seem to cause differences in the maximum asymptotic weight loss at each reactor temperature. In this study at 600°C, the maximum daf weight loss was around 40%, while the 600° line in Figure 3 was leveling in the 15% range. At 800°C the data in Figure 3 demonstrated a maximum weight loss of around 49%, which was about I.11 times the ASTM Proximate Analysis Volatile Matter of that coal. In the study reported in this paper, the coal's weight loss after 300 msec had reached almost 60% (1.24 times the ASTM Proximate Volatile Matter) and the maximum weight-loss asymptote had not been reached.

An examination of the approached asymptotes of W^* at the various temperatures suggests the validity of the "multiple reactions" model developed by several investigators and discussed by Howard (10). In Figure 2, the 450° and the 600° data appear to be approaching ultimate W^* values that are very close together, while the 800°C value of W^* is more than 20% higher. The data of Felder et al. (11) in Figure 3 indicates that the maximum weight loss W^* at 800°C is almost three times larger than the value of W^* at 600°, with weight loss curve at 700°C still increasing after 1000 msec of reaction exposure time. Suuberg et al. (9) in their listing of the five stages of devolatilization states that carbon oxides, hydrocarbons, tar and hydrogen are released in the fourth stage from 700° to 900°C. It would be logical to suggest that the reactions occurring in this temperature range would be strongly influenced by variations in the mass and heat transfer mechanisms caused by differences between reactor operating conditions. Also, the primary volatile hydrocarbon species being evolved in this temperature range would be susceptible to secondary decomposition and/or cracking reactions. Thus, the pyrolysis reaction chain probably includes a complex mix of both parallel and successive reactions.

CONCLUSIONS

A Herrin (Illinois) No. 6 coal was devolatilized in nitrogen in a laboratory laminar flow reactor system. The reactions took place at 450°, 600° and 800°C for reaction residence times ranging from 130 to 480 msec at Reynolds Numbers of 235 -308. The experimental data can be reasonably approximated by a single reaction decomposition model; $dW/dt = k (W^* - W)$; with the pre-exponential found to be 16035 sec^{-1} and the apparent activation energy being equal to 68.12 KJ/mole (16.27 kcal/mole). This reactor system stimulates a rather efficient reaction as evidenced by the fact that, after only 300 msec exposure at 800°C, the coal's weight loss had reached almost 60% (1.24 times the ASTM Proximate Analysis Volatile Matter) and the maximum weight-loss asymptote had not been reached.

At the lower temperatures of this experimental study, 450° through 600°C, knowledge of the particle heatup time is quite important. Estimates by previous investigators of the time-period before the "onset of devolatilization weight loss" occurs were substantially smaller than the actual experimental values observed in this study. There is considerable evidence that the particle heating rate and the flow conditions within the reactor system have a significant bearing on not only the pyrolysis rate, but also on the maximum weight loss of the coal which could be achieved at each reactor exposure temperature. Also, implications are that the overall devolatilization is both a parallel and a successive series of reactions, each influenced by the interrelated mass and heat transfer mechanisms occurring in that specific reactor system.

A predictive model useful in representing the reactive behavior of high-volatile coal at relatively low temperatures must incorporate a consideration of the very complex mix of mass and heat transfer effects. The development of such a model is the next stage of this continuing investigation.

ACKNOWLEDGMENTS

This research effort was supported by the U.S. Department of Energy through their Contract No. DE-FG22-82PC50802. The cooperative help of the SIU-C College of Engineering and Technology and the SIU-C Coal Extraction and Utilization Research Center is also gratefully acknowledged and appreciated.

REFERENCES

(1) Courty, P., and Chaumette, P., "Syngas: A Promising Feedstock In The Near Future", Energy Progress, 7, 23-30, (March 1987).

(2) Khan, M.R., and Kurata, T.M., "The Feasibility Of Mild Gasification Of Coal: Research Needs", Report No. DOE/METC-85/4019, Morgantown Energy Technology Center, U. S. Department Of Energy, Morgantown, West Virginia, (July 1985).

(3) Badzioch, S., and Hawksley, G.W., "Kinetics Of Thermal Decomposition Of Pulverized Coal Particles", Ind. Eng. Chem., Process Des. Dev., 9, 421, (1970).

(4) Kobayashi, M., "Devolatilization Of Pulverized Coal At High Temperatures", Ph.D. Thesis, Department of Mechanical Engineering, Massachusetts Institute of Technology, Cambridge, Massachusetts, (1976).

(5) Nsakala, N., Essenhigh, R.N., and Walker, P.L., Jr., "Studies On Coal Reactivity: Kinetics Of Lignite Pyrolysis In Nitrogen at 808°C", Combustion Science and Technology, 16, 153, (1977).

(6) Agreda, V.H., Felder, R.M., and Ferrell, J.K., "Devolatilization Kinetics and Elemental Release In The Pyrolysis Of Pulverized Coal", EPA Report No. EPA-600/7-79-241, U.S. Environmental Protection Agency, Washington, D.C., (November 1979).

(7) Wu, R-C.R., "Reaction Model and Standardized Test Procedure For Coal Devolatilization In A Laminar Flow Reactor", M.S. (Engineering) Thesis, Thermal and Environmental Engineering Department, Southern Illinois University, Carbondale, Illinois, (August 1984).

(8) Moslehi, A., "Devolatilization Of An Illinois Coal In A Laminar Flow Reactor", M.S. (Engineering) Thesis, Thermal and Environmental Engineering Department, Southern Illinois University, Carbondale, Illinois, (January 1985).

(9) Suuberg, R.M., Peters M.A., and Howard, J.B., "Product Composition And Kinetics Of Lignite Pyrolysis", Ind. Eng. Chem., Process Des. Dev., 17, 37, (1978).

(10) Howard, J.B., "Chapter 12: Fundamentals Of Coal Pyrolysis and Hydropyrolysis", in "Chemistry Of Coal Utilization, Second Supplementary Volume", M.A. Elliott, Editor, John Wiley & Sons, New York, pp. 727-739, (1981).

(11) Felder, R.M., Kau, C-C., Ferrell, J.K., and Ganesan, S., "Rates And Equilibria Of Devolatilization And Trace Element Evolution In Coal Pyrolysis", Report No. EPA 600/7-82-027, U.S. Environmental Protection Agency, Washington, D.C., (April 1982).

TABLE 1

EXPERIMENTAL REACTOR OPERATING CONDITIONS

	REACTOR TEMPERATURE		
Reactor Temperature	723 K (450°C)	873 K (600°C)	1073 K (800°C)
Dried Coal Feed Rate (gm/min)	0.46	0.46	0.46
Nitrogen Gas Flow Rate (L/min at 20°C, 1 atm)			
Main Gas Stream	20	20	20
Solids-Carrier Gas Stream	1	1	1
Combined Gas Velocity,(m/sec)	0.412	0.497	0.574
Total Gas Flow Reynolds Number	308	274	235
Coal-Solids Residence Time, msec			
Particle Flow Path Length			
10 cm	186	155	137
20 cm	336	280	227
30 cm	473	393	318

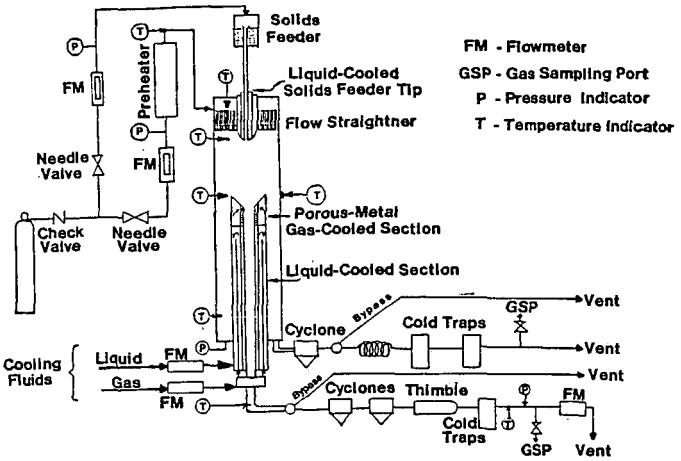

Figure 1. Experimental Laminar-Flow Reactor System

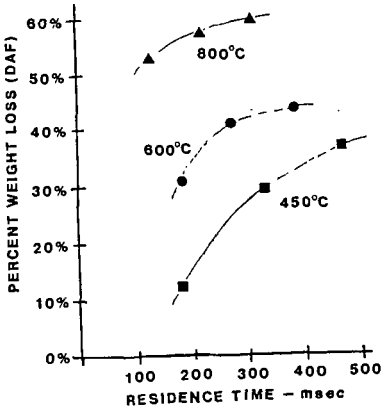

Figure 2. Weight-Loss (DAF) Versus Time, Herrin (Illinois) No. 6 Coal, This Study

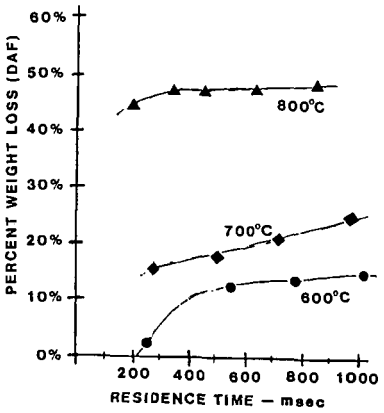

Figure 3. Weight-Loss (DAF) Versus Time, Western Kentucky No. 11 Coal, Felder et al. (Reference 11)

The Role of Coal Devolatilization in Comprehensive Combustion Models

B. Scott Brewster, Larry L. Baxter, and L. Douglas Smoot

Brigham Young University, Provo, UT 84602

Introduction

Pulverized coal combustion is a complex interaction of several processes, including particle dispersion, gas-phase mixing, particle heatup and mass transfer, particle and gas reactions, recirculating and swirling fluid mechanics, radiative heat transfer, mineral matter phase transformations, and pollutant formation and destruction. Comprehensive models which include submodels for many of these processes have been developed by several investigators (1-4) to predict local conditions inside combustors. This paper focuses on the role of coal devolatilization submodels in such predictions.

Previously reported studies of the effects of devolatilization kinetics on overall combustor characteristics have demonstrated that combustion efficiency, flame front location, and fluid dynamical structure, are all sensitive to devolatilization rate over the range of published values (5). Similar effects were noted in this study. Based on these findings, the rate of mass evolution during devolatilization is considered to be important to flowfield and particle predictions. However, devolatilization rates are currently not well established, and this paper will not address this issue further.

The objectives of this paper are (1) to present theoretical results from an investigation of several thermal effects on devolatilization for single particles and in a comprehensive predictive model and (2) to illustrate the importance of considering chemistry/turbulence interactions when extending the model to allow for variable composition of the coal volatiles. The comprehensive model that was used is PCGC–2, Pulverized Coal Gasification or Combustion–2 Dimensional (axisymmetric). Thermal effects that were investigated include variable particle heat capacity, particle emissivity, heat of reaction during devolatilization, and volatiles heating value.

Variable Particle Heat Capacity

Merrick (6) suggested the following function for coal heat capacity:

$$c_v = \left(\frac{R}{a}\right)\left[g_1\left(\frac{380}{T}\right) + 2g_1\left(\frac{1800}{T}\right)\right] \qquad 1)$$

where g_1 is given by

$$g_1(z) = \frac{e^z}{\left[\frac{(e^z-1)}{z}\right]^2} \qquad 2)$$

These equations can be used for both coal and char and predict a monotonic increase in c_v with temperature. However, because composition varies with time, the increase in c_v for a heating and reacting particle may not be monotonic due to changes in average atomic weight (6). The high temperature limit for Equation 1 is 3R/a, which agrees with principles of physical chemistry.

Using Equation 1, Merrick obtained agreement between predicted and experimental values within about 10% over the temperature range of the available data (0-300°C) for various coal ranks (15-35% volatile matter). Graphite and char heat capacities were correlated within 5% over the range 0-800°C.

Calculations were carried out for single particles of 40 and 100 microns and for coal-water-slurry to test the effect of variable heat capacity on particle temperature and devolatilization rate. Particle heat capacities were calculated as the weighted sum of the heat capacities for raw coal, char, and ash. Gas temperature was assumed constant at 2100 K. Constant heat capacity cases were calculated using heat capacities calculated at 350 K and 525 K for the coal and char components, respectively. The two-equation model was used for devolatilization, with coefficients suggested by Ubhayakar et al. (7). The average atomic weights for the coal and char were assumed to be 8.18 and 12.0, respectively, with the latter corresponding to pure carbon. The heat capacity of ash was taken to be (6)

$$c_v = 593.3 + 0.586\,T \qquad 3)$$

The heat capacity of the particles at constant pressure was assumed equal to the heat capacity at constant volume. Radiative heat transfer and particle blowing were taken into account. However, oxidation was neglected to more clearly illustrate the effects of heat capacity.

Profiles of temperature and devolatilization rate for the 100-micron particles are shown in Figure 1. The gas temperature is also shown for comparison. Calculations for the 40-micron coal particles and coal-water slurry droplets showed similar effects of variable heat capacity during particle heatup. The initial heatup rate for the 100-μm particles is approximately 1.6×10^5 K/s for both constant and variable c_p. As particle temperature increases, heatup of the particle with variable c_p is retarded by the increasing value of c_p, as shown in Figure 1a, resulting in a temperature difference between the two particles of as much as 500 degrees K. This temperature lag results in a 50 percent increase in the time required for particle ignition and a slight decrease in the devolatilization rate, as shown in Figure 1b. The slower heatup rate during devolatilization allows a greater portion of the particle to devolatilize via the low-temperature reaction, thus giving an ultimate volatiles yield that is approximately 5 percent lower than for the particle with constant c_p.

As shown in Figure 1a, the heatup rate decreases markedly during devolatilization, due to the blowing effect. This effect was similarly predicted by Ubhayakar and coworkers (7). The asymptotic temperature of both particles is approximately 200 degrees less than the gas temperature, due to radiative heat losses to the walls of the reactor, which were assumed to have a temperature of 1000 K.

Calculations were also performed with the comprehensive code (PCGC–2) for particles with constant and variable heat capacity. Contour plots of temperature for the constant and variable c_p cases are shown in Figures 2a and 2b, respectively. As shown, the temperature fields are similar, except that the temperature is somewhat lower in the variable c_p case. This can be seen by noting that the isotherms in Figure 2b are generally shifted toward the exit and centerline. The lower gas temperature was predominantly a result of the decrease in volatile yield from the coal. The delay in particle ignition caused by variable c_p is also apparent in Figure 2b on the centerline at the inlet.

The effect of variable heat capacity on total burnout is shown in Figure 3. The curve for variable c_p is shifted to the right, resulting in a decrease of approximately 3 percent in particle burnout at the exit of the reactor. This effect is consistent with the delayed ignition and slightly slower devolatilization rate observed in the single particle calculations. Interestingly, the decrease in burnout is approximately equal to the decrease in ultimate volatiles yield predicted for the single particles, even though particle oxidation was not ignored in the comprehensive predictions.

Particle Emissivity

Total emissivities for coal particles have been reported with large variation, as summarized by Solomon et al. (8). Measurements by Brewster and Kunitomo (9) for micron-sized particles suggest that previous determinations of the imaginary part of the index of refraction for coal may be too high by an order of magnitude. If so, the calculated coal

emissivity for these particles based on previous values may also be too high. However, the experimental work of Baxter et al. (10) indicates that the effective emissivity of 100-micron coal particles of several ranks of coal at low temperatures is probably not less than 0.7.

To investigate the sensitivity of devolatilization to coal emissivity, calculations were again performed for single particles and with the comprehensive code. For the single particle cases, emissivity was varied between 0.9 and 0.1. In the comprehensive code calculations, emissivity was varied from 0.9 to 0.3. The wall temperature was 1250 K in the former and 1000 K in the latter.

Little effect of emissivity was noted in either set of calculations. The high gas temperature in the single particle calculations made convection/conduction the principal mode of heat transfer. In the comprehensive code simulations, the secondary air was swirled (swirl no. = 2), and the flow field was recirculating. Thus the particles were heated largely by contact with hot recirculating gases and not by radiation. In larger furnaces, or in reactors where the particles do not immediately contact hot gases, radiation may contribute significantly to particle heating, and in this case, greater sensitivity to the value of particle emissivity would be expected.

Heat of Reaction

A similar investigation was initiated on the effect of heat of reaction for devolatilization. Investigators disagree on both the magnitude and sign of the heat of reaction. Reported values range from -65.3 kJ/kg to +334 KJ/kg (6,11). Merrick (6) speculates that the source of the disagreement is related to the effect of variable heat capacity. The heat of reaction probably varies with coal type. However, our preliminary conclusions are that devolatilization calculations are insensitive to this parameter, which agrees with the conclusion of Solomon and Serio (11). Investigation of the effect of heat of reaction is continuing.

Volatiles Heating Value

The heating value of the coal volatiles must be known in order to calculate the energy released by gas-phase reactions. This heating value is a function of volatiles composition, which is a function of burnout. However, in comprehensive combustion simulations that treat the effects of chemistry/turbulence interactions (discussed in the next section), both heating value and composition of the volatiles are often assumed constant.

The effect of variable heating value was not tested in single particle calculations, because gas-phase reactions were not included in this model. The sensitivity of the comprehensive code to changing volatiles heating value was tested in an approximate manner by increasing the heat of formation of the coal. Since the volatiles enthalpy is calculated from a particle heat balance, and over 80 percent of the total particle mass loss was due to devolatilization, increasing the the heat of formation of the coal effectively increased the volatiles heating value. A value was chosen such that the adiabatic flame temperature of the coal at a stoichiometric ratio of unity was increased by about 200 K. Since the simulations were performed for fuel-lean (combustion) conditions, the actual gas temperatures increased by 50-75 K.

The results of this investigation are shown in Figures 2 and 3. As shown in Figure 2c, the gas temperatures are seen to be higher with the increased heat of formation of coal. Otherwise the temperature fields are quite similar. The higher temperatures are due to a combination of higher heating value and greater volatiles yield. The latter effect dominates everywhere except in the near-burner region. The higher temperature significantly affects coal burnout, as shown in Figure 3, with a large portion of the impact coming from the volatile yield in the early regions of the reactor. The magnitude of the variation of the offgas heating value was arbitrary in this case, but is regarded as representative of actual coals and possibly conservative.

Volatiles Composition

The variation of char and coal offgas composition with burnout has been correlated by both simple and complex reaction schemes (12-14). Accounting for this variation is not difficult for the particles. However, dealing with this variable composition and its interplay with gas phase turbulent mixing and kinetics is both complex and computationally expensive.

The successful prediction of turbulent and mean flow properties is a difficult proposition in typical combustion environments (15). Although reasonable success has been achieved for some simple flows, the complexity of reacting, swirling, turbulent flows often exceeds the capability of even sophisticated turbulence models. The added complexity of chemical effects on these predictions and the effect of turbulence on the mean reaction rates compounds the problem. Indeed, combustion investigators have identified this problem as one of the critical needs of combustion research (16).

Several approaches to the problem have been proposed. Some of these were recently reviewed and compared to data by Smith and Fletcher (17). The approach used in the current paper is the statistical, coal gas mixture fraction model. The detailed theory and assumptions of this model are given elsewhere (1). Only a brief discussion is given here.

The statistical, coal gas mixture fraction model involves convolving instantaneous properties over the turbulent statistics of the mixture to get time-mean properties. The statistics of the mixture is represented by the multivariate probability density function of a number of independent progress variables. The instantaneous mixture properties must all be represented as functions of only these progress variables.

The current code PCGC–2 allows for two progress variables. One progress variable is typically used for the inlet gas mixture fraction and the other is used for the coal offgas mixture fraction. The coal offgas composition is therefore assumed constant. Chemical kinetics are assumed fast for major gas species (intermixing of fuel and oxidizer is rate-limiting), so that the mixture is in local instantaneous equilibrium, and local properties depend only on the local elemental composition and enthalpy. With the two mixture fractions, the local composition is specified. Enthalpy fluctuations are assumed to be correlated with fluctuations in the stoichiometric ratio, as given by the two mixture fractions. Time-mean properties are therefore calculated by a double integral over the joint probability density function of the two mixture fractions. The evaluation of this integral consumes a significantly greater fraction of the computational time than any other single task in the code, even though a table of equilibrium properties is used to minimize the time spent performing equilibrium calculations.

Additional progress variables are required if coal offgas composition is to be allowed to vary. Each group of elements that are evolved from the coal must be tracked independently. Each additional progress variable for which the statistical variance is taken into account will increase the computational burden of this approach substantially. An investigation of the importance of variable coal offgas composition in a comprehensive code that treats chemistry/turbulence interactions has never been reported. Such an investigation would determine the extent to which such effects should be taken into account. It may be possible to ignore the turbulent fluctuations of some or all progress variables when allowing offgas composition to vary. If so, the computational burden would be reduced significantly.

The computational effort involved with the convolutions is not the only significant consideration in treating large numbers of progress variables. A multi-variate probability density function is required to perform the convolution. However, transport equations are typically written to describe individual probability density functions. To the extent that the fluctuations in the mixture fractions are independent of each other, the multi-variate pdf's will be equal to the product of the individual pdf's. However, as the number of progress variables increases, this independence will be difficult to maintain. Predicting the correlation coefficients will be difficult and the relevance of the model could be compromised.

A study of the impact of turbulent fluctuations on overall predictions was conducted to evaluate their importance. In this study, the fluctuations were either arbitrarily neglected or included, and the results of the comprehensive predictions under these assumptions were

compared. Similar results are shown by Smith and Fletcher (17). These results are an extension of their work, focusing on the effect of the coal offgas fluctuations. Figures 4, 5, and 6 show the results of ignoring turbulent fluctuations in the coal gas mixture fraction on gas temperature, total particle burnout, and centerline NO_x concentration. The coal gas mixture fraction η represents the degree of mixing between the coal volatiles and the inlet gas. As expected, neglecting the fluctuations in inlet gas mixture fraction had little effect on the calculations, since both the primary and secondary streams were air at 300 and 589 K, respectively.

The effect of ignoring the fluctuations in η on gas temperature can be seen by comparing Figures 2a and 4. Ignoring the fluctuations caused a high temperature ridge at the location of mixing between the primary and secondary streams, as can be seen by the higher concentration of isotherms in Figure 4. Taking the fluctuations into account smoothed the high temperature peaks. Similar observations were made by Smith and Fletcher (17) when they ignored turbulent fluctuations in both mixture fractions. Because the rate of mixing of fuel and oxidizer is reduced when turbulent fluctuations are ignored, the particle burnout is lowered as shown in Figure 5.

The above results were obtained assuming that the mixing is rate-limiting. The kinetics of NO_x formation and destruction are of the same order of magnitude as the turbulent mixing rates. Therefore, both mixing and kinetic considerations must be made to predict NOx concentrations. The model used to do so has been previously reported (18) and incorporated as a submodel in PCGC–2.

Figure 6 shows the effect of the fluctuations on pollutant predictions. In Figure 6a, turbulent fluctuations were ignored both in the calculation of major species, and in the calculation of the pollutant species, which are decoupled from the calculation of major species. In Figure 6b, turbulent fluctuations were taken into account for both calculations. As shown, the predicted NO levels are quite sensitive to rigorous accounting for the effects of turbulence on chemistry. When turbulent fluctuations are taken into account, oxygen from the secondary mixes more rapidly with the primary, and more NO_x is formed. Although data were not available for comparison with this calculation, previously reported calculations have shown that solutions taking the turbulence into account agree more closely with data (18).

Conclusions

Coal devolatilization is typically responsible for flame ignition and the ignition point and volatile yield of the devolatilization reactions have large impacts on overall combustion characteristics.

The temperature and composition dependence of particle heat capacity alters comprehensive code predictions of particle temperature, particle ignition, particle burnout, gas ignition and combustion efficiency. The effect is predominantly linked to the predicted ignition point of the coal and the extent of devolatilization.

For typical operating conditions of entrained-flow reactors (cold walls, hot gas), the value of coal particle emissivity does not significantly affect comprehensive code predictions. Preliminary results indicate that predictions are also insensitive to heat of devolatilization, but further investigation of this effect is needed. These conclusions may be different in situations with less dominant conductive/convective heat transfer.

The heating value of the coal offgas affects coal burnout and, to a lesser extent, gas temperature. This effect is attributed to the volatile yield of the coal under different heating conditions. Correlations of offgas heating value with particle burnout may improve comprehensive code predictions.

Turbulent fluctuations have an important impact on the mean reaction rate of coal offgas with the gas mixture. Further investigation of the importance of variable coal offgas composition in comprehensive codes and the importance of including the effect of turbulent fluctuations is proceeding.

Acknowledgements

This study was conducted principally under subcontract to Advanced Fuel Research, Inc., who was under contract to the Morgantown Energy Technology Center (Contract No. DE-AC21-86MC23075). Mr. Justin Beeson is the contract officer. Some of the single particle calculations were performed by Mr. Larry Baxter while he was on leave at Sandia National Laboratories in Livermore, California.

List of Symbols

a	average atomic weight of coal or char (kg/kg-mol)
c_v	constant volume heat capacity (J/kg-K)
g_1	function defined by Equation 2
R	universal gas constant (8314.4 J/kg-mol/K)
T	temperature (K)
z	parameter in Equation 2

Literature Cited

1. Smoot, L.D. and P.J. Smith, *Coal Combustion and Gasification,* Plenum Press, New York (1985).
2. Lockwood, F.C. and A.S. Abbas, "Prediction of a Corner-Fired Utility Boiler," *21st Symposium (International) on Combustion,* The Combustion Institute, Munich, West Germany, August 3-8 (1986).
3. Boyd, R.K. and J.H. Kent, "Three-Dimensional Furnace Computer Modelling," *21st Symposium (International) on Combustion,* The Combustion Institute, Munich, West Germany, August3-8 (1986).
4. Truelove, J.S., "Prediction of the Near-Burner Flow and Combustion in Swirling Pulverized-Coal Flames," *21st Symposium (International) on Combustion,* The Combustion Institute, Munich, West Germany, August 3-8 (1986).
5. Fletcher, T.H., "Sensitivity of Combustion Calculations to Devolatilization Rate Expressions," Sandia National Laboratories, SAND85-8854 (1985).
6. Merrick, D., "Mathematical Models of the Thermal Decomposition of Coal. 2. Specific Heats and Heats of Reaction," *Fuel,* **62**, 540-6 (1983).
7. Ubhayakar, S.K., D.B. Stickler, C.W. von Rosenberg, Jr., and R.E. Gannon, "Rapid Devolatilization of Pulverized Coal in Hot Combustion Gases," *16th Symposium (International) on Combustion*, The Combustion Institute, Pittsburgh, Pennsylvania, 427-36(1977).
8. Solomon, P.R., M.A. Serio, R.M. Carangelo, and J.R. Markham, "Very Rapid Coal Pyrolysis,"*Fuel,* **65**, 182-94, (1986).
9. Brewster, M.Q. and T. Kunitomo. "The Optical Constants of Coal, Char, and Limestone," *J. Heat Trans.,* **106**, 678-83, (1984).
10. Baxter, L.D., D.K. Ottesen, and T.H. Fletcher, "Spectral Emission Characteristics of Coal Particles," Western States Section/The Combustion Institute, 1987 Spring Meeting, Provo, Utah, April 6-7 (1987).
11. Solomon, P.R. and M.A. Serio, "Evaluation of Coal Pyrolysis Kinetics," NATO Workshop on "Fundamentals of Physical-Chemistry of Pulverized Combustion," Les Arces, France, July 28-August 1 (1986).
12. Smoot, L.D., P.O. Hedman and P.J. Smith, "Mixing and Kinetic Processes in Pulverized Coal Combustors, User's Manual for a Computer Program for 1-Dimensional Coal Combustion or Gasification (1-DICOG)," Final Report Volume II prepared for EPRI, Contract No. 364-1-3, (1979).
13 Niksa, S. and A.R. Kerstein, "The Distributed-Energy Chain Model for Rapid Coal Devolatilization Kinetics. Part I: Formulation," *Combustion and Flame,* **66**, 95-109 (1986).

14. Serio, M.A., D.G. Hamblen, J.R. Markham, and P.R. Solomon, "Kinetics of Volatile Product Evolution in Coal Pyrolysis: Experiment and Theory," *Energy & Fuels,* **1**, 138-152 (1987).
15. Sloan, D.G.,P.J. Smith, and L.D. Smoot, "Modeling of Swirl in Turbulent Flow Systems," *Prog. Energy Comb. Sci.,* **12**, 163-250 (1986).
16. Smoot, L.D. and S.C. Hill, "Critical Requirements in Combustion Research," *Prog Energy Comb.Sci.,* **9**, 77-103 (1983).
17. Smith, P.J. and T.H. Fletcher, "A Study of Two Chemical Reaction Models in Turbulent Coal Combustion," Winter Annual ASME Meeting, Anaheim, AMD-Vol. 81, December 7-12 (1986).
18. Hill, S.C., L.D. Smoot, and P.J. Smith, "Prediction of Nitrogen Oxide Formation in Turbulent Coal Flames," *Twentieth Symposium (International) on Combustion,* The Combustion Institute, 1391-1400 (1984).
19. Smoot, L.D., P.O. Hedman, and P.J. Smith, "Pulverized-Coal Combustion Research at Brigham Young University," *Prog. Energy Combust. Sci.,* **10**, 359-441 (1984).

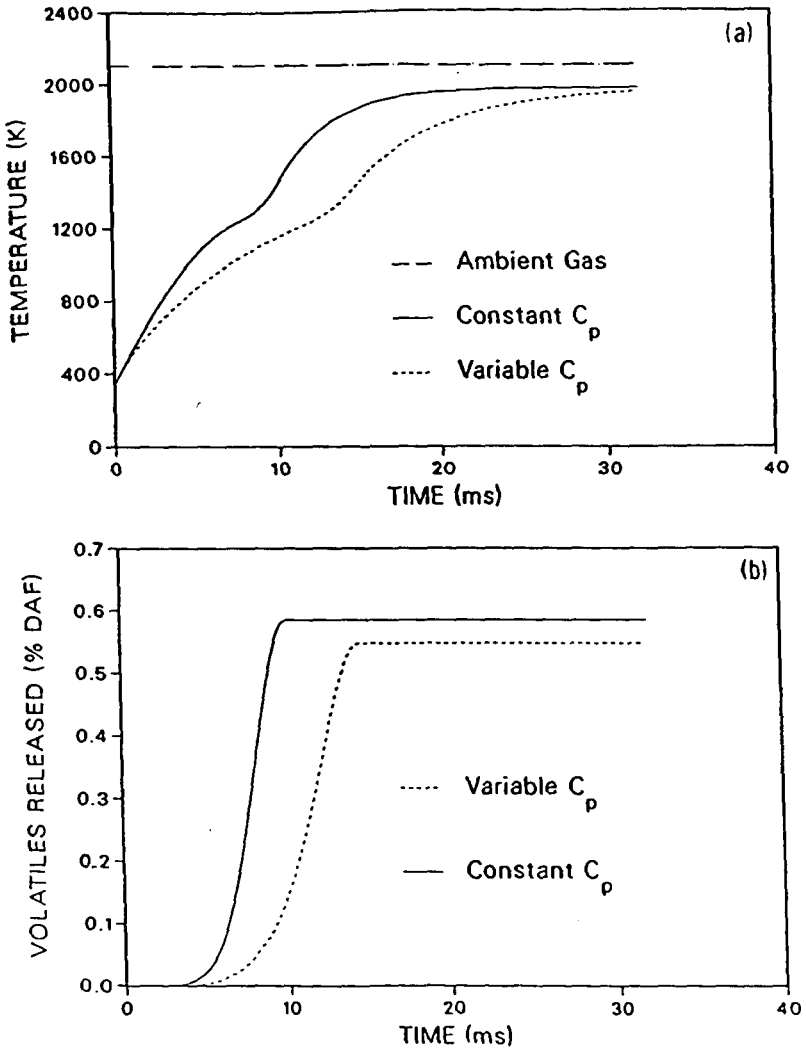

Figure 1. Variations of (a) particle temperature and (b) mass loss when different particle heat capacity formulations are used. The variable C_p case uses the correlation of Merrick (6).

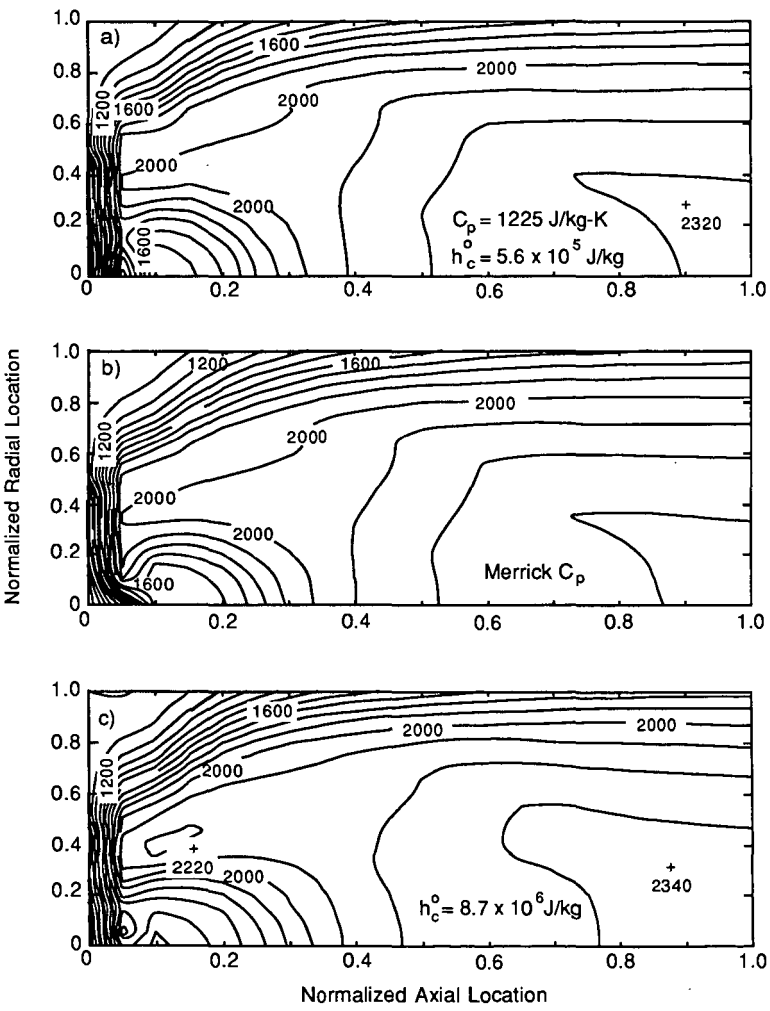

Figure 2. Contour plots of temperature for (a) constant particle heat capacity, (b) Merrick variable heat capacity, and (c) increased heat of formation of coal (h^o_c).

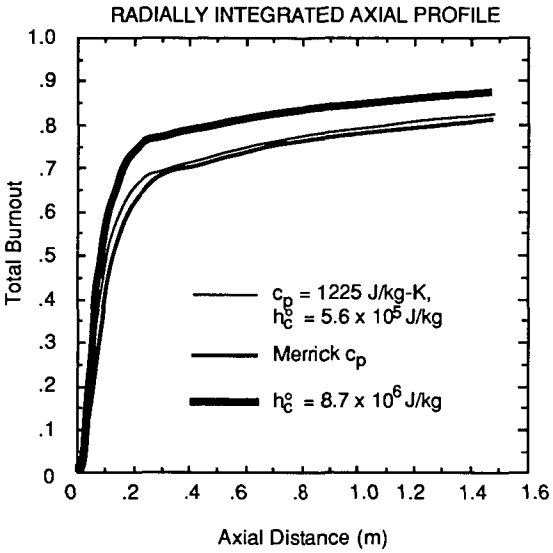

Figure 3. Effect of variable heat capacity and increased volatiles heating value on total particle burnout

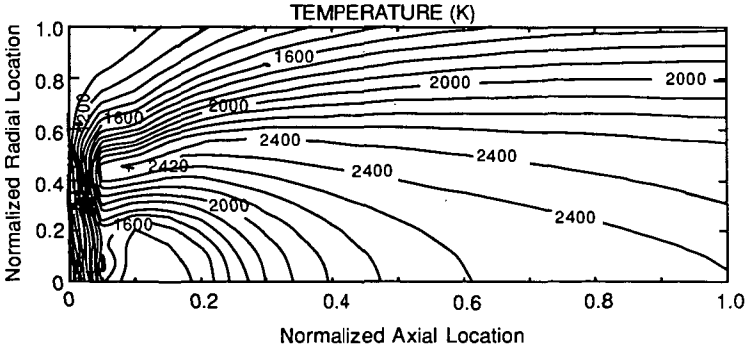

Figure 4. Gas temperature isotherms predicted when fluctuations in coal gas mixture fraction are neglected.

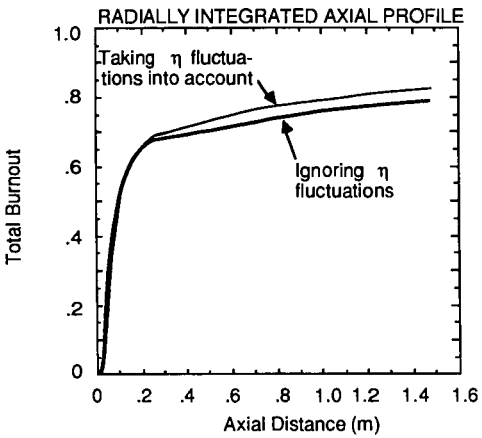

Figure 5. Effect of neglecting fluctuations in coal gas mixture fraction on total particle burnout.

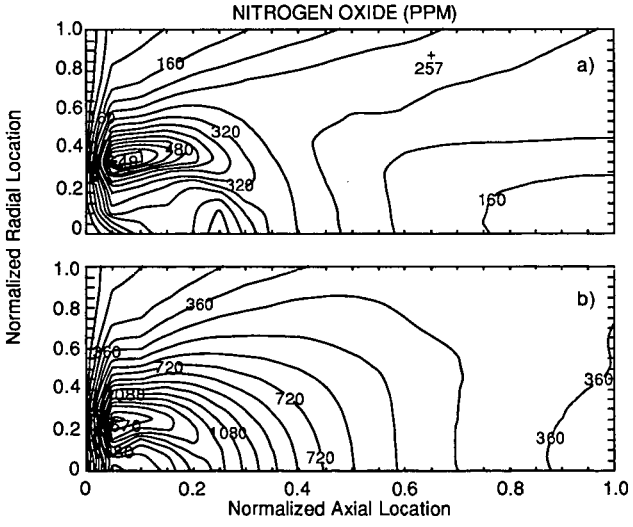

Figure 6. Predicted NO concentration (a) neglecting turbulent fluctuations of coal gas mixture fraction and (b) taking fluctuations into account.

Effect of Pressure on Pyrolysis of a Sub-bituminous Coal in an Entrained-Flow Reactor

Mohammad Fatemi, Alan W. Scaroni, Chun Wai Lee and Robert G. Jenkins

The Pennsylvania State University
Combustion Laboratory
405 Academic Activities Building
University Park, PA 16802

Introduction

To help produce advances in gasification technologies it is necessary to generate data on the effect of coal properties and operating variables on the pyrolysis/gasification behavior of coals under conditions similar to those in advanced-concept gasifiers; usually a high temperature-high pressure environment for entrained coal particles. Since relatively little data are available on coal pyrolysis/gasification at elevated pressure, especially in entrained flow systems, the primary objective of this study was to provide information on the effect of pressure on product yield and composition during pyrolysis.

The thermal decomposition of coal produces solid char or coke plus liquid and gaseous volatile matter (1):

$$\text{coal} \xrightarrow{\text{heat}} \text{solid (char or coke)} + \text{liquid (tar)} + \text{gas (CO, } CO_2\text{, } CH_4\text{, etc)}$$

The char consists mainly of carbon along with small amounts of hydrogen, oxygen, nitrogen and sulfur as well as the ash produced from the mineral matter. Tars are vapors at the pyrolysis temperature and pressure. The quality and quantity of char, tar and gases produced during pyrolysis depend on coal type, temperature, heating rate, pressure, residence time and particle size (1).

Two general techniques have been used for coal pyrolysis studies (2): captive sample, where the coal is stationary or fixed during a run, and entrained-flow, where the coal is fed and products withdrawn continuously. Most data on pressure effects have been obtained using captive sample techniques (3-9). For example, Anthony et al. found a substantial reduction in weight loss with increasing pressure for the pyrolysis of a bituminous coal above 873 K (4). Suuberg et al. also reported a reduction in weight loss and tar yield with increasing pressure (7).

The entrained-flow technique, however, has been used more in recent years by researchers (10-16). Sundaram et al. examined the effect of pressure on pyrolysis of a sub-bituminous coal under various inert gas pressures (Ar, He and N_2) in an entrained-flow reactor (12). They reported that the tar yield increased with increasing pressure of helium, while it decreased with increasing pressure of argon. They also reported that the total carbon conversion went through a maximum before decreasing with increasing pressure. Serio et al., on the other hand, reported a reduction of about 25% in tar yield with increasing pressure for four different coals(13). A study similar to the one reported here on Montana Rosebud coal under the same pressure conditions but at higher temperatures and residence times has also been reported by Bissett (14).

Experimental

An entrained-flow reactor, which was capable of subjecting pulverized coal particles to temperatures and pressures of 1373°K and 1000 psig respectively for a range of particle residence times was used in this study. The reactor, which is equipped with a computerized data acquisition system for accurate monitoring of the experimental conditions, is shown schematically in Figure 1. Pulverized coal is injected into the furnace by entrainment in a cold gas stream (primary gas) as it passes through a semi-venturi. The coal laden gas flows through a water-cooled injector probe fixed at the top of the

furnace. A secondary gas stream which is preheated during its passage upward through an annular region surrounding the reactor tube enters the furnace near the tip of the injector probe. Char is collected by a water-cooled probe which can be adjusted over a range of distances from the bottom of the furnace. This gives the flexibility to change the pyrolysis residence time. Another method of changing residence times is to adjust the gas flow rates of the gases passing through the furnace.

Char is separated from the product stream in a filter vessel installed downstream of the collector probe. The particle-laden stream enters the cylindrically-shaped vessel tangentially and at a point midway up the vessel. The solid char falls into a sample vessel at the bottom of the cylinder, while much of the tar is trapped by a 20 μm stainless steel filter at the top of the vessel. The solid pyrolysis products and the material trapped by the filter both were extracted in a conventional Soxhlet apparatus using tetrahydrofuran (THF) as the solvent. The THF solubles, which are used to represent the tars produced during pyrolysis, were obtained by evaporating the solvent after extraction. The THF insolubles are used to represent the char yield.

Proximate analyses were performed on the chars using a Leco MAC-400 analyzer. Ultimate analyses were also performed on chars and tars using a Leco CHN-600 analyzer. Sulfur contents were measured by a Leco sulfur analyzer. The gas stream leaving the collector vessel is routed through an on-line Carle gas chromatograph which is capable of monitoring the following gases: H_2, N_2, O_2, H_2S, CO, CO_2, CH_4, C_2H_2, C_2H_4, C_2H_6, H_2O, SO_2, and C_3 + C_4 hydrocarbons. An infrared gas analyzer is used to continuously monitor the carbon monoxide concentration in the outlet gas stream to determine when the reactor has reached steady-state operation. Gas composition measured by the GC is then determined for steady-state pyrolysis. The furnace is operated from a remote control panel and monitored by computer.

Samples of sized Montana Rosebud sub-bituminous coal, with mean particle size of 57μm, were used in this study. Proximate and ultimate analyses of the raw coal are shown in Table 1. Pyrolysis experiments were performed at a temperature of 1189°K, applied N_2 pressures of 100-900 psig and residence times between 0.1 to 1.7 seconds. Coal particle residence times in the furnace were determined by using a computer flow model, which is a modified version of the one developed by Tsai for entrained-flow reactors operated at atmospheric pressure (17). We modified the flow model programs for use under our high-pressure entrained-flow reactor conditions.

Weight loss due to pyrolysis was calculated by using ash as a tracer. On a dry-ash-free basis, the governing equation is:

$$\Delta W = 100\% \left[1 - \frac{A_0 (100 - A_1)}{A_1 (100 - A_0)} \right]$$

where ΔW is the calculated weight loss on a daf basis, A_0 is the proximate ash content of the dry coal and A_1 is the proximate ash content of the dry char produced during pyrolysis. An assumption in this calculation is that mineral matter in the coal does not undergo transformations during the pyrolysis which would change the quantity of ash produced upon ashing the chars (15). Tar yields were calculated from the total amount of THF solubles collected, about 5-15%, and expressed as weight percent of coal (daf) fed into the reactor. Total gas yields were calculated from the difference between the weight loss and tar yield.

Results and Discussion

The effect of pressure on weight loss for pyrolysis at 1189°K, 0.3-1.0 seconds residence time and up to 900 psig applied N_2 pressure is shown in Figure 2. It is observed that at short residence times (0.3 and 0.5 seconds) increasing the pressure reduces the weight loss, but at a longer residence time (1.0 seconds) increasing the pressure increases the weight loss slightly after going through a minimum at 178 psig. The weight loss of the Montana Rosebud coal increased steadily with increasing residence time and reached a maximum at 1.0 seconds.

Figure 3 shows the effect of pressure on tar yield at 1189°K, 0.3-1.0 seconds residence time and up to 900 psig applied N_2 pressure. The tar yield increased significantly with pressure up to 178 psig for all residence times and, with the exception of short residence time (0.3 sec) tar, then continued to increase with increasing pressure but at a slower rate. The data are in agreement with those of Solomon et al., who reported similar tar yields for the Montana Rosebud coal at 1089°K and 0.47 seconds residence time (16). The data are also in general agreement with those of Sundaram et al. (12) who reported an increase in tar yield from a sub-bituminous coal with increasing pressure of helium.

Yields and composition of gaseous products are shown in Figures 4 and 5, respectively. Comparison of Figures 2, 3 and 4 indicate that the trend for total gas yield is consistent with the effect of pressure on weight loss and tar yield. The total gas yield drops as the pressure increases from 100 to 178 psig then increases slightly with further increase in pressure. This is also in a good agreement with the data of Solomon et al. At short residence time (0.3 seconds) CO and CO_2 yields increased significantly with increasing N_2 pressure while the CH_4 yield decreased. Reduction in CH_4 yield with increasing pressure has been reported by Serio et al. (13) In the experiments carried out at residence times higher than 0.3 seconds CO concentrations were higher than CO_2, and the concentration of CH_4 was higher than that of C_2H_4 which, in turn, was higher than C_2H_6. This is in good agreement with the data of Sundaram et al. (12) but agrees with that of Serio et al. (13) only for the CH_4, C_2H_4 and C_2H_6 hydrocarbon gases.

The effect of pressure on the C/H ratio of the tar and char produced from pyrolysis is shown graphically in Figure 6 and 7, respectively. It can be seen in Figure 6 that the C/H ratio of the tars remains relatively constant except at short residence times where there is a significant drop in the C/H ratio at 178 psig. Figure 7, on the other hand, shows that the C/H ratio of the char decreases significantly as pressure increases. At short residence times the C/H ratio of the char drops from over 1.8 at 100 psig to below 1.4 at 178 psig then remains relatively constant. At the longer residence time the C/H ratio decreases gradually from over 2.2 at 100 psig to 1.8 at 900 psig N_2 pressure.

Conclusions

Pyrolysis of a Montana Rosebud subbituminous coal in a high pressure entrained flow reactor revealed the following:

1. Based on the weight loss, tar and gas yield, and C/H ratio of the tar and char, it appears that a significant change in pyrolysis behavior occurs at a pressure between 100 and 178 psig.

2. Weight loss and gas yield decrease with increasing pressure up to about 200 psig, and above this pressure there is no significant effect.

3. Tar yield is most affected by the pressure, increasing significantly with increasing pressure up to 200 psig.

4. The maximum tar yield was observed at a low residence time (0.3 seconds) and 178 psig applied N_2 pressure.

5. The CH_4 and C_2H_6 yields decreased significantly with increasing pressure, with C_2H_6 diminishing above 300 psig pressure for a residence time of 1.0 second.

References

1. Normand, M. L., "Heterogeneous Kinetics of Coal Char Gasification and Combustion," *Prog. Energy Combust. Sci.*, Vol. 4, 1978, pp. 221-270. (Pergamon Press Ltd., Great Britain).

2. Anthony, D. B. and Howard, J. B., *A.I.Ch. E. J.*, Vol. 22, 1976, pp. 625-656.

3. Anthony, D. B., Howard, J. B., Hottel, H. C. and Meissner, H. P., 15th Symposium (Int.) on Combustion, *The Combustion Institute*, Pittsburgh, PA, 1975, pp. 1303-1317.

4. Anthony, D. B., Howard, J. B., Hottel, H. C. and Meissner, H. P., *Fuel*, Vol. 55, 1976, pp. 121-128.

5. Solomon, P. R. and Colket, M. B., 17th Symposium (Int.) on Combustion, *The Combustion Institute*, Pittsburgh, PA 1979, pp. 131-143.

6. Suuberg, E. M., Peters, W. A. and Howard, J. B., *Ind. Eng. Chem. Process Des. Devel*, Vol. 17, 1978, pp. 37-46.

7. Suuberg, E. M., Peters, W. A. and Howard, J. B., *Fuel*, Vol. 59, 1980, pp. 405-412.

8. Niksa, S., Russel, W. B., Saville, D. A., 19th Symposium (Int.) on Combustion, *The Combustion Institute*, Pittsburgh, PA, 1982, pp. 1151-1158.

9. Arendt, P. and van Heek, K., *Fuel*, Vol. 60, 1981, pp. 779-787.

10. Kobayashi, H., Howard, J. B. and Sarofim, A. F., 16th Symposium (Int.) on Combustion, *The Combustion Institute*, Pittsburgh, PA, 1977, pp. 411-425.

11. Solomon, P. R., Hamblen, D. G., Goetz, G. J. and Nsakala, N. Y., *Preprints. Div. Fuel Chem.*, Am. Chem. Soc., Vol. 26, No. 3, 1981, pp. 6-17.

12. Sundaram, M. S., Steinberg, M., and Fallon, P. T., *Preprints, Div. Fuel Chem.*, Am. Chem. Soc., Vol. 28, No. 5, 1983, pp. 106-129.

13. Serio, M. P., Solomon, P. R. and Heninger, S. G., *Preprints, Div. Fuel Chem.*, Am. Chem. Soc., Vol. 31, No. 3, 1986, pp. 210-221.

14. Bissett, L. A., *Preprints, Div. Fuel Chem.*, Am. Chem. Soc., Vol 31, No. 3, 1986, pp. 222-229.

15. Jenkins, R. G. and Scaroni, A. W., Proceedings of the Sixth Annual Gasification Contractors Meeting, DOE/METC -86/6043, 1986, pp. 171-181.

16. Solomon, P. R., Serio, M. A. and Hamblen, D. G., Proceedings of the Sixth Annual Gasification Contractors Meeting, DOE/METC-86/60 43, 1986, pp. 182-191.

17. Tsai, C. N., "An Experimental Investigation of the Initial Stages of Pulverized Coal Combustion," Ph.D. Thesis, The Pennsylvania State University, 1985.

Table I

Characteristics of Montana Rosebud Subbituminous Coal Used in Pyrolysis Experiments

Proximate Analysis	wt% (dry)
Moisture	—
Volatile Matter	42.7
Ash	9.7
Fixed Carbon (by diff.)	47.6
Ultimate Analysis	**wt% (daf)**
Carbon	74.3
Hydrogen	6.0
Nitrogen	1.0
Sulfur	1.5
Oxygen (by diff.)	17.2

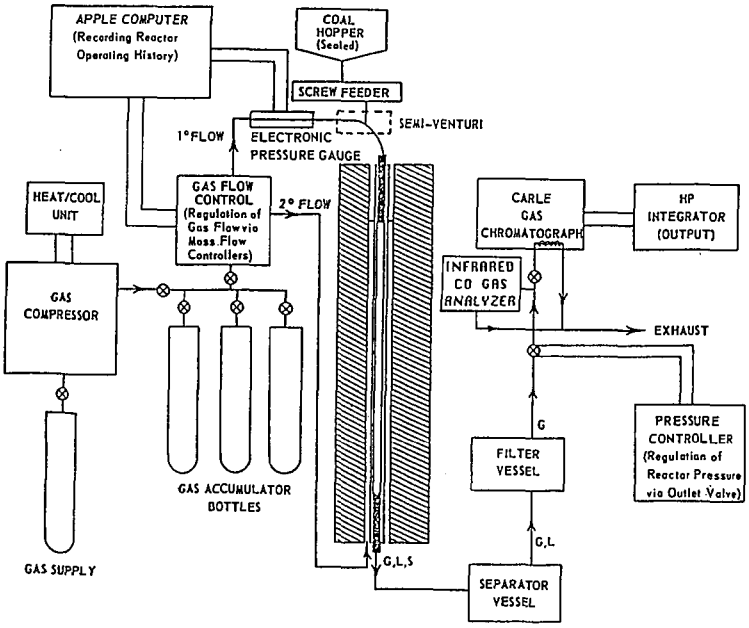

Figure 1. REACTOR CONFIGURATION

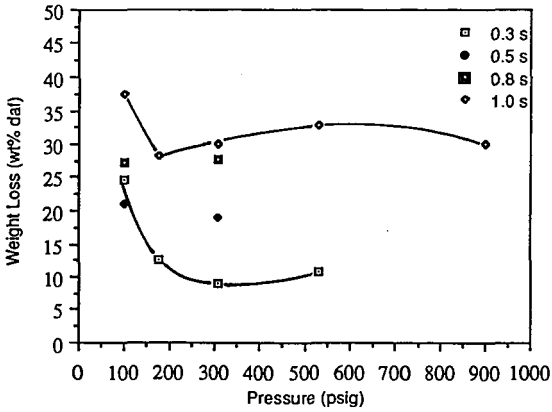

Figure 2. Effect of Pressure on Pyrolysis Weight Loss from Montana Rosebud Coal at 1189 K

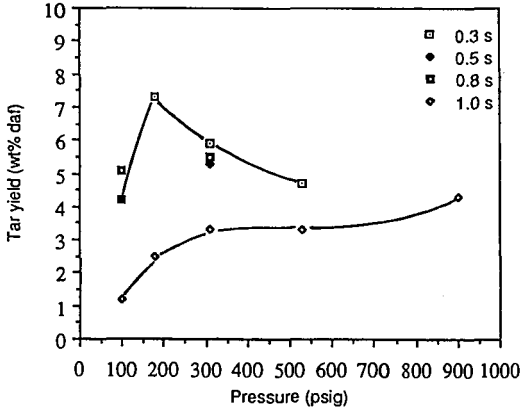

Figure 3. Effect of Pressure on Pyrolysis Tar Yield from Montana Rosebud Coal at 1189 K

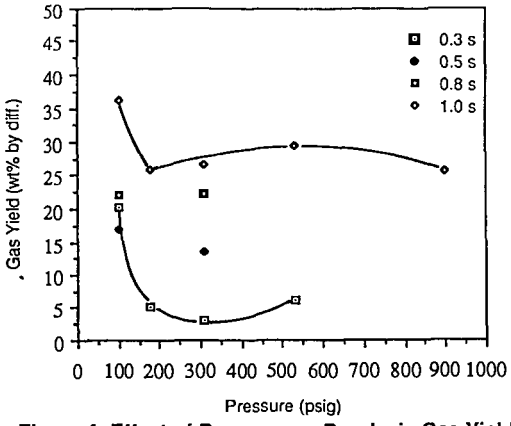

Figure 4. Effect of Pressure on Pyrolysis Gas Yield from Montana Rosebud Coal at 1189 K

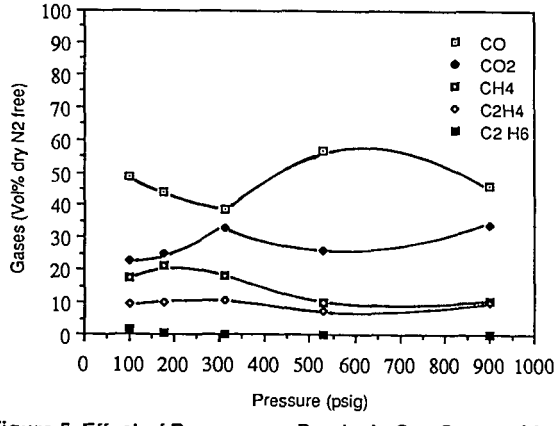

Figure 5. Effect of Pressure on Pyrolysis Gas Composition from Montana Rosebud Coal at 1189 K and 1.0 s

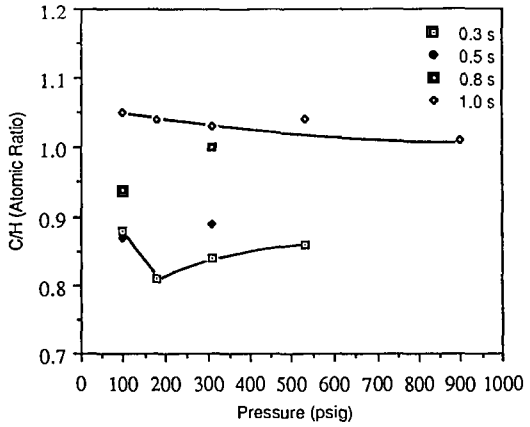

Figure 6. Effect of Pressure on C/H Ratio of Tar from Pyrolysis of Montana Rosebud Coal at 1189 K

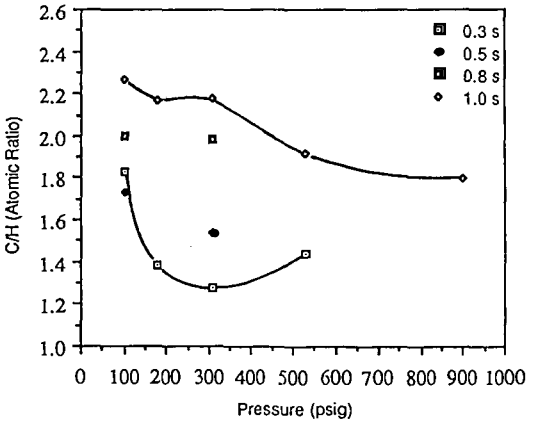

Figure 7. Effect of Pressure on C/H Ratio of Char from Pyrolysis of Montana Rosebud Coal at 1189 K

MODELING OF COAL PYROLYSIS UNDER THE CONDITIONS OF AN ENTRAINED PHASE REACTOR

W. Wanzl, P. Kaßler, K.H. van Heek, H. Jüntgen
Bergbau-Forschung GmbH, D-4300 Essen 13, West Germany

INTRODUCTION

Experimental laboratory work has shown that yield and quality of liquid products from coal pyrolysis can be controlled and optimized to a certain extent by suitable coaction of the primary thermal coal decomposition reactions and the secondary cracking or hydrocracking of the volatiles. The results indicate that favorable process conditions are provided in an entrained phase transport reactor which enables high heating rates for fast primary coal pyrolysis together with optimum residence time of the volatiles for secondary cracking and hydrocracking in the heated reactor zone. From that point of view the question arises how thermal coal decomposition can be described at high heating rates and whether transport limiting processes are involved in the overall reaction step. Especially for reactor design it is necessary to clarify to what extent experimental kinetic data gained at low heating rates can be applied to heating conditions like in a fluidized bed or in an entrained phase reactor.

KINETIC EXPERIMENTS

Low Heating Rates - Thermobalance Experiments

For experimental investigations of the influence of heating rate on the kinetics of coal pyrolysis three different types of equipment have been used as shown in Fig. 1. In previous work at low heating rates the course of product formation - total weight loss, tar, and gas - depending on temperature was measured in non-isothermal experiments in a thermobalance /1/. The low heating rate of some K/min in the thermobalance allows, beside the recording of the decrease in mass of the coal sample, a continuous analysis of the product gases (including detection of H_2O) and, by difference between total mass loss and total gas formation, the calculation of tar formation.

The mass loss curve as well as the curves for the different gaseous components show a certain structure which indicates that the volatiles are liberated in several single reactions for each component. The reactions can in a first order regarded as a set of independent parallel reactions. This model of non-isothermal reaction kinetics allows a mathematical description of product formation . With the model equations the measured curves can be described by fitting activation energy E and frequency factor k_o.

High Heating Rates - Grid Heater Experiments

The verification of the measured kinetic data at high heating rates has been carried out in experiments with a grid heater and with a Curie-point pyrolysis equipment. Schwandtner /2/ used a grid heater in the vacuum chamber of a time of flight mass spectrometer and applied heating rates up to 3000 K/s. The fast response signal of the mass spectrometer enabled kinetic measurements at high heating rates. According to theoretical calculations with the equations describing the non-isothermal reaction kinetics Schwandtner found a significant influence of the heating rate on the gas formation curves, which were shifted towards higher temperatures, respectively towards later times. But additionally, the gas release was shifted with rising particle

size as shown in Fig. 2. For coal grains exceeding 0.4 mm in diameter furthermore a tailing at the end can be noticed. With further enlargement of the grain size up to 1 mm and more the gas formation rate becomes independent of time. This means a reaction order of 0, which expresses the increasing influence of heat conductivity at these experimental conditions. This effect can be explained by the assumption that the heat transfer into the grain limites at certain heating rate and particle size the overall pyrolysis reaction. By a simple calculation of the temperature profile in the coal particle and integration of the total gas formation in the particle on the basis of a shell model the measured curves can be fitted as shown in Fig. 2.

High Heating Rates - Curie-Point Experiments

By using a different heating technique similar investigations were carried out with a pressurized Curie-point equipment which allows high heating rates above 10,000 K/sec and by that nearly isothermal pyrolysis experiments /3/. The method for measuring the critical particle diameter above which the transition from chemical reaction control to transport rate control occurs, involves measuring the yield of pyrolysis products, mainly the tar, at incomplete coal decomposition reaction. At a given heating rate and pressure, mass loss is independent of particle diameter at low particle size. By increasing particle size a distinct drop in the mass loss is noted as shown in Fig. 3, indicating that mass and/or heat transfer effects inhibit the escape of the volatiles from the particle. The critical particle diameter can, therefore, be determined by the change in the trend of mass loss versus particle size and finally plotted as function of heating rate (Fig.4).

HEAT TRANSFER CALCULATIONS

In order to achieve a more precise separation between the experimentally measured mass and enthalpy transport effects and their relevance for the measurement of kinetic pyrolysis data, model calculations were performed. The model assumes a spherical coal grain with its surface heated time dependently. It includes reaction enthalpies uniformly distributed in the coal particle. Intraparticle temperature profiles are then calculated using boundary conditions specific to the different heating methods in each apparatus.

The result of a calculation reproducing the conditions in the Curie-point measurements at a heating rate of 6.000 K/s for grain sizes at and above the critical radius (0.1 mm and 2 mm respectively) is shown in Fig. 5. The temperature profiles show quite clearly the existence of the measured critical diameters being in a first approximation a result of heat conduction within the coal. These radii are the limit up to which the heating rate can cause intra particle temperature gradients. The thermobalance uses a heating rate of 3 K/s, slow enough to prevent temperature gradients within the particle. With grain sizes below 0.1 mm also the pyrolysis yields of the Curie-point apparatus at heating rates up to 10,000 K/s may be evaluated without having to account for non-isothermal coal grains (Fig. 6).

As a consequence, looking at temperature profiles in a grain with the surface heated up instantaneously, as an upper limit for the conditions in an entrained phase reactor, internal temperature profiles die out after some ten miliseconds. These are time increments of the order of magnitude needed to reach thermal equilibrium between gas and coal within the very beginning of the reaction tube. The description of reaction kinetics in such a reactor type should therefore be possible on the basis of experimental data gained with the thermobalance and the curie point apparatus.

REFERENCES
1) Schwandtner, D.: Entgasung von Steinkohlen bei Aufheizgeschwindigkeiten oberhalb 10^5 grd/min, Thesis, Aachen. 1971
2) Wagner, R., W.Wanzl, K.-H. van Heek.: Fuel 64 (1985) 571.
3) Bunthoff, D., W.Wanzl, K.-H. van Heek, H. Jüntgen: Erdöl und Kohle Vol. 36 (1983) 326

ACKNOLEGDEMENT
The work was carried out within the frame of the IEA-Pyrolysis project (sponsored by the governments of Germany, Sweden, and United Kingdom) and within the project Anwendungsorientierte Grundlagenforschung (sponsored by the Bundesminister für Forschung und Technologie, Germany).

	thermobalance	wire-net-technique	Curie-point-technique
apparatus	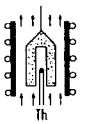	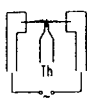	
sample size mg	1,500	10	5
heating rate K/s	0.05	200-1,500	10,000
final temperature °C	1,000	1,000	adjustable
			isothermal experiments
results	kinetics of product formation E, k_0, n, V_0 for H_2, CO_x, C_xH_y, BTX and tar	kinetics of particle swelling from high speed camera studies	kinetics of product formation E, k_0, n, V_0 for H_2, CO_x, C_xH_y, BTX and tar
	product yield		product yield

Fig. 1: Laboratory Equipment for Pyrolysis Experiments

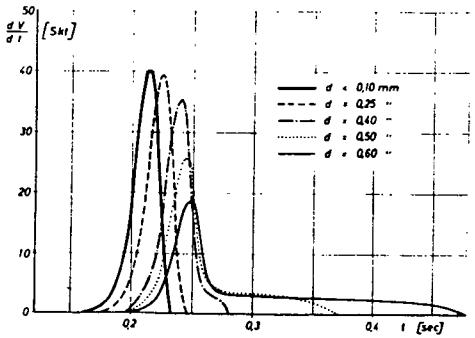

Fig. 2: Calculated Devolatilization Curves (E_a = 240 kJ/mol, $k_o = 10^{11}$ min^{-1})

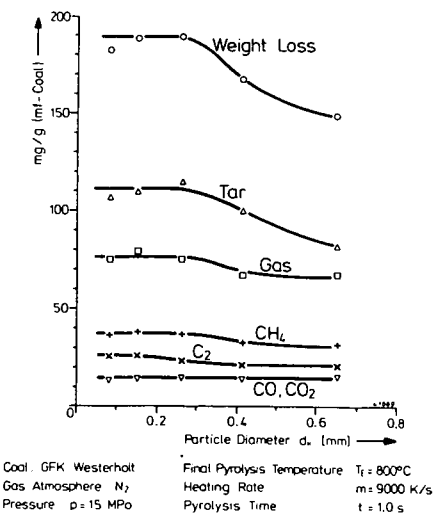

Fig. 3: Influence of Particle Size at High Heating Rates

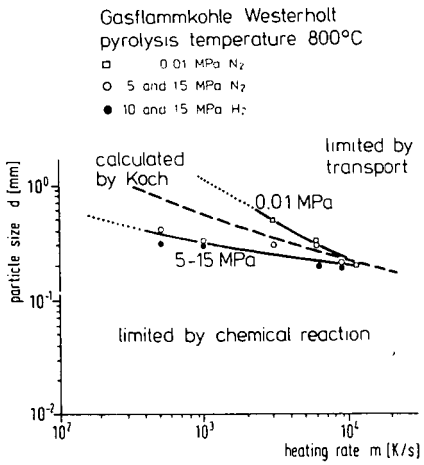

Fig. 4: Reaction Rate Limiting Step Depending on Heating Rate and Pressure

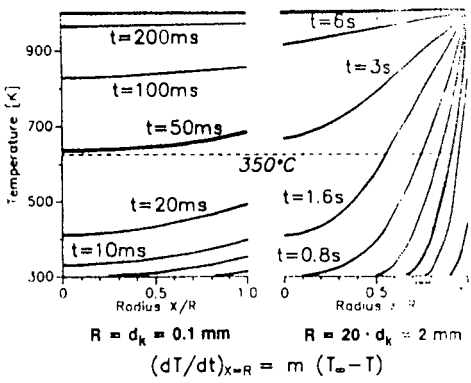

Fig. 5: Internal Profiles at and above Critical Radius d_k

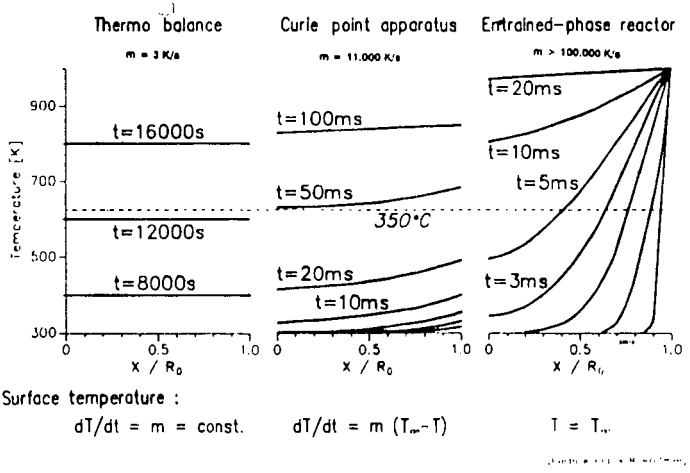

Fig. 6: Intra - Particle Temperature Gradients at Different Experimental Conditions

EFFECT OF HEAT TRANSFER ON TAR AND LIGHT GASES FROM COAL PYROLYSIS

J. D. Freihaut, W. M. Proscia, D. J. Seery

United Technologies Research Center
East Hartford, CT 06108

INTRODUCTION

Recent evidence has demonstrated that the products of coal pyrolysis vary with the conditions of heating. Both the reactivity of the char and the chemical composition of the evolved species vary with thermal flux during pyrolysis. Because of the inherent complexity of coal, it is difficult to uncouple the actual heat transfer process and the effects of variations in individual parameters in most pyrolysis experimental designs. Typical ranges of heat transfer rates available in a number of devolatilization reactor systems are indicated in Fig. 1. A particular reactor system may have additional constraints imposed by the nature of the heat flux source or transfer media - acceptable particle size of the parent coal, ambient pressure in which devolatilization can be performed, spectral distribution of a radiant source, residence time in the heat transfer field, etc. Some practical size constraints of wire grid and entrained flow reactor systems are noted in Figure 1.

This report presents the results of a study of coal pyrolysis in three different reactors covering a wide range of heating conditions. The specific purpose of the investigation was to determine if the rate of heat delivery to a high volatile bituminous coal during the tar formation and evolution phase has a significant effect on the tar yields and molecular weight distribution for a high volatile bituminous coal. From the point of view of understanding coal devolatilization and the development of fundamental kinetic models, the investigation is geared to determining whether the same tar formation and evolution processes are occuring in widely different regimes of heat transfer rate and modes of heat transfer. The heavy hydrocarbons yields and chemical characteristics provide a type of observable monitor, to generate a microscopic model of the devolatilization/pyrolysis process.

EXPERIMENTAL

Reactor Characterization

The influence of transport on coal devolatilization necessitates the characterization of reactor heat transfer properties in detail. Figure 1 displays the power density regimes required for a given heating rate of inert, spherical particles having thermal capacities equivalent to coal. Also shown are the range of power density capabilities of the heated grid and flash lamp reactors employed in this investigation and the corresponding regimes for entrained flow reactors. The heated grid system employed in this investigation generates power densities of 1-6 watts/cm^2 at grid temperatures between 600^{o}K and 1200^{o}K. The flash lamp system generates power densities, in the form of transient irradiance levels. Time averaged levels from 200 watts/cm^2 to greater than 700 watts/cm^2 were employed. Entrained flow reactors generally operates in the 10-100 watts/cm^2 regime. Final particle

temperatures of 1000°K or greater can be obtained in each system, but for significantly different transient times.

UTRC Heated Grid (HG)

The heated grid experiments are conducted by imposing a controlled voltage across a folded No. 325 mesh stainless steel screen. The screens are prefired, then loaded with 20-30 mg of coal by evenly distributing the coal between the folds of the screen. Simultaneous, real time measurements of applied voltage across the screen, current flow, and temperature of the screen are made by a rapid data acquisition system. The grid, char and tar are quenched by impingement of high velocity helium jets on the grid at the end of the heating program. The light gases evolved are measured by a FT-IR gas analysis system attached directly to the heated grid cell. Details of the UTRC heated grid apparatus have been given previously (Ref. 1, 2). The power density fields in vacuum conditions consist mainly of irradiance, whereas in the presence of ambient gases there can be significant gas conduction depending on the thermal conductivity of the gas. The power density fields were determined by synchronously measuring delivered current and voltage while measuring the temperature of the screen at pseudo steady-state conditions, and normalizing with respect to screen surface area. Depending on the heat transfer and heat capacity properties of the sample relative to the screen and ambient gas, the sample can couple to the local power density field. Such coupling has been demonstrated to change the observed temperature trajectory of the screen relative to an unloaded screen area (Ref. 1, 2). The main element of interest is the magnitude of the power density levels established by the heated grid system in the 600°K to 1000°K screen temperature regime, the temperatures of tar formation and evolution in such heating systems (Refs. 3, 4, 5).

UTRC Flash Lamp (FL)

Details of the flash lamp reactor have been given previously (Ref. 6). Under the range of capacitor voltage levels used in this investigation and with the particular match of lamp characteristics and driving circuit parameters the shape of the pulse did not vary significantly. The magnitude of the irradiance level delivered to the inside of the reactor was controlled by varying the neutral density filter and/or the capacitor bank voltage levels. The real time irradiance levels of the flash pulse were monitored by fast response pyrolelectric detectors. The detectors employed were calibrated with NBS irradiance standard lamps and a NBS traceable radiometer system used in conjunction with a chopped Argon ion laser. Pyroelectric detectors have a nearly constant response to wavelength from the UV to IR spectral regimes. Because of the possibility of inducing photochemical reactions with the UV component of the flash pulse, the reactors employed were pyrex, as were the neutral density filters. The delivered radiation is characterized by wavelengths ranging from 0.4 to 2.0 microns with peak intensities between 0.8 and 1.1 microns.

Entrained Flow Reactor (EF)

In the entrained flow reactor, coal is entrained in a primary gas and injected into a hot wall furnace, through which a preheated secondary gas is flowing whose temperature is matched with the wall. Entrained coal/char particles flow in a pencil-like stream down the center of the furnace tube and

are collected by a water cooled probe. Figures 2, 3 and 4 display the overall reactor design, aerosol-char separation device and the aerosol and char separation trains. Approximately 75% of the total reactor flow is diverted to the aerosol train. Both the cyclone (char) train and impactor (aerosol) train are followed by final filters. These filters consist of porous metal disks to ease in removal of tar species. Approximately 90% of the tar mass appears to collect on the final filters, with some deposition on stages 7 and 8 of the impactor train. SEM analysis of the impactor and cyclone stages as well as the final filters reveal the phase separator extracts particulates and aerosols less than 2 microns from the particulate flow at 75% gas flow removal. Tar material deposited on the final filter substrates consists almost entirely of condensed heavy hydrocarbons having no particulate boundary structure. Particulate material is efficiently removed by the impactor and cyclone stages.

Because the coals were initially size separated by aerodynamic means, it was originally thought that the size specific ASTM ash could be used as the basis for calculating mass fraction loss via the ash tracer technique. However, using this value gave negative weight loss results for the low wall temperature runs. Inspection of the gas analysis system data and the filter stages of the cyclone and impactor trains indicated substantial devolatilization was occurring. It became apparent that the feed system was not delivering coal particles having the same average ash content as measured for the gross sample for this particular size cut. Consequently, the reactor system was operated in the cold wall, cold flow mode with the delivered coal particles collected in stage 0 of the cyclone separator considered as representative of the actually delivered samples. It was noted that immeasurably small samples of fines were deposited in the impactor train or subsequent stages of the collection system.

Tar Sampling and Handling

Tar yields in the heated grid reactor are determined by weighing the condensible material deposited on the inside of the reactor walls and filters placed between the reactor and FT-IR gas cell. Tar yields in the flash lamp reactor are defined as the THF soluble portion of the condensibles found inside the reactor and on the filters placed between the reactor and FT-IR gas cell. These tars may contain material extracted from char particles in addition to "desorbed" (vaporized molecules, ejected molecular clusters and colloidal fragments) species evolved in the flash heating process. Relative molecular weight distributions of tars were determined with the THF soluble (room temperature, ten minute ultrasonic bath) portion of the evolved species. Entrained flow reactor tars were defined as the THF soluble portion of the material removed from the filtering system. All samples were passed through a 0.5 micron filter before injection into the SEC system. The details of the SEC have been given previously (Ref. 7).

RESULTS AND DISCUSSION

Tar yields and relative molecular weight distributions were obtained for PSOC1451. The elemental analysis for the mesh and aerodynamically separated coal samples are given in Table Ia. Table Ib lists the elemental compositions observed for the 20 - 30 micron cut of the parent coal PSOC 1451 D sample, the delivered particles captured in stage 0 of the cyclone collector, and the residual particles remaining in the feeder bed after several runs. Obviously,

the feed system delivers 20 - 30 micron particles having lower average mineral densities than that observed for the gross parent sample. The residual particles, that is, the particles left in the feeder bed have higher average mineral densities than the gross parent sample. Despite the fact that the size separation system and the feeder system both employ aerodynamic principles, segregation does occur in the reactor feed process. As a result it was deemed necessary to perform cold flow runs with each sample to generate baseline ash data for determining mass raction yields by ash tracer calculations. Results for tar yields, number average (Mn), and weight average (Mw) molecular weights are summarized in Table II. The data have been arranged in order of increasing net power density. The incident power density has been estimated from reactor property measurements indicated above and heat balance calculations assuming coal particles are spherical, with emissivity and absorptivity of 0.9, and heat capacity of 0.3 cal/gm-C. The particle sizes listed are an arithmetic average diameter of the high and low cutoff of the mesh range. The entrained flow tar yields are estimates based on one atmosphere runs performed in the flash lamp and heated grid reactor where particles were heated to the same final temperatures.

The limits of the molecular weight distributions range from 100-3500 for the heated grid and entrained flow tars, and from 100-5000 for the flash lamp tars. Previous investigators have obtained similar results for average molecular weights and for the range of the MWD's of various coal tars, and coal extracts (see Table III).

Pressure Effect in a Particular Reactor

Heated grid and flash lamp experiments were conducted at atmospheric and low pressures. The entrained flow reactor was operated at one atmosphere only. Comparisons of heated grid and flash lamp data given above (Table II) reveal a highly coupled dependency between mass and heat transfer parameters in determining molecular weight characteristics of the evolved tars. Larger MWD moments are obtained with the heated grid apparatus under low pressure conditions relative to atmospheric pressure for a given power program input (Fig. 5). The low pressure tars obtained in this apparatus have a significantly larger fraction of high MW species than the corresponding atmospheric pressure tars. Tar yields are reduced by 30% or more, depending on specific conditions, while molecular weight moments are reduced. These results are consistent with the results of Unger and Suuberg (Ref. 8) and others (Ref. 9, 10).

The same MWD pattern emerges at the lowest power density inputs employed with the flash lamp apparatus. That is, the low pressure tars have significantly higher molecular weight moments than the corresponding tars formed in one atmosphere of helium or argon (Fig. 5). However, at the next highest irradiance level (285 w/cm^2) the tars formed in one atmosphere of helium have larger moments than the corresponding low pressure conditions. These results can be understood relative to the variation in heat transfer conditions. Particles subject to a radiant pulse in low pressure conditions can only cool by an ablative process whereas particles radiantly heated in the presence of an ambient gas are cooled by conduction across a boundary layer as the particle temperature rises. In low pressure conditions the tars formed within the heating particle become hot enough to undergo some secondary cracking reactions in the evolution process. Depending on its thermal conductivity, the moderating influence of the ambient gas can be appreciable,

resulting in a lowering of the net power density delivered to the particles. Consequently, the lowest irradiance level employed was not sufficient to heat the 50 micron particles, in the presence of helium, to desorb more than 5 to 10% of the coal mass as tars. In vacuum conditions, on the other hand, the observed tar yield was ~23% for the lowest irradiance level. In one atmosphere of argon the yield was ~19% with MWD moments similar but somewhat lower than the corresponding vacuum run. The results also indicate that the change in irradiance level from an average level of 225 w/cm^2 to 285 w/cm^2 in low pressure conditions results in thermal cracking reactions of the tars as they are evolving from the correspondingly hotter particles. Light gas - CH_4, CO, C_2H_2, C_2H_4, HCN-yields associated with such high temperature reactions of tars are also increased. Although increases in CH_4 and CO are observed in the heated grid gas yields when the tar evolution process is performed in pressure as opposed to vacuum, significant changes in C_2H_2 and HCN are not observed for this coal type with a change in ambient pressure alone.

Variation in Molecular Weight Distributions with Power Density Level

The influence of power density on tar yields and MWD's was explored by utilizing the multi-reactor approach discussed previously. The effect of large differences in power density is explored by comparing results from different reactors for a particular ambient gas environment (Figure 6). The heated grid tars, which were devolatilized at the lowest incident power fields are observed to have lower number average and weight average molecular weights than the flash lamp tars, devolatilized at the highest power densities. The main mode of energy transfer is radiation in these reactors when operated in low pressure conditions, although the wavelength distribution of the radiation is shifted to the visible and near IR for the flash lamp relative to the heated grid. The molecular weight moments of the entrained flow reactor tars vary substanially with residence time. In order to compare results to the other reactors, the shortest residence time tars should be examined since these presumably will have experienced the smallest degree of gas-phase secondary reactions. The tars produced in the 900^{o}C, 40 msec residence time conditions have slightly lower molecular weights than the atmospheric pressure heated grid tars while the 1000^{o}C, 40 msec tars show similar moment characteristics. In both cases the initial tars (low residence time) show molecular weight moments less than the vacuum tars formed in the heated grid. Relative to the flash lamp tars generated in either vacuum or pressure conditions the EF reactor tars have lower moment and distribution characteristics.

Devolatilization Modeling and Coal Structure

For a given set of heat transfer conditions and particle size, it can be difficult to distinguish between mass and heat transfer effects on volatiles product distributions and characteristics (Ref. 11). Both phenomena can appear to effect any one observable similarly by introducing intraparticle or extra-particle (particle-gas boundary layer or entrainment stream) secondary reactions in evolving tar species. Lumped parameter measurements - tar yield, char yield, gas yield, weight loss - are not informative and can even be misleading for a microscopic understanding of coal devolatilization. Kinetic comparisons based on one yield characteristic or product type grossly oversimplify the complexity of the process and can be even more misleading. The results reported in this investigation indicate that detailed

characteristics of tar species generated under one set of reactor conditions can give more insight into the devolatilization process, but only if careful consideration of reactor conditions are included and detailed comparisons are made to results obtained with other reactors on the same analytical bases. A combination of tar characteristics and light gas yields and composition for a wide range of reactor conditions are necessary before a comprehensive understanding of coal devolatilization can be established.

The significant change in relative MWD's of desorbed tars with heat transfer rate in low pressure conditions strongly implies a wide distribution of bonding types, ranging from predominantly physical association to covalent bonding, among a wide distribution of organic structure sizes, molecular to colloidal. The "tar" characteristics depend on the rate (power density field) at which thermal energy is delivered to the organic matrix, the mode of energy delivery and mass transport conditions. Such behavior is not unlike that exhibited by large, thermally labile organic molecules which are observed to desorb from a given substrate intact, via pyrolysis fragmentation, or in both forms, depending on the specific mass and heat transfer conditions and the nature of the molecular interactions between the adsorbed molecules and substrate (Ref. 12-19). From a devolatilization perspective high volatile bituminous coals behave as if they contain a wide range of organic structures, molecular and colloidal, attached to a polymeric-like substrate by a variety of physical and chemical bonding types. The presence of specific fractions of physically and chemically bonded species has been postulated to interpret the plastic behavior and generation of intraparticle pyridine extratables during the rapid heating of an Appalachian provide high volatile bituminous coal (4, 40). The size characteristics of the desorbed species varies depending on whether pyrolysis fragmentation or desorption of relatively large species is emphasized by the heating conditions employed in devolatilization as well as mass transport related parameters.

Acknowledgements

The authors are grateful to Dr. D. Maloney for providing tar samples for comparisons. D. Santos and G. Wagner provided critical technical assistance in carrying out this investigation. Partial funding was provided by the Department of Energy under Contract DE-AC22-84PC70768.

TABLE Ia

PSOC 1451 (HVA BIT - Appalachian Province)
Elemental Composition

Mesh <d>	-270+325 49	-100+140 127	-50+70 254	-25+35 604	-20+25 774
%DAF					
C	82.38(0.47)*	82.26(0.36)	82.28(0.36)	80.66(2.80)	78.40(4.87)
H	5.44(0.03)	5.54(0.03)	5.58(0.02)	5.71(0.28)	5.69(0.20)
N	1.60(0.03)	1.62(0.02)	1.63(0.01)	1.56(0.08)	1.52(0.14)
S+O	10.58(0.55)	11.10(0.45)	10.48(0.37)	12.26(3.30)	14.13(4.83)
Ash	5.89(0.55)	10.78(0.69)	9.11(1.32)	24.39(18.9)	32.50(29.6)

* Numbers in parentheses represent one standard deviation.

<d> = Arithmetic average of particle range in microns

TABLE Ib

ELEMENTAL COMPOSITION OF PARENT, DELIVERED AND RESIDUAL PARTICLES:
PSOC 1451D, 20 - 30 MICRON PARTICLES

SAMPLE	%C	%H	%N	%S+O	%ASH*
PARENT-1	75.19	4.94	1.48	9.66	8.69
PARENT-2	75.25	4.95	1.45	9.52	8.80
PARENT-3	75.00	4.91	1.45	9.82	8.80
PARENT-4	75.06	4.90	1.45	9.78	8.80
DELIVERED-1	78.49	5.08	1.53	10.08	4.80
DELIVERED-2	78.54	5.08	1.50	10.36	4.50
DELIVERED-3	78.56	5.12	1.51	10.09	4.69
DELIVERED-4	78.59	5.08	1.48	10.01	4.80
RESIDUAL-1	74.46	4.91	1.41	9.49	9.69
RESIDUAL-2	74.42	4.89	1.43	9.84	9.39
RESIDUAL-3	74.45	4.90	1.45	9.99	9.19
RESIDUAL-4	74.44	4.91	1.45	9.78	9.39

TABLE II

TAR YIELDS AND MOLECULAR WEIGHTS

REACTOR/ PARAMETERS	PARTICLE SIZE [m]	ATM.	POWER DENSITY [W/CM^2]	Mn	Mw	% TAR YIELD	RUN I.D.
HG 450/2 *	49	VAC	0.62	626	839	14.2	229B
HG 550/2	49	AR	0.74	510	703	14.9	238A
HG 600/10	49	VAC	0.88	594	775	25.1	239A
HG 550/2	49	VAC	0.94	664	960	35.3	232C
HG 600/10	49	HE	1.3	522	692	12.7	242A
HG 350/1	49	VAC	1.8	655	948	20.0	224B
HG 800/2.5	49	VAC	1.9	621	855	21.0	221A
HG 800/2.5	49	VAC	1.9	610	843	24.4	237B
HG 800/2.5	254	VAC	2.0	639	869	25.1	246A
HG 800/2.5	127	VAC	2.1	616	841	28.4	245A
HG 800/2	774	VAC	2.3	616	875	24.3	253A
HG 800/2.5	774	VAC	2.3	632	869	23.3	247A
HG 800/2.5	49	AR	2.3	520	734	17.5	235C
EF 900/3 **	64	N2	50.0	485	698	****	017
EF 900/9	64	N2	-	490	709	-	018
EF 900/22	64	N2	-	382	560	-	019
EF 1000/3	64	N2	80.0	531	766	****	020
EF 1000/9	64	N2	-	406	596	-	021
EF 1000/22	64	N2	-	275	407	-	022
FL 1.8/30 ***	49	HE	225(32)	686	1059	6.0	705J
FL 1.5/60	49	HE	285(40)	784	1184	12.0	703C
FL 1.5/90	49	HE	430(60)	699	1134	19.0	704B
FL 2.2/60	49	HE	730(96)	545	898	17.0	706E
FL 1.8/30	49	AR	225(122)	714	1121	19.0	707C
FL 1.8/30	49	VAC	225	764	1180	23.0	709B
FL 1.5/60	49	VAC	285	663	1054	28.4	713B
FL 2.2/60	49	AR	729(293)	630	955	22.0	708B

Footnotes:

* HG X/Y - heated grid with 1000 C/sec ramp to X C, hold for Y sec, then 1000° C/sec ramp to 800°C, hold for 2.5-Y sec. The 600/10 runs are an exception: ramp to 600°C and hold for 10 sec.

** EF X/Y - entrained flow with X C gas temperature and Y" sampling position
900°C: 3"= 40 msec; 9" = 110 msec; 22" = 250 msec
1000°C: 3"= 40 msec; 9" = 100 msec; 22" = 230 msec

*** FL X/Y - flash lamp with X KV capacitor bank voltage and Y% neutral density filter. Values are time-averaged delivered irradiance; values inside parentheses are time-averaged net power density calculated from heat balance considerations. See Table III for characteristics of flash pulses.

***** - Not measured directly; at 3" residence time is estimated be about 20% (daf) of the parent coal mass from heated grid and flash lamp investigations. This yield represents the major fraction of the total volatile yields (Ref. 25) in 40 msec.

TABLE III

COMPARISON OF MOLECULAR WEIGHTS OF COAL DERIVED COMPOUNDS

SAMPLE	TECHNIQUE	Mn	Mw	MWD RANGE	INVESTIGATOR(S)
Pitt #8	SEC THF				this work
1 atm HG tar		500-525	675-750	100-3500	
vac HG tar		575-675	775-975	100-3500	
EF tar		275-550	400-775	100-3500	
1 atm FL tar		550-800	900-1200	100-5000	
vac FL tar		650-775	1050-1200	100-5000	
Pitt #8	SEC/VPO pyridine				Oh (1985)
HG tars:					
1 atm		350	-	100-1200	
vac		400	-	100-1200	
HG char extracts:					
1 atm		450	-	100-1500	
vac		500	-	100-1500	
Pitt Bruceton	SEC/VPO THF				Unger & Suuberg (1984)
HG tars:					
1 atm		500-700	-	100-4000	
vac		750-900	-	100-4000	
HG 1 atm char extracts:		750-1000	-	100-4000+	
Pitt #8 CO2 laser	SEC				Ballantyne et al. (1983)
1 atm tar	THF	223?	394?	60-3000	
Low Beam Shaw 84.2% C 115°C pyridine raw coal extract	Ebullio-scopy pyridine	870	-	-	Dormans & van Krevelen (1960)

REFERENCES

1. Freihaut, J.D., Zabielski, M.F. and Seery, D.J., Nineteenth Symposium (Int'l.) on Combustion, The Combustion Institute, 1159 (1982).

2. Freihaut, J.D. and Seery, D.J., ACS Div. of Fuel Chem., Preprints, 27, No. 2, 89 (1982).

3. Howard, J.B. in Chemistry of Coal Utilization, Sec. Supp. Vol. (ed. by Elliott, M.A.), John Wiley and Sons, New York, 340ff (1981).

4. Fong, W.S., Khalil, Y.F., Peters, W.A. and Howard, J.B., Fuel, 65, 195 (1986).

5. Suuberg, E.M., et al., Seventeenth Symposium (Int'l.) on Combustion, The Combustion Institute, Pittsburgh, 117 (1979).

6. Freihaut, J.D. and Seery, D.J., Proceedings of the International Conference on Coal Science, IEA, 957 (1985).

7. Freihaut, J. D., Proscia, W. M. and Seery, D. J. Proceedings of the Third Annual Pittsburgh Coal Conference, 684 (1986).

8. Unger, P.E., and Suuberg, E.M., Fuel, 63, 606 (1984).

9. Oh, M.S., Ph.D. Thesis, M.I.T., Cambridge, MA, 1985.

10. Solomon, P.R., Squire, K.R., and Carangelo, R.M., Proceedings of the International Conference on Coal Science, IEA, 945 (1985).

11. Kaiser, M., Wanzl, W., van Heek, K.H. and Juntgen, H., Proceedings of the International Conference on Coal Science, IEA, 899 (1985).

12. Cotter, R.J., Analytical Chemistry, 52, No. 14, 1589A.

13. Van der Peyl, G.J.Q., Haverkamp, J. and Kistemaker, P.G., Internat. Jnl. of Mass Spectrometry and Ion Physics, 42, 125 (1982).

14. Beuhler, R.J., Flanigan, E., Greene, L.J. and Friedman, L., J. Amer. Chem. Society, 96, No. 12, 3990 (1974).

15. Heresch, F., Schmid, E.R. and Huber, J.F.K., Anal. Chem., 52, 1803 (1980).

16. Posthumus, M.A., Kistemaker, P.G. and Meuzelaar, H.L.C., Analytical Chemistry, 50, No. 7, 985 (1978).

17. Cotter, R.J., Analytical Chemistry, 52, 1770 (1980).

18. Stoll, R. and Rollgen, F.W., Org. Mass. Spec., 14, No. 12, (642) (1979).

19. Kistemaker, P.G., Lens, M.M.J., Van der Peyl, G.J.Q., and Boerboon, A.J.H., Adv. in Mass Spectrometry, 8A, 928 (1980).

Fig. 1 Reactor Heat Transfer Regimes

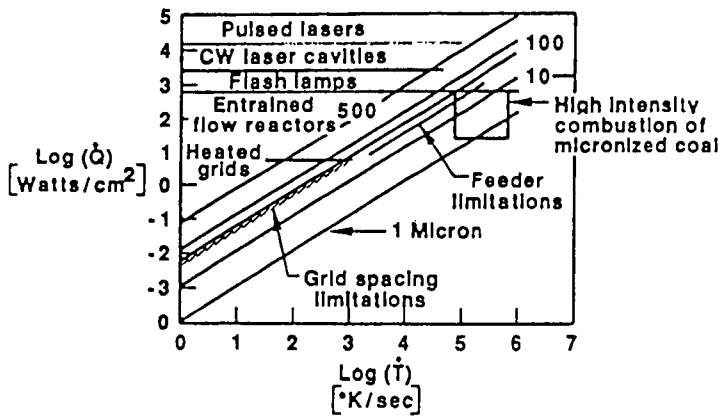

FIGURE 2

ENTRAINED FLOW REACTOR FOR COAL DEVOLATILIZATION

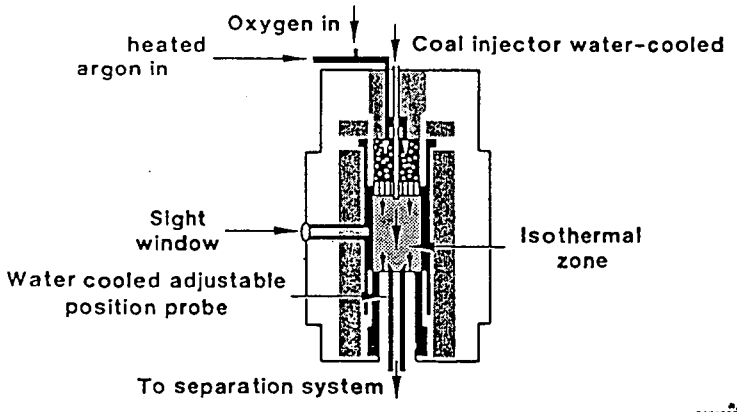

FIGURE 3

AEROSOL - CHAR SEPARATION APPARATUS

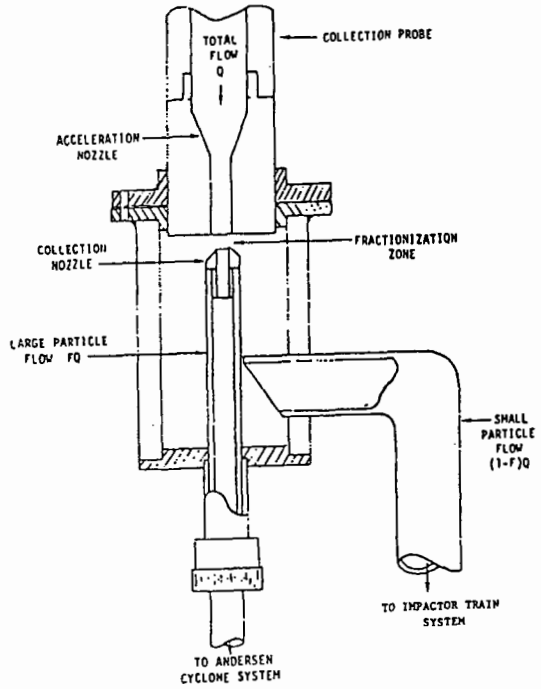

FIGURE 4

SAMPLE COLLECTION SYSTEM

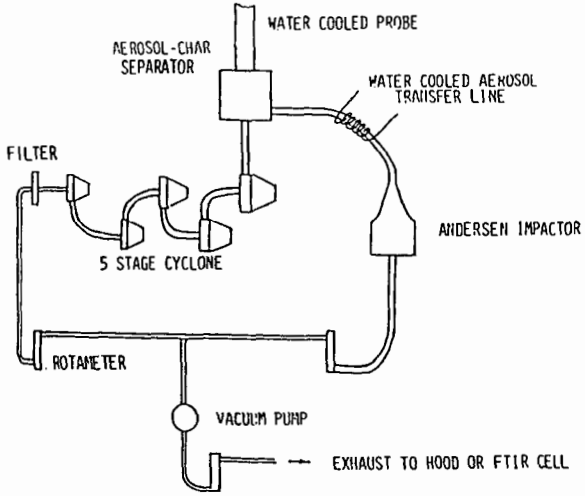

FIG. 5

EFFECT OF PRESSURE

On tar molecular weight distributions

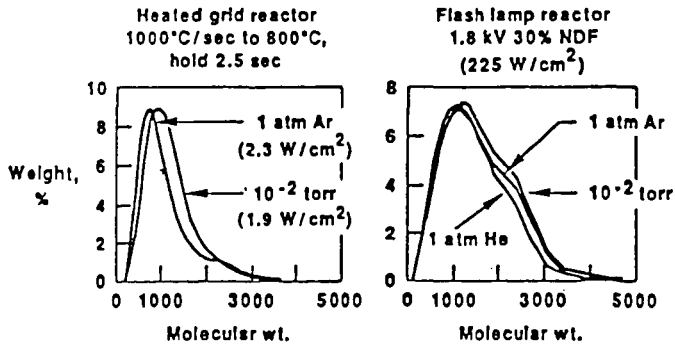

FIG. 6

EFFECT OF DIFFERENT REACTORS

On tar molecular weight distributions

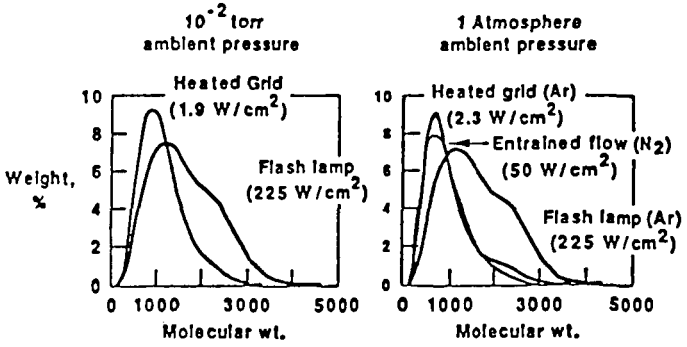

Pyrolysis of Coal at High Temperatures

Peter F. Nelson, Ian W. Smith and Ralph J. Tyler

CSIRO Division of Fossil Fuels, PO Box 136, North Ryde 2113, Australia

Introduction

Pyrolysis of coal at high heating rates is the initial step in its utilization by combustion, gasification or liquefaction. This involves the thermal decomposition of the coal's organic structure and the release of volatile products, which may account for up to 70% weight loss of the coal. Knowledge of the behaviour of the many volatile species liberated during pyrolysis is warranted, since their composition, rate of release and secondary reactions will have an important influence on such practical considerations as ignition, rate of combustion and trace gaseous and particulate emissions.

For many coals the condensed volatile species, or tar, comprise a major part of the volatile yield in coal devolatilization(1). They have been suggested as an important source of soot during coal combustion(2,3), and they have potential as models of coal structure. Thus an understanding of secondary reactions of tars is necessary for a complete model of coal devolatilization to be developed. The tars can crack to form soot, char and gases. Secondary reactions of the char involving ring condensation and gas evolution (mainly CO and H_2) will influence reactivity of the char towards gasification or combustion.

This paper presents data on the pyrolysis of a subbituminous coal and of tar produced by the rapid pyrolysis of this coal in a small fluidised bed reactor and in a shock tube. Kinetic parameters for light gas formation from secondary reactions of the tar have been determined. The results also provide evidence that secondary reactions of the tar are a source of polycyclic aromatic hydrocarbons (PAH) observed during pyrolysis. Data are also presented to show the effect of preparation conditions on the combustion kinetics of chars produced by rapid pyrolysis.

Experimental

The design and operation of the fluidised bed pyrolyzer has been described previously(1,4,5), as has the shock tube used for the high temperature cracking (6,7). Light gases were analyzed by gas chromatography. Tar components were recovered from the fluidised bed pyrolyzer by filtration through a Soxlet thimble held at liquid nitrogen temperature, extracted with dichloromethane and analyzed by high resolution gas chromatography(5). Millmerran subbituminous coal was used for all experiments (analysis wt%; C, 79.1; H, 6.5; N, 1.2; S, 0.6; O (diff.), 12.6).

Chars for the combustion studies were prepared, using a large-scale fluidised bed pyrolyser at temperatures of 540, 600 and 800°C. The product char was separated hot from the pyrolyser product gas, cooled, sampled, and then sieved to give size-graded fractions. The combustion reactivity of the char was determined using a flow reactor, and an ignition apparatus(10). The char samples contained appreciable amounts of volatile matter, the 600°C material having a standard VM yield of 16.6% (daf), and a hydrogen content of 4.0%.

Results

Kinetic parameters for secondary cracking of tar

Pyrolysis reactions of the coal under rapid heating conditions were separated from decomposition reactions of the tar to allow the vapour phase cracking reactions to be investigated free from influences of the original coal or char. This was

achieved by linking a fluidised bed pyrolyzer, operating at a low temperature (600°C) to minimise secondary reactions, to a shock tube capable of providing temperatures up to 2000K and residence times of 1-2 ms.

Arrherius parameters for the rates of formation of CH_4, C_2H_2, C_2H_4, C_3H_6, C_6H_6 and CO were determined and are presented in Table 1. Rates of production of C_2H_4 and C_3H_6 yielded activation energies of 230 and 260 kJ mol^{-1} respectively and are thus in excellent agreement with typical Arrhenius parameters obtained for the pyrolysis of long chain gaseous hydrocarbons(11,12). Thus the likely precursors of these alkenes are long chain n-alkyl groups. Recent studies(13) have shown that Millmerran flash pyrolysis tar contains at least 23 wt% n-alkyl groups of which about 40% are present as free alkanes and alkenes and the balance are bound to other structures, probably as substituted aromatics. Yields of C_2H_4 and C_3H_6 observed from the tar cracking are in excellent agreement with this n-alkyl content.

Kinetics for the lumped disappearance of long chain alkanes and alkenes have also been determined for pyrolysis in the fluid bed reactor. These results are presented in Fig. 1 and give an activation energy of 237 kJ mol^{-1} in good agreement with literature values for the decomposition of n-octane(11) and n-hexadecane(12).

Activation energies for the formation of CH_4, C_6H_6 and CO from the tar cracking are low and in the range 110 - 140 kJ mol^{-1}. This implies that many different functional groups in the tar contribute to the formation of these species with very different rates leading to a low apparent activation energy.

Formation of Polycyclic Aromatic Hydrocarbons (PAH)

Tar reactions have been identified as a source of the soot produced in both pyrolysis and combustion systems(2,3). Recent results(5) have also shown that the predominant components of the tar produced at temperatures greater than 800°C in the fluid bed reactor are PAH with up to five rings.

Mechanisms postulated for the formation of PAH in the combustion of simple hydrocarbons in flames include both ionic(14) and free radical(15) processes. The species observed, and which are regarded as important intermediates in the formation of the larger aromatic species, include phenylacetylene, styrene, indene, naphthalene and acenaphthalene. The free radical mechanisms involve addition reactions of aromatic radicals (predominantly benzyl and phenyl) to unsaturated aliphatics such as acetylenic species and stabilisation of the adduct by the formation of simembered rings. Recently Homann(16) has shown that these species occur in approximately equivalent relative amounts in flames burning a very wide variety of fuels.

The predominant species produced from coal pyrolysis at high temperatures where tar cracking is important are remarkably similar to those found in the flame studies. Fig. 2 shows yields of phenylacetylene, styrene and indene obtained from the pyrolysis of Millmerran coal in the fluid bed reactor. Analysis of the tar by FTIR shows that acetylenic species have also undergone addition reactions with the larger aromatic species.

The similarity of the species distribution observed for the coal pyrolysis products and the flame products strongly suggests that a common mechanism is responsible for the formation of PAH in these two systems. Thus in addition to their importance for soot formation, secondary reactions of volatiles are an important source of PAH formed in combustion.

Char reactivity

The combusion reactivity of the three chars determined in the flow reactor (production temperatures 540, 600 and 800°C respectively) is given in Fig. 3(a). At a

combustion temperature of ~700°C the reactivities of the chars show an inverse relationship to their preparation temperature the lower the preparation temperature the higher the reactivity(17). At 1000°C these differences have largely disappeared.

The question then arises as to the relative contributions to the observed reactivity by the consumption of the volatile and solid components of the char. The data in Fig. 3(a) were determined using a flow reactor when the particles and hot gas were mixed some distance before the burning suspension passed the positions in the reactor where rate measurements were made. There is some indication(17) that the volatile matter is evolved rapidly, and that the burning rate data are for the consumption of the solid char after the volatiles have been released.

Support for this view is given by Rybak et al.(10) where the reactivity of the 600°C char was determined from a measurement of particle ignition temperature. It was found that the ignition temperature was affected by the volatile content of the char - the more times the char was cycled through the heated ignition reactor (in the absence of oxygen), the higher the ignition temperature ultimately measured. Fig. 3(b) shows that the reactivity of the char reduces with increasing heating time (increasing number of cycles through the reactor) in a manner similar in relativity to the reactivity change with pyrolysis temperature shown in Fig. 3(a). After eight cycles the reactivity is close to that measured in the flow reactor (and in a quite different reactor at the Sandia Laboratories(18)).

References

1. Tyler, R.J. Fuel 1980, 59, 218
2. Seeker, W.R., Samuelsen, G.S., Heap, M.P. and Trolinger, J.D. Eighteenth Symposium (International) on Combustion, p.1213, The Combustion Institute, 1981.
3. McLean, W.J., Hardesty, D.R. and Pohl, J.H. Eighteenth Symposium (International) on Combustion, p.1239, The Combustion Institute, 1981.
4. Tyler, R.J. Fuel 1979, 58, 680.
5. Nelson, P.F. and Tyler, R.J. Twenty-first Symposium (International) on Combustion, in press, 1987
6. Doolan, K.R., Mackie, J.C. and Weiss, R.G. Combust. Flame 1983, 49, 221.
7. Doolan, K.R., Mackie, J.C. and Tyler, R.J. Fuel 1987, 66, 572.
8. Edwards, J.H. and Smith, I.W. Fuel, 59, 674-680, 1980.
9. Mulcahy, M.F.R. and Smith I.W., Proc. Conf. CHEMECA 70, Session 2, pp101-118, Butterworths, 1970.
10. Rybak, W., Zembrzuski, M. and Smith, I.W., 21st Symposium (International) on Combustion, 1986 (in press).
11. Doolan, K.R. and Mackie, J.C. Combust. Flame 1983, 50, 29.
12. Rebick, C. in Pyrolysis, Theory and Industrial Practice (L.F. Albright, B.L. Cryres and W.H Corcoran, Eds) p.69, Academic, 1983.
13. Nelson, P.F. Fuel, in press
14. Hayhurst, A.N. and Jones, H.R.N. J. Chem. Soc. Faraday Trans. 2, 1987, 83, 1.
15. Bittner, J.D. and Howard, J.B. Eighteenth Symposium (International) on Combustion, p.1105, The Combustion Institute, 1981.
16. Homann, K.H. Twentieth Symposium (International) on Combustion, p.857, The Combustion Institue, 1985.
17. Young, B.C. Proc. Int. Conf. on Coal Science, p.260, Dusseldorf, 1981.
18. Mitchell, R.E. and McLean, W.J. 19th Symposium (International) on Combustion, p.1113, The Combustion Institute, 1982.

Table 1 Kinetic parameters for formation of products from tar cracking in the shock tube.

Species Formed	A/s^{-1}	$E_a/kJ\ mol^{-1}$
CH_4	7×10^6	110
C_2H_2	5×10^9	220
C_2H_4	2×10^{12}	230
C_3H_6	5×10^{13}	260
C_6H_6	7×10^6	110
CO	2×10^8	140

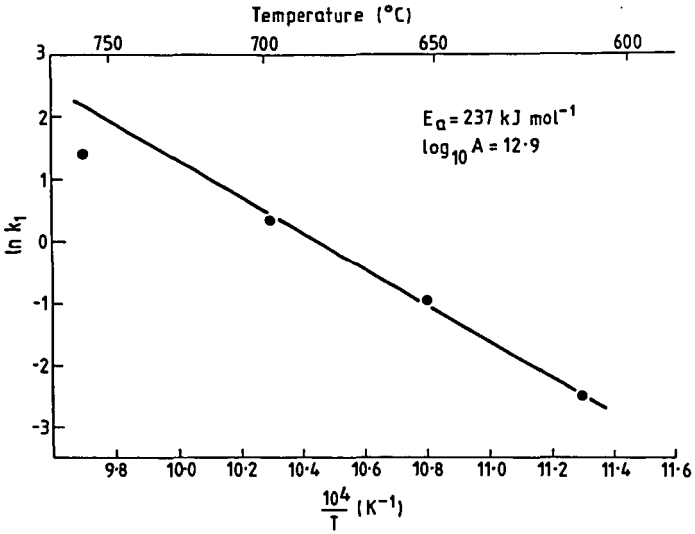

Fig. 1 Arrhenius relationship for polymethylene disappearance in fluidised bed reactor.

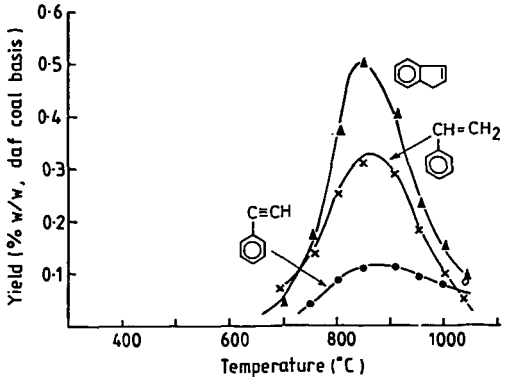

Fig. 2 Yields of indene, styrene and phenylacetylene as a function of temperature for pyrolysis of Millmerran coal.

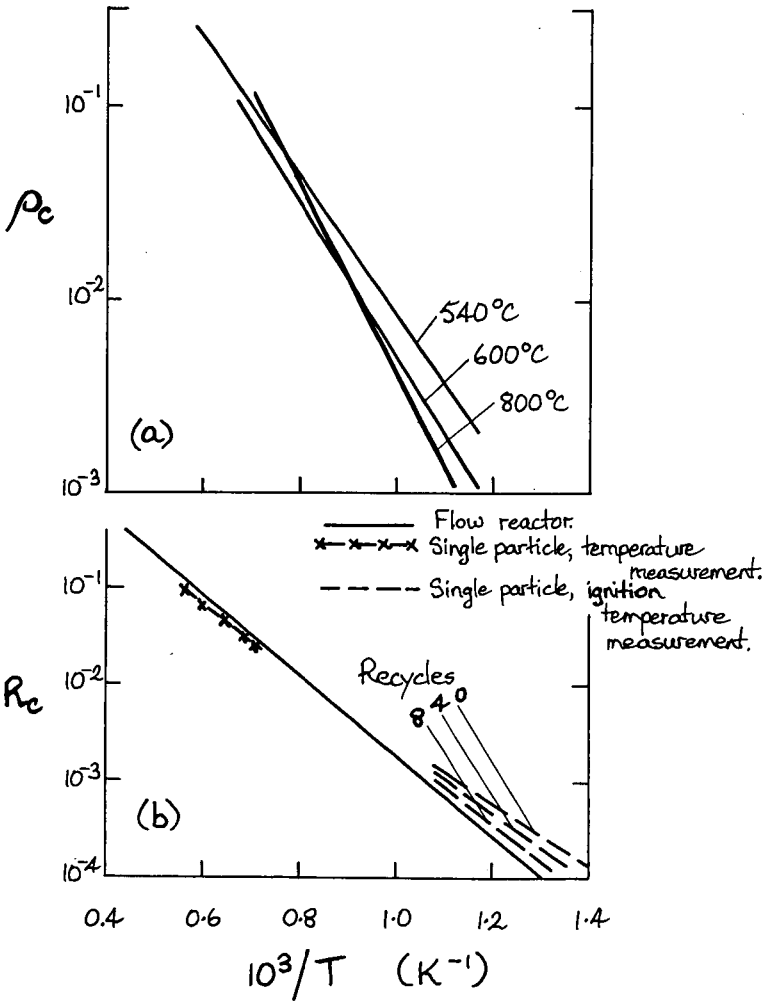

Fig.3. Reactivity of Sub-bituminous Coal Char: (a) as a function of pyrolysis temperature; (b) by various techniques, showing effect of heating time.

LOW TEMPERATURE ISOTHERMAL PYROLYSIS OF ILLINOIS NO. 6 AND WYODAK COAL

Francis P. Miknis, T. Fred Turner, and Lonny W. Ennen

Western Research Institute
Box 3395, University Station
Laramie, Wyoming 82071

INTRODUCTION

Despite what appear to be sufficient supplies of petroleum and natural gas to meet current U.S. energy needs, it is almost certain that future U.S. energy demands will be met in part by synthetic fuels produced from solid fossil fuels. The vast U.S. reserves of coal, in particular, have and will continue to receive considerable attention as a source of synthetic fuels. There are, however, certain fundamental constraints that limit the efficient processing and conversion of coal to synthetic fuels. Besides their chemical and physical heterogeneity, coals have highly aromatic chemical compositions. The high carbon aromaticity means that coals are hydrogen-deficient and as such do not readily convert to liquid and gaseous products. Consequently, innovative approaches are required to efficiently convert these hydrogen deficient materials to useful synthetic fuels.

Most coal conversion processes require thermal processing; therefore, pyrolysis is an important initial step in all coal utilization and conversion processes. Although coal pyrolysis has been studied extensively for several decades (1-4) it continues to be an active area of coal research. In part, this is a result of coal researchers' awareness of the need to understand pyrolysis in relationship to the basic structure of coal.

As a first step towards a systematic approach to understanding the relationship between coal structure and its conversion during pyrolysis, isothermal decomposition studies in the temperature range of 375°C to 425°C have been conducted on Illinois No. 6 and Wyodak coals. While prevailing attitudes favor the use of nonisothermal techniques to study coal pyrolysis, these techniques do not easily allow direct measurement of all the reaction products. Consequently, detailed chemical analyses of the reaction products are usually absent in such studies. In particular, intermediate states such as the metaplast are seldom measured directly.

With isothermal methods, it is possible to measure all the products of thermal decomposition including soluble intermediates. In addition to obtaining the overall weight conversions to products, detailed chemical and spectroscopic analyses can be obtained for each product class. For example, elemental analyses of all the products provide detailed carbon, hydrogen, sulfur, nitrogen, and oxygen balances. Solid and liquid state ^{13}C NMR measurements can be used to determine the partitioning of aliphatic and aromatic carbon in the products.

EXPERIMENTAL

Coal Samples

Isothermal pyrolysis experiments were conducted on Illinois No. 6 high volatile bituminous and on Wyodak subbituminous coal samples. Both coals were crushed and screened to obtain a 20/45 mesh particle size distribution. The initial crushed sample was thoroughly mixed and successively riffled to obtain aliquots of approximately 22 grams. Pyrolysis studies were conducted on samples taken from these aliquots. Ultimate and proximate analyses and carbon aromaticities of the two coals are given in Table 1.

Table 1. Analyses of Coal Samples

	Illinois No. 6	Wyodak
Proximate (% mf)		
Ash	8.1	8.0
Volatile Matter	39.0	47.0
Fixed Carbon	52.9	45.0
Ultimate (% mf)		
Hydrogen	5.3	5.5
Carbon	74.0	67.5
Nitrogen	1.0	0.8
Sulfur	3.4	0.7
Oxygen (diff)	8.3	17.5
Ash	8.1	8.0
Carbon Aromaticity	0.673	0.657

Pyrolysis Reactor System

The isothermal pyrolysis studies were carried out in a heated sand-bath reactor system described in detail elsewhere (5). In this system, nominally 10- to 20-gram samples were heated to reaction temperature by quickly immersing a tube reactor containing the coal sample into a preheated fluidized sand-bath. Typically, the coal sample reached the predetermined reaction temperature in less than 2 minutes. The reaction was quenched by removing the reactor from the sand bath and spraying liquid CO_2 on its surface. A helium sweep gas flow rate of 30 cc/min was used to remove the products from the reaction zone. The liquid product was collected in a dry-ice trap. Gaseous products were analyzed by gas chromatography, either by collecting the total gaseous product in an evacuated vessel or by analyzing the product gas on-line.

Material balances were calculated by measuring the weight change of the coal sample, the weight of collected liquid, the volume of collected water, and the weight of each gas component. The gas evolution curves were integrated, taking into account analytical system delays and backmixing, to calculate the total amount of gas evolved during each experiment. The reactor material balance closures were typically $100.2 \pm 0.7\%$.

Product Analyses

Elemental analyses (CHN and S) were obtained on the solid and liquid reaction products using standard instrumental techniques. Molecular weights were determined by vapor phase osmometry, using pyridine or methylene chloride as a solvent. Liquid state ^{13}C NMR measurements were made on a Varian CFT-20 or a JEOL 270 MHz NMR spectrometer. Solid state ^{13}C NMR measurements of the solid products were obtained at the NSF Regional NMR Center at Colorado State University. Gas analyses were obtained on a Hewlett Packard 5830 gas chromatograph modified to obtain complete gas analyses as frequently as every 3 minutes.

RESULTS AND DISCUSSION

Soluble Intermediate

One objective of this work was to investigate the transient nature of intermediate products that are formed during pyrolysis. Generally, global models of coal pyrolysis involve some form of intermediate (6-9). The simplest of these models can be written (9),

$$\text{coal} \xrightarrow{k_1} \text{intermediate} \xrightarrow{k_2} \text{products} \qquad 1)$$

The intermediate is often referred to as "thermobitumen" (10) or "metaplast" (6). Thermobitumen is the primary tar or bitumen formed during the initial stages of pyrolysis and acts as a plasticizer for the coal. Metaplast refers to coal which has been transformed into a fluid mass via depolymerization reactions, i.e., a metastable, plastic state. Neither material is defined in terms of solubility in a given solvent as, for example, the term bitumen is in oil shale pyrolysis. In fact, van Krevelen et al. (11) preferred the term metaplast to avoid the connotation that thermobitumen is a completely soluble material in a common petroleum solvent. Nevertheless, the properties and kinetic behavior of the soluble portion of the intermediate are known to affect the plasticity and conversion behavior of coals (12,13).

In this work, the residue coal from each isothermal pyrolysis experiment was extracted with chloroform to obtain information about the chloroform soluble portion of the intermediate. Chloroform was chosen over other commonly used solvents, such as pyridine, because it does not appreciably dissolve the raw coal and gives fairly high yields of soluble products from pyrolyzed caking coals (12).

Only small amounts of material were extractable with chloroform at any stage of pyrolysis for either coal (Figures 1 and 2). In the context of the simple model (Equation 1), the data in Figures 1 and 2 illustrate that either 1) $k_2 >> k_1$, and the soluble material is not retained long enough to plasticize the coal or 2) significant devolatilization occurs directly from the raw coal, without involving an intermediate state. The latter has been suggested to account for the increase in volatile matter with pyrolysis temperature, as well as development of fluidity in coal (9). We have observed a similar behavior of soluble intermediates during isothermal pyrolysis of New Albany shale from Kentucky, and have concluded that the greater the carbon aromaticity of the source material, the greater is the direct conversion of source material to products (primarily residue) (14).

Properties of Residue Products

Global models of coal pyrolysis, such as that depicted by Equation 1, do not incorporate any components of coal structure, although the ultimate yields of pyrolysis products are determined to a large degree by the carbon structure of the raw coal. With isothermal pyrolysis methods and solid state ^{13}C NMR techniques, it is now possible to measure changes that occur in the carbon structure of coal as a function of time and temperature. In addition, by obtaining the ultimate and proximate analyses of the residue coals, it is possible to monitor these changes quantitatively on a mass basis. These data were collected during the 425°C experiments for Wyodak and Illinois No. 6 coals (Figure 3).

The data in Figure 3 confirm that the aliphatic carbon weight loss behavior is similar to that of the total carbon. Conversely, the aromatic carbon remains relatively constant with time. Chou et al. (15) have observed a similar behavior of chars produced from flash pyrolysis of Illinois No. 5 coal at charring temperatures from 300°C to 800°C. These data support the theory that coal devolatilization

involves primarily the breaking of aliphatic carbon bonds and that the aromatic carbon tends to remain in the residue (16).

Total Aromatic Carbon in Products

During pyrolysis of fossil fuels, a net increase always occurs in the amount of aromatic carbon in the products (tar plus residue) over that in the starting material. This increase results from aromatization reactions of aliphatic moieties and the associated release of light, high hydrogen-content aliphatic species. Aromatization of hydroaromatic structures, such as tetralin, is a likely mechanism for contributing to the increase in aromatic carbon.

The extent of aromatization during pyrolysis can be determined by combining solid and liquid ^{13}C NMR measurements and the carbon mass balance data (Figures 4 and 5). For some experiments NMR carbon aromaticity and/or total organic carbon measurements were not obtained because insufficient quantities of tars were produced. In these cases the amount of aromatic carbon in the tar was estimated using the weight percent of produced tar and the average values of organic carbon and/or carbon aromaticities from other experiments at the same temperature. These data are denoted by the symbol ⊖ (Figures 4 and 5). The increases in aromatic carbon content for the Illinois No. 6 and Wyodak coals are about 18% and 10%. The reason for the low values is that only about 10% of the raw coals was converted to tars at the longest time (480 min) and highest temperature (425°C) studied.

An interesting feature of the data is that the net production of aromatic carbon approaches its limiting value during the early stages of pyrolysis (Figures 4 and 5). For example, at 425°C the net production of aromatic carbon for the Illinois No. 6 coal has reached 95% of the limiting value within 2 minutes (Figure 4c). Similar behavior is noted for the Wyodak coal. Thus, aromatization of the aliphatic moieties appears to be a very facile chemical reaction; however, it is not possible from these data to determine to what extent these reactions occur directly in the solid coal or in the produced tars.

ACKNOWLEDGMENTS

The authors wish to acknowledge the Colorado State University Regional NMR Center, funded by NSF Grant No. CHE-8208821, for providing the solid state ^{13}C NMR data. This material was prepared with the support of the U.S. Department of Energy, Grant No. DE-FG22-85PC80531. However, any opinions, findings, conclusions, or recommendations expressed herein are those of the authors and do not necessarily reflect the views of DOE.

DISCLAIMER

Mention of specific brand names or models of equipment is for information only and does not imply endorsement of any particular brand.

REFERENCES

1. Anthony, D. B. and J. B. Howard. AIChE Journal 22, 625 (1976).

2. Howard, H. C. in Chemistry of Coal Utilization, (H.H. Lowry Ed.), John Wiley, New York, 1963, 340-394.

3. Howard, J. B in Chemistry of Coal Utilization, 2nd Supplementary Volume (M.A. Elliot, Ed) Wiley-Interscience, New York 1981, 665-784.

4. Gavalas G. R. Coal Pyrolysis, Elsevier, New York, 1982.

5. Conn. P. J. , H. J. Rollison, and F. P. Miknis. Laramie, Wy., October 1984, DOE Report, DDE/FE/60177-1791.

6. Chermin, H. A. G., and D. W. van Krevelen. Fuel, 36, 85 (1957).

7. Unger, P. E., and E. M. Suuberg. 18th Symposium (International) on Combustion, The Combustion Institute, Pittsburgh, PA, 1981, 1203-1211.

8. Schaub, G., W. A. Peters, and J. B. Howard. AIChE Journal, 31, 903 (1985).

9. Gaines, A. F. Pure and Appl. Chem., 58, 833 (1986).

10. Berkowitz, N. An Introduction to Coal Technology, Academic Press, New York, 1979, p. 152.

11. van Krevelen, D. W., F. J. Huntjens, and H. N. M. Dormans. Fuel, 35, 462 (1956).

12. Dryden, I. G. C. and K. S. Pankhurst. Fuel, 34, 363 (1955).

13. Loison, R., Peytavy, A. F. Boyer, and R. Grillot, in Chemistry of Coal Utilization (H.H. Lowry, Ed) John Wiley, New York, 1963, 150-201.

14. Turner, T. F., F. P. Miknis, G. L. Berdan, and P. J. Conn, ACS Div. of Petrol. Chem. preprints, 32(1), 149 (1987).

15. Chou, M. M., D. R. Dickerson, D. R. McKay, and J. S. Frye. Liq. Fuels Technol., 2, 375 (1984).

16. van Krevelen, D. W., and J. Schuyer. Coal Science, Elsevier, Amsterdam, 1957, p 191.

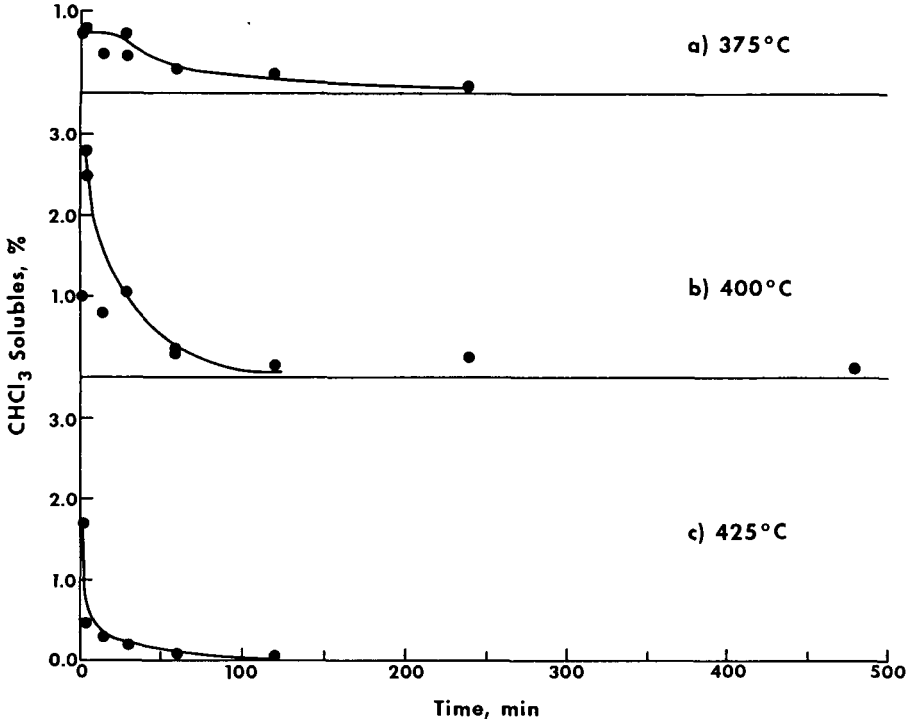

Figure 1. Chloroform-Extractable Material in Illinois No. 6 Coal vs. Time at a) 375°C, b) 400°C, and c) 425°C.

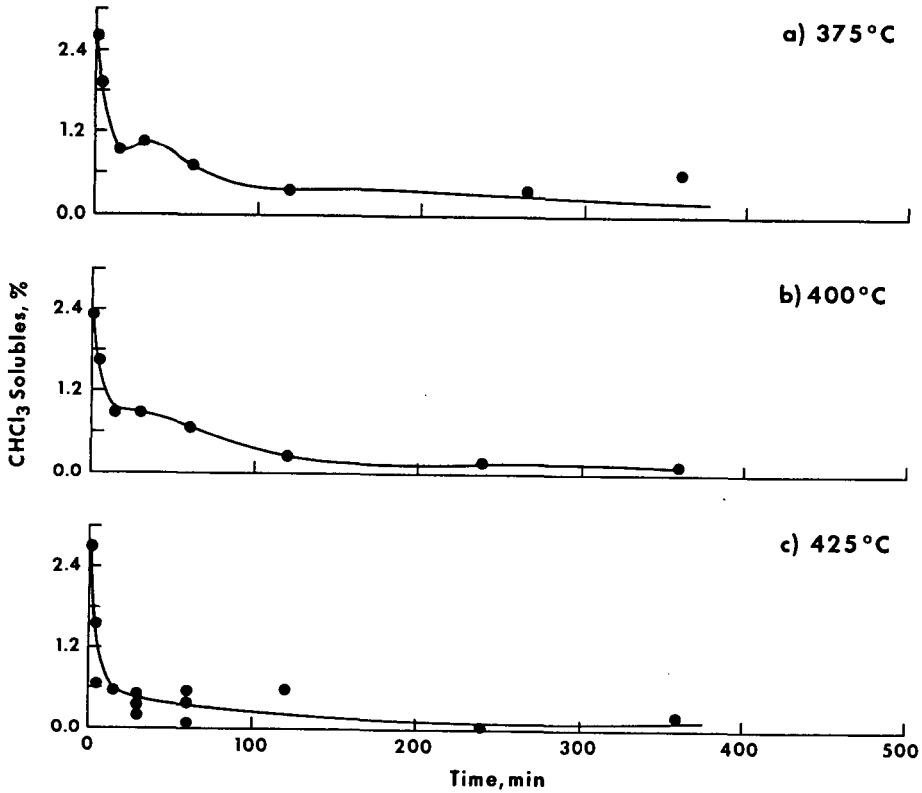

Figure 2. Chloroform-Extractable Material in Wyodak Coal vs. Time at a) 375°C, b) 400°C, and c) 425°C.

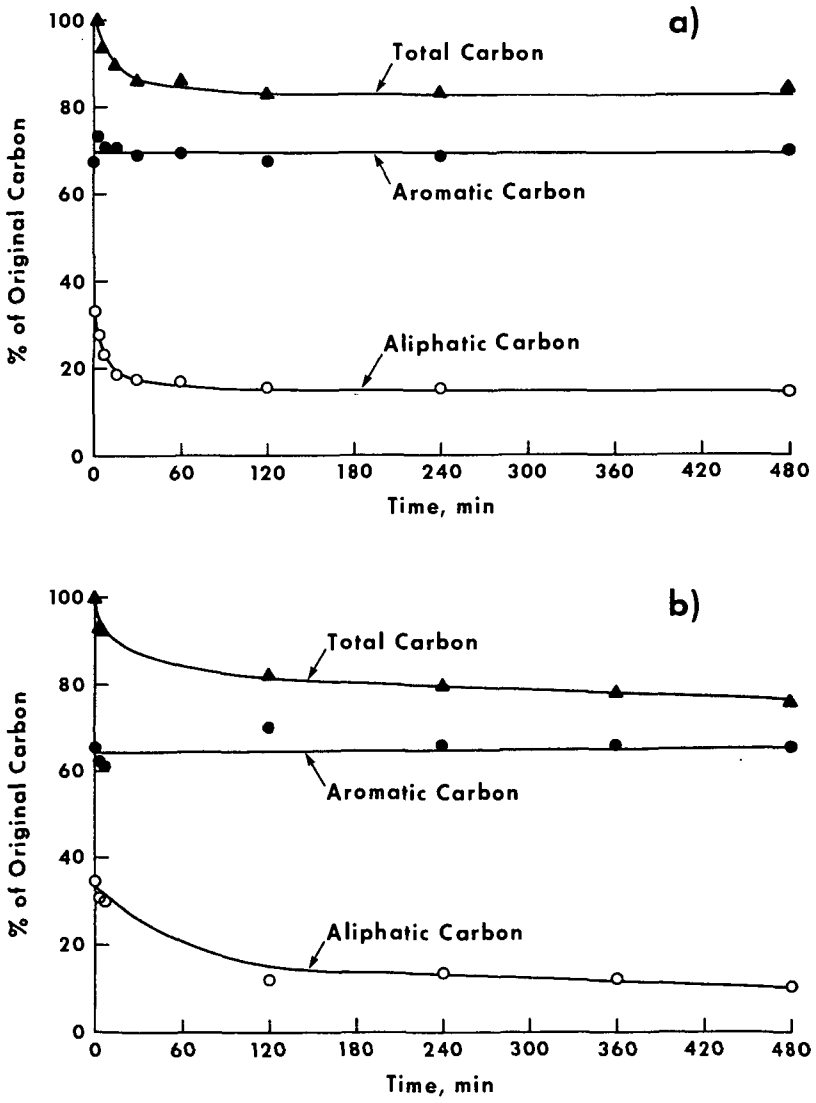

Figure 3. Distribution of Carbon Types vs. Time at 425°C for a) Illinois No. 6 and b) Wyodak Coal.

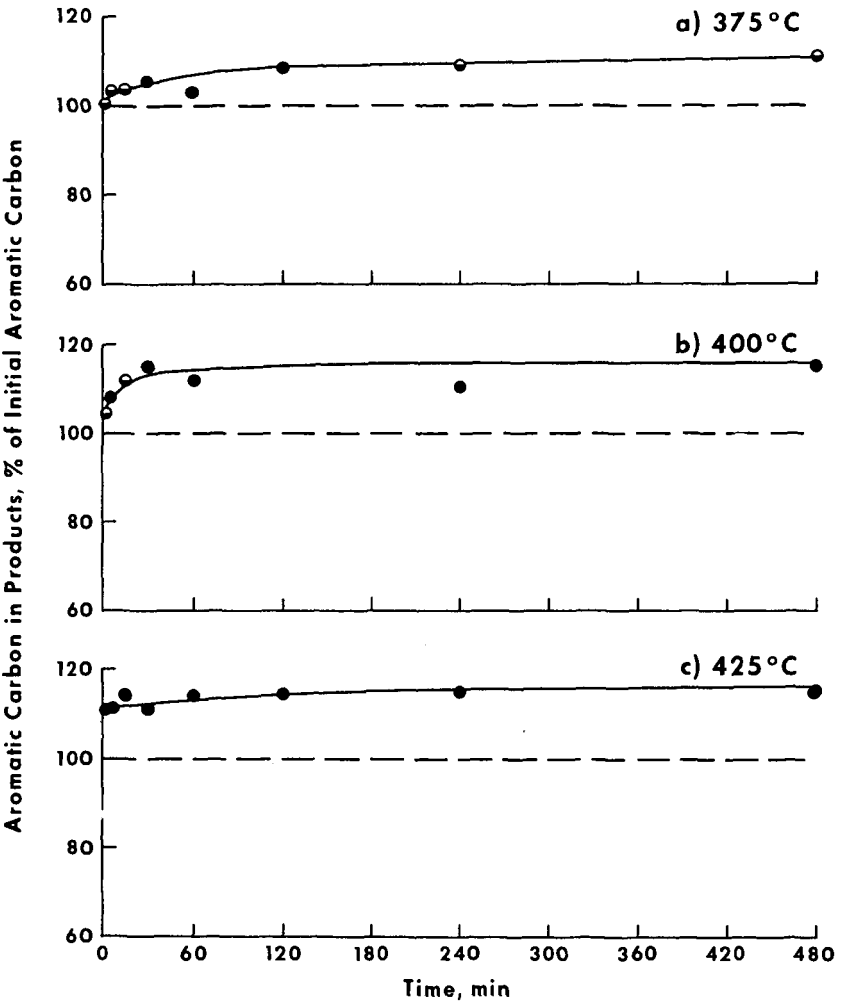

Figure 4. Total Aromatic Carbon in Products vs. Time for Illinois No. 6 Coal at a) 375°C, b) 400°C, and c) 425°C.

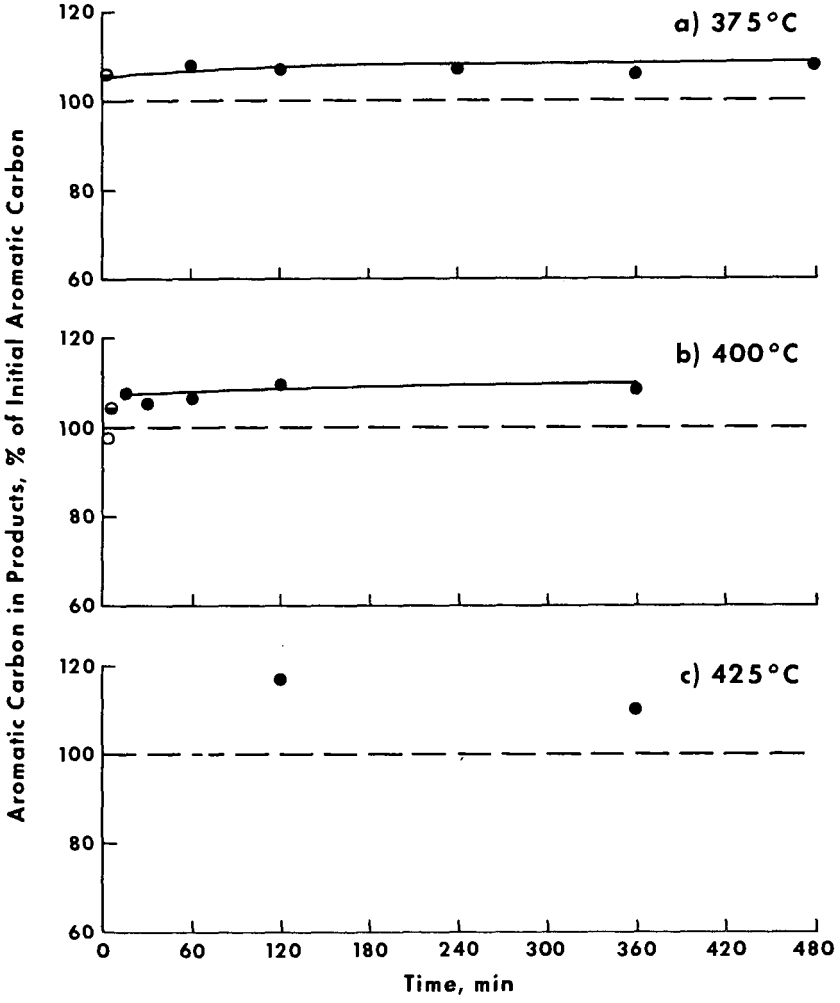

Figure 5. Total Aromatic Carbon in Products vs. Time for Wyodak Coal at a) 375°C, b) 400°C, and c) 425°C.

CHANGES IN THE DEGREE OF SUBSTITUTION OF PAC FROM PYROLYSIS OF A HIGH VOLATILE BITUMINOUS COAL

Mary J. Wornat, Adel F. Sarofim, and John P. Longwell

Department of Chemical Engineering, Massachusetts Institute of Technology
77 Massachusetts Avenue, Cambridge, Massachusetts 02139

INTRODUCTION

When pyrolyzed, coal forms a complex mixture of polycyclic aromatic compounds (PAC), many of which carry functional groups as substitutes for ring hydrogen. Further subjection of PAC to pyrolytic conditions causes changes in their composition--manifested partly by changes in the degree of substitution. The presence or absence of substituent groups is of importance to environmental issues concerning both the sources of environmental PAC and their health effects. Researchers (22,26,36,45) studying PAC in the air, water, and soil have tried to deduce information about the PAC source fuels and their process temperatures from relative abundances of certain alkylated and unalkylated PAC.

Focussing particularly on alkyl and amino substituents, several researchers (14,18,30,31,32,54) have attempted to establish a link between biological activity (i.e., carcinogenicity or mutagenicity) and the presence or absence of substituent groups. Results to date indicate that biological activity is a complex function of the identity of the parent PAC, the nature of the functional group, the size of the functional group (18,32), and the position of the substitution (2,3,21,33,34,47)--all factors that influence the electron distribution within the compound. It is logical that these factors should also be the ones that govern PAC reactivity under pyrolytic conditions, but a thorough investigation of all of these influences lies beyond the scope of any single work. It is our objective to determine how the degree of substitution and the nature of the substituent groups influence the pyrolysis behavior of coal-derived PAC.

Previous work has already revealed some information about pyrolysis-induced changes in substitution of PAC from coal pyrolysis. Serio (46) has used nuclear magnetic resonance spectroscopy (NMR) to show that increasing pyrolysis severity by either temperature or time effects an increase in aromaticity and a decrease in the presence of functional groups. Employing Fourier transform infrared spectroscopy (FT-IR), Solomon, et al. (50) and Freihaut and Seery (13) report that high temperature coal tar exhibits a considerable reduction (as compared to lower temperature tar) of IR absorption in the regions associated with functional group attachment to aromatic rings. Other researchers (5,25,53) have used gas chromatography-mass spectrometry (GC-MS) to identify some specific alkylated PAC produced in coal pyrolysis experiments. We are unaware of any work to date that reports total mass yields of substituted and unsubstituted PAC from coal pyrolysis.

EXPERIMENTAL EQUIPMENT AND PROCEDURES

To produce the PAC of this study, 44-53 μm particles of PSOC 997, a Pittsburgh Seam high volatile bituminous coal, are fluidized in argon and fed at a rate of 2.5 g/hour into the laminar flow, drop-tube pyrolysis furnace of Figure 1. Details of the furnace appear elsewhere (41). An optical pyrometer is used to measure furnace

temperature, which can be set to values of 1000 K to 2000 K by adjustment of the electrical power input. Particle residence time, or "drop distance," is controlled by adjusting the vertical position of the water-cooled collection probe. As pyrolysis products exit the reaction zone at 5.3 std l/min, they encounter 17.1 std l/min of argon quench gas at the top of the collection probe and another 4.8 std l/min through the walls of the probe inner tube as they travel the length of the collection probe. Leaving the probe, they enter an impactor for size-separation of the solid pyrolysis products. Char particles, the larger of these, deposit on the first stages; aerosols (i.e., PAC-coated soot) end up on the lowest impactor stages and the Millipore teflon filter (hole size, .2 μm) following the impactor. After passing through the filter, the gases are channeled to infrared detectors for measurement of CO and CO_2 and to a flame ionization detector for measurement of hydrocarbon volatiles. A small portion of gas is diverted to a 750 ml glass bulb for subsequent GC-MS analysis.

After all products are weighed, the aerosols are placed in teflon-capped, 30-ml amber glass bottles of Caledon distilled-in-glass HPLC grade dichloromethane (DCM) and sonicated for five minutes. Syringe-fulls of the particle/liquid suspension are passed through a Millipore teflon filter (hole size .2 μm) to remove the soot particles from the PAC/DCM solution. The mass of the residue soot is taken and subracted from that before sonication to give the mass of the PAC. Triplicate 100-μl aliquots of the PAC/DCM solution are removed, evaporated, and weighed according to the procedure of Lafleur, et al. (27) to verify the PAC yields. This latter procedure gives $\geq$ 90% recovery for naphthalene and 100% recovery for species of $\geq$ three rings, so negligible PAC mass is lost during evaporation since, in our experiments, one-ring aromatics and lighter hydrocarbons stay in the gas phase; only aromatics of $\geq$ two rings condense onto the soot.

The PAC/DCM solutions undergo analysis by GC-MS, HPLC, and FT-IR. The GC component of the GC-MS system is a Hewlett-Packard Model 5890, equipped with a Quadrex Super Cap Series, methyl silicone (film thickness .10 μm) high temperature, aluminum clad capillary column (15 m x .2 mm i.d.). Sample volumes of .1 μl are introduced into the splitless injector, maintained at 300°C. The detector is kept at 320°C, and the column temperature is programmed from 40°C to 320°C at 10°C/min. The mass spectrometer, Hewlett-Packard Model 5970, operates in electron impact mode at an ionizing voltage of 70 eV. Mass spectra are taken at a frequency of .77 scans/second, over a mass to charge ratio range of 41 to 600.

The HPLC system, fully described elsewhere (28), consists of a Perkin-Elmer Series 4 quaternary solvent delivery system coupled to a Model LC-85B variable wavelength ultraviolet (UV) detector. 1.5 ml/min of DCM (same grade as above) flows through the steric exclusion column (50 cm long x 10 mm i.d.), which is packed with 500 Å Jordi-Gel poly(divinylbenzene). Samples are injected through either a 6-μl or a 100-μl Rheodyne injection loop, and a microswitch on the injector actuates the data system to insure reproducible starting times. As demonstrated in another publication (28), substituted PAC elute in the first 23.9 ml; unsubstituted, afterward. The proportions of the UV response areas before and after 23.9 ml are taken to represent respectively the proportions of substituted and unsubstituted PAC. (To alleviate uncertainty about the relative UV response factors for the two classes of PAC, we have collected the eluates before and after 23.9 ml for one sample, concentrated them under nitrogen, and subjected them to the microbalance weighing procedure (27) mentioned above. Because the UV area technique gives good agreement with the weighing procedure, this latter, more time-consuming procedure is unnecessary.)

For FT-IR analysis, drops of the PAC/DCM solutions are placed on KBr discs (20 mm x 2 mm), and the solvent is allowed to evaporate. The discs are placed in an IBM Model IR/32 Fourier Transform Infrared Spectrometer, equipped with a Globar source and a mercury-cadmium telluride detector. The resulting absorbance spectra represent 64 scans, taken at a resolution of 8 cm^{-1}. To insure that the PAC composition is uniform over the surface of the disc, each disc is rotated slightly two times for additional determinations.

RESULTS AND DISCUSSION

Figure 2 displays the yields of soot and PAC collected on the aerosol filter for the two sets of experiments: Set 1, constant drop distance (6 in) and variable temperature, and Set 2, constant temperature (1375 K) and variable drop distance. First, it should be noted that our maximum PAC yield of ~9% lies significantly below the 24-26% primary tar yields obtained from experiments conducted under less severe conditions (7,46). Our maximum PAC yield or "zero point" thus corresponds to a significant degree of primary tar conversion (~65%). Evident from Figure 2 are the drop in PAC yield and the compensating rise in soot yield as pyrolysis conditions increase in severity--by an increase in either temperature or distance. The constancy of the sum of PAC and soot yields (21.34% $\pm$ 0.97% for Set 1; 19.86% $\pm$ 1.09% for Set 2) supports the previously reported notion that PAC serve as precursors to soot (9,17,24,42,52). It should be borne in mind, however, that our experiments and ones done prior to them (41) also show small temperature- and time-induced decreases in the yields of char, CO_2, and hydrocarbons and an increase in that of CO.

To better understand this apparent transformation of PAC to soot, it is necessary to investigate the compositional changes in the PAC that accompany their conversion. We have chosen to describe compositional changes of the PAC in terms of their aromatic ring number distribution and their degree of functional group substitution. A discussion of changes in the ring number distributions of coal-derived PAC will appear elsewhere (55); this paper focusses on pyrolysis-induced changes in the degree of substitution.

The question of how the degree of substitution changes can be partially answered by the GC-MS total ion chromatograms in Figure 3, featuring PAC from three Set 1 experiments. Since PAC elute in the order of decreasing volatility or of increasing molecular weight, addition of a functional group brings about a small increase in retention time; addition of an aromatic ring, a large increase. Readily apparent from Figure 3 is the loss of compositional complexity as temperature is raised. The lowest temperature sample is comprised of a multitude of peaks, many unresolved, which correspond to unsubstituted PAC and their substituted homologs. As temperature increases, the number of peaks diminishes drastically. Large gaps emerge between clusters of unsubstituted PAC isomers--indicating a marked depletion in the substituted species.

Even though GC-MS can easily give a qualitative picture of substitutional differences in PAC from coal, it is extremely difficult to use GC-MS quantitatively due to the unresolvability of some peaks, the uncertainty of response factors, the limited number of species included in available mass spectra libraries, and the virtual indistinguishability of mass spectra of some isomeric PAC (at least for mass spectra from systems with electron impact ionization sources (6,19,23)). Even if all of these difficulties are surmounted, the usefulness of GC-MS still extends only to the portion of the PAC sample that is gas chromatographable, i.e., to the

vaporizable components. (It should be noted that this vaporization limitation of GC-MS systems promises to soon be eliminated by the introduction of new supercritical fluid chromatography-MS systems (35).)

Unlike GC, HPLC is limited in applicability only by component solubility in the mobile phase; but, except for microcolumn HPLC techniques (43), the price for the wider range of component applicability is the loss of separation efficiency as evident in peak resolution. This "drawback" can be an advantage in analyzing mixtures as complex as fossil fuel products, however, because HPLC methods can be tailored to make bulk separations according to one or two structural parameters. We have recently developed a method with a steric exclusion HPLC column that takes advantage of a nonexclusion effect to separate substituted from unsubstituted PAC (28). Non-nitrogen-containing PAC with alkyl, phenyl, hydroxyl, carbonyl, carboxyl, etheric, esteric, cyano, or nitro functional groups elute as size-excluded species. Unsubstituted PAC are adsorbed onto the column and elute later (28). Nitrogen-containing PAC are also delayed by adsorption unless they have a substituent group that sterically blocks the N atom from the adsorption site (29).

Figure 4 presents the results of applying this technique to the PAC from the two sets of experiments. Yields of substituted PAC fall monotonically with either increasing temperature or drop distance. Over the temperature interval investigated in Set 1, the drop is by two orders of magnitude; over the distance interval in Set 2, the drop is by almoat an order of magnitude. Yields of unsubstituted PAC, on the other hand, exhibit a dual behavior. They appear to be insensitive to pyrolysis conditions at temperatures $\leq$ 1312 K for Set 1 and at distances $\leq$ 4 inches for Set 2. Beyond these "critical values," however, they too decay with an increase in either temperature or distance. Again the decline is more dramatic for the experiments in Set 1.

The qualitative similarity of the curves in Figure 4a to those in 4b suggests that the data of the two sets of experiments be compared as plots versus a parameter of pyrolysis severity--such as total PAC yield--that accounts for both temperature and time effects. The result of combining Figures 2 and 4 appears in Figure 5, which contains data from Sets 1 and 2 as well as experiments conducted at combinationa of temperature and distance not covered by these Sets.

The fact that all the data (to a first approximation) lie on the same lines suggests the following for the ranges of temperature (1125 to 1473 K) and time (approximately .050 to .325 sec particle residence times, corresponding to drop distances of 2 to 6 in) investigated:

1) The split between substituted and unsubstituted PAC is solely a function of PAC yield (or conversion) and depends on temperature or time only as much as these variables affect PAC yield (or conversion).

2) Since pyrolysis at long time and low temperature can give the same results as at short time and high temperature, the PAC conversion reactions have a narrow distribution of activation energies.

3) It is more practical to relate substituted and unsubstituted PAC yields to total yield than to temperature and residence time, quantities whose measurements tend to be more system- and method-dependent.

It is convenient to approximate the S (substituted PAC) and the U (unsubstituted PAC) curves in Figure 5 as two line segments of different slope, intersecting

at a critical PAC yield Y_c, tbe point after which there is net loss of unsubstituted PAC. The value of Y_c is 4.5 mass% of coal--corresponding to 48% PAC conversion if the point of maximum PAC yield is taken as 0% conversion. Since both S and U must be 0 at Y = 0, the equations for the lines can be obtained easily in terms of Y, the total PAC yield:

Regime 1: $Y_o \geq Y \geq Y_c$ $\quad U = U_o \quad S = Y - U_o$

Regime 2: $Y_c \geq Y \geq 0$ $\quad U = (U_o/Y_c)Y \quad S = (1 - U_o/Y_c)Y$

Thus for these experiments, once the critical yield Y_c and the initial yield of unsubstituted PAC U_o have been experimentally determined, the yields of substituted and unsubstituted PAC can be calculated solely from measurement of Y. The equations imply a ratio of S to U that, in Regime 1, decreases with decreasing Y and, in Regime 2, stays constant. The data match these approximations much better at large Y than at small Y, however, because the relative error of the straight line approximations for S and U becomes greater as Y decreases. Since secondary pyrolytic reactions depend much less on the parent coal than do the primary pyrolytic reactions, one might expect PAC from other coals (especially other bituminous coals) to exhibit the same "two line" behavior of U and S yields (albeit with different values of Y_c and U_o).

The transition from Regime 1 to Regime 2 in Figure 5 suggests a change in the nature of the functional groups associated with the substituted PAC. Figure 6 displays the FT-IR spectra of samples from three Set 1 experiments--each labeled with the functional groups conventionally assigned (4,48) to peaks at particular bands. These spectra appear unretouched, i.e., their baselines have not been "corrected" to screen out the drift allegedly due to scatter (44,49,51). The prominent functional group absorbances occur at 2850-2980 cm^{-1} and 1370-1460 cm^{-1} for alkyl groups; at 3150-3550 cm^{-1} for OH or the NH of amides or amines; at 1260-1280 cm^{-1} for etheric C-O; and at 1690-1730 cm^{-1} for carbonyl groups. The three oxygen-containing groups--hydroxyl, ether, and carbonyl--are the same as those reportedly found in coals of $\geq$ 80% carbon (1).

Socrates (48) cautions against comparing changes in relative intensities of functional groups' bands to get changes in their relative amounts because signals associated with particular functional groups can be augmented (and sometimes shifted) by certain adjacent atoms or functional groups (e.g., the intensity of the C-H aromatic stretch band at 1600 cm^{-1} can be enhanced by either ring nitrogen or hydroxyl groups (51)). Nevertheless, we can make some qualitative observations from the spectra in Figure 6. Most noticeable is that the OH or NH groups responsible for the 3150-3550 cm^{-1} band in Figure 6a disappear by 1312 K (6c) and remain absent from the spectra of samples produced at higher temperatures. This observation is consistent with the ^1H NMR determination of a temperature-induced drop in hydroxyl content of the bituminous coal tars of Collin, et al. (8). If, as recommended (50), aromatic H is represented by the 700-900 cm^{-1} band and aliphatic, by the 2800-3000 cm^{-1} band, then Figure 6 also reveals a reduction in aliphatic (or hydroaromatic) hydrogen relative to aromatic hydrogen--a reduction consistent with the results of Solomon, et al. (50) for tars of another Pittsburgb Seam bituminous coal. Figure 6 also implies a relative decrease in etheric functionalities and a relative increase in carbonyl functionalities as temperature increases. PAC thus appear to adhere to the following order of reactivity:

hydroxyl- and/or amino-substituted PAC > alkyl- and ether-substituted PAC > unsubstituted PAC and PAC with carbonyl groups.

It is instructive to compare this experimentally observed order of reactivities with what might be predicted from frontier orbital theory. According to this theory (11), the bonding between two reactants participating in any of a number of kinds of reactions (e.g., concerted, free radical, ionic) occurs by overlap of the highest energy occupied molecular orbital (HOMO) of one species with the lowest energy unoccupied orbital (LUMO) of the other. Reactions are most energetically favored for high HOMO energies and low LUMO energies. If the reactant providing the LUMO is fixed, then the reactivities of compounds reacting with this species will follow the order of the compounds' HOMO energies. Except for a minus sign, ionization potentials are "roughly the energies of the HOMOs" (11), so lower ionization potentials denote higher energy HOMOs and higher reactivities. Figure 7 displays the values of ionization potentials, measured by photoionization mass spectrometry, as reported by Franklin, et al. (12) for a variety of one- and two-ring PAC. Figures 7a, b, and e show that the reactivity of an aromatic species is increased by an increase in either the number of alkyl substitutents or the number of carbons within an alkyl substituent. Figure 7c reveals the strongly activating effect (relative to benzene) of an amino N attached directly to the aromatic ring. Figure 7d shows the activating effect of etheric or hydroxyl groups and the slightly deactivating effect of the carbonyl group. Thus PAC reactivity, as inferred from ionization potentials, follows the order:

$$\text{aromatic amines} > \text{aromatic ethers} \cong \text{multialkylated PAC} \cong \text{phenols} > \text{monoalkylated PAC} > \text{unsubstituted PAC} \geq \text{carbonyl-substituted PAC},$$

consistent with our experimental observations.

The above order helps to explain the behavior of the S curve in Figure 5. In Regime 1, the substituted PAC are composed of a significant portion of very reactive compounds with hydroxyl and/or NH, etheric, and alkyl functional groups. The S curve falls steeply as these very reactive substituted PAC disappear. By the end of Regime 1, the total mass of substituted species--especially that of the most reactive ones--is severely reduced. The slope of the S curve thus becomes less steep.

Interpretation of the U curve in Figure 5 is less clear-cut. In addition to the values in Figure 7, Franklin, et al. (12) provide ionization potentials for some PAC of $\geq$ two rings (e.g., anthracene, 7.55 eV; benzo[c]phenanthrene, 8.12 eV; and acenaphthylene, 8.73 eV), which indicate a variation in reactivity among the unsubstituted PAC as well. Two alternatives emerge to account for the behavior of the U curve.

Alternative 1 holds that there is a significant difference between the reactivities of the unsubstituted PAC and the substituted PAC with the more activating functional groups (amino, hydroxyl, ether, multialkyl). While these highly reactive substituted PAC are present (Regime 1), soot formation is dominated by the conversion of these species. There may be conversion reactions within the unsubstituted PAC class to accomodate differences in individual species' reactivities, but there is negligible transfer into the class from conversion of substituted PAC or out of the class from conversion of unsubstituted PAC to soot in Regime 1. At the end of Regime 1, however, the remaining substituted species are much less reactive than those initially present, and there is no longer a large disparity between the reactivities of the substituted and unsubstituted PAC. The unsubstituted PAC begin to convert to soot too, and the U curve declines in Regime 2.

Alternative 2 suggests that, although the substituted PAC are more reactive as a class than the unsubstituted PAC, there are certain unsubstituted PAC with reactivities comparable to those of the more reactive substituted PAC. These more reactive unsubstituted PAC convert to soot in Regime 1, where their loss is offset by a gain in unsubstituted PAC produced by reactions of substituted PAC. As pyrolytic conditions become more severe (Regime 2), conversion of unsubstituted PAC to soot prevails over production of unsubstituted PAC. The balance is upset, and the U curve declines.

The two Alternatives represent fairly extreme cases. It is certainly likely that the true interpretation lies somewhere between these extremes, but our data do not permit us to be any more exact at this time.

The three pronounced peaks between 700 and 900 cm^{-1} in the spectra of Figure 6 arise from aromatic C-H out-of-plane deformation. The position of each peak denotes the number of adjacent ring hydrogen atoms; 830-900 cm^{-1}, one lone H atom; 800-860 cm^{-1}, two adjacent H atoms; 735-820 cm^{-1}, three to five adjacent H atoms (40,48). Figure 8 portrays the variation in distribution of aromatic hydrogen for the six samples analyzed. Although selective removal of PAC with substituents at certain positions would have some influence on the distribution of aromatic H atoms, one might expect the overall loss of substituted PAC to cause a general shift toward a higher number of adjacent H atoms. Figure 8 displays a slight decrease in the fraction of lone H--more pronounced in Regime 1 ($8.7 \geq Y \geq 4.5$)--that could be considered consistent with the loss of substituted PAC. Less amenable to explanation, however, is the increase in two adjacent H at the expense of the three adjacent H in Regime 2 ($Y < 4.5$)--a sign, perhaps, that other factors are also at work, e.g., destruction of heterocyclic structures and ring build-up processes that can form PAC of larger ring number and a higher degree of peri-condensation. Figure 8 allows no conclusions to be drawn about the relative reactivities of different positional isomers of substituted PAC.

EXTENSION: IMPLICATIONS FOR SOOT FORMATION

The conversion of PAC to soot can be approximated by the following scheme:

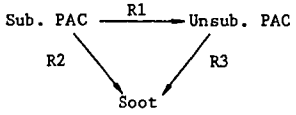

where the three reactions are depicted as irreversible since our experiments never show a net production of substituted PAC or a net destruction of soot. Although many uncertainties remain about the relative dominance of the three reactions, the data imply the following about this network:

1) In both Regimes, at least one of either R2 or R1-R3 must occur.

2) R3 must occur in Regime 2. It occurs in Regime 1 only if R1 = R3.

3) If soot forms via the combination R1-R3, then R1 = R3 in Regime 1 and R1 $\leq$ R3 in Regime 2.

4) If soot cannot form via the combination R1-R3, then R2 must occur throughout Regimes 1 and 2; and R3 must occur only in Regime 2.

It would appear that if conversion of substituted PAC to soot does first entail conversion to unsubstituted PAC, then it does not merely involve removal of the substituent group: Lewis and Edstrom (38) report 7,12-dimethylbenz[a]-anthracene to form significantly more soot than benz[a]anthracene. Davis and Scully (10) and Glassman (16) report the alkylated naphthalenes and benzenes to have higher sooting tendencies than their unalkylated homologs. If benzene, naphthalene, and benz[a]anthracene are less likely to form soot than their alkylated derivatives, then it is unlikely that conversion of an alkylated PAC to soot proceeds via the removal of the alkyl group to form the unalkylated homolog.

If, as asserted by others (20,24,37), the conversion of PAC to soot involves the formation of a reactive free radical, then PAC reactivity should correlate with the ease of radical formation. The formation of a σ-type radical (e.g., phenyl, naphthyl) by abstraction of a ring-attached H atom or methyl group requires approximately 100 kcal/mole (37)--a high bond dissociation energy due to the localization of the resulting free electron. To form π-type radicals like benzyl, however, requires only about 77 kcal/mole because the resulting unpaired electron is resonance-stabilized (37). Alkyl-substituted PAC would then be expected to be more reactive than unalkylated PAC.

Substituted PAC with hydroxyl groups can evidently form radicals even more easily. Gavalas (15) reports the profound activating effect of a hydroxyl group substituted in the ortho or para position of an aromatic unit (Ar) linked by a methylene bridge. Because of keto-enol tautomerism, dissociations of the type

$$HO\text{-}Ar\text{-}CH_2\text{-}X \longrightarrow HO\text{-}Ar\text{-}CH_2^{\cdot} + X^{\cdot} \qquad (X = H,\ CH_3,\ Ar,\ CH_2\text{-}Ar)$$

are very highly energetically favored over the type

$$Ar\text{-}CH_2\text{-}X \longrightarrow Ar\text{-}CH_2^{\cdot} + X^{\cdot}.$$

Activation energies for the dissociation of aryl and aryl/alkyl ethers lie in the same range as those of aromatics with alkyl substituents or methylene bridges (15). Thus our experimentally observed order of depletion of PAC parallels that suggested by ease of radical formation: hydroxyl-substituted PAC > alkyl- and ether- substituted PAC > unsubstituted PAC.

CONCLUSIONS

1. As observed in previous studies in our laboratory (42), there is a constancy of summed PAC and soot yields that indicates a conversion of PAC to soot.

2. The ability to separate substituted PAC from unsubstituted PAC reveals differences in their pyrolysis behaviors: At low temperatures ($\leq$ 1312 K at 6 in) or short times (drop distances $\leq$ 4 in at 1375 K), yields of substituted PAC fall markedly with an increase in either temperature or time; yields of unsubstituted PAC remain constant. Both classes of PAC react away, however, at higher temperatures or longer times.

3. Plotting substituted and unsubstituted PAC yields versus total PAC yield Y reconciles data taken at constant distance and variable temperature with those taken at constant temperature and variable distance. Because substituted and unsubstituted PAC yields prove to be solely functions of Y, Y aptly serves as a single parameter for pyrolysis severity since it accounts for variations in composition due to either temperature or time.

4. For the bituminous coal investigated, the yields of substituted and unsubstituted PAC suggest two PAC conversion regimes. Although reactivities may vary from species to species within a class, at low PAC conversions, substituted PAC as a class clearly display a much higher decay than the unsubstituted PAC: Substituted PAC yields fall by a factor of ~3.5; whereas the unsubstituted PAC show no net change. Though still evident at high PAC conversion, differences in the two classes' decays are much less pronounced. Unsubstituted PAC yields remain appreciably above those of the substituted PAC, but both classes undergo significant conversion to soot.

5. Conversion of PAC corresponds to differences in the kinds of functional groups present. At high values of Y, FT-IR shows that there are significant amounts of PAC with alkyl, ether, carbonyl, and hydroxyl and/or amino groups. Further pyrolysis, however, effects selective removal of the hydroxyl- and/or amino-substituted PAC. As the unsubstituted PAC become more prevalent, relative contributions from alkyl and ether functionalities go down and carbonyl substitution becomes slightly more significant.

6. Without specifying the kind of reaction mechanism, we can apply frontier orbital theory to PAC conversion reactions. This theory, along with values of ionization potentials found in the literature (12), suggests that PAC reactivity follows the order:

   aromatic amines > aromatic ethers $\cong$ multialkylated PAC $\cong$ phenols > monoalkylated PAC > unsubstituted PAC $\geq$ carbonyl-substituted PAC,

   which is consistent with our experimental results.

7. If we restrict the PAC conversion reactions to involve free radical formation, then we again see agreement between theory and experiment. Less energy is needed to form free radicals from PAC with hydroxyl, alkyl, and ether substituents than from unsubstituted PAC.

ACKNOWLEDGEMENTS

The authors gratefully acknowledge the National Institute of Environmental Health Sciences (Grant NIH 5 P30 ES02109) for support of this research. They also wish to express their appreciation to Professor Preetinder S. Virk and Dr. Arthur L. Lafleur for their helpful discussions and to Ms. Elaine F. Plummer for the GC-MS analyses.

REFERENCES

1. A. Attar and G. G. Hendrickson, "Functional Groups and Heteroatoms in Coal," Chapter 5 in Coal Structure, ed. by R. A. Meyers. New York: Academic Press (1982).
2. G. M. Badger, "Carcinogenic Hydrocarbons," Chapter 1 in The Chemical Basis of Carcinogenic Activity. Springfield, Illinois: Charles C. Thomas (1962).
3. T. R. Barfknecht, B. M. Andon, W. G. Thilly, and R. A. Hites, "Soot and Mutation in Bacteria and Human Cells," pp. 231-242 in Chemical Analysis and Biological Fate: Polynuclear Aromatic Hydrocarbons, ed. by M. Cooke and A. J. Dennis. Colombus, Ohio: Batelle Press (1981).
4. N. Berkowitz, "The Methods of Coal Chemistry," Chapter 3 in Coal Science and Technology 7: The Chemistry of Coal. New York: Elsevier (1985).

5. H. Borwitzky and G. Schomburg, "Separation and Identification of Polynuclear Aromatic Compounds in Coal Tar by Using Glass Capillary Chromatography Including Combined Gas Chromatography-Mass Spectrometry," Journal of Chromatography 170: 99-124 (1979).
6. M. V. Buchanan and M. B. Wise, "Negative Ion Processes for the Unambiguous Identification of Polycyclic Aromatics," Preprints of Papers, American Chemical Society, Division of Fuel Chemistry 31(1): 191-197 (1986).
7. C. C.-S. Chang, "Thermal Reactions of Freshly Generated Coal Tar Over Calcium Oxide," Ph.D. Thesis, Massachusetts Institute of Technology, Department of Chemical Engineering (1986).
8. P. J. Collin, R. J. Tyler, and M. A. Wilson, "Influence of Pyrolysis Temperature on the Aromatic Fraction of Flash Pyrolysis Tars," Fuel 59: 819-820 (1980).
9. A. D'Alessio, A. DiLorenzo, A. F. Sarofim, F. Beretta, S. Masi, and C. Venitozzi, "Soot Formation in Methane-Oxygen Flames," pp. 1427-1438 in Proceedings of the Fifteenth Symposium (International) on Combustion (1974).
10. R. A. Davies and D. B. Scully, "Carbon Formation from Aromatic Hydrocarbons II," Combustion and Flame 10: 165-170 (1966).
11. I. Fleming, Frontier Orbitals and Organic Chemical Reactions. London: John Wiley and Sons (1976).
12. J. L. Franklin, J. G. Dillard, H. M. Rosenstock, J. T. Henson, K. Draxl, and F. H. Field, Ionization Potentials, Appearance Potentials, and Heats of Formation of Gaseous Positive Ions. Washington: National Bureau of Standards (1969).
13. J. D. Freihaut and D. J. Seery, "An Investigation of Yields and Characteristics of Tars Released During the Thermal Decomposition of Coal," Preprints of Papers, American Chemical Society, Division of Fuel Chemistry 26(2): 133-148 (1981).
14. R. C. Garner and C. N. Martin, "Carcinogenic Aromatic Amines and Related Compounds," Chapter 4 in Chemical Carcinogens, Volume 1, Second Edition, ed. by C. E. Searle. ACS Monograph 182. Washington: American Chemical Society (1984).
15. G. R. Gavalas, "Thermal Reactions of Coal," Chapter 3 in Coal Science and Technology, Volume 4: Coal Pyrolysis. New York: Elsevier (1982).
16. I. Glassman, "Environmental Combustion Considerations," Chapter 8 in Combustion, Second Edition. Orlando, Florida: Academic Press (1987).
17. S. C. Graham, J. B. Homer, and J. L. J. Rosenfeld, "The Formation and Coagulation of Soot Aerosols Generated by the Pyrolysis of Aromatic Hydrocarbons," Proceedings of the Royal Society of London A 344: 259-285 (1975).
18. W. H. Griest, B. A. Tomkins, J. L. Epler, and T. K. Rao, "Characterization of Multialkylated Polycyclic Aromatic Hydrocarbons in Energy-Related Materials," pp. 395-409 in Polynuclear Aromatic Hydrocarbons, ed. by P. W. Jones and P. Leber. Ann Arbor, Michigan: Ann Arbor Science Publishers (1979).
19. A. Hase, P. H. Lin, and R. A. Hites, "Analysis of Complex Polycyclic Aromatic Hydrocarbon Mixtures by Computerized GC-MS," pp. 435-442 in Carcinogenesis--A Comprehensive Survey Volume 1. Polynuclear Aromatic Hydrocarbons: Chemistry, Metabolism, and Carcinogenesis, ed. by R. I. Freudenthal and P. W. Jones. New York: Raven Press (1976).
20. B. S. Haynes and H. Gg. Wagner, "Soot Formation," Progress in Energy and Combustion Science 7: 229-273 (1981).
21. S. S. Hecht, M. Loy, and D. Hoffmann, "On the Structure and Carcinogenicity of the Methyl Chrysenes," pp. 325-340 in Carcinogenesis--A Comprehensive Survey Volume 1. Polynuclear Aromatic Hydrocarbons: Chemistry, Metabolism, and Carcinogenesis, ed. by R. I. Freudenthal and P. W. Jones. New York: Raven Press (1976).

22. R. A. Hites, "Sources and Fates of Atmospheric Polycyclic Aromatic Hydrocarbons," Chapter 10 in Atmospheric Aerosol: Source/Air Quality Relationships. ACS Symposium Series 167: 187-196 (1981).
23. R. A. Hites and G. R. Dubay, "Charge-Exchange-Chemical Ionization Mass Spectrometry of Polycyclic Aromatic Compounds," pp. 85-87 in Carcinogenesis--A Comprehensive Survey Volume 3. Polynuclear Aromatic Hydrocarbons, ed. by P. W. Jones and R. I. Freudenthal. New York: Raven Press (1978).
24. J. B. Howard and W. J. Kausch, Jr., "Soot Control by Fuel Additives," Progress in Energy and Combustion Science 6: 263-276 (1980).
25. B. M. Hughes, J. Troost, and R. Liotta, "Pyrolysis/$(GC)^2$/MS as a Coal Characterization Technique," Preprints of Papers, American Chemical Society, Division of Fuel Chemistry 26(2): 107-120 (1981).
26. R. E. Laflamme and R. A. Hites, "The Global Distribution of Polycyclic Aromatic Hydrocarbons in Recent Sediments," Geochimica et Cosmochimica Acta 42: 289-303 (1978).
27. A. L. Lafleur, P. A. Monchamp, E. F. Plummer, and E. L. Kruzel, "Evaluation of Gravimetric Methods for Dissoluble Matter in Extracts of Environmental Samples," Analytical Letters 19: 2103-2119 (1986).
28. A. L. Lafleur and M. J. Wornat, "Multimode Retention in High-Performance Size Exclusion Chromatography with Polydivinylbenzene: I. Polycyclic Aromatic Hydrocarbons" (submitted to Analytical Chemistry).
29. A. L. Lafleur and M. J. Wornat, "Multimode Retention in High-Performance Size Exclusion Chromatography with Polydivinylbenzene: II. Heterocyclic Aromatic Compounds" (in progress).
30. R. C. Lao, R. S. Thomas, H. Oja, and L. Dubois, "Application of a Gas Chromatograph-Mass Spectrometer-Data Processor Combination to the Analysis of the Polycyclic Aromatic Hydrocarbon Content of Airborne Pollutants," Analytical Chemistry 45: 908-915 (1973).
31. D. W. Later, T. G. Andros, and M. L. Lee, "Isolation and Identification of Amino Polycyclic Aromatic Hydrocarbons from Coal-Derived Products," Analytical Chemistry 55: 2126-2132 (1983).
32. D. W. Later, E. K. Chess, C. W. Wright, R. B. Lucke, D. D. Mahlum, and B. W. Wilson, "Mass Spectrometric and Chromatographic Methods Applied to the Isolation and Identification of Tumorigenic Polycyclic Aromatic Hydrocarbons in Coal Liquefaction," presented at the Thirty-Second Annual Conference on Mass Spectrometry and Allied Topics, San Antonio, Texas (1984).
33. D. W. Later and B. W. Wright, "Capillary Column Gas Chromatographic Separation of Amino Polycyclic Aromatic Hydrocarbon Isomers," Journal of Chromatography 289: 183-193 (1984).
34. E. J. Lavoie, D. T. Coleman, N. G. Geddie, and J. E. Rice, "Studies of tbe Mutagenicity and Tumor-Initiating Activity of Methylated Fluorenes," Chemico-Biological Interactions 52: 301-309 (1985).
35. M. L. Lee, personal communication (1987).
36. M. L. Lee, G. P. Prado, J. B. Howard, and R. A. Hites, "Source Identification of Urban Airborne Polycyclic Aromatic Hydrocarbons by Gas Chromatographic Mass Spectrometry and High Resolution Mass Spectrometry," Biomedical Mass Spectrometry 4(3): 182-186 (1977).
37. I. C. Lewis, "Chemistry of Carbonization," Carbon 20: 519-529 (1982).
38. I. C. Lewis and T. Edstrom, "Studies of the Thermal Behavior of Some Polynuclear Aromatics," Proceedings of the Fifth Conference on Carbon. New York: Pergamon Press, 413-430 (1963).
39. D. McNeil, "High Temperature Coal Tar," Chapter 17 in Second Supplementary Volume of Chemistry of Coal Utilization, ed. by M. A. Elliott. New York: John Wiley and Sons (1981).
40. K. Nakanishi, Infrared Absorption Spectroscopy--Practical. San Francisco:

Holden-Day (1962).
41. R. D. Nenniger, "Aerosols Produced from Coal Pyrolysis," Sc.D. Thesis, Massachusetts Institute of Technology, Department of Chemical Engineering (1986).
42. R. D. Nenniger, J. B. Howard, and A. F. Sarofim, "Sooting Potential of Coals," pp. 521-524 in Proceedings of the International Conference on Coal Science. Pittsburgh: Pittsburgh Energy Technology Center (1983).
43. M. Novotny, A. Hirose, and D. Wiesler, "Separation and Characterization of Very Large Neutral Polycyclic Molecules in Fossil Fuels by Microcolumn Liquid Chromatography," Analytical Chemistry 56: 1243-1248 (1984).
44. P. C. Painter, R. W. Snyder, M. Starsinic, M. M. Coleman, D. W. Kuehn, and A. Davis, "Fourier Transform IR Spectroscopy: Application to the Quantitative Determination of Functional Groups in Coal," Chapter 3 in Coal and Coal Products: Analytical Characterization Techniques. ACS Symposium Series 205, ed. by E. L. Fuller. Washington: American Chemical Society (1982).
45. F. G. Prahl, E. Crecellus, and R. Carpenter, "Polycyclic Aromatic Hydrocarbons in Washington Coastal Sediments: An Evaluation of Atmospheric and Riverine Routes of Introduction," Environmental Science and Technology 18: 687-693 (1984).
46. M. A. Serio, "Secondary Reactions of Tar in Coal Pyrolysis," Ph.D. Thesis, Massachusetts Institute of Technology, Department of Chemical Engineering (1984).
47. B. D. Silverman and J. P. Lowe, "Diol-Epoxide Reactivity of Methylated Polycyclic Aromatic Hydrocarbons (PAH): Ranking the Reactivity of the Positional Monomethyl Isomers," pp. 743-753 in Polynuclear Aromatic Hydrocarbons, Proceedings of the Sixth International Symposium, ed. by M. Cook, A. J. Dennis, and G. L. Fisher. Colombus, Ohio: Batelle Press (1982).
48. G. Socrates, Infrared Characteristic Group Frequencies. New York: John Wiley and Sons (1980).
49. P. R. Solomon, R. M. Carangelo, P. E. Best, J. R. Markham, and D. G. Hamblen, "Analysis of Particle Composition, Size, and Temperature by FT-IR Emission/Transmission Spectroscopy," Preprints of Papers, American Chemical Society, Division of Fuel Chemistry 31(1): 141-151 (1986).
50. P. R. Solomon, D. G. Hamblen, and R. M. Carangelo, "Applications of Fourier-Transform IR Spectroscopy in Fuel Science," Chapter 4 in Coal and Coal Products: Analytical Characterization Techniques. ACS Symposium Series 205, ed. by E. L. Fuller, Jr. Washington: American Chemical Society (1982).
51. P. R. Solomon, D. G. Hamblen, R. M. Carangelo, J. R. Markham, and M. R. Chaffee, "Application of FT-IR Spectroscopy to Study Hydrocarbon Reaction Chemistry," Preprints of Papers, American Chemical Society, Division of Fuel Chemistry 30(1): 1-12 (1985).
52. E. E. Tompkins and R. Long, "The Flux of Polycyclic Aromatic Hydrocarbons and of Insoluble Material in Pre-Mixed Acetylene-Oxygen Flames," Proceedings of the Twelfth Symposium (International) on Combustion: 625-633 (1969).
53. F. J. Vastola and L. J. McGahan, "The Development of Laser Micropyrolysis of Coal Macerals," Preprints of Papers, American Chemical Society, Division of Fuel Chemistry 31(1): 53-59 (1986).
54. B. W. Wilson, R. Pelroy, and J. T. Cresto, "Identification of Primary Aromatic Amines in Mutagenically Active Sub-Fractions from Coal Liquefaction Materials," Mutation Research 79: 193-202 (1980).
55. M. J. Wornat, A. F. Sarofim, and J. P. Longwell, "Changes in the Aromatic Ring Number Distribution of PAC from Pyrolysis of a High Volatile Bituminous Coal" (in progress).

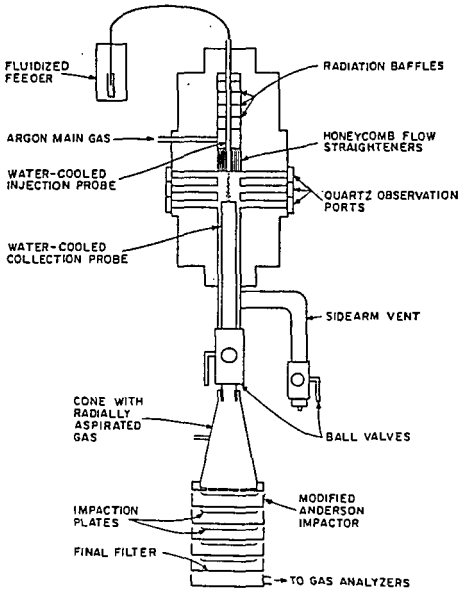

FIGURE 1: THE PYROLYSIS FURNACE AND COLLECTION SYSTEM

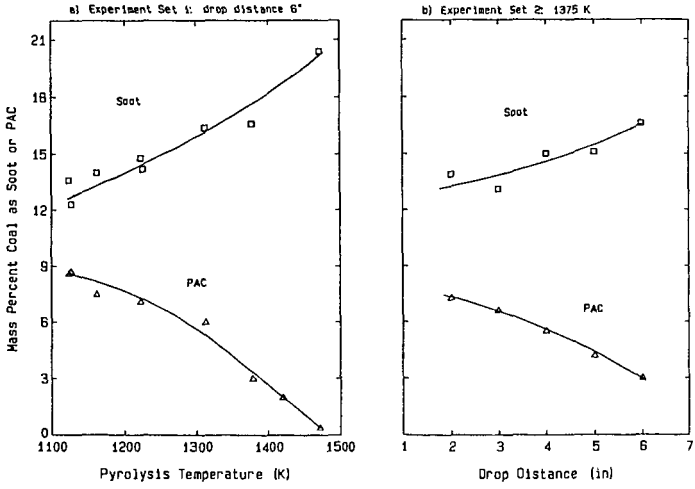

FIGURE 2: SOOT AND PAC YIELDS AT VARIOUS PYROLYSIS CONDITIONS

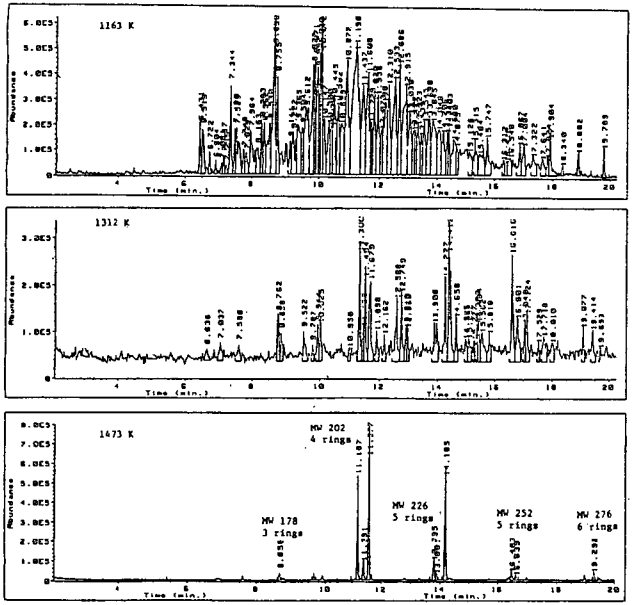

FIGURE 3: PAC TOTAL ION CHROMATOGRAMS FOR THREE PYROLYSIS TEMPERATURES

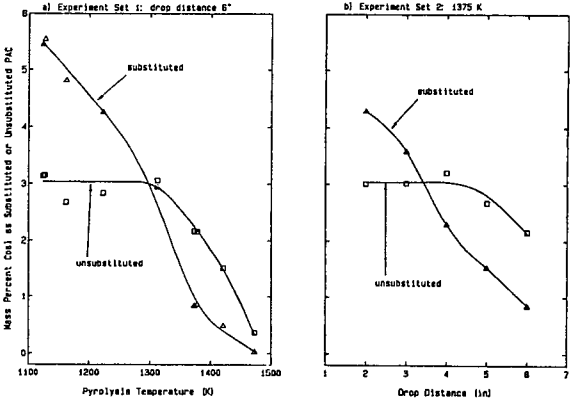

FIGURE 4: YIELDS OF SUBSTITUTED AND UNSUBSTITUTED PAC

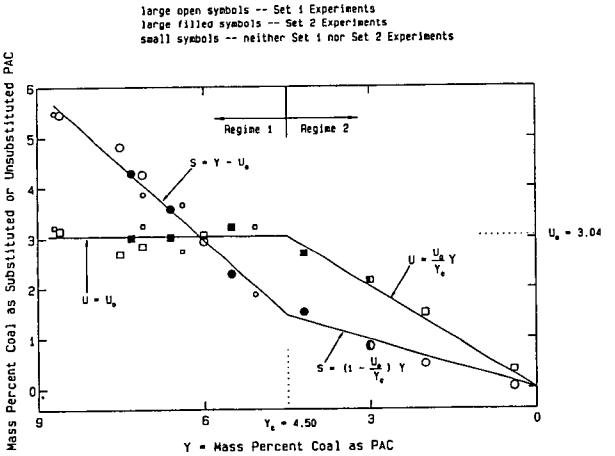

FIGURE 5: SUBSTITUTED AND UNSUBSTITUTED PAC YIELDS VERSUS TOTAL PAC YIELD

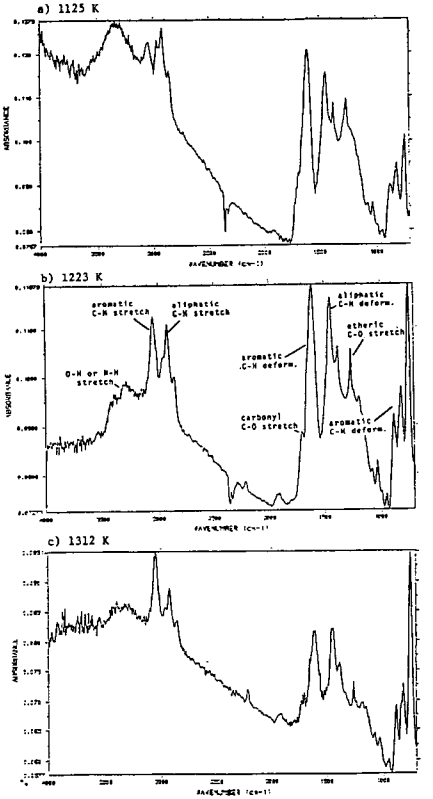

FIGURE 6: FT-IR SPECTRA OF PAC FOR THREE PYROLYSIS TEMPERATURES

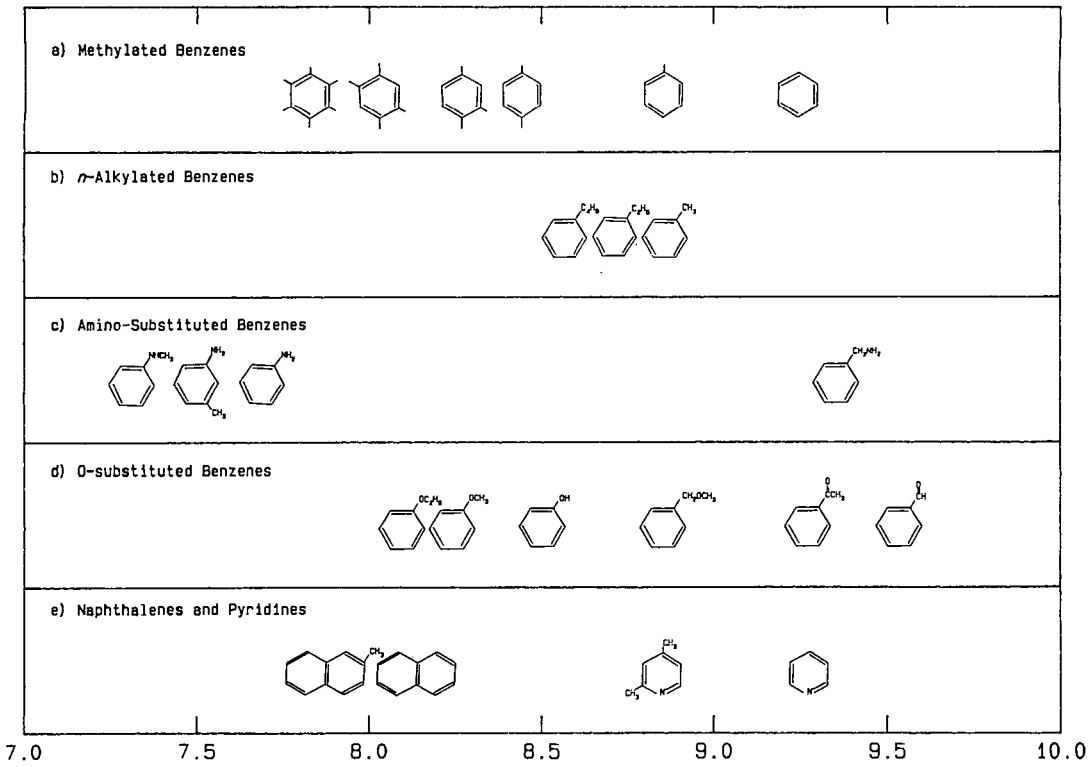

FIGURE 7: IONIZATION POTENTIALS (eV) OF AROMATICS

from Franklin, *et al.* (12)

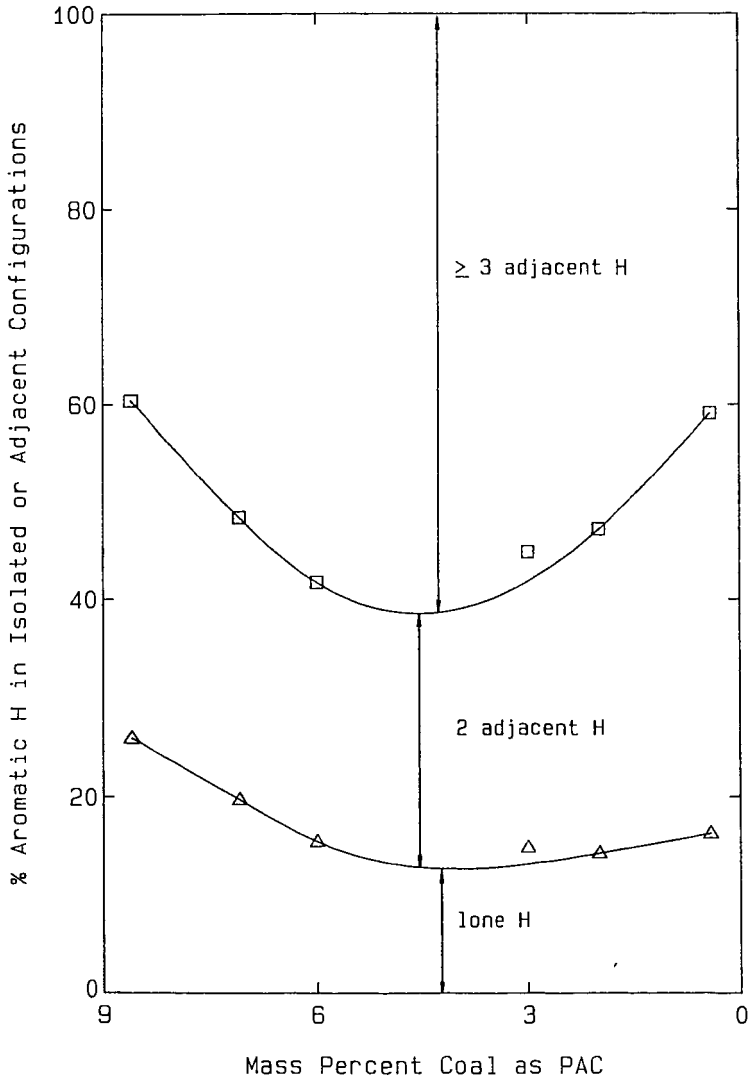

FIGURE 8: VARIATION IN AROMATIC H ADJACENCY FROM FT-IR

THERMOLYSIS OF SURFACE-ATTACHED 1,3-DIPHENYLPROPANE: IMPACT OF SURFACE IMMOBILIZATION ON THERMAL REACTION MECHANISMS

A. C. Buchanan, III and C. A. Biggs

Chemistry Division
Oak Ridge National Laboratory
P. O. Box X
Oak Ridge, Tennessee 37831-6197

INTRODUCTION

Attempts to understand the thermal chemistry of coal at the molecular level are severely complicated by its inherent properties: a diverse array of structural units (e.g., aromatic, hydroaromatic, and heterocyclic aromatic clusters connected by short aliphatic and ether links) and functional groups (e.g., phenolic hydroxyls, carboxyls, and basic nitrogens) in a cross-linked macromolecular framework with no repeating units (1,2). One simplifying experimental approach has been the study of individual model compounds that highlight structural features in coal. A complicating feature in the interpretive extrapolation of model compound behavior to coal is the possible modifications in free-radical reactivity patterns resulting from restricted translational mobility in the coal where breaking one bond in the macromolecular structure will result in radical centers that are still attached to the residual framework. We are modeling this phenomenon by studying the thermolysis of model compounds that are immobilized by covalent attachment to an inert surface. Previous studies of surface-immobilized bibenzyl (1,2-diphenylethane) showed that immobilization can profoundly alter free-radical reaction pathways compared with the corresponding fluid phase behavior (3). In particular, free-radical chain pathways became dominant decay routes leading to rearrangement, cyclization, and hydrogenolysis of the bibenzyl groups. In this paper we describe preliminary results on the effects of surface immobilization on the thermolysis of 1,3-diphenylpropane, whose fluid phase behavior has been extensively investigated (4-8).

EXPERIMENTAL

Surface-immobilized 1,3-diphenylpropane (~~DPP) was prepared at saturation coverage by the condensation at 225 °C of excess p-HOPh$(CH_2)_3$Ph with the surface hydroxyl groups of a fumed silica (Cabosil M-5, Cabot Corp., 200 m^2/g) according to the procedure described previously for surface-immobilized bibenzyl (3). Excess phenol was removed by heating at 300 (Batch A) or 270 °C (Batch B) for 0.5 h under a dynamic vacuum. The lower temperature used for Batch B appears to minimize a trace amount of reaction (ca. 0.02%) that occurs during this purification stage. GC analysis following a base hydrolysis assay procedure (3) gave coverages of 0.586 (Batch A) and 0.566 (Batch B) mmol ~~DPP per gram of final product. The starting phenol was prepared by the acid catalyzed condensation of cinnamyl alcohol ($PhCH{=}CHCH_2OH$) and phenol (9) followed by catalytic hydrogenation (10% Pd/carbon) of the olefinic intermediate.

Thermolysis (in sealed, evacuated tubes) and product analysis procedures have been thoroughly described elsewhere (3). Typically 0.3-0.4 g of surface-attached material (0.17-0.23 mmol ~~DPP) are employed, and volatile products are collected in a cold trap and then analyzed by GC and GC-MS. In a separate procedure surface-attached products are liberated as phenols following digestion of the silica in 1 N NaOH, silylated to the corresponding trimethylsilyl ethers, and analyzed as above.

RESULTS AND DISCUSSION

Thermolyses have been performed at 345 and 375 °C, and the product distributions for the four major primary products and the major secondary products are shown as a function of ~~DPP conversion in Figure 1a. The two lowest conversion runs (1.50 and 1.94%) were obtained at 345 °C, while the remainder of the data was obtained at 375 °C. Results from the two different high coverage batches of ~~DPP were consistent in terms of products detected and their relative yields. The only difference observed was a slightly slower reaction rate for batch B (ca. 30%) perhaps reflecting a slightly higher purity as a result of purification at the lower temperature (see experimental section).

We find that at low conversions (<~3%) ~~DPP cracks to form four major products in essentially equal amounts as shown below.

$$\sim\sim Ph(CH_2)_3Ph \rightarrow \underset{1}{\sim\sim PhCH_3} + \underset{2}{PhCH{=}CH_2} + \underset{3}{\sim\sim PhCH{=}CH_2} + \underset{4}{PhCH_3} \qquad 1)$$

Thermolysis of liquid DPP at very low conversions also gave a correspondingly simple product distribution as shown in Eq. 2 (4).

$$Ph(CH_2)_3Ph \rightarrow PhCH_3 + PhCH{=}CH_2 \qquad 2)$$

Hence at low conversions, the surface-immobilized DPP is reacting in an analogous fashion to liquid DPP. The additional product pair observed in the thermolysis of ~~DPP results from the fact that the two ends of the DPP molecule are no longer equivalent upon covalent surface attachment. The initial rate of the ~~DPP reaction is 15-20% h^{-1} at 375 °C for the two batches (based on a 2.3-3.0% conversion after a 9 min reaction period), and this decomposition rate is comparable to that measured for liquid DPP (ca. 19% h^{-1}) (4). This further indicates that surface immobilization at high coverage is not perturbing the initial reaction behavior of the DPP moiety.

The facile decomposition of liquid DPP was demonstrated to arise from a radical chain route whose chain propagation steps are shown in Eqs. 3 and 4 (4). In the case

$$Ph\dot{C}H_2 + PhCH_2CH_2CH_2Ph \rightarrow PhCH_3 + Ph\dot{C}HCH_2CH_2Ph \qquad 3)$$

$$Ph\dot{C}HCH_2CH_2Ph \rightarrow PhCH{=}CH_2 + Ph\dot{C}H_2 \qquad 4)$$

of ~~DPP, two distinct benzylic radicals can be formed by hydrogen abstraction (Eq. 6) following a small amount of initial homolysis (Eq. 5). Each radical can then undergo a rapid β-scission process (Eqs. 7 and 8) to produce the surface bound and free styrene products (3 and 2 respectively) analogous to Eq. 4. The free and surface-immobilized benzyl radicals propagate the chain by reacting with ~~DPP (Eq. 6; R = $PhCH_2$) to form the free and surface bound toluene products (4 and 1 respectively) while regenerating 5 and 6.

$$\sim\sim Ph(CH_2)_3Ph \rightarrow \begin{cases} \sim\sim Ph\dot{C}H_2 + PhCH_2\dot{C}H_2 & 5a) \\ \sim\sim PhCH_2\dot{C}H_2 + Ph\dot{C}H_2 & 5b) \end{cases}$$

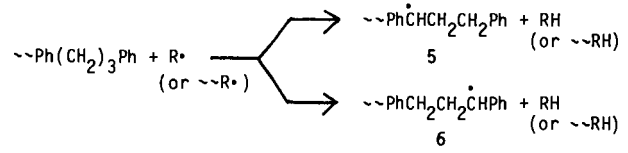

6a)

6b)

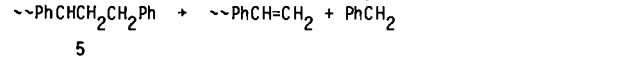

7)

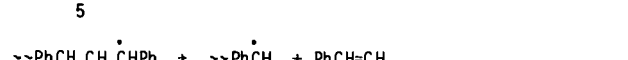

8)

No selectivity is observed for the two possible decay routes that form the product pairs 1 and 2 or 3 and 4. This suggests that at low conversions, radicals 5 and 6 are formed with equal probability and that their β-scission reactions (Eqs. 7 and 8) occur at equal rates. Trace quantities of other primary products (each <0.05 mol% of the products) including free and surface bound PhC_2H_5 (Eq. 6; R = PhC_2H_4) and free bibenzyl (from benzyl radical coupling) are also detected.

As the conversion of ~~DPP increases, there is a divergence in the yields of the four main products (Fig. 1a), and several secondary products are formed in small but increasing yields. The most significant of these (reaching about 2.8 mol % of the products at 23% conversion) is ~~$Ph(CH_2)_3Ph$~~, 7 (identified by GC-MS as the corresponding bistrimethylsilyl ether after workup). The formation of this doubly attached product arises from a secondary reaction that consumes 3, perhaps via addition of surface-attached benzyl radical (which would normally have reacted to form 1) to the surface-attached styrene. Additional secondary products observed at higher conversion include several unidentified isomers of composition corresponding to ~~$C_{23}H_{22}$~~. These products also involve the consumption of surface bound styrene (and a ~~DPP) and have a formal analog, 1,3,5-triphenylpentane, amongst the secondary products detected in the thermolysis of liquid DPP (4). However even at the highest conversion studied (23%), the secondary products sum to only 5 mol % of the total products. The radical chain decomposition of surface-immobilized DPP is a very efficient process with an estimated kinetic chain length (c.l.≡ (PhVi + ~~PhVi)/4PhEt) of 200 at 345 °C. This calculation assumes that there is no selectivity in the initial homolysis (Eq. 5) and that all PhC_2H_4• start chains.

One of the most interesting features to emerge from this study is an observed selectivity for the radical chain reaction path that forms 1 and 2 relative to that which forms 3 and 4 as the conversion increases. This is most clearly seen in Fig. 1b where the styrene to toluene yield ratio (these products are not consumed in secondary reactions) is used as an indicator of this selectivity. The ratio increases monotonically from a value of 1.00 (±0.02) indicating no selectivity at conversions <4% to a value of 1.41 (±0.04) at 23% conversion. We previously observed in the case of surface-immobilized bibenzyl that reaction rates of radical chain pathways are very sensitive to changes in surface coverage (3). These studies also indicated that unimolecular steps such as Eqs. 7 and 8 should be unaffected by such surface coverage changes. The observed regiospecificity in the reaction of ~~DPP at higher conversions may indicate that, as the molecules of ~~DPP become spread apart on the surface, hydrogen abstraction at the benzylic carbon that is farthest from the surface is becoming favored, i.e., selectivity for formation of 6 (Eq. 6b) relative to 5 (Eq. 6a). However the complication resulting from the formation of secondary products, which likely involve the reaction of 5 and 6, does not allow a firm

conclusion to be reached at this time. Additional insights into the cause of this regiospecificity should be gained from current studies being performed at lower initial surface coverages.

CONCLUSIONS

Covalent attachment of organic compounds onto an inert silica surface has proven to be a successful methodology for exploring the thermal reaction chemistry of coal model compounds under surface-immobilized conditions at temperatures relevant for coal thermolysis. Previous studies of surface-attached bibenzyl showed that restrictions on free-radical mobility can have a significant impact on reaction rates and on the nature and composition of the reaction products when compared with fluid phase behavior. The current investigation of the thermolysis of surface-immobilized 1,3-diphenylpropane has shown that facile decomposition of the trimethylene link by means of a radical chain process can still occur under surface-immobilized conditions. For ~~DPP no selectivity is observed at low conversions for the two competing radical chain decay pathways that cycle through benzylic radicals **5** and **6**. However at higher conversions, a selectivity is observed favoring the radical chain route cycling through **6**. Experiments are in progress to determine if this selectivity is a result of regiospecific hydrogen transfer on the surface at lower surface coverages.

ACKNOWLEDGMENTS

This research was sponsored by the Division of Chemical Sciences, Office of Basic Energy Sciences, U.S. Department of Energy under contract DE-AC05-840R21400 with Martin Marietta Energy Systems, Inc.

REFERENCES

1. Davidson, R. M. In Coal Science; Gorbaty, M. L. Larsen, J. W., Wender, I., Eds.; Academic Press: New York, 1982; Vol 1.

2. Green T.; Kovac, J.; Brenner, D.; Larsen, J. W. In Coal Structure; Meyers, R. A., Ed.; Academic Press: New York, 1982; Chapter 6.

3. (a) Buchanan, III, A. C.: Dunstan, T. D. J.; Douglas, E. C.; Poutsma, M. L. J. Am. Chem. Soc. **1986**, 108, 7703. (b) Poutsma, M. L.; Douglas, E. C.; Leach, J. E. Ibid. **1984**, 106, 1136.

4. Poutsma, M. L.; Dyer, C. W. J. Org. Chem. 1982, 47, 4903.

5. (a) Gilbert, K. E.; Gajewski, J. J. J. Org. Chem. 1982, 47, 4899. (b) Gilbert, K. E., Ibid. 1984, 49, 6.

6. Sweeting, J. W.; Wilshire, J. F. K. Aust. J. Chem. 1962, 15, 89.

7. (a) Benjamin, B. M.; Raaen, V. F.; Maupin, P. H.; Brown, L. L.; Collins, C. J. Fuel **1978**, 57, 269. (b) Collins, C. J.; Raaen, V. F.; Benjamin, B. M.; Maupin P. H.; Roark, W. H. J. Am. Chem. Soc. 1979, 101, 5009.

8. King. H.-H.; Stock, L. M. Fuel **1984**, 63, 810.

9. Jurd, L. Tetrahedron Lett. 1969, 33, 2863.

Figure 1. Thermolysis of ~~Ph(CH2)3Ph

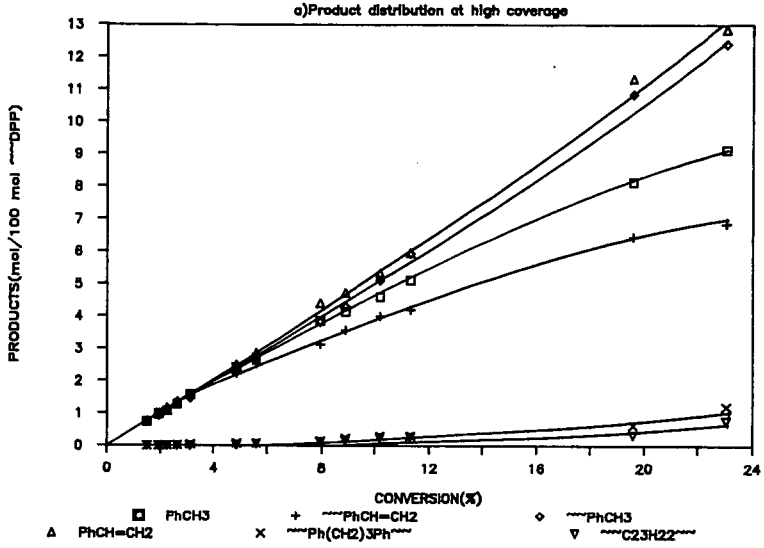

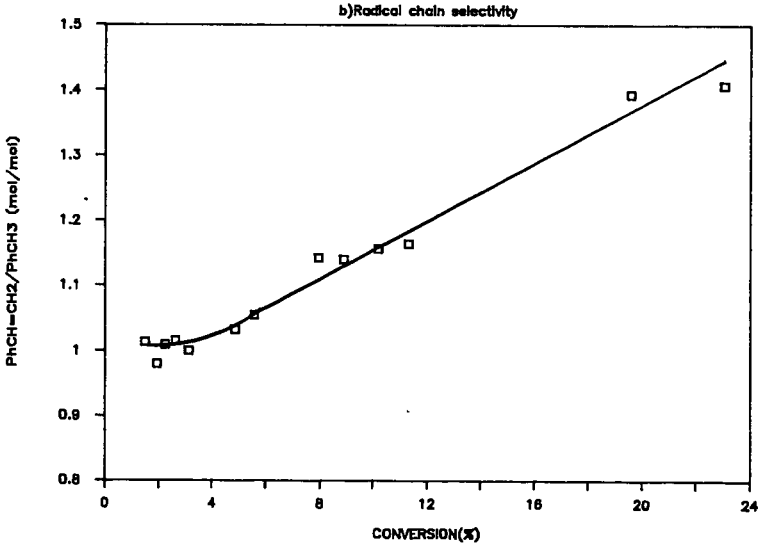

THE CASE FOR INDUCED BOND SCISSION DURING COAL PYROLYSIS

Donald F. McMillen, Ripudaman Malhotra, and S. Esther Nigenda

Department of Chemical Kinetics, SRI International
333 Ravenswood Ave., Menlo Park, CA, 94025

INTRODUCTION

Most coal pyrolysis models invoke spontaneous thermal scission of inherently weak bonds as the sole pyrolytic reaction leading to depolymerization of coal structures (1).* In this view, bond scission is dependent only on temperature; the only additional chemical factors that impact the "net" cleavage are scavenging and crosslinking of thermally generated radicals, which can be affected primarily by varying heating rates and other factors that affect heat and mass transport. In contrast to this traditional picture, data obtained by various researchers (partly in the context of coal liquefaction), when taken together, provide a strong argument that induced scission of strong bonds plays a significant role during coal pyrolysis. In this paper we attempt to summarize this argument.

The types of bond cleavage occurring during pyrolysis have been obscured in part because of the inherent difficulty of obtaining mechanistically significant pyrolysis activation energies. It is now well appreciated (3,4) that the apparent activation energy for a mixture that decomposes by a sequence of parallel first order reactions can, under conditions of rising temperature, lie below that of any member of the sequence. This factor is evidently responsible for reported activation energies as low, or lower than, 15 kcal/mole. Thus, when coupled with plausible unimolecular scission A-factors ($10^{14.5}$ to $10^{15.5}$) and a 5 to 15 kcal distribution of activation energies, rates measured under non-isothermal conditions have been shown to correspond to mean activation energies of 50 to 65 kcal/mol (5). This result has quite naturally been taken as evidence supporting the original presumption of weak bond thermolysis. However, 50 to 65 kcal/mol activation energies in no way exclude bond scission that is chemically induced by other components in the pyrolyzing substrate. In the following paragraphs, we outline some of the evidence that such induced bond scission can take place under pyrolysis conditions, and show how including them helps explain certain coal conversion phenomena.

EVIDENCE FOR THE OCCURENCE OF INDUCED BOND SCISSION DURING PYROLYSIS

Analogy with Coal Liquefaction. Since the acceptance of the weak-bond-scission/radical-capping model in coal pyrolysis has followed in large part on the acceptance of a similar model in coal liquefaction, and it has now been shown that such a model is inadequate (6-9) for liquefaction, it should also be considered whether the model is inadequate for pyrolysis. The traditional model relegates the liquefaction solvent to a role of merely scavenging thermally generated radicals. However, liquefaction effectiveness of various polycyclic aromatic hydrocarbons (PCAH) has been shown very distinctly not to correlate with scavenging, or radical-capping, effectiveness (6,9). For instance, 9,10-dihydroanthracene and its parent hydrocarbon are generally seen to be

*In the most mechanistically complete model of coal pyrolysis presented to date, Gavalas and co-workers have included bond scission induced by ipso attack of H-atoms on linkages to aromatic rings (2). Their suggestion seems to have been either largely ignored, or considered to be a minor side reaction in the production of volatiles.

substantially inferior to dihydrophenanthrene and dihydropyrene, even though dihydroanthracene is a markedly better scavenger. The inferiority of anthracene is most pronounced in the case where the solvent has no hydroaromatic hydrogen to transfer to the coal, but can only assist in shuttling hydrogen from one part of the coal structure to another (10-12). Under these conditions, the traditional mechanism requires in-situ formation of hydroaromatic, which then acts as the capping agent. Dihydroanthracene is not only the most effective scavenger (13) but because of thermochemical and kinetic considerations, is the hydroaromatic most readily formed by hydrogen transfer from coal structures. Nonetheless, it is typically much less effective than either of the other two PCAH.

Since it is clear that the hydrogen being "shuttled" is not serving merely to scavenge fragments of bonds that have already been broken, it is very likely that this hydrogen shuttling is actually inducing bond scission. It is interesting to note that liquefaction under shuttling conditions not only provides the most striking examples of the inadequacy of the traditional liquefaction mechanism, but also resembles coal pyrolysis, in that all of the hydrogen demand must be supplied by the coal itself.

Strong Bond Cleavage by Solvent Mediated Hydrogenolysis. We have used model compound studies (6,8) to show that in hydroaromatic-aromatic PCAH systems, hydrogen-transfer-induced bond scission (hydrogenolysis) of bonds too strong to thermolyze can be significant on liquefaction time scales, even in the absence of H_2 pressure. In addition, we have used hybrid coal/model-compound studies to show (7) that such cleavage tends to be accelerated by the presence of coals, and moreover, to occur by a hydrogen transfer process that does not involve the production of free H-atoms. This "radical hydrogen-transfer" (RHT) occurs in a direct bimolecular process from cyclohexadienyl "carrier" radicals formed from PCAH solvent or coal structures.

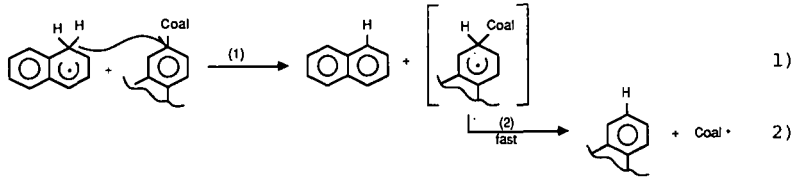

The existence of this reaction was for a long time obscured by the fact that it is often in competition with elimination and addition reactions of free H-atoms. Evidence for RHT has now been presented by several groups (14-16). While an addition-elimination sequence can yield the same products as RHT, side reactions (H_2 formation and ring hydrogenation) are associated with elimination addition. For this reason, a shift in the competition between H-transfer by the RHT process and an elimination-addition process can have a substantial impact on the utilization efficiency of solvent or coal hydrogen (6). Thus, we suggest not only that hydrogen-transfer-induced bond scission may be important in coal pyrolysis as well as in liquefaction, but also that the mode of hydrogen transfer may be more critical in pyrolysis, where the available hydrogen is limited to that which can be transferred from the relatively hydrogen-rich portions of the coal structure. The importance of hydrogenolysis mediated by solvent radicals (or coal radicals) moves such radicals from the category of species for which the only goal is to prevent retrograde reactions, to species which can, in addition, be sources of bond cleavage activity.

Strong-Bond Scission in Pyrolysis of Coal Models. Direct evidence for induced scission of alkyl-aryl linkages in the nominal absence of solvents can be seen in the pyrolyses of polymeric coal models consisting of aliphatic linkages between PCAH clusters. Solomon and co-workers have pyrolyzed a series of polymers $(\text{-Ar-CH}_2\text{-CH}_2\text{-})_n$ at 400 to 430°C and analyzed the tars by field

ionization mass spectrometry (17). This analysis revealed that polymeric coal models purposely synthesized to decompose entirely by thermolysis of the weak central bond, provide, in addition, a small but significant amount of product indicative of cleavage of the much stronger aryl-alkyl linkage.

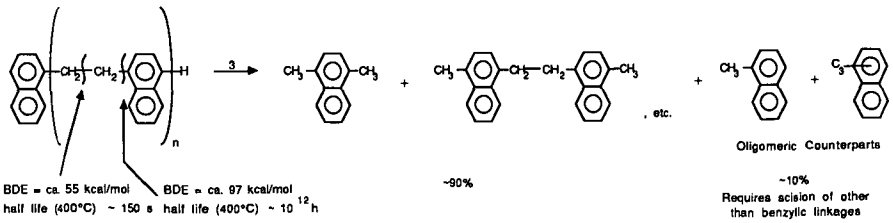

The known strengths of the two bonds (18) are such that at 400°C, the thermolysis half-life of the weaker bond is several hundred seconds, whereas the half-life of the stronger bond would be 10^{10} times longer -- wholly unobservable if thermolysis were the only available cleavage route.

These results with weakly bonded polymers are parallel to those of Buchanan (19) and co-workers who have shown that when bibenzyl is immobilized by bonding to a silica surface, induced bond-scissions become substantially more important than they are in the liquid phase. The yield of benzene and ethylbenzene ranges from about 40 to 70% of the yield of toluene. In other words, for every one to two bibenzyl linkages that break spontaneously, there is another, very strong bond whose scission is induced by hydrogen transfer. As discussed by Buchanan, the restraint provided by the bonding makes radical-radical reactions less likely, and unimolecular reactions such as rearrangement and H-atom elimination more likely. The latter reaction can then lead to hydrogenolysis of an adjacent bibenzyl structure.

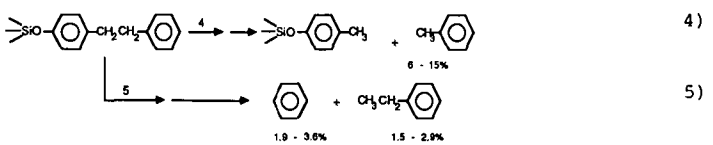

4)

5)

Similarly, earlier work by Van Krevelen (20) on polymers that contained no weak linkages whatsoever had shown that when heated in a nitrogen stream at 3°C/min, these single methylene bridged polymers were roughly half converted into volatile material during the 30 minute passage through the 450 to 550°C temperature range.

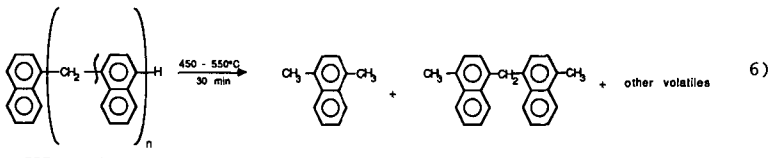

6)

For the case of the methylene-bridged naphthalene polymer, where the central linkage has a bond strength of ~ 85 kcal/mol (18), the thermolysis half-life even at 550°C would be $>10^3$ hours.

Pyrolysis of O- and C- Alkylated Coals. Various groups have shown that the methylation of coals (17,21), particularly low-rank coals, prior to pyrolysis improves the yields of the volatiles. These yield increases have been attributed to inhibition of retrograde reactions involving phenolic -OH, but they can also reflect an increased contribution from induced bond scission processes. This has been illustrated recently by Stock and co-workers (22) who have examined the product of O- methylated and O- and C- benzylated coals and found not only the expected cleavage (thermolysis) of the weak O-benzyl and C-benzyl bonds, but also the cleavage of the much stronger phenyl-C bond.

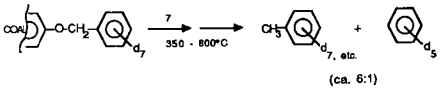

7)

IMPORTANCE OF INDUCED BOND SCISSION

The above results provide a very clear demonstration that induced scission of strong bonds in known structures does take place under pyrolysis conditions. These results suggest, but do not prove, that such cleavages also take place in coals during pyrolysis. However, the pertinent question we have to ultimately consider is whether such cleavage is of any significance to the practice of coal pyrolysis. In the following paragraphs we show that the same competing H-transfer steps we have found to be important under liquefaction conditions can account for striking variations in the yields of oil and gas resulting from modest changes in pyrolysis conditions.

Oil and Gas Yield Variations in Hydropyrolysis. Gorbaty and Maa have reported (27) that the product distribution in a fixed-bed hydropyrolysis is critically dependent upon whether the reaction temperature exceeds the threshold above which there is a pronounced exotherm. The incremental yields obtained by a switch of the pyrolysis gas from N_2 to H_2 go almost exclusively to oil if the temperature remains below this threshold, but go almost exclusively to gas if the threshold temperature is exceeded. These results are shown in Figure 1. As indicated by the authors, the higher temperatures produced in the exotherm evidently result in more ring hydrogenation and ring opening (followed by cleavage of the newly produced side chains), yielding more gas.

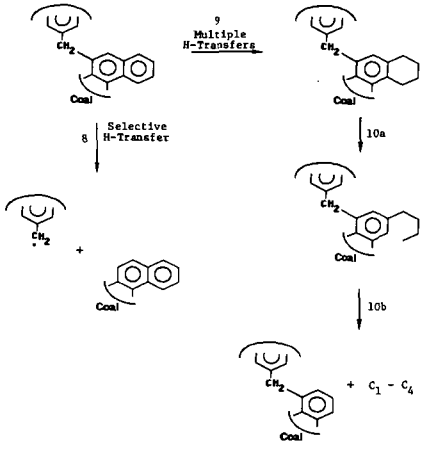

8)

9)

10)

Higher gas production with increasing temperature is, of course, a well known trend in hydroliquefaction. The question is, what factors are responsible for the change, and what makes it so sharp. In the most general terms, it is clear that a shift in product distribution is a result of a shift in competing reaction types. More specifically, we suggest that it results from a changing competition between free H-atom addition and the H-transfer via the radical hydrogen-transfer (RHT) process. Both of these processes, in that they put an H-atom on the ipso positions of aromatic structures bearing critical linkages, can lead to the fragmentation necessary to produce oils. However, under conditions where free H-atoms dominate, hydrogen is transferred much more unselectively to aromatic ring positions, regrardless of whether or not they bear linkages. Consequently there are, as suggested in reactions 9 and 10, many more side reactions that lead to excessive gas formation.

To understand why dominance by free H-atoms leads to very inefficient use of transferred hydrogen to cleave linkages, it is necessary to consider the fate of the "non-ipso" radicals -- cyclohexadienyl radicals in the coal structure formed by H-transfer to positions <u>not</u> bearing any linkage. In contrast to the ipso-radicals, which result in rapid and irreversible cleavage of the linkage, the non-ipso radicals are sufficiently long-lived to allow subsequent bimolecular reactions. Either the initial hydrogen transfer can be followed by further hydrogen transfers to produce reduced-but-uncleaved product, or the non-ipso radical can transfer a hydrogen transfer back to an aromatic by RHT (6) leading to no <u>net</u> change.*

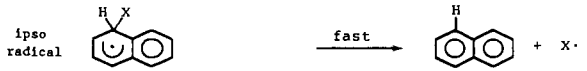

11)

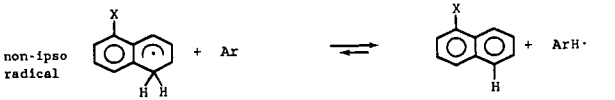

12)

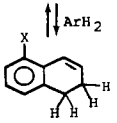

13)

*Cleavage of the ipso radical ArX· will generally be so rapid as to be irreversible regardless of the nature of X·. For instance, we estimate, from the known bond strengths (18,24), that elimination of an unstablized primary radical (a simple alkyl chain) from the 9-position of a phenanthrene ring has a half-life at 400°C of about 10^{-8} seconds; that is, sufficiently short to make transfer of a second hydrogen from any available source (ArH_2, H·, H_2, ArH·) uncompetitive.

The effectiveness of the aromatic pool in regaining "wastefully" transferred hydrogen is a function of the nature and concentration of the aromatic and the temperature. At a given temperature, the rate of this retrieval of hydrogen increases with increasing aromatic concentration in the solvent (or in the coal if there is no solvent). On the other hand, to the extent that the concentration of aromatic is too low, the non-ipso radicals will obtain a second hydrogen (e.g., from another molecule of ArH_2) to yield uncleaved dihydro product. At higher temperatures, the endothermic reactions

$$ArH^{\cdot} \rightarrow Ar + H^{\cdot} \quad \Delta H^{\circ}(Ar = PCAH) > 25 \text{ kcal/mol} \qquad 14)$$

are shifted to the right, and any given Ar becomes less effective as a "reservoir" for H-transfer activity. This means that the non-ipso radicals will have a greater opportunity to obtain a second hydrogen to form dihydro-aromatics. Such dihydronaphthalene-type species are very reactive and will be rapidly further reduced to tetrahydro products. The dihydro and tetrahydro products are then subject to ring-opening and loss of all or part of the newly formed chains as C_1 to C_4 hydrocarbons.

What helps make the shift in incremental yields from oil to gas so dramatic is the fact that the decreasing effectiveness of the aromatic pool with increasing temperature provides the system with marked feedback potential. When the temperature reaches the point where ineffectiveness of the solvent pool in regaining H-atoms allows sufficient ring hydrogenation such that the heat evolved exceeds the fixed-bed heat transfer capability, the temperature begins to rise faster. This rise further decreases the ability of the aromatic pool to regain wastefully transferred H-atoms, ring hydrogenation is further promoted, the temperature goes up still faster, and so on, in an accelerating manner.

Role of Coal Fragments in Induced Bond Scission. All of the results summarized here support, in one way or another, the hypothesis that aromatic/hydroaromatic reaction media, and H_2 as well, serve not only to scavenge coal radicals, but also to generate hydrogen transfer activity. Making the very probable assumption that the connections in coals consist of some weak covalent linkages, which will undergo thermal scission regardless of the reaction medium, and some linkages so strong they will cleave only when induced to do so by hydrogen transfer, it becomes clear that the radicals generated by scission of the weak links have a much more important role to play than merely being "capped" by hydroaromatic species (or H_2). To the extent they are non-hydroaromatic radicals (eg., benzyl), these radicals typically have no hydrogenolysis activity: they cannot transfer a hydrogen to a cleavable substrate because they cannot, in so doing, form an aromatic system. If not capped, such thermally generated radicals may indeed become involved (as the conventional view would have it) in retrograde reactions. The important point however, and the one not included in most pyrolysis pictures, is that when the scavenger is a hydroaromatic, the capping process actually contitutes a chain transfer step that converts a radical with no hydrogenolysis activity into a radical that can induce hydrogenolysis.

$$ArCH_2^{\cdot} + PhenH_2 \rightarrow ArCH_3 + PhenH^{\cdot} \quad \Delta H^{\circ} = -5 \text{ kcal/mol} \qquad 15)$$

The potential role of coal radicals in providing hydrogenolysis activity suggests that the high reactivity of coals in the initial stages of conversion may result from a "burst" of coal radicals that is large compared to the steady state level of $ArH^{\cdot}$ supplied by the hydroaromatic media. If this is the case, then the conversion of inactive, non-donor radicals into $ArH^{\cdot}$ carrier radicals (by either the solvent or by hydroaromatic coal species) could help explain the initial high reactivities of coals. If the number of initiating radical species is too high to be quickly disposed of via the normal termination pathways of the medium (i.e., radical disproportionation), then there should be a significant increase in activity. In hybrid studies involving mixtures of coals and model compounds,

we observed (7) that the addition of coal substantially increases the model compound hydrogenolysis rate. At 400°C, the rate in the modest liquefaction solvent, tetralin, was increased by a factor of about forty. In the more effective solvents, dihydrophenanthrene and dihydropyrene, the rate was increased by a factor of two to three. Thus, under the liquefaction conditions of these experiments, some species generated by the coal (presumably free radicals) very clearly were a source of bond cleavage activity, not merely something to be scavenged. In the absence of evidence to the contrary, it is reasonable to assume that the same phenomenon occurs under pyrolysis conditions.

Coal Pyrolysis in Reactive Vapors. An awareness of the triple role of aromatic/hydroaromatic media (radical scavenger, agent for conversion of inactive radicals into hydrogenolytically active radicals, and retriever of wastefully transferred hydrogen) raises questions about the relative merits of two different approaches to augmenting hydrogenolysis activity in coal pyrolysis: the use of high pressure hydrogen and the use of hydroaromatic PCAH vapor.

The use of hydrogen pressure to augment volatiles yields during coal pyrolysis is not a new approach. H_2 is, of course, a thermodynamically powerful reducing agent. However, owing to the strength of the H-H bond, H_2 is kinetically ineffective at low temperatures (in the absence of a catalyst). Unfortunately, the low temperature range of coal pyrolysis (300 to 500°C) is precisely the region in which coals become highly reactive and in which they seem particularly suuceptible to oxidative retrograde reactions. In fact, it is already well appreciated (26) that the presence of H_2 actually tends to decrease volatiles yields (relative to pyrolysis in a vacuum) at temperatures below about 600°C. Consideration of the kinetics of the reaction by which H-atoms are produced from H_2 emphasizes why this is the case.

$$ArCH_2^{\cdot} + H_2 \rightarrow ArCH_3 + H^{\cdot} \qquad \Delta H^{\circ} = +16 \text{ kcal/mol} \qquad 16)$$

$$\log k_{16,400}(1\ m^{-1}s^{-1}) \simeq 1.7$$

For Ar = phenyl, this reaction is 16 kcal/mol endothermic (18) in contrast to the analogous "scavenging" reaction shown above (reaction 15), which is 5 kcal/mol exothermic, and at least 100 times faster at 400°C (at equivalent concentrations of the respective "scavengers").

$$\log k_{15,400}(1\ m^{-1}s^{-1}) \simeq 3.8$$

While the hydrogen carrier radical generated ($ArH^{\cdot}$) is not nearly as active as $H^{\cdot}$ on a per molecule basis, it, as discussed above, is much more efficient in transferring hydrogen selectively to places where it is utilized for cleavage, and it cannot abstract another H-atom to uselessly form H_2. In addition, in the low temperature pyrolysis region, near-molar concentrations of such PCAH and their hydroaromatic derivatives can be generated at pressures in the vicinity of one atmosphere, whereas, maintenance of 1M [H_2] requires about 800 psi. Finally, the Ar/ArH_2 mixtures are themselves sources of these hydrogenolytically active radicals (by reverse radical-disproportionation (25,26) that can rival in numbers the radicals thermally generated from the coal structures. Thus, it seems likely that heating the coal in the presence of ArH_2/Ar vapors (or with "pre-loaded" Ar/ArH_2) could offer some of the conveniences of pyrolysis, and be, in the 350 to 500°C temperature range, a more effective way of inducing hydrogenolysis in the coal structures than is provided by heating in hydrogen pressure. The recent work of Gorbaty and co-workers (27) will presumably shed some light on the practicality of this approach, as well as providing data that will help to unify the chemical pictures of coal liquefaction and gasification.

CONCLUSION

In summary, experimental evidence now strongly supports the hypothesis that induced cleavage of strong bonds is a significant part of coal pyrolysis as well as liquefaction. Furthermore, conversion results indicate that shifts in the modes of hydrogen transfer affect hydrogen utilization efficiency and product distribution, and that variations in reaction conditions do indeed have an impact on the induced bond scission processes. Therefore we suggest that the most fruitful working hypothesis for coal pyrolysis/gasification research is that such induced bond scissions can be substantial and are subject to manipulation, and assert that attempts at manipulation are more likely to be successful to the extent that we obtain an improved understanding of the chemistry of these cleavage processes.

ACKNOWLEDGEMENT

The authors wish to acknowledge the support of the U.S. Department of Energy under Contract DE-FG22-86PC90908.

REFERENCES

1. See, for example: Solomon, P. R.; Hamblen, D. G., "Measurements and Theory of Coal Pyrolysis," Report No. DOE/FE/05122-1668, Contract No. DE-AC21-81FE05122, 1984; Howard, J. B., "Fundamentals of Coal Pyrolysis and Hydropyrolysis," in Chemistry of Coal Utilization, Second Supplementary Volume, M. A. Elliot, ed., John Wiley and Sons, New York, 1982, pp. 665-784.
2. Gavalas, G. R.; Cheong, P. H.; Jain, R., Ind. Eng. Chem. Fundam., 1981, 20, 113.
3. Anthony, D. B.; Howard, J. B.; Hottel, H. C.; Meissner, H. P., Fuel, 1976, 55, 121.
4. Jüntgen, H., Fuel, 1984 63, 731.
5. Solomon, P. R.; Serio, M. A., "Evaluation of Coal Pyrolysis Kinetics," presented at NATO Workshop on "Fundamentals of Physical Chemistry of Pulverized Combustion, Les Arcs, France, July 28 - August 1, 1986.
6. McMillen, D. F.; Malhotra, R.; Chang, S.-J.; Nigenda, S. E., Am. Chem. Soc., Div. Fuel Chem. Prep., 1985, 30(4), 297.
7. McMillen, D. F.; Malhotra, R.; Chang, S.-J.; Hum, G. P., Energy and Fuels, 1987, 1, 193.
8. McMillen, D. F.; Malhotra, R.; Chang, S.-J.; Fleming, R. H.; Ogier, W. C.; Nigenda, S. E., "Mechanisms of Hydrogen Transfer and Scission of Strongly Bonded Coal Structures in Donor-Solvent Systems," Fuel, accepted for publication.
9. Finseth, D. H; Bockrath, B. C.; Cillo, D. L.; Illig, E. G.; Sprecher, R. F.; Retcofsky, H. L.; Lett, R. G., Am. Chem. Soc. Div. Fuel. Chem. Prep., 1983 28(5), 17.
10. Orchin, M.; Columbic, C.; Anderson, J. E.; Storch, H. H.; U.S. Bureau of Mines Bull. No. 505, 1951.
11. Davies, G. O.; Derbyshire, F. J.; Price, R. J., J. Inst. Fuel, 1977, 50, 121.
12. McMillen, D. F., unpublished work.
13. Bockrath, B. C.; Bittner, E.; McGrew, J., J. Am. Chem. Soc., 1984, 106, 135.
14. Bilmers, R. L.; Griffith, L. L.; Stein, S. E., J. Phys. Chem., 1986, 90, 517.
15. Choi, C.-Y.; Stock, L. M., J. Org. Chem., 1984, 40, 2871.
16. Metzger, J. O., Angew. Chem. Int. Ed. Engl., 1986, 25, 80.

17. Solomon, P. R.; Squire, K. R., Am. Chem. Soc. Div. Fuel Chem. Prep., 1985 30(4), 193.

18. a. McMillen, D. F.; Golden, D. M., "Hydrocarbon Bond Dissociation Energies,". Ann. Rev. Phys. Chem., 1982, 33, 497.
b. Benson, S. W., Thermochemical Kinetics, 2nd ed., John Wiley and Sons Inc., New York, 1976.

19. Buchanan, A. C.; Dunstan, T. D. J.; Douglas, E. C.; Poutsma, M. L., J. Am. Chem. Soc., 1986, 108, 7703.

20. Wolfs, P. M. J.; van Krevelen, D. W..; Waterman, H. I., Fuel, 1960, 39, 25.

21. Chu, C. J.; Cannon, S. A.; Hauge, R. H., Margrave, J. L., Fuel, 1986, 65, 1740.

22. Rose, G. R.; Zabransky, R. F.; Stock, L. M.; Huang, C.-B.; Srinivas, V. R.; Tse, K.-T., Fuel, 1984, 64, 1339.

23. Gorbaty, M. L.; Maa, P. S., Am. Chem. Soc., Div. Fuel Chem. Prep., 1986, 31(4), 5.

24. Herndon, W. C., J. Org. Chem., 1981, 46, 2119.

25. King, H.-H.; Stock, L. M., Fuel, 1982, 61, 257.

26. Stein, S. E., "A Fundamental Chemical Kinetics Approach to Coal Conversion," in Advances in Chemistry Series, 192, American Chemical Society, Washington, DC, 1982, p. 97.

27. a. Neskora, D. R.; Schlosberg, R. H., U.S. Patent No. 4,385,981.
b. Gorbaty, M. L., private communication.

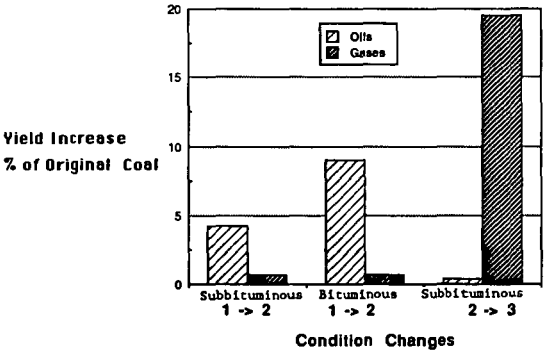

Each of the three sets of bars should be viewed in isolation from the other two. Each represents the distribution of the additional yields obtained as a result changing from one set of conditions to another.

Cond. 1. 372 -> 465°C, 35 min, N_2
Cond. 2. 372 -> 465°C, 35 min, H_2
Cond. 3. 372 -> 525°C, 85 min, H_2

Taken from the data of Gorbaty and Maa, 1986.

Figure 1. Incremental Yields Resulting from Gas and Temperature Changes in Coal Pyrolysis

Modelling the Thermal Reactions of Benzyl Phenyl Sulfide

by

Martin A. Abraham[1] and Michael T. Klein*
Department of Chemical Engineering
University of Delaware
Newark, DE 19716

The reactions of benzylphenylsulfide (BPS) neat, in benzene, in tetralin and with added thiophenol were studied. A free-radical mechanism described the neat pyrolysis of BPS to the major products toluene, thiophenol, diphenyldisulfide, and diphenylsulfide. An analytical rate expression deduced from this mechanism was consistent with results from both neat pyrolysis and reaction with additives. The secondary reactions of primary products were detailed.

Our interest in the resolution of reaction fundamentals in supercritical fluid (SCF) solvents has motivated careful study of the thermolysis pathways, kinetics and mechanisms that will generally occur in parallel with any possible solvolysis. Since reactions with a SCF solvent of compounds containing oxygen (Lawson and Klein, 1985; Townsend and Klein, 1985) and nitrogen (Abraham and Klein, 1985; Tiffany, et al., 1984), but not sulfur, have been reported, our interest extended to the reactions of benzylphenylsulfide (BPS). Herein we report on a mathematical model of BPS pyrolysis that is based on our own experiments and also the literature base on which our work is built.

Previous studies suggest that neat pyrolysis of BPS proceeds by a free-radical mechanism (Attar, 1978). The mechanism likely involves fragmentation of the C-S bond to a free-radical pair followed by stabilization through hydrogen abstraction, from either a hydrogen donor source, such as tetralin, or other hydrocarbon molecules in the reaction mixture. Fixari and coworkers (1984) pyrolysed BPS in benzene and in tetralin. For reaction in benzene, they postulated that BPS cleaved to a benzyl-phenylthiyl radical pair, which stabilized primarily by recombination. For reaction in tetralin, hydrogen abstraction was from tetralin, which led to a tetralyl radical intermediate whose disproportionation ultimately led to naphthalene. Huang and Stock (1982) also describe a free-radical mechanism for BPS decomposition. Thus the literature provides a good foundation from which to model the reaction of BPS.

Our investigation into the reactions of BPS addressed its neat pyrolysis first. Special attention was paid to derivative experiments, used in a detailed probe of the mechanism, which included reaction in the hydrogen-donor

1 Current address:
Department of Chemical Engineering
University of Tulsa
Tulsa, OK 74104

*Correspondence

solvent tetralin, reaction in the inert solvent benzene, reaction with the addition of thiophenol, and the pyrolysis of diphenyldisulfide. This provided a basis with which to summarize the experimental results in terms of plausible reaction pathways and a reaction model.

EXPERIMENTAL

The reactants, solvents, and GC standards were all commercially available and used as received. A typical experimental procedure was as follows: the reactants, solvent, and the demonstrably inert (Townsend and Klein, 1985) internal standard biphenyl were loaded into batch "tubing bomb" reactors comprising one Swagelok port connector and two caps of 1/4" nominally sized stainless steel parts. The tubing bombs were sealed and immersed in a constant temperature sandbath. In approximately two min, the reactors reached the nominal reaction temperature and, after the desired time had passed, reactions were quenched by insertion of the reactor into a cold water bath. A representative initial concentration of BPS was 0.5 mol/L.

Spectrophotometric-grade acetone or reagent-grade tetrahydrofuran was used to collect all material from the reactors in one phase. Product identification was accomplished on an HP 5970 series GC/MSD equipped with a 60m DB-5 fused-silica capillary column. Quantitation of individual product yields was by GC using an HP 5880 instrument with the same type of capillary column and a flame ionization detector. Response factors were estimated from analyses of standard mixtures, which allowed quantitative calculation of product yields and, hence, an observed product index (OPI). This was the sum of the mass of identified GC-elutable products divided by the initial mass of reactant charged.

RESULTS

The reactions of benzylphenylsulfide (BPS) with a set of coreactants complemented the study of its neat pyrolysis and allowed a deeper probe of operative pathways and mechanisms. Reaction in the hydrogen-donor solvent tetralin highlighted unimolecular fission steps, whereas reaction in benzene allowed determination of the overall reaction order. Experiments with added thiophenol probed a major non-primary pathway, and the secondary reaction of diphenyldisulfide (DPDS) was investigated through its neat pyrolysis. The experimental conditions and major products are summarized in Table 1.

The presentation of the results is organized into sections that describe, respectively, neat pyrolysis and the derivative copyrolysis experiments. Within each section, the identity of all products and the temporal variation of the yields ($y_i = n_i/n_{BPSo}$) of major products are presented first. This is followed by examination of product selectivity (y_i/x) and the effect of the loading of additive i ($S_i = n_{io}/n_{BPSo}$). Likely pathways and their kinetics are presented in the discussion.

Neat pyrolysis. Toluene was the major product of the neat pyrolysis of BPS. Other major products were DPDS, diphenylsulfide (DPS), and thiophenol; diphenylmethane and bibenzyl were minor products. The temporal variations of the yields of major products from pyrolysis at 300°C are shown in Figure 1, which indicates, by their initially positive associated slopes, that toluene, DPDS and thiophenol were primary products. OPI was greater than 0.9 at a BPS

conversion $x = 0.9$, which occurred after 120 min. The pseudo-first order rate constants and associated Arrhenius parameters for the disappearance of BPS during neat pyrolysis are summarized in Table 2.

Reaction in tetralin. Thermolysis of BPS in tetralin led to toluene and thiophenol as major products along with minor amounts of diphenylmethane and DPDS. The temporal variations of the yields of the major products from thermolysis at 340°C are shown in Figure 2, which indicates, by their initially positive slopes, that both toluene and thiophenol were primary products. OPI remained above 0.9 at a BPS conversion of 0.95, which occurred after 120 min. BPS disappearance in tetralin was described by the pseudo-first order rate constants indicated in Table 2. For reaction at 300°C, $k_{rel} = k_{TET}/k_{NEAT} = 0.087$, indicating that BPS reaction in tetralin was much slower than its disappearance during neat pyrolysis.

The effect of tetralin loading on the reaction of BPS was studied over the range $S_T = n_{TETo}/n_{BPSo}$ from 0.0 to 2.0 at 300°C. Increasing S_T simultaneously decreased BPS conversion (x) and increased selectivity ($s_i = y_i/x$) to the major products toluene and thiophenol. This is illustrated in Figure 3, where x and y_i/x are plotted vs. S_T for a constant reaction time of 50 min. During neat pyrolysis ($S_T = 0$) of BPS, x was approximately 0.9 after 50 min, whereas it was only 0.15 at $S_T = 2.0$ after the same reaction time. The selectivity to toluene increased from 0.4 to 1.0 and the selectivity to thiophenol increased from 0.1 to 0.8 as S_T increased from 0.0 to 2.0.

Reaction in Benzene. Reaction of BPS in benzene at 275°C at varying initial BPS concentrations allowed determination of an apparent overall reaction order. The resulting pseudo-first order rate constants for the disappearance of BPS are plotted vs. initial BPS concentration in Figure 4. The best-fit straight line has a slope of approximately 0.2, indicating an overall reaction order of 1.2 in BPS concentration over the range of conditions examined. The pseudo-first order rate constant corresponding to the neat pyrolysis concentration of 0.6 mol/L in Figure 4 is 4.47×10^{-3} min^{-1}, somewhat less than the experimentally determined neat pseudo-first order rate constant of 0.01 min^{-1} at the same concentration.

Reaction with Thiophenol. Pyrolysis of BPS at 300°C in the presence of thiophenol with initial molar ratios [$S_{THP} = n_{THPo}/n_{BPSo}$] ranging from 0.0 (neat pyrolysis) to 1.68 yielded toluene, DPDS, and DPS as major products; diphenylmethane and bibenzyl were minor products. Figure 5 summarizes the temporal variation of product yields for $S_{THP} = 1.68$. The disappearance of BPS in the presence of thiophenol was characterized by a pseudo-first order rate constant of 0.0445 min^{-1}, comparable to that observed from neat pyrolysis.

The effect of added thiophenol on BPS decomposition is illustrated in Figure 6, a plot of BPS conversion and major product selectivities vs. S_{THP} for a constant reaction time of 20 min at 300°C. As S_{THP} increased from 0 to 1.68, x decreased from approximately 0.85 to 0.7, whereas toluene and DPDS selectivity (y_{TOL}/x_{BPS}; y_{DPDS}/x_{BPS}) increased from 0.3 to 0.7 and 0.6 to 1.3, respectively. Evidently thiophenol functioned as a hydrogen donor to the benzyl radical, and the thus-formed phenylthiyl radical underwent termination by coupling.

Neat pyrolysis of Diphenyldisulfide. Neat pyrolysis of DPDS at 300°C yielded DPS as a primary product; thiophenol was a minor product. OPI was 0.9 at 60 min, which corresponded to a DPDS conversion and DPS yield of 0.7. Thus the selectivity of the reaction of DPDS to DPS was essentially 1.0, which implies the formation of elemental sulfur. The disappearance of DPDS was characterized by a pseudo-first order rate constant of 0.0196 min^{-1}.

DISCUSSION

The literature and present results for neat pyrolysis and reaction in tetralin combine to provide the basis for development of the mathematical model.

BPS Thermolysis Mechanism. The decomposition of BPS is reasonably interpreted as a set of free radical steps like those described by Attar (1978), Miller and Stein (1979), and Huang and Stock (1982). Illustrated in Figure 7a, a consistent sequence of steps is initiated through fission at the relatively weak (bond dissociation energy ≈ 53 kcal/mol (Fixari et al., 1984)) C-S bond. BPS consumption also occurs through hydrogen abstraction by the initiation-generated benzyl or phenylthiyl radicals, which leads to toluene or thiophenol and a BPS radical. Abstraction of hydrogen from thiophenol by a benzyl radical will produce toluene and a phenylthiyl radical. Termination by radical recombination can involve: two phenylthiyl radicals, yielding DPDS; two benzyl radicals, producing bibenzyl; or other radicals (BPS radicals, for example), yielding unobservable, higher-molecular-weight oligomers. An additional elementary step is required to account for the minor amounts of diphenylmethane observed and also the secondary conversion of DPDS to DPS. Note that the latter might not actually occur in a single elementary step.

Pseudo-steady state analysis of the elementary steps of Figure 7 allows derivation of an analytical rate expression. Under the condition of a steady state, the rate of initiation must equal the rate of termination of radicals; we also consider the concentration of each radical β_1, β_2, and μ to be in a pseudo-steady state. Thus, with the overall BPS reaction rate as in Eq. 1,

$$r = [BPS](k_1 + k_2\beta_1 + k_3\beta_2) \tag{1}$$

the balances on β_1 and β_2, which yield Eq. 2 and 3 for β_1 and β_2, respectively,

$$\beta_1 = k_1[BPS]/(k_2[BPS] + k_5[THP]) \tag{2}$$

$$\beta_2 = \frac{1}{2}\left[-\frac{k_3[BPS]}{2k_4} + \sqrt{\left(\frac{k_3[BPS]}{2k_4}\right)^2 + \frac{2}{k_4}(k_5\beta_1[THP] + k_1[BPS])}\right] \tag{3}$$

allow formulation of the overall rate of decomposition as in Eq. 4.

$$r = k_1[BPS]\left\{1 + \frac{k_2[BPS]}{k_2[BPS] + k_5[THP]} + \frac{k_3^2[BPS]}{4k_1k_4}\left(\sqrt{1 + \frac{8k_1k_4}{k_3^2[BPS]}\left(\frac{k_5[THP]}{k_2[BPS] + k_5[THP]} + 1\right)} - 1\right)\right\} \tag{4}$$

For very low loadings of thiophenol, or at low conversion during neat pyrolysis, the rate expression of Eq. 4 reduces to

$$r = 2k_1[BPS] - \frac{(k_3[BPS])^2}{4k_4}\left(\sqrt{1-\frac{8k_1k_4}{k_3^2[BPS]}} - 1\right) \qquad (5)$$

Thus the overall BPS reaction rate is a combination of a first-order term and higher-order terms and is therefore consistent with the experimentally determined reaction order of 1.2.

The dependence of r (Eq. 4) on the addition of thiophenol to the reaction mixture provides further scrutiny of the mechanism of Figure 7. This is the derivative of the rate with respect to thiophenol concentration, shown as Eq. 6.

$$\frac{dr}{d[THP]} = -\frac{k_1k_2k_5[BPS]^2}{(k_2[BPS] + k_5[THP])^2}\left\{1 - \frac{1}{\sqrt{1+\frac{8k_1k_4}{k_3^2[BPS]}\left(1+\frac{k_5[THP]}{k_2[BPS]+k_5[THP]}\right)}}\right\} \qquad (6)$$

Since the square root term in Eq. 6 is greater than unity, the term in the braces must be positive. Thus the rate of reaction decreases with increases in thiophenol loading. This is consistent with the observed decrease in conversion with the increase in thiophenol loading illustrated in Figure 6.

The observed effect of thiophenol loading on product selectivities also probes the candidate mechanism. According to Figure 7, the rate of toluene formation is

$$d[TOL]/dt = k_2\beta_1[BPS] + k_5\beta_1[THP] \qquad (7)$$

which, after substitution for β_1 from Eq. 2 reduces to

$$d[TOL]/dt = k_1[BPS] \qquad (8)$$

It is convenient to use the instantaneous selectivity $s_1 = dy_{TOL}/dx$ as a vehicle with which to analyze the overall selectivity $s_2 = y_{TOL}/x$. Since $r = [BPS]_o dx/dt$ and $d[TOL]/dt = [BPS]_o dy_{TOL}/dt$, s_1 is given as Eq. 9.

$$s_1 = d[TOL]/r = k_1[BPS]/r \qquad (9)$$

Differentiation with respect to thiophenol concentration, holding [BPS] constant as in the present experiments, provides Eq. 10 as the sensitivity of the instantaneous selectivity to the addition of thiophenol.

$$ds_1/d[THP] = -k_1[BPS]r^{-2}(dr/d[THP]) \qquad (10)$$

Thus, since $dr/d[THP]$ is always negative, as shown in Eq. 6, s_1 will always increase with increases in [THP]. Hence the increase in s_2 observed experimentally is consistent with the mechanism of Figure 7.

Likewise, the elementary step leading to DPDS suggests Eq. 11 for its formation rate.

$$d[\mathrm{DPDS}]/dt = k_4\beta_2^{\,2} \tag{11}$$

This combines with the pseudo-steady state concentration of β_2 from Eq. 3 to allow formulation of Eq. 12

$$\frac{d\,[\mathrm{DPDS}]}{dt} = \frac{k_4}{2}\left[-\frac{k_3\,[\mathrm{BPS}]}{2k_4} + \sqrt{\left(\frac{k_3\,[\mathrm{BPS}]}{2k_4}\right)^2 + \frac{2k_1\,[\mathrm{BPS}]}{k_4}\left(\frac{k_5\,[\mathrm{THP}]}{k_2\,[\mathrm{BPS}] + k_5\,[\mathrm{THP}]} + 1\right)}\right] \tag{12}$$

for the overall rate of formation DPDS. This, in turn, allows the determination of s_1 for DPDS and, hence, $ds_1/d[\mathrm{THP}]$ for DPDS as Eq. 13.

$$\frac{d\left(\frac{d\,[\mathrm{DPDS}]}{dt}\right)}{d\,[\mathrm{THP}]} = +\frac{k_1 k_2 k_5\,[\mathrm{BPS}]^2}{(k_2\,[\mathrm{BPS}] + k_5\,[\mathrm{THP}])^2}\left\{1 - \frac{1}{\sqrt{1 + \frac{8k_1k_4}{k_3^2\,[\mathrm{BPS}]}\left(1 + \frac{k_5\,[\mathrm{THP}]}{k_2\,[\mathrm{BPS}] + k_5\,[\mathrm{THP}]}\right)}}\right\} \tag{13}$$

Eq. 13 predicts that the selectivity to DPDS will increase as the concentration of thiophenol in the reaction mixture increases. This was observed experimentally, as shown in the plot of s_2 for DPDS vs. thiophenol loading of Figure 6.

Thermolysis of BPS in tetralin is by the neat pyrolysis steps and additional steps involving tetralin and its derived radicals. These are illustrated in Figure 7b, steady-state analysis of which allows formulation of the overall BPS reaction rate as Eq. 14:

$$r = k_1[\mathrm{BPS}]\left\{1 + \frac{k_2[\mathrm{BPS}]}{k_2[\mathrm{BPS}] + k_5[\mathrm{THP}] + k_6[\mathrm{TET}]}\right\} + \frac{k_3(k_3[\mathrm{BPS}] + k_7[\mathrm{TET}])}{4k_1k_4}\left\{\sqrt{1 + \frac{8k_1k_4[\mathrm{BPS}]}{(k_3[\mathrm{BPS}] + k_7[\mathrm{TET}])^2}\left(\frac{k_5[\mathrm{THP}]}{k_2[\mathrm{BPS}] + k_5[\mathrm{THP}] + k_6[\mathrm{TET}]} + 1\right)} - 1\right\} \tag{14}$$

In the limit of high tetralin loading, Eq. 14 reduces to $r = k_1[\mathrm{BPS}]$, less than one-half the rate predicted for neat pyrolysis. This is consistent with the experimentally determined rate constants listed in Table 2. Under these conditions, the rates of toluene and thiophenol formation are given by Eq. 15,

$$d[\mathrm{TOL}]/dt = d[\mathrm{THP}]/dt = k_1[\mathrm{BPS}] \tag{15}$$

which shows that added tetralin will increase the selectivity to both toluene and thiophenol.

CONCLUSIONS

1. Neat pyrolysis of benzylphenylsulfide was through a free-radical mechanism to toluene, thiophenol, and diphenyldisulfide. Pseudo-steady state analysis of consistent elementary steps allowed formulation of the rate expression as:

$$r = k_1 [BPS] \left\{ 1 + \frac{k_2 [BPS]}{k_2 [BPS] + k_5 [THP]} + \frac{k_3^2 [BPS]}{4 k_1 k_4} \left(\sqrt{1 + \frac{8 k_1 k_4}{k_3^2 [BPS]} \left(\frac{k_5 [THP]}{k_2 [BPS] + k_5 [THP]} + 1 \right)} - 1 \right) \right\} \qquad (4)$$

Results of experiments with a set of co-reactants were consistent with the rate expression and aided in the elucidation of the mechanism.

2. The overall reaction order for pyrolytic decomposition of BPS was 1.2. This is consistent with the theoretical rate expression derived from the postulated mechanism.

ACKNOWLEDGEMENTS

We gratefully acknowledge the support of this work by the Petroleum Research Foundation and Standard Oil.

NOMENCLATURE

k_i	rate constant
n_i	mole number of i
OPI	Observed Product Index, $\Sigma weight_i / weight_{BPSo}$
r	reaction rate, mol L^{-1} min^{-1}
S_i	coreactant loading, n_{io}/n_{BPSo}
s_1	instantaneous selectivity of i, dy_i/dx
s_2	integral selectivity of i, y_i/x
x	conversion, $1-n_{BPS}/n_{BPSo}$
y_i	molar yield of i, n_i/n_{BPSo}
[ ]	concentration, mol L^{-1}

Chemical Species

BPS	Benzylphenylsulfide, $PhCH_2SPh$
DPDS	Diphenyldisulfide, PhSSPh
DPS	Diphenylsulfide, PhSPh
THP	Thiophenol, PhSH
TOL	Toluene, $PhCH_3$

Greek Symbols

β_1	benzyl radical
β_2	phenylthiyl radical
μ	BPS radical

Subscripts

o	initial condition

LITERATURE CITED

Abraham, M.A.; Klein, M.T. Ind. Eng. Chem. Product Research and Development 1985, 24, 300.

Attar, A. Fuel 1978, 57, 201-212.

Fixari, B.; Abi-Khers, V.; LePerche, P. Nouveau Journal De Chimie 1984, 8(3).

Huang, C.B.; Stock, L.M. ACS Division of Fuel Chemistry Preprints 1982, 27 (3-4),28-36.

Lawson, J.R.; Klein, M.T. Ind. Eng. Chem., Fundam. 1985, 24, 203-8.

Miller, R.E.; Stein, S.E. ACS Division of Fuel Chemistry Preprints 1979, 24(3), 271-77.

Tiffany, D.M.; Houser, T.J.; McCarville, M.E.; Houghton, M.E. ACS Division of Fuel Chemistry Preprints 1984, 29(5), 56-62.

Townsend, S.H.; Klein, M.T. Fuel 1985, 64, 635-8.

Table 1: Experimental conditions for the reactions of Benzyl Phenyl Sulfide.

Additive	Temperature (°C)	Major Products
Neat	275-386	Toluene, Thiophenol Diphenyldisulfide, Diphenylsulfide
Tetralin	300-386	Toluene, Thiophenol
Benzene	275	Toluene, Thiophenol Diphenyldisulfide, Diphenylsulfide
Thiophenol	300	Toluene, Diphenyl-disulfide, Diphenyl-sulfide

Table 2: Pseudo-first-order rate constants summarizing the reactions of Benzyl Phenyl Sulfide.

Temperature (°C)	Neat Pyrolysis	In Tetralin
275	0.0182±0.0039	-
300	0.0334±0.0019	0.0029±0.0006
340	0.175±0.045	0.0269±0.0008
386	0.530±0.046	0.3467±0.0284
$\log_{10}A(min^{-1})$	7.25	13.4
E^*(kcal/mol)	22.6	41.7

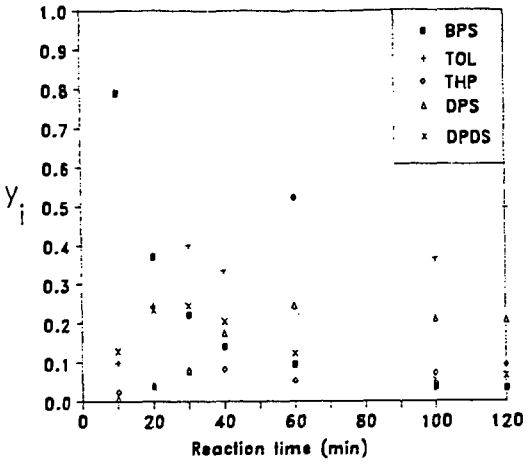

Figure 1: Temporal variation of the yields of the products of neat BPS pyrolysis at 300°C.

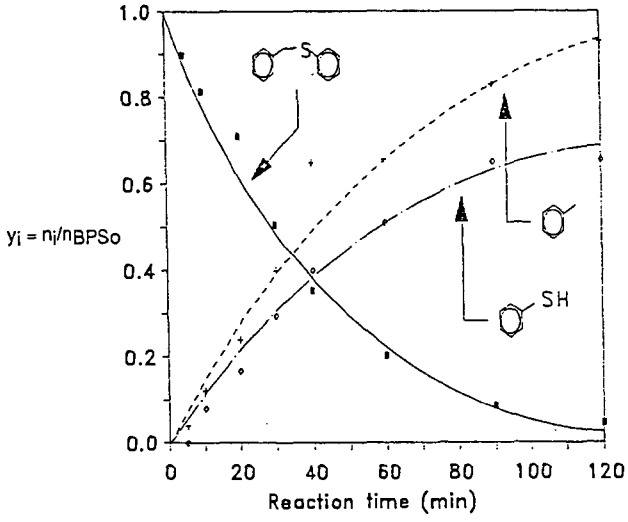

Figure 2: Temporal variation of the yields of the products of BPS thermolysis in tetralin at 340°C.

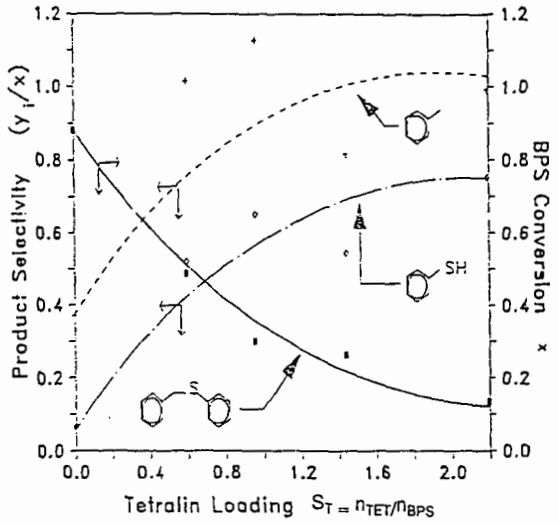

Figure 3: Dependence of product selectivity and BPS conversion on tetralin concentration during reaction at 300°C.

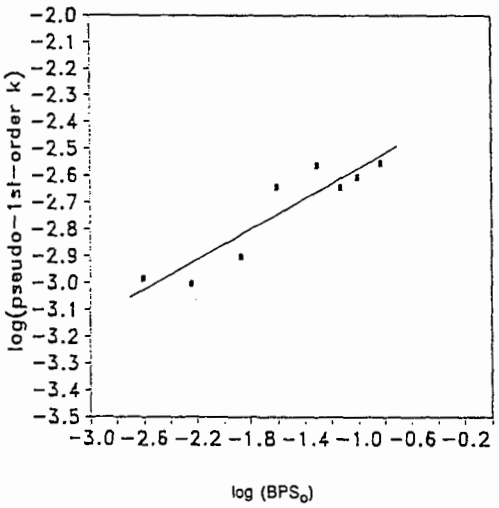

Figure 4: Overall order of reaction of BPS in benzene.

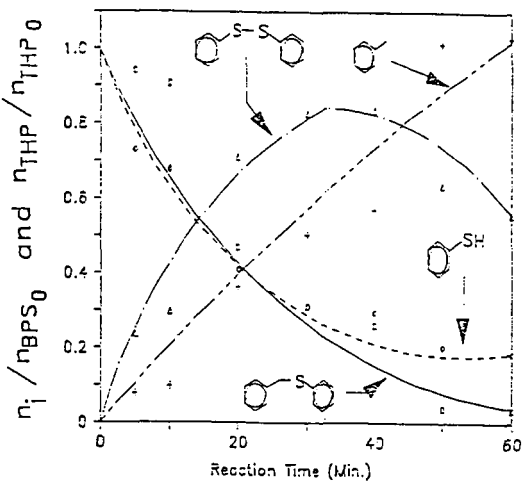

Figure 5: BPS pyrolysis at 300°C with added thiophenol: $S_{THP} = n_{THP}/n_{BPS} = 1.68$.

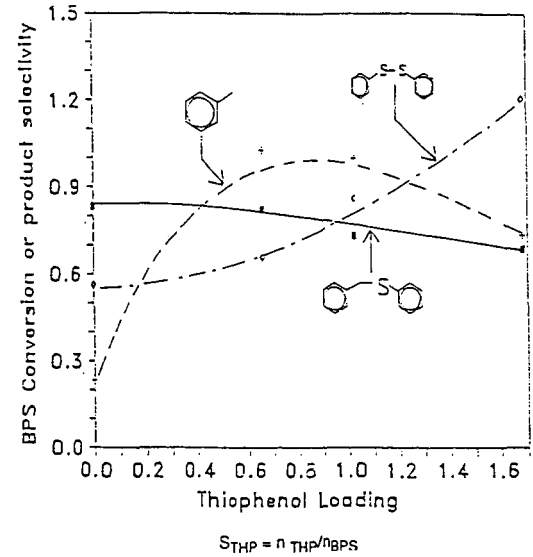

Figure 6: Dependence of product selectivity and BPS conversion on thiophenol concentration during reaction at 300°C.

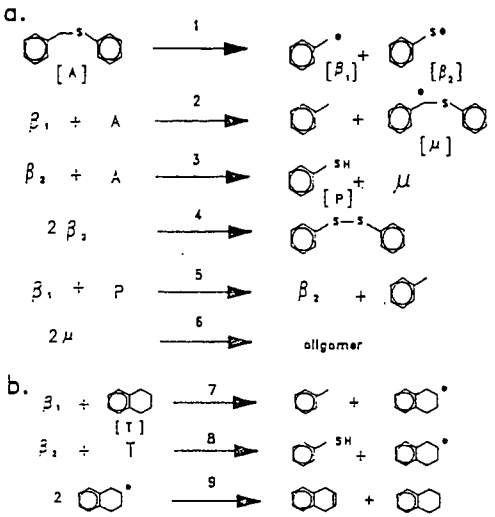

Figure 7: Free-radical steps for BPS reaction: (a) Neat pyrolysis; (b) Additional steps for reaction with tetralin.

A NOVEL APPLICATION OF ^{31}P NMR SPECTROSCOPY TO THE ANALYSIS OF ORGANIC GROUPS CONTAINING -OH, -NH AND -SH FUNCTIONALITIES IN COAL EXTRACTS AND CONDENSATES

A. E. Wroblewski, R. Markuszewski, and J. G. Verkade
Fossil Energy Program, Ames Laboratory
and
Department of Chemistry, Iowa State University, Ames, Iowa 50011

Abstract

Over one hundred model organic compounds including phenols, aliphatic alcohols, aromatic acids, aliphatic acids, amines, and thiols have been derivatized with two members of a phospholane series of phosphorus-containing reagents, namely, $ClPOCH_2CH_2O$ and $ClPOCMe_2CMe_2O$. Measurement of proton-decoupled ^{31}P chemical shifts of these derivatives reveals that, in general, the resonances fall into well-separated regions for derivatized classes of these organic compounds. Both phosphorus reagents were also tested on pyridine extracts of Illinois No. 6 coal, revealing the presence of various phenols, carboxylic acids, and aliphatic alcohols. Similar derivatization of a low-temperature pyrolysis condensate from Illinois No. 6 coal showed no detectable concentrations of carboxylic acids, a relatively small amount of aliphatic alcohols, but considerable quantities of a variety of phenols. The current scope and limitations of this NMR technique and its applicability to the quantitation of -OH, -SH and -NH functionalities in organic solutions of coal-derived materials are discussed.

Introduction

Analysis of coal-derived materials, such as low-temperature pyrolysis condensates, is usually carried out by GC/MS methods. However, these techniques are relatively non-routine and time consuming. As an alternative as well as complementary approach, IR and NMR spectroscopic procedures have been developed in recent years. Although direct analysis of complex mixtures obtained in coal processing can sometimes be performed,[1] derivatization of certain classes of compounds with suitable reagents is advantageous in NMR spectroscopy if the reagent introduces an NMR-reactive label that gives a resonance signal specific for the component being analyzed.

Previous determinations of OH functionalities in coal-derived materials have been performed by silylation[2-6] or acetylation[6,7] followed by IR[5], FT-IR[2,7] and/or ^{1}H [2,3,6], ^{29}Si [4], and ^{13}C NMR[2,6] measurements. In other studies, derivatization of various phenols with hexafluoroacetone allowed observation of ^{19}F NMR signals associated with the adducts.[6,8,9] The ^{31}P nucleus is also suitable for NMR monitoring. The P(V) reagents diethylchlorophosphate and chloro(dimethyl)thiophosphinate have been used for the derivatization of variety of phenols; however, the resonances of the respective aromatic esters spanned regions of only about 1 ppm.[10] In contrast, three P(III) organophosphorus reagents were examined previously in this laboratory, of which 2-chloro-1,3,2-dioxaphospholane appeared to be very promising in terms of widening the chemical shift range to achieve better peak separation.[11]

In this report, we present preliminary results on the scope and limitations of 2-chloro-1,3,2-dioxaphospholane **(1)**[12] and its 4,4,5,5-tetramethyl analogue **(2)**[13] as reagents for the derivatization and analysis by ^{31}P NMR spectroscopy of a variety of phenols, aliphatic alcohols, carboxylic acids,

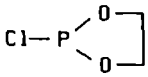

1

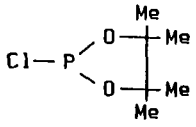

2

amines, and thiols. In addition, the applicability of both reagents to the identification of components bearing -OH, -NH, and -SH functionalities in coal extracts and pyrolysis condensates is assessed. The condensates were obtained from a low-temperature preheating step intended to modify a chemical leaching process for desulfurization of coal.[14]

Experimental

An NMR tube (10 mm) was charged under N_2 with chloroform-d (2.0 mL), chlorophospholane (**1**, 0.20 mL or **2**, 0.25 mL), and triethylamine (0.31 mL). For qualitative measurements, the standard solutions were reacted at room temperature with model compounds (a drop of liquid or a few crystals of solid). ^{31}P NMR spectra were recorded after successive additions of different model compounds until the reagent was almost exhausted. For application to coal-derived materials, approximately 100-200 mg of the coal extracts or pyrolysis condensates were added to the standard solutions, and ^{31}P NMR spectra were recorded after 15 minutes.

The extracts and condensates were prepared from an Illinois No. 6 coal. For preparation of the extract, about 1 g of coal was refluxed for 2 hr. with dry pyridine under N_2. The condensate was obtained by pyrolyzing another sample of the same Illinois No. 6 coal at 455° for 45 min. in a protective atmosphere of N_2 and collecting the volatiles condensing in an air-cooled column packed with glass beads. For a 25-g charge of coal, the yield of condensate was about 1-2 g.

Results and Discussion

Regions associated with the ^{31}P NMR resonances for representative model phenols, aliphatic alcohols, carboxylic acids, amines, and thiols derivatized with **1** and **2** are shown in Figures 1 and 2, respectively.

Derivatization of phenols with **1** at room temperature afforded the respective 2-aryloxy-1,3,2-dioxaphospholanes instantaneously. Most of these compounds gave ^{31}P NMR resonances in a rather narrow region (128.5 to 129.1 ppm). Only derivatives of di-ortho substituted phenols showed signals at lower field (131.0 - 131.5 ppm), with a low-field limit of 136.42 ppm for 2,6-di-t-butyl-4-methylphenoxy-1,3,2-dioxaphospholane. With reagent **2**, better separation of the ^{31}P NMR signals of derivatized phenols (138.0 - 139.7 ppm) and di-ortho substituted phenols (142.9 - 143.7 ppm) was achieved. In these cases, the reaction was completed at room temperature in less than five minutes, except for 2,6-di-t-butyl-4-methylphenol which did not react at all, presumably because of its bulky nature.

Carboxylic acids rapidly reacted with **1** and **2** to give derivatives displaying ^{31}P NMR signals between 127.4 and 129.5 ppm, and between 134.8 and 136.2 ppm, respectively. Although the sets of resonances for phenols and

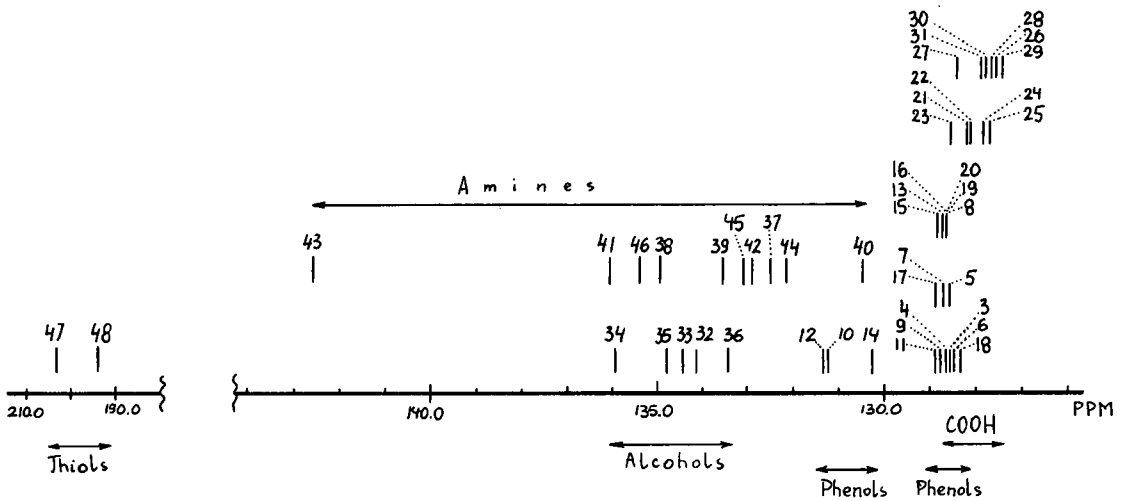

Figure 1. ^{31}P NMR chemical shifts (in ppm relative to 85% H_3PO_4) for selected model compounds derivatized with 2-chloro-1,3,2-dioxaphospholane (**1**) [secondary standard: $\delta(^{31}P)$ 175.90 ppm].
PHENOLS: **3**, phenol, 128.59; **4**, o-cresol, 128.70; **5**, m-cresol, 128.60; **6**, p-cresol, 128.53; **7**, 2,3-xylenol, 128.74; **8**, 2,4-xylenol, 128.64; **9**, 2,5-xylenol, 128.81; **10**, 2,6-xylenol, 131.30; **11**, 2,3,5-trimethylphenol, 128.90; **12**, 2,4,6-trimethylphenol, 131.42; **13**, 3,4,5-trimethylphenol, 128.72; **14**, catechol, 130.30; **15**, resorcinol, 128.83; **16**, p-methoxyphenol, 128.62; **17**, 2-methylresorcinol, 128.95; **18**, p-methoxyphenol, 128.37; **19**, α-naphthol, 128.63; **20**, β-naphthol, 128.62.
AROMATIC ACIDS: **21**, benzoic, 128.24; **22**, p-toluic, 128.19; **23**, m-phthalic, 129.54; **24**, 2,5-dihydroxybenzoic, 127.89; **25**, 2,4,6,-trimethoxybenzoic, 127.71. ALIPHATIC ACIDS: **26**, oleic, 127.56; **27**, mandelic, 128.47; **28**, succinic, 127.63; **29**, 3,3-dimethylglutaric, 127.47; **30**, indole-3-acetic, 127.77; **31**, trans-cinnamic, 127.93.
ALIPHATIC ALCOHOLS: **32**, isoamyl, 134.10; **33**, benzyl, 134.45; **34**, menthol, 135.93; **35** benzhydrol, 134.70; **36**, triphenylcarbinol, 133.41. AMINES: **37**, aniline, 132.55; **38**, o-toluidine, 134.92; **39**, anthranilic acid, 133.56; **40**, diphenylamine, 130.46; **41**, proline, 136.10; **42**, 4-methylpiperidine, 137.80; **43**, 2,6-dimethylpiperidine, 142.60; **44**, 4-methylpiperazine, 137.17; **45**, carbazole, 133.10; **46**, indole-3-acetic acid, 135.37. THIOLS: **47**, 1,3-propanedithiol, 203.12; **48**, benzenethiol, 194.28.

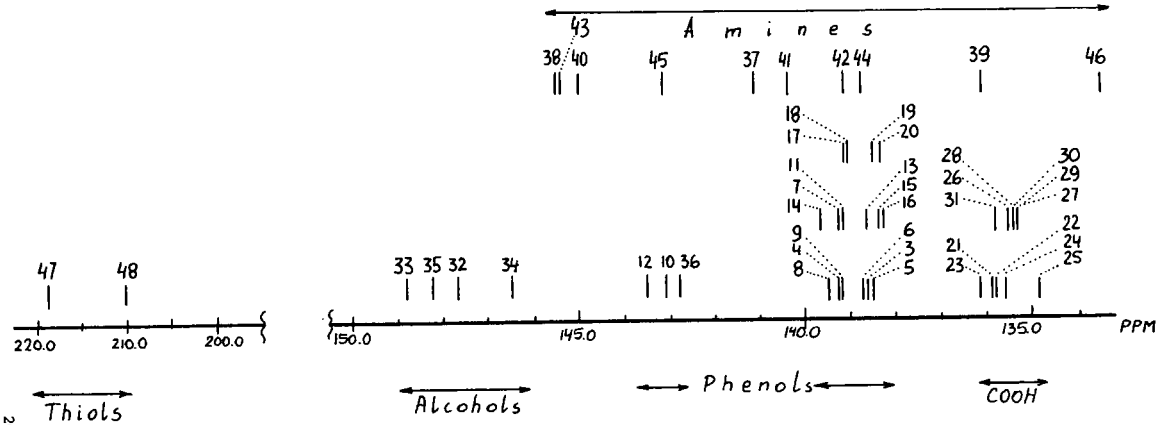

Figure 2. ^{31}P NMR chemical shifts (in ppm relative to 85% H_3PO_4) for selected model compounds derivatized with 2-chloro-4,4,5,5-tetramethyl-1,3,2-dioxaphospholane (2) [secondary standard $\delta(^{31}P)$ 175.90 ppm].
PHENOLS: **3**, phenol, 138.70; **4**, o-cresol, 139.29; **5**, m-cresol, 138.60, **6**, p-cresol, 138.83; **7**, 2,3-xylenol, 139.29; **8**, 2,4-xylenol, 139.52; **9**, 2,5-xylenol, 139.21; **10**, 2,6-xylenol, 143.04; **11**, 2,3,5-trimethylphenol, 139.21; **12**, 2,4,6-trimethylphenol, 143.55; **13**, 3,4,5-trimethylphenol, 138.68; **14**, catechol, 139.71; **15**, resorcinol, 138.44; **16**, m-methoxyphenol, 138.33; **17**, 2-methylresorcinol, 139.14; **18**, p-methoxyphenol, 139.08, **19**, α-naphthol, 138.54; **20**, β-naphthol, 138.36.
AROMATIC ACIDS: **21**, benzoic, 135.89; **22**, p-toluic, 135.81; **23**, m-phthalic, 136.17; **24**, 2,5-dihydroxybenzoic, 135.62; **25**, 2,4,6-trimethoxybenzoic, 134.91. ALIPHATIC ACIDS: **26**, oleic, 135.51; **27**, mandelic, 135.41; **28**, succinic, 135.49; **29**, 3,3-dimethylglutaric, 135.43; **30**, indole-3-acetic, 135.48; **31**, trans-cinnamic, 135.80.
ALIPHATIC ALCOHOLS: **32**, isoamyl, 147.76; **33**, benzyl, 148.80; **34**, menthol, 146.53; **35**, benzhydrol, 148.24; **36**, triphenylcarbonol, 142.82. AMINES: **37**, aniline, 141.19; **38**, o-toluidine, 145.56; **39**, anthranilic acid, 136.14; **40**, diphenylamine, 145.00; **41**, proline, 140.41; **42**, 4-methylpiperidine, 139.15; **43**, 2.6-dimethylpiperdine, 145.48; **44**, 4-methylpiperazine, 138.75; **45**, carbazole, 143.14; **46**, indole-3-acetic acid, 133.46. THIOLS: **47**, 1,3-propanedithiol, 217.85; **48**, benzenethiol, 210.31 ppm.

carboxylic acid derivatized with **1** were partially superimposed, good separation of these regions was observed when **2** was used as the derivatizing reagent.

Aliphatic hydroxy functionalities can also be analyzed by ^{31}P NMR spectroscopy after derivatization with the reagents **1** and **2**. Alkoxyphosphites derived from **1** presented ^{31}P NMR signals between 133.4 and 136.0 ppm, while those obtained from **2** revealed absorptions from 146.4 to 148.8 ppm, with exception of derivatives of tertiary alcohols (triphenylcarbinol and t-butanol) which resonated far upfield (both at 142.8 ppm). In both cases the regions of absorptions for derivatized aliphatic alcohols are well separated from those of phenols and carboxylic acids.

^{31}P NMR resonances of amines derivatized with reagents **1** and **2** are widely spread, overlapping regions represented by aliphatic alcohols, phenols and carboxylic acids. On the other hand, ^{31}P NMR signals of compounds having the P-N bond are significantly broader than those from other derivatives, thus making their assignment to amines easy.

The few thiols examined showed that the ^{31}P NMR signals for their reaction products with **1** and **2** (190 to 210 ppm and 210 to 220 ppm, respectively) are downfield from the regions observed for phenols and aliphatic alcohols. Thus, the technique shows good promise for identification of SH-bearing groups.

Derivatization of a low-temperature pyrolysis condensate from Illinois No. 6 coal with **1** and **2** revealed the almost exclusive presence of a variety of phenols (Figures 3 and 4, respectively). In addition, residual quantities of aliphatic hydroxyl groups were detected at 135 - 135.5 ppm and 147 - 148 ppm, respectively. No carboxylic acids were found, however. An identification of phenols was carried out by the addition of selected authentic compounds to the derivatized condensate containing an excess of **2**. This procedure allowed us to tentatively assign most of the prominent signals to specific substituted phenols (Figure 4). The presence of such a variety of phenolic compounds is consistent with the well-documented role that phenols play during low-temperature pyrolysis of coal.[15,16]

A pyridine extract of Illinois No. 6 coal was derivatized with both reagents to give deep-brown opaque solutions. Examination of these solutions by ^{31}P NMR spectroscopy showed broad absorptions (Figures 5 and 6), which revealed the presence of mostly phenols (at 138-140 ppm), together with a small amount of di-ortho substituted phenols (at about 143 ppm). In addition, significant amounts of carboxylic acids were found in the extract at 135-136 ppm. Identification of particular phenolic and/or acidic components was precluded by the breadth of signals. Furthermore, the extract derivatized with **1** displayed apparently significant amounts of aliphatic OH functionalities (at about 135 ppm), while the extract derivatized with **2** showed only a relatively small quantity of this functionality. This contradictory result is currently under further investigation.

Conclusions

Reagents of the type **1** and **2** provide improved ^{31}P chemical shift dispersion for compounds derived from carboxylic acids, phenols, alcohols, amines, and thiols. Therefore, they offer considerable promise for the

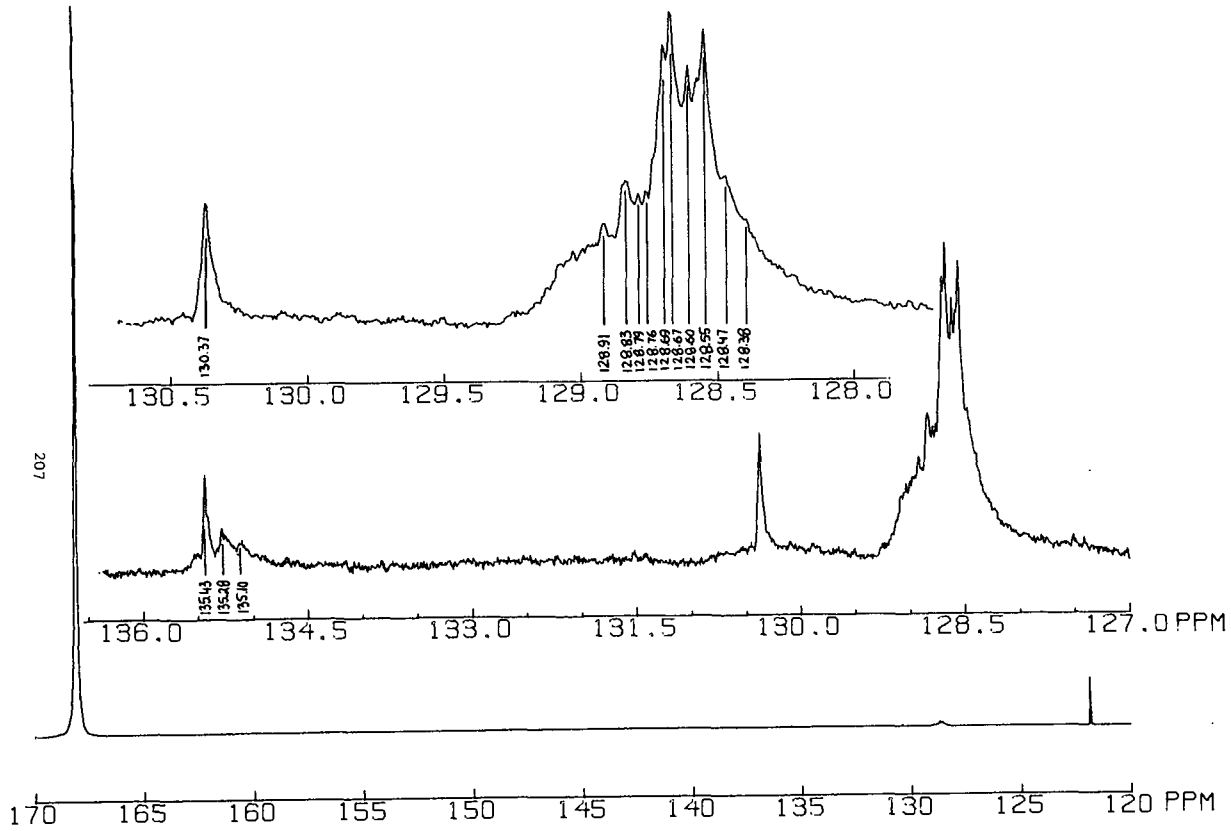

Figure 3. ^{31}P NMR spectrum of low-temperature pyrolysis condensate of Illinois No. 6 coal derivatized with **1**.

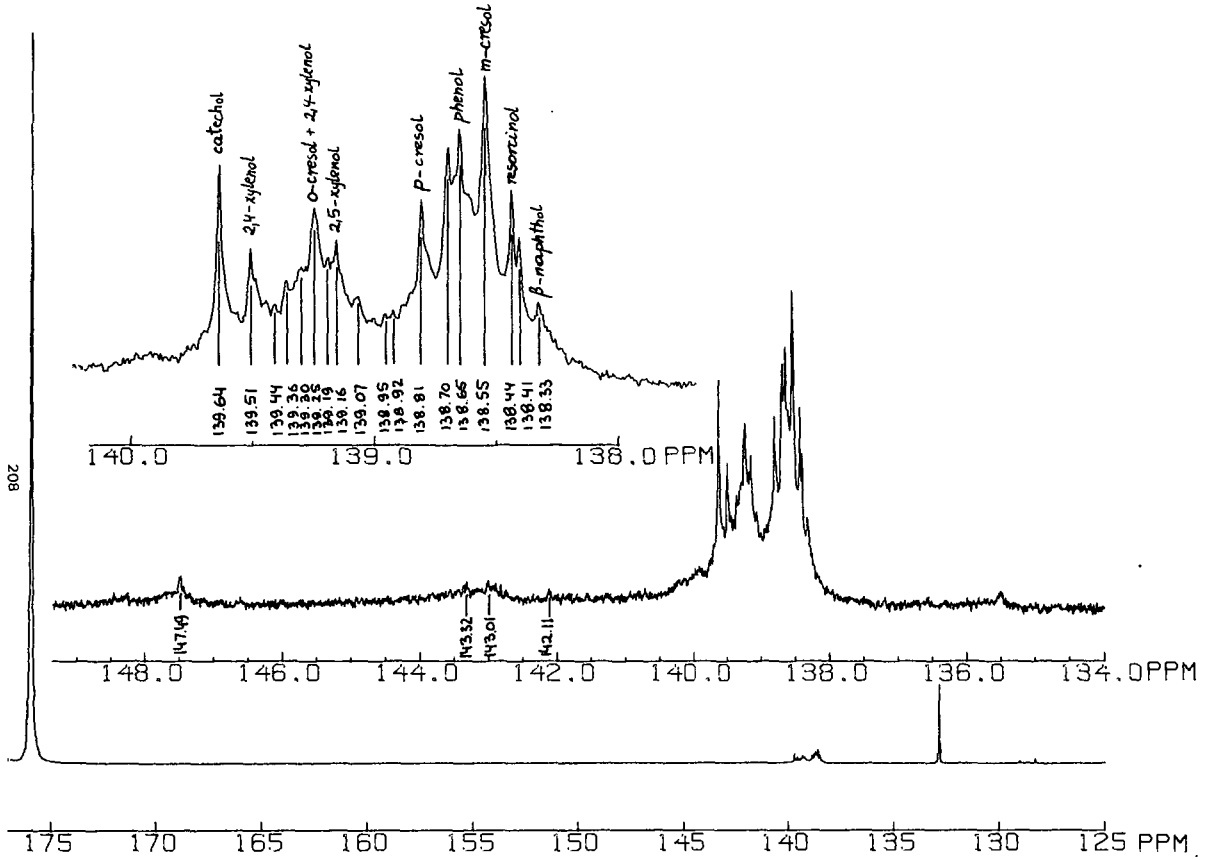

Figure 4. ^{31}P NMR spectrum of low-temperature pyrolysis condensate of Illinois No. 6 coal derivatized with **2**.

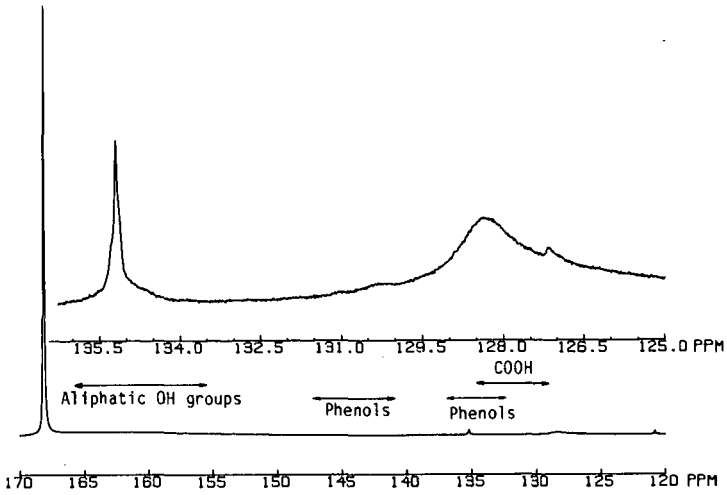

Figure 5. ^{31}P NMR spectrum of a pyridine extract of Illinois No. 6 coal derivatized with **1**.

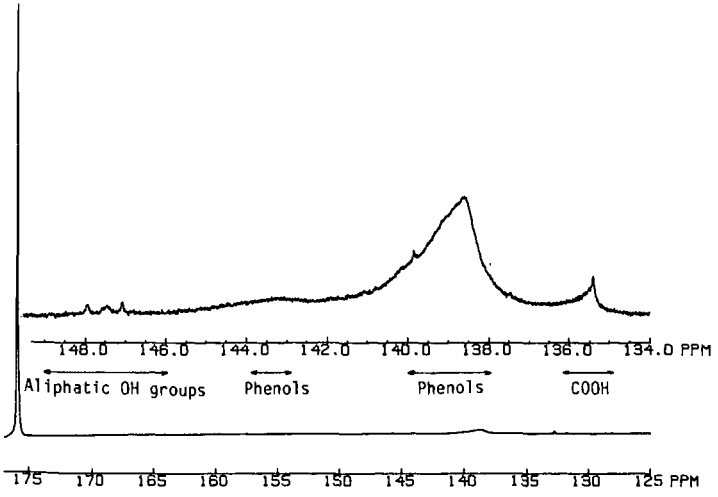

Figure 6. ^{31}P NMR spectrum of a pyridine extract of Illinois No. 6 coal derivatized with **2**.

identification (and possibly quantification) of coal-derived organic moieties bonded to -OH, -NH, and -SH functionalities. Such a capability will be extremely useful in characterizing coal extracts, pyrolysis condensates, and liquefaction products.

Acknowledgements

Ames Laboratory is operated for the U. S. Department of Energy by Iowa State University under Contract No. W-7405-ENG-82. This work was supported, in part, by the Assistant Secretary for Fossil Energy through the Pittsburgh Energy Technology Center. Special thanks are due to Dr. N. D. Shah for providing the low-temperature pyrolysis condensate.

References

1. Kanitskaya, L. V., Kushnarev, D. F., Polonov, V. M., and Kalabin, G.A., Khim. Tverd. Topl., 19, 76-82 (1985); Engl., pp. 70-76.
2. Snape, C. E. and Bartle, K. D., Fuel, 58, 898 (1979).
3. Schweighardt, F. K., Retcofsky, H. L., Friedman, S., and Hough M., Anal. Chem., 50, 368 (1978).
4. Coleman, W. M. and Boyd, A. R., Anal. Chem., 54, 133 (1982).
5. Friedman, S., Kaufman, M. L., Steiner, W. A., and Wender I., Fuel, 39, 33 (1960).
6. Snape, C. E., Smith, C. A., Bartle, K. D., and Matthews, R. S., Anal. Chem., 54, 20 (1982).
7. Snyder, R. W., Painter, P. C., Havens, J. R. and Koenig, J. L., Appl. Spectrosc. 37, 497 (1983).
8. Matthews, R. S., Stadelhofer, J. W., and Bartle, K. D., Erdol, Kohle, Erdgas, Petrolchem., 34, 173 (1981).
9. Bartle, K. D., Matthews, R. S., and Stadelhofer, J. W., Appl. Spectrosc. 34, 615 (1980).
10. Pomfret, A., Bartle, K. D., Barret, S., Taylor, N., and Stadelhofer, J. W., Erdol, Kohle, Erdgas, Petrolchem., 37, 515 (1984).
11. Schiff, D. E., Verkade, J. G., Metzler, R. M., Squires, T. G., and Venier, C. G., Applied Spectrosc., 40, 348 (1986).
12. Lucas, H. J., Mitchell, F. W., and Scully C. N., J. Am. Chem. Soc., 72, 2491 (1950).
13. Zwierzak, A., Can. J. Chem., 45, 2501 (1967).
14. Markuszewski, R., Mroch, D. R., and Norton, G. A., in Fossil Fuels Utilization: Environmental Concerns, R. Markuszewski and B. D. Blaustein, eds., Am. Chem. Soc., Washington, D. C. 1986, pp. 42-50.
15. Karr, C., in Chemistry of Coal Utilization, Suppl. Vol., H. H. Lowry, ed., J. Wiley, New York, 1963, pp. 539-579.
16. Gavalas, G. R., Coal Pyrolysis, Elsevier, Amsterdam, 1982.

Time-Resolved Pyrolysis Mass Spectrometry of Coal: A New Tool for Mechanistic and Kinetic Studies

Tanmoy Chakravarty, Henk L.C. Meuzelaar, Willem Windig and George R. Hill

University of Utah, Biomaterivals Profiling Center
391 South Chipeta Way, Suite F, Research Park
Salt Lake City, Utah 84108

Rashid M. Khan

Morgantown Energy Technology Center
Morgantown, West Virginia 26505

INTRODUCTION

Most coal devolatilization studies so far have focussed on the determination of reaction rates for reactions occurring under widely different conditions encountered in liquefaction, gasification, coking or combustion processes. Published rates on more or less comparable coals may differ by several orders of magnitude, especially when obtained at high temperatures (>1000 K) and/or high heating rates (10^2-10^5 K/s) (1,2).

At the present state-of-the-art in coal devolatilization research, more emphasis should perhaps be placed on elucidating the mechanisms of the chemical reactions underlying the observed phenomena. When studying thermal conversion reactions in coal it seems correct to concentrate first on the so-called "primary" reactions before attempting to elucidate the many possible secondary reaction pathways. This is especially true since most secondary reaction pathways are strongly influenced by reactor design and experimental conditions.

The devolatilization behavior of coal will be determined primarily by the chemical composition of coal and secondly by the experimental conditions. Under properly designed vacuum micropyrolysis experiments working with sufficiently small particles (<50 μ diameter), it is possible to avoid mass and heat transport limitations (3) and minimize the secondary reactions. Using premium coal samples from Argonne National Laboratory (4) the chemical composition can be well defined and possibly characterized by major factors such as rank and depositional environment (5). Recent advances in pyrolysis mass spectrometry (Py-MS), viz, time-resolved Py-MS (TR Py-MS), along with multivariate analysis techniques enable extraction of underlying chemical components (6) from a single experiment; thus reducing the uncertainty due to varying reactions conditions in different experiments. This paper demonstrates the feasibility of obtaining valuable mechanistic and kinetic data using microgram amounts of carefully selected coal samples under properly designed reaction conditions using TR Py-MS techniques in combination with advanced multivariate data analysis methods.

EXPERIMENTAL

A sample of hvAb Pittsburgh #8 coal was picked up in large chunks from the mine mouth and subsequently ground and sieved under nitrogen. Ultimate and proximate analysis data are shown in Table I. Sample preparation was discussed earlier (7) in detail.

(Time-Resolved Pyrolysis Mass Spectrometry)

Time-resolved Py-MS analyses were done under the following conditions: Curie-point temperature 610°C, temperature-rise time 5.4 s, total heating time 10 s, electron energy 12 eV, mass range scanned 50 to 200 amu, scanning speed 1000 amu/s, number of scans 41, total scan time 8 s. Each spectrum scanned was stored separately in the IBM 9000 computer.

(Multivariate Data Analysis)

In order to give all the variables an equal contribution, and for reasons explained by Malinowski (8), factor analysis was done on the "correlation around the origin" matrix. For this study, the number of factors used was selected by determining the leveling off of the slope (8) and the ratio of the eigenvalue (9). Deconvolution of the components was performed by using a combination of "pure mass" (8,10) and "variance diagram" (VARDIA) (6) techniques.

(Kinetic Analyses)

Kinetic analysis was based on the total ion current plot. The assumption was made that each maximum in the bimodal curve reflects a single rate process and that a first order rate equation describes the process. The parameters computed based on the maximum rate of generation at the peak of the curve are listed in Table I. The distributed activated energy model (11) was used as an alternative approach.

RESULTS AND DISCUSSION

The time-resolved total ion current (TIC) profile of the Pittsburgh #8 coal sample is shown in Figure 1b. The TIC profile has a distinctly bimodal character with a pronounced low temperature maximum near 370°C and a larger, high temperature maximum near 560°C. These temperatures, estimated from the temperature/time profile of the blank Curie-point pyrolysis filament (shown in Figure 1a) are believed to be accurate within 5%. The time-integrated spectrum of the coal sample, shown in Figure 2, shows that the most abundant homologous ion series in the pyrolysis mass spectra of fresh whole coals are the "phenols". Other major components dominating the spectra are the "benzenes", "naphthalenes" and the short chain aliphatic hydrocarbons. This matches with the results from this laboratory obtained on 102 Rocky Mountain coals (5).

Using the multivariate data analysis procedures, mentioned before, the evolution profiles of the components (separate groups of correlated mass peaks) were obtained. These profiles, labeled A, B, C and D are shown in Figure 1c. The corresponding numerically extracted spectra showing the composition of each component along with the total variance percentage are shown in Figure 3a, b, c and d.

The low temperature component A appears to represent a vacuum distillable oil consisting largely of aromatic hydrocarbon series ("benzenes", "naphthalenes" and "biphenyls/acenaphthenes"). Bench scale vacuum extraction studies of a hvBb Hiawatha coal showed the naphthene rich distillable fraction to represent approx. 4% of the fresh coal (12). It is now rather widely accepted that coal deposits go through an "oil formation window" during their coalification history in a similar manner observed for oil shale deposits. Maximum oil generation is likely to occur in coals of high volatile bituminous rank. Interestingly, in our experience this component is not readily observed under typical thermal analysis conditions.

Components B, C, and D together make up the main pyrolysis event in Figure 1b. Component B appears at a somewhat lower temperature than components C and D. The near symmetrical shape of the intensity profiles of components B and C indicates a depolymerization (such as found in thermoplastic materials) degradation behavior leading to rapid, complete pyrolysis without major charring tendencies. Component D, however, behaves more like a crosslinking substance (such as found in thermoplastic materials) with a wider temperature profile and a slow, high temperature tail indicating incomplete pyrolysis, presumably accompanied by char formation.

Which structural moieties, if any, are represented by components B, C and D? Identification of component D is relatively straightforward. As shown in Figure 3d, this component is dominated by a strong series of alkyl substituted phenols and resembles the Py-MS patterns of pure vitrinites (13) and fossil wood (14) samples.

Highly similar patterns have been observed in numerically extracted component spectra of various coal data sets obtained by Py-MS (15). Consequently, component D appears to represent the abundant vitrinite macerals present in the Pittsburgh #8 coal sample.

Component B is the early component in the "depolymerization" region (see later) and is characterized by branched or alicyclic hydrocarbons. This component is also characterized by a prominent ion series at m/z 60, 74, 88, 102, etc. (most prominent in the corresponding loading spectra, not shown here), as marked by stars in Figure 3b and thought to represent short chain fatty acids. Patterns similar to Figure 3b can be observed in Messel shale (16) as well as in sporinite concentrates (13) and may represent liptinitic structural moieties present in several different coal macerals.

The numerically extracted spectrum of component C (Figure 3c) reveals an entirely different chemical structure consisting nearly exclusively of aliphatic hydrocarbon moieties. On the basis of previously reported Py-MS studies of model compounds and maceral concentrates (13), this component is believed to consist primarily of straight chain alkanes, alkenes and alkadienes. Under the low voltage electron ionization conditions used in this experiment, short chain alkanes ($<C_{15}$) produce mainly the alkene and alkadiene molecular ion series as well as various fragment ion series, which are visible in Figure 3c. Mixtures of straight chain aliphatic hydrocarbons such as seen in Figure 3c are typical of the pyrolyzates of polyethylene-like structures such as found under vacuum micropyrolysis conditions in liptinitic macerals derived from fossil plant cuticles (17) and or algal materials (16).

It should be mentioned, however, that by selecting a limited mass range (m/z 50-200) many important small molecules (e.g., CH_4, NH_3, H_2O, HCN, CO, CH_2O, CH_3OH, H_2S, HCl, CO_2 and various C_2 compounds) are ignored in addition to many large organic molecules. This limits the characterization of the char forming process, as well as making it hard to compare our data with the data of other workers on the kinetics of evolution of small molecules (18, 19).

In spite of these limitations, the data obtained on the kinetic parameters seem to match very well with our understanding of the events marked by the two distinct humps in Figure 1b. The activation energy of 10 Kcal mol^{-1} is reasonable to expect for the thermophysical kinetics related to "desorption" of the mobile phase. The latter value of 62 Kcal mol^{-1}, which also matches with the value calculated using the distributed activation energy model, is expected for thermochemical kinetics for breaking of ethylene bridges between aromatic rings and agrees well with reported values for this step (2).

The observation of three different types of thermal behavior, as judged from the shape of the deconvoluted components, namely "desorption" (vacuum distillable component A), "depolymerization" (thermoplastic components B and C), and "thermal degradation" (thermosetting component D) points to the need for a kinetic model with at least three different reaction order terms. The desorption process is likely to have a reaction order between 0 and 1. The thermosetting (char formation) terms, on the contrary, would be expected to exhibit reaction orders substantially greater than 1. Only the two thermoplastic components (B and C) should follow first order unimolecular decomposition pathways under our vacuum micropyrolysis conditions. We are working on the development of a devolatilization model based on these TR Py-MS observations. In principle, this methodology can be applied to the "pure" maceral constituents of coal. Once the kinetic models for each maceral type are well established, a useful devolatilization model for the "mixture" coal might be within reach. In conclusion, computer-assisted TR Py-MS techniques enable deconvolution of chemical components, thereby allowing more insight into the chemistry of coal devolatilization.

ACKNOWLEDGEMENTS

Funding for this work was supported by the Department of Energy (Grant No. DE-FG22-84PC70798) and the National Science Foundation (Contract CDR-8322618). Furthermore, the authors wish to thank Dr. Clint Williford for supplying the parameters for the Distributed Activation Energy Model.

REFERENCES

1. Howard, J. B., Peters, W. A., Serio, M. A., EPRI Report No. AP-1803, Palo Alto, California (April 1981)
2. Solomon, P. R., Serio, M. A., Carangelo, R. M. and Markham, J. R., Fuel 65, 182 (1986)
3. Bliek, A., van Poelje, W. M., van Swaaij, W. P. M., van Beckum, F. P. H., AICHE Journal, 31, No. 10, 1666 (1985)
4. Vorres, K. S., Janikowski, S. K., in Karl S. Vorres (editor) ACS Preprint, 32, No. 1, 492 (1987)
5. Meuzelaar, H. L. C., Harper, A. M., Hill, G. R. and Given, P. H., Fuel 63, 793 (1987)
6. Windig, W., Jakab, E., Richards, J. M., Meuzelaar, H. L. C., Anal. Chem., 59, 317 (1987)
7. Chakravarty, T., Meuzelaar, H. L. C., Technical report to METC, Department of Energy, April 1986
8. Malinowski, E. R., Howery, D. G., Factor Analysis in Chemistry, John Wiley & Sons, 1980, New York
9. Wirsz, D. F., Blades, M. W., Anal. Chem., 58, 51 (1986)
10. Knorr, F. J., Futrell, J. H., Anal. Chem., 51, 1236 (1979)
11. Anthony, D. B., Howard, J. B., AICHE Journal, 22, 4, 625 (1976)
12. Unpublished results.
13. Meuzelaar, H. L. C., Harper, A. M., Pugmire, R. J., Karas, J., Int. J. of Coal Geo., 4, 143 (1984)
14. Metcalf, G. S., Windig, W., Hill, G. R., Meuzelaar, H. L. C., Coal Geology, in press (1987)
15. Yongseung, Yun., Jakab, E., McClennen, W., Hill, G. R., Meuzelaar, H. L. C., ACS Preprints, 32, No. 1, (1987)
16. Meuzelaar, H. L. C., Windig, W., Futrell, J. H., Harper, A. M., Larter, S. R. , ASTM STP 902, Thomas Aczel, Ed., ASTM, Philadelphia, (1986)
17. Nip, M., Tegelaar, E. W., Brinkhuis, H., de Leeuw, J. W., Schenck, P. A., Holloway, P. J., Adv. in Org. Geochem., in press (1987)
18. Suuberg, E. M., Peters, W. A., Howard, J. B., Ind. Eng. Chem., Process Design and Develop., 17, 37 (1978)
19. Campbell, J. J., Stephens, D. R., ACS Preprints 21, No. 7, 94 (1976)

TABLE I

ANALYSIS OF COAL

	C	H	N	S	O	H/C	BTU/lb
Ultimate Analysis (DAF)	83.75	5.46	1.56	2.15	7.08	0.78	13,976

	Moisture	Ash	Volatile Matter
Proximate (as rec'd)	0.57	7.27	37.86

TABLE II
KINETIC PARAMETERS CALCULATED FROM TIME-RESOLVED PY-MS DATA

	Thermal Extraction Step	Bulk Pyrolysis Step
Energy of Activation, Kcal mol^{-1}	10	62(60)*
Frequency Factor, s^{-1}	10^5	$10^{12}(10^{13}**)$

* reference (2)

** Distributed Activation Energy Model

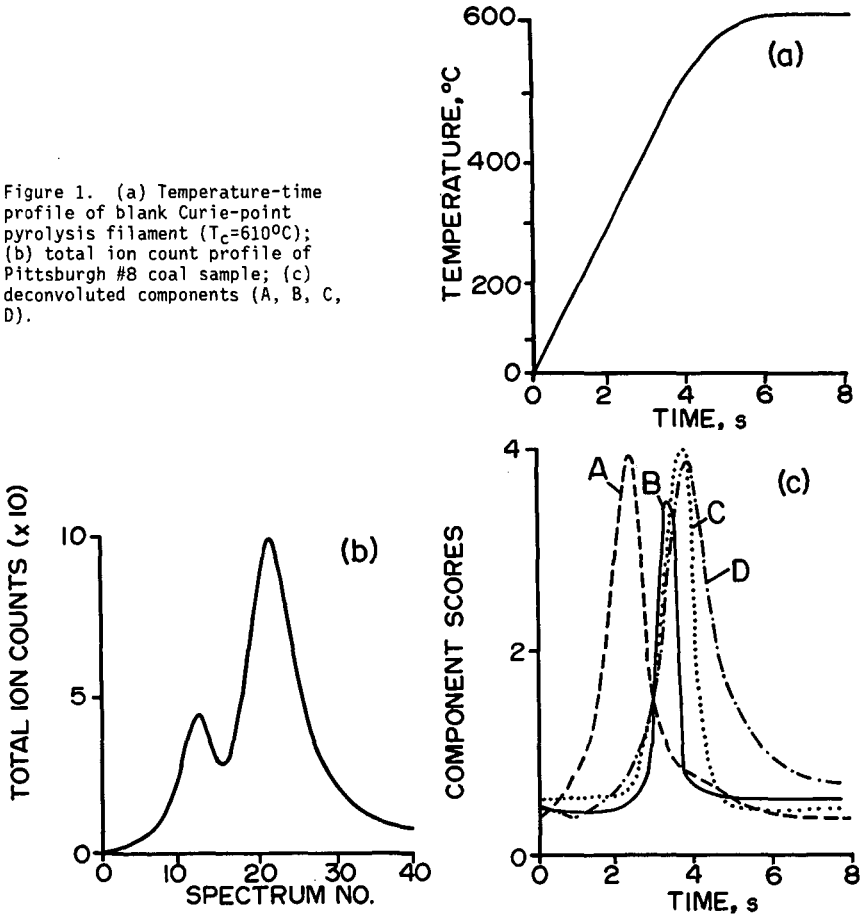

Figure 1. (a) Temperature-time profile of blank Curie-point pyrolysis filament (T_c=610°C); (b) total ion count profile of Pittsburgh #8 coal sample; (c) deconvoluted components (A, B, C, D).

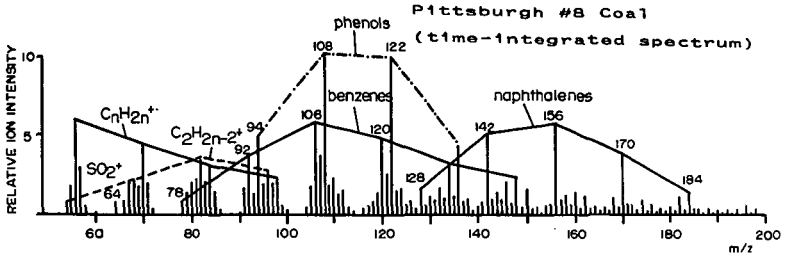

Figure 2. Time-integrated spectrum obtained by summing all 41 spectra recorded during time-resolved pyrolysis MS run. Note dominant series of homologous molecular ions characteristic of rank (hvAB) as well as of depositional environment and weathering status. Compare with deconvoluted spectra in Figure 3.

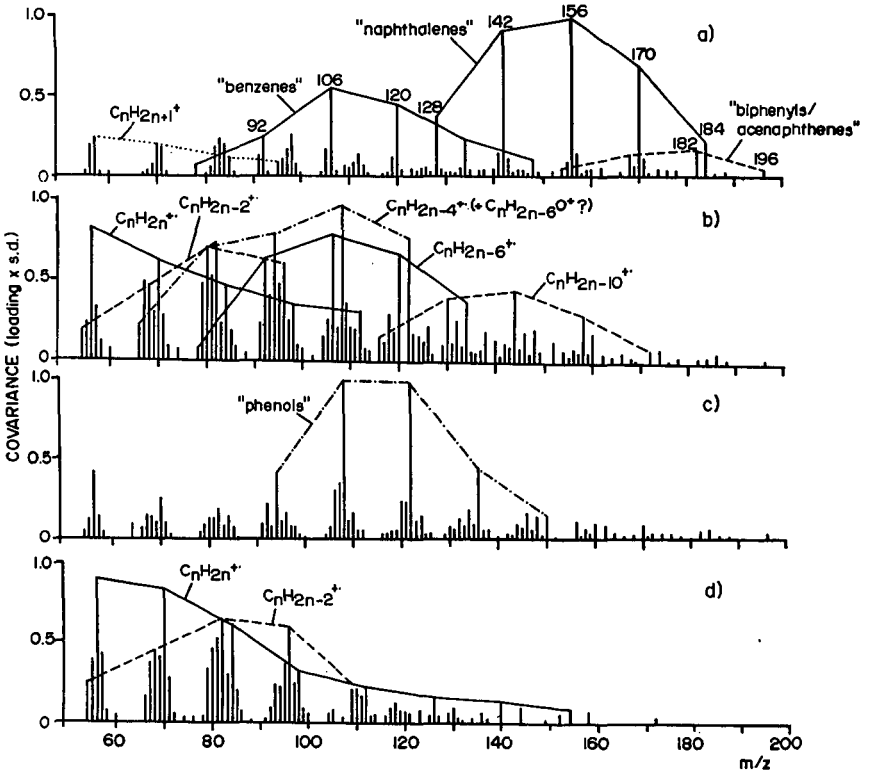

Figure 3. Numerically extracted ("deconvoluted") spectra of the four components shown in Figure 1. Note differences in % variance represented (summed variance of the four components is 99% of the total variance in all 41 spectra).

EPR STUDY OF THE CATALYTIC EFFECTS OF MINERALS ON FREE RADICAL FORMATION DURING COAL PYROLYSIS

M.S. Ali and W.R.M. Graham

Department of Physics, Texas Christian University
Fort Worth, Texas 76129

A systematic *in situ* study of free radicals in Pittsburgh No. 8, acid treated coal (ATC) as a function of temperature and residence time has been carried out using the electron paramagnetic resonance (EPR) technique at temperatures up to 900 K. The catalytic effects of pyrite, pyrrhotite, calcite, and clays on free radical formation during pyrolysis have been examined.

INTRODUCTION

Various investigators have reported that the inherent mineral matter in coal may have a positive effect during conversion processes (1-3). Pyrite and pyrrhotite are of particular interest since pyrite, which is the major iron-sulfur compound in coal, is known to affect various stages in coal processing, and pyrrhotite, which is formed from pyrites under liquefaction conditions, has been found in one study (4) to influence conversion efficiency, although other work is in disagreement with this conclusion (5).

Since the formation of free radicals by the rupture of coal bonds during pyrolysis is believed to be an important step in liquefaction, the EPR technique has been used to advantage in studies on pyrolyzed and heat-treated coals (6,7). Recently Srinivasan and Seehra (8,9) have reported results of studies on the effects of pyrite and pyrrhotite on free radical formation in two West Virginia coals which were heated to ~900 K. Observing that the maximum increase in the number of free radicals occurred at ~800 K for coal samples containing 8% added pyrite, with a somewhat smaller increase for pyrrhotite, they concluded that both the conversion of pyrite to pyrrhotite and pyrrhotite itself contributed to the enhancement in the number of free radicals. An overall increase in the number of free radicals which was smaller on heating in H_2 than in vacuum, was interpreted as indicating that free radicals were stabilized by hydrogen.

An important point to note about the studies so far (8,9) on the effects of pyrite and pyrrhotite on free radical formation, is that the EPR measurements were carried out on coal samples which had been sealed in evacuated or gas-filled sample tubes, heated in a furnace, and then cooled. This procedure may preclude the observation of information on transient effects, which may be lost on cooling down the sample before EPR measurements are taken. A significant objective of the present work therefore, was to examine mineral effects on radical formation *in situ* during pyrolysis at temperatures up to 900 K. A step in this direction was recently reported by Seehra and coworkers (10) who carried out *in situ* measurements on samples of raw coal, and were able to de-

tect several distinct stages in pyrolysis based on the variation in spin concentration as the temperature increased during pyrolysis.

EXPERIMENTAL PROCEDURE

The coal samples used in this work were derived from a ground sample (C19825 in reference 14) from the Pittsburgh No. 8 seam, a high volatile bituminous coal, which has been the subject of several previous EPR investigations in this laboratory (11-13) and has been otherwise extensively characterized (14). Mineral samples used include pyrite from Custer, South Dakota, pyrrhotite from Falconbridge, Ontario, and calcite. Standard clay samples of well crystallized kaolinite (KGa-1), illite (IMT-1), and montmorillonite (SCa-2) were obtained from the Clay Minerals Society.

Small samples for EPR studies were prepared by thoroughly grinding mineral/coal mixtures so that the average particle size was much smaller than the microwave skin depth (15). The coal and mineral were dispersed in KBr in the ratio 1:100 (16), and then ground further in a ball grinder using plexiglass vials and balls to avoid metal contamination. Samples were placed in vacuum and usually used immediately following grinding; however, when necessary, they were stored for 24 h under nitrogen, with no observable deterioration in the EPR spectrum.

The low temperature ash fraction (14.5%) from the Pittsburgh No. 8 coal has been analyzed to contain 16% pyrite, 25% calcite, 8% quartz, with the remaining 54% composed of kaolinite, illite, expandable clays, and other minerals. For experiments designed to study the evolution of free radicals in the absence of the inherent mineral matter, acid treated samples were used. These were prepared by boiling raw coal with 5M HCl for 30 minutes, thoroughly washing with acetone and ethanol, and then drying at 375 K for 8 h. Subsequent preparation proceeded as already described for raw coal.

Prior to carrying out the EPR measurements, each coal sample was placed in a 4 mm o.d. quartz sample tube which was evacuated through a side arm. The sample tube was inserted into a double-walled quartz dewar inside the microwave cavity. Nitrogen gas heated by passage over a series of two chromel-alumel heater elements flowed through the dewar. By suitable adjustment of the gas temperature and flow rate, the sample temperature, as measured by a chromel-alumel thermocouple, could be raised to 900 K with a stability of ±1 K. The Varian TE_{102} mode cavity was maintained at room temperature by means of refrigerated water circulating inside a jacket which surrounded, and was in good thermal contact with the cavity. The signal intensity from a sample of DPPH fixed to the cavity wall was unchanged by heating the sample inside the dewar, confirming that the sensitivity of the cavity was not affected.

EPR measurements were made at ~9 GHz using a Varian V-4500 spectrometer equipped with 100 kHz field modulation. The arrangement for pyrolysis experiments has already been described; low temperature experiments on the acid following demineralization were done using a Varian variable temperature

accessory. Field measurements were made using a Harvey-Wells NMR gaussmeter and a Hewlett-Packard frequency counter. The spectrometer is interfaced to an IBM XT computer which is used for data acquisition, calibration, storage, and analysis.

RESULTS AND DISCUSSION

Figure 1 shows plots of the absolute temperature (T) versus the product of the temperature and the intensity of the EPR absorption obtained by numerical double integration of the observed line profile (IT). The results illustrated are for a sample of raw Pittsburgh No. 8 coal and for two other samples, coal + 8% pyrite and coal + 8% pyrrhotite, heated for 20 minutes at ~40 K intervals. In the case of raw coal there is no significant change in free radical concentration until ~600 K, after which it rises, but at a slower rate than the curves for the samples with mineral added. Both of the latter samples show evidence of an intermediate step in which a small increase in concentration is followed by a decrease, before the onset of the steep rise at ~600 K. The preliminary step is similar to that observed by Seehra *et al.* (10) for *in situ* measurements on three raw coals, but was not observed in their earlier study (8,9) on the effects of the addition of pyrite and pyrrhotite in which measurements were made after heating outside the cavity. The number of free radicals increases faster for added pyrrhotite than for pyrite until it reaches a peak at 800 K and then drops rapidly thereafter. The pyrolysis of the raw coal and coal + 8% pyrite continues to yield additional free radicals up to the cutoff in the data at 900 K. This continued enhancement of the free radical yield in coal + 8% pyrite samples contrasts with the earlier observations for samples pyrolyzed outside the cavity and recorded cold (8,9), where all three samples showed a decline in free radical concentration back to prepyrolysis levels, and suggests the importance of *in situ* observations in monitoring the dynamic process. The observation that at temperatures up to 800 K the coal + 8% pyrrhotite sample shows higher concentrations of free radicals than pyrite, which then continues to enhance free radical formation as the yield from pyrrhotite declines, suggests that the catalytic activity of the pyrrhotite has been depleted, while in the coal + 8% pyrite sample the pyrite continues to convert to pyrrhotite which then enhances the free radical yield. This tends to support the view that the conversion to pyrrhotite as well as the mineral itself are positive influences.

A significant question is the possible influence of the inherent mineral matter on radical yield. In an attempt to investigate this possibility samples of acid treated coal were studied. Figs. 2(a) and (b) show the EPR spectrum of the raw coal at room temperature (296 K) and after heating at 814 K, respectively. The room temperature spectrum shows evidence of Fe^{3+} at $g \approx 4.4$ which is probably contained in clays, and a broad weak signal underlying the free radical signal at $g \approx 2.0$, which may be from metallic iron. Pyrite, with Fe^{2+}, has no EPR spectrum; however, after heating, conversion of pyrite to pyrrhotite has occurred, and a strong ferromagnetic resonance signal is

observed at center field. The spectrum shown in Fig. 2(c) of ATC-1 at room temperature shows that the Fe^{3+}-bearing mineral has been removed, and Fig. 2 (d) recorded at 869 K shows no evidence of converted pyrrhotite. Finally, when 8% pyrite is added to ATC-1, heating to 871 K again reveals the presence of pyrrhotite as shown in Fig. 2 (e). The spectrum shown in Fig. 2 (f) of a glass of the HCl which was used in the demineralization, shows evidence of the iron extracted from the coal.

Figure 3 shows the IT versus T curves obtained for two samples of acid treated coal (ATC-1 and ATC-2) which were heated *in situ* for ~85 min at ~40 K intervals, compared to the curve for the same ground sample of raw coal before acid treatment which was heated for ~20 min at each interval. The consistently higher concentration of free radicals generated in the pyrolysis of the raw coal compared to the ATC supports the contention that the inherent mineral component contributes to the radical yield.

Prior to examining the influence on free radical yield of adding specific minerals to the ATC, a series of experiments was carried out to determine the effect of residence time. Figs. 4(a) - (e) show the time evolution of radical concentration for ATC with added pyrite, pyrrhotite, calcite, clays (4% kaolinite, 2% illite, 2% montmorillonite), and a mixture of calcite and pyrite. In each case the results were obained by pre-heating the dewar in the cavity to ~830 K, inserting the sample tube, and beginning to record observations after 5 minutes residence. It is seen that the maximum in free radical concentration occurs for widely different residence times for the various coal/mineral combinations. In particular, the radical concentration for ATC-1 + 8% pyrrhotite reaches a maximum after only 10 min, while at least 50 min are required for ATC-1 + 8% pyrite. This again points to the importance of converted pyrrhotite. A mixture of 4% calcite + 4% pyrite added to ATC appears to be even more effective. Radical concentration increases rapidly in the first 5 minutes, and after 30 minutes has reached a maximum. By contrast, the addition of clays, pyrite, or calcite separately, appears to produce no drametic increases.

Plots of the the relative concentration of free radicals as a function of temperature for ATC and ATC with the five minerals mentioned earlier are shown in Fig. 5. At temperatures up to ~825 K the number of free radicals produced is generally best for a mixture of calcite and pyrite. Pyrrhotite also enhances free radical yield, but only up to ~800 K. Pyrite appears to be much less effective when added to the ATC than it was when added to the raw coal. Pittsburgh No. 8 coal does, of course, contain calcite, and these results at least raise that this inherent calcite and the pyrite together play a role in the observed increase in free radical concentration shown in Fig. 1.

CONCLUSIONS

Several conclusions may be drawn from the results reported here. The increase in radical concentration observed on the addition of pyrrhotite to ATC in contrast to the relative ineffectiveness of pyrite supports the view

that the conversion of pyrite to pyrrhotite and pyrrhotite itself are responsible. Of interest, is the apparent positive influence of calcite on free radical yield. In studies on the pyrolysis of Pittsburgh No. 8 coal in helium and hydrogen at temperatures up to 1300 K Franklin *et al.* (17,18) found strong effects by calcium minerals. In particular, they concluded that $CaCO_3$ and its decomposition product during pyrolysis CaO, are especially active in cracking oxygen functional groups and aromatics. We note however, that the free radical yield shows substantial enhancement only when in the presence of pyrite.

ACKNOWLEDGMENTS

This work was supported by the TCU Research Fund and in part by The Welch Fund.

REFERENCES

1. P.H. Given, D.C. Cronauer, W. Spackman, H.L. Lovell, A. Davis, and B. Biswas, Fuel *54*, 34 (1975).
2. D.K. Mukherjee and P. B. Chowdhury, Fuel *55*, 4 (1976).
3. B. Granoff and P.A. Montano, in *Chemistry and Physics of Coal Utilization 1980,* B.R. Cooper and L. Petrakis, ed. (AIP, New York, 1981) pp. 291-308.
4. P.A. Montano and B. Granoff, Fuel *59*, 214 (1980).
5. N.J. Mazzocco, E.B. Klunder, and D. Krastman, "Study of catalytic effect of mineral matter level on coal reactivity", Pittsburgh Energy Technology Center Rep. DOE/PETC TR-81/1 (1981).
6. H.L. Retcofsky, M.R. Hough, M.M. Maguire, and R.B. Clarkson, in *Coal Structure*, ACS Adv. Chem. Ser. 192, 37 (1981).
7. L. Petrakis and D.W. Grandy, *Free Radicals in Coals and Synthetic Fuels* (Elsevier, New York, 1983).
8. G. Srinivasan and M.S. Seehra, Fuel *61*, 1249 (1982).
9. G. Srinivasan and M.S. Seehra, Fuel *62*, 792 (1983).
10. M.S. Seehra, B. Ghosh and S.E. Mullins, Fuel *65*, 1315 (1986).
11. V.M. Malhotra and W.R.M. Graham, Fuel *64*, 270 (1985).
12. V.M. Malhotra and W.R.M. Graham, J. Appl. Phys. *57*, 1270 (1985).
13. V.M. Malhotra and W.R.M. Graham, Fuel *64*, 579 (1985).
14. J.K. Kuhn, F. Fiene, and R. Harvey, "Geochemical Evaluation and Characterization of a Pittsburgh No. 8 Coal and a Rosebud Seam Coal), Morgantown Energy Technology Center Rep. DOE/METC CR-78/8 (1978).
15. L.S. Singer, Proc. 5th Carbon Conf. *2*, 37 (1963).
16. H.L. Retcofsky, M.R. Hough, M.M.Maguire, and R.B. Clarkson, Appl. Spectrosc. *36*, 187 (1982).
17. H.D. Franklin, W.A. Peters, F. Cariello, and J.B. Howard, Ind. Eng. Chem. *20,* 670 (1981).
18. H.D. Franklin, W.A. Peters, and J.B. Howard, Fuel *61*, 155 (1982).

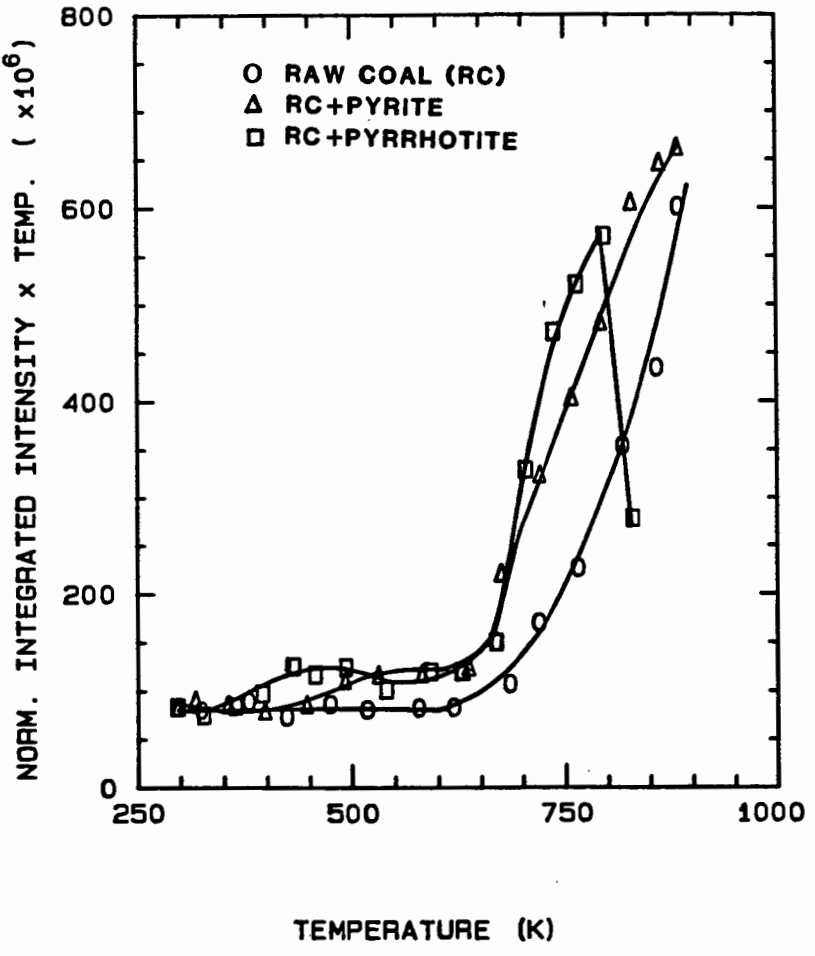

Fig. 1. Plot of IT versus T for raw coal, raw coal + 8% pyrite, and raw coal + 8% pyrrhotite.

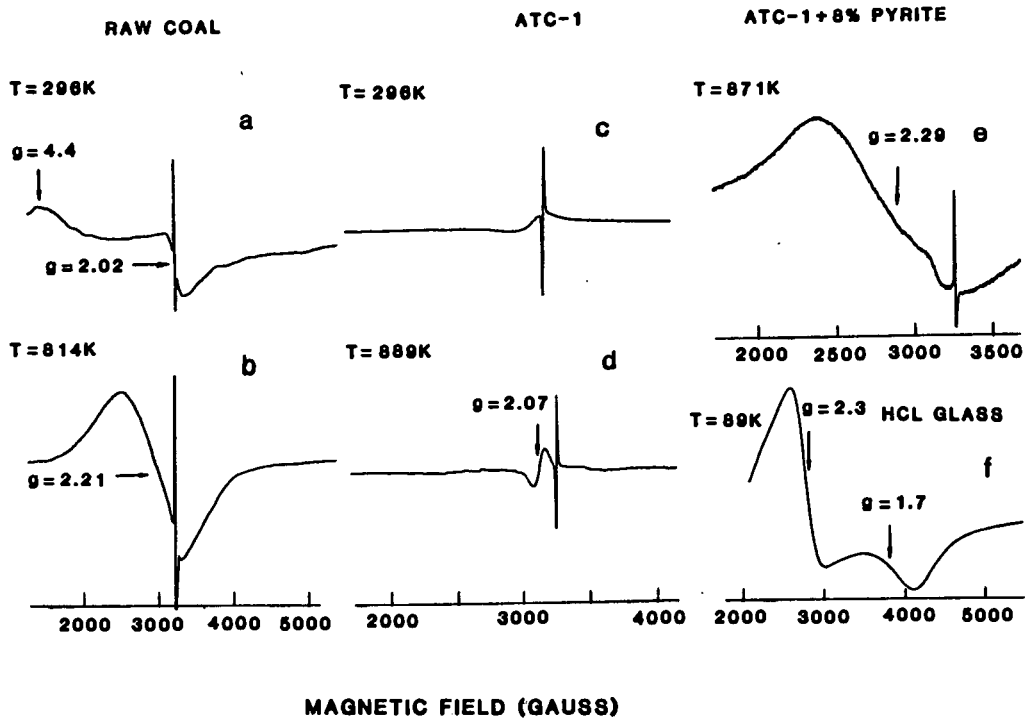

Fig. 2. EPR spectra of raw coal at (a) 296 K and (b) 814 K; ATC-1 at (c) 296K and (d) 869 K; (e) ATC-1 + 8% pyrite at 871 K; and (f) a glass at 89 K of the HCl extract from demineralization.

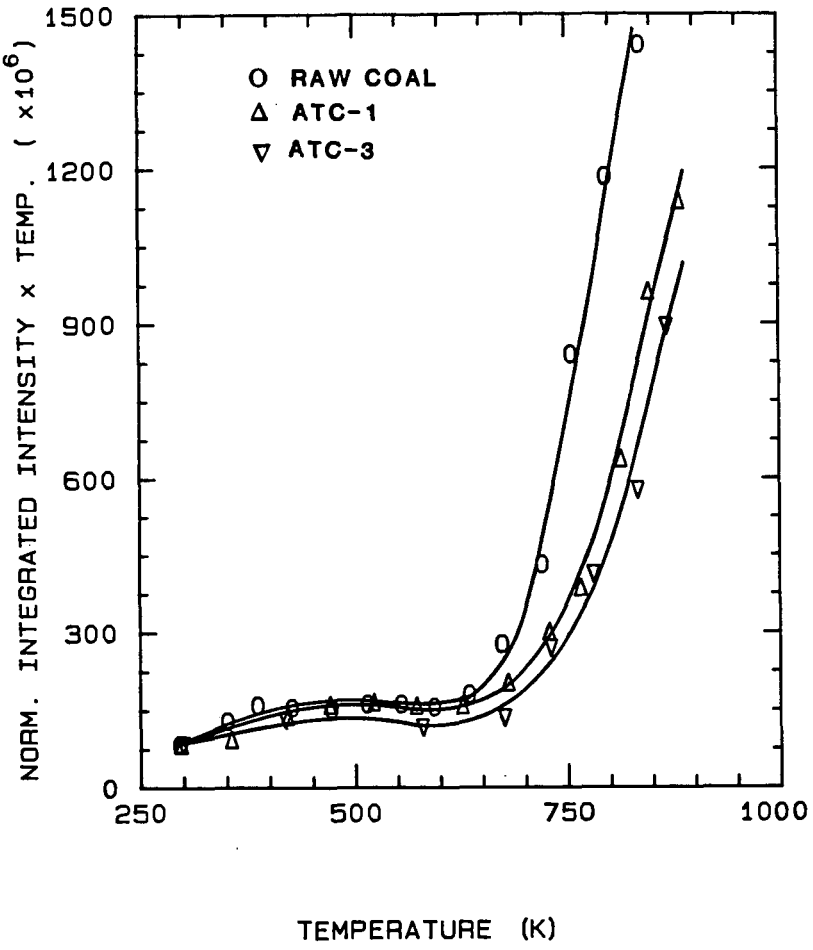

Fig. 3. Plot of IT vs. T for ATC-1, ATC-3, and raw coal.

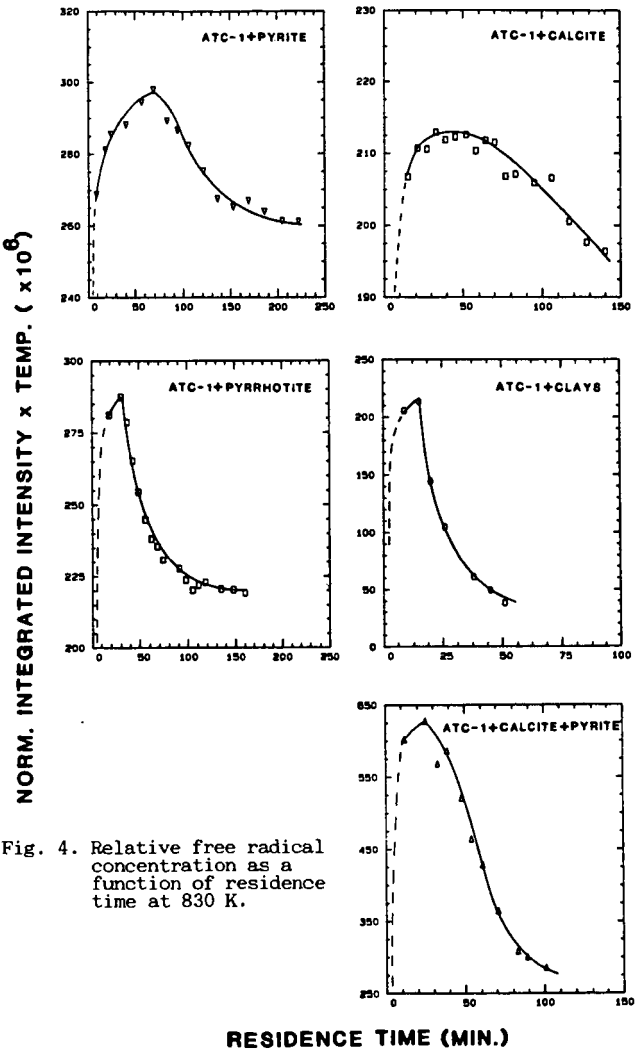

Fig. 4. Relative free radical concentration as a function of residence time at 830 K.

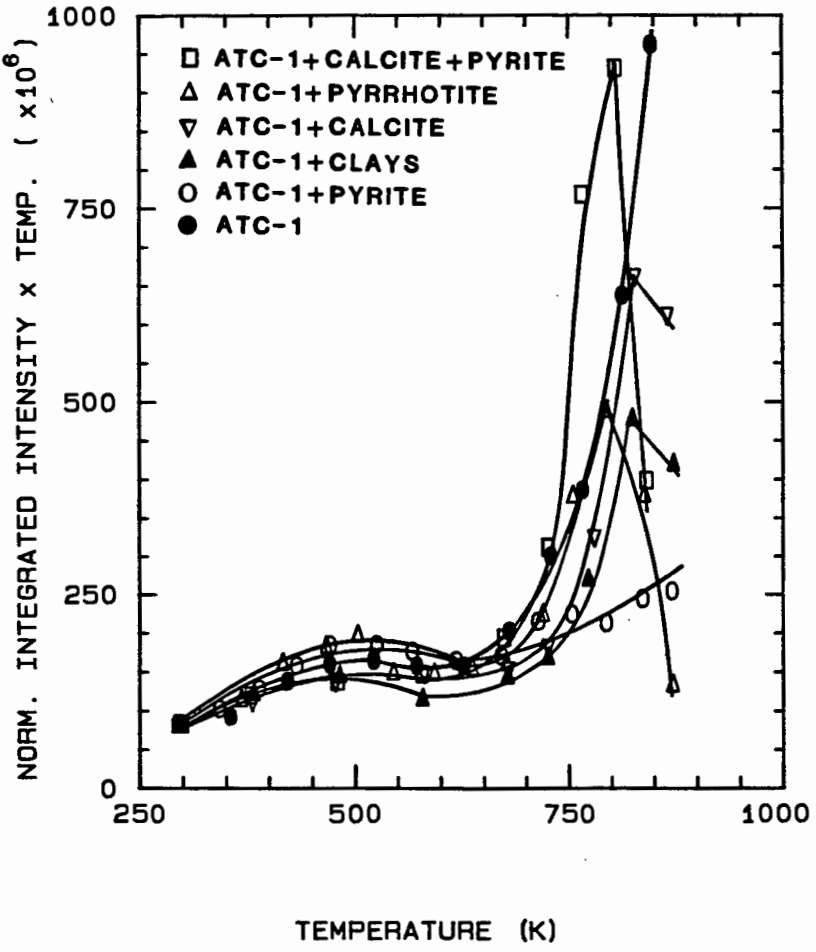

Fig. 5. Plot of IT vs. T for ATC-1 and ATC-1 + 8% various minerals.

COPPER CATALYZED LOW-TEMPERATURE PYROLYSIS AS A MEANS FOR UPGRADING LOW-RANK SOLID FUELS

S. Stournas, M. Papachristos and G. B. Kyriakopoulos

Chemical Engineering Department, National Technical University
42 Patission Street, 106 82 Athens, Greece

ABSTRACT

Low-rank solid fuels (lignite and peat) are characterized by a high oxygen content on a DAF basis, a large proportion of which belongs to carboxyl and hydroxyl groups. These groups being thermally labile, the oxygen content of low-rank coals can be substantially decreased (and their heat content per unit mass correspondingly increased) by subjecting them to simple pyrolytic treatment.

It has been found that the behavior of certain types of lignite and peat is similar to that of simple carboxylic acids, in that the thermal decarboxylation process can be catalyzed by specific metal ions. Thus when lignite and peat, in the presence of small amounts of copper, are pyrolyzed at low temperatures (160°-200° C), they readily undergo decarboxylation and dehydration and their higher heating values on a DAF basis show increases of the order of 30%. When uncatalyzed, these same reactions require temperatures in excess of 300° C.

INTRODUCTION

Among the known fossil fuel reserves those of the low-rank coals (i.e. lignite and peat) remain underutilized, despite their significant potential as a readily recoverable energy resource. The main problem associated with these solid fuels is their low heat content per unit mass, which in turn is due to the high moisture and ash content but also to the relatively low heating value of the DAF coal itself.

It has been a well known fact for many years[1] that, on moving from high rank to low rank coals, the ratio of oxygen content to carbon content increases substantially; it is not unusual for a lignite coal to contain around 30% oxygen on a DAF basis, whereas peat approaches 40%.

It is evident that the upgrading of lignite and peat to forms that come close to hard coal in properties and performance may involve:

a. Moisture removal through the various drying processes[2]
b. Ash removal through processes such as leaching[3] and flotation[4]
c. Oxygen removal from the DAF coal

The first two approaches deal with the separation of the fuel component (DAF coal) from extraneous materials (moisture and ash), whereas the third approach is concerned with the chemistry of the fuel component itself.

The higher oxygen content of low-rank coals is coupled with marked differences in the relative contents of the various oxygen functionalities. This is particularly pronounced in the case of the carboxyl group, which is one of the main oxygen functionalities occuring in lignite and peat but is almost totally absent in coals

of bituminous and higher ranks.[3,4] An efficient means of decarboxylation, therefore, could lead to a significant improvement of the overall properties, and particularly the heat content of lignite and peat.

The decarboxylation of low-rank coals can be achieved by heating the coal at a high enough temperature. Thus, simple heating of lignite to about 330° C leads to decarboxylation and an increase of about 21% in the gross calorific value of the coal.[7] Similar results were obtained by heating low-grade solid fuels at about 400° C either in the presence of base[8] or in the presence of acid,[9] whereas processes involving even higher temperatures have also been reported.[10,11]

It is apparent that, for thermal decarboxylation of low-rank coals to take place to any significant extent, temperatures in excess of 300° C are required. However, it has been known for a long time that copper will catalyze the decarboxylation of carboxylic acids,[12,13] and the mechanism of this reaction has been studied in detail.[14,15] The purpose of the present study was to assess the possibility of utilizing copper as a catalyst for the decarboxylation of lignite and peat at low temperatures, thus making the process energetically more efficient.

EXPERIMENTAL

Three types of coal were used in this study, Megalopolis lignite, Ptolemais lignite, and Philippi peat; their characteristics are given in Table I. The experimental procedure was similar to that described in a preliminary report on the heat-treatment behavior of two of the above coals[16] and is summarized below.

Samples of about 10 g of each coal (40 to 200 mesh) were slurried with 20 mL of a dilute aqueous solution of cupric sulfate; the copper content was equal to 1% or 3% of the DAF coal of the sample. An amount of sodium carbonate equivalent to the copper sulfate was dissolved in distilled water and was added to the previous slurry with stirring. The coal was then filtered off under mild suction and washed with distilled water. This method achieved an intimate mixture of the coal under study with copper in the form of cupric carbonate. The treated coal was then transferred to a porcelain crucible and placed in an oven at the desired temperature (140° - 400° C) for a period of 30 minutes. This length of time was found adequate for low temperature pyrolysis after a series of experiments with varying heating durations. For comparison purposes, blank samples of coal (i.e. containing no copper) were subjected to exactly the same procedure, except that the initial slurry was made with distilled water.

RESULTS AND DISCUSSION

The measured higher heating values of the various samples, before and after heat treatment, are shown in Tables II, III, and IV. It can be seen that thermal treatment invariably increases the heat content of Megalopolis lignite and Philippi peat; the magnitude of the increase, however, depends both on the temperature of the treatment and on the presence of copper as the decarboxylation catalyst. This behavior can be more easily visualized if one refers to figures 1 and 2, which illustrate the increase in higher heating value as a function of temperature and copper content.

TABLE I
COAL CHARACTERISTICS

	Megalopolis Lignite	Philippi Peat	Ptolemais Lignite
As Received Basis			
Moisture (%)	45.0	16.1	56.3
Volatile Matter (%)	24.4	45.8	18.0
Fixed Carbon	12.5	16.7	12.1
Ash (%)	18.1	21.4	13.7
HHV (MJ/Kg)	9.02	12.72	7.05
DAF Basis			
C %	60.4	56.7	63.2
H %	5.9	5.5	5.2
S %	2.9	1.1	1.6
N %	1.8	1.8	1.6
O % (by difference)	29.0	34.9	28.4
HHV (MJ/Kg)	24.42	20.36	23.43

TABLE II
CHANGE IN CALORIFIC VALUE (DAF BASIS) AS A FUNCTION OF TREATMENT TEMPERATURE AND COPPER CONTENT
MEGALOPOLIS LIGNITE

Treatment Temperature(°C)	Higher Heating Value (MJ/Kg)		
	No Cu	1% Cu	3% Cu
No Heat Treatment	24.42	24.25	24.28
140	24.45	24.64	24.70
160	26.06	30.43	30.08
200	26.74	30.98	31.24
250	27.67	31.62	31.82
300	33.34	34.07	33.16

TABLE III
CHANGE IN CALORIFIC VALUE (DAF BASIS) AS A FUNCTION OF TREATMENT TEMPERATURE AND COPPER CONTENT
PHILIPPI PEAT

Treatment Temperature(°C)	Higher Heating Value (MJ/Kg)		
	No Cu	1% Cu	3% Cu
No Heat Treatment	20.36	20.25	20.38
140	20.38	20.39	20.56
160	20.44	20.57	21.83
200	20.55	23.87	25.63
250	21.38	24.36	26.12
300	25.84	28.05	28.79

In the case of Megalopolis lignite (Figure 1) it is evident that the presence of copper is of minor significance up to about 140° C. the temperature being too low even for the catalyzed decarboxylation to take place. Starting at around 160° C. however, the catalytic effect of copper becomes significant and an increase of the order of 20% is observed in the higher heating value of the heat-treated lignite. Increasing the concentration of copper from 1%

to 3% appears to have essentially no effect on its catalytic activity. When the heat-treatment temperature reaches 300° C, the role of copper becomes much less significant, inasmuch as the rate of decarboxylation is quite fast even in the absence of catalyst.

In the case of Philippi peat (Figure 2) the experimental results display a similar pattern, except that the onset of significant catalytic activity of the added copper does not occur until the heat-treatment temperature has reached about 200° C. It is also worth noting that in this particular case the catalytic effect of copper is more pronounced at the higher metal concentration (3%).

TABLE IV
CHANGE IN CALORIFIC VALUE (DAF BASIS) AS A FUNCTION OF TREATMENT TEMPERATURE AND COPPER CONTENT
PTOLEMAIS LIGNITE

Treatment Temperature(°C)	Higher Heating Value (MJ/Kg)		
	No Cu	1% Cu	3% Cu
No Heat Treatment	23.51	23.22	23.43
160	23.56	23.90	24.06
200	25.26	25.54	26.36
250	25.66	26.34	26.58
280	-	-	25.64
300	26.35	27.34	23.73
320	26.88	28.35	22.95
340	-	-	22.50
370	29.66	29.27	22.59
400	-	-	22.66

As can be seen in Table IV and Figure 3, the behavior of Ptolemais lignite is quite different than that of the other two coals under the experimental conditions that were employed. In the presence of 1% copper, the increase in higher heating value of the pyrolysis residue is only slightly higher than the one occuring in the absence of catalyst. In the presence of 3% copper the results are even more remarkable, in that the higher heating value of the residue starts decreasing at around 250° C and falls below that of the unheated sample at temperatures above 300° C. It thus appears that, in the case of Ptolemais lignite, the presence of copper can lead to the evolution of combustible gases in addition to carbon dioxide and water. The exact nature of this reaction is currently under investigation in our laboratory.

Due to the loss of volatiles (mostly carbon dioxide and water), the mass of the fuel that is recovered after heat treatment is lower than the original one; this loss of mass increases with increasing temperature. The recovery of total heat content, however, is almost quantitative (over 98% in most cases) up to a treatment temperature of 200° C. At higher temperatures the observed heat loss is more pronounced, due to evolution of combustible gases such as carbon monoxide. In the case of Ptolemais lignite the loss of both mass and heat content is much more significant in the presence of 3% copper. Figure 4 is an illustration of typical heat recovery patterns, i.e. the total heat content of the pyrolyzed coal as a percentage of the amount that was contained in the sample before thermal treatment.

The process described in this paper appears to offer the possibility of additional improvements in the quality of the treated coals, including:

a. Lowering of the ash content of the treated coals, probably due to the leaching of the water-soluble components during the slurrying operation.

b. Lowering of the sulfur content.

c. Decrease of the hydrophilicity of the coal, thus making it potentially more amenable to ash-removing processes such as flotation and gravity separation.

The magnitude and mode of occurence of the above effects are currently under study.

CONCLUSIONS

In two of the three samples of low-rank coals that were studied in the course of this work, the addition of small amounts of copper appears to catalyze decarboxylation of the coals in a manner reminiscent of the copper catalyzed decarboxylation of carboxylic acids. As a result, low temperature (160°-250° C) heat treatment in these cases leads to an increase of about 25-30% in the higher heating value of the DAF coal.

The third coal, Ptolemais lignite, offers a different picture. Decarboxylation in the presence of copper is more sluggish, and it appears that other reactions are also being catalyzed, leading to the evolution of combustible gases at comparatively low temperatures.

REFERENCES

1. Van Krevelen, D.W., 1950. Fuel, 29: 269
2. Rozgonyi, T.G. and Szigeti, L.Z., 1985. Fuel Processing Technol., 10: 1
3. Wang, Z.Y., Ohtsuka, Y. and Tomita, A., 1986. Fuel Processing Technol., 13: 279
4. Mitchell, D.R. and Charmbury, H.B., 1963. Chapter 8 in Lowry, H.H., (Ed.), "Chemistry of Coal Utilization", Suppl. Volume. J. Wiley, New York
5. Whitehurst, D.D., Mitchell, T.O. and Farcasiu, M., 1980. Coal Liquefaction. Academic Press, New York, p. 18
6. Doolan, K.R. and Mackie, J.C., 1985. Fuel, 64: 400
7. Elliott, D.C., 1980. Fuel, 59: 805
8. Sharma, D.K., 1983. NSTA Technol. J., 8(2): 93
9. Van Raam, L. and Ruyter, H.P., 1981. Eur. Patent 26011. Chem. Abstracts, 95: 45957
10. Mitsubishi Heavy Industries, 1981. Jap. Patent 157494. Chem. Abstracts, 96: 126107
11. Koppelman, E., 1977. U.S. Patent 4,052,168
12. Dougherty, G., 1928. J. Am. Chem. Soc., 50: 571
13. Fieser, L.F. and Fieser, M., 1967. Reagents for Organic Synthesis. J. Wiley, New York, pp. 157, 158, 163
14. Schambach, R., 1980. Ph.D. Thesis, Univ. of Pittsburgh
15. Cohen, T., Berninger, R.W. and Wood, J.T., 1978. J. Org. Chem. 43: 837
16. Stournas, S., Papachristos, M., and Kyriakopoulos, G.B., 1987. Fuel Processing Technol., in press

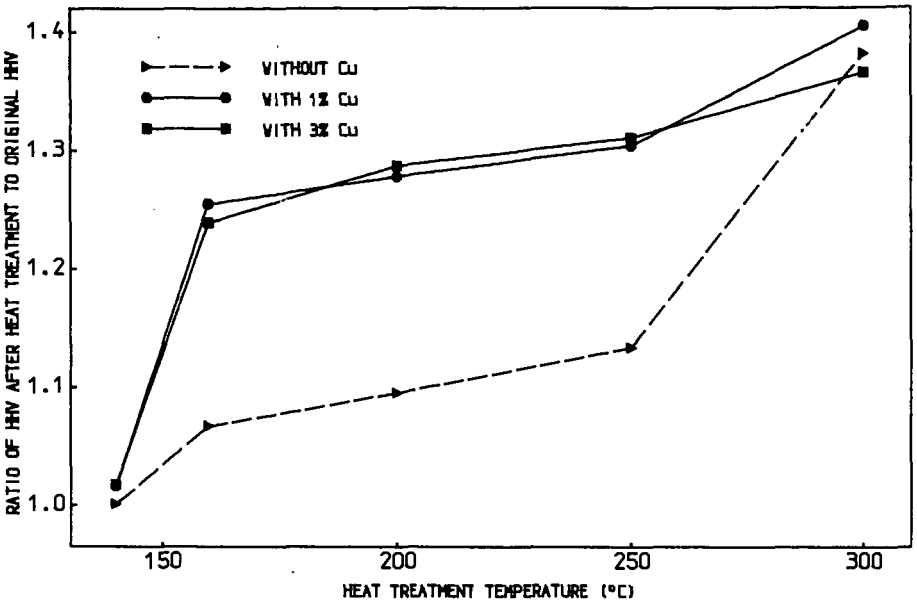

FIGURE 1. LOW TEMPERATURE PYROLYSIS OF MEGALOPOLIS LIGNITE

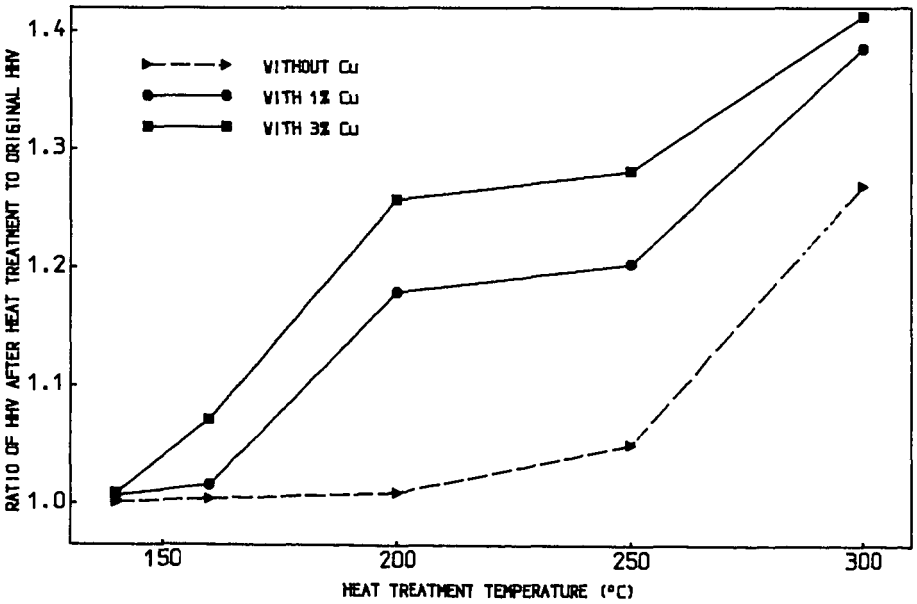

FIGURE 2. LOW TEMPERATURE PYROLYSIS OF PHILIPPI PEAT

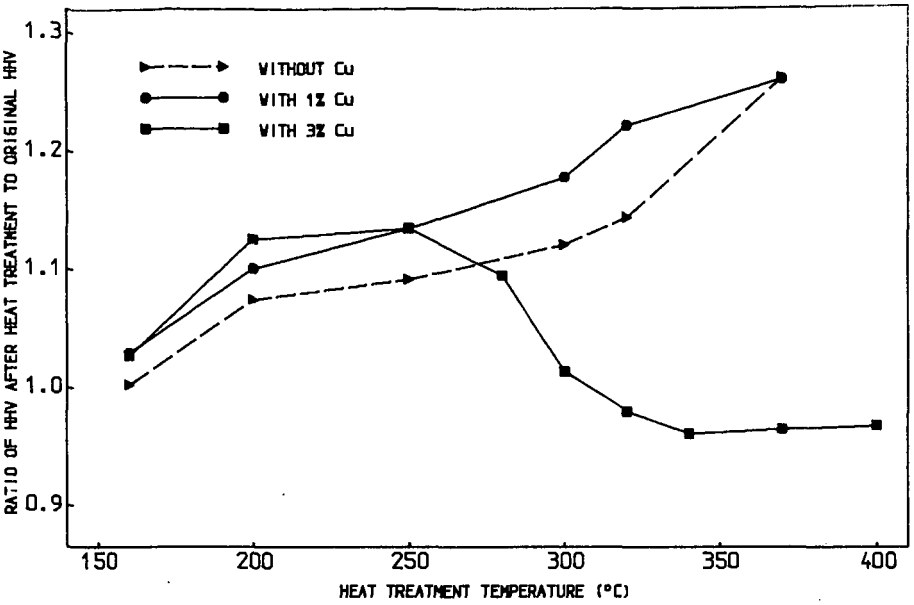

FIGURE 3. LOW TEMPERATURE PYROLYSIS OF PTOLEMAIS LIGNITE

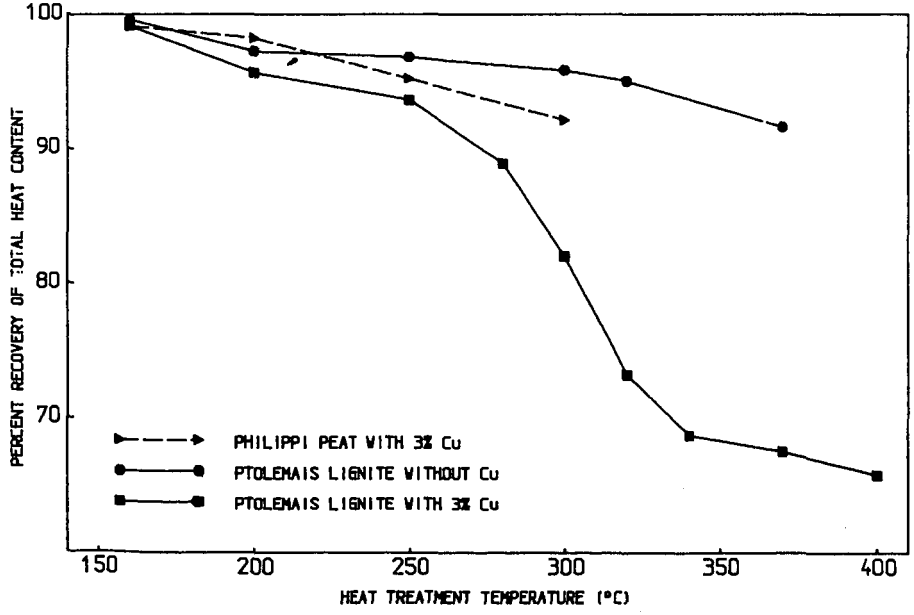

FIGURE 4. RECOVERY OF TOTAL HEAT CONTENT IN THE PYROLYSIS RESIDUE

PYROLYSIS OF WILSONVILLE COAL LIQUEFACTION RESIDUES

By W. A. Leet and D. C. Cronauer
Amoco Oil Company
P. O. Box 400
Naperville, Illinois 60566

Wilsonville coal liquefaction residues including vacuum tower bottoms (VTB), critical solvent deashing (CSD) product resids, and CSD ash concentrates were pyrolyzed via isothermal thermogravimetric analysis. Pyrolysis yields of gas, liquid, and coke were found to be insensitive to temperature over the range of 800-1200°F. The yields of pyrolysis products generated from the CSD resids indicate that the CSD resids represent the more thermally reactive and volatile portions of the VTB. The tendency of such resids to form coke upon pyrolysis correlates with phenolic hydroxyl content. Unusually low gas plus liquid yields for the relatively hydrogen rich ash concentrates correlates with high heteroatom and mineral matter contents. Differences observed in pyrolysis yields for samples from Wilsonville runs made with and without recycle of unconverted coal and mineral matter further characterize the role of such recycle.

INTRODUCTION

In the development of coal liquefaction processes, the pyrolysis (notably delayed and fluid coking) of coal liquefaction residues (resids) has been incorporated into liquefaction process design to supplement liquid yields. The following report presents an update on the viability of low temperature pyrolysis for the processing of coal liquefaction resids. Specifically, the report examines short contact time pyrolysis yields from various liquefaction resids generated at the Advanced Two-Stage Coal Liquefaction R&D Facility at Wilsonville.

EXPERIMENTAL

Liquefaction resid samples were obtained from the coal liquefaction facility at Wilsonville, AL.[1] The Wilsonville pilot plant was operating in a two-stage mode with direct coupling of the thermal liquefaction and catalytic (hydrotreater) reactors as shown in the schematic, Figure 1. After flashing and vapor recovery, the residual vacuum bottoms (VTB) cut was fed to a critical solvent deashing (CSD) unit (currently designated the ROSE-SR process by Kerr McGee Corp.) to reject an ash concentrate and recover an ash free-resid. The VTB product, CSD resid, and CSD ash concentrate from three Runs were studied. In Run 250D, the liquefaction feed solvent consisted of recycle distillates plus CSD resid. In Runs 250H and 251E, the recycle of VTB resid, including unconverted coal and mineral matter, was added to the feed solvent. In Run 251E, catalyst was also loaded into the thermal liquefaction reactor.

All three runs were made with Illinois No. 6 coal at essentially the same reaction conditions. The relevant characterization data are presented in Table I for the runs of interest.

Thermogravimetric (TGA) was used to screen pyrolysis coke, liquid, and gas yields as a function of temperature. Traditionally operated under an inert atmosphere at a preprogrammed heating rate of 5-50°C/min., an isothermal TGA procedure was developed to mimic the more rapid heating rates characteristics of short contact time pyrolysis processes. Provision was made to collect and weigh the liquids as well as recovered "coke" (residual mineral matter, unconverted coal, and coke). Gas yields were calculated by difference. Although representative process variable effects and product quality data could not be obtained due to the small sample sizes involved, such screening provided a relative measure of pyrolysis yields among samples as a function of temperature.

RESULTS

Preliminary screening of the coke yield of the Wilsonville samples was carried out by standard and isothermal TGA runs. Initial screening of Run 250H VTB indicated that coke yields were insensitive to heating rate, sample size, and purge nitrogen flow rate. Pyrolysis yields for Run 250D and Run 250H VTB products are plotted in Figure 2 as a function of pyrolysis temperature. The insensitivity of the yields to pyrolysis temperature over the range (800-1200°F) investigated suggests that the VTB cuts are highly aromatic and not readily thermally cracked under pyrolysis conditions. Such high aromaticity is due to the condensed structure of the original coal feedstock and the liquefaction and concomitant retrogressive reactions to which it is subjected in the liquefaction process. The decrease in liquid yields with VTB recycle, which is seen in comparing products of Run 250D with those of Run 250H and 251E, is attributed to additional solubilization and reaction of recycled VTB organic matter in the liquefaction reactors. This leads to the formation of more highly condensed resids.

For the key Wilsonville runs on bituminous coal, average pyrolysis liquid yields are plotted versus feed H/C ratio in Figure 3. The liquid yields, despite diminished vapor phase cracking of the volatiles evolved in the TGA experiments, are comparable to average Exxon simulated fluid coking yields for samples of resids from the H-Coal and SRC-I processes.[2-4] Such results support a physical picture in which fluid coking of Wilsonville resids lead primarily to vaporization of remaining volatiles with little concomitant liquids upgrading. Liquid yields obtained from pyrolysis of the CSD resids represent the more volatile fractions of the thermally reactive portion of the CSD feeds. Moreover, considering the high H/C ratio, the CSD ash concentrates yield unusually low quantities of liquid product upon pyrolysis. The organic matter rejected in the ash concentrate represents highly condensed and nonvolatile aromatic structures which are heteroatom rich and exhibit strong interactions (adsorption and/or chemical bonding) with the ash mineral matrix.

To examine the coking tendencies of the Wilsonville Streams, selected CSD feed and product resids were fractionated by sequential Soxhlet extraction with n-pentane, toluene, and tetrahydrofuran (THF) to oil (pentane soluble),

asphaltene (pentane insoluble, toluene soluble), preasphaltene (toluene insoluble, THF soluble), and lumped ash/unconverted coal/coke (THF-insoluble) fractions. Although arbitrary in measure, such a fractionation scheme permits a finer resolution of the chemistry involved in terms traditionally applied to coal-derived products. The fractions in turn were pyrolyzed at 1100°F to examine the propensity of each to form coke. The results are summarized in Table II for VTB and CSD resids.

Comparison of the results of Table II shows that all three VTB cuts are similar in character. Coke yields from CSD feed oils, asphaltenes, preasphaltenes, and THF-insoluble residues average about 4, 47, 67, and 89 wt%, respectively, seemingly independent of the actual feed contents of each fraction. Given Soxhlet extraction data of a Wilsonville CSD feed, linear weighting of the above ratios by concentration results in a prediction of actual coke make accurate to ± 3%. Deviations from the cited averages and resultant yield predictions coincide with shifts in phenolic hydroxyl activity measured by FTIR. Decreasing coke make in the pyrolysis of 250D, 250H, and 251E VTB organic fractions (oils, asphaltenes, and preasphaltenes) parallels decreasing phenolics content of the whole resid (Figure 4). Quick calculations show that this simple ratio approach also predicts well the coke make of the CSD ash concentrates, underpredicting coke yield by only 1%. As with the VTB cuts, the deviations can be correlated with phenolic hydroxyl content via FTIR.

Attempts to correlate the CSD product resid fractions of Table II proved less successful. The material which is recovered as product resid represents the more volatile and thermally reactive components of the VTB cuts. As the nature of such material varies with liquefaction severity and subsequent CSD unit operation, the tendency of the various CSD resid fractions (oils, asphaltenes, etc.) to form coke appears to vary greatly with coal feedstock and process configuration. The CSD resid oil fraction makes up the bulk of the VTB oil fraction recovered by extraction and solidification. The CSD resid asphaltene and preasphaltene fractions form less coke than their VTB product counterparts; thus they appear to represent the more volatile fractions and cracked products of the parent VTB resid fractions. Among the three CSD resids studied, like results are obtained for coke yields from the Soxhlet fractions for Runs 250D and 251E. Again, the increased coke make of Run 250H asphaltene and preasphaltene fractions relative to the corresponding fractions of 250D and 251E CSD resids coincides with an increase in the phenolic hydroxyl content of the whole resids.

CONCLUSIONS

Despite an increase of liquid yields due to the development of two-stage liquefaction processes, Wilsonville liquefaction resids are similar to those obtained from older liquefaction processes in that they give similar yields when subjected to thermal pyrolysis. The resids are highly aromatic and hence resistant to thermal cracking, leading to a pyrolysis in which liquid recovery is effected by limited cracking and extensive vaporization of lighter oil and asphaltenic fractions. Heteroratom content and retrogressive reactions[5] partially masked by poorly understood organic-inorganic interactions with the mineral matter play a dominant role in determining the nature of the liquefaction resids.

ACKNOWLEDGEMENT

The analytical support of R. W. Tumbula and the suggestions of B. A. Fleming are acknowledged.

REFERENCES

1. Lamb, C. W., Nalithan R. V., and Johnson T. W., "Process Development Studies of Two-Stage Liquefaction at Wilsonville," Am. Chem. Soc. Dic. Fuel Chem. Preprints, 31(4), 240, 1986.

2. "Fluid Coking of Coal Liquefaction Residues," Interim Technical Progress Report for First Residue, DOE FE-2422-10, June, 1977.

3. "Fluid Coking of Coal Liquefaction Residues," Interim Technical Progress Report for the Second and Third Residues, DOE FE-2422-21, October, 1978.

4. "Fluid Coking of Coal Liquefaction Residues," Final Technical Progress Report for Fourth Residue," DOE FE-2422-28, January, 1979.

5. Hoover, D. S., "Investigation of Deleterious Coking Mechanisms," Final Report, EPRI AP-4451, February, 1986.

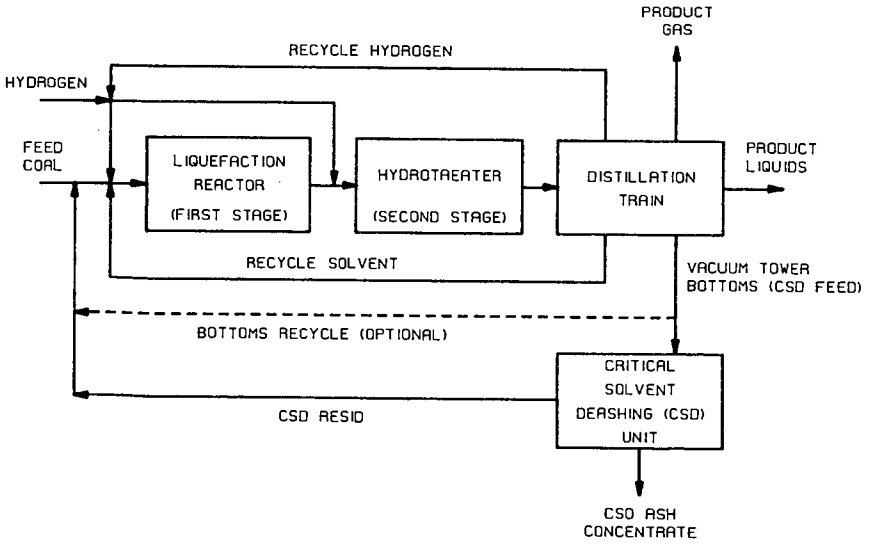

Figure 1. Wilsonville flowsheet.

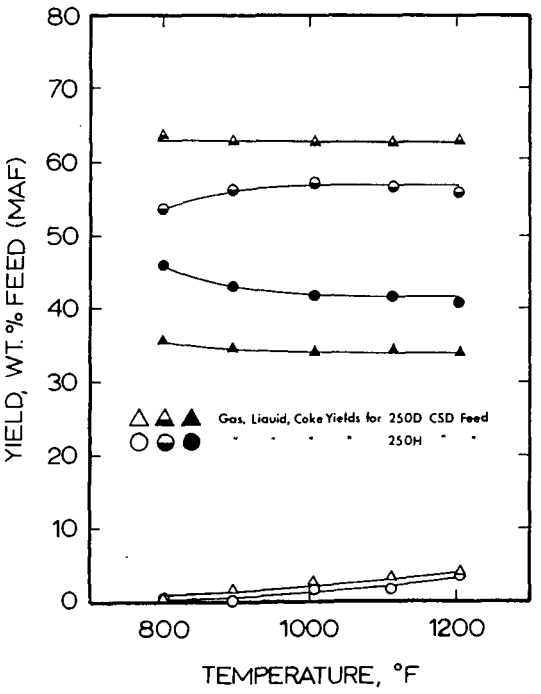

Figure 2. TGA pyrolysis yields for Wilsonville Run 250D and 250H VTB's.

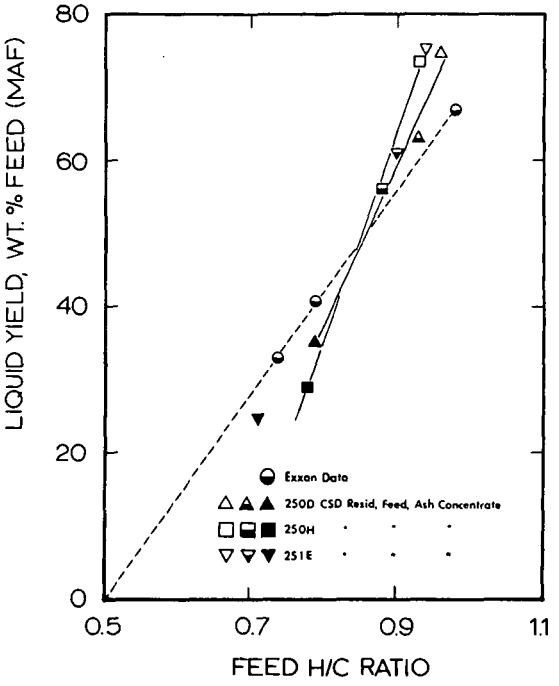

Figure 3. Average liquid yield vs. feed H/C ratio for pyrolysis of Wilsonville resids.

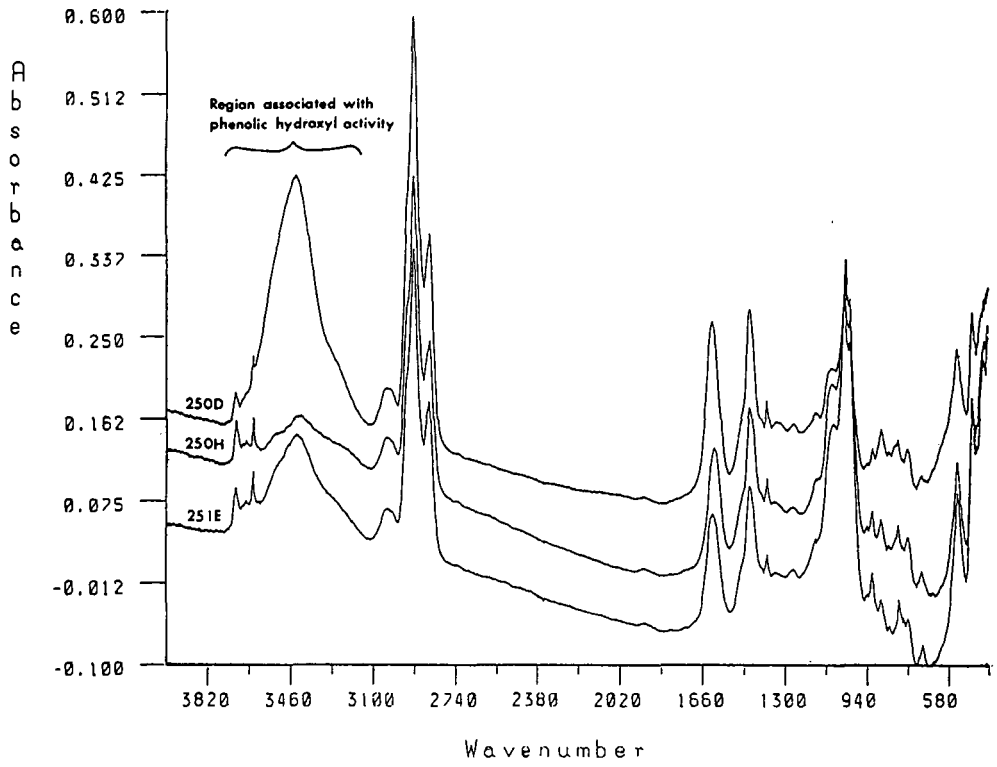

Figure 4. FTIR spectra of VTB's.

TABLE I

ANALYTICAL CHARACTERIZATION OF WILSONVILLE COAL LIQUEFACTION RESIDS
FOR KEY RUNS ON ILLINOIS NO. 6 BITUMINOUS COAL

	Run Number and Date								
	250D (020586)			250H (031786)			251E (060586)		
	VTB	CSD Resid	CSD Ash Concentrate	VTB	CSD Resid	CSD Ash Concentrate	VTB	CSD Resid	CSD Ash Concentrate
Proximate Analysis									
Moisture, wt%	0.09	0.05	0.31	0.10	0.05	0.39	0.08	0.20	0.40
Volatiles, wt%	67.8	84.4	28.7	58.1	86.5	18.6	56.9	82.9	22.6
Fixed Carbon, wt% (by diff.)	22.3	14.8	35.2	24.9	13.5	35.3	20.0	16.7	30.9
Ash, wt%	9.8	0.8	35.8	16.9	0.0	45.7	23.6	0.24	46.2
Ultimate Analysis[1]									
C, wt%	81.2	90.2	56.3	74.2	90.3	46.3	69.5	88.9	46.4
H, wt%	6.29	7.25	3.72	5.43	7.04	3.03	5.20	6.95	2.75
N, wt%	1.26	1.10	1.07	1.24	1.45	1.21	1.13	1.16	1.01
S, wt%	0.98	0.27	2.86	1.58	0.34	4.10	1.85	0.31	3.58
O, wt%	2.09	1.54	4.65	3.66	1.80	5.78	3.29	2.63	5.27
Atomic H/C	0.93	0.96	0.79	0.88	0.93	0.78	0.90	0.94	0.69
Soxhlet Extraction									
Oils, wt%	46.4	22.2	3.1	29.3	39.8	0.8	33.2	39.8	1.5
Asphaltenes, wt%	24.0	49.7	18.7	21.4	27.2	3.0	17.7	34.3	4.1
Preasphaltene, wt%	8.8	27.0	8.5	13.1	33.0	12.9	9.4	25.5	12.2
Ash + Coke + Unconverted Coal, wt%	20.8	1.2	69.7	36.2	0.0	83.3	39.7	0.3	82.2

[1] Uncorrected for mineral matter.

TABLE II

PYROLYSIS YIELDS OF WILSONVILLE RESID FRACTIONS AT 1100°F

Wilsonville Run No.	Extracted Fraction	Feed Composition, Wt%	Pyrolysis Coke Yield, Wt% Feed Sample
	I. VTB FRACTIONS		
250D	Oils	46.4	7
	Asphaltenes	24.0	52
	Preasphaltenes	8.8	74
	Ash + Unconverted Coal + Coke	20.8	88
250H	Oils	29.3	4.5
	Asphaltenes	21.4	49
	Preasphaltenes	13.1	68
	Ash + Unconverted Coal + Coke	36.2	91
251E	Oils	33.2	1.9
	Asphaltenes	17.7	46
	Preasphaltenes	9.4	58
	Ash + Unconverted Coal + Coke	39.7	89
	II. CSD PRODUCT RESID FRACTIONS		
250D	Oils	22.2	8
	Asphaltenes	49.7	26
	Preasphaltenes	27.0	40
	Ash + Unconverted Coal + Coke	1.2	76
250H	Oils	39.8	4.5 ± 0.7
	Asphaltenes	27.2	49 ± 2.3
	Preasphaltenes	33.0	58 ± 3.5
	Ash + Unconverted Coal + Coke	0.0	--
251E	Oils	39.8	3.7
	Asphaltenes	34.4	37
	Preasphaltenes	25.5	51
	Ash + Unconverted Coal + Coke	0.3	86

OXIDATIVE DIMERIZATION OF METHANE OVER LITHIUM-PROMOTED ZINC OXIDE

H.S. Zhang, J.X. Wang, D.J. Driscoll and J.H. Lunsford

Department of Chemistry
Texas A&M University
College Station, TX 77843

INTRODUCTION

The heterogeneously catalyzed oxidative dimerization of methane has received considerable attention in recent years. A variety of materials have now been examined which include the main group oxides (1,2), the rare-earth oxides (3,4) and a number of doped transition (5) and main group metal oxides (6). Work in this laboratory has focused primarily on the latter materials, and in particular Li-doped MgO (7,8). Over this material it is postulated that methane is activated via hydrogen atom abstraction by $[Li^+O^-]$ centers which are present under reaction conditions on the surface of the catalyst. Subsequent steps in the mechanism involve the release of these radicals from the surface into the homogeneous gas phase where they then undergo coupling reactions to produce the selective C_2 products.

The formation of $[Li^+O^-]$ centers has also been reported on Li-doped ZnO (9,10). This material is considerded to be a non-basic semiconductor, whereas, MgO is considered to be a basic insulator. Li-doped ZnO was chosen for examination not only because of its ability to produce potentially active centers, but also to determine the effect of basicity on the catalytic properties. Recent work by Matsuura *et al*. (11) has shown that this material is indeed active for the oxidative dimerization of methane. In the present study, this material will be examined in further detail in an effort to identify the active site on the catalyst surface and to determine the overall mechanism for final product formation.

EXPERIMENTAL

The catalysts were prepared by adding zinc oxide (ZnO) and lithium carbonate (Li_2CO_3) to deionized water and evaporating the water, while stirring, until only a thick paste remained. The paste was dried in air at 140°C overnight. This material was then pressed, broken into small chips, loaded into the reactor and preconditioned at 750°C for 4 h under a flow of oxygen before exposure to the reactant gases. The unpromoted ZnO catalyst was prepared and pretreated in the same manner, except for the addition of Li_2CO_3.

The catalytic studies were carried out in a conventional fused-quartz flow reactor operated at atmospheric pressure. Typical reactant feeds consisted of a 2:1 methane:oxygen feed diluted with a helium carrier gas at a total flow of 50 ml/min. Reaction temperatures ranged from 600 to 770°C. Product analysis was accomplished by conventional GC techniques. Further details on this system can be found in previous papers by Lunsford and co-workers (3,7).

The EPR spectra were obtained using a Varian E-6S spectrometer at 77 K. Quenching studies were carried out using the technique previously developed in this laboratory by Wang *et al*. (12). In this

work, the samples were quenched into liquid oxygen after exposure to 180 torr of gaseous oxygen at 730°C for 1 h.

RESULTS

Catalyst Preconditioning

The method used to pretreat the catalyst was found to have a strong influence on the reaction stability. Samples preconditioned for 3 h at 650°C in air rapidly deactivated, regardless of the reaction temperature, methane/oxygen ratio or the sample purity. However, by increasing the pretreatment temperature to 750°C and employing a 50 ml/min oxygen flow a steady state could be rapidly attained. In this case, a steady state reaction was achieved after only 2.5 h and was maintained even after 130 h on stream. Therefore, to ensure that all results were obtained after steady state had been reached, samples were pretreated at 750°C for 4 h under an oxygen flow and measurements were not begun until after 12 h on line.

Catalytic Studies

In order to gain insight into the overall reaction mechanism the effects of temperature, Li-doping levels and reactant partial pressures on reactivity were examined in detail. The effect of temperature is considered first and the results are illustrated in Figure 1. Methane conversion continually increased with increasing temperature over the entire range examined. The C_2 selectivity slowly increased to a maximum at a temperature of approximately 675°C while a reverse temperature dependence was observed for the C_1 selectivity. The increase in C_2 selectivity with increasing activity is contrary to expected behavior; however, a similar trend was previously observed during the oxidative dimerization of methane over Li-doped MgO catalysts (7). The activation energy determined for this reaction, over the temperature range of 550 to 700°C was 51 kcal/mol.

The effect of lithium doping was examined and a plot of methane conversion, C_2 selectivity, C_1 selectivity and C_2 yield (which is defined as the product of conversion and selectivity) *vs* lithium doping into ZnO is presented in Figure 2. Methane conversion reached a maximum over the pure oxide; however, selectivity to C_2 products was extremely low. Addition of lithium resulted in a decrease of methane conversion, but the C_2 selectivity rapidly increased and eventually leveled off at a doping level of approximately 1.0 wt% Li. A corresponding decrease in the C_1 was also observed. The major component in the C_1 fraction was CO_2 (>90%) while the C_2 portion consisted of a mixture of ethane and ethylene at a constant ratio of $C_2H_4/C_2H_6 = 0.85$. The surface areas of these used materials decreased from 0.5 m^2/g over the pure oxide to a constant value of ~0.1 m^2/g over all of the lithium-doped samples.

In one experiment a used catalyst was thoroughly washed to remove any residual Li_2CO_3 from the surface. This material exhibited an activity for C_2 formation which was comparable to the original catalyst; however, the rate of C_1 product formation increased considerably.

The variation of reactivity with respect to oxygen partial pressure is presented in Figure 3. This data was obtained over a 0.9 wt% Li/ZnO catalyst at 720°C; however, similar behavior was also observed at a reaction temperature of 660°C. As the oxygen partial pressure was increased, methane conversion continued to increase. At low oxygen partial pressures the formation of selective C_2 products

was favored whereas, as expected, high oxygen partial pressues tended to promote the production of non-selective CO and CO_2.

Maximum C_2 Yields

In order to obtain the maximum C_2 yields catalytic runs were carried out over 4 g of a 0.9 wt% Li/ZnO catalyst at several different temperatures and these results, along with some typical conversion and selectivity data, are summarized in Table I. A maximum C_2 yield of 15% was obtained at a temperature of 750°C. Higher yields apparently could be obtained at higher temperatures; however, at these temperatures the catalyst appeared to enter a molten phase. It is of value to compare these yields with those previously obtained over the Li/MgO catalysts (7). At 720°C under similar reactant feed conditions a C_2 yield of 18% was observed. The value of 11% obtained here at 720°C is obviously lower, but still within the range of the more active methane conversion catalysts thus far reported.

Table I.

MAXIMUM C_2 YIELD

Temperature(°C)		650	700	720	750
Selectivity(%)	CO_2	44.0	39.6	42.4	43.7
	CO	4.9	1.4	0.0	3.0
	C_2H_4	10.4	22.2	26.9	28.7
	C_2H_6	40.7	36.8	30.7	24.6
	Total C_2	51.1	59.0	57.6	53.3
Conversion(%)	CH_4	5.1	13.9	18.7	28.2
	O_2	11.7	25.3	35.2	55.5
C_2 Yield(%)		2.6	8.2	10.8	15.0

Catalyst: 4g 0.9 wt% Li/ZnO; Flow rates: He = 42.5 ml/min, CH_4 = 5.0 ml/min, O_2 = 2.5 ml/min.

EPR Studies

Quenching of all of the doped materials from high temperature in the presence of oxygen resulted in the detection of $[Li^+O^-]$ centers. No $[Li^+O^-]$ signal, or O^- signal, was detected over pure ZnO. The variation of $[Li^+O^-]$ concentration with respect to lithium doping is presented in Figure 2 along with the selectivty and conversion data obtained under steady state reaction conditions.

DISCUSSION

To simplify presentation of the mechanism it is best to divide the discussion into two sections: (1) methane activation and (2) stable product formation.

Methane Activation

The presence of $[Li^+O^-]$ centers in the quenched samples once again suggests that this site is most likely responsible for the initial methane activation. Although the $[Li^+O^-]$ concentration curve

does not correlate well with the conversion curve in Figure 2, relatively good agreement is observed with the C_2 yield curve, and there is even better agreement with the C_2 selectivity curve. Furthermore, in the absence of these centers (i.e. over the pure oxide) the formation of both ethane and ethylene is negligible which provides additional support for the fact that $[Li^+O^-]$ centers are required to promote selective C_2 product formation. In accord with the earlier work over Li-doped MgO catalysts it is proposed that methane is activated via hydrogen atom abstraction by $[Li^+O^-]$ centers to produce the methyl radical (7).

Stable Product Formation

The conversion and selectivity data presented in Figure 2 clearly show that selective C_2 product formation is not favored on the pure oxide surface. In addition, as C_2 selectivity increased the surface area of the catalyst fell by a factor of approximately 5. This further suggests that the catalyst surface is not entirely responsible for the selective product formation. In agreement with the earlier Li/MgO work, it is once again proposed that ethane and ethylene are formed via coupling of the radicals in the gas phase and not on the surface (7).

The formation of the non-selective products, CO and CO_2, is also briefly considered. As mentioned above, reaction on the catalyst surface appears to be a major source for these products. In addition, the data of Figure 1 indicates that the selectivity for these products increases at temperatures greater than approximately 700°C. This is believed to be due to the further oxidation of the C_2 products. This route apparently is only important at these elevated temperatures. High oxygen partial pressures also tends to promote complete oxidation products (Figure 3), but it is not possible to determine whether this is promoted on the surface or in the gas phase from this data.

Lithium carbonate on the surface appears to moderate the non-selective activity of the zinc oxide, but it has no effect on the selective oxidative dimerization reaction. When the carbonate was removed only the non-selective reactions were affected. Since zinc oxide itself is not a strongly basic oxide, one may conclude that basicity is not a prerequisite for the selective reaction.

CONCLUSIONS

The mechanism for the oxidative dimerization of methane over Li-doped ZnO is similar to that previously proposed for the same reaction over Li-doped MgO. Surface-generated gas phase methyl radicals are produced from the interaction of methane with $[Li^+O^-]$ centers. Gas phase coupling reactions provide the primary route for the formation of the selective C_2 products. Non-selective C_1 product formation is most likely promoted on the pure oxide surface. A strongly basic oxide is not required for the selective oxidative dimerization of methane.

ACKNOWLEDGMENTS

This work was supported by the National Science Foundation under Grant No. CHE-8405191.

REFERENCES

1. Keller, G.E. and Bhasin, M.M., J. Catal., 73, 9 (1982).
2. Sofranko, J.A., Leonard, J.J. and Jones, C.A., J. Catal., 103, 302 (1987).
3. Lin, C.H., Campbell, K.D., Wang, J.X. and Lunsford, J.H., J. Phys. Chem., 90, 534 (1986).
4. Otsuka, K., Jinno, K. and Morikawa, A., J. Catal., 100, 353 (1986).
5. Jones, C.A., Leonard, J.J. and Sofranko, J.A., J. Catal., 103, 311 (1987).
6 Ali Emesh, I.T. and Amenomiya, Y., J. Phys. Chem., 90, 4785 (1986).
7. Ito, T., Wang, J.X., Lin, C.H. and Lunsford, J.H., J. Am. Chem. Soc., 107, 5062 (1985); Ito, T. and Lunsford, J.H.,Nature (London), 314, 721 (1985).
8. Driscoll, D.J., Martir, W., Wang, J.X. and Lunsford, J.H., J. Am. Chem. Soc., 107, 58 (1985).
9. Haber, J., Kosinski, K. and Rusiecka, M., Discuss. Faraday Soc., 58, 151 (1974).
10. Schirmer, O.F., J. Phys. Chem. Solids, 29, 1407 (1968).
11. Matsuura, I., Utsumi, Y., Nakai, M. and Doi, T., Chem. Lett., 1981 (1986).
12. Wang, J.X. and Lunsford, J.H., J. Phys. Chem., 90, 5883 (1986).

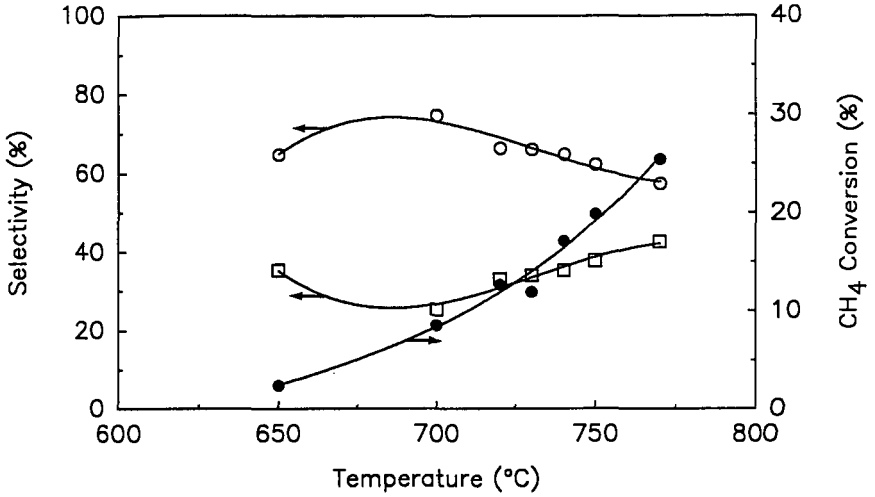

Figure 1. Methane conversion and product selectivity as a function of temperature: ● methane conversion; □ C_1 selectivity; ○ C_2 selectivity. Catalyst: 0.9 wt% Li/ZnO.

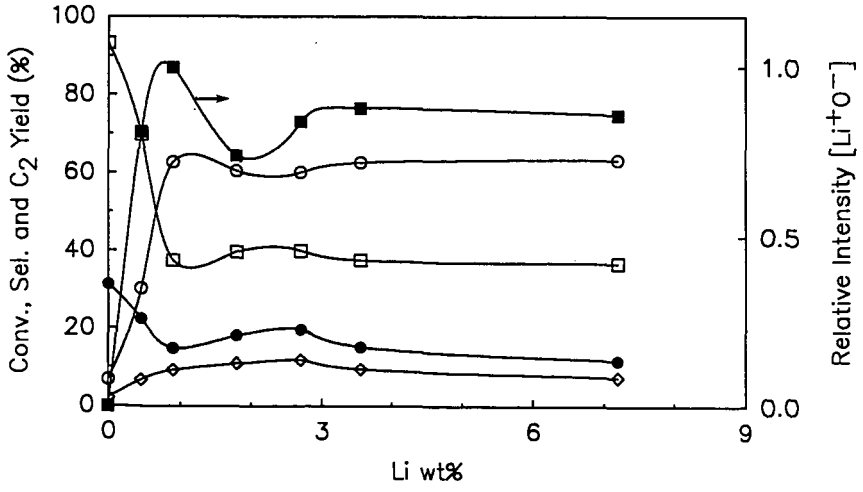

Figure 2. Methane conversion, product selectivity and C_2 yield as a function of Li-doping into ZnO: ●methane conversion; □C_1 selectivity; ○C_2 selectivity; ◇C_2 yield; ■ $[Li^+O^-]$ concentration. Temp: 750°C.

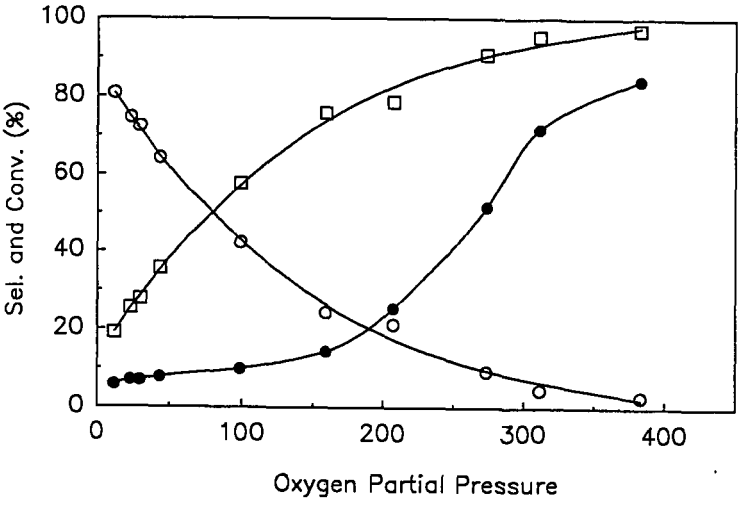

Figure 3. Methane conversion and product selectivity as a function of oxygen partial pressure: ●methane conversion; □ C_1 selectivity; ○ C_2 selectivity. Catalyst: 0.9 wt% Li/ZnO; Temp: 720°C.

CATALYTIC PARTIAL OXIDATION OF METHANE TO HIGHER HYDROCARBONS

R.J. Tyler and C.A. Lukey

CSIRO Division of Fossil Fuels, PO Box 136, North Ryde, NSW 2113, Australia

1. INTRODUCTION

The direct conversion of methane to higher hydrocarbons such as ethylene is currently a very active research area. Olefins are of particular importance as they represent intermediates suitable for oligomerisation to transport fuels. Jones et al. (1) recently reviewed the potential for methane conversion and described results using Mn-based redox type catalysts in both cyclical (using air and methane alternately) and continuous reactors. Bytyn and Baerns (2) reported the activity of PbO-based catalysts and concluded that the acidity of the surface influences the reaction pathway, with high acidity resulting in poor selectivity to the desired hydrocarbons. Otsuka et al. (3,4) described results for a variety of catalysts including rare earths, transition metal elements, alkali and alkaline earth compounds and halide doped mixtures. Lunsford et al. (5,6) were the first to report the use of a Li-doped magnesia and postulate that methane activation occurred at $[Li^{+}O^{-}]$ centres. This catalyst is notable in that it does not contain metal ions of variable oxidation state and the active species is thought to involve the anion. A remarkable feature of the published data is the variety of surfaces that promote the reaction and the similarity of many of the reported product distributions. This suggests that after the initiation step the hydrocarbon building steps probably occur via a gas phase mechanism (1).

The present paper reports results obtained using a Li/MgO catalyst with CH_4/O_2 mixtures and describes the influence of contact time and oxygen concentration on reaction rate and product selectivities. Implications for the reaction mechanism are also discussed.

2. EXPERIMENTAL

Catalysts were prepared by procedures similar to those described by Ito and Lunsford (5) and calcined in air at 850°C before use. Initial Li loadings were equivalent to a Li/Mg atomic ratio of 0.58. However subsequent analysis showed substantial loss on firing and to some extent during reaction.

Experiments were conducted using quartz or alumina fixed-bed reactors and a continuous flow of feed gas. Pseudo-contact times (W/F) equivalent to the weight of catalyst (g) divided by the feed gas flowrate at operating conditions (ml s^{-1}) were varied in the range 0.01 to 2. Temperatures were in the range 550 to 850°C. Exit gas analysis was performed by gas chromatography (hydrocarbons) and continuous gas analysers (CO, CO_2 and O_2). In some experiments water analyses were also carried out enabling oxygen balances to be determined (usually 100 ± 5%) and hydrogen yields to be calculated from a hydrogen balance. Confirmation of hydrogen yields by analysis was obtained in selected experiments.

3. RESULTS AND DISCUSSION

3.1 Reaction rates

Figure 1 shows the dependence of the methane conversion rate (mmol CH_4 min^{-1} g^{-1} catalyst) on the pseudo-contact time (W/F) for a range of O_2 concentrations using 17.3 g of catalyst at 770°C. The methane content of the feed gas was held constant at 90% and the oxygen concentration was varied between 1 and 9.4% with the balance being nitrogen.

As expected, the methane conversion rate increased as the level of oxygen in the feed gas increased. However, for each oxygen level there was a marked decline in

methane conversion rate as the contact time increased (i.e. as the gas velocity through the reactor decreased). The possibility that this effect was caused by limitations in the mass transfer of reactants across the boundary layer to the external surface of the catalyst was checked using standard calculation procedures (7). In all cases the reactor was found to be operating well outside the regime where external mass transfer limitations apply. Presumably the observed decline in methane conversion rate with increasing contact time results from operating the reactor in an integral mode where the variation in W/F results in different average reactant and product concentrations and hence different reaction rates. The possibility of rate suppression by one or more of the products reducing catalyst activity must also be considered.

3.2 Methane conversion and product selectivity

Methane conversion (percentage of input methane converted to products), oxygen consumption (percentage of input O_2 consumed) and product selectivity (amount of input methane converted to a specific product as a percentage of total methane converted) for feed gases containing 1.1 and 9.4% O_2 are illustrated in Fig. 2 as a function of W/F. At the lower O_2 concentration (Fig. 2a), total O_2 consumption was achieved at the longest contact time when CH_4 conversion reached 3%. Selectivity to hydrocarbons was very high at 94% for W/F = 0.3, of which 91% corresponded to C_2 hydrocarbons and 3% C_3 hydrocarbons, principally propane. At total O_2 consumption, hydrocarbon selectivity was still high at 93% with C_3's increasing to 5% and consisting principally of propylene. Increasing contact time resulted in an increasing conversion to ethylene with a corresponding decrease in ethane. Carbon dioxide was the dominant carbon oxide product.

With 9.4% O_2 in the feed gas (Fig. 2b) the selectivity to hydrocarbons showed a strong dependence on contact time, declining from 85% at W/F = 0.3 to 76% at 1.5. C_3 hydrocarbons, mainly propylene, reached 6% at the longer reaction times. The loss in hydrocarbon selectivity appears to be due to an increasing contribution from secondary reactions in the presence of a higher O_2 concentration and is reflected in increasing selectivity to carbon oxides. This is accompanied by an increased production of ethylene and decline in ethane.

Minor yields of other hydrocarbons were observed, including butenes, butadiene and, at higher temperatures, benzene, toluene and acetylene. These products all demonstrate an increasing contribution from secondary gas phase reactions as operating conditions became more severe. Hydrogen was also observed in the product stream in amounts equivalent to about 15% of the hydrogen liberated by the methane conversion and also depended upon reaction severity. Hydrogen could arise by pyrolysis of ethane to ethylene or possibly by decomposition of reaction intermediates such as formaldehyde.

The dependence of CH_4 conversion, O_2 consumption and product selectivity on O_2 concentration in the feed gas is summarised in Fig. 3 for a fixed W/F value of 1.5. Hydrocarbon selectivity declined linearly with increasing O_2 concentration in the feed gas (CH_4 constant at 90%) accompanied by increasing formation of carbon oxides. Ethane selectivity declined rapidly with increasing O_2 concentration whereas ethylene increased and eventually reached a plateau of 42%. In other experiments where total O_2 consumption was achieved, ethylene selectivity reached a maximum and then declined with increasing contact time suggesting that secondary, undesired production of carbon oxides adversely affected ethylene production. O_2 consumption showed a small decrease with increasing O_2 content whereas CH_4 conversion increased markedly, reaching 11% with 9.4% O_2 in the feed gas.

3.3 Reaction sequence

Ito et al. (5,6) proposed that the initial step in the catalytic conversion was the formation of a methyl radical by hydrogen abstraction from a methane molecule at a

thermally generated $[Li^+O^-]$ site. Recombination of two methyl radicals either on the surface or in the gas phase produced ethane. Ethylene was thought to arise from partial oxidation or pyrolysis reactions of ethane. Carbon oxides arose from either oxidation of methyl radicals or further oxidation of C_2 products.

In an attempt to clarify the reaction sequence, experiments were conducted at short pseudo-contact times using a small catalyst bed (<0.5 g) in order to examine the product distribution at low extents of reaction. Figure 4 shows the dependence on temperature of CH_4 conversion, O_2 consumption and product selectivity at a fixed W/F of 0.05 using a 50% CH_4/5% O_2/45% He feed gas mixture. Clearly at temperatures below about 700°C CH_4 conversion and O_2 consumption were low, C_2 hydrocarbon selectivity was also low and carbon oxides were the major products below about 650°C. Increasing the temperature resulted in increasing C_2 selectivity, which reached a broad maximum of 75% between 750 and 800°C. Below 650°C ethane was the only hydrocarbon species, with selectivity to ethylene increasing at higher temperatures. These data suggest that, at least in the early stages of the reaction, ethane and carbon oxides are formed by parallel rather than sequential reactions. The reactions involved must have different activation energies, resulting in a changing product distribution with increasing temperature.

Further evidence in favour of this reaction sequence is depicted in Figure 5. These data were derived at short residence times (W/F = 0.01-0.1) with a feed gas consisting of 95% CH_4/5% O_2. Product selectivities are shown as a function of methane conversion, and the diagram includes a curve representing O_2 consumption. At the higher conversions C_2 selectivity started to decline and carbon oxides to increase owing to secondary oxidation as the oxygen consumption approached 100%. However, extrapolation of the selectivities back to zero conversion provides evidence of the primary reaction products without contribution from secondary processes. In this example and in all other experiments only ethane and carbon oxides formed intercepts. Ethylene and C_3 hydrocarbon selectivities extrapolate to zero at zero CH_4 conversion indicating that these products arise from secondary reactions of ethane. The increase in carbon oxides at higher conversion must be associated with further oxidation of product hydrocarbons.

The simultaneous formation of ethane and carbon oxides again suggests that in the early stages of the reaction these products arise from parallel rather than sequential reactions. There is thus no direct route to ethylene. These so-called 'primary selectivities' at zero conversion are considered to be an intrinsic property of the catalyst and as such provide a useful means of comparing the performance of different catalysts.

CONCLUSIONS

Product selectivity from the catalytic partial oxidation of methane over a Li/MgO catalyst is very dependent on contact time, O_2 concentration and temperature. Very high selectivities to hydrocarbons (>90%) can be achieved provided high CH_4:O_2 ratios (>50:1) are used. The reaction sequence involves the initial formation of ethane and carbon oxides via parallel reactions. There is no direct route to ethylene, which arises from secondary reactions of ethane.

ACKNOWLEDGEMENTS

This study forms part of a larger nationally coordinated program on the direct conversion of methane involving CSIRO, the Melbourne Research Laboratories of The Broken Hill Proprietary Company Ltd. and Australian universities. Funding under the National Energy Research Development and Demonstration Program is gratefully acknowledged. The technical skills of A. McCutcheon and J. Smith contributed significantly to this investigation.

REFERENCES

1. Jones C.A., Leonard J.L. and Sofranko J.A. Energy Fuels 1987, 1, 12-16.
2. Bytyn W. and Baerns M. Appl. Catal. 1986, 28, 199-207.
3. Otsuka K., Jinno K. and Morikawa A. J. Catal. 1986, 100, 353-359.
4. Otsuka K. and Komatsu T. J. Chem. Soc. Chem. Commun. 1987, 388-389.
5. Ito T. and Lunsford J.H. Nature 1985, 314, 721-722.
6. Ito T., Wang J., Lin C. and Lunsford J.H. J. Am. Chem. Soc. 1985, 107, 5062-5068.
7. Edwards J.H., personal communication.

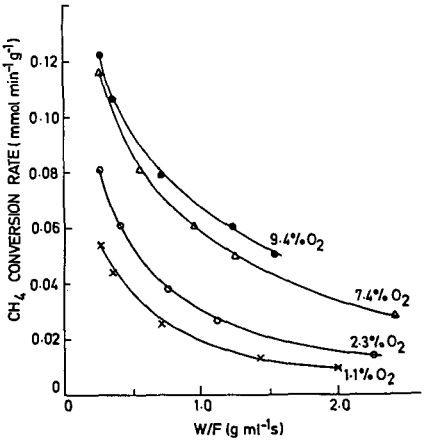

Figure 1. Influence of pseudo-contact time and oxygen level in feed gas on methane conversion rate at 770°C (feed gas 90% CH_4)

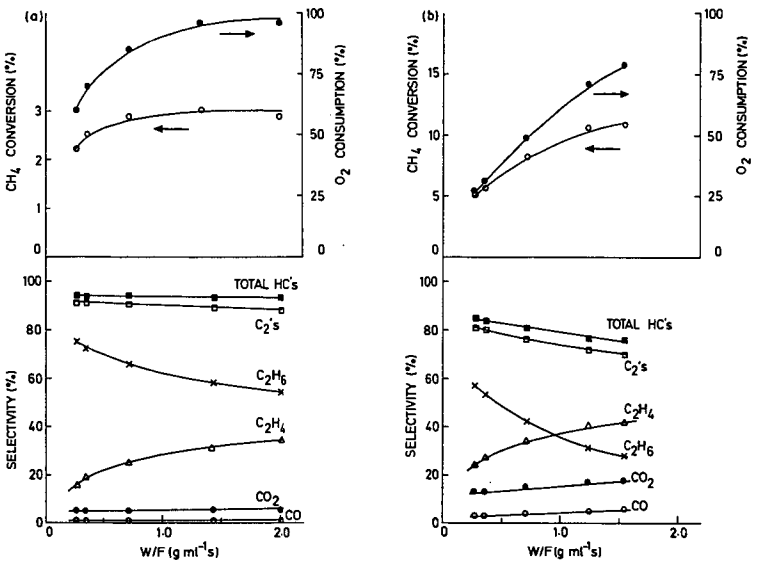

Figure 2. Influence of pseudo-contact time on methane conversion, oxygen consumption and product selectivities at 770°C. (a) Feed gas 1.1% O_2, 90% CH_4. (b) Feed gas 9.4% O_2, 90% CH_4

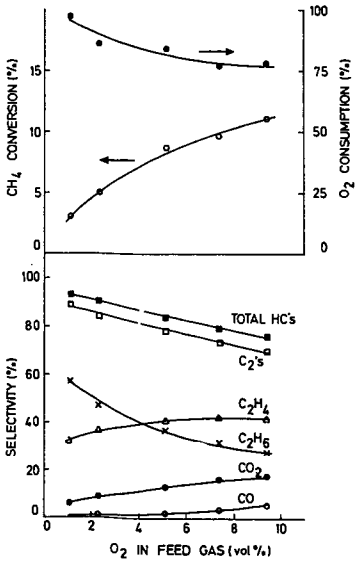

Figure 3. Influence of oxygen level in feed gas on methane conversion, oxygen consumption and product selectivities at 770°C (W/F = 1.5 g ml^{-1}s)

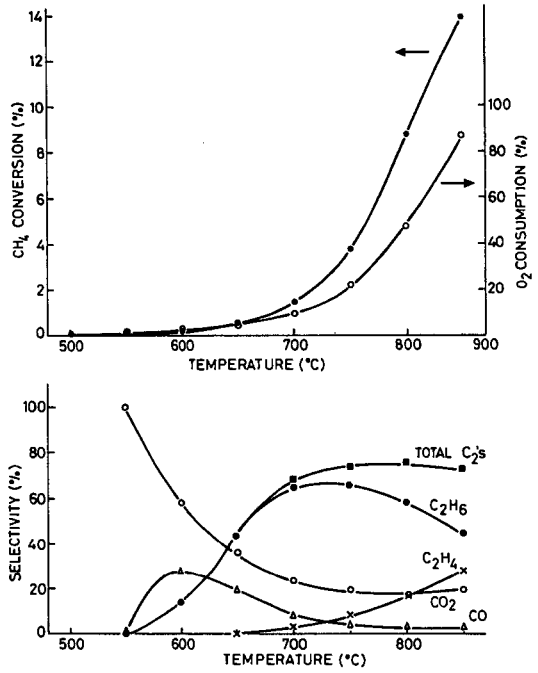

Figure 4. Effect of temperature on methane conversion, oxygen consumption and product selectivity (feed gas 50% CH_4, 5% O_2)

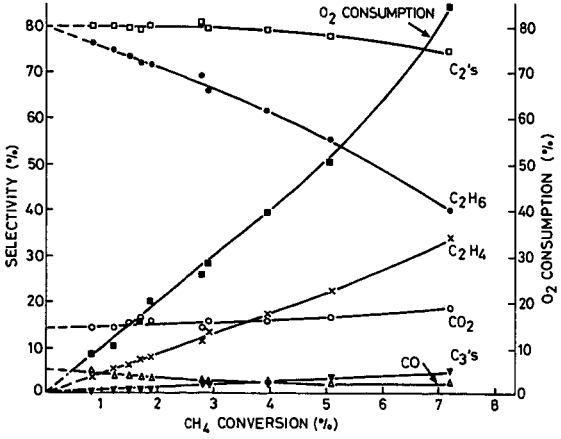

Figure 5. Variation of product selectivity and oxygen consumption with methane conversion at 750°C (feed gas 95% CH_4, 5% O_2)

THE DIRECT CONVERSION OF METHANE TO METHANOL BY A HIGH PRESSURE PARTIAL OXIDATION REACTION

H. D. Gesser, N. R. Hunter, L. A. Morton, P. S. Yarlagadda and D. P. C. Fung*

Department of Chemistry, University of Manitoba, Winnipeg, Manitoba, R3T 2N2 and *Energy Research Laboratory, CANMET, Department of Energy, Mines and Resources, Ottawa, K1A 0G1, Canada.

INTRODUCTION

The conversion of methane to a liquid storageable fuel is a desirable alternative to compressed natural gas. The simplest liquid is methanol presently formed by the steam reforming of methane to synthesis gas followed by the high pressure catalytic conversion of the synthesis gas to methanol. The process is most economic for large (2000 tonne/day) plants and must be located near large reserves of natural gas or near an appropriate pipeline. The simpler partial oxidation route offers the advantage of directly converting methane to methanol in a single step reaction. The potential for the partial oxidation route together with an economic evaluation has been reported by Edwards and Foster (1) who showed that, provided the selectivity for methanol formation is about 77%, the partial oxidation route has an economic advantage over the conventional synthesis route with no penalty for conversions as low as 4%.

Much has been published on the combustion of methane to CO_2 and H_2O but very little has been concerned with the intermediate formation of methanol.[2] Gesser et al. (2) recently reviewed the controlled oxidation of CH_4 to CH_3OH emphasizing the free radical mechanistic aspects. The heterogeneous catalytic studies was reviewed by Foster (3) and Pitchai and Kleir (4). Although the literature indicated some potential catalysts (5) no commercial viable reaction system has been developed. Before embarking on a study of the catalytic conversion of CH_4 to CH_3OH we attempted to establish a base-line study by examining the homogeneous reaction (6,7,8,9) and here report a summary of the results with methane.

EXPERIMENTAL

The experiments were performed in a glass lined tubular reactor (0.36 cm ID, 3.3 mL heated volume). Reaction temperature was indicated by a steel sheathed thermocouple probe in the reaction zone.

Gases (2% N_2 in CH_4 and pure O_2) from the respective cylinders were thoroughly pre-mixed before entering into the reactor by passing them through a mixing cross filled with Teflon turnings. Nitrogen was deliberately introduced into the feed gas so as to act as an internal reference. The pressures at various points were monitored by cslibrated pressure transducers. The reaction products were analyzed by gas chromatography with a thermal conductivity detector using an 8-port sampling valve and two columns -- 5A molecular sieve and a Porapak S column.

Using N_2 as an internal reference it was possible to measure the changes in the ratio $(CH_4/N_2)_{in}$ to $(CH_4/N_2)_{out}$ and so determine the conversion and material balances. Selectivity was calculated in terms of total carbon products. The water yield was invariably greater than that of the methanol. Formaldehyde was found in trace quantities and was determined colorimetrically (10).

Experiments were conducted by first adjusting the gas flows and, when stable, the temperature of the reactor was raised to the desired value. The on-line analysis was then performed over a period of several hours.

The residence time was usually about 2 minutes but varied from 0.2 to about 5 min with no obvious effects on the products.

RESULTS

The effect of temperature on CH_3OH conversion at different temperatures and pressures is shown in Figure 1. At higher O_2 concentrations the increase in temperature significantly increases the conversion. The possible CH_4 conversion is a maximum of twice, and a minimum of half, the O_2 consumed. Calculated conversion of greater than twice the O_2 consumed were due to errors in the CH_4/N_2 ratios

measured and the accompanying errors in the differences of two large numbers. Material balances were usually good (within 100 ±10%) for carbon but poor for oxygen.

The results in Figure 2 show the effect of temperature on the methanol selectivity at various O_2 concentrations. As the temperature is increased the selectivity passes through a maximum which is at lower temperatures for lower O_2 concentrations.

The methanol selectivity decreases as the O_2 concentration increases as shown in Figure 3.

The effect of pressure on the methanol selectivity was determined in another reactor (0.4 cm ID, 5.7 mL reactor volume). The results are given in Table 1 and clearly show that for a given oxygen concentration in the feed gas and, given reaction temperature, pressure had a positive influence on methanol selectivity; especially at above 50 atm. Thus, at an oxygen concentration of 5 to 6% in the feed gas and a reaction temperature of about 453°C, the methanol selectivity increased from 65% at 35 atm to 76% at 50 atm and at 65 atm it was 83%. A similar trend was observed at the other oxygen concentrations used in this study.

DISCUSSION

Much of the earlier work on partial oxidation of methane has been conducted in static reactors (11,12). Limited studies have been performed employing flow reactors at high pressures (13,14,15). Boomer et al. (16) showed that at a pressure of 180 atm, temperature of 475°C and 3.2% oxygen concentration in the feed gas, a maximum methanol selectivity of 74% could be obtained. The methane conversion at the above conditions was only 1.9%. Similar results were reported by Pichler and Reder (14), and Wiezevich and Frolich (15). Brockhaus and Franke (17) from their studies on the partial oxidation of methane under cool flame conditions were able to obtain a combined selectivity of methanol and formaldehyde of up to 91%. However, the conversion per pass was of the order of 2%. In comparison to all of the studies reported to this date on homogeneous gas phase oxidation of methane, our results seem to be the most promising in that a methanol selectivity of 83% at a conversion level of 8% per pass could be obtained.

The high methanol selectivities observed in our experiments can be explained by the type of the reactor used and the reaction conditions employed in the study. Several workers (18,19) have identified surface reactions such as oxidation, decomposition of oxygenated products and coke formation to be responsible for the decrease in methanol selectivity. Surface reactions were found to be important in metal reactors, packed reactors and also at low reaction pressures (20). In our study, probably the surface reactions were of less importance due to the use of a glass lined and/or high pressure where diffusion to reactor wall would not be significant.

The proposed mechanism for the partial oxidation of methane at high pressure (12) suggests that the reaction between the peroxide radical CH_3O_2 and methane resulting in the formation of methylhydroperoxide and methyl radicals may compete strongly with the decomposition of the peroxide radical. The methylhydroperoxide radical then decomposes into methoxy and hydroxy radicals and methanol is formed by a reaction between the methoxy radical and methane. Hence, higher pressures favour the methanol selectivity and our results as shown in Table 1 support this view. Although in the present work the maximum reaction pressure employed was 65 atm, earlier experiments (6,21) showed that an increase in pressure to 125 atm had lower methanol selectivity. Thus at an oxygen concentration of 5% in the feed gas the methanol selectivity was found to decrease from 81% at 50 atm to 25% at 125 atm. The maximum methanol selectivity may occur between 65 and 125 atm and this has yet to be established.

CONCLUSIONS

In this study we showed that methanol selectivities of 75 to over 80% at 8 to 10% conversion levels per pass could be obtained during the partial oxidation of methane in the tubular reactor operated at about 65 atm, 450°C and a residence time of about 4 min. The methanol selectivity was observed to depend significantly on

the oxygen concentration in the feed gas and reaction pressure. Oxygen concentrations less than 5% and reaction pressure higher than 50 atm were found to be conducive for higher methanol selectivity.

ACKNOWLEDGEMENT

The authors are grateful to Energy, Mines and Resources, CANMET of Canada for providing the financial support during the entire study.

REFERENCES

1. Edwards, J. H., Foster, N. R., Fuel Science & Technology Int'l 4, 365 (1986).
2. Gesser, H. D., Hunter, N. R., Prakash, C. B., Chemical Reviews, 85, 235 (1985).
3. Foster, N. R., Appl. Catal., 19, 1 (1985).
4. Pitchai, R., Klier, K., Catal. Rev. Sci. Eng., 28, 13 (1986).
5. Liu, H. F., Liu, R. S., Liew, K. Y., Johson, R. E., Lunsford, J. H., J. Am. Chem. Soc., 106, 4117 (1984).
6. Hunter, N. R., Gesser, H. D., Morton, L. A., and Prakash, C. B., Proceedings of the VI International Symposium on Alcohol Fuels Technology, Ottawa, May 21-25 (1984).
7. Hunter, N. R., Gesser, H. D., Morton, L. A., and Fung, D. P. C., Proceedings of the 35th Canadian Chemical Engineering Conference, Calgary, Oct. 6-9 (1985).
8. Gesser, H. D., Hunter, N. R., Morton, L. A., U.S. Patent No. 4,618,732, Issued Oct. 21, 1986.
9. Yarlagadda, P. S., Morton, L. A., Hunter, N. R., and Gesser, H. D., Fuel Science & Technology Int'I (in press).
10. Newitt, D. M., Haffner, A. E., Proc. Roy. Soc. London, A134, 591 (1932).
11. Lott, J. L., The selective oxidation of methane at high pressure, Ph.D. Thesis, University of Oklahoma (1965).
12. Newitt, D. M., Szego, P., Proc. Roy. Soc. London, A147, 555 (1934).
13. Pichler, H., Reder, R., Angewandte Chemie, 46, 161 (1933).
14. Wiezevich, P. J., Frolich, P. K., Ind. Eng. Chem., 26, 267 (1934).
15. Boomer, E. H., Can. J. Res., 15B, 375 (1937).
16a. Boomer, E. H., Thomas, V., Can. J. Res., 15B, 401 (1937).
16b. Boomer, E. H., Thomas, V., Can. J. Res., 15B, 414 (1937).
16c. Brockhaus, R. and Franck, H.-J., Deutsches Patentant 2,743,113 (1979).
17. Mahajan, S., Menzies, W. R., Albright, L. F., Ind. Eng. Chem. Process Des. Dev., 16, 271 (1977a).
18a. Mahajan, S., Nickolas, D. M., Sherwood, F., Menzies, W. R., Albright, L. F., Ind. Eng. Chem. Process Des. Dev., 16, 275 (1977b).
18b. Mahajan, S., Nickolas, D. M., Sherwood, F., Menzies, W. R., Albright, L. F., Ind. Eng. Chem. Process Des. Dev., 16, 275 (1977b).
19. Lott, J. L., Sliepcevich, C. M., Ind. Eng. Chem. Process Des. Dev., 6, 67 (1967).
20. Chou, T. C., Albright, L. F., Ind. Eng. Chem. Process Des. Dev., 17, 454 (1978).
21. Gesser, H. D., Hunter, N. R., Morton, L. A., Prakash, C. B., The Production of methanol by the controlled oxidation of methane at high pressures, Final Report submitted to Energy, Mines and Resources Canada (1984).

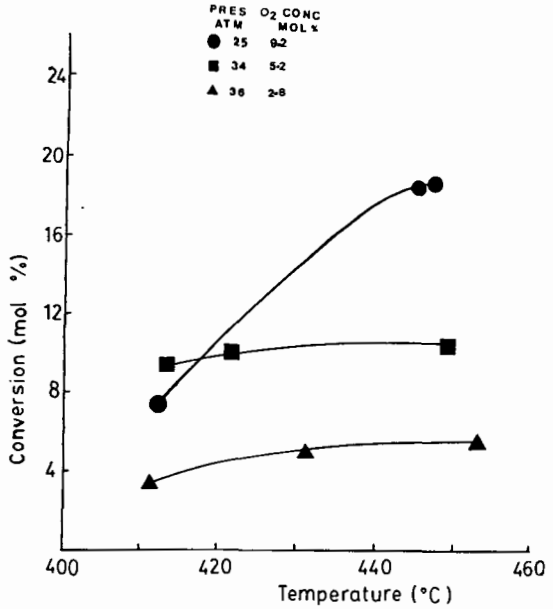

Figure 1. Effect of reaction temperature on conversion at different combinations of reaction pressure and oxygen concentrations in the feed gas.

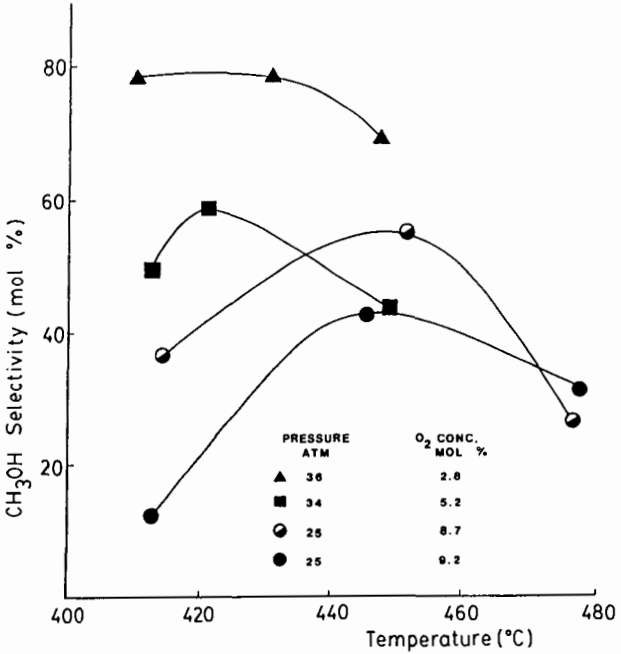

Figure 2. Variation in methanol selectivity with reaction temperature.

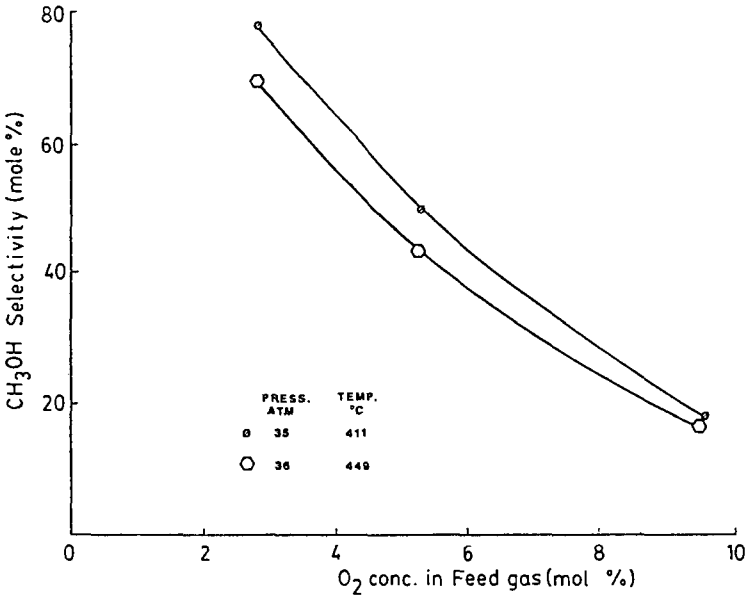

Figure 3. Effect of oxygen concentration in the feed gas on methanol selectivity.

Table I. The effect of varying reaction pressure on methanol selectivity at different oxygen concentrations in the feed gas.

Run #	Reaction Conditions			Residence Time	Conversion	Selectivity, mol%*			CH_3OH
	Temperature °C	Pressure atm	O_2 Conc. mol%	min	mol%	CH_3OH	CO	CO_2	Yield mol%
29	455	34.0	10.3	2.5	7.5	59.8	25.1	15.1	4.5
28	453	34.7	6.0	3.5	8.1	64.9	20.7	14.7	5.3
27	450	34.4	2.1	3.2	3.9	77.0	10.7	12.3	3.1
26	453	50.0	8.0	2.8	7.5	56.5	23.9	19.3	4.3
24	451	50.0	6.7	3.7	9.5	76.0	12.6	11.4	7.2
25	451	50.0	3.5	4.6	5.9	76.7	12.6	10.7	4.5
32	456	65.4	7.4	4.5	11.0	66.5	22.6	10.9	7.3
31+	456	65.3	5.1	4.1	8.0	83.0	10.7	6.4	6.6
33	468	65.6	2.6	3.7	5.3	81.5	9.6	8.9	4.3

*Average of at least 4 on-line analysis.
+Reducing the heated zone from 45 cm to 35 cm increased the CH_3OH selectivity to 84.5%.

Methane Polymerization Using a Hollow Cathode

Paul Meubus* and Gilles Jean**

*Université du Québec à Chicoutimi,
Qué. Canada G7H 2B1

**CANMET Laboratories, Ministry of Energy, Mines and Resources
Ottawa, Ontario, Canada K1A 0G1

Introduction

The polymerization of methane, or other low-molecular weight hydrocarbons, in the presence of electrical discharges or in low temperature plasmas, has been the subject of a large number of reports in the literature (1-3). Common features are the operation under vacuum and the production of radicals diffusing towards the reactor wall with subsequent polymerization to a solid product. The gas phase is generally composed of hydrocarbons up to C_5. The polymerization of hydrocarbons can be initiated through the positive-ion molecule type reaction and the radical molecule type reaction (4). The hollow cathode is a medium of high interest for generating a large concentration of highly energetic electrons, leading to the possible formation of CH_4^+ ions.

Preliminary results obtained in this lab (5-6) have shown that methane conversion can be effected using a hollow cathode as the source of polymer initiators. The present work investigates the effects on the process of the cathode metal used (Tungsten, Tantalum and a Tungsten-Platinum solid solution) as well as the influence on the yield of the gas used as a diluent (argon and helium).

Theory

Within the hollow cathode, an atom or molecule is ionized following energy transfers resulting from atom - electron collisions or charge transfer (7). With mixtures of Ar-CH_4 and He- CH_4, the ionization step of methane takes place according to the reactions:

$$Ar + e \rightarrow Ar^+ + 2e \qquad (1)$$
$$Ar^+ + CH_4 \rightarrow Ar + CH_4^+ \qquad (2)$$

Also, argon metastables $^3P_2$ (11.54 eV) and $^3P_0$ (11.72 eV) can be generated:

$$Ar + e \rightarrow Ar^* + e \qquad (3)$$
$$Ar^* + CH_4 \rightarrow Ar + CH_4^+ + e \qquad (4)$$

Similar reactions may occur with He* which presents a metastable level at 19.8 eV, this particle being then much more energetic than the argon metastables. The polymerization then proceeds following the equation:

$$CH_4^+ + CH_4 \rightarrow C_2H_n^+ + n/2\ H_2 \qquad (5)$$

the chain reaction yielding CmH+n. Termination of the process occurs when low velocity electrons are available:

$$C_mH^+_n + e \rightarrow C_mH_n \qquad (6)$$

The steps described are not unique and low velocity electrons can also lead to the formation of radicals, this likely occurring at the outlet of the cathode:

$$CH_4 + e \rightarrow CH_3^* + H^* + e$$

$$CH_3^* + CH_4 + H^* \rightarrow C_2H_6 + H_2 \qquad (7)$$

and the process continues through hydrogen abstraction.

Experimental

The reactor is shown in Figure 1. It consisted mainly of an arc discharge with a cylindrical hollow cathode 4 cm long and 0.2 cm thick. The cathode materials used were tungsten, a solid solution of tungsten and platinum and finally tantalum. The anode was made of stainless steel with a water-cooled tungsten discharge tip. The electrodes were located in a cooling chamber where the polymer obtained was collected on the water-cooled walls. A Varian 1015SL quadrupole mass spectrograph was used for the effluent gas analysis. High purity argon and chemical pure (99.9% purity) methane were used in mixtures up to 25% methane by volume. Depending on the experiment, the electrode gap was adjusted between 1.5 and 4.0 mm. The cathode furnace was adjusted to 2400°K while the arc discharge was started and the required methane flow added to the main argon stream. Further adjustments were then made in order to operate at the pre-determined conditions. The duration of an experiment was typically 10 minutes and the initial adjustments lasted about 30 seconds. At the end of the run, the polymer deposited on the cooled wall of the reactor was collected, together with the carbon appearing on the electrodes. They were weighed to the nearest ±0.1 mg.

Results and Discussion

The main product resulting from the conversion of methane using the hollow cathode is a solid polymer. Figure 2 illustrates the relationship between polymer yield, defined as weight of polymer/weight of methane fed, and E/P (E = electric field between electrodes, $V\text{-}cm^{-1}$; P= pressure, Torr). This yield is a function of the average electron energy. The maximum polymer yield is about 50% higher in helium than in argon, the corresponding E/P value for helium being about twice the one required for argon. The higher polymer yields obtained with helium are possibly related to a higher rate of formation of CH_4^+. For instance:

$$He^* + CH_4 \rightarrow CH_4^{++} + 2e \qquad (8)$$

$$CH_4^{++} + CH_4 \rightarrow 2\ CH_4^+ \qquad (9)$$

taking into account the presence of the highly energetic He^+ (ionization voltage 24.6V) and He^* (19.8V).

When Helium is used as diluent higher CH_4 concentrations do not seem to significantly affect the maximum polymer yield (Figure 3). In argon, increases in methane concentration lead to decreasing polymer yields as shown in Figure 4 curve 2 B. Higher polymer yields can be obtained at high concentration by increasing the cathode voltage. At high methane concentration only methane, acetylene and ethylene were found in the gas phase which is probably the result of propagation reaction steps having been interrupted by termination reactions with slow electrons or radicals recombination.

Another interesting feature observed in the case of CH_4/He mixtures is the complete absence of carbon deposits. The hydrocarbon species present are characterized by higher diffusivities in He than in Ar (8). This may be responsible for higher deposition rates of the hydrocarbon species present in the gas phase on the reactor wall. It could also, at least partly, explain the decreasing effect of competitive reactions leading to the formation of carbon when argon is used as a diluent gas.

Besides tungsten (work function Q_W = 4.6 eV), tantalum (Q_{Ta}= 4.1 eV) and a tungsten-platinum solid solution were used to study the influence of cathode material on polymer yield. The work function of the W-Pt cathode was evaluated to be 6.5 eV. This result compares rather closely with the 6.3 eV obtained for the Pt cathode.

These cathodes were tested with Ar+CH_4 mixtures. Figure 4 illustrates the comparative behaviour of W-Pt and W cathodes. For 10% CH_4 mixtures a high yield is obtained for the W-Pt cathode, the yield decreasing with increasing electrons energy (curve 1A). For the 25% CH_4 mixture the yield increases with increasing electron energy for both the W-Pt and the W cathodes (Curve 1B and 2B). Tungsten cathodes operating at the same conditions show significantly lower conversions, although the behaviour of yield vs E/P is the same (curves 2A and 2B).

The current density for the W-Pt cathode is estimated to be 10% that obtained with the W cathode. The drift velocity being similar in both cases, one would expect a lower electron concentration (of the same energy) for W-Pt cathodes. As a consequence, lower rates of formation of polymerization promotors and lower polymer yields should be obtained with the W-Pt cathode compared to the W cathode. To explain the higher yields observed the assumption is then made that the W-Pt cathode surface does play a catalytic role whose contribution increases as electron energy decreases (6). Figure 5 shows the relative behaviour of tantalum and tungsten cathodes. Although the thermoemissive characters of Ta and W are rather similar, tantalum does show only an increase in yield with a corresponding increase of electron energy (curve 1C, Figure 6).It is possible that catalytic effects are absent in this case, in opposition to the tungsten behaviour (curve 2A).

Conclusion

Using helium instead of argon in the polymerization of methane, by means of a hollow cathode, increases the rate of polymerization and suppresses carbon formation. These conclusions only apply to low methane concentrations (10%). Tungsten (1), tantalum (2) and a solid solution tungsten-platinum (3) have been used for making hollow cathodes. Besides being the site of highly energetic collisional processes, cathodes 1 and 3 seem to play a catalytic role in the formation of polymerization promoters. In this respect, cathode 3 shows high yields of polymer formation.

Acknowledgement

The authors are indebted to the Federal Ministry of Supply and Services and to the Federal Ministry of Energy, Mines and Resources Canada for financial support under contract no. 3ST23440-5-9233.

References

1. A.M. Millard, Techniques and Applications of Plasma Chemistry, J.R. Hollahan and A.T. Bell, eds. Wiley, New York (1974).

2. M. Shen, Plasma Chemistry of Polymers, Marcel Dekker, New York (1976).

3. H. Yasuda, Thin Film Processes, J.L. Vossen and W. Kern, eds., Academic Press, New York (1978).

4. C.E. Melton, J. Chem. Phys., 33, 647 (1960).

5. P. Meubus, Conversion du Méthane en Essence Automobile par Réactions en Cathode Creuse. Report to Can. Feder. Ministry of Energy, Mines and Resources (1986).

6. P. Meubus, Polymerization of Methane in a Hollow Cathode Discharge, 35th Canadian Chemical Engineering Conference, Calgary, Canada, October 6-9 (1985). Paper 7-63.

7. J.B. Hasted, Physics of Atomic Collisions, Butterworth, London (1964).

8. R.J. Jensen, A.T. Bell and D.S. Song, Plasma Chemistry and Plasma Processing, Vol. 3, 2, 1983.

Figure 1 Outside view of reactor

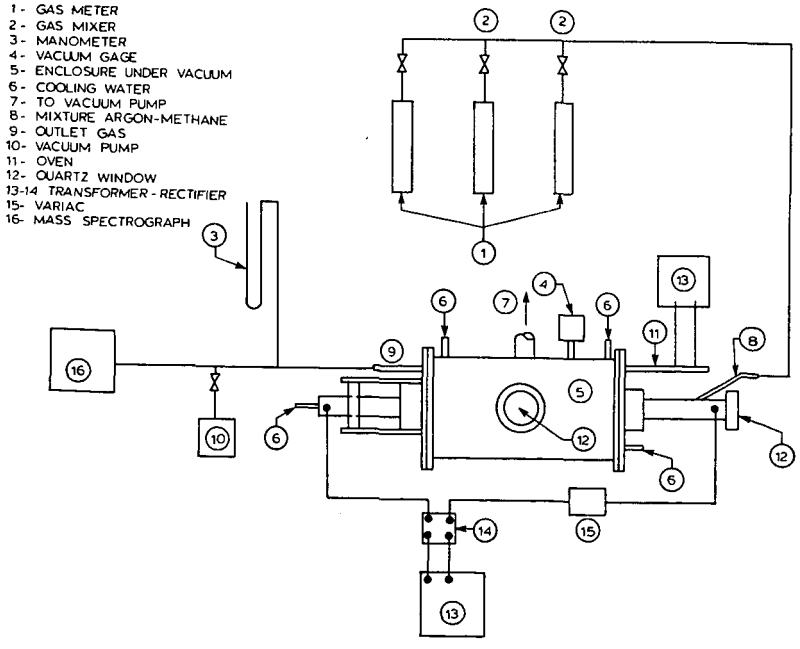

Figure 2. EFFECT OF GAS DILUENT

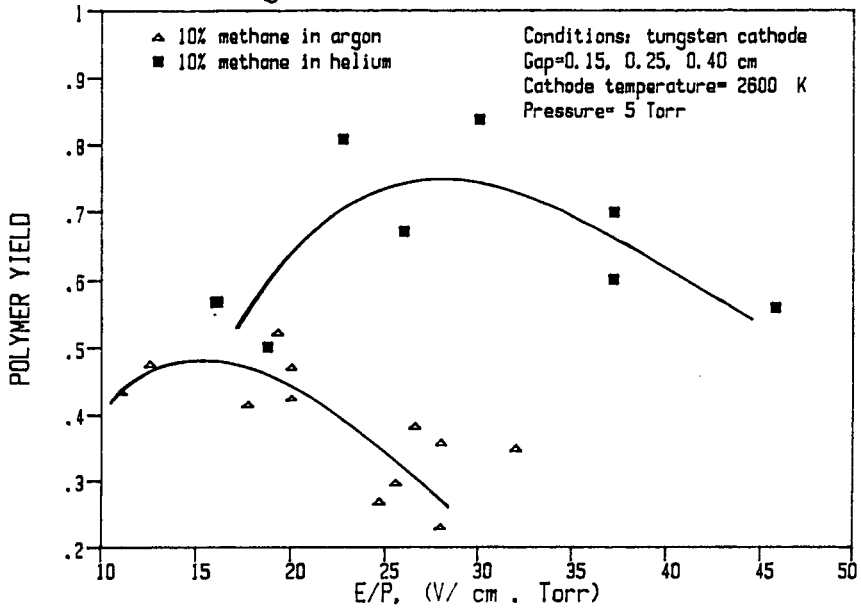

Figure 3. EFFECT OF METHANE CONCENTRATION

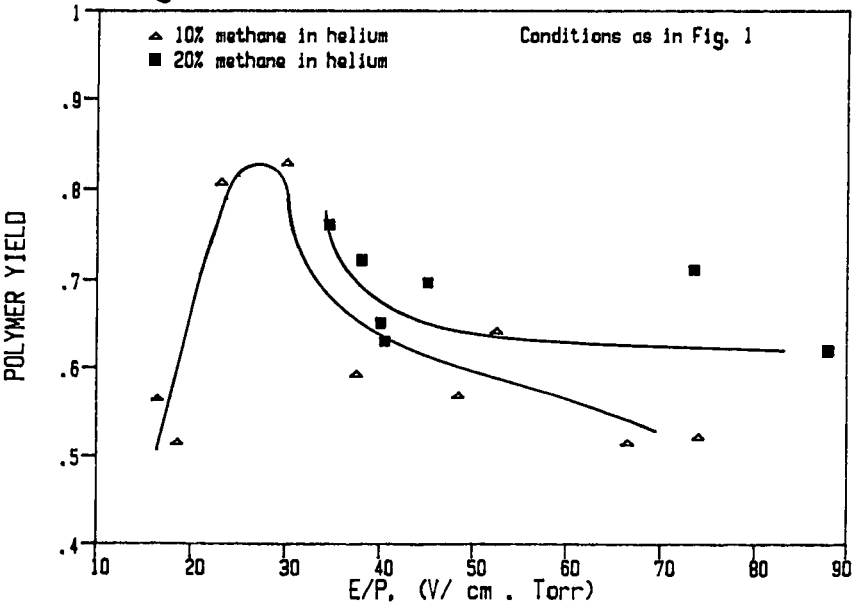

Figure 4. EFFECT OF CATHODE MATERIAL

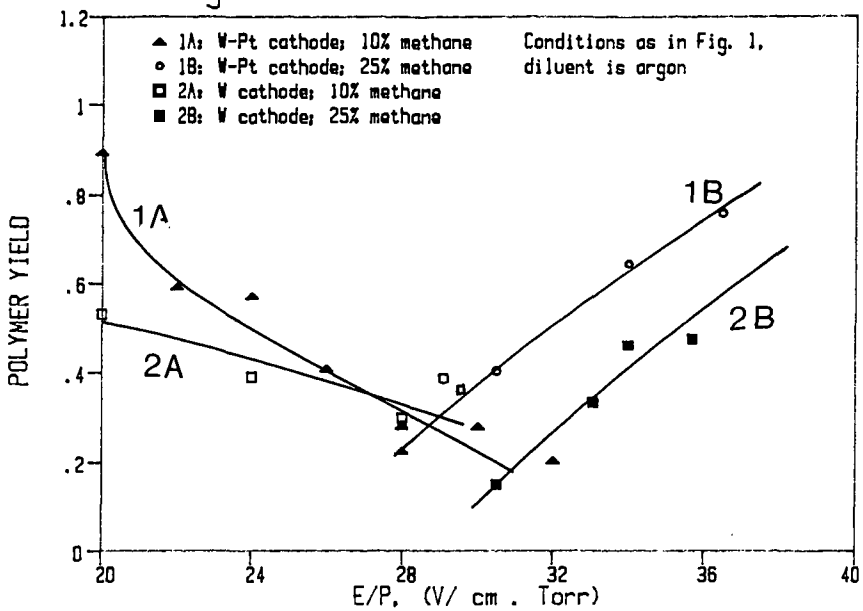

Figure 5. BEHAVIOR OF TANTALUM CATHODE

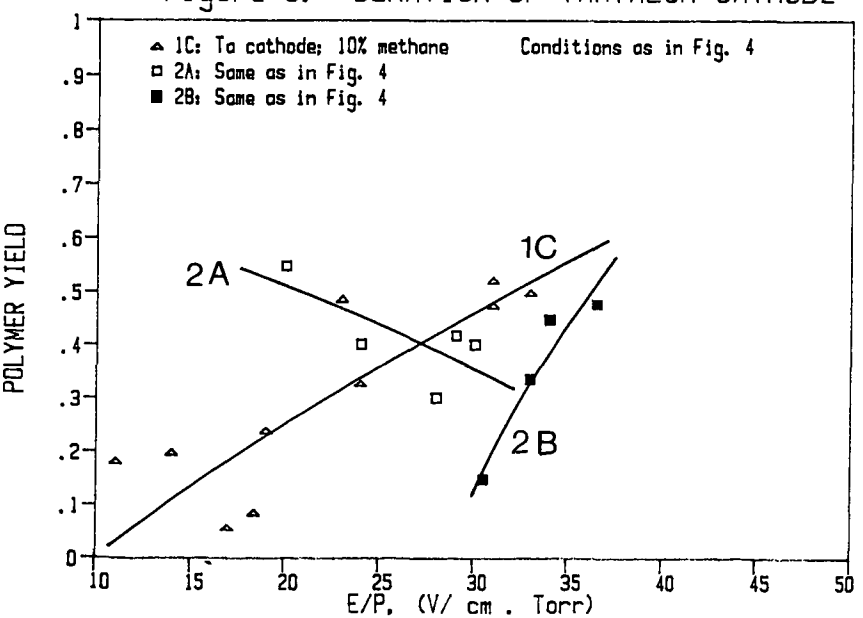

Methane Partial Oxidation in Alternating Electric Fields

R. G. Mallinson and C. M. Sliepcevich

School of Chemical Engineering and Materials Science
University of Oklahoma
Norman, Oklahoma 73019

S. Rusek

Technical Center
Owens-Corning Fiberglas
Granville, Ohio 43023

ABSTRACT

In this work, methane and oxygen mixtures have been oxidized to form methanol and smaller amounts of formaldehyde, methyl formate, formic acid and ethanol. Substantial amounts of water are also produced, as well as a small amount of ethane. The oxidation takes place at ambient conditions of temperature and pressure in an alternating electric field which is generated between cylindrical plates with a gap of 0.060 inches. Conversions were linearly dependent on the RMS voltage in experiments using up to 10 kV RMS. Among square, triangular, and sinusoidal wave forms, only small differences in performance were observed over the range of frequencies studied, from 25 to 200 Hertz. The effects of oxygen concentration, space time, frequency, and field plate area have also been examined on a limited basis. The power consumption to the power supply has been measured to determine the efficiency of this system, in which substantial heat is released. The yield of methanol is from seven to nine percent of the methane converted in which methane conversions of five to ten percent are obtained when an oxygen limited feed is used. Substantial amounts of the methane converted appear as carbon monoxide and carbon dioxide, both of which are somewhat inhibited by operation with the oxygen limited feed, although product inhibition during recycle experiments was not observed.

INTRODUCTION

There is currently a great deal of interest in the production of organic oxygenates via partial oxidation. Of particular interest is the conversion of methane to liquid fuels such as methanol, as well as the synthesis of other single and multiple carbon products such as formaldehyde, ethanol and acetic acid. Most current research involves the use of heterogeneous catalysts (1), although there has been some effort in examining thermal routes (2). It is only in the relatively old literature that the partial oxidation of methane in the presence of electric fields appears.

EXPERIMENTAL

The experimental reaction system was operated in three different configurations, however most of the results of this paper were obtained in the single pass mode. Figure 1 illustrates this configuration. Oxygen and methane are fed through individual rotameters and mixed and then flow to the reacto inlet. The reactor is the reaction vessel from an OREC model 03V5-0 ozone generator. The outer shell is a stainless steel cylinder with an outlet at the bottom. This shell serves as one electrode. The inside diameter of this outer shell is 77 millimeters. Within this shell, a glass tube is fitted which has a sealed bottom and the inner electrode which covers the inside surface of the glass tube. The gap between the outer wall of the glass tube and the inner wall of the shell is nominally 1.5 mm. Thus the

"active" reactor volume is in the shape of an annulus with an axial length of 332 mm. No analysis of the mixing characteristics was conducted, but it may be expected that there is some degree of backmixing. The volume of the reactor, between the electrodes, is about 118 cc, and the electrode area about 787 square centimeters. (The last experiment was conducted with one half of this plate area.) The outer shell has a water jacket made of PVC for control of the temperature by use of a water recirculation system or tap water.

After the gases have passed through the reactor, they pass through a dry ice/acetone trap to remove any condensable products. Following this, a small portion of the stream is diverted to a paramagnetic oxygen analyzer and, for later experiments, to a Carle gas chromatograph for analysis of the gaseous reactants and products. The thermal responses for all species detected were calibrated with known standards.

Power to the electrodes is provided by an Elgar AC power supply and a Wavetek function generator is used to generate the triangular wave used in the experiments discussed here. An oscilliscope is used to monitor the waveform, voltage level and frequency. A digital voltmeter is also used to monitor the RMS voltage.

A few experiments were run in a recycle configuration, illustrated in Figure 2. Mass flow controllers were used to add methane and oxygen to the system in a make-up gas stream. A Cole-Parmer diaphragm pump was used to recirculate the gas stream, with a bypass valve to maintain pressures slightly above atmospheric in all parts of the system.

RESULTS AND DISCUSSION

Initial runs were conducted at conditions previously established as optimal for a standard set of conditions (3). The feed flow rate was 566 cc/min at 71 ° F with a composition of 24.4 volume percent oxygen and 75.7 percent methane at a pressure of 12 inches of water. The reactor was maintained at 155 ° F. The electric field was maintained at 8 kV RMS at a frequency of 200 Hz using a triangular waveform. Under the standard conditions, the conversion of methane was about 15 percent and that of oxygen about 24 percent. Replicate experiments showed that the conversions of methane and oxygen varied ± 15 percent and ± 10 percent, respectively. The fractional yields of the primary liquid products under these conditions, water and methanol, were about .07 for methanol and .33 for water. The fractional yield is defined as the moles of a product produced per mole of methane reacted. This is used for water even though it is not a carbon based product. Thus about 7 percent of the methane converted formed methanol. Although methanol was the primary product, smaller amounts of other one and two carbon oxygenates were also formed. These products include formaldehyde, ethanol, methyl formate and formic acid. Qualitative GC/MS data showed the presence of numerous other compounds in minute quantities.

Run 4 was conducted to determine the variation on the oxygen conversion with changes in the field voltage. The oxygen concentration in the exit stream was used as an indicator of reactivity before more detailed analyses were made with later runs. In this experiment, the field was increased in increments from zero volts and allowed to equilibrate for several minutes. No decrease in the exit gas oxygen concentration was observed below 5 kV. At and above 5 kV the steady state oxygen concentration in the exit gas stream decreased linearly with increasing voltage. The system could attain a maximum RMS voltage of about 8kV at a frequency of 200 Hz. At 8 kV, the exit oxygen concentration was about 19.5 percent, or a conversion of 22 percent. A later run, run 25, was made to assess the effect of the frequency on the conversion and this, too, was found to be linear with decreased conversions at lower frequencies. In this run, the line power to the power supply was monitored and at a frequency of 50 Hz, the power consumed was approximately 30 percent of that at 200 Hz. The power used at 200 Hz was 350 Watts. There did appear to be some selectivity enhancement under these

conditions, as the methanol produced had decreased to about 43 percent of its amount at 200 Hz. However, the decrease in conversion would have a significant influence on the optimal frequency for operation.

Because significant amounts of carbon dioxide and water were produced, as well as the desired organic oxygenates, it was desirable to see if these might be inhibited by introduction of these species to the inlet stream of the reactor. Depending on the kinetics, it might be expected that significant quantities of these two species might drive the equilibrium in a favorable direction. In run 19, the inlet mole fraction of oxygen was reduced to .188 and a mole fraction of carbon dioxide of .085 was added, with the balance methane and the total inlet flow rate 485 cc/min. No differences could be detected in the results compared to runs at standard conditions, thus indicating that no equilibrium constraint appears to be limiting for carbon dioxide.

Run 20 was similar to run 19 except that an inlet mole fraction of water of .021 was used instead of the carbon dioxide. The water was added by saturating the inlet gas stream through a bubbler assembly. As with run 19, no remarkable results were observed here.

Although the reactor was being heated to 155 ° F, no work had previouly been done to determine the effect of temperature on the reactions. Run 14 was made at ambient temperature, and it was observed that no effects due to the lower temperature were present. All runs subsequent to run 14 were, therefore, made at ambient temperature. It was noted that, in fact, significant quantities of heat were generated and a stream of cooling water was passed through the reactor water jacket to maintain ambient conditions. Measurements of the temperature rise of the cooling water through the jacket and its flow rate were made on several occasions. Although the accuracy may be considered poor, it appears that a significant fraction of the input power to the system may be dissipated as heat.

Because of the complete oxidation of a fraction of the methane to carbon dioxide, several experiments at lower increments of inlet oxygen concentration were made. The lowest concentration examined was about 1 percent oxygen. In run 23, the inlet mole fraction of oxygen was .012. The power required to maintain the 8 kV field increased somewhat, to 377 Watts. The conversion of the methane decreased substantially to .059, and the small amount of oxygen was about 49 percent converted. The yield of methanol remained near the standard value, about .073. The yield of water was substantially reduced, to .125, as might be expected with significantly less oxygen available. Interestingly, ethane now became a significant product from the methane. This would certainly indicate active methyl species participating in the reaction sequence. Another reactor configuration was used for one run, in which only the oxygen was passed through the reactor. This stream was then immediatlely mixed with methane to determine whether only active oxygen species, primarily ozone, might be the primary locus of the reactions. No reaction at all was observed in this case, and the literature on ozone chemistry agrees with the inability of ozone to significantly attack methane. Clearly the observed reactions indicate direct participation of active methane species.

A last standard experiment was made with one half of the inner electrode plate area. The results indicated that, while conversions tracked the decrease in the area, the power did not decrease by 50 percent. Thus, the inverse extrapolation for scale up would be that a 100 percent increase in the plate area, suitably configured, would result in a doubling of the quantities converted, but at less than a doubling of the power requirement, which is a favorable conclusion. The quantity of power used as "overhead" in the power supply was not determined. Attempts to measure the actual power used in the reactor field were unsuccessful, but it has already been mentioned that substantial heat was generated.

In the recycle configuration, two experiments were made. The only difference between them was the recycle flow rate. The carbon dioxide absorber shown in Figure 2, was not used for these runs. For run 29, the recycle flow rate, including make up gas, was 2.1 l/min, and for run 30, 1.0 l/min was used. The composition of gas entering the reactor was .005 mole fraction oxygen, once the reaction

had been underway for a short time. A material balance on the carbon and oxygen was made at the end of each run. The condensed products could only be removed after the system was shut down. The carbon balance was able to account for 73 percent of the carbon in the methane cumulatively provided to the system, initially and during the run. At the end of a ninety minute run, for run 30, about 112 millimoles of carbon, as methane, had been fed to the system, of which about 55 remained in the system or was lost in the GC bleed stream. About 2.6 millimoles of carbon went to produce ethane, about 4.7 as carbon dioxide and 5 as carbon monoxide. 15 millimoles of methanol were produced, but other organic compounds were not quantified and could be approximately 5 more millimoles. Thus, in this initial system configuration, approximately 13 to 17 percent of the methane used was converted to useful products. It may be that better material balances will enhance that figure to some extent.

On line GC analysis of the gases showed that ethane increased to a maximum of 1.2 and 1.4 millimoles in the system for the two runs, with the lower recycle rate having the higher maximum. Both maxima occurred about 40 minutes into the run, afterwhich the concentrations both decreased by about 0.2 millimoles at the end of the 90 minute runs. Ethane, therefore appears to exhibit an equilibrium behavior. The carbon monoxide produced showed an induction period for the first 20 minutes, then continued increasing until the end of the run. Both experiments had virtually the same amount of carbon monoxide. Carbon dioxide increased linearly with time after also showing some induction during the first 20 minutes of the runs. However, the carbon dioxide produced at the higher recycle rate was significantly higher. At the end of the runs, the 2.1 l/min recycle rate had produced 6 millimoles of carbon dioxide, while the lower recycle rate had produced 4.7. One might think that the shorter contact time of the higher recycle rate would serve to minimize larger extents of oxidation.

The oxygen balance was able to account for 87 percent of the oxygen fed to the system. It might be noted that the oxygen conversion per pass was essentially 100 percent, and that higher inlet concentrations might alter the results obtained. Of the 40 millimoles of oxygen provided during the run, 5 appeared as carbon monoxide, 9.4 as carbon dioxide and 12 as water. Methanol accounted for 7.5 millimoles of the total.

The most significant result of the recycle experiments was that the percent methanol in the liquid product increased from one percent in the single pass runs to 12 percent for the recycle runs. Water concentration also increased, however.

Lastly, mention should be made that a number of other single pass experiments were conducted, both in search of other interesting reactions and in attempting to elucidate the reaction pathways of the methane-oxygen system. These runs were made at the standard conditions except that the species of the feed mixtures were altered. Mixtures examined were: carbon dioxide-methane, carbon monoxide-methane, hydrogen-nitrogen and carbon monoxide-hydrogen. Except for a trace amount of material produced from the carbon dioxide-methane mixture, no reactions were detected.

SUMMARY

The results from a number of scoping runs examining a number of variables have been presented for the oxidation of methane in an alternating electric field. Several features of these results point the way to further needed experiments to determine the possibilties for production of light organic oxygenates from this process. Fundamental studies to determine the mechanistic paths would also be useful to help focus further research on the optimal conditions for maximizing the yields of desirable products and for determining the economic potential of the process.

ACKNOWLEDGEMENTS

This work was funded by Owens-Corning Fiberglas. We wish to thank John Olinger, Jim Wintgens and Dick Fowler for helpful discussions. Also, Jim Wintgens was involved in the

developmental work which led to this research.

REFERENCES

(1) Pitchai, R. and K. Klier, *Catal. Rev.-Sci. Eng.*, **28,** 13 (1986).

(2) Luckett, G. A. and B. Mile; *Combustion and Flame*, **26,** 299 (1976).

(3) Rusek, S. and J. Wintgens, unpublished results (1985).

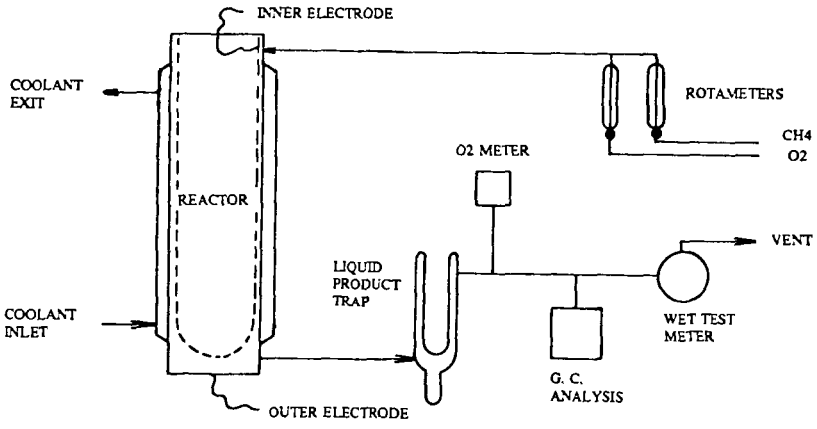

Figure 1. Single pass reactor system.

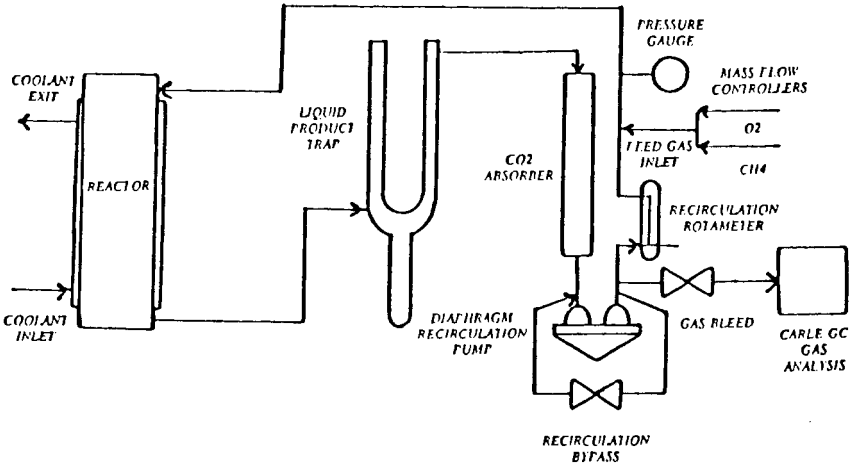

Figure 2. Recycle Reactor System.

NICKEL SITE OF METHANE CATALYSIS IN THE METHYL REDUCTASE ENZYME

J. A. Shelnutt, A. K. Shiemke,* R. A. Scott*

Sandia National Laboratories, Albuquerque, NM 87185
*University of Illinois, Urbana, IL 61801

Introduction

Methyl reductase is the enzyme of methanogenic bacteria that catalyzes the two-electron reduction of the methyl group of 2-(methylthio)ethanesulfonic acid (methyl-S-CoM) to methane and HS-CoM (1,2). The methyl group of methyl-S-CoM ultimately comes from the six-electron reduction of CO_2 by hydrogen, which also provides the reducing equivalents needed by methyl reductase. The nature of the catalytic site of methyl reductase is of current interest from the point of view of developing biomimetic C_1 chemistries directed toward methane synthesis and activation. In particular, Sandia is using molecular graphics and energy optimization techniques to design macromolecular catalysts that mimic the structure of sites of proteins that carry out C_1 chemistry. The goal is to produce catalysts whose function is the oxidation of low molecular weight hydrocarbon gases to generate liquid fuels or, alternatively, the reduction of abundant inorganic resources such as CO_2 to generate gaseous fuels. Unfortunately, the catalytic sites of many of the enzymes of interest, e. g. methyl reductase and methane monooxygenase, have not been characterized by X-ray crystallography and other structural techniques.

With the goal of learning more about the structure of one of these naturally occurring sites of C_1 chemistry, we have obtained the first resonance Raman spectra of the nickel-macrocycle, called F_{430} (1 in Figure 1), at the site of catalysis in methyl reductase (3). To help us structurally interpret the Raman spectra of the enzyme we have also obtained Raman spectra of solutions of the major forms of F_{430} (salt-extracted and cytosol-free) at room temperature and at 77 °K and also, under similar solution conditions, spectra of a nickel-corphinoid derivative (2 in Figure 1) that is related to F_{430} (3-5). By analogy with the spectra of the model nickel-corphinoid 2, the F_{430} Raman spectra characterize the coordination geometry of the nickel(II) ion in F_{430} complexes in coordinating and non-coordinating solvents. In addition, the spectra give some information concerning macrocycle ruffling in the solution complexes. Although some conclusions about the F_{430} site in methyl reductase can be made, the structure of F_{430} in the protein environment is uniquely different from F_{430} and the F_{430} model compound in the solutions we have investigated.

Materials and Methods

Methyl reductase was prepared and purified as described previously (6). F_{430} was isolated in two forms. Free F_{430} was isolated from the cytosol by methods described before (7); F_{430} was also extracted from the holoenzyme using a lithium-bromide procedure (6). The structure 1 of salt-extracted F_{430} has been determined (8) and is shown in Figure 1. A nickel-corphinoid derivative related to F_{430} and shown in 2 of Figure 1 was kindly provided by A. Eschenmoser, A. Pfaltz, and A. Fässler (9).

Samples of each chromophore ($2\text{-}10\times10^{-5}$ M) in aqueous solution buffered with 10 mM phosphate at pH 7 were used for obtaining resonance Raman spectra. Spectra of liquid solutions were obtained using a cylindrical cell partitioned into two compartments. The spectra of two samples were obtained simultaneously by rotating the cell at 100 Hz so that the two sample solutions were alternately probed by the laser radiation. The Raman difference instrumentation used for

detection and separation of the spectra of the two samples has been described previously (10). Peak positions were obtained from the fast-Fourier-transform smoothed spectra. For spectra run simultaneously the accuracy when comparing the frequency of the same Raman line in the two spectra is about ± 0.3 cm^{-1}. Occasionally, the solution of F_{430} or the corphinoid derivative was in one side of the cell and the reference side contained only the neat solvent. Subtraction of the solvent Raman lines could then be accurately accomplished leaving the spectrum of only the solute.

Raman spectra at 77 °K were not obtained in the Raman difference mode, but separately using an EPR dewar with a transparent tail (Wilmad). The sample was contained in a 4-mm NMR tube and was frozen by plunging the tube into liquid N_2. Reproducibility in the frequency of lines in these spectra are about 1 cm^{-1}.

Signal averaged Raman spectra were obtained using the 441.6-nm line of a HeCd laser (Omnichrome) or the 413.6-nm line of a krypton ion laser (Coherent). The spectral resolution was 4 cm^{-1}. Raman difference spectra were obtained using standard 90° scattering geometry; for spectra of frozen solutions a backscattering geometry was used. Absorption spectra as well as individual scans of the Raman spectrum were used to monitor sample integrity. No decomposition of F_{430} or the nickel-corphinoid model was observed.

Results

F_{430} and the model nickel-corphinoid complexes have an absorption band in the 410-440-nm region of the visible spectrum (9,11). Therefore, excitation of the Raman spectrum using 441.6-nm or 413.1-nm laser light is near the visible absorption band and, consequently, resonance enhancement of the Raman scattering occurs. In the case of the enzyme, resonance enhancement of the chromophore's spectrum permits us to selectively probe the macrocyclic cofactor without interference from the Raman spectrum of the protein matrix. Structural details of the F_{430} site in the protein can then be inferred from differences between the spectrum of protein-bound F_{430} and the spectra of F_{430} complexes in various solution environments. The spectra of all of the complexes are somewhat similar regardless of the position of the laser wavelength relative to the absorption band maximum of the particular complex. In fact, the frequencies and intensities of the lines are so similar that the corresponding lines in each of the spectra can easily be identified as can be seen in Figures 2-4. The Figures show typical spectra of salt-extracted F_{430}, cytosol-free F_{430}, and methyl reductase.

Figure 2 shows the Raman spectrum of LiBr-extracted F_{430} at room temperature and at 77 °K. Two forms are present at room temperature. Form A has Raman lines at 1293, ~1380, 1534, and (from other Raman data not shown) ~1625 cm^{-1}; the second form B has lines at higher frequencies—1312, ~1382, 1555, and 1629 cm^{-1}. At low temperature form A disappears and only B remains.

Free F_{430} at room temperature is predominantly a single form with Raman lines at 1293, 1387, 1529, and 1623 cm^{-1} (Figure 3). The frequencies are similar but distinct from the corresponding lines of the A form of salt-extracted F_{430}. There is also some evidence of a small fraction of a form with lines near those of the B form in the weak shoulders of the high frequency lines. At low temperature this form is more abundant as evidenced by the appearance of lines at 1311, 1378, 1546, and 1616 cm^{-1} that are barely noticeable in the room temperature spectrum. There is also evidence for a second form at low temperature in the lines at 1292 and 1628 cm^{-1}. It is clear that this form is not the same as the one present at room temperature because the 1529-cm^{-1} line is not present or else is shifted to near 1546 cm^{-1}.

The Raman spectrum of methyl reductase at room temperature is markedly different from both the spectrum of salt-extracted F_{430} and free F_{430}. (Compare the spectra in Figure 4 with the corresponding spectra in Figures 2 and 3.) First, the Raman lines are clearly much narrower than for the solution F_{430} complexes. Second, frequencies of the two strong lines at 1575 and 1653 cm^{-1} are much higher than the corresponding lines of the F_{430} species. In contrast, the lines in the 1280-1400-cm^{-1} region of the methyl-reductase spectrum have frequencies comparable to F_{430}.

Differences between room temperature and 77-°K spectra of methyl reductase are much smaller than observed for F_{430} in solution. Increases in the intensity of the lines at 1312, 1553, and 1632 cm^{-1} indicate an enhanced fraction of a form of F_{430} with frequencies closest to those of salt-extracted F_{430} at 77 °K.

Discussion

Raman spectra of the F_{430} forms and the F_{430} model compound 2 are similar. For example, the nickel-corphinoid bis-methanol complex has several weak lines in the 1280-1400-cm^{-1} region and two strong lines at 1556 and 1627 cm^{-1} (4). Thus, the frequency of the lines and the intensities are similar for F_{430} and the model compound. The spectral similarities indicate that the nickel corphinoid 2 is generally a good structural model for F_{430} forms.

In previous work it was noted that the two strong highest frequency lines shift systematically with increasing coordination number (4). For example, the separation between the two lines decreases from 93 cm^{-1} for the 4-coordinate species (in CH_2Cl_2) to 84 cm^{-1} for a 5-coordinate NCS^- complex (in CH_2Cl_2) and to 71 cm^{-1} for the 6-coordinate MeOH complex. In fact, for a variety of solvents that axially ligate, the 6-coordinate separation is found to be 71±3 cm^{-1} (5). Ruffling of the corphinate macrocycle may also influence the separation (vide infra).

Salt-extracted F_{430}. Assuming that the separation of the two strong lines is indicative of coordination number for F_{430} as well as the model, we predict that aqueous salt-extracted F_{430} is a mixture of a dominate 6-coordinate complex referred to above as species B (with a separation of 1629 − 1556 = 73 cm^{-1}) and a minor 4-coordinate species A (with a separation of 1625 − 1534 = 91 cm^{-1}). Indeed, the separation varies from 62-75 cm^{-1} for F_{430} 6-coordinate complexes in other coordinating solvents (5). The existence of a mixture of a 6-coordinate high-spin species and a 4-coordinate S=0 species is supported by the intermediate value found for the magnetic moment (2.0 μ_B for F_{430} versus ~2.8 μ_B predicted for a pure S=1 species) (12).

The axial ligands are probably H_2O molecules rather than some component left bound to F_{430} after extraction from the protein. Water is a weak ligand which would account for the equilibrium mixture at room temperature. At 77 °K the equilibrium shifts overwhelmingly toward the bis-aquo F_{430} complex.

Cytosol-free F_{430}. Water appears to be a poorer ligand for free F_{430} than for the salt-extracted form, since at room temperature aqueous free F_{430} is almost entirely a 4-coordinate form. This conclusion is based on an observed separation of the strong high frequency lines of 94 cm^{-1}—a value close to the separation for the 4-coordinate model compound 2. By comparison, in strongly coordinating solvents and in the presence of CN^-, free F_{430} converts to a 6-coordinate form with a separation of 63-77 cm^{-1} (5).

At 77 °K free F_{430} appears to be a mixture of two forms with lines at 1616 and 1628 cm^{-1}. The separations of the 1616- and 1628-cm^{-1} lines from the 1546-cm^{-1} line are 70 and 82 cm^{-1} for the two forms. EXAFS and XAS measurements at 4 °K are consistent with free F_{430} (the same as heat-extracted F_{430}) existing as a mixture of predominantly a 4-coordinate, ruffled species with short Ni-N bonds (1.9 Å) and a minor 6-coordinate, planar species with longer Ni-N bonds (2.1 Å) (13). The Raman data is in agreement with this result. The species with the 70-cm^{-1} separation is probably the coordinated species and the 82-cm^{-1} separation species would then be the more abundant 4-coordinate, ruffled species. A 5-coordinate complex is unlikely for a nickel corphinate in a coordinating solvent where two axial ligands would be readily available and formation of the 6-coordinate complex would be favored. Alternatively, the two species could be different ruffled species, for example, the two species obtained by a 90 ° rotation of the saddle structure resulting from S_4 ruffling and inversion of the half chair conformation of the hydropyrrolic rings (12,15).

Comparison of the F_{430} forms. Eschenmoser and coworkers have suggested that the sole difference between free and salt-extracted forms of F_{430} is a di-epimerization at positions 12 and 13 in which the hydrogen and carboxylic acid at each position exchange places (12). The structural change also occurs upon heating salt-extracted F_{430} or upon heat-extraction of F_{430} from methyl reductase. The 12,13-diepimer of salt-extracted F_{430} results in a corphinate structure that can undergo S_4 ruffling more readily than F_{430} for steric reasons. Ruffling affects axial ligation because it allows the central core of the macrocycle to contract about the nickel ion. Thus, salt-extracted F_{430} is more coordinatively unsaturated at the nickel ion as a result of its larger core size, and, therefore, has a higher affinity for axial ligands than free F_{430} which can easily ruffle.

The Raman results are in agreement with this structural interpretation. At room temperature salt-extracted F_{430} is mostly the 6-coordinate bis-H_2O complex, whereas free F_{430} at room temperature is 4-coordinate based on the Raman results. Further, the fraction of salt-extracted F_{430} that is 4-coordinate has a Raman spectrum that is distinct from 4-coordinate free F_{430} based on the Raman line frequencies. For example, the 1534-cm^{-1} line of salt-extracted F_{430} is at 1529 cm^{-1} for the diepimer. This difference is probably solely the result of the rearrangement of the substituents at the 12 and 13 positions of the corphinoid macrocycle.

Methyl reductase. The narrowing of the Raman lines of methyl reductase is most likely a result of greater homogeneity at the F_{430} site in the protein environment relative to the solution environment of the F_{430} forms. This indicates a very specific structure for the F_{430} site in the protein.

It is also clear from the large differences in frequency that the chromophore or its environment is unique in some way. The uniqueness may be a result of (1) a novel coordination geometry, (2) an unusual corphinate ligand conformation, or (3) a difference between the structure of the chromophore's peripheral substituents in the native protein and after salt extraction. We have observed that no oxygen, sulfur, or nitrogen ligand complex has come close to giving the frequencies observed for the two strong high frequency lines of methyl reductase. The separation of (1653 - 1575 =) 78 cm^{-1} for methyl reductase is however compatible with either 5- or 6-coordination although so far no ligand examined gives the high frequencies observed for these Raman lines. Thus, the second and third possibilities mentioned above should not be ruled out.

At 77 °K a form similar to the aqueous 6-coordinate form of salt-extracted F_{430} is beginning to make an appearance. At 4 °K the Ni X-ray absorption edge is

similar for methyl reductase and salt-extracted F_{430} (14). Thus, at 4 °K the salt-extracted F_{430} form may predominate in the protein.

Conclusions

The nickel-tetrapyrrole derivative in the methyl-reductase enzyme resides in a unique protein environment. We have not yet been able to find an equivalent structure for F_{430} in solution based on the Raman spectra. Nevertheless, the Raman data suggest that F_{430} in the protein has at least one axial ligand and occupies a site in the protein with a low degree of heterogeneity.

The free form of F_{430} shows evidence of ruffling in that multiple forms are observed in the low temperature Raman spectrum and the species cannot all be ascribed to axial ligand complexes. This low temperature behavior is also noted for the model nickel-corphinoid in non-coordinating solvents such as methylene chloride (5). On the other hand, salt-extracted F_{430} shows no evidence of ruffling, but displays higher affinity for axial ligands than the diepimer.

It is thought that the axial coordination sites of nickel may serve as a binding site for methyl-S-CoM or perhaps the methyl group that is reduced to methane in the reaction. Nickel corphinoids are known to have higher affinity for axial ligands than nickel porphyrins (15) and the unusual affinity may play a role in methane catalysis. The nickel corphinoids also exhibit different behavior in the photolysis of axial ligands than the nickel porphyrins (16). A Ni(I) intermediate may be involved in the reduction of the bound methyl group to methane (17).

Macrocycle flexibility may also play a role in methane catalysis as has been proposed for vitamin B_{12} (Co-corrin) enzymes involved in biological methyl-transfer reactions (18,19). In these reactions an axial Co-CH_3 complex is known to be an intermediate. Efforts to further elucidate the roles of axial ligation and macrocycle flexibility in the catalytic properties of F_{430} in methyl reductase are continuing using resonance Raman and transient Raman spectroscopic techniques.

Acknowledgements

We thank Professor Albert Eschenmoser for kindly providing the model F_{430} complexes. This work performed at Sandia National Laboratories and supported by the U. S. Department of Energy Contract DE-AC04-76DP00789 and the Gas Research Institute Contract 5082-260-0767.

REFERENCES

1. Wolfe, R. S., Trends Biochem. Sci. 1985, **10**, 396.
2. Hartzell, P. L.; Wolfe, R. S., Proc. Natl. Acad. Sci. USA 1986, **83**, 6726.
3. Shiemke, A. K.; Scott, R. A.; Shelnutt, J. A., J. Am. Chem. Soc. 1987, submitted.
4. Shelnutt, J. A., J. Am. Chem. Soc. 1987, in press.
5. Shelnutt, J. A. unpublished results.
6. Ellefson, W. L.; Wolfe, R. S., J. Biol. Chem. 1981, **256**, 4259.
7. Gunsalus, R. P.; Wolfe, R. S., J. Biol. Chem. 1980, **255**, 1891.
8. Pfaltz, A.; Juan, B.; Fassler, A.; Eschenmoser, A.; Jaenchen, R.; Gilles, H. H.; Diekert, G.; Thauer, R. K., Helv. Chim. Acta 1982, **65**, 828.
9. Fässler, A.; Pfaltz, A.; Kräutler, B.; Eschenmoser, A., J. Chem. Soc. Chem. Commun. 1984, 1365.
10. Shelnutt, J. A., J. Phys. Chem. 1983, **87**, 605.
11. Livingston, D. A.; Pfaltz, A.; Schreiber, J.; Eschenmoser, A.; Ankel-Fuchs, D.; Moll, J.; Jaenchen, R.; Thauer, R. K., Helv. Chim. Acta 1984, **67**, 334.

12. Pfaltz, A.; Livingston, D. A.; Jaun, B.; Diekert, G.; Thauer, R. K.; Eschenmoser, A., Helv. Chim. Acta 1985, **68**, 1338.
13. Eidsness, M. K.; Sullivan, R. J.; Schwartz, J. R.; Hartzell, P. L.; Wolfe, R. S.; Flank, A.-M.; Cramer, S. P.; Scott, R. A., J. Am. Chem. Soc. 1987, in press.
14. Shiemke, A. K.; Scott, R. A., unpublished results.
15. Eschenmoser, A., Ann. N. Y. Acad Sci. 1986, **471**, 108.
16. Ondrias, M. R.; Findsen, E. W.; Crawford, B. A.; Shelnutt, J. A., J. Am. Chem. Soc. 1987, submitted.
17. Juan, B.; Pfaltz, A., J. Chem. Soc. Chem. Commun. **1986**, 1327.
18. Wood, J. M. in "B_{12}" Vol 2, ed. Dolphin, D., Wiley: New York, 1982, p.151.
19. Geno, M. K.; Halpern, J., J. Am. Chem. Soc. 1987, **109**, 1238.

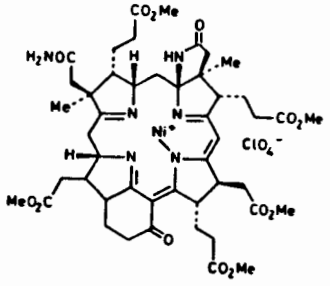

1

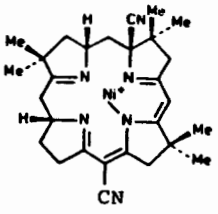

2

Fig. 1. Structures of F_{430} (1) and the model nickel–corphinoid derivative (2).

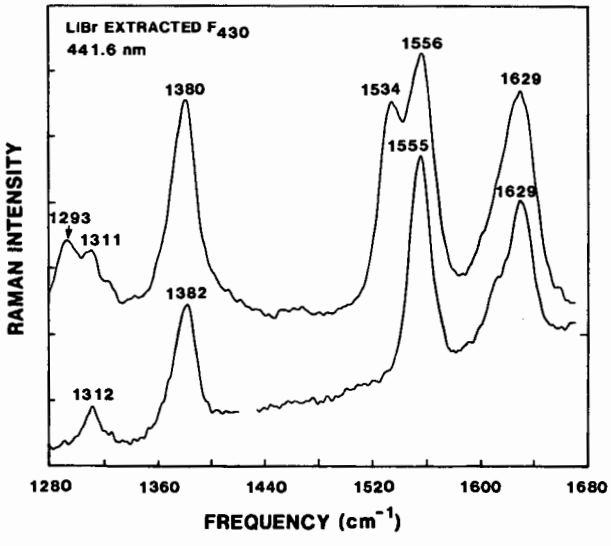

Fig. 2. Resonance Raman spectrum of salt-extracted F_{430} at room temperature (top) and at 77 °K (bottom) in aqueous 10 mM phosphate buffer.

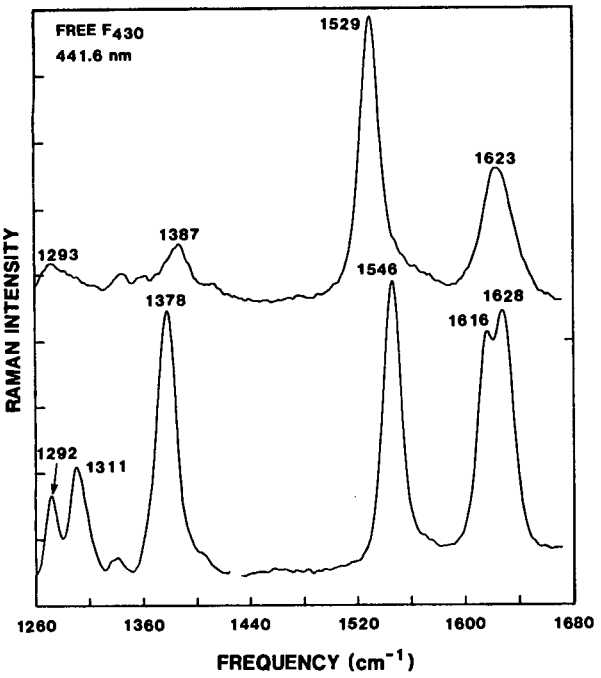

Figure 3. Resonance Raman spectrum of cytosol-free F_{430} at room temperature (top) and at 77°K (bottom) in aqueous 10 nM phosphate buffer.

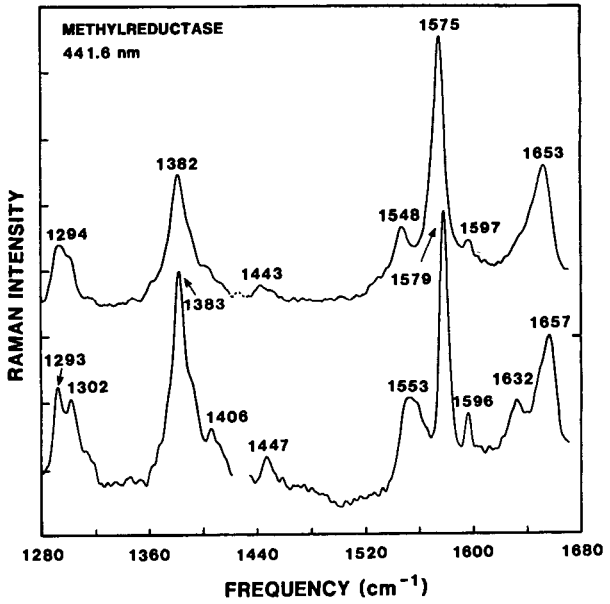

Figure 4. Resonance Raman spectrum of methyl reductase at room temperature (top) and at 77°K (bottom) in aqueous 10 nM phosphate buffer.

THE TESTING OF CATALYSTS FOR ALKANE ACTIVATION*

Frances V. Stohl, John A. Shelnutt,
Barry Granoff and Daniel E. Trudell

Sandia National Laboratories, Albuquerque, NM 87185

Introduction

Low oil prices have caused a decrease in the exploration for and development of new oil reserves in the United States. This, combined with an increase in U.S. oil consumption, has resulted in an increased dependence on foreign oil. In June 1986, 40% of the oil used in the U.S. was supplied by foreign sources as compared to 32% in 1983 (1); it is likely that this dependence on foreign oil will continue to increase. This leaves the U.S. vulnerable to sudden, drastic fluctuations in our liquid fuel supply. To minimize this dependence on foreign oil, it is necessary to find new sources for liquid fuels. One potential new source is methane, which makes up about 90% of natural gas. Methane can be partially oxidized to alcohol that could be used directly as liquid fuel or converted to gasoline by Mobil's methanol to gasoline process (2). Economic analyses (3) of potential processes for the conversion of methane to liquid fuel have shown that the use of partial oxidation to form methanol, in contrast to existing conventional methods of forming methanol from syngas, could make a methane to gasoline process economically feasible. Research is needed, however, to find catalysts that are capable of oxidizing methane to methanol with high conversions and high selectivities.

Most work performed on methane partial oxidation has used metal oxide catalysts at high temperatures and pressures (4-6). These studies have shown that catalytic oxidation of methane to methanol is possible, but conversion and selectivity are low. Liu, et. al. (7) have shown that Mo supported on silica is an effective catalyst for the partial oxidation of methane to methanol and formaldehyde when nitrous oxide is present as the oxidant. At a conversion level of 3%, the combined selectivity to CH_3OH and HCHO was 78%, with CO being the principal other product. Using ^{3}Li-doped MgO at a temperature of approximately 500^{o}C, Driscoll, et. al. (8) were able to show that methyl radicals were formed when methane was passed over the surface of this catalyst. The surface methoxide ions were converted to methanol by reacting with water in the system. The mechanism was similar to the one proposed for the partial oxidation of CH_4 over a Mo/SiO_2 catalyst (7).

Watson and Parshall (9-11) have reported that organolanthanide complexes can react with the C-H bond as shown by isotope exchange reactions using labeled methane. In this case, the catalyst was a dicyclopentadienyl methyllutetium compound. It was proposed that an electrophilic reaction took place between methane and the electron-deficient lanthanide complex.

Janowicz, et. al. (12) have shown that an iridium complex can convert alkanes into hydridoalkylmetal complexes, and that the insertion reaction proceeds through a three-center transition state.

* This work supported by the U.S. Dept. of Energy at Sandia National Laboratories under Contract DE-AC04-76DP00789.

The hydrido products can then be converted to functionalized alkyl halides by treatment with mercuric chloride followed by halogens. Analogous rhodium complexes were shown to undergo similar C-H insertions, but the products were less stable than with the iridium complexes (12). Jones and Feher (13,14) have also shown that alkane C-H bonds can be activated by homogeneous Rh(I) compounds.

Methane can be selectively converted to methanol biochemically via a monooxygenase enzyme (15). Organisms capable of utilizing methane as their sole carbon and energy source are called methanotrophs. In the organism Methylococcus capsulatus, the monooxygenase enzyme has been shown to be capable of utilizing a variety of alkanes, alkenes, ethers, alicyclic compounds, etc. (15). The soluble methane monooxygenase from M. capsulatus was resolved into three fractions by ion exchange chromatography, but the molecular structures are unknown.

Several other naturally occurring enzymes, such as cytochrome P450 (16), can also catalyze the conversion of alkanes to alcohols at low temperatures and pressures. In an attempt to mimic the activity of these enzymes, we have initiated a program to tailor-make catalysts for the direct conversion of methane to methanol. Our work focuses on the use of metalloporphyrins, and relies on computer-aided design to guide the synthesis of novel catalytic materials. The molecular design techniques are being combined with structural studies (17) of biological catalysts to identify the important characteristics of the active site, the development of activity and selectivity tests to determine structure-activity relationships, and the synthesis of designed catalysts.

Porphyrins are being used because they are present in enzymes that perform C_1 chemistry (methyl reductase, methyl transferase), have versatile structures that can be controlled, and can be synthesized with many different metals. Porphyrins have also shown significant activity for oxidation of long chain alkanes (C5+) (18,19).

The objective of this paper is to describe the catalyst activity and selectivity tests we are developing and to report on the results of testing several commercially available porphyrins. To get structure-activity relationships, it is necessary to develop several different activity tests using alkanes with varying chain lengths. We started with a cyclohexane test using previously reported conditions (20) so that our results could be compared to literature results. Additional tests we have developed to date use hexane and butane as reactants. In the future, tests will be developed using ethane and methane as reactants.

Experimental Procedures

Materials

The catalysts used in this work included iron tetraphenyl porphyrin (FeTPPCl), manganese tetraphenyl porphyrin (MnTPPCl) and iron pentafluorophenyl porphyrin ($FeTF_5PPCl$). The first two catalysts were obtained from Porphyrin Products and the third from Aldrich. Methylene chloride (99+%) was used as the solvent in all tests. The oxidant was iodosylbenzene (C_6H_5IO) prepared from the reaction of iodosobenzene diacetate with NaOH (21). The alkanes used for the various tests were cyclohexane (99+%), hexane (99%), and butane (99.5%).

Reaction Conditions

Reactions with cyclohexane and hexane were performed in the liquid phase in an argon atmosphere glove-box. Each run had 1.4 cm^3 solvent and 0.6 cm^3 cyclohexane (or 0.7 cm^3 hexane). The ratio of reactant:oxidant:catalyst was 1100:20:1 (20) on a mole basis. These reactions were carried out at atmospheric pressure and ambient temperature (about 30°C in the glove-box) for 2 hours. Reactants were stirred at 1000 rpm.

The oxidation of butane was carried out under 5 psig pressure by bubbling butane at a flow rate of about 12 cm^3/min through a solution containing 2 cm^3 methylene chloride, 0.005 mmol catalyst, and 0.1 mmol oxidant. A condenser was attached to the reactor to minimize the loss of methylene chloride. The condenser temperature was set at 7°C so that butane condensation did not occur. At this temperature, small quantities of methylene choride vaporized so that additional solvent was added during the run to maintain constant volume. The reaction temperature was 19°C. After 6 hours, the flow of butane was stopped, the pressure gradually released, and the excess butane was allowed to outgas from the methylene chloride prior to analysis of the products.

Product Analyses

Oxidation products were identified using GC/MS techniques and quantified using capillary column gas chromatographic techniques with commercially available compounds as standards. Product yields are reported on the basis of the amount of oxidant added to the reactor.

Catalyst Characterization

The porphyrins were analyzed using UV-vis spectroscopy. Spectra were taken of both as received and used porphyrins to determine if any degradation of the porphyrin occurred during reaction.

Results and Discussion

Cyclohexane tests were run first in order to compare our results with published values (20). Initial runs used FeTPPCl. Tests with iodosylbenzene, prepared using previously reported procedures (21), resulted in low cyclohexanol yields, which were thought to be due to a high concentration of contaminants in the oxidant. Infrared (IR) spectra of the oxidant showed the presence of iodobenzene (C_6H_5I). Other phases could not be identified. Extensive cleaning using water and chloroform was carried out; the IR pattern of the product showed a significant decrease in the amount of iodobenzene present. The results we obtained for FeTPPCl and $FeTF_5PPCl$ with this purified batch of oxidant are shown in Table 1. The reported cyclohexanol yields (20) were 10.1% for FeTPPCl and 66.6% for $FeTF_5PPCl$. Our yields for both porphyrins are significantly higher than the literature values suggesting that we may have prepared a purer oxidant.

An additional test performed with MnTPPCl showed a much greater cyclohexanol yield than obtained with FeTPPCl. UV-vis analyses of the three catalysts before and after reaction showed that the FeTPPCl degraded during reaction, whereas the $FeTF_5PPCl$ and MnTPPCl showed no significant degradation. The extent of FeTPPCl degradation and the cyclohexanol yield from the run with FeTPPCl as a function of time are shown in Figures 1 and 2. A comparison of the results in these two figures indicates that some reaction still occurred even after the porphyrin was completely degraded. A test carried out with

reactant, oxidant and solvent, but no porphyrin, did not yield any cyclohexanol. This indicates that the iron species resulting from the degradation had some activity. The cause of the higher activity of MnTPPCl as compared to FeTPPCl is not definitively known. It could be entirely due to the degradation of the FeTPPCl or could be partially due to FeTPPCl degradation and partially due to differences in the activities of the two metals. This cannot be proven from these runs. Additional studies are being performed to determine the effects of different metals on catalyst activity.

The main structural difference between FeTPPCl and $FeTF_5PPCl$ is the replacement of hydrogens with fluorines on the phenyl rings. Steric and electronic effects of the fluorines prevent catalyst degradation to produce a more stable catalyst. The fluorines may also cause the catalyst to be more active (20). Runs with MnTPPCl and $FeTF_5PPCl$ that were carried out for about 16 hrs did not show any increase in yield beyond the first two hours, suggesting that the reactions might be limited by the amount of oxidant remaining. It has been suggested (20) that the oxidant can be further oxidized by an Fe-oxygen intermediate species of the porphyrin to give iodoxybenzene ($C_6H_5IO_2$) during these reactions. The iodoxybenzene is not an oxidant. We are currently performing studies to determine the fate of the iodosylbenzene in these reactions.

Activity testing with hexane was performed under the same conditions as with cyclohexane so that yields could be compared. Results for this test are shown in Table 1. The total hexanol yield is lower than the total cyclohexanol yield under the same conditions. The hexanol from the run with $FeTF_5PPCl$ consists of 1% 1-hexanol, 28% 2-hexanol and 27% 3-hexanol. These results show that selectivity to the 1-hexanol is very low and the total yield has decreased in going from the cyclic compound to the straight chain. The decrease in the yield of the 2- plus 3- alcohols in the hexane run, as compared to the cyclohexanol yield with the same catalyst, is proportional to the number of methylene groups. Hexane has 4 secondary carbons whereas cyclohexane has 6, and the yield of 2- plus 3- hexanols is 2/3 of the yield of cyclohexanol.

The run with butane yielded 35% butanol consisting of 34% 2-butanol and 1% 1-butanol. The concentration of butane in the methylene chloride under the test conditions was measured using Raman spectroscopy. The results showed that there was about 8% butane (on a mole basis). This is significantly lower than the 20% hydrocarbon present in the reactions with cyclohexane or hexane. The results of the tests with cyclohexane and hexane cannot be directly compared to the results of the butane tests because of the lower reactant concentration and the differences in reaction times and temperatures. Therefore, additional testing is being carried out to enable this comparison.

Conclusions

The results of the cyclohexane tests carried out for longer times indicate that it is necessary to determine what happens to the oxidant during the reaction, since the results suggest that oxidant is depleted even at low alcohol yields. If a more effective oxidant is found, yields should be significantly higher. The results with butane suggest that we may have a good test procedure for use with shorter chain alkanes. To be able to compare results from tests using cyclohexane and hexane to butane (and to future tests with ethane and methane), it will be necessary to determine the effects of different

reactant concentrations and different reaction times and temperatures.

References
1. Hirsch, R.L., Science 235, 1467, 1987.
2. Williams, R., Oil & Gas J., 76, May 14, 1984.
3. Dautzenberg, F.M., Garten, R.L. and Klingman, G., ACS Division of Ind. Eng. Chem. 21st State-of-the-Art Symposium, Marco Island, Florida, June 15-18, 1986.
4. Foster, N.R., Appl. Catal. 19, 1, 1985.
5. Jones, C.A., Leonard, J.J. and Sofranko, J.A., Energy and Fuels 1, 12, 1987.
6. Sofranko, J.A., Leonard, J.J. and Jones, C.A., J. Catal. 103, 302, 1987.
7. Liu, H.-F., Liu, R.-S., Liew, K.Y., Johnson, R.E. and Lunsford, J.H., J. Am. Chem. Soc. 106, 4117, 1984.
8. Driscoll, D.J., Martin, W., Wang, J.-X. and Lunsford, J.H., J. Am. Chem. Soc. 107, 58, 1985.
9. Watson, P.L. and Parshall, G.W., Acc. Chem. Res. 18, 51, 1985.
10. Watson, P.L., J. Am. Chem. Soc. 105, 6491, 1983.
11. Parshall, G.W., Chemtech, 628, 1984.
12. Janowicz, A.H., Periana, R.A., Buchanan, J.M., Kovac, C.A., Stryker, J.M., Wax, M.J. and Bergman, R.G., Pure and Appl. Chem. 56, 13, 1984.
13. Jones, W.D. and Feher, F.J., J. Am. Chem. Soc. 104, 4240, 1982.
14. Jones, W.D. and Feher, F.J., Organometallics 2, 562, 1983.
15. Woodland, M.P. and Dalton, H.J., Biol. Chem. 259, 53, 1984.
16. Griffin, B.W., Peterson, J.A., and Estabrook, R.W. in "The Porphyrins", ed. Dolphin, D., Academic Press, New York, p.333, 1979.
17. Shelnutt, J.A., Shiemke, A.K. and Scott, R.A. ACS Division of Fuel Chem. Preprints, Aug. 31 - Sep. 4, 1987 (in preparation).
18. Mlodnicka, T., J. Mol. Catal. 36, 205, 1986.
19. Cook, B.R., Reinert, T.J. and Suslick, K.S., J. Am. Chem. Soc. 108, 7281, 1986.
20. Nappa, M.J. and Tolman, C.A., Inorg. Chem. 24(26), 4711, 1985.
21. Saltzman, H., and Sharefkin, J.G., "Org. Synth." 43, 60, 1963.

Table 1. Yields of alcohols reported as a percent of the initial oxidant input to the reactor.

REACTANT	CATALYST	TOTAL YIELD	1-ALC* YIELD	2-ALC YIELD	3-ALC YIELD
Cyclohexane	FeTPPCl	14			
	MnTPPCl	42			
	$FeTF_5PPCl$	84			
Hexane	$FeTF_5PPCl$	56	1	28	27
Butane	$FeTF_5PPCl$	35	1	34	

* ALC = alcohol.

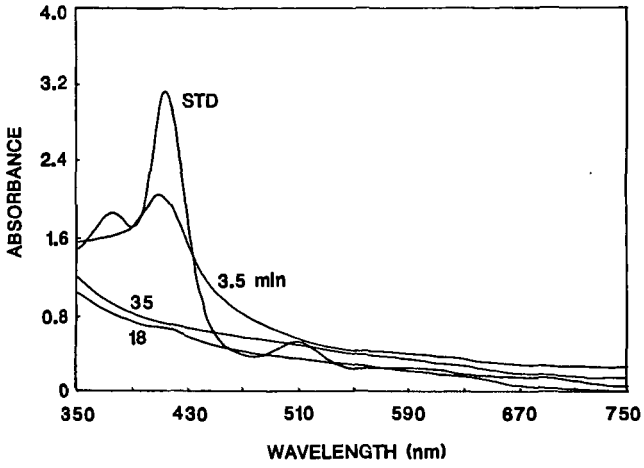

Figure 1. Comparison of UV-vis spectra of FeTPPCl (STD) with catalyst removed (at 3 times) from a reaction with cyclohexane.

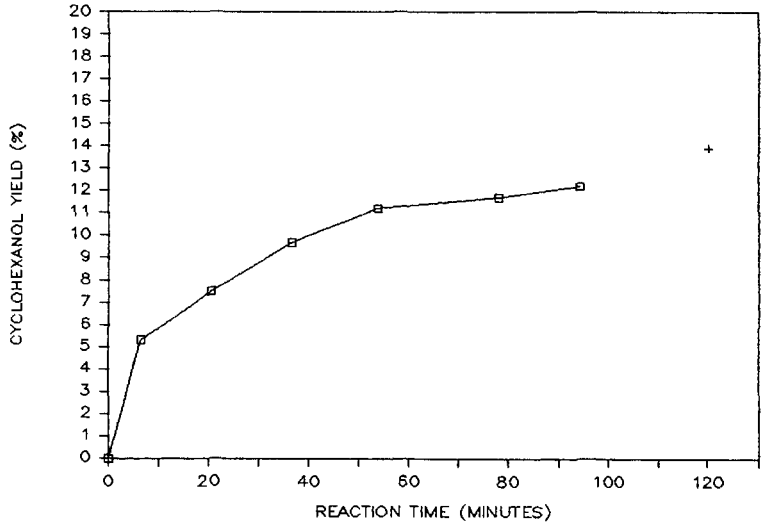

Figure 2. Cyclohexanol yield vs. run time. Catalyst = FeTPPCl. □ = samples pulled from reaction using a syringe (manual injection into GC). + = sample removed from reactor after end of run (automatic injection into GC).

ALKANE ACTIVATION BY OXIDE-SUPPORTED ORGANORHODIUM COMPLEXES

Jeffrey Schwartz

Princeton University
Princeton, NJ 08544

INTRODUCTION

"Homogeneous" catalysis, or catalysis by discrete, soluble transition metal complexes, is dominated by studies of such species in "soft" ligand environments (e.g., consisting of phosphines, sulfides or carbonyls). Historically, one focus of research in this field has been the elucidation of changes in reactivity of a complex which are effected by subtle modification of the ligand environment of the metallic center. It is of interest to us to determine how a gross change in this ligand environment affects the reactivity of a metal system bound to it; specifically, we aim to elucidate changes in rules of molecular reactivity which occur when the "soft" ligand environment of a transition metal complex is replaced by a "hard", oxygen-based one. In this context, solid metallic oxides were chosen to provide this oxygen-based ligation.

THE CHEMISTRY OF OXIDE-BOUND RHODIUM(ALLYL)COMPLEXES

We chose to focus our attention[1] on the chemistry of oxide-ligated rhodium complexes, given the many interesting and important reactions which exist for this metal in "classical", "soft-ligand"-based homogeneous catalysis. In our work we have used a variety of chemical and spectroscopic procedures to characterize our complexes.

Tris(allyl)rhodium reacts with hydroxyl groups of silica with evolution of 1 equiv of propylene to give Rh(III) species [SiO]Rh(allyl)$_2$, 1. (We use the terminology "[SiO]" simply to indicate covalent bonding between the oxide and the metal. Details of this interaction are not yet known, although preliminary results of EXAFS studies suggest that several oxygen atoms of the support interact with a given rhodium center.)

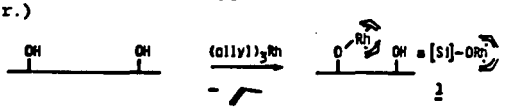

1

Hydrogen reacts slowly with 1 at room temperature. During this time 1 eq of propane is evolved. Hydrogen uptake measurements correlate with the amount of propane thus obtained and these data are consistent, stoichiometrically, with the formation of [SiO]Rh(allyl)H, 2. The infrared spectrum of 2 shows strong absorptions attributable to the allyl and hydride ligands (ν_{Rh-H} = 2010 cm^{-1}; weaker absorption at 1800 cm^{-1}). If hydrogenation is attempted before chemical deposition has occurred (i.e. before formation of 1 is complete) tris(allyl)rhodium adsorbed on the oxide rapidly reacts to give a black material which shows no infrared transmission, and which may be rhodium metal.

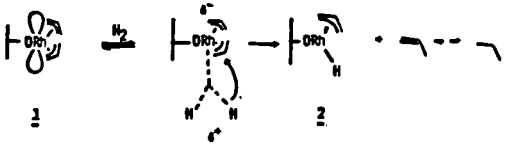

1 2

A series of XPS experiments was performed on 2 to corroborate its assignment. A single Rh species was found with an oxidation potential at 308.0 eV (Rh 3d 5/2 vs Si 2p). Thermolysis of this material at 400° followed by XPS analysis revealed

that rhodium metal had been formed (oxidation potential at 307.25 eV). XPS data obtained for 2 falls outside a range of values (308.4 eV to 311.3 eV) which has been determined for Rh(III) salts, a range which overlaps with that for typical Rh(I) complexes (307.6 eV to 309.6 eV). XPS data for covalent organometallic complexes, however, must be interpreted with caution: although 2 is <u>formally</u> a complex of Rh(III), actual positive charge build-up on the metal in this hydride-ligated species may be quite low.

To further probe the nature of the interaction between the metal complex and the oxide support, procedures were developed[2] for vapor phase deposition of tris(allyl)rhodium onto single crystal hydroxylated TiO_2 in ultra-high vacuum; deposition and a subsequent hydrogenolysis procedure were investigated through a series of UPS measurements made on the surface oxygens of the oxide. These demonstrated that attachment of the bis(allyl)rhodium moiety to TiO_2 was associated with a removal of electron density from the surface oxygens, consistent with the notion that this moiety is a strong electrophile (perhaps stronger than proton). Replacement of one of the allyl ligands by hydride revealed by UPS a build-up of charge on the surface oxygens. Thus the role of hydride as a strong donor ligand toward rhodium, mentioned above in discussions of XPS analyses, is corroborated by these UPS results. Variation in binding energies for surface oxygens as a function of other ligand changes in the coordination sphere of the rhodium demonstrate the *covalent* nature of the interaction between the metal complex and the oxide, which apparently behaves as a conventional "donor" ligand.

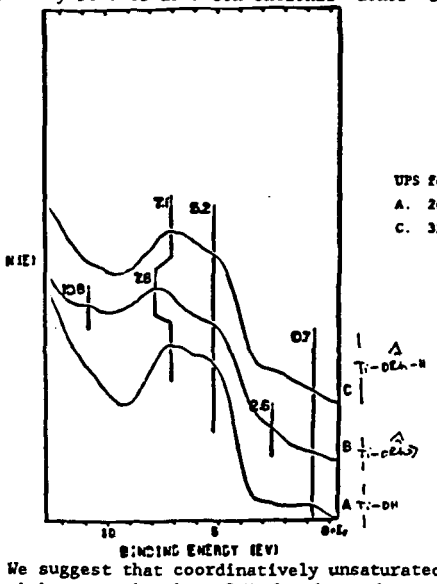

UPS for Rh(allyl)(H) formation on titanium dioxide (001).
A. 205L water/8' Ar+ B. 2420L tris(allyl)Rh/ (A)
C. 3230L H_2/(B)

We suggest that coordinatively unsaturated 1 is electrophilic in its reactivity. Activation of H_2 has been observed by aqueous Rh(III) and by numerous metal oxides. In these cases, the concept of "heterolytic" activation of hydrogen has been developed; the coordinatively unsaturated metal conter acts as a sink for "H^-", and a base in the environment of the metal center stabilizes the released proton. When 2 is exposed to D_2, H-D exchange between the atmosphere and residual hydroxyl groups of the silica support is observed, consistent with the notion that in the presence of 2 H_2 or D_2 act as a source of H^+ or D^+. Complex 2 also catalyzes rapid (< 1 min) equilibration of 50:50 H_2-D_2 mixture at room temperature.

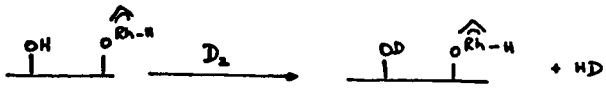

ACTIVATION OF ALKANES

Simple alkanes are conceptual analogs of dihydrogen in that they both should be able to form a two center, three electron bond with an unsaturated metal center utilizing electron pairs in bonding σ orbitals; analogous intramolecular C-H bond coordination is now well established experimentally and has been calculated to be

facile intermolecularly. To probe interactions between alkanes and 2, we studied their reaction in the presence of D_2 gas. Sequential H-D exchange occurred when 2 was used to catalyze this process between ethane, for example, and D_2 (see entry 1). Decomposition of 2 (heating at 400° under one atmosphere of hydrogen for 4 hrs) gave a black species which showed no infrared absorptions attributable to Rh–H stretching modes. This species showed catalytic activity for H-D exchange which was different from that of 2: whereas 2 gives rise to a distribution of deuterated ethanes relatively high in d_1- and low in d_6-ethane, this other black substance gives rise to a bimodal pattern showing a high degree of d_6-ethane relative to d_1 (see entry 2). We had noted that simple thermolysis of 2 yields rhodium metal (by XPS analysis) and, therefore, we compared this black material with rhodium on silica obtained by conventional methods. Interestingly, rhodium on silica thus prepared behaves in a fashion similar to that noted for the pyrolysate (see entries 3 and 4).

(1) $\equiv$Rh(allyl)H/SiO_2
(2) Rh/SiO_2 prepared from $\equiv$Rh(allyl)H/SiO_2 at 400°, 1 atm H_2
(3) Rh/SiO_2 prepared from $RhCl_3$ (aqueous), 400°, 1 atm H_2
(4) Rh/SiO_2 prepared from $RhCl_3$ (methanol), 150°, 1 atm H_2
(5) Rh/KBr prepared from $Rh(allyl)_3$/KBr, room temp., 1 atm H_2
(6) Rh film

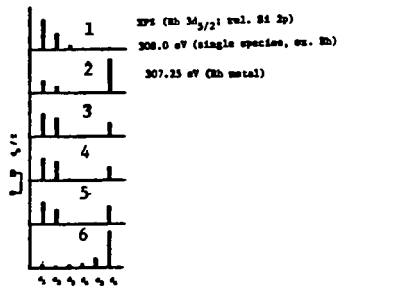

ACTIVATION OF METHANE

We proposed that methane could be activated by an intramolecular ligand rearrangement route from a two-electron, three-centered intermediate analogous to that one proposed for activation of H_2, and we have demonstrated that methane can replace hydrogen in the hydrogen activation step shown in Scheme 2. For example, when 1 is treated with H_2 2 results; similarly we found that when 1 was treated with methane, a mixture of hydride complexes 2 and 5 were obtained. Hydrogen also reacts with hydridochloride complex 3 to give dihydride 4, and therefore 3 was treated with methane. This results in the formation of methyl chloride (0.85 equiv); activation of methane was confirmed by use of $^{13}CH_4$. Here, infrared analysis performed on rhodium-containing materials showed the presence of dihydride 4, and broadened absorption centered at 2040 cm^{-1} suggested that 4 could be contaminatd with another hydride species, perhaps a (methyl)rhodium(hydride) complex 6; (for the analogous[SiO]Rh(H)Bu, ν_{Rh-H} = 2010 cm^{-1}). Indeed when this material (6) was treated with chlorine, methyl chloride was obtained (0.2 equiv). These observations can be explained[3] by the sequences shown below.

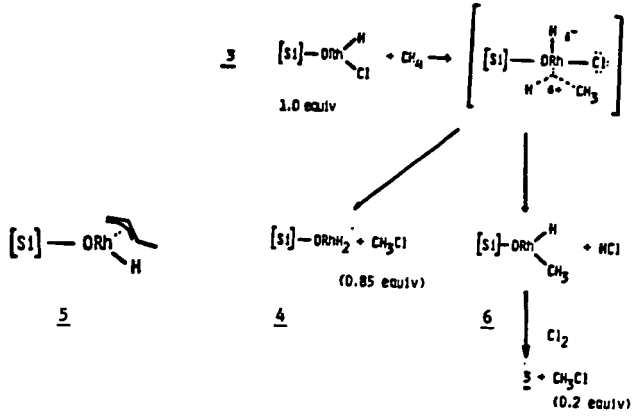

OXIDE-DEPENDENT DEPOSITION AGGREGATION

Although we had noted that a variety of oxides could be used for chemical attachment of organorhodium complexes, we had not originally studied how variation in the oxide itself affects the structure or reactivity of complexes bound thereto, and deposition control was attained only by adjusting total content of hydroxyl groups on the oxide. The subtle notion was not considered that relative locations might vary of reactive hydroxyl groups on oxides of different structure, although this distribution of reactive sites would control deposition of one equivalent of an organometallic with regard to another. Silica and alumina are among the most commonly used oxides, in general, for chemical attachment to reactive organometallic complexes, and we found[4] that an interesting oxide-dependent deposition phenomenon distinguishes these two materials: although for both we utilize samples containing a large excess of acidic hydroxyl groups relative to total rhodium deposited, we note that for silica, deposition of rhodium complexes occurs selectively to generate dimers; on alumina (of comparable total acidity) monomers are formed.

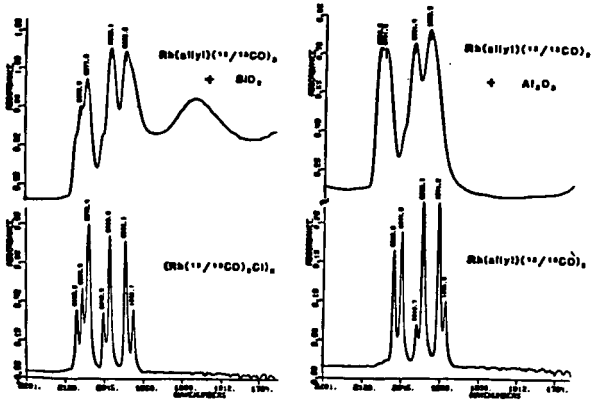

· Rhodium carbonyl compounds bound to silica are not structurally stable under hydrogen[4]. This can be demonstrated by noting changes in the infrared spectrum of carbonyl compounds formed on deposition and after subsequent treatment with H_2. Specifically, we note a relative decrease in intensity attributable to terminal carbonyl ligation and an increase in intensity attributable to bridging or "semi-bridging" carbonyl groups. We note that rhodium hydride species (2 or 4) on silica are also structually unstable under H_2 with regard to clusterification. When these reactions were followed by infrared spectroscopy evidence was obtained for the presence of intermediary molecular hydrogen adducts. Thus, although it is a commonly held assumption that degradation under hydrogen of catalytically ac ive complexes to metallic particles occurs first by reduction of the complex to the metal and then by aggragation, our data suggest that a complementary route, namely aggregation followed by degradation, must also be considered. It is interesting to note that dihydrido or dicarbonyl complexes of rhodium bound to either alumina or titanium dioxide do *not* demonstrate any evidence for analogous clusterification under H_2. Clearly the surface properties of all of these oxides must be better elucidated to understand differences in reactivity imparted to the covalently bound complexes by their various oxide ligands.

1. Alkane Activation by Oxide-Bound Organorhodium Complexes, Schwartz, J. *Acc. Chem. Res.* , 1985, *18*, 302-308, and references cited therein.

2. Investigation of a Model Catalytic System in Ultrahigh vacuum: The Adsorption of $Rh(allyl)_3$ on the TiO_2 (001) Surface, Smith, P.; Bernasek, S. L.; Schwartz, J.; McNulty, G. S. *J. Am. Chem. Soc.* 1986, *108*, 5654-5655.

3. Activation of Alkanes by Oxide-Supported Organorhodium Complexes, Kitajima, N.; Schwartz, J. *Proceedings of the Fourth International Symposium on Homogeneous Catalysis - Fundamental Research in Homogeneous Catalysis, Volume III*, 1986, 1003-1014.

4. Oxide-Dependent Deposition and H_2-Promoted Aggregation of Organo-rhodium Complexes, McNulty, G. S.; Cannon, K.; Schwartz, J. *Inorg. Chem.* 1986, *25*, 2919-2922.

Activation of Methane on Iron, Nickel, and Platinum Surfaces. A Molecular Orbital Study

Alfred B. Anderson and John J. Maloney

Chemistry Department, Case Western Reserve University
Cleveland, Ohio 44106

The activation of alkane CH bonds is the first step in hydrogenolysis and oxidation catalysis. It is clear from simple consideration of metal-hydrogen bond strengths ($\gtrsim$250kJ/mol) and CH bond strengths (434 kJ/mol for breaking the first CH bond in methane) that oxidative addition and not hydrogen atom abstraction will be the route followed on metal surfaces. In contrast, O^- defect centers at oxide surfaces do abstract hydrogen atoms from methane, forming gas phase methyl radicals (1). The greater strength of an OH bond over a CH bond allows this to happen; a molecular orbital analysis has been published recently (2). Though kinetic studies of alkane reactions on metal surfaces are large in number, little is known about catalyst surface composition and structure or the structure and electronic factors responsible for CH activation by metals. The purpose of the present work is to explore mechanisms, activation energies, and orbital interactions associated with the oxidative addition of a methane CH bond to several idealized clean transition metal surfaces.

The metals chosen for our theoretical exploration, iron, nickel, and platinum, have been the topics of several systematic methane catalysis and surface science studies in recent years. A theoretical study of the oxidative addition of methane to an iron surface indicated the reaction was exothermic with an activation energy barrier of roughly 88 kJ/mol (3). In that study, low barriers were also found for dehydrogenation of CH_x (x= 1-3) fragments and this is reflected in the ability of iron particles to catalyze the high temperature pyrolysis of natural gas to graphite fibers as studied recently by Tibbetts (4). Early work using iron surfaces was unsuccessful in yielding activation energies, probably because contaminants lowered the activity (5).

In the case of nickel, activation energies are higher on single crystal surfaces than on films and supported metal particles. Estimates are 88 kJ/mol on Ni(110) (6), 71 kJ/mol on Ni(111) (7), and 0 (8) and 30 (9) kJ/mol on Ni(100). On a Ni film 42 kJ/mol has been reported (5) and independent studies of methane activation by silica supported nickel yield similar barriers, 29 (10) and 25 (11) kJ/mol.

Activation of n-alkanes on platinum has been studied (12,13). Activation energies are about 46 kJ/mol on Pt(110) (13) and the inactivity of Pt(111) (12) has been interpreted to mean that n-alkane CH activation energies must be greater than 67 kJ/mol (13).

Because of various experimental difficulties in the early work, only the recently determined activation energies, 71 kJ/mol for Ni(111) and 30 kJ/mol for Ni(100) are likely to be accurate (5,9,13). The other values are in greater doubt.

Theoretical Method

The atom superposition and electron delocalization molecular orbital (ASED-MO) method (14) used in this paper is a semiempirical

theoretical approach which uses valence Slater orbitals (15) and experimental ionization potentials (16) as input data. The ASED-MO method is a simple way to predict certain molecular data from atomic data. Its structure and energy predictions are often quite accurate, but in general it is best used to establish and explain chemical trends.

Surfaces were modeled using the bulk-superimposable clusters in Figure 1. Atoms with which methane interacts directly in the transition state are shaded. Adsorption studies were performed assuming high-spin molecular orbital occupations with lower levels in the d band doubly occupied and upper levels singly occupied. The Fe_{13} and Fe_{14} clusters had 38 unpaired electrons, the Fe_{11} cluster 30 and the Ni_{10} and Pt_{10} clusters 6 unpaired electrons. The cluster structures are bulk-superimposable and based on well-known lattice constants (17).

Methane activation on Fe(100) and (110) surfaces

Key numerical results are in Table I and transition state structures are in Figure 2. The activation energy for inserting an Fe(100) surface atom into a methane CH bond is 32 kJ/mol and occurs when the bond is stretched 0.36 Å. On a "roughened" surface site, consisting of an Fe ad-atom placed on top in a bulk-like position, the activation energy decreases slightly to 27 kJ/mol. The bonding in the transition state is best characterized as CH donation to the surface and the electronic structure for the ad-atom case is in Figure 3. This figure is representative of all other transition states discussed in this work. The stretching causes one of the 3-fold degenerate $\underline{t}$ symmetry methane orbitals to become destabilized. Its bending of 22 deg away from the tetrahedral direction contributes further to the destabilization and also causes a small stabilization in one of the other $\underline{t}$ orbitals. The lowest orbital is destabilized by the distortion. Interactions with the surface consist in a small stabilization of the lowest orbital and mixing of both of the upper orbitals from the $\underline{t}$ set with the Fe orbitals to form clearly-defined C···H···Fe and C···Fe σ bonding orbitals. The main occupied antibonding counterpart orbital energy lies in the half-filled d band region and participation of the CH σ^* orbital in it removes almost all H contribution; the orbital has a C···Fe σ bonding character.

The transition state structures given in Figure 2 show how the methyl groups are tilted with respect to the two Fe(100) surfaces. The activated CH bonds are bent away from the tetrahedral directions, as are the newly-forming metal-carbon bonds. On these surfaces the deviations from the tetrahedral directions are nearly symmetric; numerical values for structure parameters are in Table I.

The total Mulliken overlap between the atom inserting into the CH bond and the surface cluster decreases when the atom is playing its activating role. Values given in Table I indicate a smaller decrease for the Fe/Fe(100) surface than for Fe(100). Furthermore, the bond order between the adsorbed Fe atom and the surface is less than between a surface atom and its neighbors.

The close-packed Fe(110) surface is much less reactive. The activation energy for site A is 118 kJ/mole and for site B it is 135 kJ/mol - see Figure 2 and Table I. The methyl tilts from vertical are less than for the (100) surface and this is symptomatic of increased steric repulsions with the closely-packed surface. The bending of the

activated CH bond away from the surface is greater than on Fe(100) and the Fe-C bonds are closer to the tetrahedral direction despite the greater Fe-C distances. There are significant changes in the bond order between the activating Fe atom and its neighbors. On the clean surface the bond order is higher than for Fe(100), indicating more near neighbors and stronger bonding. When the iron atom is activating CH, its overlap decreases more than for the (100) surface, lending further support to the idea that activating CH bonds weakens the metal bonding and that the stronger the metal bonding is, the more it must be perturbed and the weaker the activating ability of the surface. This appears to be borne out by the experimental results for (100) and (111) Ni.

Methane activation on Ni(111) and Pt(111) surfaces

Ni(111) is close-packed and the transition state structures are similar to those for Fe(110). The calculated activation energy, 64 kJ/mol, is close to 71 kJ/mol reported in (7), and provides a benchmark for our qualitative numbers. The effect of activation on the overlap of the active Ni atom with its neighbors is the same as for the close-packed Fe(110) surface.

The 43 kJ/mol activation energy calculated for Pt(111) is close to the experimentally determined value of about 46 kJ/mol for the (110) surface (13) and is smaller than implied by early studies of n alkanes on Pt(111) (12). We do not know precisely the reason for the disagreement. The calculations have uncertainty, but it is noted that the effects of transition state methane on the Pt-Pt bond order are more like those for the open Fe(100) surface than the close-packed Fe and Ni surfaces. We also note early work which stated Ni(111) was inactive compared to Ni(110) (6), yet very recent experiments yield a barrier for the Ni(111) surface close to our calculated value. Impurities may have passivated the (111) Ni surfaces in the early work.

Conclusions

The oxidative addition of methane to the iron, nickel, and platinum surfaces considered here is characterized by the insertion of a surface metal atom into a CH bond. Transition state CH bond stretches amount to around 0.4-0.5 Å. In the transition state two methane CH σ oribtals hybridize with the metal s and d band orbitals to form metal-H and metal-C bonds and the antibonding counterpart to these σ donation interactions is stabilized by mixing with the empty CH σ^* orbital to give additional C-metal bond order. Our finding of charge donation to the metal surfaces in most of the transition states conflicts with the conclusions of Saillard and Hoffmann (19) who used stylized structure models and Extended Hückel calculations, but never actually studied properties along reaction paths for activating methane.

We have found that the close-packed iron(110) surface is a much weaker CH activator than the more open (100) surface and that an adatom on the (100) surface is the most active site of all. These activities correlate with the inverse of the bond order between the activating surface atom and its neighbors. These bond orders undergo larger absolute and percentage changes when the activation energy is high, indicating a contribution to the barrier comes from a weakening of metal bonding at the transition state. Hydrogen atoms have been noted to weaken iron bonding in custers while carbon atoms

strengthened iron overlaps (3). It is obvious that adsorption should affect metal bonding. The relative activation of close-packed and open surfaces toward methane could also have been anticipated.

Depite being close-packed, Ni(111) activates methane with a barrier half of that for Fe(110). Our calculated value is in good agreement with recent experiments and experimental estimates for Ni(100) and Ni films are less, as expected from the above theoretical results for iron. Pt(111) is predicted to be more active than Ni(111) and, therefore, much more active than Fe(110). An updated experimental look at Pt(111) is in order.

Acknowledgement

We are grateful to the Gas Research Institute for supporting this research.

REFERENCES

1. Driscoll, D. J.; Lunsford, J. H. J. Phys. Chem. 1985, 89, 4415.

2. Mehandru, S. P.; Anderson, A. B.; Brazdil, J. F. J. Phys. Chem. 1987, 00, 0000.

3. Anderson, A. B. J. Am. Chem. Soc. 1977, 99, 696.

4. Tibbetts, G. G. J. Cryst. Growth 1984, 66, 632; 1985, 73, 431.

5. Wright, P. G.; Ashmore, P. G.; Kemball, C. Trans. Faraday Soc. 1958, 54, 1692.

6. Schouten, F. C.; Kaleveld, E. W.; Bootsma, G. A. Surf. Sci. 1977, 63, 460.

7. Lee, M. B.; Yang, Q. Y.; Tang, S. L.; Ceyer, S. T. J. Chem. Phys. 1986, 85, 1693.

8. Schouten, F. C.; Gijzeman, O. L. J.; Bootsma, G. A. Surf. Sci. 1979, 87, 1.

9. Hamza, A. V.; Madix, R. J. Surf. Sci. 1987, 179, 25.

10. Gaidai, N. A.; Babernich, L.; Guczi, L. Kinet. Katal. 1974, 15, 974.

11. Kuijpers, E. G. M.; Jansen, J. W.; van Dillen, A. J.; Geus, J. W. J. Catal. 1981, 72, 75.

12. Firment, L. E.; Somorjai, G. A. J. Chem. Phys. 1977, 66, 2901.

13. Szuromi, P. D.; Engstron, J. R.; Weinberg, W. H. J. Phys. Chem. 1985, 89, 2497.

14. Anderson, A. B. J. Chem. Phys. 1975, 62, 1187.

15. Clementi, E.; Raimondi, D. L. J. Chem. Phys. 1963, 38, 2868.; Richardson, J. W.; Nieuwpoort, W. C.; Powell, R. R.; Edgell, W. F. J. Chem. Phys. 1962, 36, 1057; Basch, H.; Gray, H. B. Theoret. Chim. Acta, 1966, 4, 367.

16. Lotz, W. J. Opt. Soc. Am. 1970, 60, 206; Moore, C. E. Atomic Energy Levels, Natl. Bur. Std. (U.S.) Circ. 467 (U.S. Govt. Printing Office, Washington, D. C., 1958).

17. ASM Metals Reference Book, 2nd ed (American Society for Metals, Metals Park, Ohio, 1984).

18. Saillard, J.-Y.; Hoffmann, R. J. Am. Chem. Soc. 1984, 106, 2006.

Table I. Calculated transition state properties. Structure parameters are with reference to Figure 2. The CH_3 tilt is from the vertical and bends are from the tetrahedral direction. The C-M bend and M-H and M-C distances are derived; other structure variables were optimized. The $M-M_n$ overlap includes next-neighbor contributions and is calculated in the Mulliken definition.

surface	h_C(A)	x_C(Å)	CH_3 tilt (deg)	CH bend (deg)	CM bend (deg)	M-H(Å)	M-C(Å)	$M-M_n$ overlap value	$M-M_n$ overlap change(%)	ΔCH(Å)	E_a (kJ/mol)
Fe(100)	2.25	0.0	25	22	25	1.65	2.25	2.10	-9	0.36	32
Fe/Fe(100)	2.18	-0.57	37	22	22	1.57	2.25	2.13	-4	0.44	27
Fe(110) (A)	2.35	-0.05	12	34	11	1.66	2.35	2.39	-18	0.46	118
Fe(110) (B)	2.28	-0.30	16	35	8	1.58	2.30	2.37	-18	0.54	135
Ni(111)	2.15	-0.1	12	34	12	1.57	2.15	1.42	-17	0.51	64
Pt(111)	2.30	0.0	15	30	15	1.63	2.30	1.93	-8	0.36	43

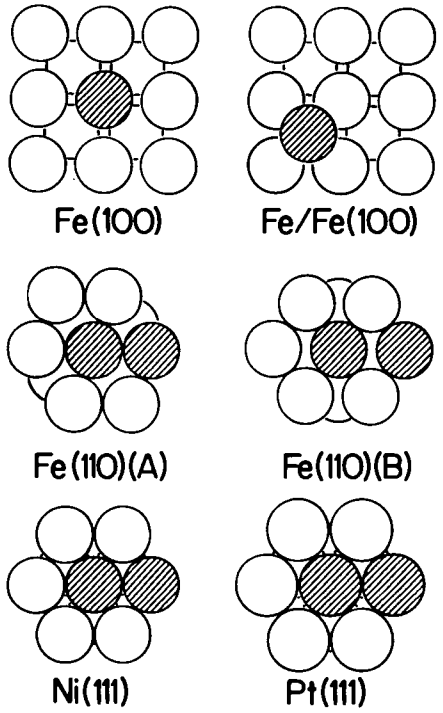

1. Cluster models used for the calculations. Shaded atoms are those associated with methane in Figure 2.

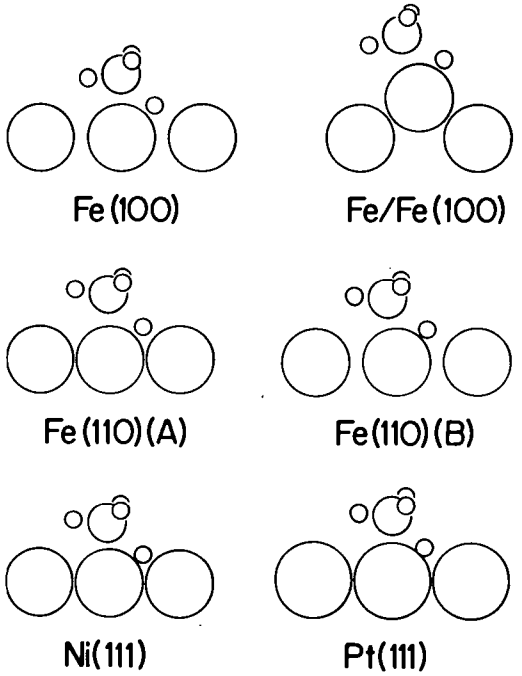

2. Calculated transition state structures.

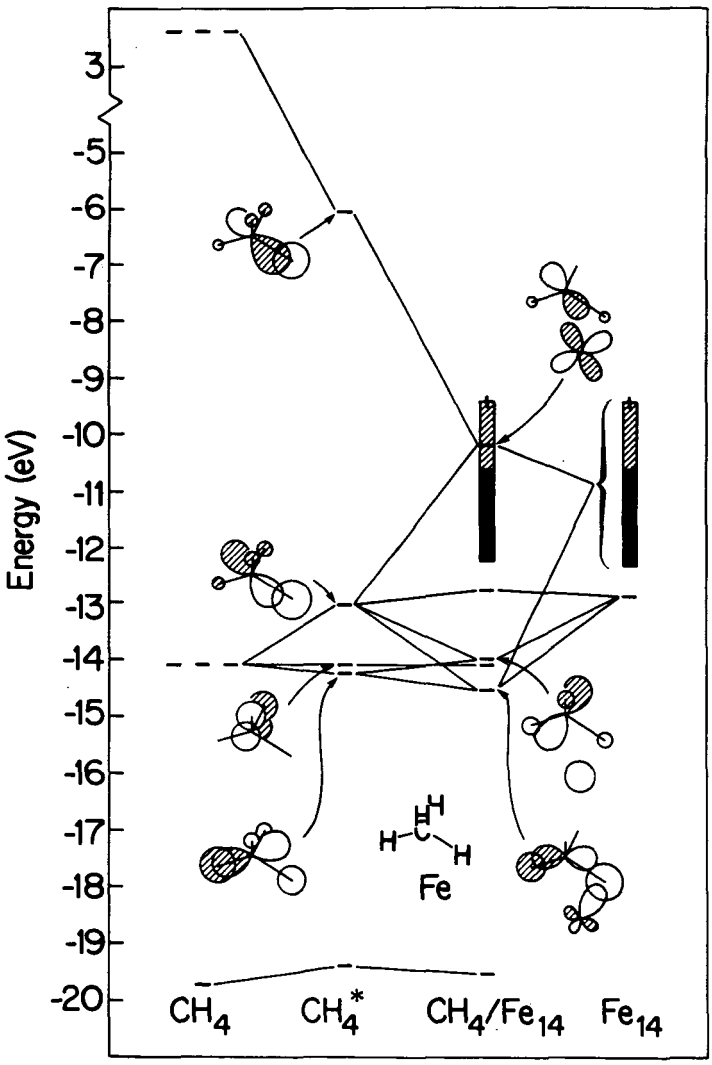

3. Orbital interactions between CH_4 and the ad atom on Fe(100). Energy levels of distorted methane with the cluster removed are in the CH_4* column. Orbitals in the shaded metal band region are half-filled.

Conversion of CH_4 into C_2H_2 and C_2H_4 by the Chlorine-Catalyzed Oxidative-Pyrolysis (CCOP) process: I. Oxidative Pyrolysis of CH_3Cl

A. Granada, S.B. Karra, and S.M. Senkan*

Department of Chemical Engineering
Illinois Institute of Technology
Chicago, Illinois 60616

INTRODUCTION:

Methane is available in large quantities in natural gas, thus constitutes an important raw material for the synthesis of higher molecular weight hydrocarbons. Processess exist to convert methane into acetylene, ethylene, and hydrogen using high temperature pyrolysis. However, at the high temperatures needed for the thermal decomposition of methane, the yields of more valuable liquid and gaseous products are too low due to the formation of excessive amounts of carbonaceous solids (see (1) and references therein).

In an earlier patent Gorin (2) proposed a chlorine-catalyzed process in which methane conversion was achieved via CH_4 chlorination, followed by the pyrolysis of chlorinated methanes (CM) and formation of C_2+ products and HCl. The HCl produced can either be converted into chlorine via the well-known Deacon reaction, or can be used to convert CH_4 into CH_3Cl via oxychlorination process, thus completing the catalytic cycle for chlorine. Recently, Benson (3) patented a process similar to that of Gorin (2), in which the flame reactions of Cl_2 and CH_4 were involved. Later, Weissman and Benson (4) studied the kinetics of CH_3Cl pyrolysis.

As expected from bond dissociation energy considerations, the decomposition temperatures for CM would be lower than that for methane, thus the destruction of valuable pyrolysis products, which include acetylene and ethylene would be suppressed. However, in spite of the lower temperatures required for CM pyrolysis, the formation of carbonaceous solids still is a problem (2,4), and this renders the direct pyrolysis of CMs unattractive for practical applications.

The Chlorine-Catalyzed Oxidative-Pyrolysis (CCOP) process developed ameliorates the problem of formation of solid products, while maintaining high yields for acetylene and ethylene (5,6). The CCOP process exploits the high-temperature, non-flame reactions of methane, chlorine, and oxygen, and forms an important bridge between combustion chemistry, halogen inhibition processes (7,8) and chemical reaction engineering. Although some carbon monoxide forms in the CCOP process, CO is a gaseous product thus can be handled easily. In addition, CO can itself be used to synthesize higher molecular hydrocarbons as well.

EXPERIMENTAL:

The experiments were conducted in a 2.1 cm ID quartz tube which was about 100 cm long, and was placed in a 3-zone Lindbergh furnace. A small amount of CH_3Cl/O_2 mixture was injected directly into pre-heated argon carrier gas. Experiments were reasonably isothermal as determined by thermocouples. Although laminar flow conditions were present, the deviation

from ideal plug flow behavior was determined to be in the range 10-15%, by the measurements of the concentration profiles in the radial direction.

Species profiles were determined by withdrawing gases through a water-cooled quartz sampling probe positioned centrally at the downstream of the reaction zone, followed by gas analysis by on-line mass spectrometry.

RESULTS AND DISCUSSION:

The experimental conditions investigated are presented in Table I. It should be noted that under these conditions, homogeneous gas-phase kinetics would dominate the reaction processes, with minor contributions from surface induced reactions (4,9).

TABLE I
Experimental Conditions Investigated.
T=980C, P=515 Torr, v=150 cm/s, res. time=50-250 ms

Species	Mixture A Mole percent CCOP Process	Mixture B Mole percent St. Pyrolysis
CH_3Cl	7.32	7.47
O_2	2.05	-
Ar	90.6	92.5

It was possible to conduct experiments with Mixture A indefinitely without any visible signs of formation of solid deposits at the exit of the transparent quartz reactor. Use of mixture B, however, immediately resulted in the formation of dark solid deposits, which rendered the quartz reactor opaque. The formation of solid deposits in the absence of oxygen, however, is an expected result, consistent with the findings of previous investigators (2,4).

In all the experiments the major species quantified, other than the reactants and argon, were: C_2H_2, C_2H_4, C_2H_6, C_2H_3Cl, CH_4, HCl, and CO. Minor species identified, but not quantified were: C_6H_6, H_2O, CO_2, and HCHO.

In Figure 1 the mole percent profile for CH_3Cl and temperature are presented as a function of axial position. In addition, the percent for unaccounted carbon (UC) is also presented. UC is defined as the percent of carbon unaccounted for by the measurements of major gaseous species, thus it represents a measure of extent of formation of solid products.

As seen from the UC profiles in Fig 1, the formation of high molecular weight products, which cannot be quantified by mass spectrometry, is indeed a problem in the absence of O_2. This result is consistent with our qualitative observations noted earlier and the results of Gorin (2), and Weissman and Benson (4).

In Figure 2 the mole percent profiles for HCl, O_2, and CO are presented. The HCl mole percents were calculated from chlorine atom balances, from the measurements of the overall conversion of CH_3Cl, and by assuming that no chlorine is associated with UC. The conversion of O_2 was quite low,

less than about 10%, consistent with the formation of low levels of CO, and by the absence of quantifiable amounts of CO_2 or H_2O.

In Figure 3 the profiles for H_2 and CH_4 are presented. The mole fractions for H_2 were obtained from hydrogen atom balances. In Figure 4 the profiles for C_2H_2, C_2H_4, and C_2H_3Cl are shown. These profiles suggest the eventual establishment of pseudo-stationary values for C_2H_2 and C_2H_4 at higher CH_3Cl conversions, consistent with the non-chain character of the process. As seen from these profiles, the levels of these products were not sensitive to O_2.

REACTION MECHANISM:

Detailed chemical modeling of the CCOP process suggests that CM pyrolysis starts with the well known initiation step (10):

$$CH_3Cl \;===\; CH_3 + Cl \qquad 1)$$

as well by the following route in the presence of O_2:

$$CH_3Cl + O_2 \;===\; CH_2Cl + HO_2 \qquad 2)$$

These reactions are followed by:

$$Cl + CH_3Cl \;===\; CH_2Cl + HCl \qquad 3)$$

Once formed, HCl undergoes the following fast reaction:

$$CH_3 + HCl \;===\; CH_4 + Cl \qquad 4)$$

regenerating Cl, and forming CH_4 as an inevitable by-product of CM pyrolysis. Reaction 4 also rapidly consumes the CH_3, therefore rendering CH_2Cl as the most important C_1 radical in the system.

The chemically activated recombination of CH_2Cl, as well as CH_2Cl and CH_3 then determine the major product distributions in the CCOP process. These reactions are the following:

$$CH_2Cl + CH_2Cl \;===\; [1,2\text{-}C_2H_4Cl_2]^* \qquad 5)$$

$$CH_3 + CH_2Cl \;===\; [C_2H_5Cl]^* \qquad 6)$$

where $[\ ]^*$ denotes the chemically activated adduct. The $CH_3+CH_3=[C_2H_6]^*$ reaction is unimportant because of the lower concentrations of the CH_3 radicals.

The energized adducts $[1,2\text{-}C_2H_4Cl_2]^*$, and $[C_2H_5Cl]^*$ then undergo the following parallell stabilization and decomposition reactions:

$$[1,2\text{-}C_2H_4Cl_2]^* + M \;\text{--->}\; 1,2\text{-}C_2H_4Cl_2 + M \text{ (Stabilization)} \qquad 7)$$

$$\text{------->}\; C_2H_4Cl + Cl \qquad 8)$$

$$\text{------->}\; C_2H_3Cl + HCl \qquad 9)$$

$$[C_2H_5Cl]^* + M \text{ ---> } C_2H_5Cl + M \quad \text{(Stabilization)} \qquad 10)$$

$$\text{-------> } C_2H_4 + HCl \qquad 11)$$

$$\text{-------> } C_2H_5 + Cl \qquad 12)$$

As apparent from these reactions gas density (M) has a significant impact on the nature of the ultimate product distribution. For example, at higher pressures and/or lower temperatures where M is high, collisional stabilization of the chemically activated intermediates is enhanced, thus the formation of recombination products would be favored. Conversely, at low pressures and/or higher temperatures where M is low, HCl and Cl elimination channels would gain greater significance.

These radical combination reactions are then followed by the following, again pressure-dependent, unimolecular reactions leading to the formation of C_2H_2, and C_2H_4:

$$C_2H_3Cl + M \text{ === } C_2H_2 + HCl + M \qquad 13)$$

$$C_2H_4Cl + M \text{ === } C_2H_4 + Cl + M \qquad 14)$$

$$1,2\text{-}C_2H_4Cl_2 + M \text{ === } C_2H_3Cl + HCl + M \qquad 15)$$

$$C_2H_5Cl + M \text{ === } C_2H_4 + HCl + M \qquad 16)$$

Reaction 13 is the major channel for the formation of C_2H_2 and for the destruction of C_2H_3Cl. The formation of C_2H_4 occurs primarily via reaction 11, and to a lesser extent by reactions 14, and 16.

Ethylene also undergoes the following destruction processess:

$$C_2H_4 + Cl \text{ === } C_2H_3 + HCl \qquad 17)$$

$$C_2H_4 + CH_2Cl \text{ === } C_2H_3 + CH_3Cl \qquad 18)$$

and form one of the most important C_2 radicals in the system, C_2H_3. Similar destruction channels for C_2H_2 would be too slow to be of any significance.

In the absence of oxygen, the primary reaction pathways available for C_2H_3 are its polymerization:

$$C_2H_3 + C_2H_2 \text{ === } CH_2CHCHCH \qquad 18)$$

and to a lesser extent:

$$C_2H_3 + C_2H_4 \text{ === } CH_2CHCH_2CH_2 \qquad 19)$$

or its highly-endothermic, thus slow decomposition to acetylene:

$$C_2H_3 \text{ === } C_2H_2 + H \qquad 20)$$

The $CH_2CHCH_2CH_2$ and $CH_2CHCHCH$ radicals subsequently undergo dehydrogenation, hydrogenation, further addition reactions with C_2H_3 and C_2H_2, cyclize and ultimately result in the formation of high molecular weight

carbonaceous solids. Although the detailed chemical kinetic steps leading to the formation of solid products are not fully known at present, the process nevertheless is well known to be extremely rapid (11), and reaction 18 is believed to play a pivotal role (4,12, 13).

In the presence of oxygen, however, the C_2H_3 radical has an additional fast reaction channel which effectively competes with the above processes:

$$C_2H_3 + O_2 \quad === \quad HCOH + HCO \qquad 21)$$

This elementary reaction have only recently been isolated and studied (14), and was shown to have no activation energy barrier. Consequently, oxygen has a profound influence on the processes of formation of high molecular weight hydrocarbon solids and carbon by directly intercepting the C_2H_3 radicals. The HCOH and HCO formed by reaction 21 subsequenly are converted into CO.

As evident from the above reaction mechanism, although O_2 interrupts the processess that ultimately lead to the formation of solid deposits, it does <u>not</u> directly interfere with the reactions responsible for the formation of ethylene and acetylene. This is supported by the experimental measurements presented in Figure 4, in which the mole percents for C_2H_2 and C_2H_4 remained nearly the same both in the presence and absence of oxygen at the same extent of conversion of CH_3Cl.

It is most important to note that the success of the CCOP process depends on the presence of the following combustion inhibition reaction, which also is the major route for H_2 formation:

$$H + HCl \quad === \quad H_2 + Cl \qquad 22)$$

Reaction 22, because of its lower activation energy, efficiently removes the H radicals from the system, and renders the following important combustion chain branching reaction:

$$H + O_2 \quad === \quad OH + O \qquad 23)$$

ineffective in building up the concentrations of O and OH radicals (7,8). Consequently the formation of flames, thus the destruction of CM and valuable products are prevented.

ACKNOWLEDGEMENTS: This research was supported, in part, by funds from the U.S. Environmental Protection Agency, Grant No:R812544-01-0, and the Illinois Institute of Technology.

REFERENCES:

1. Back, M.H., and Back, R.A., in Pyrolysis: Theory and Industrial Practice, Albright, L.F., Crynes,B.L., and Corcoran,W.H., Eds., Academic Press, New York, NY 1983.

2. Gorin, E., US Patent 2,320,274, 1943.

3. Benson, S.W., US Patent 4,199,533, 1980.

4. Weissman, M., and Benson, S., Int. J. Chem. Kinetics., v.16, p.307 (1984).

5. Senkan, S.M. "Production of Higher Molecular Weight Hydrocarbons from Methane", U.S. Patent Application in Progress.

6. Granada, A., Karra, S.B., and Senkan, S.M., Ind. Eng. Chem. Research, submitted, 1987.

7. Chang, W.D., and Senkan, S.M., Combust. Sci. Tech., v.43, p.49 (1985).

8. Chang, W.D., Karra, S.B., and Senkan, S.M., Combust. Sci. Tech., v.43, p.107 (1986).

9. Rotzoll, G., Combust. Sci. Tech., v.47, p.275 (1986).

10. Karra, S.B., and Senkan, S.M., "Detailed chemical kinetic modeling of the CCOP process", manuscript in preparation.

11. Trimm, D.L., in Pyrolysis: Theory and Industrial Practice, Albright, L.F., Crynes,B.L., and Corcoran,W.H., Eds., Academic Press, New York, NY 1983.

12. Frenklach, M., Clary, D.W., Gardiner, W.C., and Stein, S.E., Twentieth Symposium (International) on Combustion, p.887, The Combustion Institute, Pittsburgh 1984.

13. Colket, M.B., Twenty First Symposium (International) on Combustion, The Combustion Institute, Pittsburgh in press 1987.

14. Park, J.Y., Heaven, M.C., and Gutman, D., Chem. Phys. Lett., v.104, p.469 (1984).

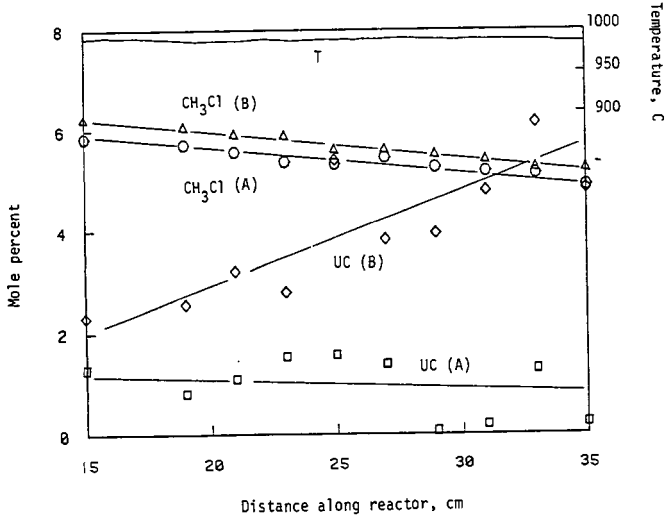

Figure 1. Profiles for CH_3Cl, UC and Temperature.

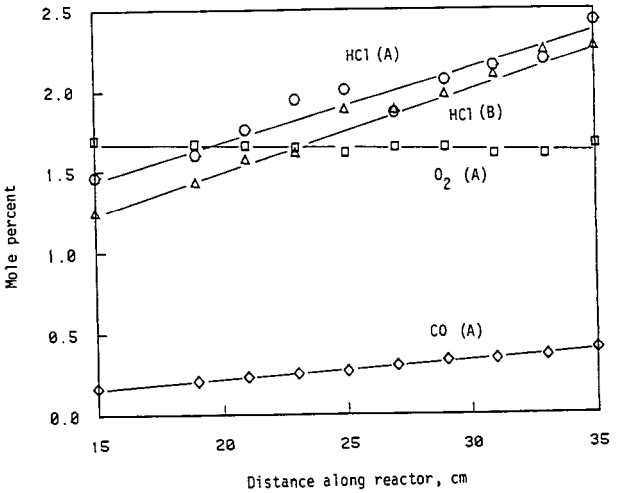

Figure 2. Profiles for HCl, O_2, CO.

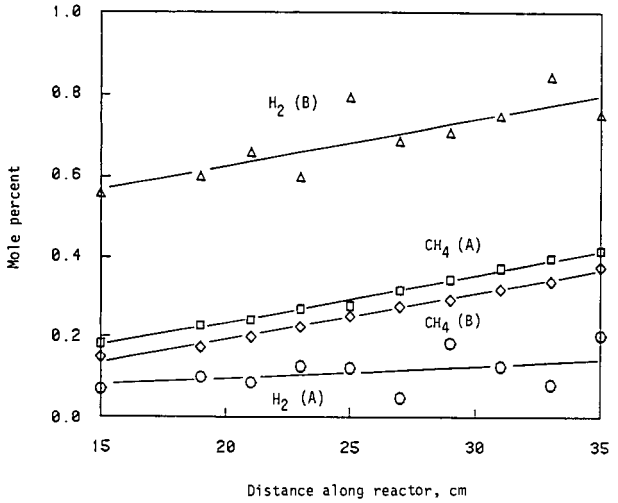

Figure 3. Profiles for H_2 and CH_4.

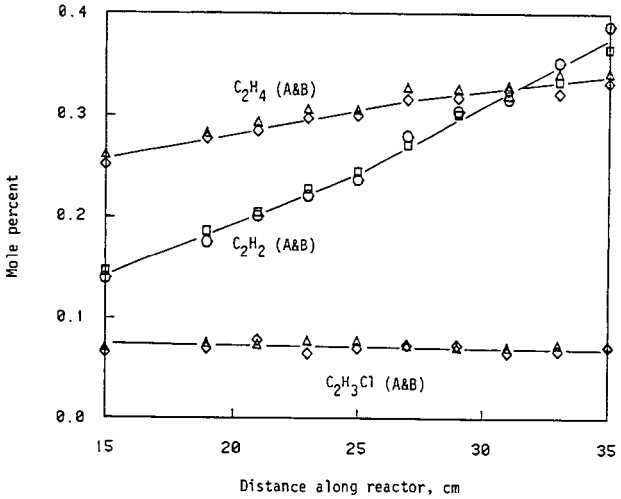

Figure 4. Profiles for C_2H_2, C_2H_4, and C_2H_3Cl.

CONVERSION OF METHANE TO GASOLINE-RANGE HYDROCARBONS

Charles E. Taylor and Richard P. Noceti
U.S. Department of Energy
Pittsburgh Energy Technology Center
P.O. Box 10940
Pittsburgh, PA 15236

Existing processes have been assembled in a novel combination capable of producing higher hydrocarbons from methane with high yield and selectivity. Methane, oxygen, and hydrogen chloride react over an oxyhydrochlorination (OHC) catalyst in the first stage to produce predominantly chloromethane and water. In the second stage, the chloromethane is catalytically converted to higher hydrocarbons, namely, paraffins, cycloparaffins, olefins, and aromatics, by an alumino-silicate zeolite. In the process described, the final hydrocarbon mixture is largely in the gasoline (C_4-C_{10}) boiling range.

The first stage of the process has been carried out under varying conditions of temperature and residence times. The conversion of reactants, the yields, and the product selectivities are tabulated over the operating range of the catalyst.

The second-stage reaction has been carried out utilizing feeds of chloromethane and various mixtures of chloromethane, dichloromethane, and trichloromethane. A long-term study on a commercial zeolite has shown no significant changes in conversions or product distribution after multiple regeneration cycles.

INTRODUCTION

Current technology for the conversion of methane to more useful compounds includes steam reforming reactions;[1] halogenation;[2] oxychlorination;[3] oxidation, including oxidative coupling and metal oxide reactions;[4] reaction with superacids;[5] and various other methods.[6] At present, these conversion schemes are unattractive because they are marked by low overall carbon conversions or poor selectivities.

In 1975, Mobil Oil Corporation patented a process for the conversion of methanol to higher hydrocarbons by reaction over a zeolite catalyst, such as ZSM-5.[7] Although later Mobil patents claimed that ZSM-5 would convert any monofunctionalized methane to higher hydrocarbons,[8] methanol was the feedstock of interest. In 1982, Ione et al.[9] reported that the conversion products of monofunctionalized methanes over zeolites were independent of the substituent and, for a given catalyst, depended only on the reaction conditions.

In work done at Allied Chemical Corporation, Pieters et al.[10,11] and Conner et al.[12,13] reported the selective functionalization of methane by reaction with oxygen and hydrogen chloride over a supported copper chloride catalyst to give tetrachloromethane as the major product. The advantages of the Allied process are significant. Reaction conditions are mild, and conversion and product distribution are stated to be functions of feed stoichiometry and temperature.

If a modification of the OHC reaction conditions produced predominantly chloromethane, a two-step process (Figure 1), in which the chloromethane oligomerization step provides the hydrogen chloride needed for methane chlorination, would be possible. Chlorine, as

hydrogen chloride, is essentially a placeholder in the methylene synthon. This is the basis of the PETC process.

The work described below demonstrates that an effective method for selective functionalization in combination with oligomerization over a zeolite catalyst provides a facile route for conversion of methane to higher hydrocarbons.

EXPERIMENTAL

The details of the two-stage laboratory reactor system are shown in Figure 2. All the reactants were introduced at slightly above atmospheric pressure from gas cylinders. Flow rates were controlled by a Brooks four-channel mass-flow controller. The feed stream for the first-stage reactor was sampled before and after the experimental run, while the product stream was continuously sampled on line during the run to obtain a mass balance around the OHC reaction. A quadrupole mass spectrometer was used to analyze the feed and product streams. Oligomerization reaction products were collected at dry ice temperatures and analyzed on a Hewlett-Packard 5880 capillary column gas chromatograph equipped with a Hewlett-Packard 5970 mass selective detector (GC/MSD).

Thermogravimetric (TG) measurements were conducted using a Perkin-Elmer TGS-2 system. Differential Scanning Calorimetry (DSC) measurements were conducted using a Perkin-Elmer DSC-2C calorimeter. Both the TG and the DSC were connected to a TADS data station. Heating rates of $10^{o}C\ min^{-1}$ were employed for 3-6 mg of activated OHC catalyst contained in a gold pan under an inert atmosphere.

The catalysts were contained between quartz wool plugs within horizontal 1- X 35- centimeter quartz tubes enclosed in split tube furnaces. Temperatures were controlled by a feedback controller.

The reactants were preheated to 175°C before entering the catalyst zone. The effluent stream was maintained at 150°C to prevent product condensation before the cold trap or in the capillary inlet to the mass spectrometer.

The oxyhydrochlorination catalyst was prepared according to the literature[10,11] by sequential layering of CuCl, KCl, and $LaCl_3$ onto a fumed silica support in nonaqueous solvents. The OHC catalyst was activated in a stream of hydrogen chloride at 300°C for ten minutes prior to use. The ZSM-5 was obtained from Mobil Oil Corporation in the ammonium form with a silica-to-alumina ratio of 70:1. The ammonium form was converted to the acid form by calcining in air at 538°C for 16 hours. The iron-promoted ZSM-5, prepared according to the method of Rao and Gormley,[14] contained 14.5% iron by weight and had a silica-to-alumina ratio of 27:1.

The reaction conditions for the oligomerization of chloromethane were similar to those reported for methanol,[15] i.e., reaction temperature of 350°C and WHSV = 1, using 1 gram of catalyst.

The zeolite catalyst was regenerated by exposure to oxygen at temperatures between 350° and 550°C until the presence of carbon dioxide in the effluent stream was no longer detected by the mass spectrometer. Removal of carbon restored the catalyst to its initial activity even after 14 cycles.

RESULTS

Conversion of methane to chloromethane

The conversion of methane to chloromethane has been observed under various reaction conditions. The data (Table I and Figure 3) show a material balance around 100% and display several trends. Note that methane conversion and polychlorination both increase as residence time and temperature increase.

The highest level of methane conversion occurred around 345°C, which is in the neighborhood of reported eutectic melting points for several $CuCl-KCl-LaCl_3$ mixtures.[11] When the temperature exceeded 350°C, conversion decreased. The DSC measurements showed an endotherm with an onset at 385°C and a maximum at 406°C. The maximum corresponds to the reported melting point of the supported $CuCl-KCl-LaCl_3$ layers.[13] The loss of activity occurs well below the experimentally determined melting point and may be explained as the result of a surface area decrease because of phase transitions in the supported phase or a loss of stratification due to diffusion.

Production of carbon dioxide and formic acid, undesirable by-products, also varied with residence time and temperature. As either the residence time or temperature increased, the amount of carbon dioxide increased while the amount of formic acid decreased. Carbon monoxide was not detected in the product stream.

The OHC catalyst is also susceptible to deactivation by exposure to oxygen in the absence of methane at temperatures greater than 100°C. Reactivation requires exposure of the catalyst to hydrogen gas at temperatures between 280° and 300°C. The catalyst is stable in air at ambient temperatures but is hygroscopic. Surface moisture is indicated by a color change from brown to green. Removal of water from hydrated catalyst by heating above 100°C in an inert gas stream gave a catalyst with less OHC activity than freshly prepared and activated catalyst.

Conversion of chloromethane to gasoline

Conversion of chloromethane over ZSM-5 to gasoline-range hydrocarbons has been observed to occur under conditions similar to those for the conversion of methanol. Two forms of the oligomerization catalyst were used in this study. One was a sample of iron-promoted ZSM-5 synthesized in our laboratory; the other was a sample of H-ZSM-5 obtained from Mobil Oil Corporation. Both catalysts produced similar products under the same reaction conditions. The gas chromatograms of the products collected from methanol or chloromethane oligomerization over ZSM-5 are shown in Figures 4 and 5, respectively. The mass selective detector allowed identification of most of the components in the samples, which are listed in Table II. Generally, the products contain ten carbons or less, and a large fraction of the product is aromatic. The presence of chlorinated aromatics was not observed for any of the oligomerization reactions conducted.

Trace amounts of 2-chloropropane and 2-chlorobutane were also found in one of the chloromethane oligomerization products. We hypothesized that these compounds had been formed by vapor phase addition of hydrogen chloride to propene and butene, products of chloromethane oligomerization. This type of addition has been reported to occur under similar conditions.[16] It was further proposed that if these

chlorinated alkanes came in contact with the zeolite catalyst, they would be oligomerized. To test the latter theory, several primary, secondary, and tertiary chlorocompounds of propane, butane, and pentane were allowed to react over ZSM-5 at the conditions for chloromethane oligomerization. In each case, the halocarbon was converted to aromatic hydrocarbons and hydrogen chloride, confirming our hypothesis.

Key to the PETC process is the ability of the ZSM-5 to convert mixtures of chloromethanes, especially those with compositions similar to the OHC product stream, without excessive deactivation due to coking. To determine the effect of feed composition on catalyst coking, mixtures of chloromethane, dichloromethane, and trichloromethane, including one with molar ratios identical to the OHC product stream (Table I, 5.14 seconds), were reacted over ZSM-5. Conversions and coke formation on the zeolite were comparable to those experienced for straight chloromethane (Figure 6) when the molar ratio of chloromethane to dichloromethane was at least 2.75 to 1 and the trichloromethane was 2.3 mole percent or less.

The effects of catalyst aging, caused by prolonged contact of the ZSM-5 with the products of reaction, mainly hydrogen chloride, have been addressed. Conversion studies were undertaken on a single 1-gram ZSM-5 sample exposed to various mixtures of chloromethane, dichloromethane, and trichloromethane under reaction conditions. When conversions dropped below 50%, the zeolite was regenerated by removal of the coke as described above. After regeneration, the initial conversion of chloromethane returned to ~100%. Product distribution exhibited no noticeable change during 800 hours of operation and 14 regeneration cycles.

Conclusion

Methane has been converted to higher hydrocarbons boiling in the gasoline range by the two-stage process described. In the first stage, mixtures of chloromethane, dichloromethane, and trichloromethane were produced by the OHC catalyst in ratios dependent on reaction temperature, residence time, and large changes in feed stoichiometry. Under the conditions described, the ratio of chloromethane to dichloromethane varied from 3.82 to 1.70 as residence time increased from 4.20 to 9.58 seconds. These experiments were conducted at a reaction temperature producing maximum methane conversion. Chloroform production also increased with increasing residence time. Tetrachloromethane formation was at or below detectability limits during all experiments.

The oligomerization of chloromethane to gasoline-boiling-range hydrocarbons occurred under conditions identical to those for methanol. Hydrogen chloride, the by-product of oligomerization, is recoverable from the product stream and may be recycled for use in the OHC step. Mixtures of chloromethane and dichloromethane in ratios of greater than 2.75 to 1, respectively, along with mixtures of chloromethane, dichloromethane, and trichloromethane in the same molar ratios as produced in the oxyhydrochlorination stage, are also oligomerized by ZSM-5. The oligomerization of the mixtures containing the polychlorinated methanes occurs without observable difference in conversion or coke deposition from that experienced for chloromethane or methanol. Long-term exposure of the zeolite to hydrogen chloride and multiple regenerations do not appear to affect either conversions or product distribution.

ACKNOWLEDGMENT

We would like to acknowledge the technical assistance of Dr. Karl T. Schroeder with the GC/MSD analysis, Dr. Sheila W. Hedges with the TG and DSC analyses, and Mr. Richard R. Anderson with the mass spectrometer.

DISCLAIMER

Reference in this report to any specific commercial product, process, or service is to facilitate understanding and does not necessarily imply its endorsement or favoring by the United States Department of Energy.

REFERENCES

1 Van Hook, J.P. Catal. Rev.-Sci. Eng. **1980**, 21(1), 1.

2 Fontana, C.M.; Gorin, E. U.S. Patent 2 575 167, 1951.

3 Kroenke, W.J.; Nicholas, P.P. U.S. Patent 4 467 127, 1984.

4 Pitchai, R.; Klier, K. Chem. Rev. **1986**, 28(1), 13.

5 Olah, G.A.; Gupta, B.; Farina, M.; Felberg, J.D.; Ip, W.M.; Husian, A.; Karpeles, R.; Lammertsma, K.; Melhotra, A.K.; Trivedi, N.J. J. Am. Chem. Soc. **1985**, 107, 7097.

6 Benson, S.W. U.S. Patent 4 199 533, 1980

7 Chang, C.D.; Silvestri, A.J.; Smith, R.L. U.S. Patent 3 928 483, 1975.

8 Chang, C.D.; Silvestri, A.J.; Smith, R.L. U.S. Patent 3 894 105, 1975.

9 Ione, K.G.; Stepanov, V.G.; Romannikov, V.N.; Shepelev, S.E. Khim. Tverd. Topl. **1982**, 16(6), 35.

10 Pieters, W.J.M.; Carlson, E.J.; Gates, E.; Conner, W.C., Jr. U.S. Patent 4 123 389, 1978.

11 Pieters, W.J.M.; Conner, W.C., Jr.; Carlson, E.J. Appl. Cat. **1984**, 11, 35.

12 Conner, W.C., Jr.; Pieters, W.J.M.; Gates, W.; Wilkalis, J.E. Appl. Cat. **1984**, 11, 49.

13 Conner, W.C., Jr.; Pieters, W.J.M.; Signorelli, A.J. Appl. Cat. **1984**, 11, 59.

14 Rao, V.U.S.; Gormley, R.J. Hydrocarbon Processing **1980**, 59(11), 139.

15 Chang, Clarence D. Hydrocarbons from Methanol; Marcel Dekker, Inc.: New York, 1983; Chapter 3.

16 Tierney, J.; Costello, F.; Dalton, D.R. J. Org. Chem. 1986, 11, 5191.

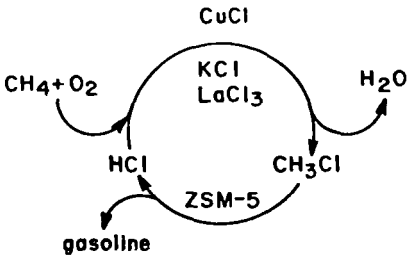

FIGURE 1. CYCLIC PATHWAY FOR THE CONVERSION OF METHANE TO GASOLINE BY THE TWO-STAGE PETC PROCESS

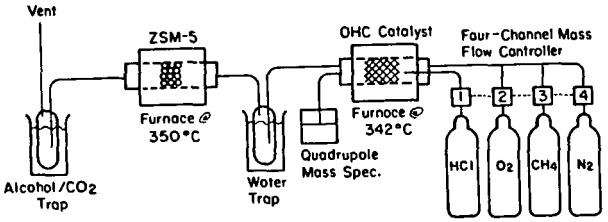

FIGURE 2. LABORATORY-SCALE UNIT FOR THE CONVERSION OF METHANE TO GASOLINE

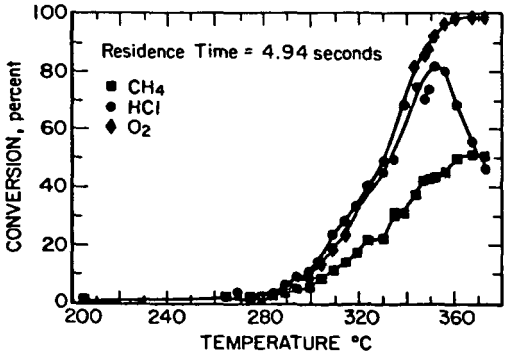

FIGURE 3. CONVERSION OF OXYHYDROCHLORINATION REACTANTS AS A FUNCTION OF TEMPERATURE

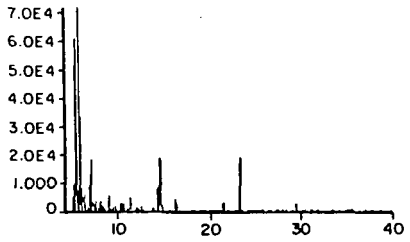

FIGURE 4. GAS CHROMATOGRAM OF METHANOL OLIGOMERIZATION PRODUCTS

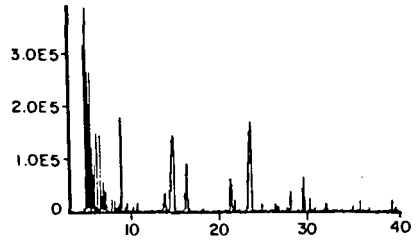

FIGURE 5. GAS CHROMATOGRAM OF CHLOROMETHANE OLIGOMERIZATION PRODUCTS

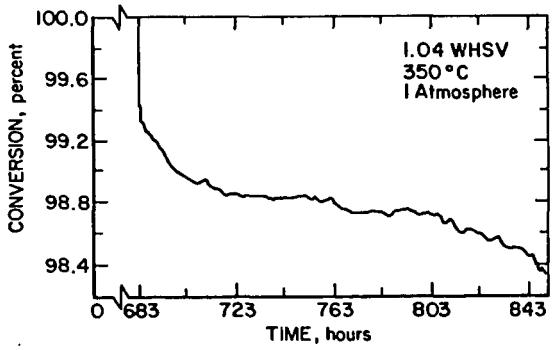

FIGURE 6. CHLOROMETHANE CONVERSION AS A FUNCTION OF TIME AFTER THE 14^{TH} REGENERATION

TABLE I

Selectivity of the OHC Reaction at 342°C

Calculated Residence Time (Sec)[a]	% Conversion[b]			% Product							CH_2Cl/CH_2Cl_2
	CH_4	HCl	O_2	CH_3Cl	CH_2Cl_2	$CHCl_3$	CCl_4	CO	CO_2	HCOOH	
4.17	25.20	30.17	34.01	75.32	19.72	1.58	0.00	0.00	0.81	2.57	3.82
5.14	28.36	39.28	38.89	73.96	21.24	1.96	0.00	0.00	0.93	1.90	3.48
8.06	38.36	50.71	55.21	68.42	25.83	2.92	0.01	0.00	1.43	1.39	2.65
6.26	36.36	57.72	57.95	67.90	26.16	2.70	0.00	0.00	1.60	1.64	2.60
6.37	45.25	62.41	62.89	66.70	27.15	3.32	0.01	0.00	1.62	1.19	2.46
7.71	42.12	96.36	97.36	64.90	27.47	3.82	0.01	0.00	2.16	1.62	2.36
9.12	53.48	98.00	92.89	57.34	32.31	5.95	0.02	0.00	3.45	0.93	1.77

[a]Residence Time = (catalyst void space)/(total inlet gas flow rate).

[b]% Conversion = 100*([IN] - [OUT])/[IN].

TABLE II

Oligomerization Product Identification

Retention Time (Min.)	Compound
5.088	Pentane
5.259	Butane
5.356	Benzene
6.255	Cyclohexane
6.638	Hexane
8.980	Toluene
13.763	Xylene
14.645	Xylene
16.352	Xylene
21.716	1,3,5-Trimethylbenzene
23.276	1,2,3 + 1,2,4-Trimethylbenzene
26.020	Tetramethylbenzene
29.506	Durene
32.078	Pentamethylbenzene

Hydrodenitrogenation of Quinoline and Coal Using Transition Metal Sulfides

Christine W. Curtis and Donald R. Cahela

Chemical Engineering Department, Auburn University, Alabama 36849

This study investigates the effectiveness of unsupported, precipitated transition metal sulfides as HYD and HDN catalysts in both a quinoline system and a coal liquefaction system. The transition metal sulfides of moderate surface areas were produced by a method developed by Chianelli and Dines (1) in the late 1970's. These materials crystallize in weakly interacting layers which allow for ready intercalation of appropriate species. A number of different transition metal sulfides have been tested for HDS activity using dibenzothiophene (2) and are good candidates for hydrodenitrogenation (HDN) studies. The degree of HYD and HDN of quinoline and the reaction products from coal liquefaction were determined using precipitated transition metal sulfides and compared to commercial transition metal sulfides, commercial hydrotreating catalysts such as $CoMo/Al_2O_3$ and $NiMo/Al_2O_3$, and platinum containing catalysts such as Pt/SiO_2 and PtS_2.

Experimental

Preparation of Catalysts. Each precipitated transition metal sulfide was prepared by dissolving the metal chloride in ethyl acetate (EA) which was then added to a slurry of lithium sulfide (Li_2S), precipitating the metal sulfide. The product was annealed with pure H_2S at 400°C, washed with 12% acetic acid and then sulfided with 10% H_2S/H_2 at 400°C for 1 hour. The metal chlorides used were $CrCl_3$, $MoCl_4$, WCl_6, $FeCl_3$ and $RuCl_3{:}3H_2O$, producing Cr_2S_3, MoS_2, WS_2, FeS_x and RuS_2. All of the chemicals required for synthesis were obtained from Alfa Chemicals.

The composition of the metal sulfides was confirmed by X-ray diffraction by matching the d spacings of the sample with the reference. The experimental data matched the standards sufficiently to confirm the identity of the metal sulfides listed above. Sulfur analyses of both the precipitated and commercial transition metal sulfides are compared to the theoretical in Table 1. Surface area measurements by dynamic B.E.T. using N_2 in He are also given in Table 1. Differences in the surface areas of different batches of a given transition metal sulfide reflect the sensitivity of the surface area to preparation methods.

A platinum on silica (Pt/SiO_2) catalyst was prepared by adding 0.44 g SiO_2 to 12.46 g of a 5% solution of hydroplatanic acid. Water was removed by vacuum rotary evaporation and the catalyst was dried for 16 hr at 50°C under 25 mm Hg. After grinding, the Pt/SiO_2 was reduced in a 40 ml/min H_2 flow producing a slivery black material. PtS_2 was obtained from Alfa Chemicals. The $NiMo/Al_2O_3$ and $CoMo/Al_2O_3$ catalysts were presulfided in a stream of 10 volume percent H_2S in H_2; sulfiding was begun at 250°C and the temperature was raised by 50°C every fifteen minutes until 400°C was reached and maintained for one hour. Both catalysts were ground before use.

Quinoline Model System. Reactions were performed with the precipitated and commercial transition metal sulfides, Pt/SiO_2, PtS_2, $CoMo/Al_2O_3$ and $NiMo/Al_2O_3$ catalysts in 15 cm^3 stainless steel tubing bomb reactors. Two weight percent quinoline in hexadecane was used as the reactant solution (5 g) with 0.025 g catalyst and 1250 psi hydrogen (cold). The reactor was maintained at 380°C while being agitated at 850 rpm. Most of the reactions were at least duplicated. Several lower temperatures were used with the Pt/SiO_2 catalyst. The liquid products were analyzed by gas chromatography using a fused silica 30 m capillary DB-5 column with a 0.2 micron film with FID detection and p-xylene as the internal standard. NH_3 was analyzed using a Chromosorb 103 column and TCD detection. Hydrogen consumption was determined using a molecular sieve column with TCD detection in conjunction with standard PVT methods.

Table 1. Analysis of Catalysts

Catalyst	Sulfur, % Sample	Sulfur, % Theoretical	Surface Area, m^2/g
Cr_2S_3-4	44.0	48.1	19.5
Cr_2S_3-C	49.6	48.1	12.5
MoS_2-3	37.7	40.1	30.8
MoS_2-7		40.1	24.1*
MoS_2-C	41.1	40.1	10.7
WS_2-2	25.1	25.9	13.5
WS_2-4		25.9	
WS_2-C	24.9	25.9	8.5
FeS-2	39.1	36.5	6.7
FeS_2-C	57.2	53.5	4.9
RuS_2-3	30.2	38.8	26.4*
			19.4
RuS_2-5			81.5*
$NiMo/Al_2O_3$			174
$CoMo/Al_2O_3$			180

*Analyses performed by Quantachrome Corporation

The concentration of the liquid phase products is given for each compound as a mole percentage of quinoline initially charged to the reactor. The data is summarized in terms of percent of maximum hydrogenation (PMH), percent hydrodenitrogenation (PHDN), and percent hydrogenolysis (PHYG). PMH is the number of moles of hydrogen required to produce the observed product distribution from quinoline as a percentage of the hydrogen required to produce the final end product, propylcyclohexane (PCH). PHDN is calculated by summing the mole percentage for the components which do not contain nitrogen. PHYG is obtained by summing the mole percentages for the compounds which have resulted from hydrogenolysis of the C-N bond.

Coal Liquefaction Reactions. Ground Kentucky #11 coal with a nitrogen content of 1.10% was used in the liquefaction reactions. Two batches of coal were used: Batch A, kept in a desiccator, dried during the course of the experiments, while the moisture content of Batch B remained fairly constant. Thermal and several catalytic reactions were performed using Batch A; the product distributions were corrected for the changing moisture composition of the coal.

Coal liquefaction reactions were performed with MoS_2, RuS_2, $NiMo/Al_2O_3$, and Pt/SiO_2 as well as thermally in 46 cc stainless steel tubing bomb reactors. The charge to the reactor was 0.5 g of coal with 0.5 g anthracene as solvent. Reactions were performed at 425°C for 60 minutes at an agitation rate of 850 rpm. Recovery of the product from the reactor was based upon the weights of the solid and liquid fractions. In calculating the product distributions, all losses were equally distributed among the solid and liquid fractions. The product distribution is reported on a maf coal basis.

The liquid and solid products were separated by sequential washing with methylene chloride - methanol (9:1 v/v) solution (MCM) and tetrahydrofuran (THF). This separation produced three fractions: MCM solubles (MCMS), MCM insolubles-THF solubles (THFS) and THF insolubles or ash-free insoluble organic matter (IOM). The MCMS fraction was further fractionated by the chromatographic method of Boduszynski et al.(3) into compound-class fractions: hydrocarbons (HC), nitrogen heterocycles (NH), hydroxylaromatics (HA) and polyfunctional compounds (PC). Model compounds such as anthracene, acridine, carbazole and 2-naphthol, were chromatographed and verified the procedure. The hydrocarbon fraction separated from the MCMS fraction was further analyzed for anthracene hydrogenation products using the same capillary column as for quinoline. The sample, dissolved in toluene with phenanthrene as the internal standard, was analyzed isothermally at

180°C. Anthracene and three major hydrogenation products were observed: 9,10-dihydroanthracene (DHA), 1,4,5,8,9,10-hexahydroanthracene (HHA), and 1,2,3,4,5,6,7,8-octahydroanthracene. In some reactions, a corrected sum (CRS) is used which includes the light cracked products produced during the reaction assuming a response factor of unity and disregarding molecular weight changes. This CRS was required to obtain reasonable recovery values due to cracking of anthracene during the reaction. The anthracene products are reported as a percentage of the anthracene charged, the sum of which represents the recovered anthracene.

Results and Discussion

The activity and selectivity of precipitated transition metal sulfides for HDN of quinoline were compared to that of $NiMo/Al_2O_3$, $CoMo/Al_2O_3$, commercial transition metal sulfides and Pt/SiO_2. Several transition metals from groups 6B and 8A were chosen. The catalysts which showed the highest level of HYD and HDN activity in the quinoline system were used for the coal liquefaction reactions.

Quinoline Reaction System. The reaction pathway (Figure 1) for quinoline under catalytic conditions has been extensively investigated by Satterfield and coworkers (4-6). In the current study, the gaseous and liquid products from both thermal and catalytic reactions were analyzed and reasonable recoveries of the liquid products were attained. Methane (CH_4) was the only hydrocarbon gas observed. The ammonia (NH_3) observed was usually much less than it should have been based upon the denitrogenation of the liquid products. Solubility experiments in hexadecane showed that ~70% of the hexadecane was absorbed by the solvent, yielding low recoveries.

The product distribution achieved from the thermal and catalytic quinoline reactions are given in Table 2. The PMH and PHDN terms are good indicators of HYD activity and HDN selectivity. Precipitated RuS_2 and supported $NiMo/Al_2O_3$ showed the highest and nearly equivalent PMH of ~49%. Precipitated MoS_2 produced a PMH of ~42% and $CoMo/Al_2O_3$, 39%, while the other catalysts yielded lesser amounts of hydrogenation, ranging from 24 to 30% PMH. The catalysts can be ranked according to their ability to hydrogenate quinoline in terms of PMH: RuS_2-3 ≐ $NiMo/Al_2O_3$ > MoS_2-3 ≐ $CoMo/Al_2O_3$ > WS_2-2 ≐ Cr_2S_3 -4 > FeS_x-2> thermal. The number to the right of the sulfide indicates the batch number. Precipitated RuS_2 achieved the highest PHDN of 10.8%; $NiMo/Al_2O_3$ and precipitated MoS_2 achieved 8.9% and 8.0%, respectively. Likewise, RuS_2-3 and $NiMo/Al_2O_3$ also gave the highest PHYG, but, in this case, RuS_2 with a PHYG of 17.3% was substantially more effective than $NiMo/Al_2O_3$ at 10.2%. The remaining catalysts and the thermal reaction showed no denitrogenation and little hydrogenolysis.

A comparison of the precipitated transition metal sulfides to their commercial or mineralogical analogues is given in Table 3. Commercial RuS_2 was not available. Only in the case of WS_2 did the commercial metal sulfide give the same degree of HYD activity as the precipitated metal sulfide. For both MoS_2 and Cr_2S_3, the precipitated sulfide gave higher HYD activity and for MoS_2 higher PHDN and PHYG.

Table 3. Activity and Selectivity Comparison of Precipitated to Commercial Transition Metal Sulfides

Catalyst	PMH, %	PHDN, %	PHYG, %
None	5.0	0.0	0.0
Cr_2S_3-4	28.8	0.0	0.0
Cr_2S_3-C	25.9	0.0	3.1
MoS_2-3	41.7	8.0	10.4
MoS_2-C	29.4	0.0	1.7
WS_2-2	30.9	0.4	2.4
WS_2-C	32.9	0.0	2.5

Since $NiMo/Al_2O_3$ and precipitated RuS_2 gave comparable PMH of quinoline, the

Table 2

Product Distribution from Thermal and Catalytic Quinoline Reactions

Type Catalyst		None	Cr_2S_3-4	MoS_2-3	WS_2-2	FeSx-2	RuS_2-3	$CoMo/Al_2O_3$	$NiMo/Al_2O_3$
Mole NH_3 x 100%									
Mole Qi		2.8	0.2±0.1	2.8±1.5	0.34±0.48	0±0	0.42±(-)		1.06±1.4
Mole% CH_4		0	0±0	0	0±0	0±0	0±(-)		0.004±0.006
H_2 consumption,%		7.7	1.5±4.9	11.8±6.9	-7.1±7.1	3.3±15.6	18.1±(-)		13.1±18.6
M Q C	PCH	0±0	0±0	1.6±0.2	0.2±0	0±0	7.7±1.0	0.5±0.0	4.1±0.4
o u h	PB	0±0	0±0	6.4±0.0	0.2±0.1	0±0	3.1±0.2	1.9±0.1	4.9±0.2
l i a	DHQt	0±0	0.6±0.5	19.7±1.1	4.8±0.1	0.5±0.1	26.8±0.4	19.9±0.8	32.1±2.6
e n r	DHQc	0±0	0.3±0.4	4.6±0.4	1.0±0.1	0.6±0.1	4.8±1.6	4.2±0.1	7.0±1.0
o g	CHP	0.2±0.3	1.2±1.1	2.4±0.7	0.5±0.1	1.4±0	1.8±0.2	1.2±0.1	3.3±0.8
% l e	PA	0±0	3.1±0.1	2.4±0.1	0.9±0	0±0	6.5±0.4	1.3±0.2	1.3±0.1
i d	Q	82.7±3.3	2.2±0.3	2.0±0.6	1.7±0	16.±5.6	1.0±0	1.6±0.0	1.2±0.4
n	THQ	17.1±3.0	92.7±1.6	61.6±0.3	90.8±5.6	81.7±5.6	48.6±3.0	69.6±0.9	46.4±2.6
e									
PMH, %		5.0±0.9	28.8±0.5	41.7±1.0	30.9±0.1	24.5±1.6	49.1±1.4	39.0±0.3	49.5±1.8
PHDN, %		0±0	0±0	8.0±0.2	0.4±0.1	0±0	10.8±1.2	2.4±0.1	8.9±0.1
PRB, %		0±0	3.1±0.1	10.4±0.1	1.3±0.1	0±0	17.3±1.6	3.7±0.4	10.2±0.0
Recovery, %		90.4±1.6	83.6±5.7	75.5±18.9	88.2±1.6	86.2±6.8	89.5±1.6	89.1±5.1	79.1±15.3

Reaction Conditions:

Time	30 min
Temperature	380°C
Agitation Rate	850 cpm
H_2 Charged Cold	1250 psig
Reactant	2 wt% quinoline in hexadecane
Reactor	15 cc microreactor
Catalyst Charge	$\frac{\sim 5.10 \times 10^{-3} \text{g catalyst}}{\text{g reaction mixture}}$

Compounds:

PCH	propylcyclohexane
PB	propylbenzene
DHQ	decahydroquinoline
CHP	2,3-cyclohexenopyridine
PA	o-propylaniline
Q	quinoline
THQ	1,2,3,4-tetrahydroquinoline

catalytic activity and selectivity of these two catalysts were tested with two individual products from quinoline hydrogenation: 1,2,3,4- tetrahydroquinoline (THQ) and 2-propylaniline (PA). The two catalysts achieved similar PMH and PHDN of THQ. $NiMo/Al_2O_3$ yielded more cis and trans decahydroquinoline (DHQ) than RuS_2 which produced more PA and nearly twice as much PHYG. When PA was used as the reactant, more hydrogenation and denitrogenation of PA was achieved with $NiMo/Al_2O_3$ than RuS_2. The lesser ability of RuS_2 to convert PA may explain the larger amount of PA observed in the THQ reaction with RuS_2.

Table 4. Catalytic Activity of $NiMo/Al_2O_3$ and RuS_2 in Several Reactant Systems

	Thermal	$NiMo/Al_2O_3$	RuS_2
Catalytic Activity with THQ as a Reactant			
PMH of THQ, %	0.7	27.8	25.4
PHDN,%	0.0	7.4	8.9
PHYG, %	0.0	8.5	14.6
Catalytic Activity with Propylaniline as Reactant			
PMH of PA, %	0.0	68.5	30.1
PHDN, %	0.0	81.4	36.5
Catalytic Activity with Propylaniline and Quinoline as Reactants			
PMH of PA, %		27.1	22.6
PHDN, %		35.6	27.1

To simulate the quinoline reaction system, 0.2 wt % quinoline was added to the PA solution (2 wt %). Quinoline served as a leveler of catalytic activity. The $NiMo/Al_2O_3$ was severely poisoned resulting in substantial reductions in both the HYD and HDN ability of $NiMO/Al_2O_3$ while RuS_2 was affected to a lesser extent showing a one-third reduction in PMH and PHDN. Thus, the presence of basic nitrogen in quinoline and THQ reduced the inherent activity of $NiMo/Al_2O_3$ to make $NiMo/Al_2O_3$ effectively equivalent to RuS_2 in both activity and selectivity in the quinoline system.

Recently, a catalyst containing 40% reduced Pt on silica has been shown to be an active HDN catalyst (7). The HDN ability of Pt/SiO_2 in the quinoline model system was investigated at temperatures ranging from 200 to 380°C as shown in Table 5. At 200°C, Pt/SiO_2 achieved the same activity as Cr_2S_3 and WS_2 at 380°C, with a PMH of ~35%. The activity of Pt/SiO_2 increased with temperature up to 340°C yielding 71% PMH and 9.8% PHDN; the PHDN was similar to that of RuS_2 with Pt/SiO_2 at 380°C. None of the products from the quinoline reaction pathway was observed; only higher boiling compounds were present. Even the solvent hexadecane was no longer present.

Table 5. Effect of Temperature on Activity of Pt/SiO_2 for Quinoline Hydrodenitrogenation

Temperature, °C	200	250	300	320	340	380
MQC | PCH	0	0	1.9	3.4	9.7	0
olu | PB	0	0	0	0	0.1	0
lia | DHQt	9.7	47.4	64.6	61.6	70.7	0
enr | DGQc	5.1	9.1	10.4	10.4	12.6	0
og | CHP	3.5	0.8	1.2	1.2	0.9	0
%le | PA	0	0	0	0	0.4	0
id | Q	0.9	1.0	0	0	0	0
n | THQ	80.8	39.8	22.1	23.4	5.5	0
e |						
PMH, %	34.0	53.4	62.1	61.8	71.3	-
PHDN, %	0	0	1.9	3.4	9.8	-
PHYG, %	0	0	1.9	3.4	10.2	-
Recovery, %	91.1	93.6	80.9	93.1	93.1	75.5

A comparison of the activity and selectivity of Pt/SiO_2, PtS_2 obtained from Alfa Chemicals and precipitated RuS_2 is given in Table 6. At 250°C, a temperature where Pt/SiO_2 showed considerable activity, PMH values of RuS_2 and PtS_2 showed equivalent HYD activity, ~29 to 30%, while Pt/SiO_2 showed considerably more, ~53%. None of the catalysts was able to denitrogenate quinoline and almost no hydrogenolysis occurred at this temperature.

Table 6. Comparison of the Activity and Selectivity of PtS_2, Pt/SiO_2 and RuS_2 in the Quinoline Model System at 250°C

Catalyst	PtS_2-C	Pt/SiO_2-1	RuS_2
PMH, %	29.1	53.4	29.8
PHDN, %	0.0	0.0	0.0
PHYG, %	0.0	0.0	0.1

Coal Liquefaction Reactions. Two precipitated transition metal sulfides, RuS_2 and MoS_2, rivaled the commercial hydrotreating catalysts, $NiMo/Al_2O_3$ and $CoMo/Al_2O_3$, respectively, in their ability to hydrogenate and denitrogenate quinoline. Thus, RuS_2, MoS_2, $NiMo/Al_2O_3$ and Pt/SiO_2 were chosen as catalysts in coal liquefaction reactions to evaluate their efficiency in hydrogenating and removing nitrogen from coal.

Anthracene was used as the solvent for the coal liquefaction reactions. Since anthracene readily cracks under catalytic hydrogenation conditions (8), some hydrocracked products were expected; however, the presence of nitrogen heterocycles in the coal system moderated catalyst activity and reduced the amount of anthracene hydrocracking. For some of the reactions, the total anthracene products, including both hydrogenated and hydrocracked species, were measured, accounting for a 97 to 101% recovery of anthracene in thermal reactions and in reactions using $NiMo/Al_2O_3$ and RuS_2. However, when Pt/SiO_2 was used, only 74% recovery of the anthracene was achieved. With quinoline Pt/SiO_2 showed the production of high molecular weight materials at 380°C; this same phenomenon may have occurred in the coal reactions at the lower reaction temperature of 340°C.

The product distributions obtained from thermal and catalytic liquefaction reactions are given in Table 7. The reactions performed at 425°C yielded nearly equivalent coal conversions ranging from 94.5% for the thermal reaction to 99.0% for the reaction with RuS_2. The amount of light hydrocarbon gases produced was almost constant for all of the reactions yielding 15% for MoS_2 and RuS_2 and 14% for $NiMo/Al_2O_3$ while the thermal reaction produced nearly 19%. Therefore, the liquid products produced were quite similar in all reactions, ranging from 75.8% for the thermal reaction to 83.3% for RuS_2-5, thereby, providing a nearly equivalent basis for directly comparing the products from different reactions.

Comparing the product distributions, the sum of the polyfunctional compounds and THFS decreased from 20.5% for the thermal case to 9.0% for MoS_2-5&7, 6.4% for RuS_2-5 and 6.7% with $NiMo/Al_2O_3$. The total amount of product soluble in MCM increased by more than 10% in the catalytic compared to the thermal reactions. Considerably more of the heavier fractions was upgraded in the catalytic reactions producing a higher percentage of the products in the hydrocarbon (HC), nitrogen heterocycle (NH), and hydroxylaromatic (HA) fractions. In Figure 2, the product fractions produced from the different reactions are plotted against the catalyst specific surface area. The HC fraction produced followed the catalyst specific area: 17% for no catalyst, 34% for MoS_2-5&7, 49% for RuS_2-5 and 59% for $NiMo/Al_2O_3$. A maximum in Figure 2 is observed in the amount of NH produced, starting at 14% in the thermal reaction reaching ~19.5 and 18.2% with MoS_2-5&7 and RuS_2, respectively, and decreasing to ~11.0% with $NiMo/Al_2O_3$. Compared to the thermal reaction, the HA fraction decreased in the presence of the catalysts according to their specific surface area. Thus, the increased solubility of the coal-derived material in the MoS_2-5&7 and RuS_2 reactions was directly reflected in an increase in the NH and HC fractions since both the PC and HA fractions decreased. $NiMo/Al_2O_3$, attaining lower NH and higher HC fractions than the transition metal sulfides, performed better as a HDN catalyst than did RuS_2 in the coal

system.

Table 7. Product Distribution of Coal Liquefaction Reactions at 425°C

Type Catalyst			None	MoS_2-5&7	RuS_2-5	$NiMo/Al_2O_3$
Surface Area, m^2/g			-	24.1	81.5	174
g cat/g reactant			0.20	0.20	0.20	0.20
Temperature, °C			425	425	425	425
H_2 Consumption, %			6.2	8.5	14.2	15.3
Recovery, %			95.3	91.8	92.2	89.3
Coal Batch			A	A & B	B	B
	M|	GAS	18.61	15.16	15.61	13.76
	A|	M|HC	17.02	34.08	48.83	58.80
	F|	C|NH	13.99	19.47	18.20	11.02
W	|	M|HA	24.36	20.11	10.33	6.74
t	C|	S|PC	9.70	2.98	0.61	1.82
	O|	Total MCMS	65.07	76.64	77.97	78.37
%	A|	THFS	10.78	6.01	5.83	4.85
	L|	PC+THFS	20.48	8.99	6.44	6.67
	|	IOM	5.54	2.19	1.05	3.04
	|	Conversion, %	94.46	97.81	98.95	96.95
M A c|		DHA	16.11	13.36	4.00	2.17
o N h|		OHA	9.83	26.88	60.23	53.04
l T a|		HHA	58.43	38.26	17.97	16.30
e H r|		ANTH	2.61	0.20	0.0	0.0
g|		Total	86.97	79.05	80.49	71.51
% e|		CRS	96.96	-	101.91	100.55
d|						

The anthracene hydrogenation products from the liquefaction reactions are plotted versus catalyst specific surface area in Figure 3. Anthracene is sequentially hydrogenated from anthracene to DHA to HHA to OHA, which then hydrocracks to lighter products. In the thermal reaction, 2.6% anthracene remained unconverted; this amount decreased rapidly below GC detectability limits under catalytic conditions. DHA and HHA were at a maximum in the thermal reaction and decreased as catalysts with increasing surface areas were used, while OHA showed a maximum at an intermediate catalyst surface area. Both the OHA maximum and decrease in the sum of the anthracene hydrogenation products were due to hydrocracking of OHA. The CRS of the anthracene products in Table 7 indicates that all the anthracene could be accounted for in hydrogenated and hydrocracked products.

Coal liquefaction reactions using Pt/SiO_2 employed two stage processing in which a thermal reaction at 425°C was performed to convert most of the coal, followed by an hour reaction at 340°C with Pt/SiO_2. The two stage reaction scheme was used to dissolve the coal in the first stage and possibly upgrade and eliminate some of the potential catalyst poisons before introduction of the catalyst. The Pt/SiO_2 did not produce either a satisfactory or a reproducible suite of products. High gas makes of ~34% were observed along with substantial losses in the HC fraction. The THFS amount was quite large ~38% compared to ~5 for the transition metal sulfides. Analysis of the anthracene solvent accounted for only ~74% of the original anthracene charged to the reactor, indicating production of higher molecular weight compounds as in the quinoline reaction.

Summary

Two precipitated transition metal sulfides MoS_2 and RuS_2 possessed both HYD activity and HDN selectivity in the quinoline model system. These transition metal sulfides rivaled the commercial hydrotreating catalysts in activity; RuS_2 was comparable to $NiMo/Al_2O_3$ and MoS_2 to $CoMo/Al_2O_3$. $NiMo/Al_2O_3$ possessed higher activity for PA hydrogenation than did RuS_2; however, RuS_2 was not as severely

poisoned by quinoline as $NiMo/Al_2O_3$. Pt/SiO_2 at 340°C was as active a catalyst for quinoline HDN as $NiMo/Al_2O_3$ at 380°C. Both precipitated MoS_2 and RuS_2 achieved upgrading in coal liquefaction reactions showing HYD activity; however, the higher surface area $NiMo/Al_2O_3$ showed greater HYD activity and considerably more nitrogen removal. Pt/SiO_2 was readily poisoned in the coal system and was not effective for coal HDN.

Table 8. Products from Two Stage Liquefaction Using Pt/SiO_2

Catalyst Loading		H_2 Consumption, %	1.65 ± 2.33
g cat/g reactant	0.20	Recovery, %	111.74 ± 12.95
Temperature, °C	425/340	Coal Batch	B
(first stage/second stage)			

	M|GAS	33.81 ± 7.15	M A c|DHA	4.48 ± 0.78
	A|M|H	-9.57 ± 11.96	o N h|OHA	40.92 ± 1.82
	F|C|NH	19.13 ± 3.85	l T a|HHA	14.79 ± 1.90
W	|M|HA	24.09 ± 1.08	e H r|ANTH	0.0 ± 0.0
t	C|S|PC	4.95 ± 0.81	g|Total	60.18 ± 4.50
	O|Total MCMS	38.95 ± 16.09	% e|CRS	73.97 ± 10.85
%	A|THFS	33.29 ± 17.92	d|	
	L|PC+THFS	38.24 ± 18.72		
	|IOM	-5.69 ± 8.97		
	|Conversion	105.69 ± 8.97		

Acknowledgements

The authors gratefully acknowledge the support of this work by the Department of Energy under Contract No. DEAC22-83PC60044.

References

1. Chianelli, R.R., Dines, M.B., Inorg. Chem., 17(10), 2758(1978).
2. Pecoraro, T.A., Chianelli, R.R., J. Catal., 67, 430-445 (1981).
3. Boduszynski, M.M., Hurtubise, R.J., Silver, H.F., Anal. Chem., 54, 375-381 (1982).
4. Satterfield, C.N., Modell, M., Hites, R.A., Declerck, C.J., Ind. Eng. Chem. Process Des. Dev., 17(2), 141 (1978).
5. Satterfield, C.N., Cocchetto, J.F., Ind. Eng. Chem. Process Des. Dev., 20, 53 (1981).
6. Satterfield, C.N., Yang, S.H., Ind. Eng. Chem. Process Des. Dev., 23, 11 (1984).
7. Guttieri, M.J., Maier, W.F., J. Org. Chem., 49, 2875 (1984).
8. Weisser, O. and Landa, S., "Sulphide Catalysts, Their Properties and Applications," Pergamon Press, New York, 1973.

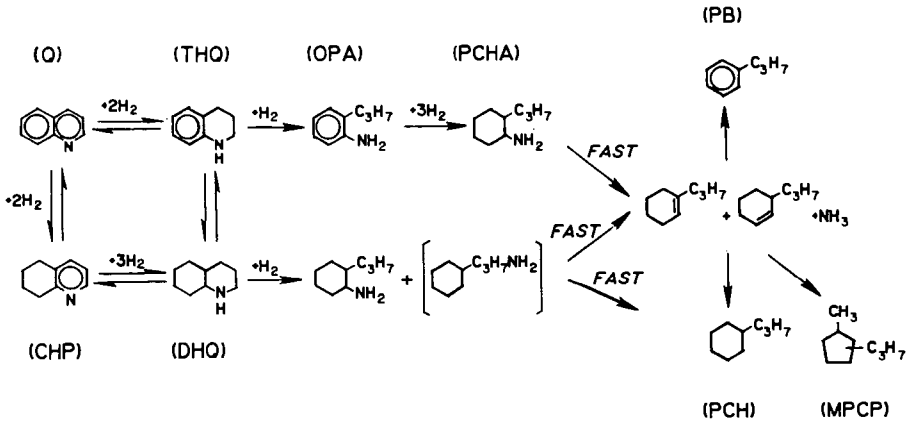

Q - quinoline

THQ - 1,2,3,4 -tetrahydroquinoline

CHP - 2,3 - cyclohexenopyridine

DHQ - decahyroquinoline (cis and trans isomers)

OPA - o-propylaniline

PCHA - propylcyclohexylamine

PB - propylbenzene

PCHE - propylcyclohexene (1,1 or 1,3)

PCH - propylcyclohexane

MPCP - methylpropylcyclopentane

Figure 1. Reaction Network.

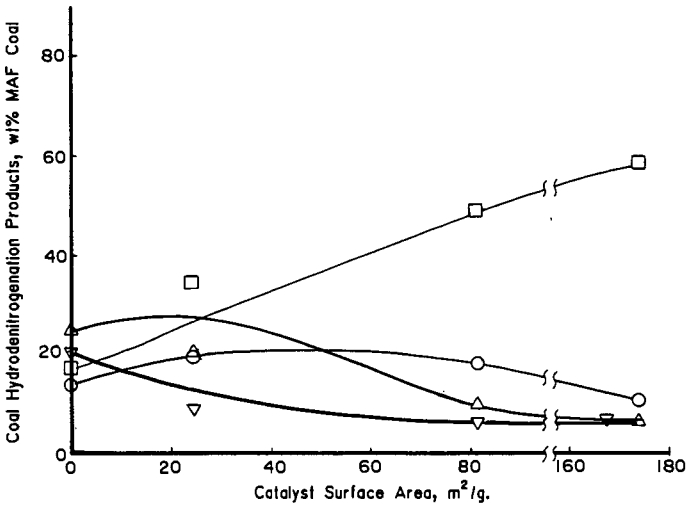

Figure 2. Effect of Catalyst Surface Area on Coal Hydrodenitrogenation Products: □-Hydrocarbons, ○-Nitrogen Heterocycles, △-Hydroxyl Aromatics, ▽-Polyfunctional Compound plus THF solubles.

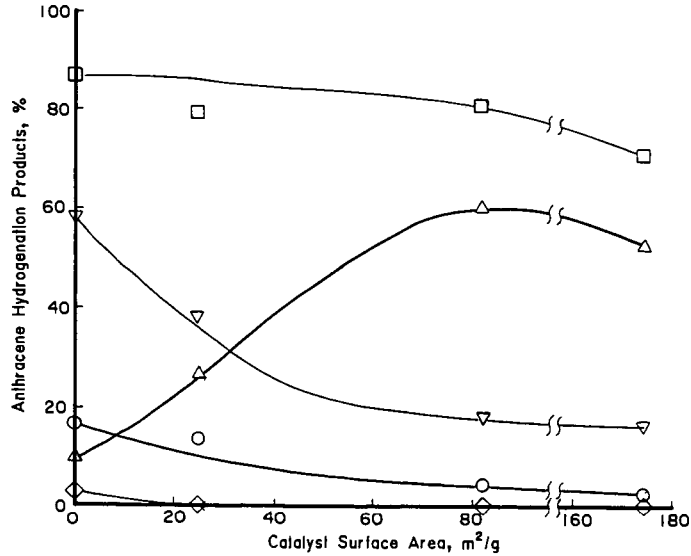

Figure 3. Effect of Catalyst Surface Area on Hydrogenation of Anthracene: ○-DHA, △-OHA, ▽-HHA, ◇-ANTH, □-Sum.

SAND87-0270C

CAUSES OF CATALYST DEACTIVATION DURING QUINOLINE HYDRODENITROGENATION*

Frances V. Stohl

Sandia National Laboratories Albuquerque, NM 87185

Introduction

Previous studies (1,2) of catalyst samples from the Wilsonville Advanced Coal Liquefaction R&D Facility have shown that the initial rapid catalyst deactivation was due to the buildup of carbonaceous deposits on the catalyst. Greater than 75% of the catalyst's hydrogenation (HYD) activity was lost as soon as coal processing began (2). Variations in the amount of carbonaceous deposits (1) on the catalysts from several different Wilsonville runs, which used two different coals and three process configurations, were due to the process configuration but not the coal type. The heaviest hydrotreater feed (from the Reconfigured Integrated Two-Stage Liquefaction configuration) in the Wilsonville runs, yielded the most accumulation of carbonaceous deposits on the catalyst and therefore the greatest deactivation (1). Hydrotreating this feed resulted in an initial 67% loss of hydrodesulfurization (HDS) activity; hydrotreating the lightest feed (from the Double Integrated Two-Stage Liquefaction configuration) yielded only a 47% decrease in HDS activity.

As a result of the work on Wilsonville catalysts, a program has been initiated to identify the hydrotreater feed components that are most harmful to the catalyst. Previous studies (3) to determine the impacts of the various chemical classes of compounds found in a hydrotreater feed on catalyst activity showed that the aliphatic and neutral polycyclic aromatic compounds yielded much less deactivation than the total hydrotreater feed and the nitrogen polycyclic aromatic compounds (N-PAC) and hydroxy polycyclic aromatic hydrocarbons (HPAH) yielded much greater deactivation. The N-PAC yielded a 95% loss of extrudate activity with 98% of the active sites poisoned. The activity losses for all of these fractions were due to poisoning of active sites and decreased effective diffusivities. Chemical analyses of the HPAH and N-PAC fractions showed that both contained significant amounts of oxygen and nitrogen so that the individual effects of the nitrogen and oxygen compounds could not be separated. Therefore, additional studies (4) were performed using both nitrogen and hydroxy model compounds. Hydrotreating phenol and 1-naphthol yielded only about 35% losses in extrudate activity. Hydrotreating indole, a weak basic pyrrolic nitrogen compound, yielded a 50% loss and carbazole, a neutral pyrrolic compound, yielded a 24% loss. In contrast, pyridinic nitrogen compounds (pyridine, quinoline, acridine) yielded about 75% losses. These results showed that the strong basic nitrogen compounds are most harmful to the catalyst.

The current work involves determining the causes of deactivation due to hydrotreating pyridinic compounds. Quinoline was chosen as the model compound for this study because it represents a type of nitrogen compound present in coal-derived materials, and a hydrodenitrogenation (HDN) reaction network has been proposed for

* This work supported by the U.S. Dept. of Energy at Sandia National Laboratories under Contract DE-AC04-76DP00789.

this compound (5,6). In the proposed reaction scheme, at low temperatures, quinoline is hydrogenated to 1,2,3,4-tetrahydroquinoline (PyTHQ). PyTHQ is cracked to o-propylaniline (OPA), and then the nitrogen is removed, as ammonia, to give propylbenzene (PBz). At high temperatures, the hydrogenation of quinoline to 5,6,7,8-tetrahydroquinoline (BzTHQ) also becomes important. BzTHQ is further hydrogenated to decahydroquinoline (DHQ), which is then cracked and denitrogenated to yield mostly propylcyclohexane (PCH). PyTHQ can also be hydrogenated to DHQ and OPA can also be hydrogenated and denitrogenated to PCH.

The initial work reported here on the causes of deactivation due to hydrogenating quinoline will cover the impact of process conditions on deactivation and the determination of the effects of the reaction scheme intermediates and products on deactivation.

Experimental Procedures

Quinoline was hydrogenated under a variety of conditions to determine the effects of process variables on catalyst deactivation. In addition, each of the intermediates formed during quinoline HDN was catalytically hydrotreated and the resultant deactivation measured. The aged catalysts were characterized and the intermediate compounds and products reported for the HDN reaction scheme (5) were quantified.

Materials

The catalyst was Shell 324M with 12.4 wt% Mo and 2.8 wt% Ni on an alumina support in the form of extrudates measuring about 0.8 mm in diameter and 4 mm in length. Prior to use the catalyst was presulfided with a 10 mol% H_2S in H_2 mixture at 400°C and atmospheric pressure for 2 hours. The structures of the model compounds used in this study are shown in Table 1.

Hydrotreating Experiments

Each hydrotreating experiment was performed in 26 cc batch microreactors with 1200 psig H_2 cold charge pressure. Runs were made for either 5 minutes or 120 minutes at either 300°C or 400°C. Unless otherwise stated, experiments were performed with 1.5g of model compound and 0.5g presulfided catalyst. The aged catalysts were Soxhlet extracted with tetrahydrofuran prior to activity testing. Elemental analyses were performed on the extracted aged catalysts.

Activity Testing

Hydrogenation activities of fresh and aged catalysts were determined by measuring the rate of hydrogenation of pyrene to dihydropyrene in 26 cc microreactors at 300°C with 450 psig H_2 cold charge pressure (7). Experiments with whole extrudates and catalyst ground to -200 mesh enabled determination of the losses of extrudate and intrinsic activities (8) respectively. Loss of intrinsic activity is proportional to the loss of active sites.

Liquid Product Analyses

Intermediates and products reported for the quinoline HDN reaction network (5) were identified using GC/MS and quantified using GC analysis with commercially available compounds as standards.

Results and Discussion

Activity Testing

The measured extrudate and intrinsic activity losses for the runs with quinoline at 300°C and 400°C for 5 minutes and 120 minutes are given in Table 2. The catalysts from all these runs had extrudate activity losses ranging from 73 to 84% and intrinsic activity losses from 85 to 94%. The differences in the measured extrudate activities of the catalysts from the two times at a given temperature are not significant. However, the catalyst from the 400°C run for 120 minutes is slightly more deactivated than the catalyst from the 300°C run for 5 minutes. The intrinsic activity losses for the catalysts from the quinoline runs are all the same within experimental error. These results show that deactivation occurs very rapidly and that significant changes in time and temperature have little effect on the extent of deactivation.

Effects of variations in the catalyst to reactant ratio were tested using quinoline at 300°C for 120 minutes. A run with a 1:1 ratio yielded a 64% extrudate activity loss, whereas runs with 1:3 and 1:9 ratios gave 76% and 77% losses respectively. These results suggest that a higher catalyst to quinoline ratio yields less deactivation, which is probably due to the greater number of active sites relative to the amount of deactivating compound.

The four intermediate compounds (PyTHQ, OPA, BzTHQ, DHQ) and the two products (PBz, PCH) were each hydrotreated with catalyst at 300°C for 5 minutes and 120 minutes. The measured extrudate and intrinsic activity losses are given in Table 3. The results show that for the 5 minute runs, the three hydrogenated species (PyTHQ, BzTHQ, DHQ) yielded comparable deactivation (about 70% extrudate activity loss) to hydrotreating quinoline. For the 120 minute runs, quinoline, DHQ, and BzTHQ yielded comparable activity losses to the 5 minute runs; PyTHQ yielded significantly less deactivation (53%). With both run times, OPA caused less deactivation than the other intermediates and PCH caused the least deactivation. PBz caused deactivation by a different mechanism than quinoline, PCH or the intermediates as indicated by the low amount of active sites poisoned. The 52% extrudate activity loss caused by PBz may be due to diffusional limitations caused by the deposition of carbonaceous material in the outer regions of the catalyst. This is a different mechanism than observed for quinoline so that this compound is not important in quinoline deactivation. The results of the hydrotreating experiments with the intermediate compounds and products indicate that greater deactivation is correlated with the hydrogenated intermediates (PyTHQ, BzTHQ and DHQ) and quinoline. It is not known why PyTHQ causes less deactivation at the longer time; it may be due to the greater reaction of PyTHQ at the longer time (see below).

Elemental Analyses of the Catalysts

There is a correlation between the carbon contents of the aged catalysts (Table 4) and deactivation. Quinoline, PyTHQ, BzTHQ and DHQ caused the most deactivation and gave the highest carbon contents. PCH yielded the least deactivation and gave the lowest carbon content. However, it appears that above a certain carbon content, when the catalyst is significantly deactivated, additional carbonaceous deposits do not have much effect on activity. For example, aged catalyst from the 120 minute run with quinoline at 300°C has about a 30% higher carbon content than the catalyst from the 5 minute run and yet they both are equally deactivated.

Liquid Product Analyses

Quantitative analyses of the liquid products from the quinoline runs performed at 300°C and 400°C for 5 minutes and 120 minutes are given in Figure 1. The amount of unidentified components (components that are not intermediates or products in the reported quinoline HDN reaction scheme (5)) is equal to 100% minus the height of the bar. The quantity of unidentified compounds increased with both time and temperature. At 300°C for 5 minutes, 19% of the liquid product was unidentified whereas at 400°C for 120 minutes 86% was unidentified. These results indicate that side reactions occur to a greater extent under more severe reaction conditions. The product distribution for the 300°C run for 5 minutes also shows that the hydrogenation of quinoline to PyTHQ was very rapid. Increasing time and/or temperature yielded more OPA. None of these runs yielded significant concentrations of PBz or PCH. The 400°C run products show a higher concentration of BzTHQ than the 300°C runs in agreement with previous results (5).

The product distributions for the run with a 1:1 quinoline to catalyst ratio had 54% unidentified product, whereas the runs with 1:3 and 1:9 ratios had 44% and 24% respectively. Therefore, a higher catalyst to quinoline ratio yields more side reactions. The product distributions also showed increasing concentrations of OPA and PCH with increasing catalyst to quinoline ratios.

The product distributions for the 5 minute runs with the intermediates and products showed no significant amount of unidentified material. In addition, the only significant reaction that occurred in any of these runs was the hydrogenation of BzTHQ to about 15 wt% DHQ. In the 120 minute runs (Figure 2), PyTHQ, DHQ and BzTHQ yielded 29%, 19% and 9% unidentified product respectively. In addition, PyTHQ formed more OPA, DHQ and PCH. OPA yielded more PCH. PBz was hydrogenated to a significant amount of PCH, and BzTHQ was hydrogenated to DHQ.

There is no correlation between the amount of deactivation and the amount of unidentified material in the liquid product. This is shown by the results of the quinoline runs in Table 2 and Figure 1. In addition, the 1:1 catalyst to quinoline run yields less deactivation than the 1:3 run, but yields more unidentified material.

The rapid deactivation due to hydrotreating quinoline and the hydrogenated heterocyclic intermediates may be due to the low reaction rates of the intermediate compounds to denitrogenated products at 300°C. Some of the intermediates (PyTHQ and DHQ) are strong basic compounds (9). Therefore, these compounds would be strongly adsorbed on the catalytic sites causing site blockage. Additional studies are underway to evaluate the effects of hydrotreating the intermediates and products at 400°C and to characterize the deposits on the aged catalysts.

References

1. Stohl, F.V. and Stephens, H.P. submitted to I&EC Research.
2. Stephens, H.P. and Stohl, F.V. ACS Division of Petroleum Chemistry Preprints 30(3), 465, 1985.
3. Stohl, F.V. and Stephens, H.P. ACS Division of Fuel Chemistry Preprints 31(4), 251, 1986.
4. Stohl, F.V. Proc. Direct Liquefaction Contractors' Review Meeting, Oct. 20-22, 1986, Monroeville, PA.
5. Satterfield, C.N., Modell, M., Hites, R.A. and Declerck, C.J. Ind. Eng. Chem. Process Des. Dev. 17(2), 141, 1978.
6. Cocchetto, J.F. and Satterfield, C.N. Ind. Eng. Chem. Process Des. Dev. 20, 49, 1981.

7. Stephens, H.P. and Kottenstette, R.J. ACS Division of Fuel Chemistry Preprints 30(2), 345, 1985.
8. Stephens, H.P. and Stohl, F.V. ACS Division of Fuel Chemistry Preprints 29(6), 79, 1984.
9. Satterfield, C.N. and Cocchetto, J.F. Ind. Eng. Chem. Process Des. Dev. 20, 53, 1981.

Table 1. Model compounds.

Quinoline	PyTHQ	OPA	PBz
			
BzTHQ	**DHQ**	**PCH**	
			

Table 2. Fraction of measured extrudate and intrinsic activity losses for the runs with quinoline. Results are relative to fresh presulfided catalyst.

	EXTRUDATE		INTRINSIC	
TEMPERATURE(°C)	5 min	120 min	5 min	120 min
300	0.73	0.76	0.89	0.89
400	0.80	0.84	0.85	0.94

Table 3. Fraction of measured extrudate and intrinsic activity losses for the 300°C runs with the intermediates and products. Results are relative to fresh presulfided catalyst.

	EXTRUDATE		INTRINSIC	
REACTANT	5 min	120 min	5 min	120 min
PyTHQ	0.70	0.53	0.85	0.80
OPA	0.54	0.47	0.66	0.66
PBz	0.52	0.53	0.22	0.27
BzTHQ	0.75	0.66	0.88	0.83
DHQ	0.68	0.67	0.82	0.78
PCH	0.14	0.21	0.37	0.35

Table 4. Carbon contents of the aged catalysts from the 300°C runs reported as weight percents.

	Quin	PyTHQ	OPA	PBz	BzTHQ	DHQ	PCH
5 min	4.81	4.25	3.86	2.28	5.19	4.07	1.81
120 min	6.36	NA*	3.43	2.49	4.76	4.19	1.99

* Not analyzed.

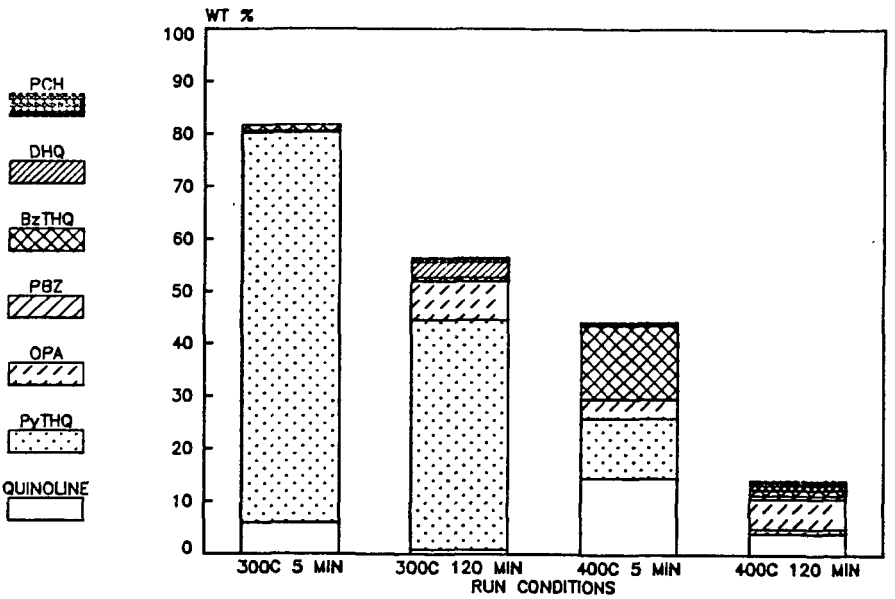

Figure 1. Liquid product analyses from the runs with quinoline.

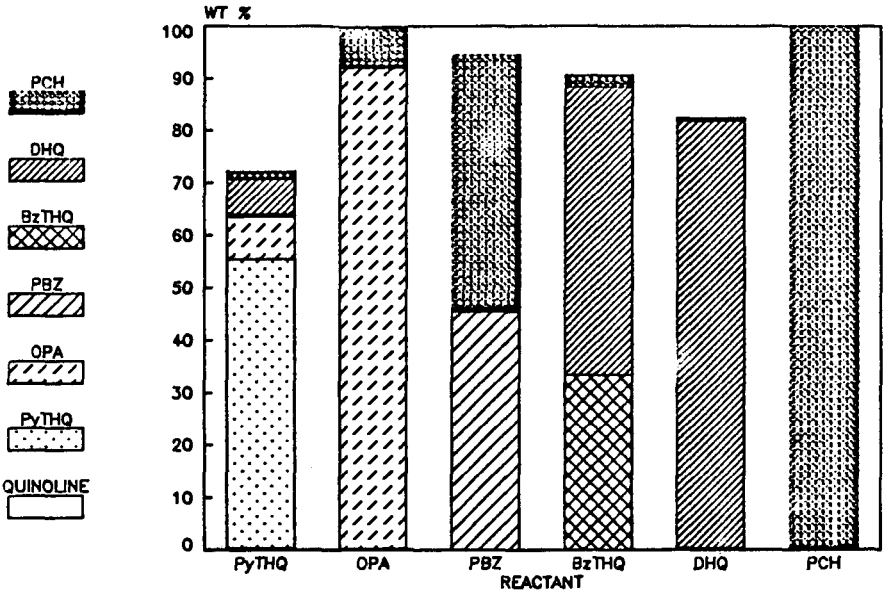

Figure 2. Liquid product analyses from the runs with the intermediates and products at 300°C for 120 minutes.

HYDROTREATMENT EFFECTS ON WILSONVILLE COAL LIQUIDS; COMPUTER-ASSISTED EVALUATION OF MULTISOURCE ANALYTICAL DATA

Koli Taghizadeh, Rita Hardy, Robert Keogh, Jack Goodman, Burt Davis
Kentucky Energy Cabinet Laboratory, Lexington, KY 40512

Henk L.C. Meuzelaar
University of Utah, Biomaterials Profiling Center
Salt Lake City, Utah 84108

INTRODUCTION

As reported earlier (1), monitoring time-dependent changes in Wilsonville coal-derived liquid (CDL) streams by means of computer-assisted direct mass spectrometry (MS) techniques enables detection of process related trends in the relative concentration of CDL components. Notwithstanding the potentially high information yield of this MS procedure, additional data is required for unambiguous identification and interpretation of some of the more complex components or trends. In fact, the CDL's produced by the Wilsonville pilot plant are routinely analyzed by an extensive array of conventional tests, including elemental analysis and solubility classes, as well as by advanced chromatographic and/or spectroscopic techniques, e.g., proton nuclear magnetic resonance spectroscopy (NMR) and carbon-13 NMR.

Unfortunately, the sheer volume of the data produced by this broad array of tests during a 2 to 3 month run makes it very difficult to discern some of the more interesting trends and effects. In the experiments reported here computerized multivariate analysis techniques such as factor, discriminant and canonical correlation analysis, were used to remove redundant data or experimental noise and to highlight relevant components and trends.

EXPERIMENTAL

A schematic flow diagram of the Wilsonville Advanced Coal Liquefaction facility in the Integrated Two-Stage Liquefaction (ITSL) mode is shown in Figure 1. The feed to the second stage hydrotreater is a mixture of thermal distillate (450^{o}F+) and Critical Solvent De-ashed Thermal Residue (CSD TR). The hydrotreater "atmospheric flashed bottoms" stream is recycled to the first stage dissolver. The temperature/time profile of the hydrotreater as well as a seven day average of the difference (ΔT) between the outlet and inlet temperature of dissolver are shown in Figure 2. The hydrotreater temperature was increased in 10^{o}F increments from 720^{o}F to 740^{o}F as the catalyst aged. However, as shown in Figure 2, several times during the run, operator responses to technical problems caused the actual hydrotreater temperature to be much lower than the set temperature. It is intended that the dissolver temperature be controlled primarily by the temperature of the preheated coal slurry, which flows from a preheater into the dissolver.

The data presented here were generated for samples collected during run No. 244 at the Wilsonville pilot plant when they were processing an Illinois No. 6 coal from a Burning Star mine. The average composition of the coal was: proximate analysis - VM 36%, FC 50%, moist. 4%, ash 10%; ultimate analysis - C 68.2%, H 4.5%, N 1.2%, S 3.3, mineral matter 10.6%, O (diff.) 12.2%. The sampling points for both hydrotreater feed and hydrotreater product (atmospheric flashed bottoms) samples are shown in Figure 1 and the days on which samples were collected are indicated in Figure 2. For consistency with earlier work (1), that numbering system was retained; unfortunately, the NMR and conventional data were not available for sample nos. 2, 3, 4, 12, 13 and 14. Therefore these samples were omitted from this data set.

Elemental carbon, hydrogen and nitrogen values were obtained using a LECO CHN-600 analyzer (2). Direct oxygen determinations were obtained by a modified Unterazucher method (3), and sulfur determinations were made on a LECO SC-132 instrument (4). The solubility class (oils, asphaltenes, preasphaltenes) and phenols determinations were described in detail elsewhere (5,6). Vacuum distillations utilized a modified ASTM D-1160 apparatus that was maintained at approximately 0.1 mmHg during the distillation. Following standard practice, the distillation was considered to be complete when cracking became noticeable.

Proton NMR samples were prepared by diluting approximately 0.25 g of the CDL with 0.25 ml of $CDCl_3$ which was doped with 1 wt. % TMS (tetramethyl silane). Spectra were recorded on a Varian EM-390 instrument. A minimum of two integrations were recorded for the proton regions determined. The proton spectra were divided into seven regions which correspond to different proton type resonances (7). Samples for carbon 13-NMR were prepared by diluting 1.5 g of the CDL with 1.0 ml of $CDCl_3$. Five mg of $Cr[acac]_3$ was added as a relaxation agent. Spectra were recorded with a Varian FT-80 spectrometer over a 4000 Hz spectral window at 20 MHz. Integrals were obtained in duplicate. The carbon 13-NMR spectra were divided into an aliphatic (0-50 ppm) and an aromatic region (100-200 ppm) (8).

Solutions for low voltage MS were prepared as follows: about 2 mg of each CDL were weighed and dissolved in 1 ml of a 1:1 benzene:methanol mixture. Solutions were stored at -10 ^{o}C prior to analysis. Low voltage MS were obtained using an Extranuclear 5000-1 quadrupole system under the following conditions: temperature rise time 5.5 s, equilibrium temperature 610 ^{o}C, total heating time 10 s, electron energy setting 12 eV, mass range scanned m/z 20-260, scanning rate 1000 amu/s, total scan time 20 s. Each sample was analyzed in triplicate and the resulting spectra were normalized using the SIGMA program package (9).

Data analysis was performed using factor analysis and canonical correlation analysis procedures, described elsewhere in more detail (10,11 and 12). Canonical correlation analysis was used to compare two data sets, e.g., on the basis of factor scores. The canonical correlation technique constructs sets of linear combinations of the variables in the two data sets in such a way that the first linear combination (canonical variate function) for the first data set and the first linear combination of the second data set show maximum correlation. The second set of linear combinations describes the maximum correlation remaining in the data set and so on.

RESULTS AND DISCUSSION

Figure 3 shows the averaged low voltage mass spectra of the hydrotreater feed and hydrotreater product (flashed bottoms). The hydrotreater feed spectrum shows relatively prominent peak series at m/z 168, 182, 196, 210 and 224, tentatively identified as acenapthenes and/or biphenyls with various of alkylsubstitution. The hydrotreater product spectrum shows major peak series at m/z 172, 186, 200, 214, and 228; these are believed to represent hydroaromatic hydrocarbons such as octahydrophenanthrenes and/or hexahydrofluorenes with possible contributions from tetrahydroacenaphthenes.

Other homologous ion series at m/z 212, 226, 240, 254 in the hydrotreated product spectrum obviously represent decahydropyrenes and perhaps decahydrofluoranthenes. Although there is no direct way to identify the various mass peaks in Figure 3, all major compound series were tentatively identified by GC/MS as well as MS/MS analysis of selected samples and compounds as well as by comparisons with GC/MS literature data on Wilsonville CDL's (13,14). Close scrutiny of Figure 3 may raise the question why the main compound series observed in the hydrotreater product does not correspond directly to the main compound series in the hydrotreater feed? An obvious answer is that the hydroaromatic compounds formed during hydrotreatment are

substantially more volatile than the corresponding aromatic parent compound series. Consequently, many of these low boiling volatiles are removed in the atmospheric distillation overhead fraction (see Figure 1).

A second aspect which should be pointed out here is that the spectra in Figure 3 represent only the CDL components which were able to reach the ion source without preheating the MS inlet system. Consequently, compounds with about 5-rings and higher are not included in Figure 3. However, as established in a separate series of experiments (1) involving preheating of the MS inlet as well as comparisons with Field Ionization MS data obtained at SRI, differences seen in Figure 3 are quite characteristic and representative of the overall changes observed as a result of hydrotreatment even if these higher components had been volatilized. In other words, the changes observed for the 2-4 ring systems in Figure 3 were qualitatively similar to those observed in higher condensed compound series.

To enable more systematic comparisons among the spectra of all 14 samples, the low voltage MS data were subjected to factor analysis. Figure 4 shows the factor score plot of the first two factors, together explaining 74% of the total variance in the data. The hydrotreater feed (categories 1-10) and hydrotreater product (categories 11-20) samples form two distinct clusters. In fact, Factor I and Factor II, with 64.4% and 9.6% of total variance respectively, appear to reveal two major trends in the data set; namely a hydrotreatment effect (Factor I) and a time + temperature effect (Factor II, compare with the time + temperature trend in Figure 2). Factors I and II explained 74% of the total variance in the data whereas the remaining 26% was largely explained by factors 3-10, none of which revealed significant components or trends.

Conventional coal liquid characterization data as well as ^{1}H and ^{13}C NMR data obtained for both sets of samples are shown in Table I. The effects of hydrotreatment are immediately apparent upon inspection of many of the parameters in Table I. However, neither the time + temperature trend, observed in the low voltage MS data nor any of the other trends which might be present are readily discernible by visual examination of the multidimensional information in Table I. Consequently, multivariate statistical analysis techniques such as factor analysis, are needed to reduce the data and reveal the main underlying trends.

To obtain a better insight into the components and trends described by the NMR and conventional data, factor analysis was performed on this data set as well. Eight factors with eigenvalues >1.0, together describing a total variance of 98.6% were obtained. The score plot of the first two factors is shown in Figure 5 with Factor I (57.4%) and Factor II (13.6%) revealing the hydrotreatment effect and time + temperature effect respectively. Again, the remaining factors (27.6%) did not reveal any clear trends or components. Encouraged by the obvious similarities between the information provided by Figures 4 and 5, we determined the degree of overlap between the two data sets by means of canonical correlation analysis.

Two major canonical correlation functions were found, CVI (can. corr. = 0.998) and CVII (can. corr. = 0.946). The integrated score plot of both data sets is shown in Figure 6. To reduce the complexity of the low voltage MS data, the average of each triplicate analysis was plotted. As expected, the same two important trends were observed with CVI showing the effect of hydrotreatment and CVII describing a combined time + temperature effect.

Figure 7 shows the absolute difference between the CVI scores of hydrotreated feed and hydrotreated products of low voltage MS and conventional and NMR data; this enables a more direct evaluation of the efficiency of the hydrotreatment process to be made. Apparently, the differences between the composition of the hydrotreater

feed and the hydrotreater product sample become somewhat less pronounced towards the end of the run, indicating a loss of hydrotreatment efficiency with time.

Finally, Figures 8 and 9 allow a more detailed chemical evaluation of the trends and components represented by CVI and CVII. The mathematically extracted mass spectra of CVI (hydrotreatment effect) and CVII (time + temperature effect) are shown in Figure 8. The positive components of the spectrum Figure 8a, representative of the hydrotreater feed, show prominent acenaphthene and/or biphenyl series at m/z 168, 182, 196, 210, and 224 (compare with Figure 3a) as well as naphthalene series at m/z 142, 156, 170, 184, and 198. The negative components show dominant hydroaromatic ion series at m/z 172, 186, 200, 214, and 228 as well as at m/z 212, 226, and 240 (also observed in Figure 3b).

Interpretation of the spectrum of the second canonical variate function in Figure 8b is less straightforward. Obviously, we are looking at a shift in the average molecular weight of the vacuum distillate fraction that is seen by the mass spectrometer. As discussed above, the upper limit of the vacuum distillate range is primarily determined by the inlet temperature of the mass spectrometer. Conversely, the lower limit of the distillation range must be primarily determined by the cut-off point of the atmospheric distillation following hydrotreatment. This cut-off point is likely to reflect the steadily increasing hydrotreater temperature shown in Figure 2. Consequently, the early samples tend to be richer in low MW components than the later samples obtained at higher hydrotreater temperatures. This appears to be reflected in the trend shown in Figure 8b. Whether Figure 8b also reflects the effect of catalyst aging, e.g. in the form of changes in qualitative composition is hard to decide due to the close correlation between time and temperature in the overall experimental design shown in Figure 2. Moreover, minor but definite changes in overall coal quality, e.g., as a result of storage and/or variations in mine output, could also have contributed to the observed trends, thereby further complicating attempts at unambiguous chemical interpretation. Obviously, if these effects are to be distinguished in future studies, the experimental design of the process conditions will need to be aimed at decoupling the effects of catalyst aging, reactor temperatures, distillation conditions and changes in feed coal composition.

The loadings (correlation coefficients) of the NMR and conventional variables on the first canonical variate function are shown in Figure 9a. Heteroatomic concentrations (N, S, O), asphaltene and benzene insolubles as well as the relative concentration of all condensed and noncondensed aromatic protons and aromatic carbon are higher in the hydrotreater feed than in the product samples. Conversely, %C, %H, oil yield, relative concentration of alkyl and cyclic protons (H-NMR) and aliphatic carbons (carbon 13-NMR) are, as expected, higher in the hydrotreater product (flashed bottoms).

Loadings of NMR and conventional data on CVII (Figure 9b) show that hydrotreater temperature (T), dissolver temperature (ΔT) and time (t) show a strong, positive correlation with CVII (negative portion). With increasing time and temperature, more hydrogen is present in the nondistillate fraction which could reflect decreased catalyst efficiency; that is, the hydrocracking activity decreases relative to the hydrogenation activity. Moreover, heteroatoms such as N and S are not removed as efficiently in the later days of the run. The fact that %O appears to be higher in the early days may well be due to phenols at m/z 136, 150, 164 or a pseduocorrelation caused by the normalization of %C, H, N, O to 100%. Also distillate yields are higher in early days, whereas the nondistillate portion increases in later days. ^{1}H-NMR data show higher alkyl beta and gamma protons in early days. The low voltage MS data in Figure 8b indicate that this might be due to the presence of highly substituted tetralins and phenols. Conversely, the ^{1}H-NMR data show that the relative concentration of cyclic alphas and some type of cyclic beta hydrogen increases in later days; the higher hydroaromatics in low

voltage MS (Figure 8b) could account for this. Overall, the time + temperature trend represented by CVII indicates a loss of catalyst efficiency accompanied by decreased distillate yield, increased aromaticity and ring condensation and a substantial increase in hydrogen in the nondistillate fraction.

A speculative interpretation of the latter observation has catalyst aging producing a more pronounced loss of bond cleavage activity than of hydrogenation efficiency, thus resulting in the formation of alicyclic structures which remain in the increasingly larger nondistillate fraction. Alternatively, one might hypothesize that a loss of efficiency in capping newly formed radicals leads to an increased condensation through regressive reactions.

ACKNOWLEDGEMENTS

This work was supported by the Commonwealth of Kentucky, Kentucky Energy Cabinet and DOE Contract No. DEFC22-85PC80009 as part of the Consortium for Fossil Fuel Liquefaction Science (administrated by the University of Kentucky). Dr. W. Windig and Mrs. M. Van are acknowledged for invaluable discussion in data analysis and manuscript preparation. We also acknowledge the superior cooperation of the staff of the Wilsonville Alabama pilot plant.

REFERENCES

1. Taghizadeh, K., Davis, B., Meuzelaar, H.L.C., 35th Annual Conference on Mass Spectrometry and Allied Topics., May (1987).
2. Leco Corp., CHN-600 Instrument Manual No. 200-340 (1983).
3. Unterzaucher, J., Analyst., 77, 584 (1952).
4. Leco Corp., SC-132 Manual 200-170 (1980).
5. Schultz, H., Mima, M.J., Prep. Pap., Am. Chem. Soc. Div. Fuel Chem., 23, (2)768, (1978).
6. Davis, B., Thomas, G., Sagues, A., Jewitt, C., Baumert, K., IMMR 80/053, April (1980).
7. Burke, F.P., Winschel, R.A., Pochapshky, T.C., U.S. DOE Contract DE-AC05-79ET-14503, Final Report, FE-14503-3., November (1983).
8. Levy, G.C., Nelson, G.L., Carbon-13 Nuclear Magnetic Resonance for Organic Chemists, John Wiley and Sons., New York (1972).
9. Windig, W., Meuzelaar, H.L.C., 34th Annual Conference on Mass Spectrometry and Allied Topics., 64, (1986).
10. Windig, W., Meuzelaar, H.L.C., Anal. Chem. 56, 2297, (1984).
11. Windig, W., Meuzelaar, H.L.C., Haws, B.A., Campbell, W.F., Asay, K.H., Anal. Appl. Pyrolysis 5, 183, (1983).
12. Halma, G., Van Dam, D., Haverkamp, J., Windig, W., Meuzelaar, H.L.C, J. Anal. Appl. Pyrolysis., 7, 167, (1984).
13. Wozniak, T.J., Hites, R.A., Anal. Chem. 57, 1320, (1985).
14. Winschel, R.A., Burke, F.P., Proceedings 8th Annual EPRI Contractors Conference on Coal Liquefaction, (1983).

TABLE I
AVERAGED NMR AND CONVENTIONAL CHARACTERIZATION DATA FOR HYDROTREATER FEED AND HYDROTREATER PRODUCT SAMPLES

Conventional Parameters*		Hydrotreater Feed (%)	Hydrotreater Product (%)	NMR Parameters*		Hydrotreater Feed (%)	Hydrotreater Product (%)
C	(1	88.70±0.13	88.89±0.19		(1	18.01±1.16	12.01±1.06
	(2	88.82±0.28	89.25±0.14	Condensed	(2	12.00±0.76	7.85±0.53
	(3	88.67±0.37	89.08±0.41	Aromatics	(3	26.18±3.59	19.89±4.80
H	(1	7.67±0.07	8.73±0.23		(1	8.26±1.21	6.00±0.57
	(2	8.85±0.25	9.76±0.09	Noncondensed	(2	9.95±1.33	4.87±0.33
	(3	5.69±0.08	6.13±0.25	Aromatics	(3	10.09±1.93	7.34±1.98
N	(1	0.83±0.06	0.70±0.12		(1	17.33±0.76	17.73±0.65
	(2	0.46±0.02	0.29±0.04	Cyclic	(2	13.08±1.64	14.70±1.72
	(3	1.98±0.07	1.68±0.07	Alpha	(3	18.77±1.67	19.76±0.82
S	(1	0.41±0.01	0.18±0.05		(1	9.89±0.71	10.03±0.29
	(2	0.24±0.02	0.03±0.01	Alkyl	(2	10.50±0.60	9.27±0.49
	(3	0.59±0.02	0.49±0.25	Alpha	(3	10.95±0.63	11.03±0.54
O	(1	2.38±0.12	1.51±0.12		(1	13.73±2.48	20.19±0.35
	(2	1.62±0.12	0.67±0.08	Cyclic	(2	16.41±0.75	20.35±1.28
	(3	3.06±0.31	2.63±0.58	beta	(3	13.52±0.71	16.42±1.35
Phenols		1.27±0.30	0.36±0.14		(1	20.61±0.95	21.22±0.66
				Alkyl	(2	22.54±0.70	24.31±0.77
Distillate		56.13±3.53	65.29±4.24	beta	(3	12.86±1.02	13.58±1.56
Nondistillate		43.87±3.53	34.71±4.24		(1	12.17±1.06	12.81±0.43
				Gamma	(2	18.46±2.61	18.64±2.89
Oils		58.28±1.60	75.79±2.90		(3	7.63±0.92	11.98±4.03
Asphaltenes		30.02±1.44	20.42±2.28	Aliphatic	(2	52.81±1.64	64.20±2.16
				Aromatic	(2	33.23±1.55	24.16±1.53
Benzene Insol.		11.70±1.53	3.79±1.10	Aromatic	(2	13.97±1.49	11.64±1.47

*(1) total sample, (2) distillable, and (3) nondistillable fraction.

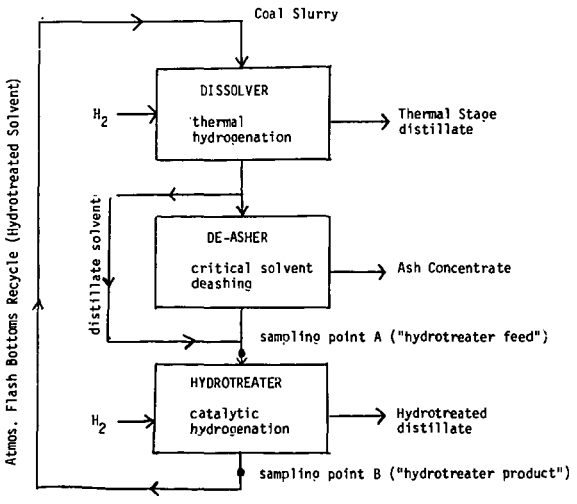

Figure 1. Wilsonville Integrated Two Stage Liquefaction (ITSL) process (simplified scheme).

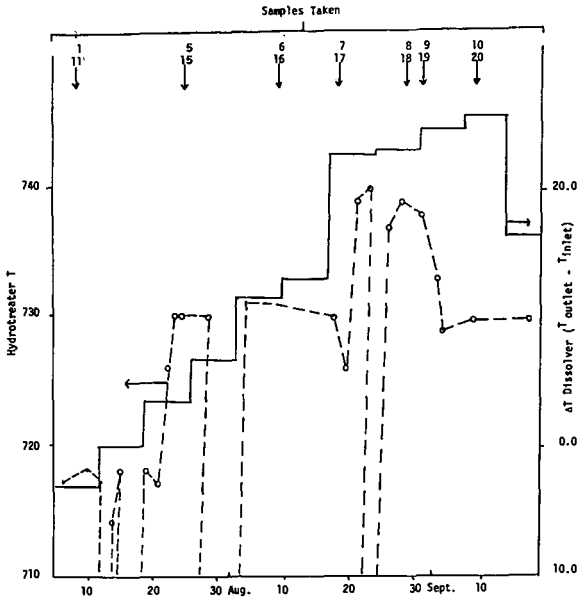

Figure 2. Temperature/-time profile of hydro-treater (--) as well as a seven day average of the difference (Δ T) between the outlet and inlet temperature of dissolver (__) and days on which samples were collected.

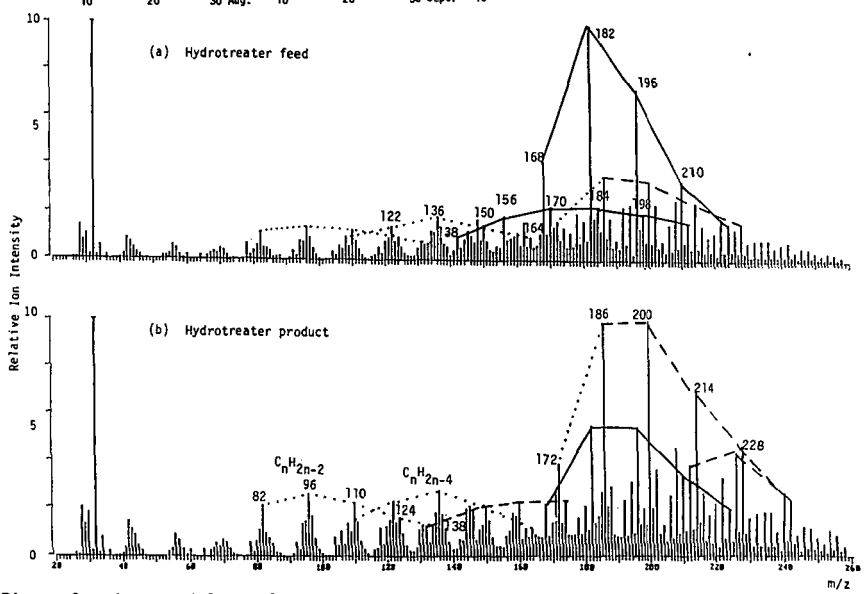

Figure 3. Averaged low voltage mass spectra of the hydrotreater feed (a) and hydrotreater product (flash bottoms) (b).

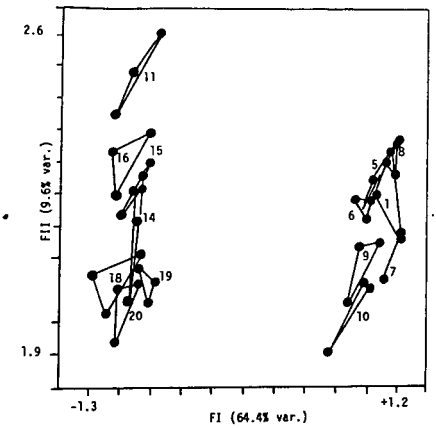

Figure 4. Factor score plot of low voltage MS data in the Factor I and Factor II subspace. Triplicate analyses of the same sample are connected by solid lines. For sample codes see Figure 2.

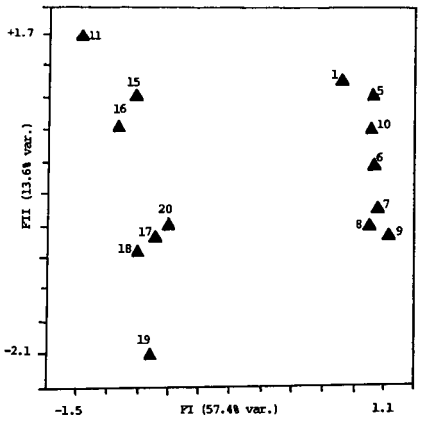

Figure 5. Factor score plot of NMR and conventional data in the Factor I and Factor II subspace, showing two cluster hydrotreater feed (1-10) and hydrotreater product (11-20). For sample codes see Figure 2.

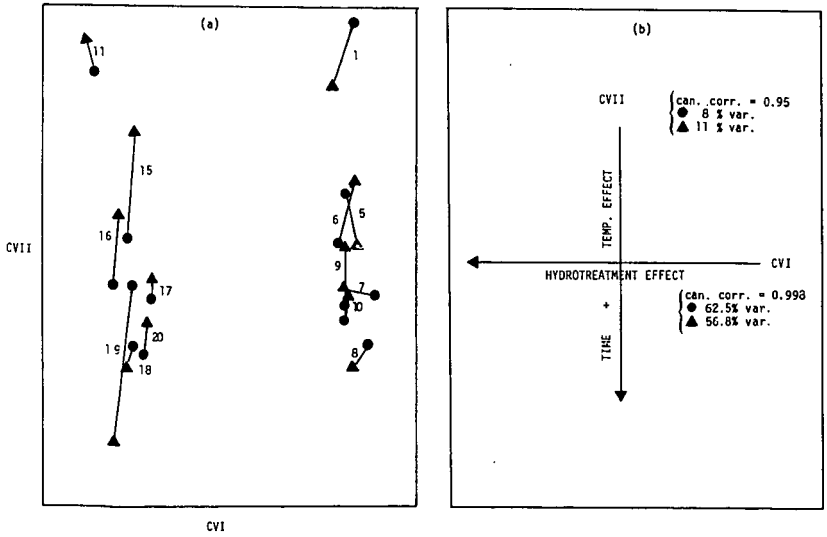

Figure 6. (a) Scores of low voltage MS (●) and scores of NMR and conventional data (▲) in the CVI and CVII subspace. Note the correlation between two data sets. (b) Interpretation of the major trends in the CVI-CVII subspace.

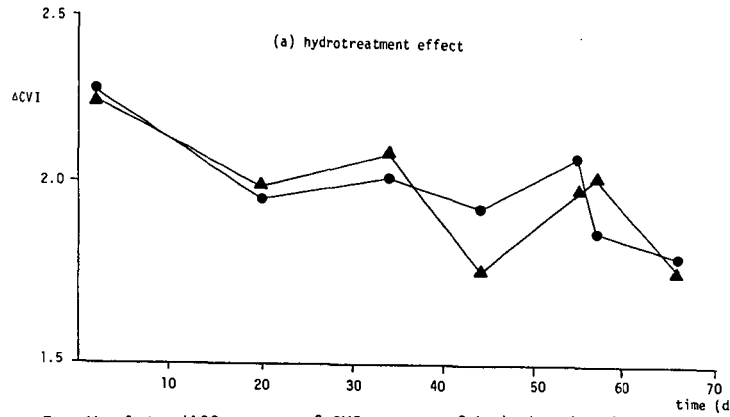

Figure 7. Absolute differences of CVI scores of hydrotreater feed and hydrotreater product for low voltage MS (●) and NMR and conventional data (▲).

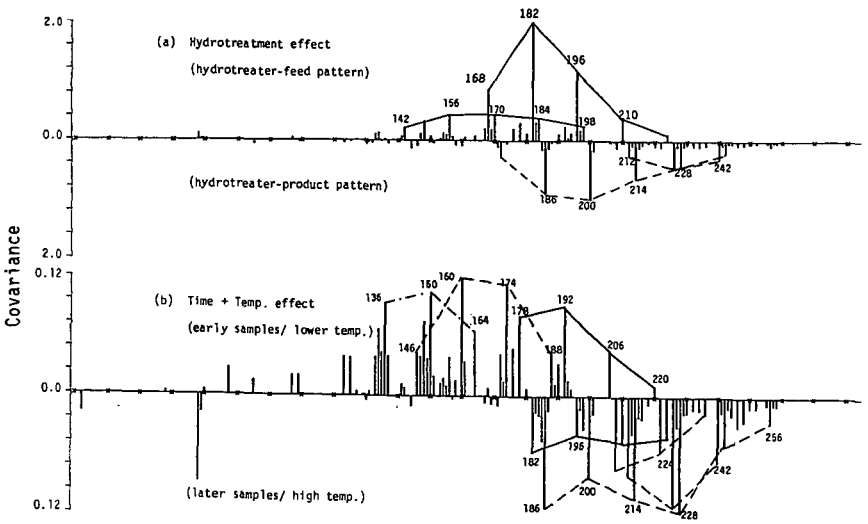

Figure 8. Mathematically extracted spectra of low voltage MS on CVI rotation (a) and CVII rotation (b).

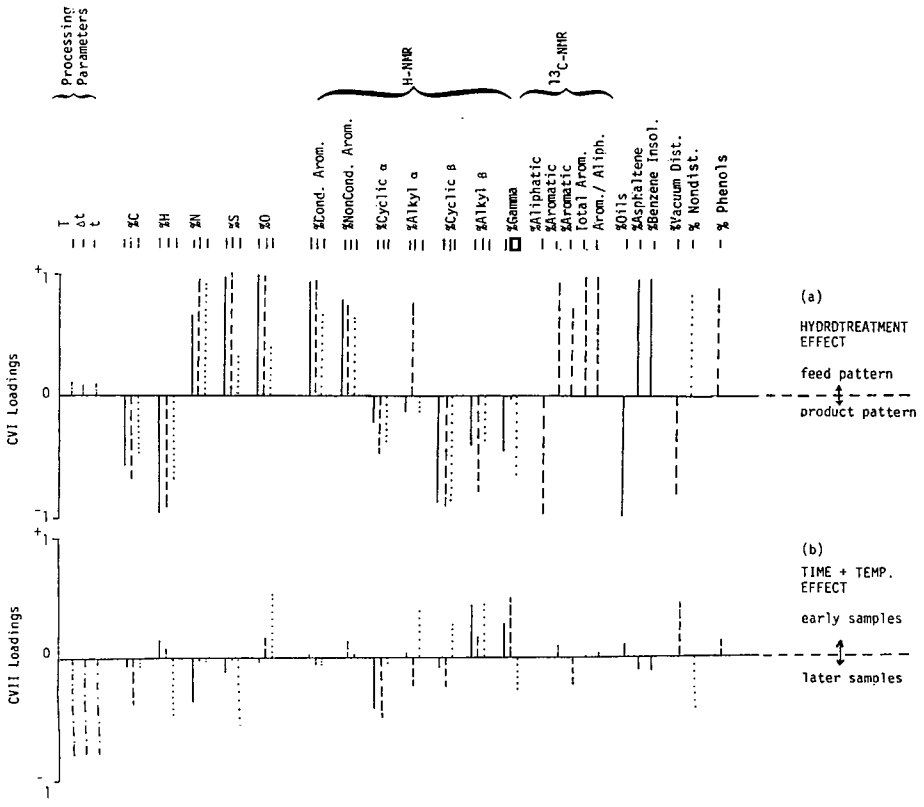

Figure 9. Loading of NMR and conventional variables on CVI (a) and CVII (b). Total sample (-), distillable fraction (--) and nondistillable fraction (...).

CONVERSION OF TETRALIN TO NAPHTHALENE DURING COAL LIQUEFACTION: A COAL RANK PHENOMENON?

B. Chawla, R. Keogh and B. H. Davis

Kentucky Energy Cabinet Laboratory
P. O. Box 13015
Lexington, KY 40512

ABSTRACT

Since coal conversion, in the presence of tetralin (a donor solvent), is believed to be a coal rank phenomenon, it seemed worthwhile to determine the role of rank upon conversion of tetralin (T) to naphthalene (N) during coal liquefactions at 385°, 427° and 445°C. The THF soluble fractions, containing T and N, were analyzed using a high performance liquid chromatographic technique. The T/N ratios, for eight coal samples of different ranks, showed a direct relationship between the coal rank and the T/N ratio. The conversion of tetralin to naphthalene was lowest for the highest rank coal, and vice versa. The T/N ratio versus rank relationship was obtained for reaction times ranging from 5 to 65 minutes.

INTRODUCTION

Coal liquefaction processes have been studied in the presence of hydrogen donor as well as non-hydrogen donor solvents during the last five decades (e.g. 1-14). Two generally accepted pathways (5, 6, 14-17) for H-transfer from a donor solvent (tetralin) to coal during coal liquefactions are shown in equations 1) to 4).

Pathway I

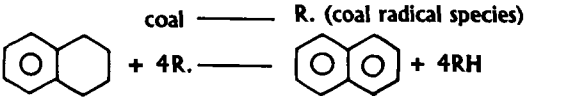

1)

2)

Pathway II

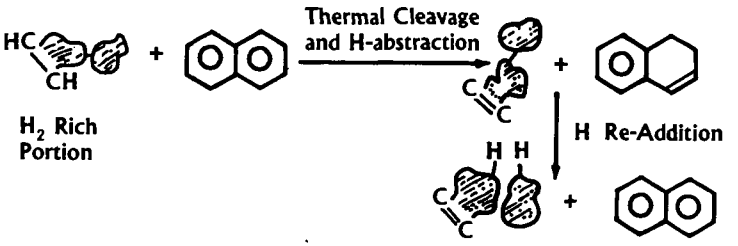

H_2 Rich Portion

3)

4)

Higher coal conversions in the presence of donor solvents have established that no matter which pathway dominates, the solvent hydrogen donor ability plays an important role in the process of coal liquefaction. However, only a small fraction of the research efforts, which are presently being made towards coal liquefaction processes, is being devoted for understanding the fate of H-donor solvent.

Tetralin (a donor solvent) involvement during coal liquefaction processes is indeed highly complex (3, 4, 16, 18) and produces various compounds such as naphthalene, 1-methylnaphthalene, 1-methylindane, indane, indene, butylbenzene, dimers and C_9 - C_{11} hydrocarbons, etc. However, the major component of tetralin conversion is naphthalene. In order to determine the role of coal rank upon conversion of tetralin (T) to naphthalene (N), we report in this paper our results on T/N ratios for liquefaction of eight coals of different ranks at 385°, 427° and 445°C.

EXPERIMENTAL

The liquefaction experiments were conducted in a microautoclave reactor of 50 ml capacity. The microautoclave was charged with 5g of coal (-100 mesh, dried overnight under vacuum of about 25 inches of Hg at 80-90°C), 7.5g of tetralin and a steel ball (1/4" dia.) for mixing. The system was pressurized with 800 psi of H_2 at ambient temperature (ca. 2000 psi at 445°C) and immersed in a heated sand bath for the desired reaction time. Typically, it required less than two minutes to reach the desired reaction temperature. To ensure thorough mixing of ingredients, the shaker speed (vertical) was set at 400 cpm. At the end of the experiment, the reactor was inserted in a cold sand bath. Once the reactor had come back to ambient temperature (within two minutes), the unreacted H_2 and other gases were slowly released. The products were removed from the reactor using tetrahydrofuran (THF) and were extracted in Soxhlet equipment to obtain the coal conversion. The extraction was continued for about 24 hours or more until the liquid extract obtained was clear.

The THF soluble reactor products were analyzed by a high performance liquid chromatographic (HPLC) technique. The technique requires only the stirring of resulting reactor products overnight with excess of THF and then injecting the THF filtrate into the HPLC system. The ratio of peak areas (number of counts) of tetralin and naphthalene can be used to obtain the T/N ratio directly (without knowing solution concentration) from a linear calibration plot of T_{area}/N_{area} versus T/N (see Figure 1). This technique was developed by optimizing the conditions for the analysis of the THF soluble reactor products:

Column:	Supelcosil, LC-PAH (25cm x 4.6mm)
Mobile Phase:	THF: H_2O, 40:60
Flow:	0.9 ml/min
Detector:	UV, λ254 (nm)

The performance of the HPLC system was checked against a standard mixture of uracil, acetophenone, benzene and toluene with CH_3OH:H_2O, 60:40 as a mobile phase with a typical flow rate of 1 ml/min.

The precision and reproducibility of the data were established by making repeated measurements for completely independent experiments performed on different days. The precision of the T/N data was found to be better than 1%. The accuracy of our results was verified by comparing the T/N ratios obtained by gc and HPLC. The maximum uncertainty in the T/N ratios was determined to be less than 5%.

The HPLC grade THF and water and the commercially available tetralin were used as supplied.

The chemical analyses of the eight coals used in this work are presented in Table 1.

RESULTS AND DISCUSSION

Effect of Coal Rank and Temperature on T/N Ratio

Coal liquefaction runs for eight coal samples were made at three temperatures, 385°, 427° and 445°C, to determine the extent of conversion of tetralin to naphthalene. The tetralin/naphthalene ratios obtained for the THF soluble reactor products are presented in Table 2. The overall variation in T/N values from 1.80 to 18.7 is very significant for the range of coal ranks covered under this study. The following observations result from the data in Tables 1 and 2:

(a) T/N ratio decreases with an increase in reaction temperature for all the coals studied.

(b) T/N ratio decreases with an increase in oxygen content of the coal. The decrease of the T/N ratio with the increase in oxygen content is much more systematic at the 427° and 445°C thermal severities, the data for 385°C are somewhat scattered.

(c) T/N ratio decreases with a decrease in carbon content of the coal and again the decrease in T/N ratio is more systematic at 427° and 445°C.

(d) The percentage coal conversion to THF soluble products (data not given in Table 2) increases with an increase in temperature - consistent with the previous observations (5, 17). Therefore, as the T/N ratio decreases, the conversion of THF soluble product increases. This relationship holds true for a particular coal at the three thermal severities: 385°, 427° and 445°C. However, this relationship does show considerable scatter when one tries to relate the T/N ratios with the conversion data for a series of coals at the higher reactor temperatures such as 445°C. This is most likely due to the secondary reactions taking place, i.e., asphaltenes and/or preasphaltenes to produce oils and gases.

As the coal rank decreases (the carbon content decreases and oxygen content increases) there will be an increase in hydrogen demand during coal liquefaction process. The higher the hydrogen consumption during the reaction, the higher is the conversion of tetralin to naphthalene. Hence the result is a lower T/N ratio. This is consistent with the observations discussed previously under (b) and (c). Therefore, the lower the coal rank, the lower is the T/N value (or higher H_2 demand).

We have made several attempts to correlate T/N ratios with various other properties of coals. However, there seem to be no other reportable relationships with the limited data base available at present.

Effect of Liquefaction Duration on T/N Ratio

In order to determine the effect of liquefaction residence time (kinetic versus equilibrium conversions) on the T/N ratio, experiments were performed at 445°C for reaction times ranging from 5 to 65 minutes. The T/N ratios obtained using two coals of different ranks (a Western Ky. #9 and a Wyodak) are presented in Figure 2. Figure 2 also displays the T/N results obtained for blank experiments performed on tetralin + H_2 in the presence of a catalyst (Ni/Mo oxide).

As shown in Figure 2, the T/N value decreases sharply with the increase in reaction time until it reaches some pseudoequilibrium value for both the coals and the blank experiments. However, the T/N values obtained for the catalytic tetralin experiments achieve a pseudoequilibrium value faster than those of coals. All reactor conditions were constant in these experiments except different coal samples and a Ni/Mo oxide catalyst for the blank runs were used. Since the pseudoequilibrium values are different for the two coals the pseudoequilibrium T/N value also appears to be coal rank dependent. The relatively low and different pseudoequilibrium T/N values for the two coals (1.3 and 1.9) as compared to that of the catalyzed (Ni/Mo) tetralin conversion reaction (4.0) clearly suggest that the conversion of tetralin to naphthalene is mainly due to the extent of the hydrogen demand during liquefaction rather than some catalytic reactions from the mineral matter. This is further supported by the fact that there was no significant conversion of tetralin to naphthalene when tetralin was heated with or without low temperature ash in presence of H_2 at 385°, 427° and 445°C.

The parallel behavior of T/N ratios of two coals of different ranks over the entire range of reaction time suggests that the T/N ratios (Figure 2) follow a parellel course in both the kinetic (ca. first 35 minutes) and the equilibrium processes ($>$ 35 minutes) and the major contribution to T/N ratio is probably through kinetically controlled processes. This phenomenon is partially supported by the fact that the conversion for most of the coals reaches its maximum value within 5 to 10 minutes (5, 17, 19).

In order to compare and understand the contributions from kinetically and thermodynamically controlled processes to T/N ratios, liquefaction experiments, using a 45 minute residence time and a 445°C reactor temperature, were performed using the eight coals. The T/N ratios obtained using the longer residence time and the 15 minute residence time are compared in Figure 3. As can be seen, a linear relationship with a slope of greater than unity (1.23) clearly suggest that tetralin is also involved in the

thermodynamically controlled process and the extent of tetralin conversion is controlled by the coal rank. Since coal conversion to THF solubles are somewhat similar (ca. 90%) for 15 minute and 45 minute liquefaction runs, the question arises: what does tetralin do during thermodynamically controlled process? One possible explanation is that during the thermodynamically controlled process, the coal rank dependent conversion of tetralin to naphthalene is due to the hydrogen demand of the secondary reactions of asphaltenes and preasphaltenes to produce the lower molecular weight components - oils and gases. On the other hand, the coal rank dependent conversion of tetralin to naphthalene during kinetically controlled process of coal dissolution is possibly due to the hydrogen demand of the production of asphaltenes and preasphaltenes from the coals. This needs to be clarified further by analyzing the liquefaction products obtained using the different reaction times and is under investigation in our laboratory.

ACKNOWLEDGEMENT

This work was supported by the Commonwealth of Kentucky, Kentucky Energy Cabinet and DOE Contract No. DEFC22-85PC80009 as part of the Consortium for Fossil Fuel Liquefaction Science (administered by the University of Kentucky).

REFERENCES

1. Pott, A.; Broche, H.; Schmitz, H.; Scheer, W., Gluckauf 1933, 69, 903.

2. Orchin, M.; Storch, H. H., Ind. Eng. Chem. 1948, 40, 1259.

3. Curran, G. P.; Struck, R. T.; Gorin, E., Ind. Eng. Chem. Process Des. Dev. 1967, 6, 166.

4. Wiser, W. H., Fuel 1968, 47, 475.

5. Neavel, R. C., Fuel 1976, 55, 237 and references cited therein.

6. Tsai, M. C.; Weller, S. W., Fuel Process Technol. 1979, 2, 313.

7. "Solvent Activity Studies" DOE/PC/50041-18, DE83, 015870, Catalytic Inc., Wilsonville, Alabama.

8. "Coal Liquefaction - The Chemistry & Technology of Thermal Processes" by D. D. Whitehurst et al., Academic Press, 1980.

9. Derbyshire, F. J.; Whitehurst, D. D., EPRI Contractor's Meeting, May 1980, Palo Alto, California.

10. Derbyshire, F. J.; Odoerfer, G. A.; Rudnick, L.R.; Varghese, P.; Whitehurst, D. D., EPRI Report, AP-2117, Vol. 1, Project 1655-1, 1981.

11. Ohe, J.; Itoh, H.; Makaba, M.; Ouchi, K., Fuel 985, 64, 902 and 1108.

12. Skowronski, R. P.; Ratto, J. J.; Goldberg, I. B.; Heredy, A., Fuel 1984, 63, 440.

13. Besson, M.; Bacaud, R.; Charcosset, H.; Cebolla-Burillo, V.; Oberson, M., Fuel Process Technol. 1986, 12, 91.

14. Storch, H. H., "Chemistry of Coal Utilization", Ed.: H. H. Lowry, Vol. II, John Wiley and Sons, 1945.

15. Heredy, L. A.; Fugasi, P., "Phenanthrene Extractions of Bituminous Coal", Coal Science Advances in Chemistry Series, No. 55, 1966, 448.

16. Whitehurst, D. D.; Farcasiu, M.; Mitchell, T. O., The Nature and Origin of Asphaltenes in Processed Coals, EPRI-AF-252, 1st Annual Report, Palo Alto, CA 1977.

17. Pina, B. B., "Hydroliquefaction Performance of Two Kentucky Coals in Solvents of Various Hydrogen-Donor Strengths', M.S. Thesis, 1984, University of Louisville, Louisville, Kentucky and references cited therein.

18. (a) Poutsma, M. L.; Youngblood, E. L.; Ostwald, G. E.; Cochran, H. D., Fuel 1982, 61, 314. (b) Shah, Y. T.; Cronaur, D. C., Catal. Rev. - Sci. Eng. 1979, 20, 209 and references therein. (c) Vernon, L. W., Fuel 1980, 59, 102. (d) Collins, C. J.; Raaen, V. F.; Benjamin, B. M; Maupin, P. H.; Roark, W. H., J. Am. Chem. Soc. 1979, 101, 5009. (e) Franz, J. A.; Camaioni, D. M., J. Org. Chem. 1980, 45, 5247. (f) Berman, M. R.; Comita, P.B.; Moore, C. B.; Bergman, R. G., J. Am. Chem. Soc. 1980, 102, 5692 and references therein.

19. Our unpublished results.

Table 1. *Coal Analysis.*

	W. Ky. #9 71154	Breckinridge 71160	W. Ky. #9 71072	W. Ky. #11 71064
1. Ash (As-Received)	30.03	6.36	9.04	9.56
2. Volatile Matter, daf	47.83	74.28	42.90	47.47
3. Fixed Carbon, daf	52.17	25.72	57.10	52.53
4. Sulfate S, daf	0.00	0.01	0.14	0.06
5. Pyritic S, daf	1.47	1.23	0.53	1.06
6. Organic Sulfur, daf	2.27	0.55	1.91	3.11
7. Total Sulfur, daf	3.74	1.81	2.57	4.23
8. Carbon, daf	84.99	80.66	79.19	78.80
9. Hydrogen, daf	6.16	8.51	5.44	5.85
10. Nitrogen, daf	1.98	2.13	2.00	1.70
11. Oxygen, daf	3.13	6.90	10.80	9.42

	W. Ky. #11 71081	G. Seam-Co. PSOC866	Wyodak-Wy. 91168	Fort Union Bed-Mt. PSOC833
1. Ash (As-Received)	4.43	17.80	6.64	10.22
2. Volatile Matter, daf	43.23	36.96	52.92	46.86
3. Fixed Carbon, daf	56.77	63.04	47.08	53.14
4. Sulfate S, daf	0.17	0.04	0.05	0.07
5. Pyritic S, daf	0.64	0.06	0.17	0.12
6. Organic Sulfur, daf	2.21	0.52	0.78	0.46
7. Total Sulfur, daf	3.01	0.62	1.00	0.64
8. Carbon, daf	78.28	75.20	71.02	68.64
9. Hydrogen, daf	5.52	5.34	5.42	4.72
10. Nitrogen, daf	1.70	1.18	1.37	1.26
11. Oxygen, daf	11.49	17.66	21.29	24.74

Oxygen by difference.

Table 2. *T/N Ratios for 15-Minute Duration Liquefactions at Three Temperatures and THF Soluble Conversions at 445°C.*

	Conversion (%)		T/N Ratio		
Coal Sample	**445°C 15 min.**	**445°C 45 min.**	**445°C**	**427°C**	**385°C**
71154 (Ky. #9)	—	94.6	4.03 ± 0.21	6.63 ± 0.62	17.40 ± 1.0
Breckinridge	—	90.6	3.51 ± 0.27	5.96 ± 0.18	18.7
71072 (Ky. #9)	—	87.6	2.78 ± 0.12	4.30 ± 0.15	10.3 ± 0.5
71064 (Ky. #11)	—	95.1	2.62 ± 0.06	3.70 ± 0.11	9.14 ± 0.05
71081 (Ky. #11)	93.6	92.7	2.37 ± 0.25	3.99 ± 0.13	11.13 ± 0.22
PSOC 866	77.2	80.2	1.86 ± 0.06	—	—
91648 (Wyodak)	89.5	90.0	2.07 ± 0.06	2.60 ± 0.04	—
PSOC 833	—	84.0	1.80 ± 0.05	2.86 ± 0.05	6.30 ± 0.10

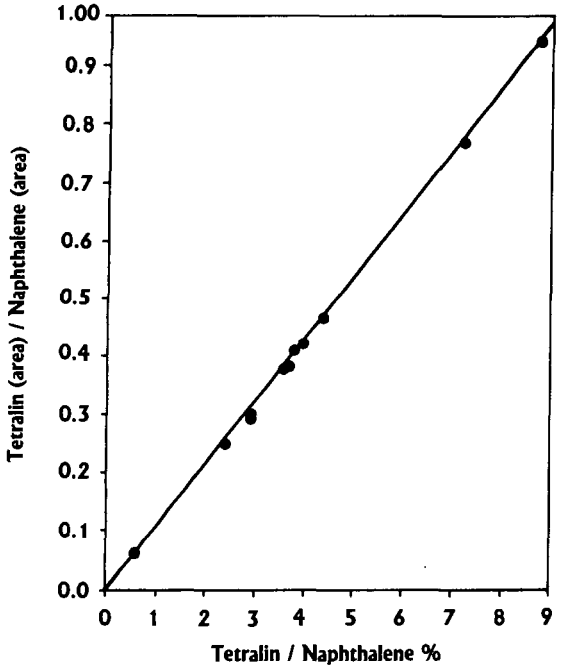

Figure 1. *Ratios of Peak areas versus T/N (wt. %) Ratios.*

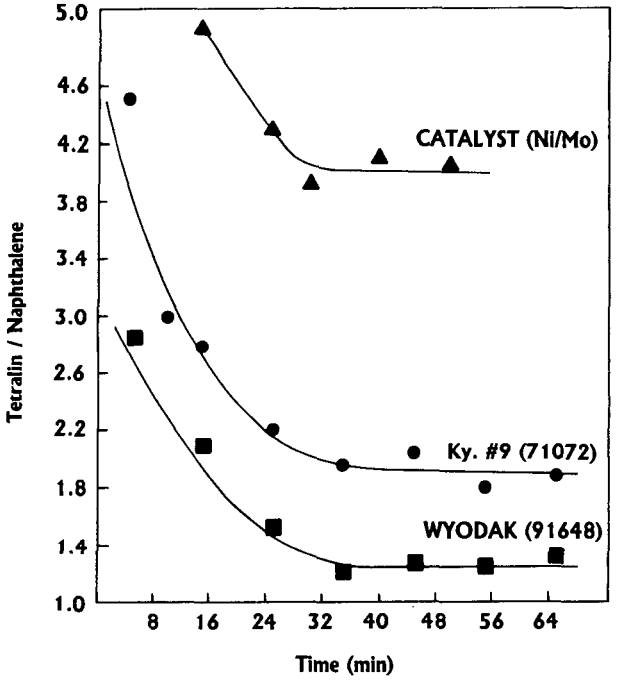

Figure 2. *T / N Ratios at 445°C.*

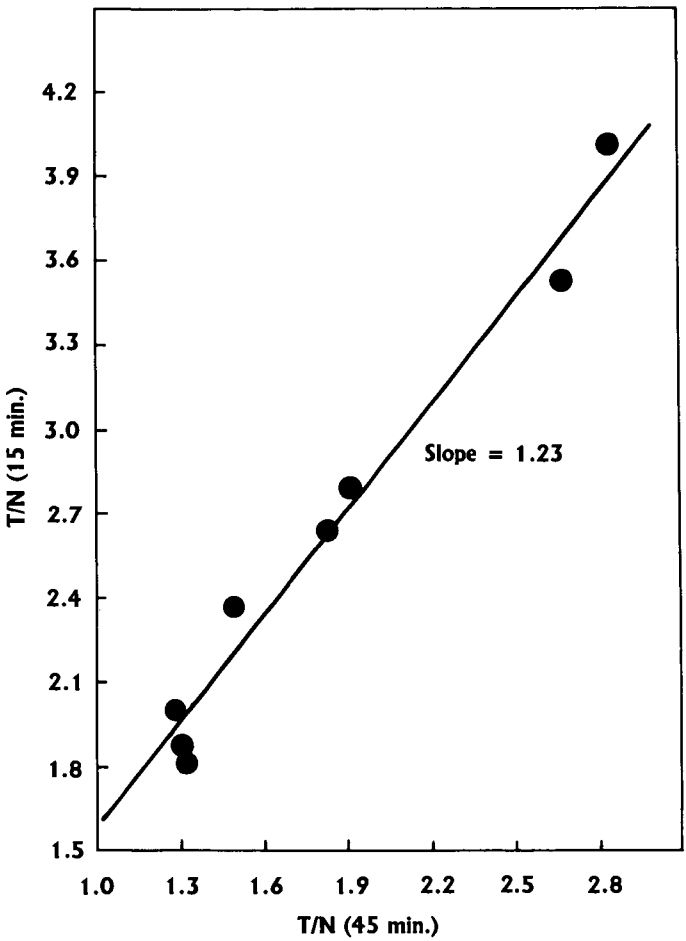

Figure 3. *Comparison Between the T / N Ratios of 15 and 45 Minutes Residence Time Runs at 445°C.*

THE ORGANIC/MINERAL INTERACTION IN COAL LIQUEFACTION BOTTOMS

W.A. Leet, F.S-C. Lee, R. Gandy, and D.C. Cronauer

Amoco Oil Corporation
P.O. Box 400
Naperville, IL 60566

ABSTRACT

Characterization of the organic/mineral matter interactions is central to the problem of solid/liquid separation in the liquefaction of coal. Samples of the vacuum tower bottoms from the liquefaction of Illinois No. 6 coal in the Wilsonville pilot plant have been studied. The techniques include various analyses such as elemental, solvent extraction, STEM, FTIR, XPS, XRD, and XRF. Surface active oxygenates associated with organic/mineral matter interaction appear to consist of both phenolics and carboxylates. The observed characteristics of the organic/mineral interactions were affected by the recycle of mineral matter and unconverted coal as part of the liquefaction feed solvent.

INTRODUCTION

The separation of unconverted coal and mineral matter from heavy coal-derived liquids is difficult. Work was undertaken to determine if an interaction between these components could be demonstrated which could prove useful in the design of efficient mineral removal processes. Specific reference is made to the use of critical solvent deashing (CSD) such as that of the ROSE-SR process of Kerr-McGee Corporation. The polar functionality of clays, carbonates, and other minerals would likely interact with heterofunctional groups in coal asphaltenes and preasphaltenes. Therefore, typical coal-derived resids and unconverted coal solids were characterized, focusing on the loading of organic oxygenates onto mineral matter.

Coal asphaltenes have been shown to have high levels of heterofunctionality(1), and the oxygenate groups are primarily phenolic(2) with low to immeasurable levels of carboxylic groups. In fact, Illinois No. 6 coal, which was used to generate the products tested in this study, was shown to contain about one-tenth(2) or less(3) of its oxygen as carboxylic groups. In addition, it has been shown(4) that coal loses carboxylic groups on heating to elevated temperatures. Therefore, since this functionality was observed in the heavy fractions and CSD operation greatly improved with the recycle of unconverted coal, we extended this study to include the characterization of recycled solids which may have served as catalytic sites for liquid upgrading and/or coking. Reference is made to the work of Wakeley, et al.(5) with respect to the nature of reactor solids accumulating during liquefaction.

EXPERIMENTAL

Samples were obtained from the Advanced Coal Liquefaction R&D Facility at Wilsonville, AL, which has been described by Lamb, et al(6). The Wilsonville pilot plant was operating in a two-stage mode with direct coupling of the thermal and catalytic (hydrotreater) reactors as shown in the schematic, Figure 1. After flashing and vapor recovery, the vacuum tower bottoms (VTB) cut was fed to a critical solvent deashing (CSD) unit to reject an ash concentrate and recover an ash-free resid. The products of two runs were studied. In run 250D, the liquefac-

tion feed solvent consisted of recycled flash distillates plus CSD-derived resid. In run 250H, a portion of the VTB, including unconverted coal and mineral matter, was added to the feed solvent. Both runs were made with Illinois No. 6 coal at essentially the same reaction conditions, and CSD operation was shown (7) to be much smoother in the latter run.

Characterization data for samples of VTB of these two runs are summarized in Table I. GPC analysis of the organic Soxhlet fractions produces identical molecular weight profiles for the two samples. The data document the higher concentration of mineral matter and unconverted coal in run 250H product as a result of recycle. The shift in the Soxhlet characterization data, specifically the decrease in the oils (pentane solubles) content, highlights a significant shift in character as a result of process recycle. Apparently, recycle leads to increased solubilization and reaction of the heavy fractions in the liquefaction reactors resulting in a more refractory resid.

The VTB cuts resids were Soxhlet extracted with tetrahydrofuran (THF) to separate the soluble organic matter from the solids. NMR analysis of the THF extracts is provided in Table II. There are large differences in the aliphatic carbon and ring size (bridgehead carbon) between the two samples. Run 250H VTB is more highly dealkylated (C_{a-s} = 12.2 vs. 18.3%) and condensed (C_{a-i} = 27.2 vs. 18.6%). This is consistent with the lower level of oils found in the VTB upon recycle. FTIR data confirm the observation. FTIR analysis also points to a nearly five-fold increase in the phenolic oxygen content of run 250D product over that of 250H. This difference is largely due to THF extractables.

The physical makeup of the THF insolubles fraction of both runs was examined by Dr. Alan Davis of Pennsylvania State University using petrographic techniques. The results indicate that the organic portion of the fractions were primarily composed of vitroplast (20 vol %), unreacted "inertinite" (9-12 vol %), and unreacted vitrinite (2-8 vol %). The 250D sample contained larger amounts of unreacted inertinite than the 250H sample. The 250H sample also contained masses of larger vitroplast spheres (secondary vitroplast) which were not seen in the 250D sample. No mesophase structures were observed and only very rare particles of coke were noted in the residues. Both samples exhibited large amounts of clays (50-55 vol %) and iron sulfides (6-13 vol %). While the clay concentrations were similar for both fractions, the concentration of iron sulfides in the 250H VTB were twice that in the 250D sample, reflecting the concentration of mineral matter by process recycle. Trace (1-4 vol %) carbonates were also identified. However, the carbonates, present also in the feed coal, were highly crystalline and exhibited none of the structure of the reactor-formed carbonates which are generated during the processing of some carboxylate-rich low-rank coals.

The mineral matter concentrated in the THF insolubles was analyzed by XRF and XRD. Analysis by XRF shows that the mineral matter of the two samples to be similar in composition (Table III), with large amounts of silicon, alumina, and iron present. XRD analysis shows the latter three components to be in the form of α-quartz, iron sulfide minerals (predominantely pyrrhotite), and aluminosilicates (principally kaolinite). Both samples exhibit traces of carbonates as noted earlier.

Ground particles of VTB before and after THF extraction were characterized by STEM and XPS. STEM analysis points to the agglomeration of iron sulfide and calcium mineral particles upon THF extraction. XPS data for mineral matter for both resids

before and after THF extraction are summarized in Table IV. The data indicate high levels of physical adsorption of organic matter on the silicate and aluminosilicate mineral surfaces in that the organic coating is removed by THF extraction. However, the iron sulfide surface exhibits significant irreversible adsorption or coking on the surface, because organics are not removed by THF extraction. A similar situation exists for calcium carbonate surfaces, but to a lesser extent than that of iron sulfide.

Elemental analysis of the organic matter in the THF insolubles fractions of the VTB cuts is given in Table V. The THF insolubles fractions of both VTB cuts are similar with significant concentrations of heteroatoms in the THF insolubles. Much of the organic oxygen shows up as strong phenolic oxygen absorption in the OH/NH stretch region of the FTIR spectrum (Figure 2). Comparison of ratios of normalized integrals and normalized intensities of the second derivatives by deconvolution shows that like amounts and types of phenolics are concentrated in the THF insolubles fractions of the two VTB cuts. The FTIR spectra also exhibit small but marked residual carboxylic acid absorption at around 1700 wavenumbers and a carboxylate band around 1530 (Figure 3). In comparison to the very weak carboxylic signal in the whole VTB, the data indicate that the carboxylate functional groups are preferentially attached to the THF insolubles portion of the resids. Acidification of the THF insolubles with 6N HCl followed by extraction with $CHCl_3$ leads to a 44% reduction in the intensity of the carboxylic acid band in the insolubles, so there is interaction with the minerals that are removed by acid treatment.

CONCLUSIONS

The separation of unconverted coal and mineral matter at Wilsonville was shown to be better when a portion of these solids were recycled with the feed solvent to the liquefaction reactor. Our analysis of the VTB feed to the separation unit indicates that such recycle leads to increased solubilization of the heavy fractions and a more refractory (condensed) resid. We also observed that some carboxylic acid functionality is retained in the heavy coal-derived fractions after coal liquefaction. This appears to be due to an interaction of these groups with the mineral matter. It has also been observed that much of the carbonaceous deposits formed on the silica and aluminosilicate clays can be removed by extraction with a polar solvent, but the organic matter deposited on the iron sulfides and carbonates are more coke-like and not readily removed.

ACKNOWLEDGEMENT

The aid of Dr. A. Davis of Pennsylvania State University in the petrographic analysis of the samples is gratefully acknowledged. The analytical support of T. F. Fleisch, G. W. Fajac, J. B. Hall, and R. W. Tumbula and the suggestions of B. A. Fleming are also acknowledged. Personnel at Wilsonville were also instrumental in handling the appropriate samples.

REFERENCES

1. Whitehurst, D. D., Farcasiu, M., Mitchell, T. O., and Dickert, J. J., "The Nature and Origin of Asphaltenes in Processed Coals," EPRI AF-480, Project 410-1 Annual Report, July, 1977.

2. Ruberto, R. G., and Cronauer, D. C., in "Organic Chemistry of Coal," J. W. Larson, ed., Am. Chem. Soc. Symp. Ser., 71, 50, 1978.

3. Dutta, P. K., and Holland, R. J., Fuel, 62, 732, 1983.

4. Mragikova, J., Sindler, S., Veverka, L., and Macak, J., Fuel, 65, 342, 1986.

5. Wakeley, L. D., Davis, A., Jenkins, R. G., Mitchell, G. D., and Walker, P. L., Fuel, 58, 379, 1979.

6. Lamb, C. W., Nalithan, R. V., and Johnson, T. W., "Process Development Studies of Two-Stage Liquefaction at Wilsonville," Am. Chem. Soc. Div. Fuel Chem. Preprints, 31(4), 240, 1986.

7. Nalithan, R. V., Lee, J. M., and Johnson, T. W., "Status of Coal Liquefaction at Wilsonville," DOE Contractor's Review Conference on Direct Coal Liquefaction, Monroeville, PA, October. 20-22, 1986.

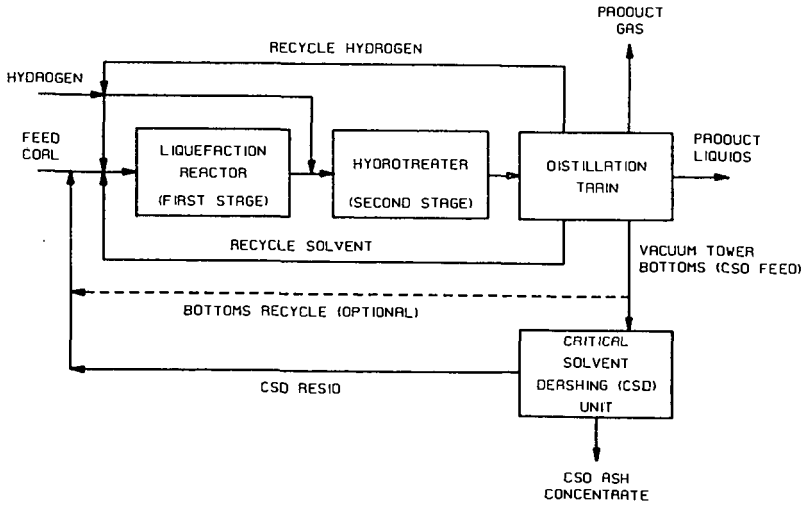

Figure 1. Wilsonville flowsheet.

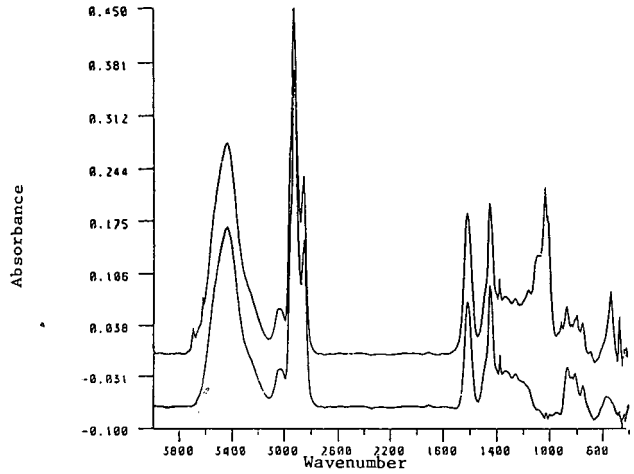

Figure 2 FTIR Spectra of Run 250D VTB and the $HCl/CHCl_3$ Insolubles from the VTB/THF Insolubles

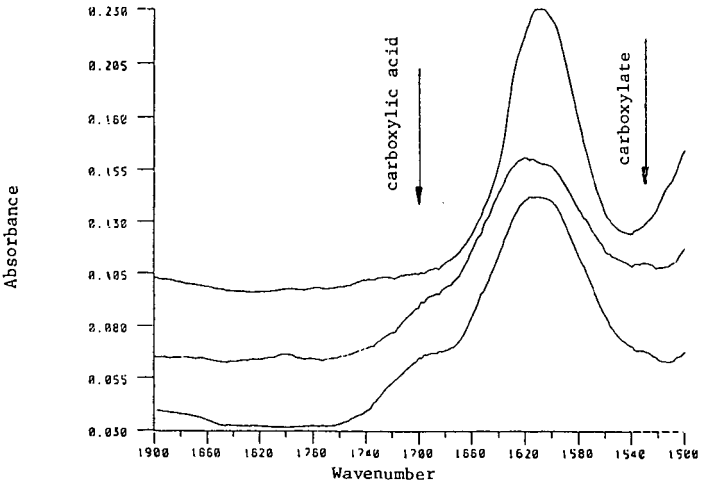

Figure 3 FTIR Spectra of Run 250H VTB (A), its THF Insolubles (B), and its $HCl/CHCl_3$ Insolubles

TABLE I

CHARACTERIZATION OF WILSONVILLE VACUUM TOWER BOTTOMS STREAMS

	Run 250D	Run 250H
Proximate Analysis (wt%)		
Moisture	0.09	0.10
Volatiles	67.8	58.1
Fixed Carbon (by diff.)	22.3	24.9
Ash	9.8	16.9
Elemental Analysis[1] (wt%)		
Carbon	81.2	74.2
Hydrogen	6.29	5.43
Nitrogen	1.26	1.24
Sulfur	0.98	1.58
Oxygen	2.09	3.66
Atomic H/C	0.93	0.88
Soxhlet Extraction[2] (wt%)		
Oils	46.4	29.3
Asphaltenes	24.0	21.4
Preasphaltenes	8.8	13.1
Coke & Unconverted Coal & Mineral Matter	20.8	36.2

[1] Uncorrected for mineral matter.

[2] Sequential extraction with n-pentane, toluene, and tetrahydrofuran.

TABLE II

NMR ANALYSIS OF THF EXTRACTS[1]

	Run 250D	Run 250H
Ha, H on aromatic C	24.1	31.1
Hα, H on a C α to ring	35.4	25.6
Hsat, H on a C β or further to ring (=CH_2-)	31.3	35.4
Hme, H on CH_3 or further to ring	9.2	7.8
Ca, aromatic C	60.6	67.3
Cat. aromatic C bearing a H	23.7	28.0
Ca-s, aromatic C bearing an alkyl C	18.3	12.2
Ca-i, aromatic C at bridgehead position	18.6	27.2
Average number of rings[2]	6	9

[1] Analyses based on combined ^1H and ^{13}C-NMR. Data is expressed as % of total C or H.

[2] Average number of aromatic rings was calculated using a number average MW of 740 (VPO).

TABLE III

METAL COMPOSITIONS OF THF INSOLUBLES BY XRF

	Run 250D	Run 250H
Al	6.3	6.5
Na	<0.1	<0.1
Mg	0.18	0.22
Si	14.3	14.3
S	1.24	1.26
K	0.97	1.07
Ca	3.2	2.0
Ti	0.25	0.31
Fe	7.4	7.8
Ba	0.03	0.03
Mn	0.04	0.02
Total Metals	34.0	33.5
Oxide Ash	63.8	62.8

TABLE IV

ATOMIC RATIOS ON PARTICLE SURFACES AT RESIDS CALCULATED FROM XPS DATA[1]

	Run 250D		Run 250H	
Atomic Ratio	Whole Resid	THF Insol	Whole Resid	THF Insol
Si/100C	1.0	11	0.8	10
Al/100C	0.0	7.3	0.6	7.1
Fe/100C	0.0	0.5	0.0	0.5
Ca/100C	0.0	1.0	0.0	1.5

[1]Adjusted to THF insolubles content basis.

TABLE V

ELEMENTAL ANALYSIS OF THF INSOLUBES[1]

	Run 250D	Run 250H
Carbon	29.5	29.8
Hydrogen	2.0	1.8
Nitrogen	0.5	0.8
Sulfur	4.4	4.3
Oxygen	6.5	5.9
Atomic H/C	0.83	0.73

[1] Uncorrected for mineral matter.

Catalyzed Reactions of Alkylaromatic Hydrocarbons Dissolved in Supercritical Fluids

F. C. Knopf, T.-H. Pang, K. M. Dooley

Dept. of Chemical Engineering, Louiaiana State University
Baton Rouge, LA 70803

INTRODUCTION

Partial oxidations of alkylaromatic compounds occur at below 600K through catalytic mechanisms that are partly free radical in nature. These side chain oxidations and hydroxylations are usually catalyzed homogeneously by transition metal complexes or mixtures of metal salts with redox capabilities. Compounds of Co, Fe, and Mn are examples; the catalytic mechanisms exhibit certain common features (1-6). These are: (i) The ions have stable oxidation states separated by +1, because chain initiation and other reaction steps involve one-electron transfers; (ii) Once a reaction sequence (chain) is initiated, thermal free-radical steps occur in parallel with metal-catalyzed steps.

Alkylaromatics require less severe oxidizing conditions than do alkanes because of their smaller (by ~ 1 ev) ionization potentials, and partially oxidized side chains deactivate the ring for further reactions by this mechanism. Peroxides and hydroperoxides are the primary products of these oxidations, but these decompose to more stable products at temperatures above about 370K. As an example, consider the oxidation of toluene to benzaldehyde/benzoic acid. Four proposed reaction networks are shown in Figure 1. The initiation step involves electron transfer to Co^{3+}, suggesting that the trivalent ion is necessary for catalysis. However, the divalent ion reacts in several benzoperoxy decomposition steps, and in practice only small amounts of Co^{3+} are necessary.

An alternative to these liquid-phase processes is to use a supercritical fluid (SCF) phase to contact solid analogs of the homogeneous catalysts. Considering the above example of toluene oxidation, the use of an SCF phase would result in a homogeneous mixture and the removal of solubility limitations on O_2. SCF mixtures have better mass transfer characteristics than typical liquids, and rapid reaction quenching of highly exothermic oxidations is possible by a pressure letdown from the SC region. A staged pressure letdown engenders another benefit, that of fractionation of reactants and products, eliminating the need for more complex downstream separations. Therefore it appears possible to exploit the capabilities of a SC mixture to provide a reaction medium for an entire class of what would normally be liquid phase oxidations. We are currently examining such catalytic oxidations in SCF-CO_2 for upgrading model coal liquid compounds that result from SCF extraction or flash hydropyrolysis processes. There are indications that alkylaromatic side-chain partial oxidation, which we have already demonstrated at SC conditions (7), will enhance the desired cracking reactions. For example, hydroxy groups ortho or para to methylene bridges facilitate bridge-bond rupture by allowing formation of a lower energy keto-enol tautomer intermediate; the half-life of the cleavage is reduced by over an order of magnitude (8). The presence of water causes cleavage of ether linkages to alcohols, which has

been observed for guaiacol pyrolysis at SC conditions (9). An example of these and similar reactions as applied to actual coal liquids is the autoxidation followed by anaerobic thermolysis of SRC in quinoline (10). The yield to combustion products at 388-453K was less than 10%.

RESULTS AND DISCUSSION

Preparing SCF-Aromatic Hydrocarbon Mixtures

Figure 2 gives the P-T diagram for a mixture of toluene and carbon dioxide as constructed from experimental data (11) and the Peng-Robinson equation of state (12), with the critical locus for a binary mixture computed by the algorithm of Heideman and Khalil (13). The TP-CP curves (1 = carbon dioxide and 2 = toluene) represent the vapor P curves for the pure liquids, from their triple points to their critical points. At point O the three-phase line ends (the liquid phases become identical) and the critical locus extends to CP_2 of pure toluene. Point a is in the SCF (F) region, point b is on the critical locus, and point c represents typical operating conditions (473K, 100 atm) for the initial reaction studies. The P-X diagram at 473K is given in Figure 3. The SCF phase on the left of the diagram contains at least 20 mol% toluene. The feed to the reactor contained only 0.7% toluene and 2.0% O_2 and therefore constituted a single phase SCF mixture.

The phase diagrams for heavier molecules dissolved in SC-CO_2 indicate that their solubilities in the SCF phase will be much lower than that of toluene. For example the equilibrium mole fraction for phenanthrene in SC-CO_2 or CO_2-air mixtures at 473K and 100 atm was found to be less than 1%. However, the solubilities of either component of a binary solid mixture of aromatic hydrocarbons can be enhanced by up to 300% over its single component solubility (14). In addition, we have shown that by mixing a small amount (less than 10%) of a volatile hydrocarbon such as methanol or toluene with the SC-CO_2 it is also possible to greatly increase the solubilities of heavy aromatic hydrocarbons considered "nonvolatile". For example the solubility of DDT in CO_2 at 100 atm and 313K was shown to increase by more than an order of magnitude in CO_2 containing 6.7% methanol (15). These solubility enhancements due to solute-solute interactions should be sufficient to bring the SC-phase concentration of any aromatic single component or mixture into the typical range for vapor-phase oxidation catalysis, about 1-5 mol%.

Partial Oxidation Catalysis

The results of toluene oxidation experiments in a tubular fixed-bed reactor using an SC feed of CO_2, toluene, and air indicate that strongly acidic catalysts such as H-Y zeolite are inactive, and that, of the many supported metal oxides tested (Co, Mo, Co-Mo, and Ni-W oxides, supported on γ-Al_2O_3), the one whose active component was mostly CoO is the most active and also the most selective for partial oxidation to benzaldehyde and benzoic acid (7). Some results comparing this catalyst to a similar one containing mostly Co_3O_4 are given in Figure 4. The turnover numbers for partial oxidation are in the 10^{-7}-10^{-4}/s range, with the reactor operated differentially at conversions less than 2%; these rates are based on moles of total active metal.

The efficacy of the CoO compared to Co_3O_4 was also observed in a recent study of p-xylene oxidation in slurry reactors (16), and is probably a manifestation of the importance of the proper Co^{2+}/Co^{3+}

ratio in the catalysis (see Figure 1). The observed turnover numbers actually exceed those of previous studies where Co(II) homogeneous catalysts were used in the absence of initiators and electron transfer promoters (as in this work). For example, at 343K the observed turnover number for Co(II) acetate-catalyzed toluene partial oxidation is only 8.3×10^{-8}/s in pure acetic acid (17). Although rates as high as 0.01/s have been found at higher temperatures (1,18,19), these were measured in the presence of initiators and electron-transfer promoters such as soluble halides. We can adapt these technological developments to the high pressure process by incorporating such additives in the feed or the catalyst.

Effect of Total Pressure

The relatively high catalyst activities in the SCF oxidation process appear to be the result of a pressure effect. Holding the feed composition constant, we varied the total pressure in the reactor from about 80-140 atm, and observed the changes in the partial oxidation rate given in Figure 5. The more than twofold increase in rate might be explained by the effect of pressure on the concentration-based rate constant, as given by transition-state theory:

$$\left(\frac{\partial \ln k}{\partial P}\right)_{T,x} = -\frac{\Delta V^{\ddagger}}{RT} + \left(\frac{1-n}{P}\right)\left[1 - \left(\frac{\partial \ln Z}{\partial \ln P}\right)_{T,x}\right] \qquad 1)$$

In the equation, $\Delta V^{\ddagger}$ is the difference in partial molar volumes of the activated complex and reactants, n is the molecularity of the reaction, and Z is the compressibility. Although this relation holds only for a single-step reaction, it can be used to roughly estimate the pressure effect here. Detailed calculations (20) using the Peng-Robinson equation of state and assuming a transition state thermodynamically similar to the product benzaldehyde [this assumption was tested for several bimolecular reactions of the type A + B → R for which the pressure variation was known, and was found to be adequate (21)] predicted an increase in a second-order rate constant of only about 30% for the pressure range of the data in Figure 5. It appears as if rate constant enhancement is not the most important consideration here.

Another possible explanation for the pressure effect is a pressure-dependent variation of O_2 concentration in the condensed "pore" phase of the catalyst. Work with microporous chars and zeolites has indicated that molecules can adsorb in multiple layers in porous media at pressures above the nominal mixture critical pressure, and that the adsorbed phase behaves almost liquid-like in terms of density and heat of adsorption (22,23). Referring to Figure 3, one would expect the capillary pores to be rich in toluene at low pressures but to become enriched in both air and CO_2 at increasing pressures. Because alkylaromatic oxidation reactions are typically of order zero to one in O_2, pore condensation phenomena could explain the rate increase; this idea is supported by the fact that the rate seemingly levels off near 140 atm, possibly indicating surface saturation.

ACKNOWLEDGEMENT

The work reported here was supported by the Louisiana Center for Energy Studies.

REFERENCES

1. Kaeding, W. W.; Lindblom, R. O.; Temple, R. G.; Mahon, H. I. Ind. Eng. Chem. Process Des. Dev. 1965, 4, 97.
2. Heiba, E. I.; Dessau, R. M.; Koehl, W. J., Jr. Prepr. - Am. Chem. Soc., Div. Pet. Chem. 1969, 14, A44.
3. Kamiya, Y.; Kashima, M. J. Catal. 1972, 25, 326.
4. Sheldon, R. A.; Kochi, J. K. Adv. Catal. 1974, 25, 272.
5. Parshall, G. W., "Homogeneous Catalysis"; Wiley: New York, 1970; Chapters 7 and 10.
6. Schuit, G. C.; Gates, B. C. In "Chemistry and Chemical Engineering of Catalytic Processes"; Prins, R.; Schuit, G. C., Eds.; Sijthoff and Noordhoff, Amsterdam, 1980; p. 461.
7. Dooley, K. M.; Knopf, F. C. Submitted to Ind. Eng. Chem. Research 1986.
8. McMillen, D. F.; Ogier, W. C.; Ross, S. J. Org. Chem. 1981, 46, 3322.
9. Lawson, J. R.; Klein, M. T. Ind. Eng. Chem. Fundam. 1985, 24, 203.
10. Hazlett, R. N.; Solash, J.; Fielding, G. H.; Burnett, J. C. Fuel 1978, 57, 631.
11. King, M. B.; Alderson, D. L.; Fallah, F. H.; Kassim, D. M.; Kassim, K. M.; Sheldon, J. R.; Mahmud, R. S. In "Chemical Engineering at Supercritical Fluid Conditions"; Paulaitis, M. E.; Penninger, J. M.; Gray, R. D., Jr.; Davidson, P., Eds.; Ann Arbor Science: Ann Arbor, MI, 1983; p. 31.
12. Peng, D.-Y.; Robinson, D. B. Ind. Eng. Chem. Fundam. 1976, 15, 59.
13. Heideman, R. A.; Khalil, A. M. AIChE J 1980, 26, 769.
14. Kurnik, R. T.; Reid, R. C. Fluid Phase Equilibria 1982, 8, 93.
15. Dooley, K. M.; Kao, C.-P.; Gambrell, R. P.; Knopf, F. C. Submitted to Ind. Eng. Chem. Research 1986.
16. Hronec, M.; Hrabe, Z. Ind. Eng. Chem. Product Res. Dev. 1986, 25, 257.
17. Zakharov, I. V.; Geletii, Yu. V. Petrol. Chem. USSR 1979, 18, 145.
18. Namie, K.; Harada, T.; Fujii, T. U. S. Patent 3,903,148, 1975.
19. Borgaonkar, H. V.; Raverkar, S. R.; Chandalia, S. B. Ind. Eng. Chem. Product Res. Dev. 1984, 23, 455.
20. Brodt, S. R. M. S. Thesis; Louisiana State University, Baton Rouge, LA, 1987.
21. Dooley, K. M.; Brodt, S. R.; Knopf, F. C. Accepted for publication by Ind. Eng. Chem. Research 1987.
22. Hayhurst, D. T.; Lee, J. C. AIChE Symp. Ser. 1983, 79(230), 67.
23. Jones, M. W.; Isaac, P. J.; Phillips, D. Trans. Faraday Soc. 1959, 1953.

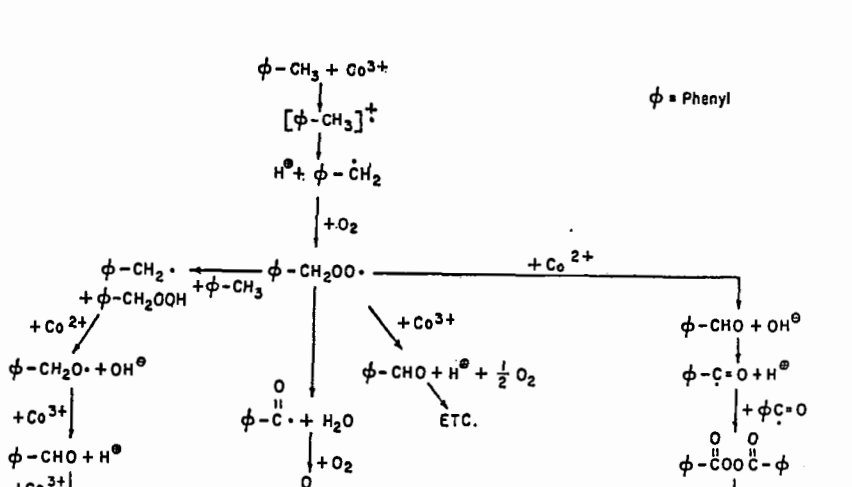

Figure 1. Reaction networks for toluene oxidation to benzaldehyde/benzoic acid, catalyzed by Co^{2+}/Co^{3+} in solution.

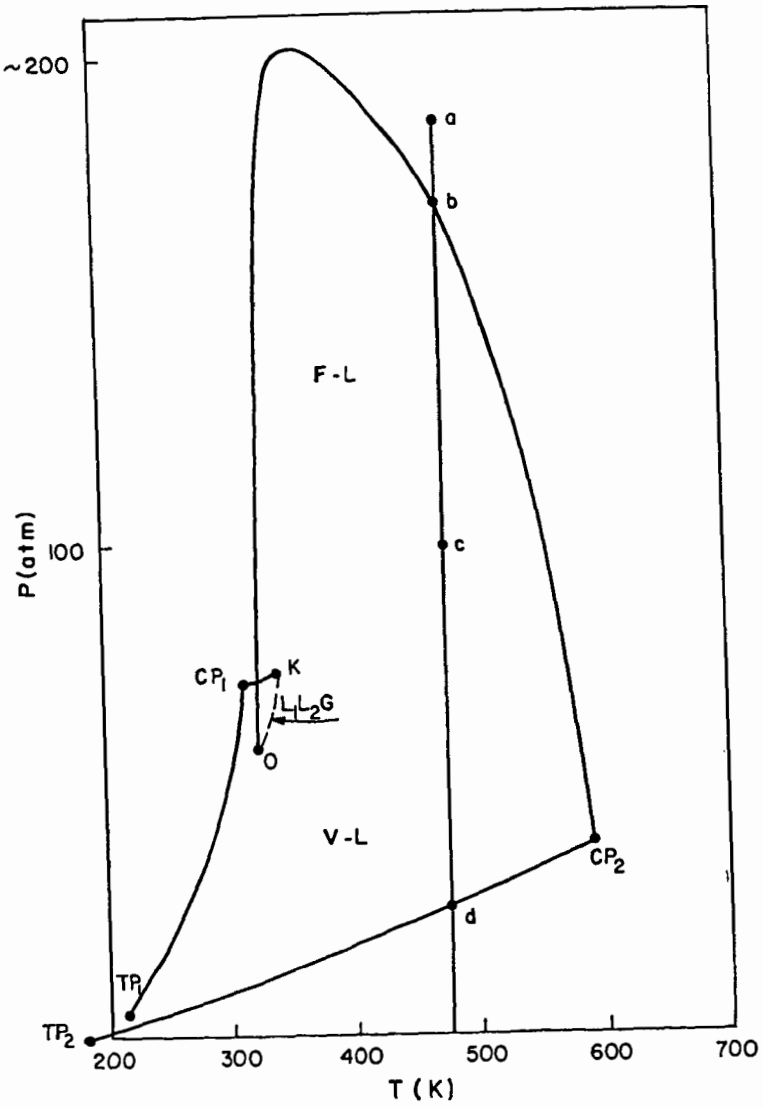

Figure 2. P-T diagram for toluene and CO_2.

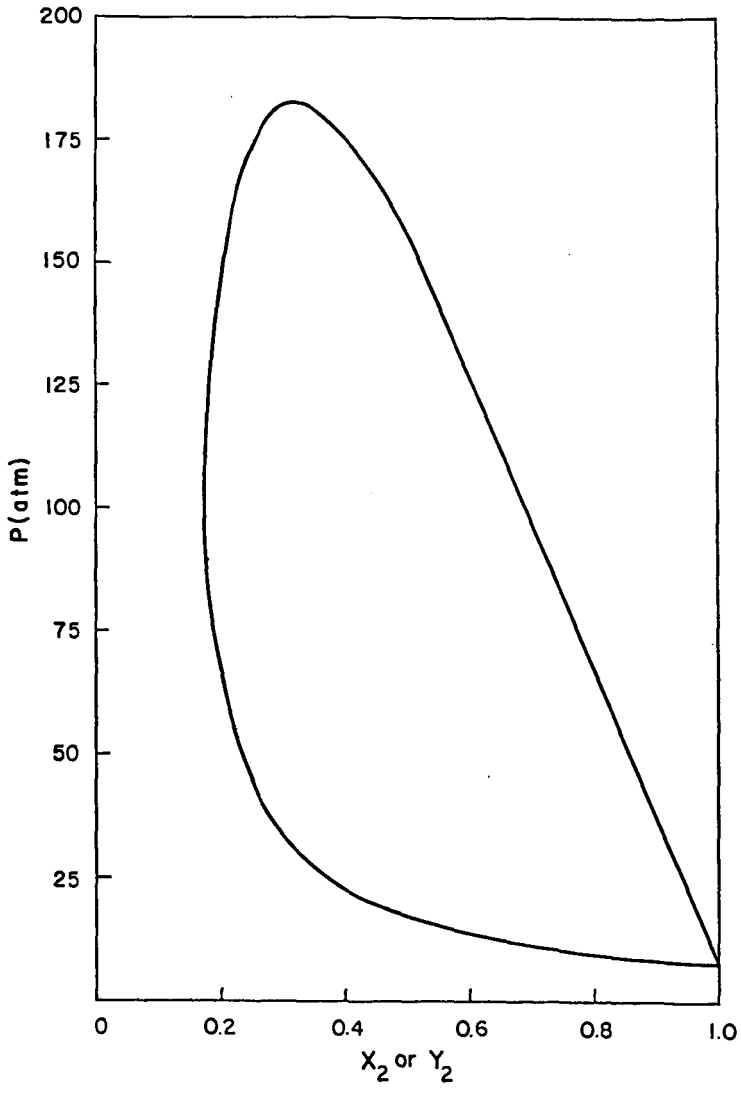

Figure 3. P-X diagram for toluene and CO_2 at 200°C.

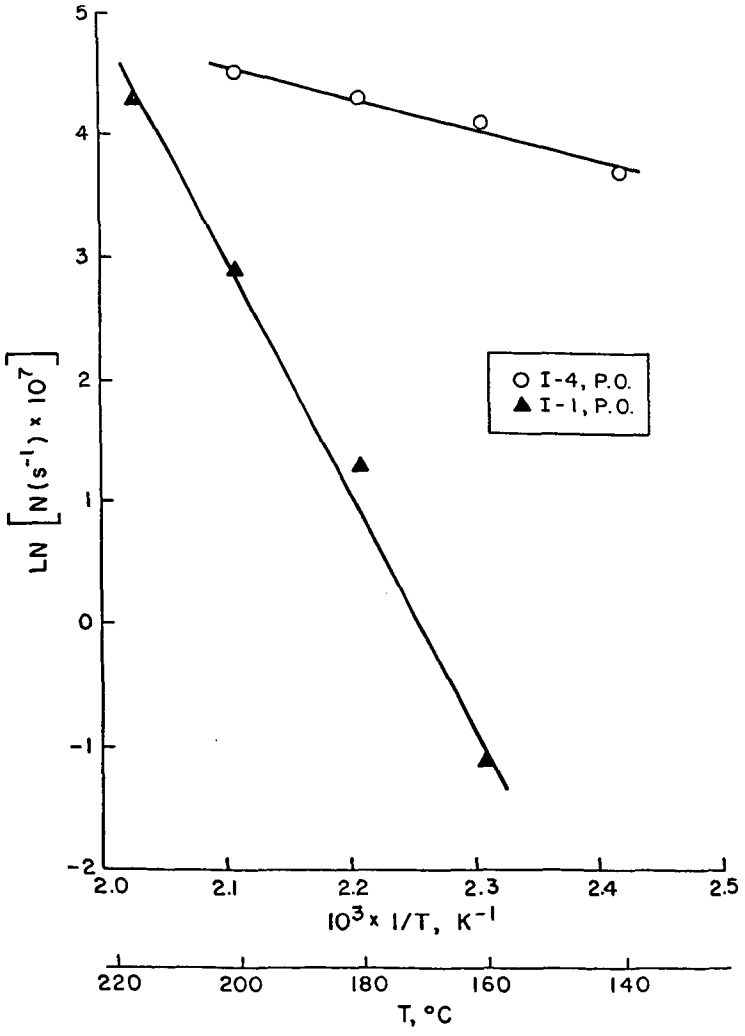

Figure 4. Turnover number for partial oxidation, for two supported Co oxide catalysts calcined at 400°C (I-1) and 200°C (I-4).

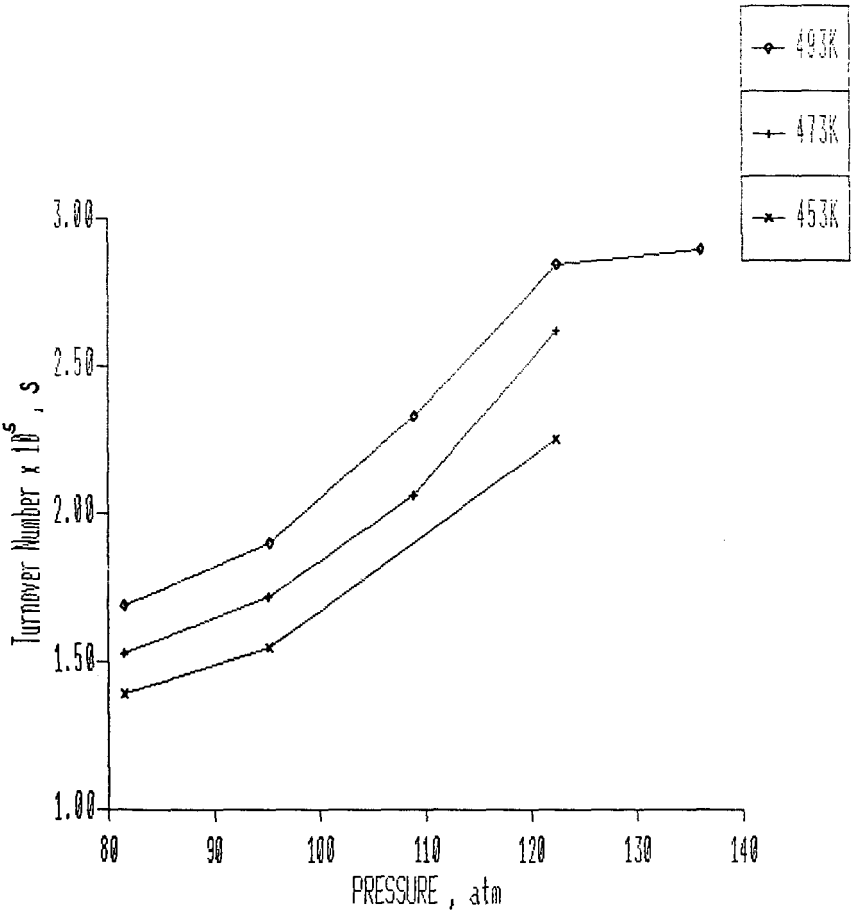

Figure 5. Turnover number per partial oxidation, for a supported Co oxide catalyst calcined at 200°C (catalyst I-4, 5% CoO).

A STUDY ON THE DISTRIBUTION OF VARIOUS CHEMICAL SPECIES IN DIFFERENT COAL LIQUIDS BY SIZE EXCLUSION CHROMATOGRAPHY - GAS CHROMATOGRAPHY - MASS SPECTROMETRY

C. V. Philip and R. G. Anthony

Kinetic, Catalysis and Reaction Engineering Laboratory
Department of Chemical Engineering, Texas A&M University
College Station, Texas 77843 - (409)845-3376

INTRODUCTION

Size exclusion chromatography - gas chromatography - mass spectrometry (SEC-GC-MS) is a unique technique which we have developed for coal liquid analysis. Size exclusion chromatography (SEC) separates molecules based on size in a short analysis time. Unlike other chromatographic techniques, SEC does not retain sample species on the column, the analysis time is fixed, and everything loaded onto the column elutes within a fixed time frame. The application of SEC is limited only by the solubility of the sample in a solvent. Since tetrahydrofuran (THF) is a good solvent for coal liquids, the separation of coal liquids by SEC is easily achieved with appropriate columns. Although size exclusion chromatography (SEC) has been used primarily for the separation and characterization of polymers based on molecular size or molecular weight, its use can be extended to the separation of smaller size molecules (1-4). Since coal-derived mixtures have several components of similar sizes, the use of SEC alone does not resolve them for the purpose of identification.

Coal liquids, petroleum crudes, and their distillation cuts have been separated into four or five fractions by SEC. These SEC fractions were analyzed by use of GC (6,7,8). The fraction collection procedure was performed manually, which was inefficient, and susceptible to human error (9,10,11,12,13). A preferred technique is to use a computer controlled fraction collection and subsequent GC-MS analysis technique (14,15,16,17,18). The automated fraction collection followed by injection of the fraction into the GC reduces analysis time, and offers an option for the collection of the desired number of fractions at predetermined time intervals. The manual collection of up to 10 one-ml fractions is also used in order to varify the effectiveness of the automated technique.

Mass spectrometers used to be expensive and complex for routine use as a GC detector. The Ion Trap Detector (ITD, Finnigan) is a low priced mass spectrometer (MS) for capillary chromatography. Three analytical tools - SEC, GC, and ITD - are incorporated into a powerful analytical system for the analysis of complex mixtures such as coal liquids, recyle solvent and anthracene oils. The SEC-GC-MS analysis of Wyodak recycle solvent is used to illustrate the speed and effectiveness of the technique.

EXPERIMENTAL

The low rank coals used in the liquefaction experiments were Texas Big Brown lignite from the Wilcox formation, Zap-2 Indian Head lignite and Beulah lignite from North Dakota and Wyodak coal from Wyoming. Mini reactors (6.3 and 20 mℓ) used mostly Autoclave high pressure fittings (11). The liquefaction solvents included anthracene oil, four recycle solvents from the coal liquefaction pilot plant at the University of North Dakota Energy Research Center (UNDERC) and water under supercritical conditions. Hydrogen, carbon monoxide and hydrogen sulphide were the reactive gases which were used in varying proportions (19). The samples of liquid products from selected

experimental conditions were used for the detailed analysis.

The product slurry as well as the recycle solvents were extracted with tetrahydrofuran (THF) and the solubles were used as samples for the analysis. The technique for the analysis is based on the integrated use of three instruments - a size exclusion chromatograph (SEC) with a 100Å SEC column, a high resolution gas chromatograph with a bonded phase wide bore fused silica column and an Ion Trap Detector (ITD, Finnigan), a mass spectrometer for capillary chromatograph (Figure 1). A sample injected into the SEC was separated based on linear molecular size and the fractions of effluents were collected at preprogramed time intervals. The SEC-GC interface is illustrated in Figure 2. The separation of each fraction is continued on the capillary column and the components were detected by the mass spectrometer (ITD). The mass spectral fragmentation data were stored on a 10 megabyte hard disk and were later analyzed by the library search using National Bureau of Standards (NBS) mass spectral data base which has fragmentation patterns of about 40,000 organic compounds. The library search was used to identify the general formula as well as probable functional groups of most major components in coal liquids. The identification of each species was achieved by using several factors including SEC retention volume (linear molecular size), GC retention time (boiling point, molecular weight) and mass spectral fragmentation pattern. Since the coal liquids contain many components, the mass spectral data of some compounds were not available in the library. A very careful evaluation of the MS fragmentation pattern was necessary to establish the identity of the compound. Identification of unknowns needed better MS fragmentation pattern and time. Once a compound was identified, the information was continously used for identifying trace amounts based on masses of the major fragments.

RESULTS & DISCUSSION

Analysis of Wyodak recycle solvent

The detailed discussion of SEC-GC-MS analysis Wyodak recycle solvent can be used to illustrate the analysis technique as well as the composition of coal liquids. Wyodak recycle solvent contains some anthracene oil distillate as well as coal depolymonization products stabilized by the liquefaction conditions. Figure 3 shows the SEC separation of Wyodak recycle solvent. The separation pattern of various chemical species and chemical groups are assigned based on reported (4-15) as well as unreported studies. When valves V_2 and V_3 (Figure 2) are engaged, the SEC effluents are collected in the sample loops of V_3 at specific intervals. The refractive index detector output shows the effect of such fraction collections as negative peaks (Figure 4). Sixteen SEC fractions of 100 μl each were collected from the Wyodak recycle solvent (Figure 4) at 0.5 min intervals. Each fraction was analyzed by injecting 0.1 μl into the GC, which used the flame ionization detector (FID). The first three fractions and the last fraction showed the GC of the solvent; so the GC of those fractions are not included in Figure 5. The first GC (Figure 5.1) corresponds to the GC of fraction #4 and the last GC (Figure 5.12) is that of fraction #15. By increasing the GC oven temperature the larger alkanes in fraction #2 and #3 can be detected. A shorter column enhances the FID response as these heavy alkanes accumulate on the column probably due to irreversible adsorption or decomposition.

Figure 5.1 shows the GC of fraction #4. It shows alkanes ranging from C_{25} to C_{30}. It is quite possible that the fraction may contain higher alkanes which are not detected due to the GC-oven temperature limit. The peaks are identified from the MS fragmentation pattern. Fraction #5 is collected after a 0.5 minute interval and its GC (Figure 5.2) shows alkanes ranging from C_{19} to C_{30}. This fraction has lower alkanes (C_{19}-C_{24}) in larger proportions in addition to smaller amounts of alkanes

(C_{25}-C_{30}) which were detected earlier in fraction #4. The peak due to C_{27} is larger relatively to other alkanes in Figure 5.1 and 5.2. Our experience with fossil fuels indicates that the straight chain alkanes (n-alkanes) have a normal distribution over a wide molecular weight range. Even in other reported works on hydrocarbon fuels an unusual enhancement of a particular straight chain alkane is not observed. The alkane fractions always contain branched alkanes such as pristane, phytane, and hopane, and some of them are called biological markers. It is quite possible that the C_{27} peak could be due to some branched alkanes co-eluting with n-C_{27}.

The GC of fraction #6 is shown in Figure 5.3, which contains mostly alkanes in the range of C_{15}-C_{24} and small amounts of C_{14} and C_{25}-C_{29}. The fraction #6 was collected 0.5 minute after fraction #5 and one minute after fraction #4. If fraction #5 had not been collected, the GC of fraction #4 and #6 which were one minute apart could have been used to qualitatively, but not necessarily qualitatively, determine all of the species. Fraction #5 has species from both fractions #4 and #6. The peak width of species eluting at these retention times is about one minute. Hence SEC fraction collection at one min (one ml) intervals would have contained all the species with less overlapping and analysis time could have been reduced to half. A short peak immediately after C_{17} is pristane (trimethylhexadecane). The short peaks that appear between the n-alkane peaks appear to be isoalkanes or branched alkanes. The baseline appears to be shifted slightly upward compared to the baseline of the GC's in Figure 5.1 and 5.2. This is probably due to a large number of possible isomers of phenolic species. GC of fraction #7 (Figure 5.4) has alkanes as small as C_{12}. The ratio of peak heights of pristane to C_{17} increases in the GC of this fraction compared to previous fractions as expected from its shorter linear molecular size. The smaller peaks between n-alkane peaks are alkylated phenols and branched alkanes.

Fraction #8 (Figure 5.5) is mostly alkylated phenols and indanols with a trace amount of smaller alkanes. The baseline shift is due to the co-elution of several large phenolic species in many isomeric forms. Fraction #9 (Figure 5.6) does not contain any alkanes. The ratio of the o-cresols to m-, p-cresols increases from fraction #8 to #9. Both m-cresol and p-cresol are structurally longer than o-cresol. Some long aromatic species such as biphenyls also appear in this fraction. Compared to fraction #8, the phenols in fraction #9 are of shorter size while the peaks appearing at long GC retention times are aromatics. It is safe to say that phenols appear before 16 minutes of GC retention time followed by aromatics after 16 minutes. The GC of fraction #10 is shown in Figure 5.7. Light phenols including xylanols and cresols present in this fraction are separated on the GC before a retention time of 8 minutes. The species appearing after 8 minutes are aromatics, mostly with alkyl side chains.

Fraction #11, whose GC is in Figure 5.8, contains phenol, which appears at 3 minutes. Phenol is the only phenolic in Fraction 11. Almost all possible isomers of one and two ring aromatics with alkyl side chains (propyl or shorter) are detected in this fraction. Since the number of species are higher, co-elutions of two or more components at one GC retention time is observed. The mass spectral fragmentation pattern can be used to assign the molecular formula and general structural nature. The identification of isomers is very difficult in a number of cases. The NBS Mass Spectral Data Base has only a fraction of the needed standard reference spectra to identify the species in this fraction. Most of the identification has been assigned based on the fragmentation patterns and boiling points derived from the GC retention times. Fraction #12 as shown in Figure 5.9 has overlapping from two types of aromatics - alkylated aromatics and polycyclic aromatics. Fraction #13 contains aromatics

with slight alkylation and the ring numbers increase as shown in Figure 5.10. Both fractions #14 and #15 (Figure 5.11, 5.12) contain only multi-ring aromatics with few alkyl side chains. One exception to the rule that SEC separates species in decreasing order of linear molecular size is that condensed ring aromatics tend to remain in the column longer. Some polycyclic aromatics such as pyrene and coronene are eluted from the gel column only after napthalene although they are much larger. More pyrene is in Fraction #15 than in Fraction #14 but the reverse is true for anthracene which appears before naphthalene.

Distribution of Alkanes in Coal Liquids

One of the major results of SEC-GC-MS studies is the discovery of an orderly pattern, by which various isomers and homologs of similar chemical species exist in coal liquids. For example almost any direct coal liquefaction process produces very similar species which differ from each other by size and extent of isomerization but with an orderly distribution pattern. Alkanes ranging from $C_{12}H_{26}$ and $C_{44}H_{80}$ are detected in almost any coal liquid. Most of these are straight chain alkanes showing an orderly continuous pattern. Neither is a particular n-alkane almost absent nor is it present in a disproportionate amount. Exceptions exist for some branched alkanes such as pristane, phytane, and hopane. These species are also called biomarkers and their concentration varies depending on the sample. The straight chain hydrocarbons, mainly the alkanes, are observed as sharp GC peaks in the GC of certain SEC fractions of lignite-derived liquids. The corresponding SEC-fractions of the anthracene oil show a "hump" in the GC. It appears that the pyrolytic conditions used in a coking oven are destroying or converting most of the straight-chain alkane species into numerous isomeric hydrocarbons. The MS fragmentation patterns of the GC "hump", are similar to that of alkanes.

Distribution of Phenols in Coal Liquids

Phenols are a major chemical lump present in coal liquids. Phenols have basically one or more aromatic ring structures with alkyl substituents. Methyl, ethyl and propyl are the most common alkyl substituents. The smallest species is the one with a hydroxyl group attached to a benzene ring. Addition of a methyl group produces three isomers - o-, m-, and p-cresols. It appears that all three are present in about the same proportion. The number of possible isomers increases as the possible number and size of alkyl substituents increases. It is expected that higher degree of alkylation can produce larger molecules in a larger number of isomeric forms, separation of which is rather difficult even by high resolution GC methods. This could be the reason why a shift in the GC baseline is observed for the SEC phenolic fractions rather than resolved peaks. Since these shifts are quite reproducible and real, it can be assumed that these "bumps" are due to a large number of components eluting continuously without resolution. Their SEC retention time suggests that they are probably phenols. The gas chromatographers who are used to fewer sharp peaks from capillary GC may prefer to resolve them. Sometimes derivatization techniques are used to obtain sharper well resolved peaks. As a matter of fact unresolved "bumps" are telling a story. Too many isomers of close molecular weight or boiling point are eluting without resolution at close retention times. Phenols do show peak tailing in most GC separation conditions. But currently available capillary columns do not show tailing as a serious problem. Peak tailing is expected to decrease as the degree of alkylation increases. Peak tailing for cresol is less than that for phenol. It is much improved for xylenols. The derivatization of phenols prior to GC separation may produce fewer well-resolved peaks but at the expense of losing some components.

Distribution of Aromatics in Coal Liquids

The number of isomers of alkylated aromatics is enormous. Lower members of alkylated benzenes such as xylenes are well-resolved and detected by FID and MS. Increased alkylation causes an increase in the number of isomers. In the case of both alkylated phenols and aromatics various isomers exist in a continuous pattern. The less alkylation gives few well-resolved isomers. The more alkylation gives a large number of isomers but in smaller concentrations.

We have observed a striking similarity in the identity of chemical species found in different types of coal liquids such as anthracene oil (A04), recycle solvents and the lignite-derived liquids from our liquefaction experiments as they are separated by SEC-GC and identified by MS. The polycyclic aromatic species which are characteristic of coking oven products from coal, such as anthracene oil and creosote oil are found in all lignite-derived liquids from our liquefaction experiments, including the liquid obtained by the dissolution of lignite in water under super critical conditions. Their relative concentration was found to increase varying with the severity which is used to produce the coal liquid. Anthracene oil has the highest concentration of polycyclic aromatics and the lignite liquefied in supercritical water has the lowest. The hydroxy aromatics, also known as alkylated phenols, which are produced under lignite liquefaction experiments, are not major components in anthracene oil.

CONCLUSIONS

The coal conversion products are compounds of at least two types of species. "a" The species which are released from the coal matrix and stabilized by the coal liquefaction process. This type of species retains most of its original structural characteristics. Most of the alkanes and alkylated phenols belong to this group. "b" The species which are characteristic of high temperature reactions. The polycyclic aromatics such as phenanthrene and pyrenes are products of high temperature chemistry. Coke ovens and even wood burning fireplaces produce these products. The liquefaction environment can cause additions of alkyl side chains to these species although higher temperature causes the dealkylation of these products. Some of these species may be existing in coal but in lower concentrations.

The coal liquefaction process generates both types of compounds. Lower temperatures favor type "a" compounds while higher temperatures tend to produce more of type "b" compounds. The SEC-GC-MS analysis data on a number of coal liquids produced under varying conditions from different coals and liquefaction solvents indicate that liquefaction temperatures below 400°C produce very little type "b" compounds although they are not totally absent. The alkylated aromatics such as alkyl indans and benzenes appear to be generated from the original coal structure although these compounds could be catatytically generated at these temperatures even from simple starting materials such as CO and H_2. Several low temperature reactions products from coal support the existence of one or two ring aromatics with other substituents, especially in low rank coals.

ACKNOWLEDGEMENTS

The financial support of the U.S. Department of Energy, (project Number DE-AC18-83FC10601), Texas A&M University Center for Energy and Mineral Resources and Texas Engineering Experiment Station is gratefully acknowledged. The Energy Research Center at University of North Dakota furnished samples for the study.

REFERENCES

1. Hendrickson, J.G., "Molecular Size Analysis Using Gel Permeation Chromatography",

Anal. Chem., 1968, *40*, 49.
2. Majors, R.E.J., "Recent Advances In HPLC Packing and Columns", *Chromatog. Sci.*, 1980, *18*, 488.
3. Cazes, J. and D.R. Gaskill, "Gel-permeation Chromatographic Observation of Solvent-solute Interaction of Low-molecular Weight Compounds", *Sep. Sci.*, 1969 4, 15.
4. Krishen, A. and R.G. Tucker, "Gel-permeation Chromatography of Low Molecular Weight Materials With High Efficiency Columns", *Anal. Chem.*, 1977 *49*, 898.
5. Philip, C.V., Anthony, R.G., "Dissolution of Texas Lignite in Tetralin", *Fuel Processing Technology*, 1980, *3*, p. 285.
6. Zingaro, R.A., Philip, C.V., Anthony, R.G., Vindiola, A., "Liquid Sulphur Dioxide - A Reagent for the Separation of Coal Liquids", *Fuel Processing Technology*, 1981, *4*, 169.
7. Philip, C.V., Zingaro, R.A., Anthony, R.G., "Liquid Sulfur Dioxide - as an Agent for Upgrading Coal Liquid", "Upgrading of Coal Liquids," Ed. Sullivan, R.F., *ACS Symposium Series No. 156*, 1981;p.239.
8. Philip, C.V., Anthony, R.G., "Chemistry of Texas Lignite Liquefaction in a Hydrogen-donor Solvent System", *Fuel*, 1982, *61*, 351.
9. Philip, C.V., Anthony, R.G., "Separation of Coal-derived Liquids by Gel Permeation Chromatography", *Fuel*, 1982, *61*, 357.
10. Philip, C.V. and Anthony, R.G., "Analysis of Petroleum Crude and Distillates by Gel Permeation Chromatography (GPC)", "Size Exclusion Chromatography", Ed. Prouder, T., *ACS Symp. Series*, 1984, *245*, 257.
11. Philip, C.V., Anthony, R.G. and Cui, Z.D., "Structure and Reactivity of Texas Lignite", "Chemistry of Low-Rank Coals, Ed. Schobert, H.H., *ACS Symp. Series*, 1984, *264*, 287.
12. Philip, C.V., Bullin, J.A. and Anthony, R.G., "GPC Characterization for Assessing Compatibility Problems with Heavy Fuel Oils", *Fuel Processing Technology*, 1984, *9*, 189.
13. Sheu, Y.H.E., Philip, C.V., Anthony, R.G. and Soltes, E.J., "Separation of Functionalities in Pyrolytic Tas by Gel Permeation Chromatography", *Chromatographic Science*, 1984, *22*, 497.
14. Philip, C.V. and Anthony, R.G. "Separation of Coal Liquids by Size Exclusion Chromatography - Gas Chromatography (SEC-GC)", *Am. Chem. Soc. Div. Fuel Chem. Preprints*, 1985, *30*, (1), 147.
15. Philip, C.V. and Anthony, R.G. "Characterization of chemical Species in Coal Liquids Using Automated Size Exclusion Chromatography - Gas Chromatography (SEC-GC)", *Am. Chem. Soc. Div. Fuel. Chem. Preprints*, 1985, *30* (4), 58.
16. Philip, C.V. and Anthony, R.G. "Separation of Coal Liquids by Size Exclusion Chromatography - Gas Chromatography (SEC-GC)", *Journal of Chromatographic Science*, 1986, *24* (10), 438.
17. Philip, C.V. and Anthony, R.G. "Gel Permeation Chromatography - Gas Chromatography - Mass Spectrometry (GPC-GC-MS) Instrumentation for the Analysis of Complex Samples", Pittsburgh Conference Atlantic City March 9-13, 1987, paper #788.
18. Philip, C.V., Moore, P.K., and Anthony, R.G. "Analysis of Coal Liquids by Size Exclusion Chromatography - Gas Chromatography - Mass Spectrometry (SEC-GC-MS)", accepted for publication in Advances in Size Exclusion Chromatography, ACS Symposium Series, 1987.
19. Anthony, R.G., Philip, C.V. and Moore P.K. "Kinetic Model Development for Low-Rank Coal Liquefaction", Final Technical Report for Low Rank Coal Liquefaction, March 15, 1983 - October 31, 1986, DOE/FC/1060-13.

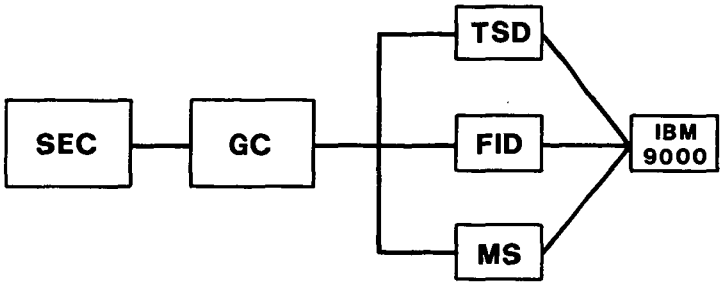

Figure 1. SEC-GC-MS instrumentation.

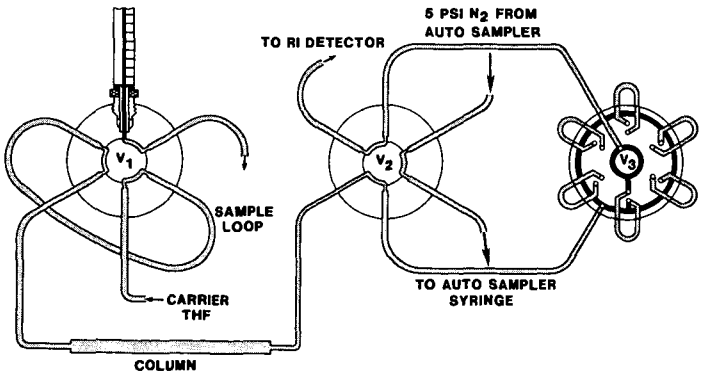

Figure 2. SEC-GC interface Note: V_3 has sixteen sample loops instead of six shown.

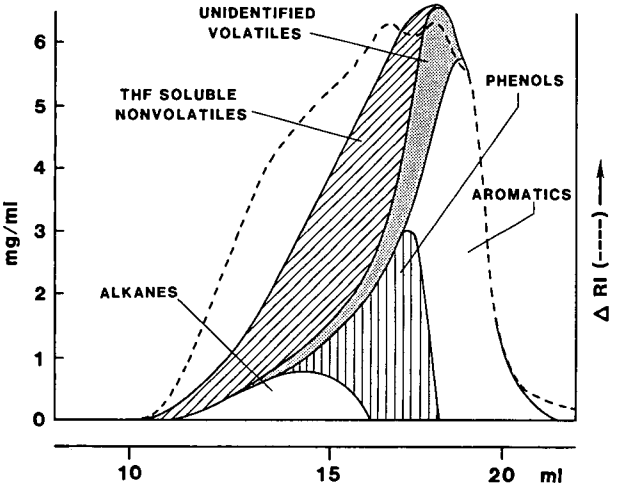

Figure 3. SEC of Wyodak recycle solvent.

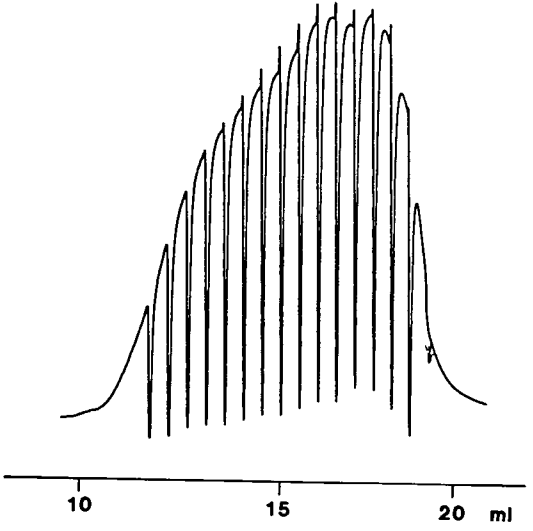

Figure 4. 100 µl fractions collected by SEC-GC interface (on-line).

SEC-GC-MS OF WYODAK RE-CYCLE SOLVENT

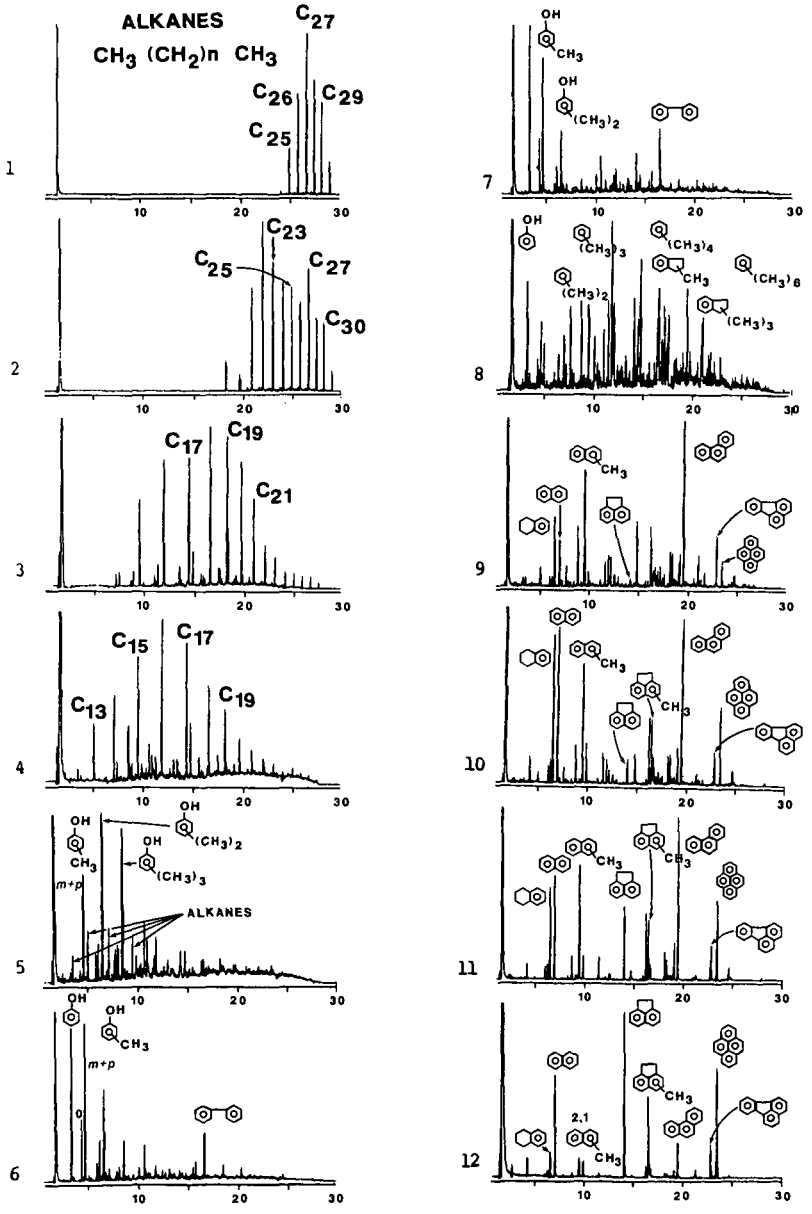

Figure 5. SEC-GC-MS of Wyodak re-cycle solvent.

THE HYDROGEN TRANSFER CYCLE FOR COAL LIQUEFACTION -- PROCESS IMPLICATIONS*

H. P. Stephens and R. J. Kottenstette
Sandia National Laboratories, Albuquerque, NM 87185

INTRODUCTION

Direct liquefaction of coal involves the conversion of a hydrogen-poor solid to a liquid richer in hydrogen by a complex set of bond ruptures and hydrogen transfer reactions. This paper reports a portion of a continuing effort to understand the utilization of hydrogen in direct liquefaction by tracing the transfer of hydrogen from the gas phase to polynuclear aromatic hydrocarbon (PAH) solvent components, and from these donor components to coal. In this portion of the effort, experiments were performed to monitor the dehydrogenation of hydroaromatic components of a coal-derived solvent that results from donation of hydrogen to coal.

In a previous paper (1), results of experiments were reported that showed the impact of a hydrogen source, either from the gas phase or from solvent containing hydroaromatic compounds, on the yield of liquefaction products. Gas-phase hydrogen was required to produce high conversion of coal to liquids only if the solvent contained low concentrations of hydroaromatic donors. Furthermore, significant consumption of gas-phase hydrogen occurred only in reactions catalyzed to promote in-situ hydrogenation of PAHs to hydroaromatics. In related experiments (2,3,4), we have sought to define effective conditions for the hydrogenation of PAHs in coal-derived solvents. The results of these studies demonstrated that 1) use of catalytic hydrogenation at relatively low temperatures favored formation of hydroaromatics; 2) use of lower temperature allows the use of lower pressure; and 3) that CO/water mixtures are effective sources of hydrogen for hydrogenation of PAHs. These results were used to establish conditions for preparing a liquefaction solvent containing high concentrations of hydroaromatic hydrogen donors. This solvent was then reacted with coal, in the absence of gas-phase hydrogen, over a range of temperatures and times to monitor the transfer of hydrogen from the hydroaromatic derivatives of three key PAHs, phenanthrene, fluoranthene, and pyrene.

EXPERIMENTAL

Materials

Feed to the solvent production reactor was prepared from a pasting solvent produced from Illinois No. 6 (Burning Star) coal by the Lummus Integrated Two-Stage Liquefaction (ITSL) process development unit (5). This material, which was too viscous to be used in our laboratory reactor, had a boiling point range of approximately 550 to 850°F. Prior to its use, it was vacuum distilled with a spinning band apparatus. The 650 to 770°F fraction, which contained 3.3% by weight phenanthrene, 4.0%

* This work supported by the U.S. Department of Energy at Sandia National Laboratories under Contract DE-AC04-76DP00789.

fluoranthene and 8.6% pyrene, was retained for these experiments. Illinois No. 6 high-volatile bituminous coal for these experiments was obtained from the Argonne National Laboratory Premium Coal Sample Program. The coal was found to have 7.3% by weight moisture and 17.5% mineral matter by low temperature ashing. Extrudates (0.8 mm diameter by 4 mm length) of Shell 324M, a 2.8% Ni, 12.4% Mo on alumina catalyst, were used for hydrogenation of the solvent. Prior to use, the catalyst was sulfided in situ with 10 mole % H_2S in H_2 at 390°C and atmospheric pressure.

Apparatus and Procedure

Solvent hydrogenation was performed in a trickle-bed reactor using steam and a 1:1 "syngas" mixture of hydrogen and carbon monoxide to simulate the products of a gasifier. The reactor consisted of six 1.0 cm ID by 15 cm long catalyst-filled stainless steel tubes connected in series. Each tube contained 9.5 g of catalyst. The reactor was thermostatted to $\pm$ 1.0°C by a forced-air convection oven and pressure was controlled to $\pm$ 10 psig with a precision back pressure regulator. After pressurizing to 800 psig with the gas mixture, the reactor temperature was brought to 300°C and water flow was initiated. Upon detection of conversion of CO/H_2O to CO_2/H_2, the coal-derived solvent flow was started. The gas mixture was delivered to the reactor at a volume hourly space velocity of 325 and steam and solvent were delivered at weight hourly space velocities of 0.07 and 0.5 respectively. The amount of steam fed to the reactor was slightly in excess of the amount required to stoichiometrically convert all of the CO. During the operation of the reactor, 0.5 mole % of H_2S was added to the gaseous feed to maintain the catalyst in the sulfided state.

Coal liquefaction reactions were performed in batch microautoclaves with slurry capacities of 8 cm^3 and gas volumes of 35 cm^3 (6). After the reactors were charged with 8g of a 2:1 ratio mixture of solvent and coal, they were pressurized to 300 psig with nitrogen. They were then heated to temperature in a fluidized sand bath while being agitated with a wrist-action shaker at 200 cycles/min. Following the heating period, the reaction vessels were quenched in water, the final temperatures and pressures were recorded, a gas sample was taken and the product slurry was quantitatively removed for analysis. All experimental variables for both the flow and batch reactors were monitored and recorded with a computer-controlled data acquisition system. Four coal liquefaction experiments were performed to correlate dehydration of the hydroaromatics with coal conversion. Reactions were performed at two temperatures, 425 and 450°C, and for times ranging from 10 to 40 minutes.

Product Analyses

Gas samples from the liquefaction reactions were analyzed for N_2, H_2, CO, CO_2, and C_1-C_3 hydrocarbons with a Carle Series 500 gas chromatograph with a hydrogen transfer system. The amounts of PAHs and hydroaromatics in the flow reactor feed and liquid product samples were determined with a Hewlett-Packard 5890 gas liquid chromatograph equipped with a capillary column. Coupled gas chromatography/mass spectrometry techniques were used to

identify the retention times of the PAHs and hydrogenated PAHs. Hydrogen content of the product was determined by elemental analysis. To calculate the amount of donatable hydroaromatic hydrogen, a portion of the coal-derived solvent that was catalytically dehydrogenated was also analyzed for hydrogen content. Conversion of coal to products was quantified by tetrahydrofuran (THF) and n-heptane solubility. Dry, mineral matter free (dmmf) basis conversions were calculated from the difference between the weight of organic coal and the insoluble organic matter resulting from THF or n-heptane extraction of the product. The n-heptane soluble materials, which contained the post-reaction solvent components, were examined by capillary column chromatography to determine the extent of dehydrogenation of solvent hydroaromatics.

RESULTS AND DISCUSSION

Solvent Hydrogenation

The extent of solvent hydrogenation can be seen in Figure 1, which is a comparison of the chromatogram of the trickle-bed reactor product to that of the feed. Analysis of the product solvent showed that 66% of the phenanthrene, 88% of the fluoranthene and 56% of the pyrene were converted to hydroaromatics. Table 1 gives the concentrations and distribution of the hydroaromatics resulting from hydrogenation of the PAHs. It was also noted from the chromatograms that the solvent contained significant amounts of alkylated phenanthrenes and pyrenes, which were also hydrogenated. However, the concentrations of these were not quantified. From the difference between the hydrogen content of the solvent (9.0%) and that of a catalytically dehydrogenated sample (8.2%), the donatable hydrogen content was calculated to be 0.8% by weight.

Coal Liquefaction and Hydrogen Donation

Table II presents a summary of the results of the coal liquefaction experiments in terms of insoluble organic material (IOM) remaining after reaction, n-heptane insoluble and soluble products formed, yield of hydrocarbon gases (C_1-C_3) and release of hydrogen to the gas phase. As can be seen from Table II, the highest reaction severity, 450°C for 40 minutes, produced a significant converion of coal to n-heptane soluble products (44%) with only a small amount (16%) of hydrogen released to the gas-phase.

Figures 2-4 trace the concentrations of the PAHs and hydroaromatics as a function of conversion of coal to the sum of the yields of n-heptane soluble materials and hydrocarbon gases. Several observations can be made with respect to hydrogen donation by the hydroaromatic species.

Comparison of the PAH and hydroaromatic concentrations resulting from experiments 2 and 3 shows that the extent of donation is directly proportional to conversion of coal to products. Though experiments 2 and 3 were performed for different times and at different temperatures, the product distributions were

nearly identical, as were the post-reaction concentrations of PAHs and hydroaromatic solvent components.

Examination of the concentration curves shown in Figures 2-4 indicates the relative ease with which the various hydroaromatics donate hydrogen during the conversion of coal. Three groups of hydroaromatics can be distinguished: First are those which donate early in the coal conversion process, as indicated by sharply decreasing concentrations at the lowest coal conversion. Tetrahydrofluoranthene, di-, tetra- and 1,2,3,6,7,8-hexahydropyrene can be placed in this group. The second group consists of hydroaromatics that donate later in the coal conversion process, as indicated by sharply declining concentrations at higher conversions. Tetrahydrophenanthrene, hexahydrofluoranthene and decahydrofluoranthene belong to this group. The third group are hydroaromatics that show a steady decrease in concentration over the entire range of coal conversion. Three compounds, dihydrophenanthrene, octahydrophenanthrene, and 1,2,3,3a,4,5-hexahydropyrene (isohexahydropyrene in Fig. 4) exhibit this behavior.

Examination of the concentration profiles for the hydrophenanthrenes indicates the existance of a multiple step donation for octahydrophenanthrene. Initially, as the concentration of octahydrophenanthrene (H_8Ph) decreases, the concentration of tetrahydrophenanthrene (H_4Ph) increases. The concentration of H_4Ph does not decrease much until the concentration of H_8Ph is substantially lower. This is consistent with the following dehydrogenation pathway which results from hydrogen donation:

$$H_8Ph \longrightarrow H_4Ph \longrightarrow Ph$$

Implications for Coal Liquefaction Processes

This study of the hydrogen transfer cycle for coal liquefaction suggests more effective ways to utilize hydrogen. The results of these experiments clearly demonstrate that an excellent coal liquefaction solvent can be produced by reaction of a coal-derived liquid with a H_2/CO/steam mixture at relatively low temperature and pressure. The resulting solvent contains a sufficient concentration of hydroaromatics to be used as the sole source of hydrogen for the liquefaction of coal. Applying these techniques for transfer of hydrogen to coal in a liquefaction process could provide several advantages: First, use of CO/H_2/steam mixtures, instead of purified hydrogen, for the hydrogenation of the solvent would eliminate the need for gas purification units. Second, operation of the solvent production reactor at a lower temperature and pressure would allow reduction of the wall thickness of the reactor vessel, thus reducing vessel cost. Third, the 650-770°F distillate cut used as a recycle solvent contains significant concentrations of the important three- and four-ring hydroaromatic donor precursors, but does not contain compounds that cause extensive catalyst deactivation. Finally, the requirement for gas-phase hydrogen and high pressure in the thermal liquefaction step would be eliminated.

REFERENCES

1. H. P. Stephens, Proceedings of the 1983 International Conference Coal Science, Pittsburgh, PA, August 1983, p. 105.
2. H. P. Stephens and R. J. Kottenstette, Preprint of Papers, American Chemical Society, Fuel Division, Vol. 30, No. 2, 345, April 1985.
3. H. P. Stephens, Proceedings of the 1985 International Conference on Coal Science, Sydney, Australia, October 1985, p. 327.
4. H. P. Stephens, Preprint of Papers, American Chemical Society, Fuel Division, Vol. 31, No. 4, 314, September 1986.
5. H. D. Schindler, J. M. Chen, and M. Peluso, Proceedings of the Seventh Annual EPRI Contractors' Conference on Coal Liquefaction, p. 2-1, EPRI AP-2718, Palo Alto, CA, November 1982.
6. R. J. Kottenstette, Sandia National Laboratories Report SAND82-2495, 6 (1983).

TABLE I Distribution of phenanthrene, fluoranthene, pyrene and hydroaromatic derivatives in hydrogenated coal-derived solvent.

Compound	Conc. in Solvent (Wt %)	Percent of PAH Mixture
Phenanthrene	1.03	34
9,10-dihydro-	0.38	13
1,2,3,4-tetrahydro-	0.79	26
1,2,3,4,5,6,7,8-octahydro-	0.81	27
Fluoranthene	0.51	12
1,2,3,10b-tetrahydro	1.96	46
6b,7,8,9,10,10a-hexahydro-	0.71	17
1,2,3,3a,6b,7,8,9,10,10a-decahydro-	1.06	25
1,2,3,3a,4,5,6,6a,10b,10c-decahydro-		
Pyrene	3.81	44
4,5-dihydro-	2.49	29
4,5,9,10-tetrahydro-	0.53	6
1,2,3,6,7,8-hexahydro-	0.98	11
1,2,3,3a,4,5-hexahydro-	0.77	9

TABLE II Summary of Results of Coal Liquefaction Experiments

Exp. No.	Temp (°C)	Time (min.)	Product Distribution (% dmmf coal basis) IOM	Hept. Sols.	Hept. Insols	C_1-C_3	Hydrogen Released to Gas Phase (% of donatable) hydrogen)
1	425	10	9.5	22.4	66.9	0.8	3.9
2	425	30	6.7	36.3	54.5	1.5	6.9
3	450	10	6.8	36.3	53.3	2.5	7.5
4	450	40	4.1	43.5	45.9	6.4	16.1

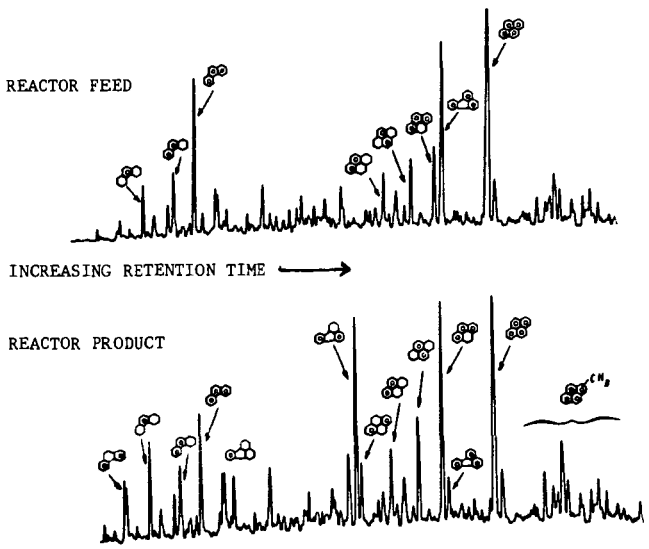

FIGURE 1. Comparison of Chromatograms of Trickle Bed Reactor Feed and Product

Fig. 2. Concentration of phenanthrene and hydrophenanthrenes vs coal conversion.

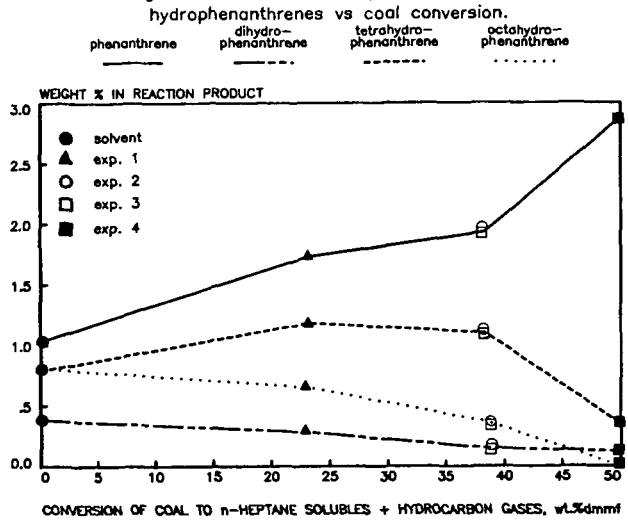

Fig. 3. Concentration of fluoranthene and hydrofluoranthenes vs coal conversion.

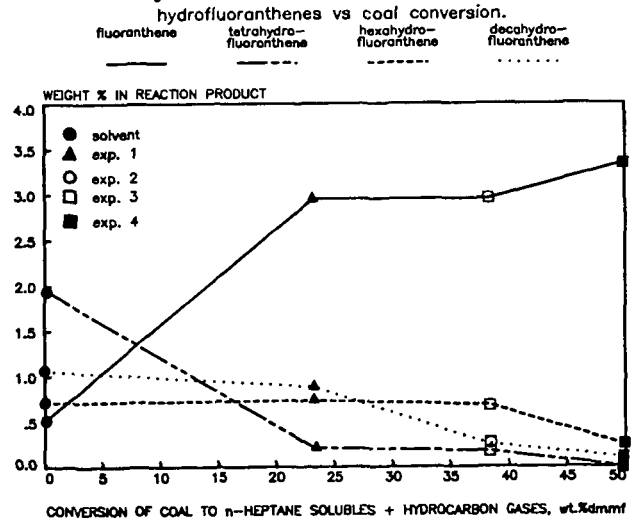

Fig. 4. Concentration of pyrene and hydropyrenes vs coal conversion.

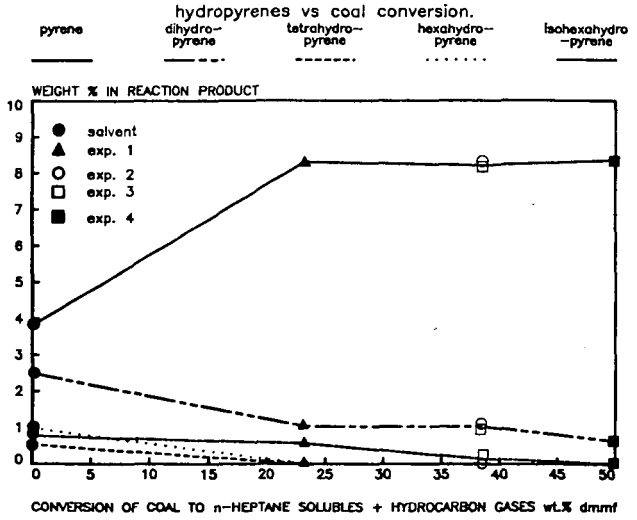

Investigation on the Nature of Steam Modified Coal

S.D. Brandes and R.A. Graff

The Clean Fuels Institute, The City College of New York
New York, New York 10031

Introduction

In previous work it was found that dramatically improved liquid yields from steam pyrolysis and mild solvent extraction of bituminous coal are obtained when the coal is first exposed to subcritical steam for short periods of time (Graff and Brandes, 1984 and 1987). This finding motivated the investigation, reported here, into the nature of coal after modification by subcritical steam.

In this work solvent swelling, a technique to determine the degree of cross-linking between macromolecular units in coal (Green, et al. 1984), has been applied. An estimate of the degree of hydrogen bonding in the coal was thereby obtained.

Treated coal was also analyzed by diffuse reflectance infrared spectroscopy (DRIS) and by an o-alkylation procedure described by Liotta (1981). The results of these three studies are described in this paper.

EXPERIMENTAL PROCEDURES

Tests were conducted using a batch of Illinois No.6 coal[1] ground under an inert atmosphere to pass 200 mesh and having the following elemental analysis (wt%, maf) : 76.1 C, 5.3 H, 1.3 N, 5.1 S, 11.8 O.[2]

Treatment

Treatments of coal samples were carried out in a series of fixed bed reactors. The reactors are constructed from lengths of stainless steel tubing (2.54cm X 1.35cm). The length of the tube was varied to accommodate different amounts of coal. By modifying the reactor chamber in this way these reactors can be used to treat 1.5 to 30 grams of coal at a time.

After loading, the reactor is placed horizontally so that there is a space above the coal for the flow of steam and gases evolved during treatment. The reactor is attached to a source of helium and/or steam and a thermocouple is wired to its midpoint. The reactor, including valves at either end, is wrapped in heating tape. A flow of helium at 50 atm is established through the reactor. With helium flowing at a minimal rate, controlled by an outlet needle valve, the reactor is heated to 300°C. This is above the condensation point of the superheated steam (265°C). Helium is then replaced by steam at 50 atm and the flow of steam is adjusted so

---

[1] We thank R. Liotta of Exxon Research and Engineering Corp. for providing this coal sample.

[2] Elemental analyses were performed by Galbraith Laboratories, Knoxville, Tennessee.

that there is a steady discharge of steam from the exit tube. The reactor is further heated to the desired treatment temperature in the first 2 to 3 minutes of steam flow. Treatment températures are in the range of 300 to 360°C. The temperature is maintained for the desired length of time (typically 15 minutes) by adjusting the voltage to the heating tape. To stop treatment, the heating tape is turned off and the steam flow replaced by helium. The reactor is allowed to cool to room temperature. The flow of helium is maintained until there is no detectable moisture in the reactor effluent. This is determined by placing a cold metal object in the flow of helium and observing any condensation which forms or by placing a piece of indicating Dryerite in the helium flow. Both inlet and outlet valves are then shut, and the tube is removed from the source of the gas.

Swelling

Swelling experiments were carried out as described in Green, et al. (1984). Samples of approximately 1g of coal were measured into 10mm X 80mm centrifuge tubes and covered with neoprene stoppers. The samples were centrifuged at 1700 rpm for approximately 10 minutes to settle the dry coal. The height of the sample (h_1) was then measured by use of an external rule. Solvents were added to the tube and the tubes were capped and shaken until there was complete homogeneity. The tubes were left to stand 18 hours and then were centrifuged again until a constant height of the solid material was attained. In the case of pyridine, because of the dark color of the solution, the tube was turned upside down in order to read the height of the solids. Experiments were done under N_2 in a glove bag unless the sample was to be deliberately exposed to air, then no precautions were taken in handling the sample in any step of the above procedure.

DRIS

Diffuse reflectance infrared spectroscopy (DRIS) was used to analyze both raw and treated coal samples which had been ground to pass 200 mesh before treating. Samples after treatment were ground and resieved, under a N_2 atmosphere, to pass 200 mesh. DRIS spectra were obtained using a Nicolet 7199 instrument. Samples were handled under nitrogen in a glove bag directly attached to the sample chamber of the machine and a purge of N_2 was maintained through the instrument. Data were acquired over approximately 13 minutes. The number of data points was 8192 over 1000 scans.[3]

O-Methylation

O-methylation of the treated coal was performed following procedures described by Liotta, et al.(1981). Typically, one gram of coal was weighed into a 250 ml round bottom flask immersed in an ice bath; 2.9 mmoles of tetra-n-propylammoniumhydroxide (TnPAH) were added. This was in slight excess of the 2.5 mmoles of acidic sites that were found, by titration, to be in raw coal. For treated coal the amount of TnPAH added was approximately 2.5 times this amount. Freshly distilled tetrahydrofuran (50-60 ml) was added while the contents were stirred with a teflon covered magnetic stirring bar.

---

[3] We thank Mr. E.W. Sheppard of Mobil Research and Development for his assistance in obtaining and interpreting the DRIS spectra.

Labeled methyl iodide ($C^{13}H_3I$),in 20% excess of the amount of TnPAH that was used, was added. Stirring was continued for 72 hours. The workup entailed removing the THF on a rotovaporizer and washing the product with 250 ml of a hot methanol and water solution (1:1 by volume). The contents of the flask were then vacuum filtered on a 80 micron filter and washed with four liters of hot water. The coal was dried in a stream of nitrogen, transferred to a soxhlet extractor, and washed with distilled water for five days. The coal was then dried in a stream of nitrogen and in a vacuum oven at 90°C for 4 hours. Stable carbon isotope analyses were performed on these samples by Coastal Science Laboratories of Austin Texas using combustion techniques.

EXPERIMENTAL RESULTS

Swelling

Values of swelling ratios for raw and treated coals are given in Table 1. The measured increase in volume depends on the amount of material present in the solid phase. If during solvent swelling some of the solid is lost by extraction, the final volume is that of a reduced amount of material. An approximate correction for this loss can be made by dividing the swelling ratio by the fraction of starting material unextracted. This correction has been made to the values in Table 1 using average values obtained in room temperature extraction of the same samples (Graff and Brandes, 1987). By accounting for the amount of material in the solvent the swelling values of the solid phase are made comparable from one sample to the other.

In pyridine and in water the steam treated coal swells more than the raw coal or the helium treated coal by a considerable amount. In benzene the raw coal swells little more than helium or steam treated coals. Pyridine breaks hydrogen bonds, benzene does not. The difference between the degree of swelling in pyridine and in benzene is a measure of the amount of hydrogen bond cross-linking. The smaller the difference the fewer the number of hydrogen bond cross-links. In Table 2 the difference values are listed. The amount of hydrogen bond association is high for steam treated coal protected under nitrogen. The helium treated sample shows less hydrogen bonding than raw coal.

Extraction in pyridine destroys essentially all of the coal's hydrogen-bond cross-links so that subsequent swelling experiments reveal the backbone structure of the coal. It is apparent from these data that there is an increase of the degree of hydrogen bonding in the treated coal as compared to the raw and helium treated samples even in the backbone of the coal after room temperature extraction. Helium treated coal, again, shows the least amount of hydrogen bond association.

When steam treated coal is exposed to air and then swelled in pyridine the swelling ratio is decreased to below that for raw coal. Exposure of helium treated coal to air has no effect on the swelling ratio. The decrease in swelling indicates an increase of cross-links of any kind. For the air exposed samples the formation of oxygen cross-links is a possibility.

To wet steam treated coal with distilled water, 0.05% by weight Xanthum gum, a polymeric thickening agent was added. When swelling experiments were conducted in water, the increase of swelling for the

treated sample over the raw coal was startling (Table 1). There is a twofold increase in the swelling value of the steam treated coal over the raw coal.

DRIS

Samples of coal treated in steam and helium, raw coal, and raw coal dried under vacuum at 90°C were examined by DRIS. There are no apparent differences among the samples in any region of the spectra except in the region attributed to -OH species (3200-3700cm^{-1}) (Fig. 1). All of the spectra generated display two bands in the hydroxyl region (Fig 2). In the raw coal sample the broad peak at 3300cm^{-1} predominates and mostly occludes the one at 3550cm^{-1}. Vacuum drying of the coal sample at 90°C does not alter this ratio. In all the treated coal samples the peak height ratio of the two is reversed. The peak at 3550cm^{-1} is clearly visible. The effect is evident whether the coal is treated in helium or steam, and it is not effected by exposure of the samples to air for brief times (less than ten minutes).

O-Methylation

The values for the relative enrichment in C-13 are given in Table 5 for raw Illinois No.6 coal, raw coal O-alkylated with labeled methyl iodide, helium treated coal, O-alkylated, and steam treated coal, O-alkylated. It is readily apparent that the steam treated coal after alkylation with the labeled methyl iodide is almost doubly enriched in C-13.

DISCUSSION

Swelling

Swelling data show that it is not a reduction of hydrogen bonding in steam treated coal that is responsible for the steam treated coal's behavior. On the contrary there is an increase in hydrogen bonding in steam treated coal. Because of the ability of water and water miscible solvents to swell the coal and the inability of water insoluble solvent to swell the coal the following conclusions have been drawn. The steam treated coal is not of the same structural makeup as the raw coal, nor as the helium treated coal. One may postulate two different structures for the modified coal. One interpretation of the data which can be made does not include any chemical interaction of the water and the coal. Residual water not removed in the drying step of the treatment process acts to hold open the coal structure. The water is miscible in pyridine and water and thus the coal swells. A possible alternative structure consists of newly formed phenolic groups created in the high pressure steam treatment. The phenols may form hydrogen bonds to each other and to the coal structure. These sites readily accept the water or water miscible solvent and cause the coal to swell more than the native structure.

DRIS

The apparent shift in the ratio of the two peaks which appear between 3200 and 3700cm^{-1} in the IR spectrum provides a significant clue in determining what changes have occurred in the structure of the coal.

The broader of the two peaks, centered around 3300cm^{-1}, is

usually associated with phenolic, alcoholic, acidic, mineral and aqueous entities in the coal structure (Fuller and Smyrl, 1985). There is no reason to believe that there is a change in the mineral matter of the coal due to steam treatment. Therefore, to interpret the observed differences between raw coal spectra and steam treated coal spectra in this region we must focus our attention on alcoholic entities, specifically phenolic -OH. The sharper peak at 3550cm^{-1} in our samples may be attributed to intramolecularly bound -OH, which are higher energy, more tightly bound species. These materials have only a small amount of hydrogen bonding to other species. A comparison of these two peaks in the spectra of raw coal and treated coal shows that there is a shift in the ratio of these two peaks. It appears that the higher energy peak increases over the lower energy one. There are three ways to interpret these observations:

1. If the total number of hydroxyl groups remains fixed, then high energy species have increased at the expense of low energy species. This implies a weakening of secondary bonding, principally hydrogen bonding.

2. A decrease in the total number of hydroxyl groups would also imply a decrease in hydrogen bonding.

3. If the shift is interpreted as principally resulting from an increase in the number of high energy hydroxyl groups (the total number of hydroxyl species increasing) the amount of hydrogen bonding in the coal could have increased. The new primary hydroxyl groups (e.g. phenols), if formed at sites which in the original coal were covalently bound, would hold the structure apart and prevent reformation of the covalently cross-linked structure. This leaves a partially depolymerized coal bound only by hydrogen bounds at the new hydroxyl functionalities.

All three of these interpretations are consistent with the tenet that the coal is partially depolymerized in steam treatment. Combined, however, with the evidence from the swelling data, which indicates an increase in the degree of hydrogen bonding in the coal, the third of the above interpretations is considered most likely.

O-Methylation

The increased hydrogen bonding exhibited in the treated coal by the swelling experiments and the presence of a shift in the hydroxyl region of the infrared spectrum strongly indicate the presence of more OH functionality. The O-alkylation procedure, first described by Liotta (1979) has proven to be an excellent quantitative way to measure the relative abundance of these groups. The use of a traceable alkylating agent, in our case C-13 labeled methyl iodide, allows for an accurate count of the number of reacted groups. Although NH, SH, and COOH sites will also react with the alkylating agent it is safe to assume that these groups are present only in minor amounts in the coal to start with and are not altered or removed in steam treatment.

The incorporation of almost twice as many labeled C-13 groups in the steam treated coal as the raw coal and the helium treated coal substatiates the speculation that steam treated coal contains more OH groups.

CONCLUSIONS

From these findings it is clear that steam treated coal has a structure altered from the raw starting coal. There is an inclusion of OH functionality in the structure which accounts for the increased hydrogen bonding and the shift in the IR spectrum. A tentative hypothesis for the increase in the extraction yields as well as the pyrolysis yields (both previously reported) is that these new hydroxyl sites are formed during the steam treatment at places in the original coal which were covalently bound. This leaves a partially depolymerized coal, cross-linked only by relatively weaker hydrogen bonds. These bonds are highly susceptible to water and water miscible solvents.

The quality of the resulting fuel produced from processing of this steam treated coal is expected to be substantially improved over that which would be obtainable from a raw coal. The weakened bonding structure of the coal will promote the production of lower molecular weight fragments. These, in turn, will be easier to upgrade. Preliminary findings from an investigation now underway suggest that although there is an increase in the number of hydroxyl sites it is at the expense of other organic oxygen in the coal. In other words the total organic oxygen content of the coal does not increase on steam treatment. This may indicate that the coal not only will be more easily upgraded as is mentioned above, but also, that this treated coal is not a worse feed for further processing than raw coal as it does not contain additional oxygen. A final point to be made is that the improved properties of steam treated coal are achieved with no expenditure of elemental hydrogen. This gives steam treated coal an economic headstart in upgrading to a more useful fuel.

ACKNOWLEDGEMENTS

The use of the o-methylation technique was suggested by Martin Gorbaty of Exxon Research and Engineering Corp. We are grateful to him and to Michael Siskin, also of Exxon Research & Engineering, for helpful discussions in the course of this work.

This work was sponsored in part by the USDOE under contract No. DE-AC21-84MC21315; W.-S. Liou, Project Manager; and M. Ghate, Chief of the Gasification and Combustion Branch.

REFERENCES

Fuller, E.L. Jr. and N.R. Smyrl (1985), "Chemistry and Structure of Coal: Diffuse Reflectance IR Spectroscopy Equipment and Techniques", Fuel, 64, 1143.

Graff, R.A. and S.D. Brandes (1984), "Coal Liquefaction by Steam Pyrolysis", ACS, Division of Fuel Chemistry Preprints, 29, (2), 104.

Graff, R.A. and S.D. Brandes (1987), "Modification of Coal by Subcritical Steam: Pyrolysis and Extraction Yields", Energy and Fuels, 1, 84.

Green, T.K., J. Kovac, and J. Larsen (1984), "A Rapid and Convenient Method for Measuring the Swelling of Coals by Solvents", Fuel, 63, 935.

Liotta, R., K. Rose, and E. Hippo (1981), "O-Alkylation Chemistry of Coal and Its Implications for the Chemicals and Physical Structure of Coal", J. Org. Chem, 46, 277.

Liotta, R. (1979), "Selective Alkylation of Acidic Hydroxyl Groups in Coal", Fuel, 58, 725.

Table 1

Swelling Ratios (Q) for Raw and Treated*
Illinois No.6 Coal

Solvent	Raw		Steam Treated			Helium Treated		
	In Air	Extracted	Under N_2	In Air	Extracted	Under N_2	In Air	Extracted
Pyridine+	2.80	1.95	3.01	2.46	1.88	2.24	2.24	1.68
Benzene	1.13	1.35	1.06	1.00	1.12	1.00	1.06	1.24
Water	0.98	1.21	1.83	1.84	0.98	1.56	1.41	1.23

*Treatments in steam and helium for 15 minutes at 50 atmospheres
+Corrected for extraction losses

Table 2

Difference in Swelling Ratio (Q)
of Pyridine and Benzene Swollen Samples

	$Q_{pyr}-Q_{benz}$
Raw	
In Air	1.67
Extracted	0.60
Steam Treated	
Under N_2	1.95
In Air	1.46
Extracted	0.76
Helium Treated	
Under N_2	1.24
In Air	1.18
Extracted	0.44

Table 3

Relative Ratio of C-13/C-12
In O-Alkylated Coals

Sample	Ratio
Raw Illinois No.6	-25*
O-methylated Raw Coal	4900
O-methylated Steam Treated Coal	8240*
O-methylated Helium Treated Coal	3789

*Average of two values

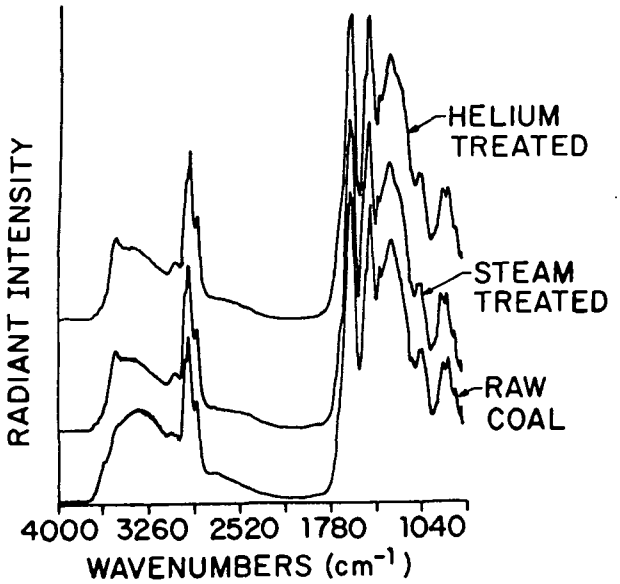

Figure 1. Comparison of DRIS Spectra of Treated Illinois No. Coal

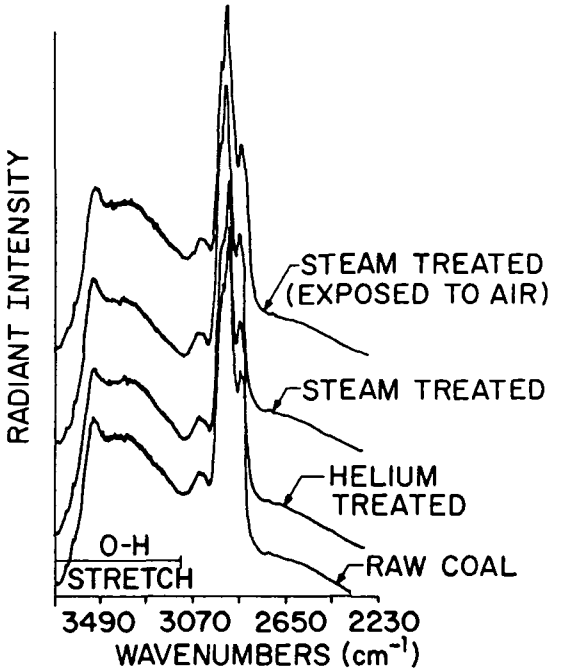

Figure 2. Comparison of the OH Stretching Region of Variously Treated Illinois No.6 Coal

Oxidation/Pyrolysis Chemistry as Related to Fuel Sooting Tendencies

Kenneth Brezinsky and Irvin Glassman

Princeton University
Mechanical and Aerospace Engineering Department
Princeton, NJ 08544

Introduction

The obvious practical importance of understanding soot formation processes has motivated a series of studies examining both the macroscopic, phenomenological parameters that affect soot formation such as flame type and temperature and the microscopic, chemical processes that may be responsible for the rate controlling soot initiation steps.

At Princeton University, premixed and diffusion flame experiments have been conducted and have revealed the relationship between the sooting tendency of hydrocarbon fuels and temperature (1,2,3). The tendencies exhibited by fuels are different when measured in the two types of flames. Under premixed conditions, an increased flame temperature has been found to decrease the formation of soot. The details of the initial fuel structure, such as the isomeric distribution of side chains, degree of conjugation and aromaticity are unimportant to the sooting tendency except insofar as they contribute to the total number of C-C bonds. The general conclusions that have been deduced are that soot forms in the post flame region from an essential precursor, probably acetylene, and the sooting tendency of a particular fuel depends primarily on the balance between the amount of soot precursor it forms (a function only of the number of C-C bonds) and the amount of precursor consuming OH radicals the fuel produces. The OH attack increases faster with temperature than does the soot precursor formation (1). The OH concentration is also proportional to the H/C ratio, which, too, is a function of the number of C-C bonds (1).

Diffusion flame experiments have led to the observation of almost completely opposite patterns. An increase in the diffusion flame temperature has been shown to increase the sooting tendency of a hydrocarbon fuel. The particular structure of the fuel affects the degree of soot formation through the mechanism by which the fuel pyrolytically decays. Since different fuels have different pyrolysis mechanisms, the nature of the initial fuel structure becomes a significant determinant in the degree of soot formation. Furthermore, soot is formed in the pre-flame, fuel region. Consequently, oxidation at the flame front consumes fuel, fuel fragments and soot particles. Particles break through the flame front and become observed as soot only when there are lowered temperatures in a localized area and insufficient oxygen to consume both the molecular hydrocarbons and the soot particles.

The details of the chemical mechanisms of the pyrolysis and oxidation processes that so strongly impact the sooting tendencies of various hydrocarbon fuels could not be revealed by the types of premixed and diffusion flame experiments that were performed. Insight into chemical mechanisms, however, has been obtained from chemical kinetic, flow reactor studies conducted at Princeton. Studies of the oxidation of benzene (4), toluene (5), ethyl benzene (6), propyl benzene (7,8), butyl benzene, alpha methyl naphthalene (10), butadiene (11), ethylene (12), propane (13), butane (14) and

other hydrocarbons have revealed many of the mechanistic steps by which these fuels decompose. A limited number of pyrolysis studies have also yielded mechanistic information for oxygen free conditions. Despite the information obtained from the flow reactor studies, the absence of a chemical, soot formation mechanism has prevented the linking of the flow reactor derived mechanisms with the pyrolysis and oxidation chemistry that must be responsible for the phenomenological observations of the flame studies.

A recently developed soot formation mechanism by Frenklach et al. (15), that evolved from a sequence of shock tube experiments on acetylene pyrolysis can serve as a partial frame work for connecting known chemical mechanisms with macroscopically determined sooting tendencies. The mechanism proposes a sequence of events starting from acetylene, proceeding through butadienyl and vinyl acetylenyl radicals to the formation of a phenyl radical (Table 1). From the phenyl radical, the growth of large polycyclic aromatics leading to soot would proceed relatively easily. This soot formation sequence should be appropriate for the post-flame region of a sooting premixed flame and the pre-flame fuel region of a diffusion flame.

In this paper, a first attempt is made at using the postulated soot formation mechanism of Frenklach et al., as a framework for relating flow reactor derived oxidation and pyrolysis mechanisms to soot related, fuel and intermediates decomposition processes. In order to logically develop the relationship, the set of Princeton experiments will first be described, the results obtained from them succinctly stated and then the proposed chemical relationships discussed.

Experimental

In both the premixed and diffusion flames the effects of temperature and fuel structure on the propensity to soot have been examined by changing the amount of diluent, usually nitrogen. Fuel structure effects were examined by the careful selection of a wide variety of hydrocarbon compounds. However, the two types of flames are very different in the manner in which the fuel and oxidizer come together at the flame front. As a consequence, there are profound effects on the above mentioned relationships between temperature, fuel structure and sooting tendency.

In a premixed flame, fuel, oxidizer and diluent are mixed upstream of the flame front and arrive at the flame front as components of a homogeneous gas. In the Princeton experiments (1), preset quantities of nitrogen and oxygen were mixed with a variable amount of fuel and fed to a Bunsen type tubular burner. The sooting limit was determined by increasing the fuel flow rate while the oxygen and nitrogen flow rate were kept constant. When luminous continuum radiation was detected at the sides of the conical flame, the fuel flow rate was decreased just enough to cause the radiation to disappear. The average fuel flow rate associated with both the appearance and disappearance of luminosity was used to calculate the critical equivalence ratio for the onset of soot. To establish the critical equivalence ratio at another temperature, the same procedure was repeated with a different preset quantity of nitrogen.

A diffusion flame is unlike a premixed flame in that the fuel and oxidizer meet in a reaction zone as a result of molecular and turbulent diffusion. The Princeton diffusion flame studies(2,3) were conducted with a burner in which a central tube delivered fuel into an outer tube containing flowing air. An excess of oxidizer led to the elongated shape characteristic of an overventilated flame. The sooting tendency of a particular fuel was established using this burner by varying the volumetric fuel + diluent flow rate for a given amount of air. When visibly obvious soot particles exited

from an annulus around the top of the flame, the soot height, i.e. the length of the luminous zone measured from the burner lip to the flame apex, was measured. Sooting heights for different fuels with different amounts of added nitrogen or argon diluent were evaluated in order to establish the sooting propensity at different temperatures.

For the chemical mechanism studies, the Princeton flow reactor was used (16). The flow reactor is a tubular, high temperature, turbulent reactor that is designed to permit the examination of oxidation and pyrolysis processes without complications due to the diffusion of heat and mass. Species concentrations with respect to time for a dilute reacting flow are obtained by withdrawing samples with a water cooled probe at discrete, well characterized locations within the tube. Analysis of the chemical content of each sample is performed with either gas chromatography or gas chromatography/mass spectrometry as is needed. Concentrations at the various locations in the reactor are related to the extent of reaction by taking into account the flow velocities within the reactor. Experiments examining the oxidation and pyrolysis of various hydrocarbon fuels have all been conducted at one atmosphere pressure and in a 900 to 1200K temperature range. The temperature range of the flow reactor, though lower than the range of hydrocarbon adiabatic flame temperatures, is nevertheless quite relevant to the chemistry of soot formation processes. The 900-1200K range corresponds both to the temperature in a flame where the initial fuel decomposition occurs and also the temperature of the zone of a flame where soot particles are first observed (17).

Results

For premixed flames, the sooting tendency (as a function of the adiabatic premixed flame temperature) for a wide variety of hydrocarbons is shown in Figure 1 (1). The critical effective equivalence ratio, i.e. the ratio of the stoichiometric oxygen necessary to convert all the fuel to CO and H_2O to the experimental amount, is used as a measure of the sooting tendency in the premixed flame. The larger is the critical equivalence ratio, the smaller is the tendency of fuel to soot. Therefore, from Figure 1 it can be seen that ethane at all temperatures has a much smaller tendency to soot than does methylnapthalene. The single, most obvious trend in Figure 1 is that for all fuels, the sooting tendency decreases as the flame temperature is increased. Furthermore, the change in sooting tendency with temperature is roughly the same for all fuels regardless of fuel type. Consequently, a vertical slice through Figure 1 at any one temperature should permit an ordering of sooting tendencies that is representative of those at all temperatures.

Such an ordering is presented in Figure 2 for a flame temperature of 2200K (1). The abscissa, "number of C-C bonds", represents the total number of carbon to carbon bonds in the parent fuel molecule when each single carbon-carbon bond is considered to contribute one, each double bond contributes two and each triple bond contributes three to the total number of bonds. The predictive correlation of Figure 2, which is independent of a detailed knowledge of isomeric structures, conjugation and even aromaticity, implies that fuel structure is an inconsequential factor in soot formation in premixed flames. The results of these premixed flame experiments along with those that have examined the post-flame region as a function of initial fuel type (18), suggests that soot formation occurs in the post flame region from a universal soot precursor whose concentration but not nature is affected by the structure of the initial fuel.

The results of a diffusion flame study of the sooting tendency of hydrocarbons as a function of temperature is shown in Figure 3 (19). The

sooting tendency is measured by the inverse of the volumetric flow rate at the smoke height. The smaller the inverse flow rate the smaller the tendency to soot. The sooting tendency of different classes of species varies widely from class to class but is relatively constant within a class. For example, aromatic compounds such as benzene, ethylbenzene and methylnaphthalene soot much easier that do the small alkenes such as propene, butene and even cyclohexene. The classes of compounds also have very different sooting temperature dependencies as revealed by the slopes of each line in Figure 3. However, in contrast to the behavior of hydrocarbon fuels in premixed flames, fuels show an increasing sooting tendency with increasing flame temperature.

A structure independent correlation of the type available for premixed flames cannot be developed from the diffusion flame results. It appears that initial fuel morphology does play an important part in the tendency of a fuel to soot as is evidenced in Figure 3 by the groupings of sooting tendency according to class of hydrocarbon. Since hydrocarbon fuels will pyrolytically decompose at the temperatures present in the oxygen-free fuel stream a distance far from the flame front, the conclusion can be drawn that the effect of initial fuel structure on sooting tendency is manifested through pyrolysis processes.

Flow reactor studies of hydrocarbon fuels, unfortunately, cannot be so concisely summarized in three plots as were the flame results. Generally, each oxidation study is conducted at rich, stoichiometric and lean equivalence ratios at one or more temperatures. From the many species concentration profiles with respect to time that are obtained, mechanistic information is deduced. The mechanism of the high temperature oxidation of benzene/phenyl radical that was developed from a series of such flow reactor oxidation studies is displayed in Figure 4 (16). This mechanism, as well as the one for butadiene that follows, were chosen for display from among the many that have been obtained from flow reactor studies because of their particular relevance to important elements of the soot formation process.

The mechanism of Figure 4 indicates that benzene is oxidized in a step by step process involving C_6, C_5 and C_4 stable radicals. At the temperature of the oxidation studies, 1000-1200K, oxidative attack was the predominant mode of decomposition, since purely pyrolytic processes are too slow. The benzene oxidation sequence as outlined ends with the ring opening formation of either butadiene or the butadienyl radical. The oxidation characteristics of butadiene have been the object of another, different set of flow reactor studies (11). These studies have resulted in the development of a mechanism that extends the benzene mechanism just presented. This butadiene/butadienyl oxidation mechanism is given in Figure 5.

Discussion

Before discussing the relationship between flame and flow reactor experimental results, the assumption must be made that the diffusion of species in flames affects the rates of reactions but not the basic pathways of a chemical mechanism that would occur in a reduced diffusion, flow reactor environment. Some preliminary, direct comparisons of flame species obtained from the probe sampling of a diffusion flame and flow reactor pyrolysis experiments appear to support this conclusion (20). Presumably, diffusion of species would also leave the basic mechanisms of oxidation and pyrolysis in premixed flame essentially unaffected.

Therefore, premixed sooting flames can be conceptually viewed as flames in which the fuel rapidly breaks down in an oxidizing environment to acetylene; the acetylene passes through the flame front, and then reacts to form soot. If the initial fuel is benzene, it is oxidized in the homogeneous

pre-flame region to mostly CO, H_2O and a small amount of acetylene. The acetylene that survives the flame front then grows through the Frenklach mechanism (15) back up to phenyl radicals and/or benzene. In some sense, the process is symmetric with respect to the flame front. The benzene oxidation mechanism derived from the flow reactor is applicable both to the rapid pre-flame benzene decomposition processes and the post-flame benzene and/or phenyl radical consumption reactions.

The pre-flame benzene decomposition oxidation reactions, if very rapid, will lead by the step by step mechanism of Figure 4 to a large buildup of acetylene. Since a large concentration of acetylene on the pre-flame side near the flame front would presumably lead to a large acetylene concentration in the post-flame region, these oxidation reactions are soot enhancing.

In contrast, any oxidation reactions in the post-flame region that consume species involved in the Frenklach soot growth mechanism will be soot retarding and perhaps even inhibiting. For example, vinyl acetylene, a key species in the soot formation mechanism, may be attacked by an O atom leading to the formation of allene and CO as indicated in Figure 5. Though the allene, through subsequent reactions may contribute species, such as acetylene, that can enter back into soot formation mechanism they do so at a lower molecular weight level with a consequent delay in the formation of soot. Therefore, the oxidation processes serve to drain species out of the soot formation route.

In a similar way, the formation of phenoxy or phenol from phenyl and/or benzene can occur in the post-flame region because of some O_2 and significant quantities of OH and O that are found there. The phenoxy quickly decomposes to cyclopentadienyl which itself will be oxidized. Thus the post-flame benzene consuming reactions interfere with the further growth of large molecules by removing or delaying the concentration growth of an essential soot building block, the phenyl radical. These reactions are therefore soot inhibiting.

Paradoxically, it appears that oxidative attack on some soot formation intermediates could actually contribute to soot formation. For example, butadienyl radical is postulated to be a key species in the route leading to the first aromatic ring. The butadienyl radical can decompose to vinyl acetylene as indicated in Figure 5 through reaction with O_2 or collision with a third body designated as M. The decomposition reaction with O_2, when the concentration of O2 is high enough, may even be faster than the unimolecular decomposition. Since it is known from sampling in flames (21) that a considerable fraction of the initial O_2 persists into the post-flame region, the accelerative effect of O_2 on the rate of soot formation may be significant.

The benzene oxidation mechanism of Figure 4, when developed into a detailed mechanism of the type now available for smaller hydrocarbons and coupled with an advanced flame model, can potentially yield an analytic prediction of the amount of acetylene that is formed in the pre-flame region and which then survives into the post-flame zone.

In diffusion flames, soot formation can be viewed conceptually to be the result of fuel pyrolysis reactions occurring in the relatively oxygen free pre-flame, fuel stream. Consequently, the soot formation mechanism of Frenklach et al., which is, in fact, a pyrolysis mechanism, would be most appropriate for the fuel stream reactions of diffusion flames. However, in contrast to the situation for premixed flames, there is no experimental indication that hydrocarbon fuels must break down to acetylene before building back up to larger molecules. Pyrolysis reactions in the fuel stream that produce directly any of the larger members of the soot formation route would contribute to an increased sooting tendency. An indication of the routes

through which fuel decomposition might feed large species into the soot formation route could come from flow reactor pyrolysis experiments augmented by higher temperature mechanistic information available in the literature.

An obvious example of such a case is the pyrolysis chemistry of benzene. Flow reactor pyrolysis experiments have indicated that though it is difficult to decompose benzene thermally, when the molecules do break apart they form vinyl acetylene, butadiene and acetylene (22). Higher temperature experiments performed in a very low pressure pyrolysis apparatus (23) revealed the formation of these same intermediates as well as others. High temperature shock tube pyrolysis experiments corroborate both of these experimental findings and emphasize the importance of phenyl radical formation (24). Clearly, benzene fuel in a diffusion flame not only will decompose pyrolytically to the starting material in the soot formation mechanism, acetylene, but also provides some of the essential vinyl acetylene and phenyl radical building blocks necessary for the formation of the polycyclic aromatics. In view of the intermediates known to be formed during benzene pyrolysis, it is not surprising that the data of Figure 3 indicate that benzene soots very easily.

However, it is not necessary that the hydrocarbon pyrolysis processes form the exact C_2, C_4 and C_6 species that appear in the soot formation mechanism. Sometimes, it is sufficient for the pyrolytic decomposition simply to produce stable intermediates which themselves appear to easily form the appropriate species. An interesting demonstration of this point results from a flow reactor examination of the major pyrolysis intermediates of iso-octane and n-octane (25). Though both fuels pyrolytic decomposed rather quickly, each one produced a different major intermediate. The pyrolysis of iso-octane was found to yield primarily iso-butene and some propene. The corresponding pyrolysis of n-octane yielded mostly ethylene and also some propene. The diffusion flame data of Figure 3 indicates that iso-octane has a significantly greater tendency to soot than does n-octane. In fact, the sooting tendency of iso-octane is close in magnitude to that of its primary pyrolysis intermediate, iso-butene. In contrast, the sooting tendency of n-octane approaches the reduced value of ethylene, its major pyrolysis intermediate. The comparison between the sooting tendency of the two isomeric octanes, and their pyrolysis intermediates is another example of the importance of initial fuel structure to sooting in a diffusion flame.

Experimental results on the addition of small amounts of oxygen to the fuel side of various sooting diffusion flames have yielded some interesting insights into the relationships between sooting tendency and chemical mechanism. The oxygen effect was found to be exceptionally strong in ethene, less so in propene, and negligible for the alkane fuels (26,27,28,29,30,31). It would appear that the normal radical pool formed during thermal pyrolysis of most fuels in diffusion flames is so large that the additional radical reactions due to the presence of small amounts of oxygen lead to no overall gain in the extent of the radical pool which governs the overall pyrolysis rate. This pyrolysis condition is true for all aliphatic hydrocarbons except ethene, and to some extent propene. For ethene, oxygen increases the radical pool extensively. Consideration of the bond strengths in ethene and propene would lead one to perhaps expect the trend postulated. Verification was shown (31) by computations in which a comprehensive chemical kinetic mechanism for the oxidation of butane (14), developed in part with flow reactor data, was adapted to apply to the pyrolysis of ethene, propene and acetylene. Although there are no experimental data for oxygen effects on accelerating the sooting of acetylene, from bond strength considerations one would expect a strong

effect and the flow reactor based computations do show substantial increase in the radical pool with oxygen addition. Similarly one would expect the same for benzene. Although no computations for benzene were performed, experimental results (29) show that oxygen accelerates the sooting of benzene.

There is, of course, a temperature effect when considering the role of oxygen in accelerating pyrolysis of fuels. The higher the temperature, the less is the accelerative effect (32,33). Most fuels show increased pyrolysis rates with oxygen addition at lower temperature (32,33). The comparisons made in the previous paragraph were for high temperatures (~1100-1300 K). In laminar diffusion flames the temperature time history of a pyrolyzing fuel element is short compared to low temperature flow and static reactors. Since it has been established that the onset of soot formation in a diffusion flame coincides with the points on the temperature profiles corresponding to about 1300 K (17,34), it is very apparent that the high temperature comparisons are the ones of importance. This temperature sensitivity can lead one to conclude that the initiation step is accelerated in addition to increasing the radical pool. The computations (31) appear to confirm this statement. The general pyrolysis mechanism does not seem to change otherwise. Flow reactor experimental results confirm that there is no appreciable, if any, accelerative effect of oxygen on the pyrolysis of propane, propene or butane (33) at high temperatures and an appreciable effect on ethene (35).

Summary

The relationships between flame studies of the sooting tendencies of various hydrocarbon fuels and chemical mechanisms derived from flow reactor experiments have been developed. The mechanisms for the oxidation of benzene and butadiene, in particular, have been related to both sooting premixed and diffusion flames despite the large difference in basic flame structure. A recently developed soot formation mechanism has provided the linking framework between chemical mechanism and observable sooting tendencies. The same framework has permitted the application of flow reactor based chemical models to the prediction and explanation of the effect of oxygen addition on sooting diffusion flames.

Acknowledgements

The authors wish to thank Mr. George Sidebotham and Mr. Harjit Hura of Princeton University for helpful discussions and for providing preliminary experimental data. The support of the Air Force Office of Scientific Research under Contract F49620-82-K-0011 is also greatly appreciated.

References

1. Takahashi, F. and Glassman, I., Combust. Sci. & Technol., 1984, Vol. 37, pp. 1-19.
2. Glassman, I. and Yaccarino, P., The Combust. Inst., 18th Symp. (Int'l.) on Combustion, 1981, pp. 1175-1183.
3. Gomez, A., Sidebotham, G. and Glassman, I., Comb. and Flame 58, 45-57 (1984).
4. Venkat, C., Brezinsky, K., and Glassman, I., Int. Symp. Combust. 19, 143 (1982).
5. Brezinsky, K., Litzinger, T.A. and Glassman, I., Int. J. Chem. Kinet. 16, 1053 (1984).
6. Litzinger, T.A., Brezinsky, K. and Glassman, I., Comb. and Flame 63, 251 (1986).
7. Litzinger, T.A., Brezinsky, K. and Glassman, I., J. of Phys. Chem., 1986, 90, 508.
8. Litzinger, T.A., Brezinsky, K. and Glassman, I., Combust. Sci. & Technol., 1986, Vol. 50, pp. 117-133.

9. Brezinsky, K., Litzinger, T.A. and Glassman, I., 21st Symp. (Int'l.) on Combustion, 1986.
10. Litzinger, T.A., Brezinsky, K. and Glassman, I., Eastern States Section/Combust. Inst. Paper #68, 1985.
11. Brezinsky, K., Burke, E.J. and Glassman, I., Int. Symp. Combust. 20, 613 (1985).
12. Westbrook, C.K., Dryer, F.L. and Schug, K.P., 19th Symp. (Int'l.) on Combustion, 1982, pp. 153-166.
13. Hautman, D.J., Schug, K.P., Dryer, F.L. and Glassman, I., Combust. Sci. & Technol. 25, 219 (1981).
14. Pitz, W.J., Westbrook, C.K., Proscia, W.M. and Dryer, F.L., Int. Symp. Combust. 20, 831 (1985).
15. Frenklach, M., Clary, D.W., Gardiner, W.C.,Jr. and Stein, S.E., 20th Symp. (Int'l.) on Combustion, 1984, pp. 887-901.
16. Brezinsky, K., Prog. Energy Combust. Sci., 1986, Vol. 12, pp. 1-24.
17. Kent, J. and Wagner, H. Gg., Int. Symp. Combust., 20th, p. 1007.
18. Harris, S.J. and Weiner, A.M., Combust. Sci. & Technol., 1984, Vol. 38, pp. 75-87.
19. Glassman, I., COMBUSTION, Academic Press, 1987.
20. Sidebotham,G. and Hura, H., Princeton University, unpublished data.
21. Bittner, J.D. and Howard, J.B., Int. Symp. Combust. 18, 1105 (1981).
22. Weckman, E., Princeton University, unpublished data.
23. Smith, R.D. and Johnson, A.L., Comb. and Flame 51: 1-22 (1983).
24. Kiefer, J.H., Mizerka, L.J., Patel, M.R. and Wei, H.-C., J. Phys. Chem. 1985, 89, 2013-2019.
25. Brezinsky, K. and Dryer, F.L., Central States/Western Section/Combustion Institute, WSSCI Paper # 3-5A, 1985.
26. Chakeraborty, B.B. and Long., R., Comb. and Flame 12, 469 (1968).
27. Deardon, P. and Long, R., J. Appl. Chem. 18, 243 (1968).
28. Jones, J.M. and Rosenfeld, J.L.J. Comb. and Flame 19, 427 (1972).
29. Wright, F.J., Fuel 53, 232 (1974).
30. Schug, P., Manheimer-Timnat, Y., Yaccarino, P. and Glassman, I., Comb. Sci. and Tech. 22, 235 (1980).
31. Hura, H. and Glassman, I., Comb. Sci. and Tech. 53, 1(1987).
32. Walker, P.W., Reaction Kinetics (Spec. Periodical Rep., Chem. Soc. London) 1, 172 (1975).
33. Murphy, S.L., Brezinsky, K. and Glassman, I., Eastern States Section/The Combustion Institute Meeting, Paper No. 10 (1982). See also Murphy, S.L., Princeton University M.S.E. Thesis, 1982.
34. Gomez, A. and Glassman, I., 21st Symp. (Int'l.) on Combustion (1986).
35. Hura, H., Princeton University, private communication (1987).

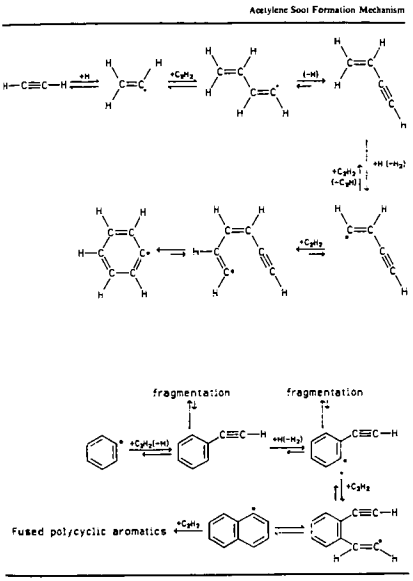

Table 1

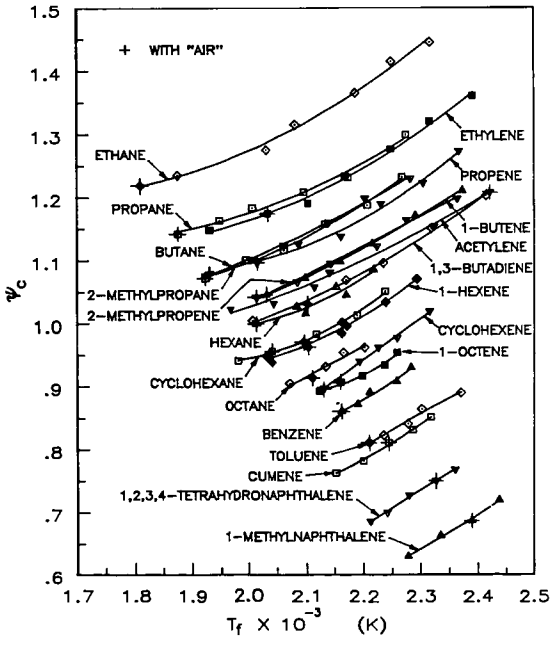

Figure 1. The critical effective equivalence ratio at sooting as a function of adiabatic flame temperature (from ref. 1)

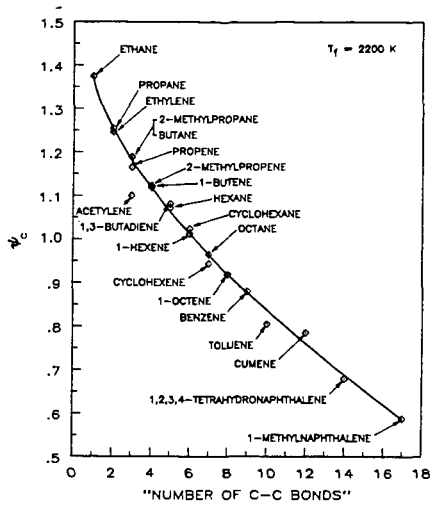

Figure 2. The correlation between the critical equivalence ratio at sooting and the number of C-C bonds (from ref. 1).

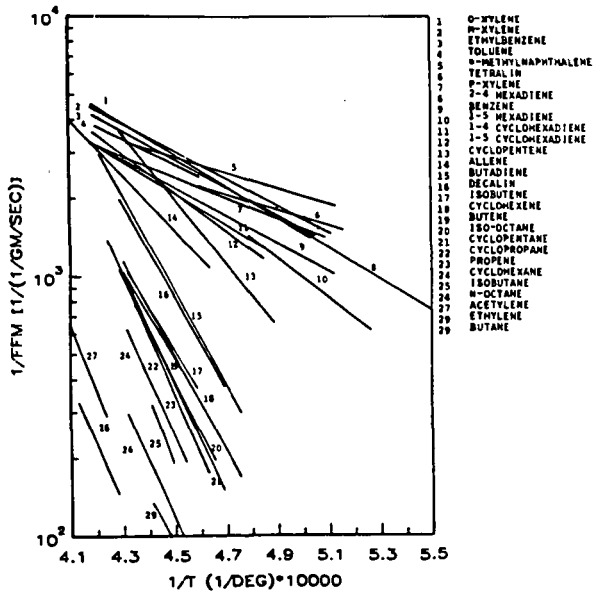

Figure 3. The sooting tendency of some hydrocarbon fuels as a function of the reciprocal of the calculated adiabatic flame temperature (from ref. 19).

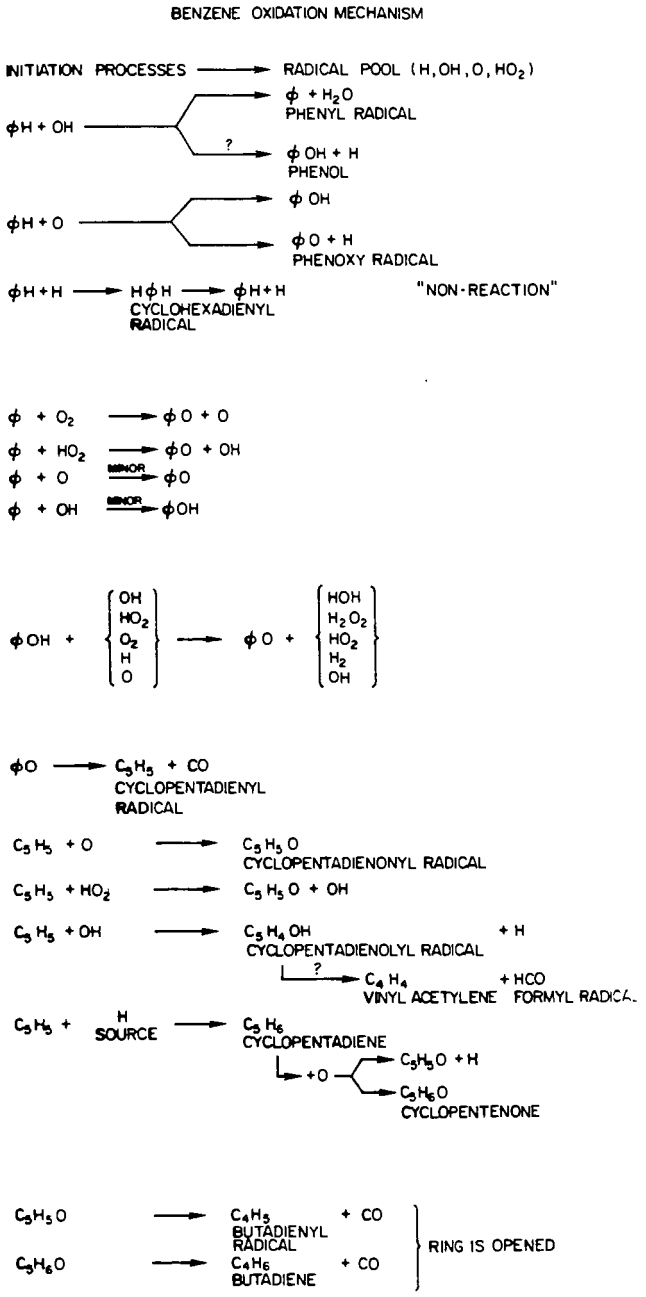

Figure 4. Benzene oxidation mechanism (from ref. 16).

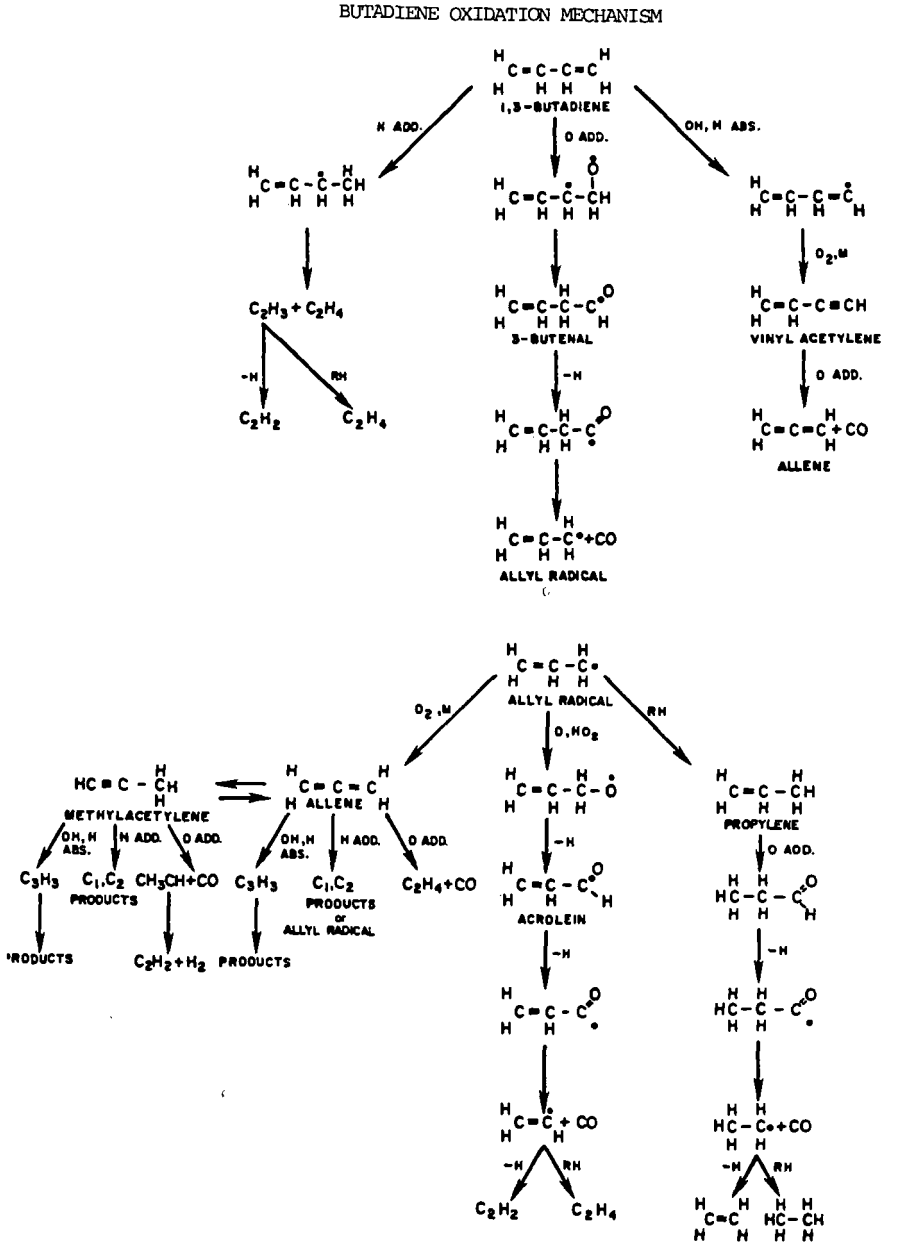

Figure 5. Butadiene oxidation mechanism (from ref. 11).

The Formation of Soot and Polynuclear Aromatic Compounds in the Low-Temperature Pyrolysis of Alkynes

by

Julian Heicklen

Department of Chemistry and Environmental Resources Research Institute, The Pennsylvania State University, University Park, PA 16802

Abstract

The pyrolysis of vinylacetylene (CH_2=CH-C≡CH), 2-methylbut-1-ene-3-yne (CH_2=C(CH_3)-C≡CH), acetylene-vinylacetylene mixtures and acetylene-styrene mixtures at 300-550°C produced polymer and adducts (or dimers) in parallel independent homogeneous second-order reactions. At the temperatures of the studies, the polymerization reaction dominates, but because the Arrhenius parameters are smaller for the polymerization process, it should become relatively less important above ≈850K. The respective Arrhenius A factors are about $10^{6.5}$ and $10^{8.0}$ M^{-1} sec^{-1} for polymerization and adduct formation (or dimerization) and the respective activation energies are about 90 and 125 kJ/mole.

The adducts (or dimers) are cyclic compounds some of which are aromatic. With continued heating they can lose hydrogen and condense to higher polynuclear aromatic compounds. The polymer chars on heating, presumably because of hydrogen evolution. The second-order removal processes dominate over unimolecular decomposition at the temperatures studied and can remain significant for temperatures in excess of 1200K. Both second-order processes should be important in soot formation.

Early Work

Soot and the aromatic compounds are well-known products of the low-temperature pyrolysis of hydrocarbons. They include polynuclear aromatic compounds, some of which are carcinogenic.

The pyrolysis of C_2H_2 has been studied for over 50 years, an early work being done by Pease (1929) who reported only polymerization at 400-600°C. Munson and Anderson (1963) studied the reaction in a flow reactor between 500 and 850°C. Apparently they were the first to show that the exclusive initial product is vinylacetylene. In a companion study, Hou and Anderson (1963) found that no free radicals were formed at temperatures up to 700°C in the pyrolysis of acetylene, vinylacetylene or diacetylene.

Cullis and Franklin (1964) studied the pyrolysis of C_2H_2 from 500-1000°C and confirmed that the sole initial product was vinylacetylene. The diacetylene seen comes from the heterogeneous decay of the vinylacetylene. They found the reaction to be second order in C_2H_2, and to be unaffected by the presence of other hydrocarbons. By comparing their results with earlier work, they concluded that a single mechanism prevails for the pyrolysis of C_2H_2 from 350-2500°C. The reaction is second order with $\log(k, M^{-1} s^{-1}) = 10.8 - 41{,}600/\theta$ where $\theta = 4.575$ T (Cullis and Read, 1970). Palmer and Cullis (1965) have pointed out that vinylacetylene is the sole initial product at temperatures at least up to 1300°C. Subsequent work by Ogura (1977) of the shock decomposition of C_2H_2 gave $\log (k, M^{-1}sec^{-1}) = 11.39 \pm 0.26 - (46{,}000 \pm 1400/\theta$ from 1000-1670K.

Extended pyrolysis of C_2H_2 does produce many other products. Stehling et al (1962) studied the reaction at 600-900°C and found benzene as the main product at 600°C with some vinylacetylene and styrene present. At 700°C, indene, naphthalene, and other unidentified products were seen. Above 800°C, H_2 and C_2H_4 became important, though they were seen along with CH_4 for very extended conversions at 600°C. The aromatic compounds are produced at temperatures up to 800°C, at which temperature they start dehydrogenating. The vinylacetylene reached a maximum concentration at 600-650°C. The aromatic compounds formed must come from reactions of vinylacetylene, either by itself or with C_2H_2.

The first study on vinylacetylene pyrolysis was done by Ikegami (1963). He studied the reaction at 300-400°C and found two processes, a rapid polymerization and a slow decomposition to produce mainly H_2, C_2H_4, C_2H_6, CH_4, and small amounts of C_2H_2. The rate was second order in C_4H_4 with a rate coefficient of $1.85 \times 10^8 \exp\{-25{,}300/1.987T\}\ M^{-1}\ s^{-1}$.

The pyrolysis of vinylacetylene was also studied by Cullis et al (1967) and Cullis and Read (1970). They studied the reaction between 300 and 620°C and found it to be quite different below and above 500°C. Below 500°C only polymerization occurred in a second order reaction with an activation energy of 28 kcal/mole. These results agree with those of Ikegami (1963). Above 500°C it was found that polymerization was accompanied by large amounts of low molecular weight products, mainly H_2 and C_2H_2, though CH_4, C_2H_4, and soot were also formed. Diacetylene and methylacetylene were not produced under any conditions.

Cullis and Read (1970) found that the addition of C_2H_2 to vinylacetylene had no effect on the vinylacetylene pyrolysis at 478°C, even for an acetylene concentration twice that of vinylacetylene. On the other hand, Yampol'skii et al (1968) found that at 800-950°C, vinylacetylene removal was slower in a mixture of 0.5% vinylacetylene and 99.5% C_2H_2 than in a mixture of 0.5% vinylacetylene and 99.5% Xe, and they reported the respective rates in terms of first order removal coefficients. Furthermore in the presence of C_2H_2, though the vinylacetylene removal rate was reduced, benzene was produced.

Polymer Formation

The pyrolyses of several alkyne systems have been studied in our laboratory from 300-550°C. The dominant product in all cases is a yellow polymer which settles on the wall of the reaction vessel. This polymer is stable at ≈300°C, but slowly becomes black over a period of weeks at higher temperatures. Presumably hydrogen is being evolved from the polymer and it becomes soot.

The systems studied include pure vinylacetylene (CH_2=CH-C≡CH), pure 2-methylbut-1-ene-3-yne (CH_2=C(CH_3)-C≡CH), vinylacetylene-acetylene (C_2H_2) mixtures and acetylene-styrene (C_6H_5CH=CH_2) mixtures. In all cases the rate of disappearance of reactants was homogeneous, second order, and unaffected by the addition of excess N_2 or He. For the pure C_4H_4 and C_5H_6 systems the reaction was second order in the reactant, whereas for the mixed systems, the removal rate for C_2H_2 or C_8H_8 was first order in each reactant. The rate coefficients and temperature ranges used are summarized in Table 1.

Presumably the polymerization occurs through a free-radical addition mechanism. For the pure C_4H_4 system the basic mechanism would be:

$2C_4H_4 \rightarrow 2R\cdot$ (H-atom transfer)	k_i
$R\cdot + C_4H_4 \rightarrow R\cdot$	k_p
$2R\cdot \rightarrow R_2$	k_t

which leads to the rate law

$$-d[C_4H_4]/dt = (2k_i + k_p(k_i/k_t)^{1/2})[C_4H_4]^2$$

The mechanism and rate law for the C_5H_6 system is analogous. Since $2k_i$ is small compared to $k_p(k_i/k_t)^{1/2}$, the overall Arrhenius A factor for the reaction is given by $A_p(A_i/A_t)^{1/2}$. The expected values for A_i and A_p are $\approx 10^8$ M^{-1} sec^{-1} since these are typical second-order reactions. Radical-radical termination reactions occur near collision frequency, and since R· is a large radical, we expect $A_t \approx 10^{11}$ M^{-1} sec^{-1}. Thus the overall A factor should be $10^8 \times (10^8/10^{11})^{1/2} = 10^{6.5}$ M^{-1} sec^{-1} in agreement with the observation of Lundgard and Heicklen (1984) for C_4H_4 and Chanmugathas and Heicklen (1985) for C_5H_6. The overall activation energy is $E_p + E_i/2$ since $E_t \approx 0$ and is about 90 kJ/mole.

For the C_2H_2-C_4H_4 system the initiation and termination steps are the same as for pure C_4H_4, since C_2H_2 self polymerization was negligibly slow under the conditions of the study. However an additional propagation step is needed:

$$R\cdot + C_2H_2 \rightarrow R\cdot \qquad k_p$$

so that

$$-d[C_2H_2]/dt = k_p'(k_i/k_t)^{1/2}[C_2H_2][C_4H_4]$$

in agreement with the observations. The values for the overall Arrhenius A factor and activation energy should be similar to those for the one-compound polymerizations, as indeed they are.

The C_2H_2-C_8H_8 polymerization is considerably more complex and not completely understood. The polymerization of either compound alone was negligibly slow under the conditions studied, yet copious amounts of polmyer were produced in the mixed system. A tentative mechanism has been suggested (Chanmugathas and Heicklen, 1987) in which initiation occurs by the interaction of $2C_8H_8$ molecules:

$$2C_8H_8 \rightarrow R_1\cdot \qquad I$$

The $R_1\cdot$ radical presumably does not add readily to styrene, but does add readily to C_2H_2

$$R_1\cdot + C_2H_2 \rightarrow R_2\cdot \qquad 2$$

where the distinction between $R_1\cdot$ and $R_2\cdot$ radicals is that the former has a styrene end group, whereas the latter has an acetylene end group. The $R_1\cdot$ radicals can also terminate:

$$2R_1\cdot \rightarrow \text{Termination} \qquad 3$$

The $R_2\cdot$ radicals add preferentially to C_2H_2 to regenerate $R_2\cdot$ type radicals, but occasionally they generate a different radical, $R_3\cdot$, which adds preferentially to styrene to give an $R_1\cdot$ type radical:

$$R_2\cdot + C_2H_2 \rightarrow R_2\cdot \qquad 4a$$
$$\rightarrow R_3\cdot \qquad 4b$$
$$R_3\cdot + C_8H_8 \rightarrow R_1\cdot \qquad 5$$

This mechanism leads to the rate laws

$$-d[C_8H_8]/dt = 2k_1[C_8H_8]^2 + k_2(k_1/k_3)^{1/2}\,[C_2H_2][C_8H_8]$$
$$-d[C_2H_2]/dt = k_2(k_1/k_3)^{1/2}[(k_4 + k_{4b})/k_{4b}][C_2H_2][C_8H_8]$$

If $2k_1 \ll k_2(k_1/k_3)^{1/2}$, then C_8H_8 removal is first-order in both reactants and the rate coefficient parameters should be similar to those for the other systems in agreement with the observations. The C_2H_2 removal rate is first-order in both reactants but is much larger than that for C_8H_8 by the factor $(k_4 + k_{4b})/k_{4b}$.

Many addition polymers have a ceiling temperature at which their rate of depolymerization equals their rate of polymerization, and the polymer is not produced at higher temperatures. Usually this occurs because the polymerization process produces C-C single bonds which are the weakest bonds in the polymer and are ruptured on heating. This does not appear to

be the case with polymers produced from acetylenes. C-C single bonds are formed but they are sandwiched between C=C double bonds giving rise to a conjugation effect. Thus the C-C single bond energies are strengthened to >400 kJ/mole while the tertiary vinylic C-H bonds are weakened to ≈335 kJ/mole. Therefore instead of depolymerization at high temperature, C-H bond scission occurs and hydrogen is released leaving behind a char (or soot). Thus the polymerization followed by charring could be an important soot-producing process in the low-temperature pyrolysis of hydrocarbons.

It is interesting to see at what temperatures the polymerization process is important. This can be computed precisely for C_4H_4 since its first-order decomposition rate has been measured recently by Hidaka et al (1986) to be $6.1 \times 10^{13} \exp(-335 \text{ kJ/mole-RT}) \text{ sec}^{-1}$. With this expression and the Arrhenius parameters obtained by Lundgard and Heicklen (1984) for total C_4H_4 removal at low temperatures where polymerization predominates, we can obtain $[C_4H_4]_{1/2}$, the concentration of C_4H_4 where equal amounts of it disappear by unimolecular decomposition and polymerization. The curve marked polymerization in Fig. 1 shows a plot of $\log([C_4H_4]_{1/2})$ vs. temperature. From this curve it can be seen that the polymerization dominates over decomposition at 1000K for C_4H_4 pressures in excess of 0.1 Torr or at 1200K for C_4H_4 presures in excess of 20 Torr. Soot formation through polymerization is important at temperatures up to at least 1200K and may be significant at temperatures up to 1400K.

Adduct Formation

Adduct formation occurs along with polymerization. Thus in the single reactant systems dimers are produced along with polymer, but no trimers or tetramers were seen. In the mixed systems adducts of the two reactants were observed. Both polymerization and adduct formation (dimerization) are initial processes as determined by examining time histories of the curves of growth. Furthermore they are completely independent of each other and do not proceed through a common intermediate. This conclusion comes from the rate laws by the following argument. Let us assume that the two processes have some common intermediate I. Then the general mechanism would be

$$\begin{aligned} A + B &\rightarrow I \\ I + A \text{ (or B)} &\rightarrow \text{Polymer} \\ nI &\rightarrow \text{Adduct} \end{aligned}$$

where A and B are the two reactants. This general mechanism requires that the rate law for polymer formation be of higher order than for adduct formation, contrary to observation. Therefore the two processes cannot have a common intermediate. The adduct formation occurs by a concerted or diradical process. Presumably the polymerization occurs via a mono radical chain mechanism.

In our laboratory, acetylene and vinylacetylene mixtures were pyrolyzed at 400-500°C in the absence and presence of O_2 or NO (Chanmugathas and Heicklen, 1986). The major product of the interaction between C_2H_2 and C_4H_4 was polymer, but benzene was also produced. Both the C_2H_2 removal and C_6H_6 formation rates were first-order in C_2H_2 and C_4H_4. The rate coefficient parameters are listed in Tables 1 and 2, respectively. Benzene formation occurred by two processes: a concerted molecular mechanism (≈60%) and a singlet diradical mechanism (≈40%).

In order to investigate the low temperature (below 500°C) pyrolysis of vinylacetylene as an avenue for polynuclear aromatic hydrocarbon formation, it is essential to look at the formation of higher molecular weight products. Due to experimental limitations, however, the two early studies (Ikegami, 1963; and Cullis and Read, 1970) in this temperature range were only able to monitor lower molecular weight products such as H_2, CH_4, C_2H_2, C_2H_4, C_2H_6, C_3H_6 and in one case benzene. Also, kinetic data were limited to vinylacetylene removal rates as a function of temperature.

Therefore, a study was undertaken in our laboratory in order to obtain more detailed kinetic information about the low-temperature pyrolysis of vinylacetylene, paying particular attention to higher molecular weight products formed during the early stages of reaction. Thus we have examined the pyrolysis of vinylacetylene at 300-450°C (Lundgard and Heicklen, 1984). Vinylacetylene removal was found to be second-order with rate coefficients similar to those reported by Ikegami (1963) and Cullis and Read (1970). In agreement with the earlier work, we found no effect of added gases (N_2, He in our case) and that the main product was polymer which coated the reaction vessel walls. However, in addition we found that 20% of the vinylacetylene was converted to styrene, a dimer of vinylacetylene. This provided the first direct evidence of how aromatics are produced from the pyrolysis of smaller hydrocarbons.

The reaction for vinylacetylene removal and C_8H_8 formation is homogeneous, second-order in reactant, and independent of the presence of a large excess of N_2 or He. However C_8H_8 formation is about half-suppressed by the addition of the free radical scavengers NO or O_2. The major reaction for C_4H_4 removal is polymerization. In addition four C_8H_8 isomers, carbon, and small hydrocarbons are formed. The three major C_8H_8 isomers are styrene, cyclooctatetraene (COT), and 1,5-dihydropentalene (DHP).

The C_8H_8 compounds are formed by both molecular and free radical processes in a second-order process with an overall $k \simeq 3 \times 10^8 \exp(-122$ kJ/mole RT) M^{-1}-sec (average of packed and unpacked cell results). The molecular process occurs with an overall $k = 8.5 \times 10^7 \exp(-188$ kJ/mole RT) M^{-1}-sec. The COT, DHP, and an unidentified isomer (d), are formed exclusively in molecular processes with respective rate coefficients of $4.4 \times 10^4 \exp(-77$ kJ/mole RT), $1.7 \times 10^5 \exp(-89$ kJ/mole RT), and $3.1 \times 10^9 \exp(-148$ kJ/mole RT) M^{-1}-sec. The styrene is formed both by a direct free-radical process and by isomerization of COT.

Lundgard and Heicklen (1984) pointed out that the mechanism for styrene formation could involve a modified Diels-Alder reaction with either of two intermediates:

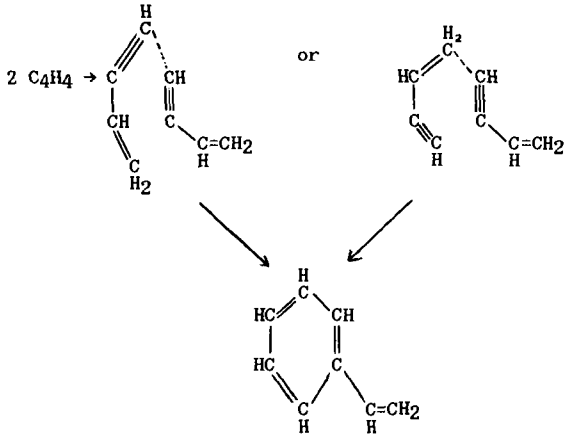

With either of the transition states it is necessary to transfer a hydrogen atom before ring closure.

In order to distinguish which intermediate is involved in styrene formation a study was made of the pyrolysis of 2-methylbut-1-ene-3-yne: $CH_2=C(CH_3)-C\equiv CH$ (hereafter referred to as C_5H_6). For this molecule the two intermediates will give different products. The head-to-head addition will give a meta-substituted product, while the head-to-tail addition will give a para-substituted product.

The pyrolysis of 2-methylbut-1-ene-3-yne (C_5H_6) has been studied from 375-450°C in a quartz reaction vessel in the absence and presence of O_2 or NO (Chanmugathas and Heicklen, 1985). From 375-425°C, the rates of disappearance of reactant and of formation of dimers are second order in C_5H_6. The major product is polymer, with the dimers accounting for about 3% of the C_5H_6 consumed. In addition toluene and p-xylene are produced, their production coming, at least in part, from decomposition of the C_5H_6 dimers ($C_{10}H_{12}$). Also trace amounts of CH_4, C_2H_4, C_2H_6, and C_3H_6 are formed. The rate coefficient parameters for C_5H_6 removal and $C_{10}H_{12}$ formation in the absence of O_2 or NO are listed in Tables 1 and 2, respectively.

The reaction mechanism for dimer formation is analogous to that in vinylacetylene (C_4H_4) pyrolysis (Lundgard and Heicklen, 1984), except that in the C_4H_4 system cyclooctatetraene is seen as an unstable product that isomerizes to styrene, whereas in the C_5H_6 system, the dimethylcyclo-octatetraene apparently is too unstable to be detected. The dimers detected were 2,6-dimethylstyrene (P4), p-isopropenyltoluene (P5), and 2 other unidentified dimers (P3) with nearly identical gas chromatographic retention times. From the effect of the radical scavengers and by comparison of the C_4H_4 and C_5H_6 systems, the following mechanistic characteristics were determined:

1) The direct formation of styrene in the C_4H_4 system comes from a

head-to-head "modified Diels-Alder" 6-member cycloaddition which proceeds through a diradical intermediate.

2) There is no conclusive evidence for a direct head-to-tail "modified Diels-Alder" 6-member cycloaddition. However, if it does occur, it does not involve diradicals, but must be concerted. Presumably this is how the unquenchable C_6H_6 is formed in the C_2H_2-C_4H_4 reaction.

3) Cyclooctatetraene is formed in concerted, non-free radical mechanisms which may proceed both by head-to-head and head-to-tail 8-member cycloadditions. For the C_5H_6 system, the head-to-head adduct isomerizes to P3, whereas the head-to-tail adduct isomerizes to P3, P4, and/or P5. Kinetic data suggest that P3 is not produced from the cyclooctatetraene intermediate, in which case, head-to-head addition would not occur.

It apears that the head-to-head additions are free radical in nature and proceed mainly through a 6-membered ring intermediate, while head-to-tail additions are a concerted molecular process and proceed mainly through an 8-membered ring intermediate.

Chanmugathas and Heicklen (1987) have found that styrene adds to acetylene in a homogenous second-order reaction with a rate coefficient of $\log\{k\{C_{10}H_{10}\}, M^{-1}\text{-sec}^{-1}\} = 8.24 \pm 0.62 - (143 \pm 9)$kJ/mole-RT from 450-550°C to produce methyl indene and 1,2-dihydronaphtahlene as initial products. These products then decay to produce indene and naphthalene, respectively.


1,2 dihydronaphthalene


naphthalene


methylindene


indene

These experiments suggest how larger polynuclear aromatic systems may be produced. Presumably if vinylacetylene were added to styrene, then vinylnaphtahlene might be produced, which in turn could add to acetylene to product anthracene and phenanthrene.

In summary we have discovered a new class of reactions: the second-order homogeneous reaction of alkynes to form adducts. There are three pieces of evidence that these reactions are homogeneous. First, all four systems studied give normal homogeneous second-order Arrhenius preexponential factors of $\log\{A, M^{-1}\text{sec}^{-1}\} \approx 8$. Second the addition of a large excess of inert gas (N_2 or He) had no effect on the rate coefficients. Third, for the one system in which packed vessels were used, the rate constants for vinylacetylene dimerization was unaffected by a change in surface-to-volume ratio of 59.

At the temperatures for which these systems were studied, the polymerization process was much more important than adduct formation. However its Arrhenius parameters are smaller than those for adduct formation (see Tables 1 and 2). Thus at higher temperatures the relative importance of adduct formation will become greater. We can use the rate coefficients for adduct formation for C_4H_4 obtained by Lundgard and Heicklen (1984) and for C_4H_4 unimolecular decomposition of 6.1×10^{13} exp{-335 kJ/mole-RT} sec^{-1} obtained by Hidaka et al (1986) to obtain $[C_4H_4]_{1/2}$ when the two processes

for C_4H_4 removal are equal. This C_4H_4 pressure is shown in Fig. 1 as a function of temperature by the curve makred dimerization. The dimerization becomes more important than polymerization at temperatures above 860K. It is equal to unimolecular decomposition at 10 Torr pressure of C_4H_4 at 1250K and can play a significant role at even higher temperatures.

The dimerization or adduct formation forms aromatic compounds which can continue to add acetylenic compounds to form polynuclear aromatic compounds which become more and more graphitic as the number of aromatic rings grow. Thus this may be an important, or even the major, path to soot formation at temperatures of $\lesssim$1200K.

References

Chanmugathas, C. and J. Heicklen, Intern. J. Chem. Kinetics, 17, 871 (1985).

Chanmugathas, C. and J. Heicklen, (1986) Intern. J. Chem. Kinetics, 18, 701.

Chanmugathas, C. and J. Heicklen (1987) submitted for publication.

Cole, J. A., J. D. Bittner, J. P. Longwell, and J. B. Howard (1984) Combustion and Flame, 56, 51.

Cullis, C. F. and N. H. Franklin (1964) Proc. Roy. Soc., A280, 139.

Cullis, C. F., I. A. Read, and D. L. Trimm (1967) Intern. Symp. Comb., 11, 391.

Cullis, C. F. and I. A. Read (1970) Trans. Faraday Soc., 66, 920.

Hidaka, Y., K. Tanaka, and M. Suga (1986) Chem. Phys. Lettr., 130, 195.

Hou, K. C. and R. C. Anderson (1963) J. Phys. Chem., 67, 1579.

Ikegami, T. (1963) Rev. Phys. Chem. Japan, 33, 15.

Lundgard, R. and J. Heicklen (1984) Intern. J. Chem. Kinetics, 16, 125.

Munson, M. S. B. and R. C. Anderson (1963) Carbon, 1, 51.

Ogura, H. (1977) Bull. Chem. Soc. Japan, 50, 1044.

Okabe, H. (1981) J. Chem. Phys., 75, 2772.

Okabe, H. (1983) J. Chem. Phys., 78, 1312.

Palmer, H. B. and C. F. Cullis (1965) "Chemistry and Physics of Carbon" P. L. Walker, ed., Marcel Dekker, NY, 1, 265.

Pease, R. N. (1929) J. Am. Chem. Soc., 51, 3470.

Stehling, F. C., J. D. Frazee, and R. C. Anderson (1962) Intern. Symp. Comb., 8, 774.

Yampol'skii, Yu. P., V. Maksimov, and K. P. Lavrovskii, J. Phys. Chem. USSR (Engl. trans.) 182, 940 (1968); Dokl., Akad. Nauk SSSR, 182, 1344 (1968).

Table 1: Summary of Total Removal Rate Coefficients

Reactant 1	Reactant 2	Log(A_1, $M^{-1}sec^{-1}$)	Log(A_2, $M^{-1}sec^{-1}$)	E_1, kJ/mole	E_2, kJ/mole	Temp.°C	Reference
C_4H_4	C_4H_4	8.57	-	105	-	300-400	Ikegami (1963)
"	"	9.32	-	117	-	336-475	Cullis and Read (1970)
"	"	6.22	-	79	-	300-450	Lundgard and Heicklen (1984)[a]
"	"	7.10	-	91	-	300-450	Lundgard and Heicklen (1984)[b]
C_5H_6	C_5H_6	6.79	-	80	-	375-450	Chanmugathas and Heicklen (1985)
C_2H_2	C_4H_4	6.26	-	71	-	400-500	Chanmugathas and Heicklen (1986)
C_2H_2	C_8H_8	7.53	6.63	91	99	450-550	Chanmugathas and Heicklen (1987)

a) Unpacked cell.
b) Packed cell.

****

Table 2: Summary of Adduct Formation Rate Coefficients

Reactant 1	Reactant 2	Log(A, $M^{-1}sec^{-1}$	E, kJ/mole	Temp.°C	Reference
C_4H_4	C_4H_4	8.50	122	300-450	Lundgard and Heicklen (1984)
C_5H_6	C_5H_6	7.40	111	375-450	Chanmugathas and Heicklen (1985)
C_2H_2	C_4H_4	8.65	126	400-500	Chanmugathas and Heicklen (1986)
C_2H_2	C_8H_8	8.27	143	450-550	Chanmugathas and Heicklen (1987)

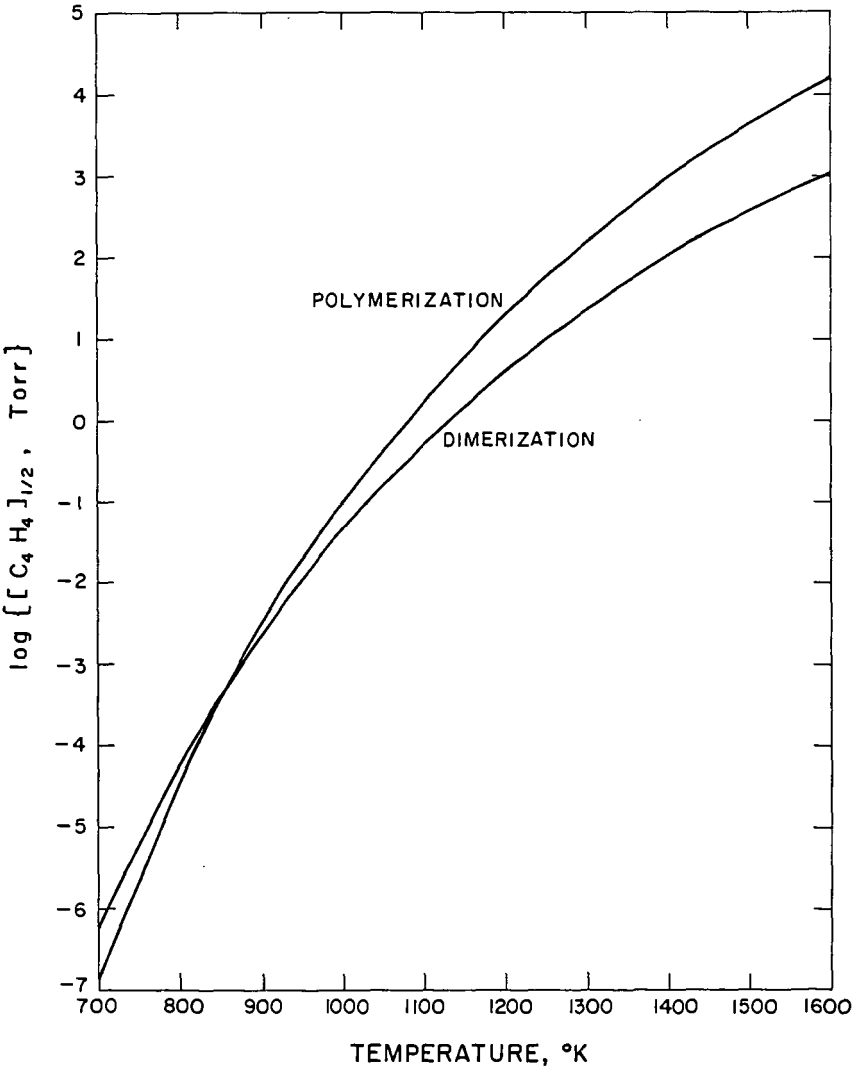

Fig. 1: Plot of the C_4H_4 pressure where unimolecular decay is equal to second-order removal vs. temperature.

Kinetic Mechanism for Pyrolysis of Acetylene Near 1000K

by M. B. Colket, III

United Technologies Research Center, East Hartford, CT 06108

INTRODUCTION

Recently a mechanism for acetylene pyrolysis was proposed to describe experimental data obtained from a single-pulse shock tube (1) over the temperature range of 1100 to 2000K. The kinetic mechanism is similar to those proposed previously (2,3) and includes mechanisms to describe formation of vinylacetylene, benzene, and phenylacetylene. Subsequently, a subset of this mechanism was modified and used (4) to match decay profiles of acetylene as well as product formation for pyrolysis data obtained in a flow reactor (5) at temperatures of 873 to 1173K.

It is the objective of this study: (a) to extend the mechanism (4) to include formation of higher molecular weight species, with a detailed discussion of growth from one to two rings; (b) to discuss the possible role of the 'odd' radical, i-C_4H_3; (c) to discuss some uncertainties with modeling PAH formation.

Description of Model

The kinetic model used in this study is listed in Table I and contains 89 reactions and 43 species. CHEMKIN and LSODE were used for integration of the rate equations. For modeling of the flow reactor data, constant temperature and pressure conditions were imposed whereas, for the shock tube data, a shock tube code modified (1) to simulate quenching in a single-pulse shock tube was utilized.

Thermodynamic parameters (except for those of vinyl radicals) are the same as those used and reported previously (1) for the lower molecular weight species. Parameters for species with molecular weights above 100 AMU were obtained from Stein (6) and are believed to be identical to those used in Frenklach, et. al. (3) Reference data for vinyl radicals and heavier species are reported in Table II. Stein's thermodynamic data for vinyl radicals were adopted since his heat of formation (68.4 kcal/mole) is higher than that used by Colket (1) (65.7 kcal/mole) and is closer to some recent determinations. In addition, Stein's reference value for entropy is higher (by 2 eu) than that used by Colket. Fortunately, the differences in values are nearly offset when determining equilibrium constants ($\ln K_{eq} = -(\Delta H - T\Delta S)/RT$) and changes in chemical kinetic modeling results are minimal.

The chemical kinetic model differs from that used previously (4) in that C_2H, C_4H_2, C_4H, i-C_4H_3, C_6H_2 and C_6H and associated reactions were included. In addition, species and reactions related to formation of polycyclic aromatics were also added. Of particular note is a modification in the dominant bimolecular initiation step. Previously the reaction

$$C_2H_2 + C_2H_2 \rightleftarrows n\text{-}C_4H_3 + H$$

was used with a rate constant of log (k/sec^{-1}) = 14.54 - 68000/4.58T. In the present study the reaction

$$C_2H_2 + C_2H_2 \rightleftarrows i\text{-}C_4H_3 + H$$

which has a lower endothermicity was employed with a rate of log (k/sec^{-1}) = 14.54-60500/4.58T. This larger rate constant for initiation is required to counterbalance termination steps omitted previously.

Formation of Fused Rings

This work was guided substantially by the significant contributions of Bittner, Howard, and Palmer (7) and of Frenklach, et. al (3). An important conclusion of the former work is that ring growth is dominated by addition of aryl radicals to triple bonds, followed by addition of acetylene to the resultant vinyllic (aromatic) radical, cyclization, and loss of an H-atom.

i.e.,

$$\dot{\phi} + C_4H_2 \rightleftarrows \phi CH\dot{C}CH$$

$$\phi CH\dot{C}CH + C_2H_2 \rightleftarrows \phi CHC(CCH)CH\dot{C}H$$

$$\phi CHC(CCH)CH\dot{C}H \rightleftarrows$$ $$\rightleftarrows H +$$

Other than reverse processes, the main competitive process which can inhibit ring growth is the thermal decomposition of the vinyllic adducts (i.e., loss of H-atoms). Bittner, et. al, reached specific conclusions regarding the importance of the thermal decomposition of the vinyllic adduct relative to its addition to acetylene. However, these conclusions may have to be re-examined, since calculations were based on low pressure flame conditions rather than those of a high pressure combustor.

Frenklach, et. al, included at least six separate reaction sequences for growth from a single to a fused ring. One reaction sequence, however, was found to dominate although a second played a minor, but contributing role. The second (minor) reaction sequence is comparable to that proposed by Bittner, et. al (see above) although phenyl radicals add to acetylene, rather than diacetylene. The dominant reaction sequence was found to be initiated by H-atom abstraction from the ortho position on phenylacetylene, followed by acetylene addition and cyclization.

$$\dot{\phi}CCH + C_2H_2 \rightleftarrows \phi(CCH)CH\dot{C}H$$

$$\phi(CCH)CH\dot{C}H \rightleftarrows$$ 

The resultant aryl radical can subsequently add to triple bonds to continue growth to higher order polycyclic aromatics. Due to the lack of experimental

rate data for reactions involving abstraction, addition, cyclization, or ring fracturing of polycyclic aromatics, Frenklach, et. al, selected generic rate constants for classes of reaction.

Rate constants for reactions involving aromatic species as listed in Table I were selected using the same technique of Frenklach, et. al, i.e., rate constants for a class of reactions are equated. Previously (3), values for several of these classes were assigned since experimental data was sparse. In this study, we have where possible updated the reaction rate data to be consistent with recently available determinations.

Predictions from the model (at 973K, 20% acetylene, and one atmosphere) are compared to the data from Munson and Anderson (5) in Fig. 1 for acetylene decay and production of benzene. In Fig. 2, predictions of production of styrene, naphthalene, and phenanthrene are shown. Although there is no experimental data from Munson and Anderson for these species, the final concentration of naphthalene is similar to other results (8) near 1000-1100K. The predicted value for styrene is about a factor of ten high.

Initially, only the dominant and minor mechanism (as identified by Frenklach, et. al) were included in the reaction sequence, specifically Mechanisms I and II:

I $\quad \phi C_2H + R \rightleftharpoons \dot{\phi}C_2H + RH \qquad (A)$

$\dot{\phi}C_2H + C_2H_2 \rightleftharpoons \phi(C_2H)CH\dot{C}H$

$\phi(C_2H)CH\dot{C}H \rightleftharpoons A2$

and

II $\quad \phi C_2H + H \rightleftharpoons \phi CH\dot{C}H \qquad (B)$

$\dot{\phi} + C_2H_2 \rightleftharpoons \phi CH\dot{C}H \qquad (C)$

$\phi CH\dot{C}H + C_2H_2 \rightleftharpoons \phi CHCH\dot{C}H$

$\phi CHCH\dot{C}H \rightleftharpoons A2H + H$

where A2 represents the 1-naphthyl radical and A2H, naphthalene.

The net contribution of the second sequence to the formation of A2H (or A2) dominates over that of the first by several orders of magnitude. For the specific conditions considered in this study, this fact can be easily explained.

At the low temperature (≈1000K) and the high initial concentrations of acetylene, forward reaction rates can be shown to dominate. Ignoring the contribution of Reaction C and taking the radical, R, in Reaction A to be an H-atom, then the relative rate is simply the rate of H-atom abstraction from the ring by H-atoms relative to the rate of H-atom addition to the acetylenic group in phenylacetylene. The value (9) of k ($C_6H_6 + H \rightarrow C_6H_5 + H_2$)

at 1000K is about 10^{10} cc/mole-sec. The rate constant for H-atom addition to acetylene, according to Ellul, et. al (10), extrapolates to 2 x 10^{12} cc/mole-sec at 1000K. Using these rate constants as estimates for k_A and k_B, respectively, Mechanism II is approximately 200 times faster than the first. The dominance of the Mechanism II becomes more apparent when the contribution of Reaction C is considered, since Reaction C is two to three orders of magnitude faster than Reaction B. Consequently, the second sequence is more than four orders of magnitude faster than the first. This is opposite to the trend observed by Frenklach, et. al. This strong discrepancy can be explained by a combination of (a) the higher temperatures of their study which enhance thermal decomposition of the radical adducts; (b) the lower partial pressures of acetylene in their study (40 torr vs. 150 torr in this study) which reduce the rate of radical addition to acetylene; and (c) the use by Frenklach of a high, temperature independent rate constant for Reaction A (with R as H-atom). Their rate constant was selected to be 10^{14} cc/mole-sec whereas, Kiefer, et. al's expression (9) gives 1.6 x 10^{12} cc/mole-sec at 1600 K.

Consequently, a reanalysis of dominant reactions occurring in a practical device should be performed for the specific ambient conditions. A preliminary analysis of the kinetic model indicates that the Mechanism II will dominate at temperatures of 1500-1700K for high pressure combustors, in which local acetylene concentrations may be at least an order of magnitude larger than considered in this and and previous studies.

Also found to contribute a minor but significant role at 973K are the overall reactions

$$\dot{\phi} + C_4H_4 \rightarrow A2H + H$$

and

$$\phi C_2H + i\text{-}C_4H_3 \rightarrow A2C_2H + H$$

both of which require H-atom shifts prior to cyclization. The second of these could be part of a very attractive sequence (as shown in Fig. 4) depending on the concentration of $i\text{-}C_4H_3$ radicals.

Role of $i\text{-}C_4H_3$

It is recognized that thermochemistry plays a significant role in the ability to model the above processes. Frenklach, et al. (11) have demonstrated quantitatively that uncertainties in thermochemistry drastically affect computed results. An interesting and possibly important thermochemical aspect of acetylene pyrolysis is due to the rather large difference between the heats of formation of the two isomers of C_4H_3, i.e., HCCCHĊH and HCCĊCH$_2$. The separation in this work was taken to be 10 kcal/mole, although Stein (6) and Bittner (12) give 8 and 15 kcal/mole, respectively. Due to its relative stability, the isomer with the unpaired electron on the secondary carbon atom ($i\text{-}C_4H_3$) becomes a dominant radical in the acetylene system. The situation is exacerbated if an isomerization step ($i\text{-}C_4H_3 \rightleftarrows n\text{-}C_4H_3$) is not included. Depending on temperature, the

concentration of i-C_4H_3 is two to three orders of magnitude higher than that of its isomer and an order higher than that of the vinyl radical. Consequently, it is logical that i-C_4H_3 plays a significant role in termination, and quite possibly in ring formation and growth.

The importance of this radical to chain termination or to ring formation and growth is dependent critically on (a) the thermodynamics of the C_4H_3 isomers; (b) the isomeration rate (equated in this work to a rate suggested (13) for the i-propyl⇄n-propyl isomeration); and (c) rate constants for reactions forming and destroying i-C_4H_3. Reactions which dominate formation of i-C_4H_3 include H-atom abstraction from vinylacetylene by phenyl, vinyl and H-atoms. The principal destruction mechanism in the present study is the isomerization to n-C_4H_3.

Uncertainties

Significant uncertainties in both rate constants and mechanisms still exist. The initiation step in acetylene pyrolysis has been a matter of unresolved dscussion for nearly thirty years. There is perhaps just as much uncertainty in the termination step(s). In this work, recombination of C_2H_3 + C_2H_3, H + C_2H_3, i-C_4H_3 + i-C_4H_3, and H + i-C_4H_3 all contributed to termination, yet there is essentially no data available on the absolute value of their rate constants (although some information on reverse reactions is available). The addition of H-atoms to acetylene is critically important to this mechanism, yet there is no data on this reaction near or above 1000K. Rate constants for reactions of similar types have been equated in this work; however, changes in rate constants depending on molecular size may be quite significant. Molecular and ionic processes have been ignored in the present study; however, there is as yet no proof against their occurrence. It is believed, however, that due to the reasonable agreement between the present model and experiments, contributions due to such reactions are perhaps small.

Conclusions

A chemical kinetic model, revised to include growth of aromatic rings predicts profiles of acetylene decay and formation of benzene, vinylacetylene, ethane, and hydrogen which are in agreement with experimental flow reactor results near 1000K. In addition the model predicts the formation of styrene, phenylacetylene, naphthalene and other fused rings. An analysis of the detailed model indicates that the dominant route for growth from a single to a fused ring is due to addition of phenyl radicals to two acetylenes. Addition of phenyl to vinylacetylene was proposed and may play a significant role depending on pressure and relative concentrations. Uncertainties associated with the role of the i-C_4H_3 radical were discussed and a mechanism involving sequential addition of i-C_4H_3 to phenylacetylene and the resultant products was proposed as a conceptually attractive mechanism for ring growth. Uncertainties related to the heat of formation and rate of isomerization to n-C_4H_3 prevent quantitative predictions as to the importance of such a mechanism.

Acknowledgements

This work has been supported by the Air Force Office of Scientific Research (AFSC) under Contract No. F49620-85-C-0012. The United States government is authorized to reproduce and distribute reprints for governmental purposes, notwithstanding any copyright notation herein.

References

1. Colket, M. B., Twenty-First Symposium (International) on Combustion. The Combustion Institute, 1987, to be published.

2. Tanzawa, T., and Gardiner, W. C., Jr., Combust. Flame 39, 241 (1980), also J. Phys. Chem. 84, 236 (1980).

3. Frenklach, M., Clary, D. W. ,Gardiner, W. C., Jr., and Stein, S., Twentieth Symposium (International) on Combustion, p. 887, The Combustion Institute, 1985; also see Frenklach, M., Clary, D. W., and Ramachandra, M. K., NASA Conractor Report 174880, May 985.

4. Colket, M. B., Palmer, H. B. and Seery, D. J. Submitted for publication, 1987.

5. Munson, M. S. B., and Anderson, R. C., Carbon 1, 51 (1963).

6. Stein, S., Personal communication, 1987.

7. Bittner, J. D., Howard, J. B., and Palmer, H. B., Soot in Combustion Systems and Its Toxic Properties, ed. by J. Lahaye and G. Prado, p. 95, Plenum Press, 1983.

8. Stehling, F. C., Frazee, J. D. and Anderson, R. C., Eighth Symposium (International) on Combustion, p. 774, Williams ad Wilkins Co., Baltimore 1962.

9. Kiefer, J. H., Mizerka, L. J., Patel, M. R., and Wei, H.-C., J. Phys. Chem. 89, 2013 (1985).

10. Ellul, R., Potzinger, P., Reimann, B., and Camilleri, P., Ber. Bunsenges. Phys. Chem. 85, 407 (1981).

11. Frenklach, M., Clary, D. W., Gardiner, W. C., Jr. and Stein, S. E., Shock Waves and Shock Tubes, Proceedings of the Fifteenth International Symposium, Ed. by D. Bershader and P. Hanson, p. 295, Stanford Univesity Press, 1986.

12. Bittner, J. D., Ph.D dissertation, Massachusetts Institute of Technology, 1981.

13. Benson, S. W., Thermochemical Kinetics, J. Wiley and Sons, New York, 1976.

TABLE I
REACTIONS FOR ACETYLENE PYROLYSIS NEAR 1000K
logk = logA + nlogT - E/R/T/2.303 *

	Reactions	Forward Rate Constant			Reverse Rate Constant		
		logA	n	E	logA	n	E
1	2C2H2=i-C4H3+H	14.54	0.0	60.5	13.49	0.0	0.2
2	H+C2H2=C2H3	12.92	0.0	2.7	12.96	0.0	41.6
3	C2H3+C2H2=n-C4H5	12.88	0.0	8.0	14.86	0.0	44.1
4	n-C4H5=C4H4+H	13.00	0.0	33.0	12.39	0.0	-5.4
5	n-C4H5+C2H2=ℓ-C6H7	12.18	0.0	5.0	14.25	0.0	41.0
6	c-C6H7=ℓ-C6H7	14.48	0.0	50.0	11.36	0.0	0.4
7	C6H6+H=c-C6H7	13.60	0.0	4.3	13.12	0.0	24.6
8	C2H3+C4H4-C6H6+H	11.60	0.0	0.0	0.00	0.0	0.0
9	C4H4+n-C4H5-A1C2H3+H	13.50	0.0	5.0	0.00	0.0	0.0
10	A1C2H3+H=A1C2H2S+H2	14.00	0.0	14.5	13.09	0.0	19.7
11	C2H4+C6H5=A1C2H3+H	11.57	0.0	2.1	12.92	0.0	1.4
12	C6H6+H=C6H5+H2	14.40	0.0	16.0	12.39	0.0	9.5
13	C2H2+C6H5=A1C2H2	12.00	0.0	4.0	13.72	0.0	42.2
14	C2H3+C4H4=C2H4+n-C4H3	13.00	0.0	10.0	13.09	0.0	9.5
15	C4H4+C6H5=C6H6+n-C4H3	12.48	0.0	0.0	13.04	0.0	3.1
16	ℓ-C6H5=n-C4H3+C2H2	13.40	0.0	36.1	11.11	0.0	0.0
17	C6H5=ℓ-C6H5	13.54	0.0	65.0	10.25	0.0	1.7
18	C2H3+C6H6=C2H4+C6H5	13.48	0.0	13.0	13.00	0.0	9.3
19	2C2H3=C4H6	13.40	0.0	0.0	17.15	0.0	104.9
20	C4H4=n-C4H3+H	15.00	0.0	100.0	12.91	0.0	-7.9
21	C6H6=C6H5+H	15.70	0.0	107.9	13.05	0.0	-3.2
22	n-C4H5+H=C4H4+H2	13.00	0.0	0.0	12.99	0.0	66.0
23	n-C4H5+H=C4H6	13.00	0.0	0.0	14.84	0.0	107.9
24	n-C4H5+n-C4H3=2C4H4	12.70	0.0	0.0	14.18	0.0	69.5
25	n-C4H5+C2H3=C4H4+C2H4	12.00	0.0	0.0	13.57	0.0	69.0
26	C2H3+H=C2H4	12.85	0.0	0.0	15.00	0.0	107.2
27	C6H5+C2H3=A1C2H3	12.60	0.0	0.0	16.11	0.0	106.5
28	C2H3+H=H2+C2H2	13.00	0.0	0.0	13.57	0.0	65.5
29	C2H4+H=C2H3+H2	14.84	0.0	14.5	13.30	0.0	11.7
30	C4H4+H=n-C4H3+H2	13.90	0.0	14.5	12.42	0.0	11.0
31	C4H6+H=n-C4H5+H2	14.00	0.0	14.5	12.76	0.0	10.9
32	C4H6+C2H3=n-C4H5+C2H4	13.18	0.0	10.0	13.52	0.0	9.5
33	C6H5+C6H6=C12H10+H	11.80	0.0	11.0	13.38	0.0	9.2
34	C2H4+M=C2H3+H+M	16.16	0.0	81.8	14.01	0.0	-25.4
35	2i-C4H3=C4H4+C4H2	11.00	0.0	0.0	14.35	0.0	47.8
36	i-C4H3+H2=C2H2+C2H3	10.70	0.0	20.0	11.18	0.0	14.8
37	C4H4=i-C4H3+H	15.20	0.0	95.0	12.72	0.0	-2.1
38	C2H+C4H4=C2H2+i-C4H3	13.60	0.0	0.0	12.48	0.0	27.9
39	n-C4H3=C2H2+C2H	14.30	0.0	57.0	13.56	0.0	3.0
40	i-C4H3=C4H2+H	12.00	0.0	49.0	12.86	0.0	-0.2
41	n-C4H3=C4H2+H	12.60	0.0	40.0	13.04	0.0	1.4
42	n-C4H3=i-C4H3	13.00	0.0	35.0	12.58	0.0	45.7
43	i-C4H3+H=C4H2+H2	13.00	0.0	0.0	14.47	0.0	55.2
44	n-C4H3+H=C4H2+H2	12.48	0.0	0.0	13.53	0.0	65.9

* NOTES: Units for A: cc,moles,sec., Units for E: kcal/mole.
= represents forward and reverse directions included in model.
- represents forward direction only included in model.

(CONTINUED NEXT PAGE)

TABLE I (continued)
REACTIONS FOR ACETYLENE PYROLYSIS NEAR 1000K
logk = logA + nlogT - E/R/T/2.303 *

	Reactions	Forward Rate Constant			Reverse Rate Constant		
		logA	n	E	logA	n	E
45	C4H4+H=i-C4H3+H2	14.49	0.0	14.5	12.62	0.0	21.9
46	C6H5+C4H4=C6H6+i-C4H3	12.18	0.0	0.0	12.31	0.0	13.8
47	C2H3+C4H4=C2H4+i-C4H3	12.70	0.0	10.0	12.36	0.0	20.2
48	C4H4=C2H+C2H3	15.70	0.0	115.0	12.93	0.0	-7.8
49	H2+M=2H+M	12.35	-.5	92.5	11.74	-.5	-11.9
50	C2H2+M=C2H+H+M	16.62	0.0	107.0	15.25	0.0	-17.9
51	C2H+H2=H+C2H2	12.85	0.0	0.0	13.60	0.0	20.5
52	C2H+C2H2=C4H2+H	13.60	0.0	0.0	14.78	0.0	15.4
53	C2H+C4H2=C6H2+H	13.60	0.0	0.0	14.97	0.0	15.1
54	C4H+C2H2=C6H2+H	13.30	0.0	0.0	14.91	0.0	8.1
55	C4H+H2=H+C4H2	13.30	0.0	0.0	14.30	0.0	13.5
56	C6H+H2=H+C6H2	13.30	0.0	0.0	14.53	0.0	10.3
57	C2H+C6H6=C6H5+C2H2	13.30	0.0	0.0	12.05	0.0	14.1
58	C4H+C6H6=C6H5+C4H2	13.30	0.0	0.0	12.29	0.0	7.0
59	C2H3+C4H2=C4H4+C2H	13.48	0.0	23.0	13.70	0.0	5.4
60	2C6H5=C12H10	12.48	0.0	0.0	16.57	0.0	108.3
61	C2H+C4H4=C2H2+n-C4H3	13.60	0.0	0.0	12.91	0.0	17.2
62	A1C2H3+H=A1C2H2+H2	14.50	0.0	14.5	13.29	0.0	11.7
63	A1C2H2S=A1C2H+H	13.00	0.0	45.0	13.11	0.0	0.8
64	A1C2H2=A1C2H+H	12.30	0.0	37.0	12.71	0.0	0.8
65	A1C2H2+C2H2=A1C4H4	12.88	0.0	8.0	14.81	0.0	44.5
66	A1C4H4=A2H+H	10.00	0.0	0.0	13.32	0.0	18.5
67	C6H5+C4H4=A2H+H	11.60	0.0	0.0	17.14	0.0	56.4
68	A1C2H+C2H3=A1C2HP+C2H4	13.70	0.0	13.0	14.02	0.0	10.5
69	A1C2H+H=A1C2HP+H2	14.40	0.0	16.0	13.18	0.0	10.7
70	A1C2H+C2H=A1C2HP+C2H2	13.30	0.0	0.0	12.85	0.0	15.2
71	A1C2H+i-C4H3-A2C2H+H	11.60	0.0	0.0	0.00	0.0	0.0
72	A1C2H+C2H3-A2H+H	11.60	0.0	0.0	0.00	0.0	0.0
73	A1C2HP+C4H4=A1C2H+i-C4H3	12.18	0.0	0.0	11.51	0.0	12.6
74	A1C2HP+C2H2=A1C2HV	12.30	0.0	4.0	13.70	0.0	41.8
75	A1C2HV=A2	11.00	0.0	0.0	14.14	0.0	53.4
76	A2C2H2=A2C2H+H	12.30	0.0	37.0	12.71	0.0	0.8
77	A2+C2H2-A2R5+H	12.30	0.0	4.0	0.00	0.0	0.0
78	A2C2H2+C2H2=A2C4H4	12.88	0.0	8.0	14.81	0.0	44.5
79	A2C4H4=A3H+H	10.00	0.0	0.0	13.32	0.0	20.7
80	A2H+H=A2+H2	14.40	0.0	16.0	12.88	0.0	10.7
81	A2H+H=A2P+H2	14.40	0.0	16.0	12.88	0.0	10.7
82	C2H3+A2H=C2H4+A2	13.70	0.0	13.0	13.72	0.0	10.5
83	C2H3+A2H=C2H4+A2P	13.70	0.0	13.0	13.72	0.0	10.5
84	A2P+C2H2=A2C2H2	12.30	0.0	4.0	13.70	0.0	41.8
85	A2C2H+H=A2C2HX+H2	14.40	0.0	16.0	13.49	0.0	10.7
86	A2C2H+C2H3=A2C2HX+C2H4	13.70	0.0	13.0	14.33	0.0	10.5
87	A2C2HX+C2H2-A3	12.30	0.0	4.0	0.00	0.0	0.0
88	A3+C2H2-A4H+H	12.30	0.0	4.0	0.00	0.0	0.0
89	A3H+H=A3+H2	14.40	0.0	16.0	13.18	0.0	10.7

* NOTES: Units for A: cc,moles,sec., Units for E: kcal/mole.
= represents forward and reverse directions included in model.
- represents forward direction only included in model.

TABLE II
Selected Thermodynamics at 300K
(from Stein(6))

Species	Identification	Heat of Formation (kcal/mole)	Entropy (eu)
C2H3	vinyl	68.4	56.5
A1C2H3	styrene	35.3	82.6
A1C2H2	A1$\dot{C}$HCH	91.2	85.2
A1C2H2S	A1$\dot{C}$CH2	83.2	83.8
A1C2H	phenylacetylene	75.2	76.4
A1C2HP	A1$\dot{C}$2H	133.6	79.0
A1C2HV	A1(C2H)$\dot{C}$HCH	146.6	95.1
A1C4H4	A1CHCHCHC$\dot{H}$CH	104.7	98.0
A2	1-naphthyl	94.4	83.6
A2P	2-naphthyl	94.4	83.6
A2H	naphthalene	36.1	79.7
A2C2H	2-naphthylacetylene	91.5	90.9
A2C2H2	A2$\dot{C}$HCH	107.4	99.7
A2C2HX	A2$\dot{C}$2H	149.9	92.1
A2C4H4	A2CHCHCHC$\dot{H}$CH	121.0	112.5
A2R5	acenaphthylene	61.7	87.2
A3	phenanthrenyl	108.5	96.8
A3H	phenanthrene	50.1	94.2
A4H	pyrene	55.2	96.5

FIG. 1 MODEL PREDICTIONS vs. DATA OF REF. 5
C2H2 and C6H6 Concentrations at 973K

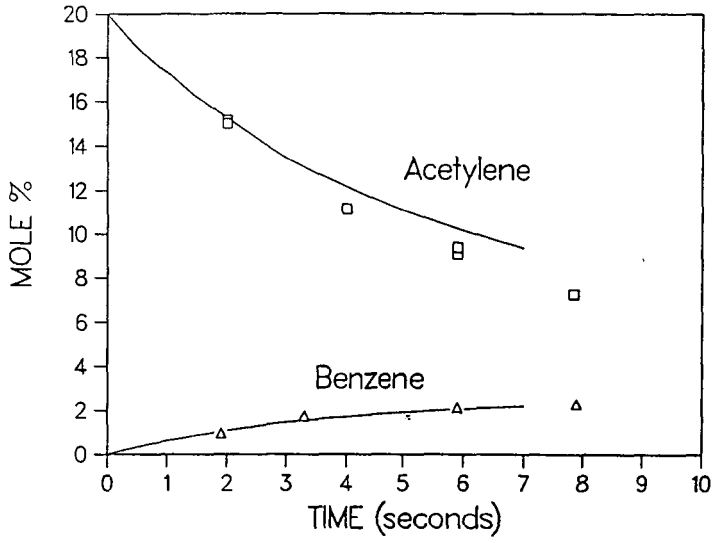

FIG. 2 PYROLYSIS OF 20% ACETYLENE AT 973K
Formation of Aromatic Products (predictions)

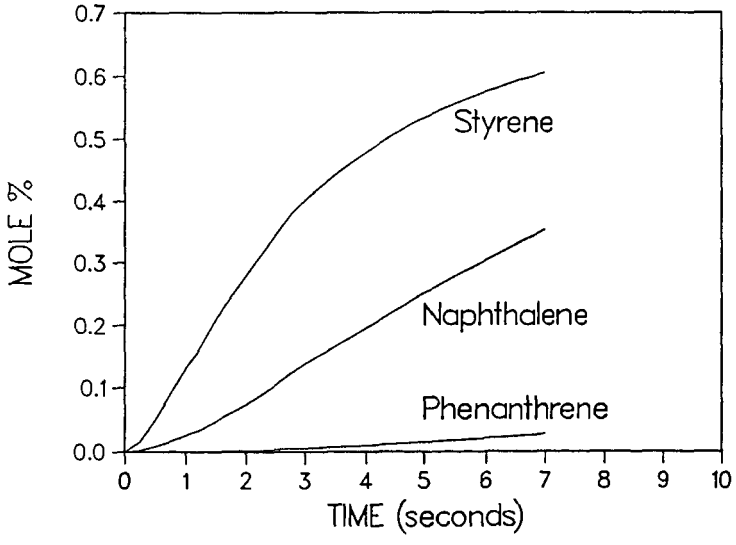

RING GROWTH BY SEQUENTIAL ADDITION OF i-C_4H_3

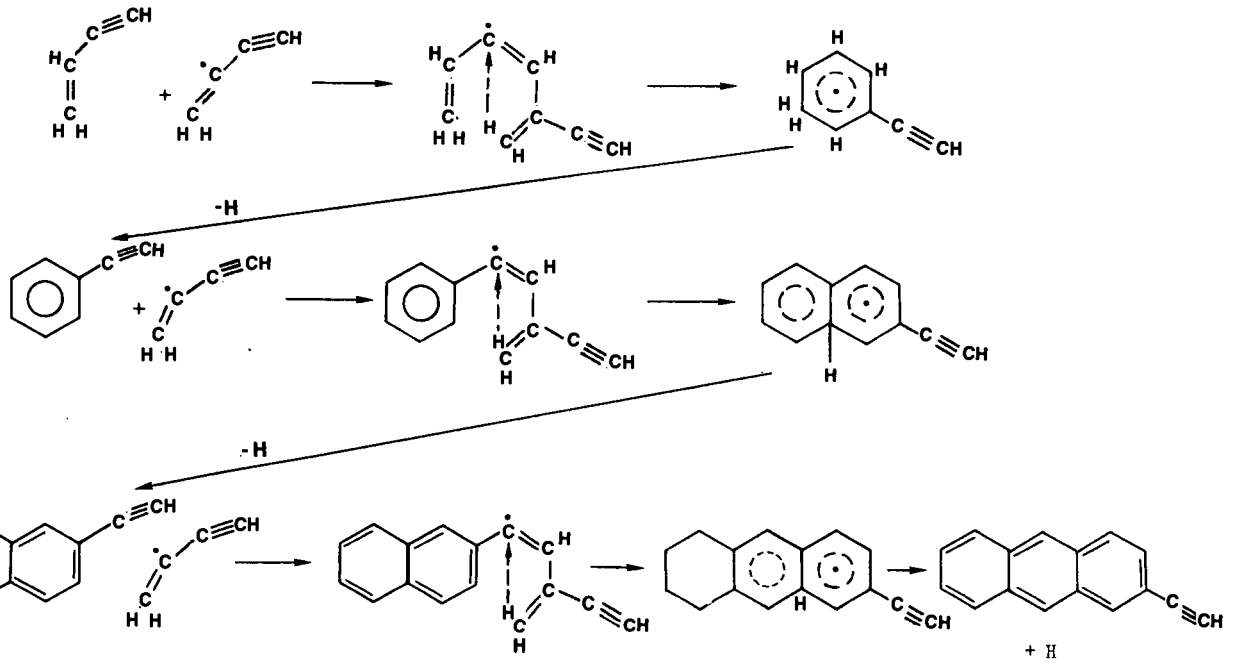

FIG. 3

87-4-89-1

A MECHANISTIC INVESTIGATION OF SOOT PRECURSORS

S. H. Bauer[a] and P. M. Jeffers[b]

[a] Department of Chemistry, Baker Laboratory,

Cornell University, Ithaca, New York 14853-1301

[b] Department of Chemistry, SUNY-Cortland, Cortland, NY 13045

INTRODUCTION

Fuels with low H/C ratios are particularly prone to soot production during combustion; aromatic species generally (but not universally) do so more readily than aliphatics. It is now well recognized that "soot" is not a singular material. Besides characterizing the variety of soots with respect to composition, volatile content, and structure, extensive efforts have been devoted to determining conditions which promote the development of soot in flames and in internal combustion engines. Many studies have been reported on the effects of inhibitors; reviews abound (1). During the past decade chemical kinetics investigations have proliferated with the hope of unraveling the mechanisms for its generation, ultimately to permit control of the types and magnitudes of soot emissions. There is general agreement on species types which initiate condensed aromatic ring growth (2); there is still disagreement as to whether ions play a major role(3); there is overall agreement on the spacial distribution of PAH in flames, as measured mass spectrometrically (4); composition constraints on fuel/oxidizer ratios for the inception of sooting, and the temperature range in flames wherein soot appears are sufficiently well-defined (5).

In this report our objectives are: **A.** To call attention to the differences and the conceptual similarities between the sooting process and a kinetic model for nucleation/condensation. **B.** List the types of precursors required for sooting, and the underlying experimental basis. **C.** Present a minimal set of reactions, with rate constants, which model the observed time evolution of condensed molecular structures (soot precursors). This list must incorporate a repetitive growth cycle for continued condensation. As a minimum, the model must semiquantitatively reproduce observed delay times for the onset of condensation. **D.** Present qualitative spectral data which support **C.**

A. The characteristic kinetic features of a typical nucleation/condensation mechanism (6) are: (a) An initial binary association sequence which reaches steady state at some small number (n) (7):

$$A_1 + A_1 \underset{}{\overset{(A)}{\rightleftharpoons}} A_2 \qquad [k_1 \; ; \; k_{-1}]$$

$$- - - - - - - - - - - - - -$$

$$A_{n-1} + A_1 \rightleftharpoons A_n \qquad [k_{n-1} \; ; \; k_{-(n-1)}]$$

Note that at this stage the rates of association/condensation are nearly balanced for each step: $k_{n-1}(A_1) \approx k_{-(n-1)}$. No activation energies are involved; association is driven by a decrease in enthalpy; dissociation is favored by an almost equal $T\Delta S$ term. This is followed by (b),

$$A_n + A_1 \xrightleftharpoons{k_n} A_{n+1}$$

$$A_{n+1} + A_1 \xrightleftharpoons{k_{n+1}} A_{n+2}$$

wherein steady state is achieved by unidirectional flow, such that $k_{n+1} \approx k_n$, with insignificant reversibility. Here the enthalpy factor completely dominates. The magnitude of n at which this "switch-over" occurs characterizes the critical size nucleus.

The contrast with soot production from C/H fragments is striking. The initial lag is due to: (α_1) the rate of pyrolysis of the fuel, to generate small reactive fragments, generally referred to as "acetylenic species", and (α_2) their partial recombination to [in some cases --- the direct production of] aromatic ring radicals; activation energies control these steps. Hence, minimal temperatures of ≈1500 K are required. It is likely that a dynamic local equilibrium similar to the steady state (a), develops between these small highly reactive radicals. When adequate levels of both types of species are attained, stage (β) follows; i.e. an essentially unidirectional growth sequence, wherein the acetylenic species add onto the aromatic radicals, in analogy with (b). Thus, there occurs a "switch-over" which has the appearance of a catastrophic onset of sooting. Since at all times in (β) the driving enthalpy for growth is countered by an opposing $T\Delta S$ term, at some higher temperature the latter quenches sooting (≈ 2100 K). This accounts for the bell-shaped generation profile [soot yield vs temperature] reported by many observers.

B. What are the essential precursors which operate in regions (α_1) and (α_2)? Observations, previously reported for shock tube pyrolysis studies of ten polycyclic aromatics (8), guided our choice of the smallest species which have to be incorporated in a minimal mechanism. For shock durations of <700 μs, over the temperature range 1500-2200 K, acetylene, tetramethylpentane, acenaphthene or acenaphthalene, when individually pyrolyzed, yielded insignificant amounts of soot. However, any aliphatic/aromatic combination under the same shock conditions produced copious amounts of soot. Clearly, two types of molecular species are required for the onset of sooting. It follows that one should anticipate longer delays when a single type is initially present because of the time required to generate the other type. Schematically,

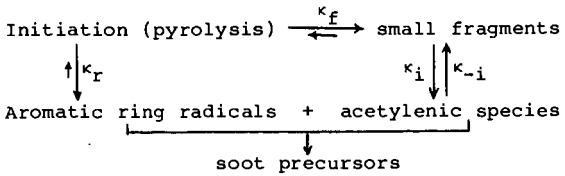

The relative magnitudes of κ_f and κ_r are determined by the structures of the fuel.

C. Two sets of reactions with appropriate rate constants are listed in Tables I and II, for benzene and toluene, respectively. We attempted to identify the smallest number of essential steps, not to list all reactions which plausibly occur concurrently with soot initiation.

C_6H_6: For the benzene pyrolysis our final set consists of 18 reactions with 18 H/C species (plus Ar), although at least twice that number of reactions and species [30] were considered during the preliminary calculations. Not included in Table I are intermediate radical stabilization steps.

We also treated the addition of acetylene as a single step:

$$C_6H_5 + C_2H_2 \rightarrow C_8H_5 + H_2;\ k_7 = 10^{13.7} \exp(-2000/RT)$$

rather than a two reaction sequence:

$$C_6H_5 + C_2H_2 \longrightarrow C_8H_6 + H;\quad k_7' = 10^{13}$$

$$C_8H_6 + H \longrightarrow C_8H_5 + H_2;\ k_7'' = 2\times10^{13} \exp(-6800/RT)$$

The typical growth cycle is illustrated by

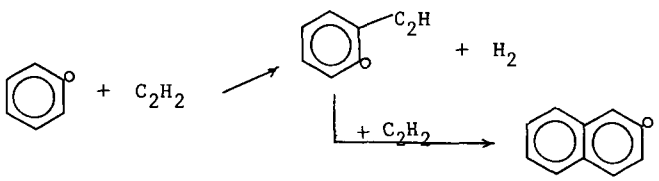

At each cycle one ring is added and a new radical is generated which repeats the cycle. As ring condensation proceeds there are possibilities for alternate routes to yield other observed products, for example R12; it was included because biphenyl is a commonly found product, although no further reactions of biphenyl occur other than the reverse of its formation. The other stable molecular products incorporated in this mechanism are C_2H_2, C_4H_2, $H_{10}C_{18}$, and $C_{22}H_{12}$. It is necessary to assign an upper limit to the largest species incorporated in the computer code; we chose $C_{22}H_{12}$ which serves as a "sink". Tests show that the concentration/time patterns for the last three species, for any selected terminus, remains essentially unchanged when the largest assumed unit was varied [$C_{18} \rightarrow C_{20} \rightarrow C_{22}$]. Clearly, the two-step growth sequence continues until the system is quenched.

Kinetic calculations, to model rates of production of soot precursors by pyrolysis, were performed with the Mitchell/Kee (9) shock kinetics program. All reactions were considered reversible, with their reverse rate constants calculated within the program by reflection through their equilibrium constants. Most of the unavailable thermodynamic parameters were estimated by Benson's group contribution recipe.

Figure 1 is a plot of the computed concentration-time profiles for 1% C_6H_6 in argon, reflected shock heated to 2120 K (initial). It shows the expected general features. During early times the mole fractions of H, C_2H_2, C_4H_2 and H_2 rise, that of C_6H_6 slowly declines and nearly steady state concentrations of C_6H_5 and C_8H_5 develop. The higher molecular weight products then slowly begin to grow, in sequence of increasing carbon content. The time dependence of the imposed cut-off at C_{22} provides a measure of the delay time for the onset of avalanche soot growth. Note that after a gradual decline, C_6H_6 drops sharply as do all the heavier species even though all reactions

were treated reversibly. $C_{22}H_{12}$ (the terminal species) increases (designated as the soot initiator). Eventually, after the lower carbon content species had passed through maximum levels, C_2H_2, C_4's and H_2 dominate.

A measure of the sensitivity of this mechanism to the rate constant for initiation (R1) was obtained by using a value derived by reflection of Frenklach's (1) estimate for the reverse of R1, 1×10^{13} mole/cc-sec, whereas the curves in Fig. 1 were calculated with k_1 about a factor of ten larger, as suggested by M. C. Lin (10); it is very close to the value reported by Fujii and Asaba (11). A faster initiation rate results, with a much earlier appearance of heavy products and considerably more extensive (eventual) destruction of benzene. When the one step phenyl radical decomposition (R5) was replaced by the sequence:

$$C_6H_5 \longrightarrow H_5C_6 \text{ (linear)} \; ; \quad k_4' = 2.4 \times 10^{12} \exp(-58{,}800/RT)$$

$$H_5C_6 \longrightarrow C_4H_3 + C_2H_2 \; ; \quad k_4'' = 1.8 \times 10^{15} \exp(-40{,}000/RT)$$

a dramatically slower depletion of all the low molecular species was indicated. This merits further investigation, possibly by direct assay of the time dependence for appearance of C_4H_3.

The proposed mechanism is sensitive to one more feature --- the initial concentration of C_2H_2. If one starts a calculation, as for Fig. 1, but with added C_2H_2 (mole fraction of 0.005), the production of all the heavy products is strongly accelerated. This accounts for our observations that soot formation from acenaphthene or acenaphthalene is significantly accelerated when C_2H_2 [or tetramethylpentane, which readily produces C_2H_2] was included in the initial mixture.

Two variations of the mechanism were found to exert a moderate effects on the rate of heavy product formation. The C_2H_2 addition sequence via one step, rather than two steps, delays somewhat the appearance of the final product. Reducing the value of k_{12} by a factor of 100 makes at most a 15-20% change in heavy species mole fractions at 5 μsec, with slightly larger differences in $C_{12}H_{10}$ and C_8H_6 concentrations at earlier times.

Finally, several factors were found to have slight or negligible effects. These non-critical factors include deletion of radical stabilization steps, incorporating an initial [artificially] high H atom concentration, the value for k_7 [acetylene addition to phenyl], and the inclusion of an alternate initiation process:

$$H + C_6H_6 \longrightarrow C_6H_7; \qquad k_1' = 4.5 \times 10^{14} \exp(-4300/RT)$$

$$C_6H_7 \longrightarrow C_4H_5 + C_2H_2; \quad k_1'' = 6 \times 10^{14} \exp(-92{,}000/RT)$$

Reduction of E_a from 92 to 80 kcal/mole for the second step had no effect. Substituting the bimolecular reaction:

$$C_6H_6 + C_6H_6 \longrightarrow C_6H_5 + C_6H_7 \; ; \quad k_1'' = (5 \times 10^{12} - 5 \times 10^{16}) \exp(-85{,}000/RT)$$

for R1 failed to provide sufficient radical species for the pyrolysis sequence to proceed.

$C_6H_5CH_3$: The adequacy of our minimalist approach to develop a mechanism for the precursor stage of sooting is illustrated by the analysis of our shock tube data for toluene. The initiation steps (Table II) differ from those for benzene (steps 1-6, Table I) but thereafter the growth sequences are the same. Here also the calculated and observed delay times are in acceptable agreement. Six additional species must be included (C_7H_8; C_7H_7; C_3H_3; CH_3; CH_4 and C_2H_6). Reactions T 1, 2, 4, 5 and 6 were taken from Mizerka and Kiefer (12). The combined effect of reactions T2, T3, and T8 is to generate rapidly significant concentrations of C_6H_5 and C_6H_6. No effort was made to determine which reaction path is most effective. At temperatures around 1800°K and higher T2 is a significant pathway for the initial breakup of toluene. The rate constant for T3 was assumed to be (1/4) that for T4, and both are exothermic. T7 is a reasonable sink for CH_3 radicals, while the recombination of C_3H_3's [T8] maintains the reaction sequence alive in a simple fashion. All the initially estimated rate constants were used in the calculations without subsequent adjustments. The possibility that there are steps in the sequence T 1→8 which are not essential for the "minimal" mechanism was not fully tested; it appears that T7 could be dropped.

Our conclusion is that a few additional steps added to the simplified mechanism proposed for benzene, can account in a quantitative way for many features of the pyrolysis of aromatics, in general. For soot production, the major pathways are evident and inherently reasonable.

D. What experimental evidence exists, or can be developed, to support the above proposals? Other than direct mass spectrometric detection of PAH, one must look for some in situ diagnostic technique. Absorption and fluorescence spectra (5) are indicated, but there are obvious limitations. The samples consist of complex brews, characterized by superposed broad spectral bands. Thus, there is little likelihood that one could identify specific species. But, we are concerned with molecular types; the saving feature is the absence of oxygen or nitrogen chromophoric structures. The recorded spectra in the near uv, visible and down to the near infrared must arise from condensed polycyclic aromatics, either the stable species, as reported in the literature (12) or their radicals. To distinguish between general turbidity and characteristic absorptions, one should measure the temporal wavelength dependence of light loss on passage through the reacting medium, and its dependence on temperature. Also, a condition for the adequacy of a minimal mechanism is that it correctly predict the temperature dependence of the time delays of the growth of condensed polycyclic aromatics.

EXPERIMENTAL

Since a large diameter shock tube was not available to measure the time dependent spectra tranverse to the shock flow, we had to resort to recording integrated absorption spectra by passing the probing beam axially along the shock direction. The data were resolved by imposing an additional integration step in the analysis. A 1" I.D. stainless steel shock tube (Fig. 2a) was fitted with a clear plastic end-wall at the driver section; a quartz window and filter terminated the test section. A He/Ne laser beam (6328 A), directed along the axis of the tube, was aimed at a small aperture inserted between the quartz end plate and the narrow band pass filter. The phototube output was recorded simultaneously with the output of two pressure trans-

ducers located 1 cm and 11 cm from the downstream end. In later experiments the laser was replaced by a Xe lamp and the phototube by a monochromator/linear array of diodes for scanning other regions of the spectrum (Fig. 2b).

The signals from the piezo-gauges allow evaluation of the shock speed and dwell time. Since the gas at different initial positions along the tube is heated for different lengths of time, the extent of light absorption (or scattering) must be integrated along the entire tube length. Let $A_n(x;t')$ be the instantaneous concentration of the n^{th} absorbing species, where $t' = t_w - x/u_r$; t_w is the laboratory time for shock reflection at the quartz window, x is the return distance from the window at the location of the reflected shock, and u_r the reflected shock speed. Then, the recorded light loss is:

$$I^{\lambda}(t')/I_o^{\lambda} = \exp\left[-\sum_n \mu_n(\lambda,T_5) \int_o^{u_r t'} A_n(t_w - x/u_r)dx\right] . \qquad [1]$$

Here we assumed that no chemical processing and no absorption (at the probing wavelength) occurs during the incident shock.

Reflected shock temperatures ranged from 1400°K to 2200°K, and were controlled by varying both the initial pressure of the test gas and the diaphragm thickness. Residence times were generally about 700 μsec, followed by a rapid quench due to expansion. Analysis by g.c. of the shock heated samples (both gas phase and condensable species) indicated that during the test time the products had not achieved their equilibrium concentrations at the reflected shock temperatures.

I. The molecular species which strongly absorb red light (He/Ne) appear after an extended induction period which is temperature dependent. [Typical shapes are illustrated by the curves in Fig. 3b.] In turn, these absorbers are removed by continued condensation. Hence the initial flattening and the subsequent slow growth of absorption. We noted that substantial light loss occurred even in some cases where little soot was produced. Curves of $\ln(I/I_0)$ vs t (corrected for emission) were sigmoidal and often saturated at $I>0$. We presume that the recorded light loss was due primarily to absorption by transient species, which are precursors of soot particles, and to a lesser extent by soot, which forms during the later stages of the experiment. The absorbing species at λ6328 must be condensed ring entities, such as the para sequence of the acene series (12), and/or radicals of similar structure (Fig. 4). For the 2% runs, the concentration-time profiles for $C_{20}H_{11}$ [designated as the representative absorber of λ6328] were integrated, per eq. [1]. These curves show all the salient features of the recorded (I/I_0) traces, i.e. the sigmoid shape following a delay, a relatively sharp rise and a slow approach to saturation. The computed times selected for minimal detection of absorption (at 3x noise level) check quite well with the measured values (Table III).

II. Absorption curves over a range of wavelengths (400-800 nm) were obtained with the second experimental configuration (Fig. 2b). Typical time/wavelength spectra at two extremes are shown in Fig. 3a and Fig. 3b. No significant differences appear over a spectral range of 20 nm. However, there are clear, significant differences between the spectral scans at 811 and 392 nm. First, the delay times are shorter and the rise times are faster for the same shock speeds, indicating more rapid rates for generating the smaller species which absorbed

near the uv, compared with the much longer delay times for the appearance of the larger species, which absorb in the near infrared. Second, a two step process appears at 800 nm, where the initial relatively fast rise is followed by a slower continued increase in absorption, demonstrating subsequent growth, since the absorption edge continues to move toward the longer wavelength.

Two types of information are presented by these plots (recorded at 100 nm intervals, 400-800 nm); delay times (t_i) which measure induction times for the development of absorbing species, and rise times $[(t_f-t_i)/2]$, which are mean inverse rates of production of these species. For any specified shock temperature (T_5), a plot of t_i vs mean λ has a positive slope, as expected for a sequential growth of absorbers with leading edges progressing toward the red. For any specified λ, t_i is longer the lower the shock speed (T_5).

Because of the restricted range of final densities covered in these experiments, the half-times for attaining the first saturation level do not permit us to determine whether the global process is first or second order. However, graphs of ln k_u ($\equiv 10^6 \ln 2/t_{1/2}, \mu s$) vs $1/T_5$ (Fig. 5) clearly show nesting of points for the sequence of λ's, as expected, assuming that the leading edges of the absorption curves measure the larger units at longer wavelengths. At any T_5, the k_u's are consistently larger when derived from 400 nm traces compared with 800 nm traces.

ACKNOWLEDGMENTS

This program was supported by the U. S. Department of Energy under contract DE-AC01-80 ER 10661.A004. We sincerely thank Dr. R. J. Kee for copies of the Sandia computer codes, Professor C. F. Wilcox, Jr. for extensive discussions of the possibilities and limitations of the Diels-Alder addition sequence, and Professor J. H. Kiefer for discussions of his shock tube pyrolysis experiments of toluene and ethylbenzene.

REFERENCES

1. Sections on SOOT & COMBUSTION GENERATED PARTICULATES can be found in every Symposium (International) on Combustion [Combustion Institute], starting with the 15th (1974) through the 21st (1986). Also: Wagner, H. Gg., 17th Symposium (International) on Combustion, The Combustion Institute, Pittsburgh, **1978**, p. 3; Haynes, B. S. and Wagner, H. Gg., Prog. Energy Comb. Sci. **1981**, 7, 229.

2. Frenklach, M., Clary, D. C., Gardiner, W. C. and Stein, S. E., 20th Symposium (International) on Combustion, The Combustion Institute, Pittsburgh, **1984**, p. 887; Bockhorn, H., Fetting, F. and Wenz, H., Ber. Bunsenges. Phys. Chem. **1983**, 87, 1067; Homan, K. H., 20th Symposium (International) on Combustion, The Combustion Institute, Pittsburgh, **1984**, p. 857.

3. Keil, D. G., Gill, R. J., Olson, D. B. and Calcotte, H. F., 20th Symposium (International) on Combustion, The Combustion Institute, Pittsburgh, **1984**, p. 1129 -- favor ionic mechanisms; Bertrand, C. and Delfan, J-L., Comb. Sci. and Tech. **1985**, 44, 25; discount significant contributions from ions.

4. Longwell, J. P., 19th Symposium (International) on Combustion, The Combustion Institute, Pittsburgh, **1982**, p.1339.

5. Smith, K. C., et al., Comb. and Flame, **1985**, 62, 157; Frenklach, M., Hsu, J. P., Miller, D. L. and Matula, R. A., Comb. and Flame, **1986**, 64, 141.

6. Bauer, S. H. and Frurip, D. J., J. Phys. Chem. **1977**, 81, 1015.

7. Bauer, S.H., Wilcox, C.F., Jr. and Russo, S., J. Phys. Chem. **1978**, 82, 59.

8. Bauer, S. H. and Zhang, L-M., 14th International Symposium on Shock Tubes and Waves, Ed. R. D. Archer and B. E. Melton, New S.W. University Press, **1983**, p. 654.

9. Mitchell, R. E. and Kee, R. J., Sandia National Laboratories, Livermore, CA, SAND-82-8205 (March, 1982).

10. Hsu, D. S. Y., Lin, C. Y. and Lin, M. C., 20th Symposium (International) on Combustion, August 1984. See also: Kieffer, J. H., et al., J. Phys. Chem. **1985**, 89, 2013.

11. Fujii, N. and Asaba, T., 14th Symposium (International) on Combustion, The Combustion Institute, p. 433 (1973).

12. Clar, E., Polycyclic Hydrocarbons, **1964**, Academic Press, London; Clar, E., The Aromatic Sextet, **1972**, J. Wiley & Sons, London; Stern, E. S. and Timmons, C. J., Electronic Absorption Spectroscopy in Organic Chemistry, **1970**, Edward Arnold, London; Karcher, W., et al., Ed., Spectral Atlas of Polycyclic Aromatic Compounds, **1983**, D. Reidel, Dorchester.

TABLE I

	MINIMAL MECHANISM (C_6H_6)	log A	E_0(cal mole^{-1})	Ref.
1.	$C_6H_6 = C_6H_5 + H$	15.7	108000.	10
2.	$C_2H + C_6H_6 = C_6H_5 + C_2H_2$	13.3	0.00	2
3.	$C_2H_2 + C_2H_2 = C_4H_3 + H$	12.3	65000.	a
4.	$C_6H_5 = C_4H_3 + C_2H_2$	14.8	82800.	b
5.	$C_4H_3 = C_2H_2 + C_2H$	10.76	52500.	2
6.	$C_4H_3 + Ar = Ar + C_4H_2 + H$	16.0	45000.	c
7.	$C_6H_5 + C_2H_2 = C_8H_5 + H_2$	13.7	2000.0	2
8.	$C_8H_5 + C_2H_2 = C_{10}H_7$	13.0	0.00	2
9.	$C_{10}H_7 + C_2H_2 = C_{12}H_7 + H_2$	13.0	2000.0	2
10.	$C_{12}H_7 + C_2H_2 = C_{14}H_9$	13.0	0.00	2
11.	$C_{14}H_9 + C_2H_2 = C_{16}H_9 + H_2$	13.0	2000.0	2
12.	$C_6H_5 + C_6H_6 = C_{12}H_{10} + H$	11.0	11000.	d
13.	$C_{16}H_9 + C_2H_2 = H_{10}C_{18} + H$	12.74	10000.	e
14.	$C_{16}H_9 + C_2H_2 = C_{18}H_9H_2$	13.0	2000.0	2
15.	$C_{18}H_9 + C_2H_2 = C_{20}H_{11}$	13.0	0.00	2
16.	$C_{20}H_{11} + C_2H_2 = C_{22}H_{12} + H$	12.74	10000.	e
17.	$H_2 + Ar = H + H + Ar$	$(12.08)T^{1/2}$	92600.	
18.	$C_6H_6 + H = C_6H_5 + H_2$	13.3	6600.	c

Footnotes for TABLE I

a. J. Warnatz, Ber. Bunsenfesell. Phys. Chem. 1983, 87, 1008 but $E_0 = \Delta H_{reaction} = 67.4$ kcal mole^{-1} (rather than 54 kcal mole^{-1}).

b. T. Asaba and N. Fujii, 13th Symposium (International) on Combustion, The Combustion Institute, Pittsburgh (1971), p.155.

c. Values of A are those given in (2), but with selected E_0's.

d. A slightly adjusted value based on --- C. T. Brooks, S. J. Peacock and B. G. Renber, J. Chem. Soc. Farad. Trans. I, 1979, 75, 652 and ref. (b).

e. Based on the reaction:

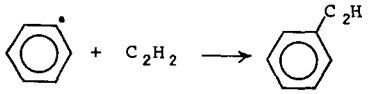

For (13) and (16) we assumed a somewhat lower A value and inserted $E_0 \approx 10$ kcal mole^{-1}, because in these the H atom is lost from the ring rather than from the added moity (C_2H_2).

TABLE II
Initiation Steps for Toluene

	MINIMAL MECHANISM ($C_6H_5CH_3$)	log A	E_0 (cal mole^{-1})	Ref.
T1	$C_7H_8 = C_7H_7 + H$	12.9	72,600	9
T2	$C_7H_8 = C_6H_5 + CH_3$	11.6	90,000	9
T3	$H + C_7H_8 = C_6H_5 + CH_4$	1+ 4log T	2,100	estimated
T4	$H + C_7H_8 = C_7H_7 + H_2$	1.6+ 4log T	2,100	9
T5	$C_7H_7 = C_3H_3 + 2C_2H_2$	14.0	84,800	9
T6	$C_7H_7 + H = C_3H_3 + C_4H_3 + H_2$	14.65	80,000	9
T7	$C_2H_6 + Ar = 2CH_3 + Ar$	14.6	88,400	estimated
T8	$C_3H_3 + C_3H_3 = C_6H_6$	13.0	-	estimated

TABLE III
Experimental Condition for Representative Shocks

Composition	p_1 (Torr)	u_1 (mm/μsec)	T_5(°K)	$\rho_5 \times 10^3$ (g/cc)	Exp'tl Δt(μsec)	Calc Δt(μsec)
2.0% toluene	110	.893	1612	1.93	340	320
"	95	.943	1700	1.64	100	
"	85	.962	1725	1.82	70	
"	65	1.02	1812	1.37	40	50
2.0% benzene	85	.926	1767	1.41	240	240
"	95	.926	1767	1.55	380	
"	85	.926	1767	1.41	360	
"	65	.980	1910	1.51	50	60
"	65	1.00	1950	1.56	50	40

p_1(Torr): total pressure of fuel plus Ar; Δt(μsec) is interval between the onset of the reflected shock and the toe of the absorption trace.

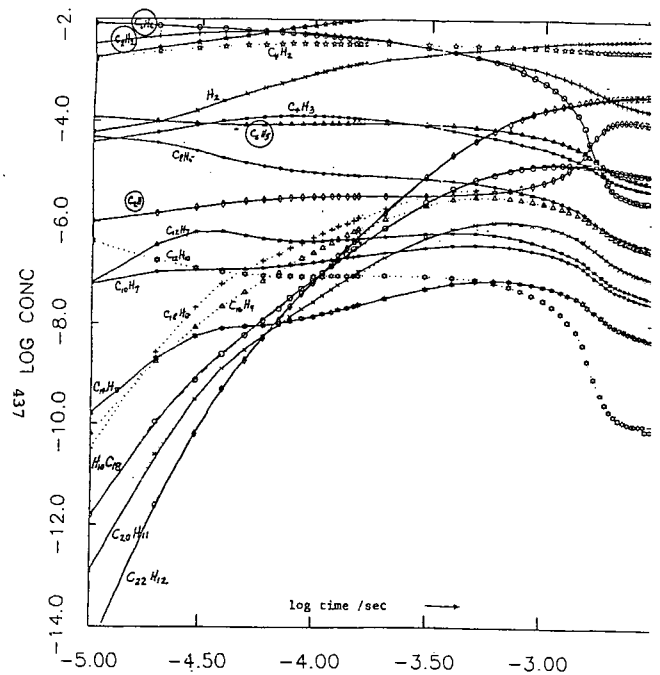

Figure 1. Calculated dependence of mole fraction on time, of various species, for shock heated 1% benzene in argon. T_5(initial) = 2120K; T_5(final) = 1907K.

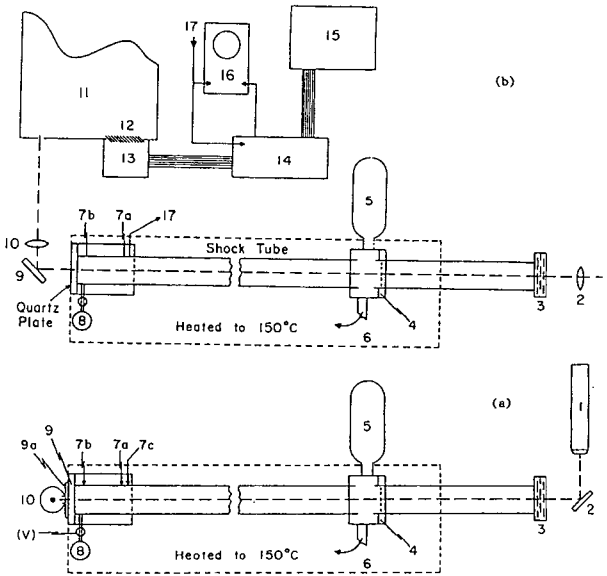

Figure 2. Schematic of shock tube and optical configuration.
(a) 1.He/Ne laser; 2.Mirror; 3.Plastic back-plate.
4. Diaphragm location; 5.Quench tank; 6. Lead to vacuum lines
7. Piezo gauges (a,b); 7c. Piezo crystal to trigger;
8. Sampling port; 9. Quartz window; 9a. Optical filter;
10. Phototube.
(b) 10. Lens; 11. Monochromator; 12. Linear array detectors;
13. Amplifiers and digitizers; 14. Read and hold; 15. Computer.

Figure 3.Absorption spectra of shock heated toluene (2% in Ar); reflected shock regime. All spectra were recorded with 20 μs resolution. t_r=0 indicates the time when the incident shock was reflected from the quartz end plate.
(a) Incident shock speed u_i=1.031 mm/μs. Compare the delay times and absorption rise times for 400nm,with (b) Incident shock speed u_i=1.020 mm/μs, of spectra at 800 nm.

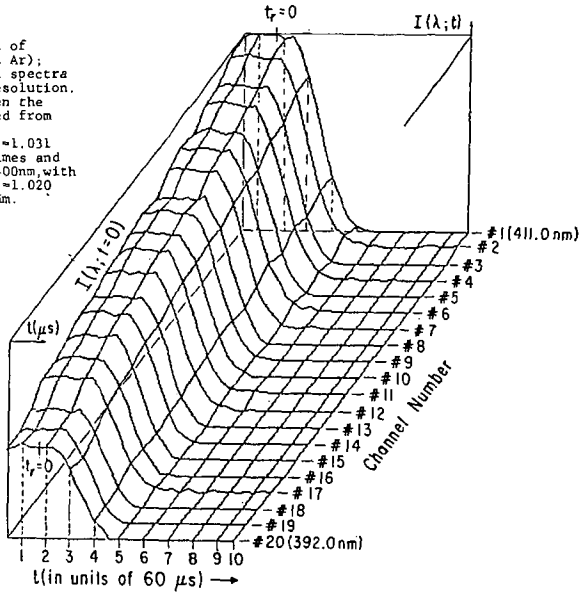

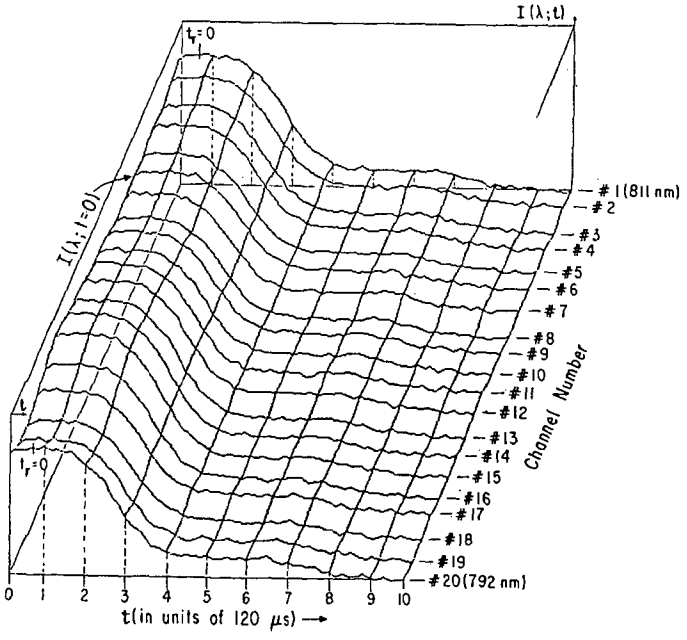

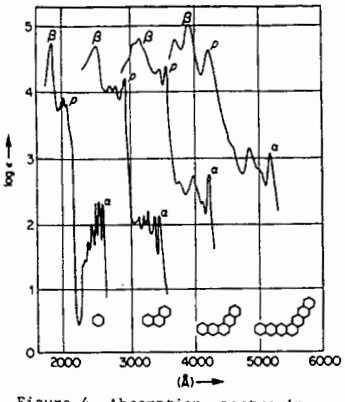

Figure 4. Absorption spectra in the phene series

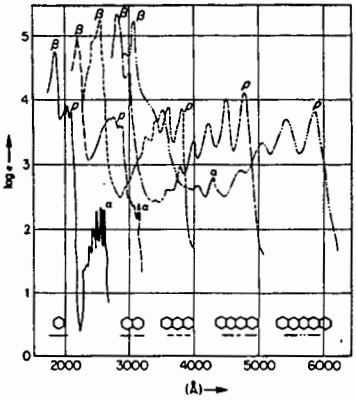

Absorption spectra of the acene series

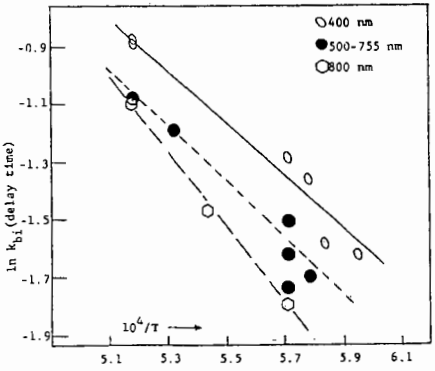

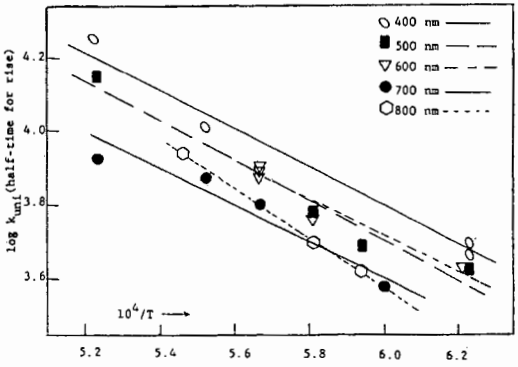

Figure 5a. The delay time for onset of absorption is the reciprocal of a mean bimolecular rate constant (arbitrary units) which decreases with the size of the absorbing units. The largest absorbers (at 800 nm) require a larger activation energy.

Figure 5b. The mean half-times for generating the larger absorbers increases with increasing size. The 800 nm absorbers require a larger activation energy (≈30 kcal/mole) compared to those which absorb at 400nm (≈24 kcal/mole).

COMBUSTION TUBE SOOT FROM A DIESEL FUEL/AIR MIXTURE

L. B. Ebert and J. C. Scanlon

Exxon Research and Engineering; Annandale, NJ 08801

C. A. Clausen

University of Central Florida; Orlando, FL 32816

INTRODUCTION

Used by the Chinese to make inks many years before Christ (1), soot was an environmental nuisance by the time of the industrial revolution (2). Today, soot can be both useful (the carbon black industry) and detrimental (diesel exhaust), so that investigations of soot can impact wide-ranging areas. Curiously, although there is intuitive understanding about the commonality of soots from a variety of sources, including furnace flames, piston engines, combustion chambers, or premixed flames (2), there is no general agreement about the detailed molecular structure of soot. Recently, Zhang, O'Brien, Heath, Liu, Curl, Kroto, and Smalley (ZOHLCKS) proposed to interrelate soot with carbon clusters of icosahedral symmetry (3). They suggested that "the polycyclic aromatic molecules known to be present in high concentrations in sooting flames may therefore adopt pentagonal rings as they grow, so as to generate spheroidal structures which maximize the number of C-C linkages," ultimately yielding a soot nucleus consisting of "concentric, but slightly imperfect spheres" (3). Thus, ZOHLCKS proposed that the spherical morphology of soot <u>particles</u> arose from soot "molecules" of nearly spherical symmetry.

In this paper, we discuss the structural and chemical characterization of soot formed in a combustion tube, in part to address the ZOHLCKS proposal, in part to develop information to compare soot to a variety of other carbonaceous materials.

EXPERIMENTAL DETAILS

Samples of soot were generated at the University of Central Florida by the combination of no. 2 diesel fuel (C-13 NMR aromaticity 19%) with air in a combustion tube of inner diameter 9.8 cm. Sample 1 was generated by injecting the air and fuel (at a mass ratio of 5:1) preheated to 75°C into the combustion tube heated to 1150°C. For sample 2, the combination of air preheated to 600°C with diesel fuel preheated to 350°C in an unheated combustion tube led to spontaneous ignition. The combustion process was allowed to proceed under basically adiabatic conditions; the flame tem-

perature reached a maximum of ~ 900° C. Further information on the diesel fuel is available (4).

X-ray diffraction was performed on a Siemens D-500 using copper radiation. Debye internal interference calculations were done as previously reported (5-7).

Elemental analysis of sample 2 was done by Galbraith. Duplicate runs made on carbon and hydrogen yielded average values of %C = 90.08 (89.94, 90.21) and %H = 1.76 (1.82, 1.69) for an average H/C atomic ratio of 0.23. The sample had 0.22%N (N/C= 0.002) and 4.64%O (O/C=0.04). Ash by thermogravimetric analysis was 0.19%.

Sample 2 was reacted with potassium naphthalene (-1) in tetrahydrofuran (THF) at room temperature. A solution of 30 minute old naphthalene radical ion (0.380 g, 2.97 mmol naphthalene in 25.810 g THF; with 2.498 g, 63.9 mmol K°) was added to 0.675 g sample 2. After 2 hours 15 minutes, there was a consumption of 0.404 g, 10.3 mmol K°, determined by weighing the solid K°; that the total K° uptake of 10.3 mmol exceeded the amount of naphthalene (2.97 mmol) suggested that the deposit was reacting. After 23 hours 15 minutes, there was a consumption of 0.536 g, 13.7 mmol K° and the solution was quenched at 0°C with the addition of solution of 2.836 g CD_3I in 1.845 g THF. The solution was allowed to stand at room temperature under inert gas for 24 hours, and then was filtered through a medium porosity frit. Following drying, the entrained solids weighed 2.589 g; following rotary evaporation, the material which passed the filter weighed approximately 0.29 g. A Bruker MSL was used for D-2 in the solid state (55.283 MHz).

RESULTS AND DISCUSSION. X-RAY DIFFRACTION.

Figure 1 gives the diffraction pattern of sample 2 over the range 15 - 105° 2θ (Cu). There are four readily observed diffraction peaks, which fall into the range normally associated with the (002), (100), (004), and (110) peaks of graphite or other benzenoid arrays. There are no (hkl) peaks having non-zero hk and non-zero l (e.g., (101)), suggesting that the material is turbostratic, meaning that there is no well-defined registry between adjacent planes (as found in the ABAB stacking sequence of graphite). The most intense peak, the (002), arises from interference between approximately parallel aromatic entities, and thus gives information about aromatic stacking. Figure 2 shows that sample 1 and sample 2 have (002) peaks of different widths. Sample 1 has d(002) at 3.63 A of width 0.122 radians, corresponding to a crystallite size in the direction of aromatic stacking of 12 A; sample 2 has d(002) at 3.60 A of width 0.070 radians, corresponding to a crystallite size of 20 A. (Scherrer constant = 0.9).

The (100) and (110) diffraction peaks give information about the size of the benzenoid array. As given in Figure 3, the linewidths of these peaks suggest sizes of 22 to 28 A, if one uses a Scherrer constant of 1.84. However, as pointed out by Warren and Bodenstein in a study of carbon blacks (8) and by Ergun (9), the use of the 1.84 constant can give unreliable results for in-plane crystallite sizes < 50 A. For crystallite sizes near 20 A (8), the Scherrer constant is about 1.4 for the (100) and about 1.6 for the (110), which then give us crystallite sizes of 21 A (100) and 19 A (110).

Knowledge of the lattice constants can allow us to predict microscopic density. For graphite, which has a_o = 2.45 A (= C - C bond distance of 1.415 A X $\sqrt{3}$) and c_o = 6.74 A, one obtains a unit cell volume of $(a^2)c \times 0.866 = 35.0\ A^3$. This unit cell has four carbon atoms, so we have 8.76 A^3/C atom. This yields a predicted density of 2.28 gram/cm^3. If we consider the effect of the different c_o of the soot on density (e.g., (002) at 3.60 A instead of 3.37 A), we calculate a unit volume of 9.36 A^3/C atom and a density of 2.13 gram/cm^3. The changes associated with a_o are smaller, and in the other direction. Intuitively, and on the basis of the (100) peak, we would expect a limiting sp^2-sp^2 bond distance of 1.39 A, and correlative a_o of 2.41 A. If we consider the effect of both the increased c_o and the possible decreased a_o on density, we find a volume of 9.05 A^3/C and a density of 2.21 gram/cm^3. The key point from these calculations is that the increase in c_o found in the soot can change the predicted density only about 7%; this change is not enough to account for the observed densities of 1.8 to 2.0 gram/cm^3 typically found in soots (M. Frenklach, personal communication).

Having appreciable amounts of hydrogen, the soot is better viewed as a "large" polynuclear aromatic rather than as a "small" graphite. Because hydrogen-hydrogen and carbon-hydrogen interactions are key structural determinants for aromatic hydrocarbons, the densities are much lower for the aromatics than for graphite: naphthalene (1.145), anthracene (1.25), phenanthrene (1.182), biphenylene (1.24), pyrene (1.27), picene (1.324), perylene (1.341), and coronene (1.38). Relating observed density to wgt% carbon for the above aromatics, we obtain

$$\text{density} = 0.10814\ (\%C) - 8.988 \qquad R = .9546$$

If one extrapolated to graphite, using the densities of these hydrocarbons as a guide, one obtains a density of only 1.826.

What do we expect for a soot of spherical carbon clusters? One must consider effects due to intramolecular scattering (analogous to the (100) and (110) peaks in benzenoid

arrays) and due to intermolecular scattering (analogous to the (002) and (004) peaks in graphite.

For intramolecular interference, we have simululated the scattering from one truncated icosahedron of bond length 1.54 A using the formalism of Debye internal interference, and the results are given in Figure 4. In the figure, the x axis is linear in k, with $k = 2\pi/d = 4\pi\sin\Theta/\lambda$ (Θ = Bragg angle, λ = wavelength of x-radiation), and one sees two peaks in the range k = 0.8 to 2.8, neither of which are observed in our soot. As one changes the bond length of the icosahedron, one will change the peak maxima in a predictable way, with the coefficient relating bond length to d value given by the Miller index of the peak (5,6). For instance, for the (002) peak in a stack of seven parallel coronene molecules, changing the interplanar spacing from 3.20 A to 3.95 A changes the observed d value from 3.16 A to 3.87 A (5, 6).

For intermolecular interference between spheroids, let us assume that we can place all carbon atoms on the surface of one spheroid at a distance of ca. 3.6 A from carbon atoms of some other spheroid. In this way, we can get a "(002)" peak at 3.6 A, as observed in the soot, but one notes that the linewidth of such a peak will correspond only to a "stack" of two aromatics (crystallite size ca. 7.2 A). If one goes to the concentric shell model (Figure 4 of ref. 3), one can obtain a larger apparent stack height; to account for the data on sample 2, one would need 5 to 6 shells (20 A/3.6 A) to obtain the observed (002) linewidth. Such an entity would have a large fraction of non-protonated (quaternary) aromatic carbon atoms, just as graphite does, and, from a chemical point of view, would be more like graphite than aromatic hydrocarbons. To address this more fully, we performed chemical experiments on sample 2.

BACKGROUND. CHEMICAL REDUCTION.

The use of potassium naphthalene (-1) in THF to reduce fossil fuel materials has been reviewed by Stock (10) and by Ebert (11). If one wants to distinguish graphite-like chemistry from polynuclear aromatic hydrocarbon chemistry, reduction by naphthalene (-1) followed by alkylation by alkyl iodide is useful because different products are obtained. Graphite is reduced by naphthalene (-1) and correlatively intercalated by K^+ and THF; the potassium intercalate is not alkylated by alkyl iodides. Aromatic hydrocarbons of reduction potential less negative than the -2.5 V (vs. SCE) of naphthalene (-1) will be reduced to anions, which can then (usually) be alkylated by alkyl iodides to give products in which the alkyl group is attached to an sp^3-hybridized carbon of the reduced aromatic.

With respect to the reduction, there has been a belief in the literature that aromatic hydrocarbons can form numer-

ous highly charged poly-anions driven by the presence of excess alkali metal. Examples include the dianion of naphthalene (10) and tetraanions of pyrene and perylene. Noting that the difference in reduction potential between the radical anion and dianion of anthracene is 0.48 V (12), one would expect the dianion of naphthalene to have a reduction potential of at least -2.98 V (vs. SCE), near that of K° itself; we are unaware of any work in which a second reduction peak has been measured for naphthalene and in fact with pyrene third and fourth reduction peaks are not seen (13).

Relevant to the shell proposal for soot of ZOHLCKS (3), Stock proposed that the reductive alkylation of coal suggested a model "in which molecular fragments of coal are peeled away from the solid as layers from an onion" (10). To address this, we performed reductive methylation (with CD_3I) of Burning Star coal to determine if methyl groups added preferentially to the "soluble" phase (14). The coal consumed 10.4 mmol K/g, and, following alkylation, 52% of the product carbon was in the "THF-soluble" phase and 48% in the "THF-insoluble" phase. Solid state ^2D NMR showed CD_3 groups in both phases, with the THF-soluble phase having only 87% of the deuterium of the insoluble phase, on a per carbon atom basis! The spectrum of the insolubles showed only a first order quadrupole split spectrum (separation = 51.7 G, indicative of three-fold rotation of bound $-CD_3$ groups) but the solubles showed a strong (averaged) central peak and a quadrupolar split line. Significantly, these results for coal, which are those expected for alkylation of aromatics and heterocyclics, are similar to what we report here for soot.

RESULTS AND DISCUSSION. REDUCTIVE ALKYLATION.

At 23 hours 15 minutes, the soot took up 15.9 mmol K/gram, correcting for consumption of potassium by naphthalene(-1). Figures 5 and 6 give the ^2D NMR of the solid solubles and insolubles, and we see that the soot has behaved like a polynuclear aromatic in being alkylated by CD_3I. Figure 7 gives the ^2D NMR of the solubles in methylene chloride, showing CD_3 groups bound primarily to sp^3 carbon, as expected for the reductive alkylation of polynuclear aromatics (15); some methylation of oxygen does occur.

One might be concerned with contamination of the THF-soluble sample by vast amounts of 1,4 dimethyl 1,4 dihydro naphthalene. Actually, naphthalene (-1) reduces methyl iodide to methyl radicals, in contrast to anions of larger aromatics which do in fact undergo alkylation (15, 16). Analysis of the THF-solubles by GC/MS, with quantification by flame ionization detection, shows the ratio of naphthalene to the most abundant dimethyl dihydro naphthalene to be 19.7/1; this is consistent with solution phase ^{13}C NMR which

shows three sharp aromatic peaks at 125.7, 127.7, and 133.3 δ, the shift positions of naphthalene itself. The underlying aromatic envelope goes from 120 to 146 δ, and there are aliphatic peaks at 14.2, 22.8, 25.9, 29.4, 29.7, 30.09, 30.34, 31.98, 34.26, and 37.46 δ. Aliphatic carbon bound to oxygen is suggested by a peak at 68 δ.

In conclusion, we see that the soot anion, in being alkylated by CD_3I, behaves as anions of larger polynuclear aromatics, such as perylene and decacyclene (16) and not like the anion of graphite with K^+. Naphthalene, with excess K^0, behaves as naphthalene (-1).

Acknowledgements--We thank Mike Matturro for giving us the atomic coordinates of the 60 atom truncated icosahedron, Rod Kastrup for for the high resolution NMR spectra, and Manny Garcia for the D-2 NMR of solid samples.

REFERENCES

1. Y. Schwob, Chem. Phys. Carbon, 15, 109 (1979).
2. H. GG. Wagner, 17th Symposium on Combustion, pp. 3-19 (1978).
3. Q. L. Zhang, S. C. O'Brien, J. R. Heath, Y. Liu, R. F. Curl, H. W. Kroto, and R. E. Smalley, J. Phys. Chem., 90, 525 (1986).
4. Oak Ridge National Laboratory report ORNL/TM-9196 (November 1983).
5. L. B. Ebert, J. C. Scanlon, and D. R. Mills, Preprints, Petroleum Division of the Amer. Chem. Soc., 28(5), 1353 (1983).
6. _____, Liq. Fuels Technology, 2, 257 (1984).
7. _____, Preprints, Petroleum Division of the Amer. Chem. Soc., 30(4), 636 (1985).
8. B. E. Warren and P. Bodenstein, Acta Cryst., 18, 282 (1965).
9. S. Ergun, Chem. Phys. Carbon, 3, 211 (1968).
10. L. M. Stock, in Coal Science, Academic, 1982, pp. 161-282.
11. L. B. Ebert, in Chemistry of Engine Combustion Deposits, Plenum, 1985, pp. 303-376,
12. A. J. Bard and L. R. Faulkner, Electrochemical Methods, Wiley, 1980, p. 701.
13. J. Mortensen and J. Heinze, Tet. Lett., 26, 415 (1985).
14. A. R. Garcia, L. B. Ebert, and B. G. Silbernagel, Extended Abstracts of the 18th Biennial Carbon Conference, July, 1987.
15. L. B. Ebert, G. E. Milliman, D. R. Mills, and J. C. Scanlon, in Advances in Chemistry Series No. 217 (Polynuclear Aromatic Hydrocarbons), Amer. Chem. Soc., 1987.
16. L. B. Ebert, D. R. Mills, and J. C. Scanlon, Preprints, Petroleum Division of the Amer. Chem. Soc., 32(2), 419 (1987).

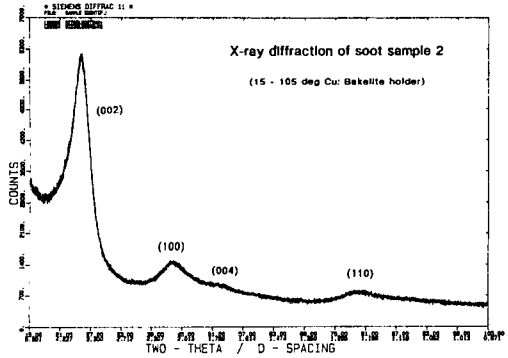

Figure 1. X-ray diffraction of sample 2.

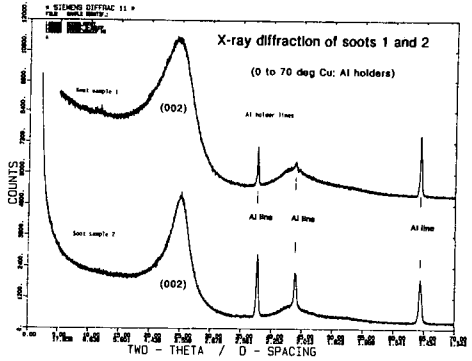

Figure 2. X-ray diffraction comparison: 1 vs. 2.

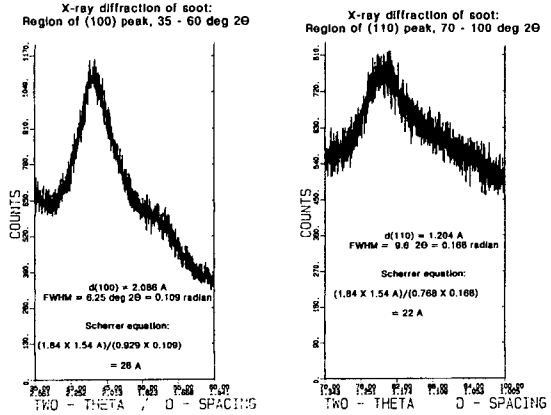

Figure 3. X-ray diffraction: (100) and (110) of sample 2

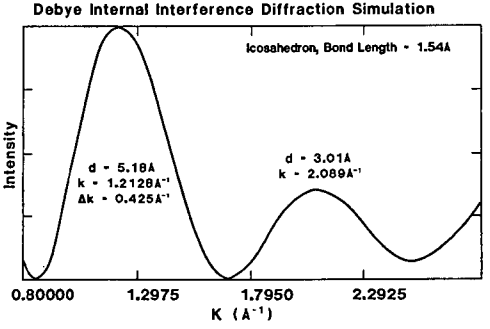

Figure 4. X-ray diffraction simulation: truncated icosahedron

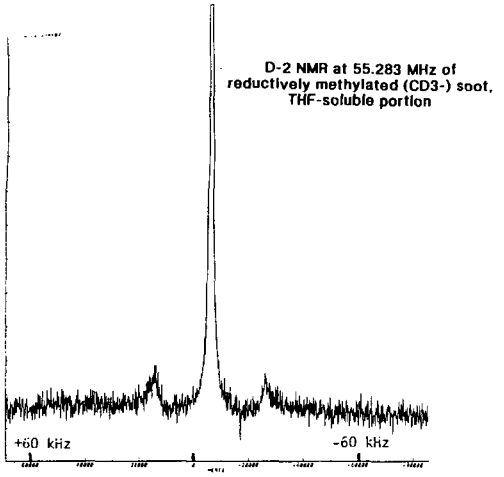

Figure 5. D-2 NMR of Me-soot THF-solubles

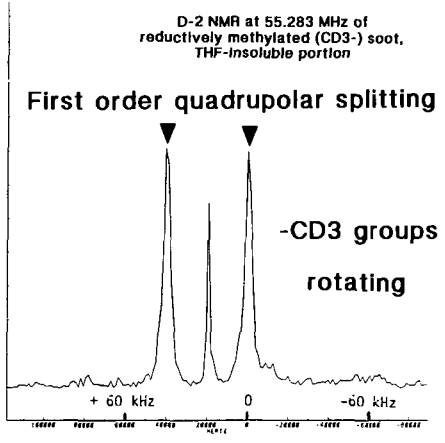

Figure 6. D-2 NMR of Me-soot THF-insolubles

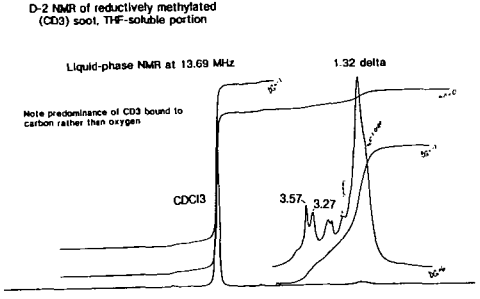

Figure 7. High resolution D-2 NMR of THF-sol

SINGLE PULSE SHOCK TUBE STUDIES ON THE STABILITY OF 1-PHENYLBUTENE-2

J. P. Cui*, Y. Z. He* and W. Tsang

Chemical Kinetics Division
National Bureau of Standards
Gaithersburg, Maryland 20899

ABSTRACT

1-Phenylbutene-2(1-PHB-2) has been decomposed in single pulse shock tube experiments. Acetylene formation is used as a measure of the rate of cleavage of the benzyl-vinyl C-C bond. The rate expression for this reaction has been found to be

$$k(1\text{-PHB-2} \rightarrow \text{benzyl} + \text{propenyl}) = 2.4 \times 10^{16} \exp(-43780/T)\ /s.$$

The A-factor for this process is unexpectedly large. It may be indicative of a larger than usual combination rate constant for vinyl radicals. Possible sources of experimental errors are considered. Our results are consistent with a bond dissociation energy for the primary vinyl C-H bond in propylene of 475±10 kJ/mol.

INTRODUCTION

This paper is concerned with the strength of the primary vinyl C-H bond in propylene. The present results should provide additional information on the energy of the vinyl C-H bond in ethylene. Within the past year there have been values ranging from 435 to 495 kJ/mol[1,2]. Any effect from methyl substitution will be far smaller than the spread of such numbers. The importance of the this quantity is due to the evidence[3] that vinyl radicals are key reactive intermediates for soot formation. Unfortunately, there is at present almost no rate data on vinyl radical reactions and the uncertainty with regard to its heat of formation prevents even the most rudimentary efforts at estimation.

The experiments are carried out in a heated single pulse shock tube[4]. Our target molecule is 1-phenyl butene-2 (1-PHB-2). The choice of this molecule is dictated by the weakening of the vinyl C-C bond by benzyl resonance and the decreased stability of the propenyl radical compared to that of the vinyl radical itself (had we chosen to work with allylbenzene). The former lowers the rate constant to a range which is more convenient for our purposes. Nevertheless, the rate constants are still very much smaller than those for alkane and alkene decomposition that we have hitherto studied. This creates certain problems. The existence of a unique reaction product, acetylene, from the decomposition of the propenyl radical, should reduce complications.

The key factors in obtaining high accuracy results from single pulse shock tube work are the great simplifications in the reaction mechanism and the use of an internal standard reaction to calibrate for the conditions in the experiments. The general methodology has been successfully used to give a complete picture of the decomposition of many organic compounds[5].

*Guest Scientists: Permanent Address, Institute of Mechanics, Academia Sinica, Beijing, China

There have been no previous studies on 1-PHB-2 decomposition. In Figure I(1), we outline a number of possible competitive unimolecular decomposition processes. From published bond energies one expect that they will be close to that for the vinyl-benzyl bond[6]. Unfortunately, these decomposition channels do not lead to unique products and it will not be possible to obtain accurate information on the rate constants for these reactions. This also makes it important to work at extents of conversion.

EXPERIMENTAL

The experiments are carried out in a heated single pulse shock tube maintained at 110 °C. All of the gas sampling system are maintained at temperatures close to or above this value. It is thus possible to work with very low volatility substances. Analysis of the products was by gas chromatography using a 30 meter polydimethylsiloxane capillary column for all substances with carbon numbers 5 or higher. For the light hydrocarbons we use a dinonylphthalate coated silica column. This column eluted acetylene between propylene and isobutene. Unfortunately, the retention time of allene also fell in this position. From separate experiments we determined that our yields of allene was uniformly of the order of 4% of the acetylene yield. The 1-PHB-2 from K & K[7]. Gas chromatographic analysis indicated that it is mostly the trans compound with about 3 % cis. There are also a number of other impurities. These included n-butylbenzene and s-butyl benzene. In these molecules, the normal C-C bonds are weakened by benzyl resonance. Since these are much more labile than vinyl C-C bonds, we observe under all conditions large quantities of their dissociation products. However under our conditions it is not possible to form acetylene from these starting materials.

In Figure I we enumerate the most likely decomposition modes of 1-PHB-2. Note that for methyl or larger alkyl radicals addition will be reversed, while the abstraction products will be the same as that for hydrogen atoms. The key conclusion from an examination of these possibilities is that under conditions of small extent of decomposition of the parent compound there is no channel that can lead to acetylene formation except through the sequence of reaction initiated by the cleavage of the propenyl-benzyl bond, followed by beta elimination of the methyl group.

Our concern with these factors arises from the high stability of the 1-phenylbutene-2 which prevents us from carrying out our experiments under conditions of enormous excesses of scavenger (100 to 1000 to 1). Indeed, a scavenger such as toluene will have rates of decomposition less than an order of magnitude slower. With a 100 to 1 ratio the scavenger will be producing more radicals than our test compound and will then have the capability of inducing decomposition. With this in mind, our highest scavenger 1,2,4 trimethylbenzene (1,2,4-TMB) to 1-PHB-2 ratio was 8 to 1. This appeared to be sufficient since our results with a 2 to 1 ratio are within experimental error the same as that at 8 to 1. The composition of the mixtures used and the range of conditions are summarized in Figure II.

The internal standard used in these studies is the reverse Diels Alder decomposition of 1-methylcyclohexene (1-MCH). We have previously established[8] its rate expression for decomposition into 2-methyl-butadiene-1,3(isoprene) and ethylene as

$k(1\text{-MCH} \rightarrow \text{isoprene} + C_2H_4) = 10^{15}\ \mathrm{Exp}(-33500/T)/s$

This standard is used because isoprene is not a reaction product in 1-PHB-2 decomposition and it elutes from our capillary column in a region where there are no interfering peaks.

RESULTS

The distribution of products from the shock induced decomposition of 1-phenylbutene-2 in the presence and absence of the scavenger 1,2,4-TMB can be found in Table I. The important points to be noted are the changes in relative concentrations. We assume that acetylene is essentially a primary product and its concentration will not be effected by the absence and presence of the scavenger. Our results are in accord with the expectation that some of the reactive radicals will be removed by the 1,2,4-TMB. However, although there is a decrease in the yields of the lighter products (for example, propylene, butadiene) relative to that of acetylene as the amount of the inhibitor, 1,2,4-TMB is increased, we cannot be certain that we have been able to stop completely the radical induced decomposition. This is not unreasonable, since as noted earlier the thermal stability characteristics of 1-PHB-2 is not that much different than the inhibitor. Thus there approaches a point where our inhibitor will in fact be contributing to the pool of active radicals. It is interesting to note that the material balance with regard to 1-MCH decomposition improves with scavenger addition. Paralleling this is the decrease in the quantity of 1-PHB-2 destroyed when the scavenger is added. Clearly in the absence of the scavenger there are radical catalyzed decomposition channels.

For our purposes we concentrate on the acetylene from 1-PHB-2 decomposition and isoprene from 1-MCH decomposition. Figure II contains the comparative rate plots for the formation of acetylene from 1-PHB-2 decomposition and isoprene from 1-MCH decomposition. The rate constants are derived from the relation

$$\mathrm{Log}(k(\text{acetylene})) = \mathrm{Log}((\text{acetylene})_f/(1\text{-PHB-2})_i)/t$$
$$\mathrm{Log}(k(\text{isoprene})) = \mathrm{Log}(1-(X*(\text{isoprene})f/(1\text{-MCH})_i)/Xt$$

where $X = 1+(((\text{MCH})_i-(\text{MCH})_f-(\text{isoprene})_f)/(\text{isoprene})f)$ and takes into account the possibility that some of the 1-MCH $((\text{MCH})_i-(\text{MCH})_f-(\text{isoprene})_f)$ will be decomposed through radical attack. We have no means of determining how much isoprene is destroyed. Thus it is essential in the 1-MCH decomposition to obtain the best possible mass balance. This is attained when the scavenger is added. As will be seen below, in the absence of scavenger comparative rate results are different than in its presence. The relation for acetylene appearance assumes negligible 1-PHB-2 disappearance. From the data in Table I it can be seen that this is attained in the studies with the scavenger. We assume that the conversion of the trans to the cis form will not effect our results. An interesting aspect of the data in Table I is that we can extract rate constants for the trans -> cis isomerization of 1-PHB-2 as well and the decomposition of nbutyl- and sbutyl-benzene. In all three cases they fall in the expected range.

The comparative rate expressions relating the rate constant for acetylene andd isoprene formation in 1-PHB-2 and 1-MCH decomposition are as follows;

$$\text{Log(k(acetylene))} = 1.308 \pm .014 \text{Log(k(isoprene))} - 3.030 \pm .034$$
(1% 1-PHB-2 and 200 ppm 1-MCH)

$$\text{Log(k(acetylene))} = 1.312 \pm .015 \text{Log(k(isoprene))} - 3.256 \pm .036$$
(1% 1,2,4 TMB; .5% 1-PHB-2 and 100ppm 1-MCH)

$$\text{Log(k(acetylene))} = 1.304 \pm .034 \text{Log(k(isoprene))} - 3.198 \pm .087$$
(2% 1,2,4 TMB; .25% 1-PHB-2 and 50 ppm 1-MCH)

Substituting into these relations the rate expression for the reverse Diels-Alder decomposition of 1-MCH given above, we obtain the following rate expression for acetylene formation in 1-PHB-2 decomposition $k(\text{acetylene}) = 3.8 \times 10^{16} \text{ Exp}(-43800/T)$ /s, $k(\text{acetylene}) = 2.6 \times 10^{16} \text{ Exp}(-43900/T)$ /s and $k(\text{acetylene}) = 2.3 \times 10^{16} \text{ Exp}(-43670/T)$ /s respectively.

It will be noted that the last two expressions are virtually identical, while the first rate expression is about 30 % larger. This is due to the contribution from the radical induced decomposition of 1-MCH and isoprene and is of the magnitude expected on the basis of our mass balance considerations. The agreement in the other two cases suggest that enough inhibitor has now been added so that the radical induced decomposition no longer poses a serious problem. The similarity in the activation is also interesting. It suggests that the contribution from the induced decomposition has very similar temperature dependence as the direct unimolecular decomposition. Our best rate expression for the breaking of the vinyl-benzyl bond is thus the average of our results in studies carried out in the presence of 1,2,4 TMB or

$$k(\text{1-PHB-2} \rightarrow \text{benzyl + propenyl}) = 2.4 \times 10^{16} \text{ Exp}(-43780/T) \text{ /s}$$

DISCUSSION

We will now use our rate expression for the breaking of the benzyl-vinyl bond to derive the bond energy of the primary C-H bond in propylene. From the usual assumption regarding the absence of temperature dependence for the reverse combination reaction, the relations are

$$\triangle H \text{ (reaction)} = \triangle E \text{(activation Energy)} + RT$$

or $\triangle H = 409.6$ kJ/mol at 1150K. Since

$$\triangle H \text{ (reaction)} = H_f\text{(benzyl)} + Hf\text{(propenyl)} - H_f\text{(1-PHB-2)} \text{ at 1150K.}$$

substituting the heat of formation of benzyl and 1-PHB-2 lead to H_f(propenyl)=269.5 kJ/mol. at 1150K. We have calculated the thermodynamic quantities of benzyl using the prescription of Benson and O'Neal[9] and a value of 205 kJ/mol for the heat of formation at 300K. This is 6 kJ/mol higher than the number recommended by McMillen and Golden[6], but is a value that we obtained some years ago on the basis of isobutyl benzene decomposition[10]. This leads to a heat of formation of 180.7 kJ/mol at 1150K. The heat of formation of 1-PHB-2 at 1150K is taken to be 80.3 kJ/mol and is based on the heat of formation of butylbenzene and an average value of 133 kJ/mol for the heat of dehydrogenation[11]. Assuming that the heat capacity of propenyl is an average of that of propene and propyne leads to

BDE(propene->propenyl+H) = 484 $\pm$ 8 kJ/mol

There have been no previous measurement of this bond dissociation energy. However, it should not be too far off from the value for ethylene. Our number is extraordinarily high and had it not been for the recent value of Shiromaru and coworkers would be the highest ever reported for such a bond. Most kinetic results appear to favor very low values.

The A-factor for acetylene formation, 2.4×10^{16} /s, is large in comparison to that for processes that involve the breaking of a benzyl-alkyl bond. In these cases A-factors are more in the range of one-half to one order of magnitude smaller. Our high number is reflected in the rate constant of the reverse recombination reaction. It is of interest to calculate the combination rate constant for benzyl attack on propenyl using our A-factor. From the estimated entropies we find that $\triangle S = 148$ J/mol-K. Substitution into the relation,

$$A_f/A_b = \exp(-\triangle S/R)/eRT$$

leads to $A_b = k_b = 11 \times 10^{10}$ 1/mol-s, with an uncertainty of a factor of 3. This is a large rate constant. It is much larger than the values for comparable processes involving alkyl radicals. Thus an interesting consequence of this study is that higher vinyl C-H bond energies not only lead to longer lifetimes for the decomposition of vinyl type radicals but predicts higher combination rates with other radicals.

In view of the unexpectedly larger recombination rates, it is important to consider possible sources of uncertainties in our measurements. The chief source of error is probably in the definition of the reaction mechanism. We have assumed that all the acetylene must be formed from the cleavage of the benzyl-vinyl C-C bond and that this will be followed by beta C-C bond cleavage. While we believe that these embody the main reactions, the fact that we are making a slope measurement means that small errors may lead to substantial errors. Probably the most serious is the assumption of beta C-C bond cleavage in propenyl decomposition and ignoring the possibility of a 1-3 bond shift leading to an allyl radical which will be fairly stable under our conditions. This assumption is based on the behavior of alkyl radicals. In the present case there may be some enhancement due to the much larger reaction exothermicity for the 1-3 shift (in excess of 60 kJ/mol). However, since we are dealing with a doubly bonded structure there will be an extra degree of strain in the transition state. Furthermore, in the decomposition of o-iodotoluene where we make the o-methylphenyl radical, which is structurally very similar to propenyl, there does not appear to be any evidence for such a shift. It should be noted that if such an effect is to make a contribution it will bias the results towards higher activation energies. The A-factor for 1-3 H-shift is smaller than that for beta C-C bond fission and this must be compensated for by a lower activation energy if this process is to make any contribution. Similarly, since the lowest energy path for acetylene formation in our system is the breaking of the benzyl-vinyl bond, then any other contribution will also lead to an increase in measured activation energy. On this basis we believe that to some extent our activation energy is an upper limit. A lower limit is set by the A-factor for the decomposition of a compound such as ethylbenzene or 4×10^{15} /s. This leads to a more "normal" A-factor 1.8×10^{10} 1/mol-s. Scaling our activation energy to obtain the same rate constant will lead to a value of 346 kJ/mol or a bond dissociation energy

of 465 kJ/mol. Taking the average of these two values we arrive at 475±10 kJ/mol as the most likely value. This is still a very large number. It is a reflection of the fact that our measured rate constants are much too small to be consistent with a low vinyl-H bond energy.

In a similar fashion it is interesting to consider the consequences of a bond dissociation energy in the 435 kJ/mol range. Assuming our rate constant to be correct, this will imply an A-factor of 3×10^{14} /s and a rate constant for. combination of close to 10^9 l/mol-s. This strikes us as an extremely low and unlikely value. Even more unlikely is the highest reported value for the C-H bond energy in ethylene since this will lead to an A-factor of 2.5×10^{17} /s and a recombination rate of 11×10^{11} l/mol-s. or larger than collisional. On the other hand, a somewhat higher rate constant for vinyl radical combination is in line with increasing evidence for a very small disproportionation to combination rate constant ratio for vinyl radicals reacting with itself.

REFERENCES

1. Shiromaru, H., Achiba, Y., Kimura, K., and Lee, Y. T. J. Phys. Chem., 1987 91,17

2. Kiefer, J. H., Wei, H. C., Kern, R. D., and Wu, C. H., Int'l J. Chem. Kin.,1985, 17, 225

3. Frenklach, M; Gardiner W. C., Clary, D. and Stein, S. E., 21st Symposium on Combustion, in press

4. Robaugh, D. and Tsang, W., J. Phys. Chem., 1986, 90, 5363

5. Tsang, W,"Comparative-Rate Single Pulse Shock Tube Studies on the Thermal Stability of Polyatomic Molecules," in Shock Waves in Chemistry (A.Lifshitz, ed) Marcel Dekker, New York, 1981, pg 59

6. McMillen, D.F. and Golden, D. M. Annu. Rev. Phys. Chem., 1982, 33, 493

7. Certain commercial materials and equipment are identified in this paper in order to specify adequately the experimental procedure.In no case does such identification imply recommendation of endorsement by the national Bureau of Standards, nor does it imply that the material or equipment is necessarily the best available for the purpose

8. Tsang, W., Int'l. J. Chem. Kin.,1978, 10, 599

9. O'Neal, H. E. and Benson, S. W., "Thermochemistry of Free Radicals" in "Free Radicals, Vol II" (J. Kochi, ed) John Wiley and Sons, 1973, pg 275

10. Tsang, W., Int'l. J. Chem. Kin., 1969, 1, 245

11. Stull, D. R., Westrum, E. F.; and Sinke, G. C.; "The Chemical Thermodynamics of Organic Compounds", John Wiley and Sons, 1969

Figure I: Important Steps in 1-Phenylbutene-2 Decomposition

1. Unimolecular Decomposition
   a. C-H bond split $C_6H_5CH2CH=CHCH_3$ -> $C_6H_5CCH=CHCH_3$ + H
      -> $C_6H_5CH_2CH=CHCH_2$ + H
   b. C-C bond splits $C_6H_5CH2CH=CHCH_3$ -> C_6H_5 + $CH2CH=CHCH_3$
      -> $C_6H_5CH_2$ + $CH=CHCH_3$
2. Radical Attack (abstraction and addition)
   a. $C_6H_5CH2CH=CHCH_3$ + R -> $C_6H_5CHCH=CHCH_3$ + RH
      -> $C_6H_5CH2CH=CHCH_2$ + RH
   b. $C_6H_5CH2CH=CHCH_3$ + H -> $C_6H_6CH2CH=CHCH_3$
      -> $C_6H_5CH2CH2CHCH_3$
      -> $C_6H_5CH2CHCH2CH_3$
3. Decomposition of Radicals
   $CH_2CH=CHCH_3$ -> $CH_2=CHCH=CH_2$
   $C_6H_5CHCH=CHCH_3$ -> $C_6H_5CH=CHCH=CH_2$ + H
   $C_6H_5CH2CH=CHCH_2$
   (stabilized)
   $C_6H_6CH_2CH=CHCH_3$ -> C_6H_6 + $CH_2CH=CHCH_2$
   $C_6H_5CH2CH2CHCH_3$ -> $C_6H_5CH_2$ + C_3H_6
   $C_6H_5CH2CHCH2CH_3$ -> $C_6H_5CHCH=CH_3$ + CH_3
   $CH=CHCH_3$ -> $CH=CH$ + CH_3
4. Decomposition Products from Impurities (nbutylbenzene, sbutylbenzene) leading to ethylene, styrene, methyl, methane, ethane, etc.

Figure II: Comparative Rate Studies on the Formation of Benzyl and Propenyl from 1-PHB-2 and 1-MCH Decomposition; 1% 1-PHB-2 and 200 ppm 1-MCH in Argon (□); 1% 1,2,4-TMB, .5% 1-PHB-2 and 100ppm 1-MCH in Argon (✱); and 2% 1,2,4 TMB, .25% 1-PHB-2 and 50 ppm 1-MCH in Argon(●). Temperature, 1092-1221 K; Residence time 500 microsecs.; Pressure, 2.5-3.5 atms.

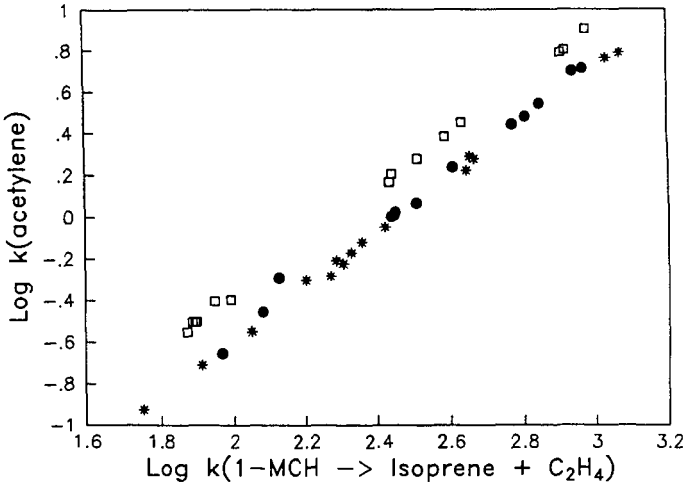

Table I: Typical Gas Analysis Results from the Decomposition of 1-Phenylbutene-2 (in units of 10^3 x mole fraction)

A) Normalized against initial mixture (composition; 964, trans 1-PHb-2; 21, cis 1-PHB-2; 12, s-Butylbenzene; 2.6 n-Butylbenzene)

Mixtures	1% (1-PHB-2) in Argon	1%(1-PH-2) 200ppm (1-MCH) in Argon		1%(1,2,4TMB) .5%(1-PHB-2) 100ppm (1-MCH) in Argon		2%(1,2,4-TMB) .25%(1-PHB-2) 50 ppm(1-MCH) in Argon	
Methane	8.3	6.6	2.0	5.8	11.4	17.6	4.5
Ethane, Ethene	6.9	8.5	2.2	4.2	8.2	8.8	1.9
Propylene	9.6	7.7	2.0	1.7	3.5	1.9	.57
Acetylene	1.3	.81	.13	.3	.74	.86	.11
Butenes	1.5	1.3	.5	.45	.8	.75	.39
1,3 Butadiene	3.5	2.5	.56	.76	1.7	1.5	.25
Benzene	2.5	1.7	.4	.57	1.2	1.2	.23
Toluene	2.8	1.8	.6	.82	1.8	2.1	.58
Ethylbenzene	3.4	2.5	.4	.5	1	.56	.12
m,p-Xylene				1.4	2.9	5.2	1.1
Styrene	6.5	5.0	1.3	2.0	3.6	3.5	.8
o-Xylene				.5	1.0	1.9	.4
Allylbenzene	5.8	4.6	1.4	1.1	2.1	1.2	
s-Butylbenzene	7.4	8.5	11.2	10.4	8		
n-Butylbenzene	2.2	2.2	2.3	2.5	2.3	2.3	2.6
1-PHB-2 trans	860	860	916	945	895	890	961
cis	62	57	30	50	76	85	35

b) Normalized against 1-MCH

Isoprene	133	34	91	178	234	53
1-MCH	807	944	904	780	744	934
Temperature(K) (based on Isoprene yields)	1160	1105	1143	1172	1185	1121

Reaction Time: 500 microsecs; Pressure: 2.8-3.2 atm.

The Correlation of Benzene Production with Soot Yield Determined from Fuel Pyrolyses

R.D. Kern, C.H. Wu, J.N. Yong, K.M. Pamidimukkala and H.J. Singh

Department of Chemistry
University of New Orleans
New Orleans, Louisiana 70148

Introduction

The rate of production of soot in pyrolytic reaction systems has been studied in shock tubes using a variety of non-intrusive analytical techniques; laser extinction (LEX)[1-6], static analysis of the product distribution from single pulse shock tubes (SPST)[7-9], and dynamic analysis of the reflected shock zone by time-of-flight mass spectrometry (TOF)[10]. The data reduction process often involves measurement of a changing bulk quantity; e.g., attenuation of a He-Ne laser beam due to absorption by high molecular weight gas phase species and discrete soot particles via LEX or deficiencies in the carbon atom mass balance via SPST or TOF. The concentrations of the various polycyclic hydrocarbons formed in the pre-particle soot chemistry phase are extremely low[9] and are below the detectability limit of the TOF technique[10] which is about 10^{-10} mol cm^{-3}. The non-detected hydrocarbons constitute the "missing" mass.

The ultimate goal of the work in this area is to write a complete chemical mechanism for soot formation. This formidable task has been attempted for acetylene[11]. Some 180 species and 600 reactions were considered in an effort to model the soot yield obtained by LEX. Both the calculated and experimental yields were very low (< 1%). Comparison of the calculated results with the measured bulk quantity was obtained by assuming that all species in the model having MW>300 absorbed 632.8 nm radiation. The summation of these high molecular weight concentrations converted to carbon atoms cm^{-3} and divided by the input carbon atom concentration yielded the computed soot yield.

The effort herein is to develop a correlation between a readily observable molecular species whose presence is diagnostic of subsequent soot formation and the bulk observables of laser extinction and mass balance deficiency.

Experimental Techniques Employed

LEX has been utilized behind incident and reflected shock waves during various observation times ranging from 0.5-2.5 ms[1-6]. In order to compare the relative sooting tendencies of fuels, a total carbon atom concentration of $2x10^{17}$ atoms cm^{-3} was chosen for such fuels as ethylbenzene, toluene, benzene, pyridine, allene, 1,3 butadiene, vinylacetylene, and acetylene. The soot yield vs the no-reaction shock zone temperature curves are bell-shaped. Aromatic compounds produced the greatest amount of beam attenuation or soot yield while

acetylene exhibited the least. The early LEX work[1-3] reported values for the absolute soot yield on the order of 80 - 90% conversion of aromatic fuels to soot. It was subsequently realized that these values were too high due in part to uncertainty of the literature value for the refractive index of soot and to light absorption by pre-particle species.[4] It was also known that a significant amount of soot formation occurred in the accompanying cooling wave.[7,8] For these and other reasons, the ordinate for soot yield plots was taken to be E(m) x soot yield with the value of E(m) left unspecified pending resolution of the uncertainties.[4,5] This adjustment cast the LEX results as a measurement of relative rather than absolute soot yields.

The thrust of the mass balance deficiency procedure was to add up all of the carbon containing products detected and subtract from the total carbon atoms in the original fuel. Aromatic compounds showed the greatest deficiencies (with the notable exception of pyridine[6]) and acetylene the least. There was good agreement with regard to the relative sooting tendencies of fuels investigated with LEX and the mass deficiencies obtained by SPST and TOF.

The TOF method offers the advantage of recording the product distribution at selected times during the reaction. Concentration profiles of various observed species are constructed within the m/e range of 12 - 300 during typical observation times of $\sim$ 0.75 ms. The data are fit with computed lines from proposed or known mechanisms. Benzene has been recorded during the pyrolyses of allene[12], 1,2 butadiene[13], and 1,3 butadiene[14]. The profiles have been modeled using the CHEMKIN program[15,16] with reasonable success.

Results and Discussion

In order to mimic the soot bells determined by LEX, benzene concentrations were modeled for the thermal decompositions of C_3H_4[12], 1,2 C_4H_6[13], 1,3 C_4H_6[14], C_4H_4[17], C_5H_5N[18], and C_2H_2[19]. In each of these pyrolyses investigated by the TOF method, the total carbon atom concentration was approximately 2 x 10^{17} atoms cm^{-3}. The benzene concentrations were calculated for each of these fuels at 1 ms as a function of no-reaction shock temperature in order to compare with the LEX work. The TOF and LEX results are shown in Figures 1 and 2. Before discussing each fuel individually, we note that the benzene concentration curves are bell shaped, that the relative amounts of benzene formed are in the same general order as the sooting tendencies, and that the benzene maximum for each fuel precedes the respective soot tendency maxima.

Allene

A 4.3% C_3H_4-Ne mixture was investigated over the temperature and total pressure range of 1300-2000 K and 0.2-0.5 atm, respectively. TOF analysis revealed that the major products were C_2H_2, C_4H_2, CH_4 and C_6H_6; lesser amounts of C_2H_4, C_2H_6, C_4H_4, and C_6H_2 were detected. The major product profiles were modeled with an 80 step reaction mechanism. The initial reactions involved the isomerization of allene to propyne[20]; both isomers decompose to yield C_3H_3 + H[21,22]. Benzene was produced via reaction of C_3H_3 with allene and by reaction of

two C_3H_3 radicals. The latter route was suggested by Hurd[23,24] in which C_3H_3 initially forms :CH–CH=ĊH via 1,2 H shift followed by cyclization to benzene. Benzene concentrations were calculated at 1 ms for various no-reaction temperatures. The resulting bell shaped curve is displayed in Figure 1 along with its respective LEX soot tendency bell[5].

1,2 Butadiene

A 3% 1,2 C_4H_6-Ne mixture was shocked over the ranges 1200–2000 K and 0.17–0.56 atm. The major stable species observed were C_2H_2, CH_4, C_2H_4 and C_4H_2. At intermediate temperatures (around 1500 K), benzene and toluene were recorded. C_2H_2 and C_4H_2 were the only major products at high temperatures. Isomerization of 1,2 to 1,3 C_4H_6 precedes extensive decomposition. The two isomers decompose according to two pathways.

$$1,2\ C_4H_6 \text{ ------> } CH_3 + C_3H_3 \qquad 1)$$
$$1,3\ C_4H_6 \text{ -----> } 2\ C_2H_3 \qquad 2)$$

The decomposition of 1,3 C_4H_6 has been studied by laser schlieren densitometry (LS) and TOF[14]. The reaction mechanism used to model the various product profiles from 1,3 C_4H_6 was employed as a subset to the mechanism for 1,2 C_4H_6. Reactions describing the isomerization and other key channels complete the model. Benzene concentrations were calculated at 1 ms and are plotted as a function of temperature in Figure 1. There are no LEX data available for comparison.

1,3 Butadiene

A 3% 1,3 C_4H_6-Ne mixture was studied over the range comparable to 1,2 C_4H_6. LS profiles obtained by Professor Kiefer provided conclusive evidence that the main pathway for decomposition was C–C bond rupture to produce two vinyl radicals. A 31 step mechanism modeled the LS profiles and the TOF profiles for 1,3 C_4H_6, C_2H_2, C_2H_4, C_4H_2 and C_6H_6[14]. The amount of benzene produced was less than that recorded for 1,2 C_4H_6 and for an equivalent amount of C_3H_4. The latter result is in agreement with the LEX work[5] which is shown in Figure 1.

Acetylene

C_2H_2 is the major product in the high temperature thermal decompositions of many hydrocarbons; C_8H_{10}[25], C_7H_8[26], C_6H_6[27–29], C_5H_5N[18], C_3H_4[12], 1,2[12] and 1,3 C_4H_6[14], and C_4H_4[30]. A radical mechanism derived largely from those previously employed by Gardiner[31] and Kiefer[32] was used to model TOF data obtained on a series of C_2H_2-Ne mixtures, 1–6.2%, over the range 1900–2500 K and 0.3–0.55 atm. The major species modeled were C_2H_2, C_4H_2, and C_6H_2. Minor amounts of C_8H_2 and C_4H_3 were recorded; benzene was not detected. Reactions from the benzene mechanism[29] were added to the model and used to calculate the relatively minor amounts of benzene detected in the SPST work by Colket[9]. The results are shown in Figure 3. Although the fit is not completely satisfying, the computed profile is satisfactory for our purpose here; namely, the benzene yield is very low compared to the major species present. Benzene concentrations for an acetylene

mixture containing 2 x 10^{17} C atoms cm^{-3} are plotted in Figure 2 along with the corresponding LEX soot bell[5].

Vinylacetylene

Pyrolysis of C_4H_4 has been studied recently by LS and TOF over the range 1500-2500 K and 0.14-0.56 atm[30]. Analysis of the LS profiles revealed that the decomposition was characterized by a heat release of $\sim$ 40 kcal mol^{-1}. The LS profiles were all concave upward which ruled out any appreciable chain acceleration reactions. TOF measurements of the major products, C_2H_2 and C_4H_2 disclosed a near constant ratio of $C_2H_2/C_4H_2 \sim 5$ which was independent of the observation time and temperature. Trace amounts of C_6H_2 were recorded at higher temperatures; C_8H_2 and benzene were not detected. These facts support the proposal that the mechanism is molecular and occurs via the reactions

$$C_4H_4 + M \text{ -----> } 2\ C_2H_2 + M \qquad 3)$$
$$C_4H_4 + M \text{ -----> } C_4H_2 + H_2 + M \qquad 4)$$

The LS profiles and the TOF profiles were fit with rate constants derived for this two channel dissociation. These conclusions are in conflict with two other shock tube reports that propose a radical mechanism for the pyrolysis in which the first step is C-H bond rupture[33,34].

$$C_4H_4 \text{ -----> } C_4H_3 + H \qquad 5)$$

The initiation is followed by a sequence of radical reactions. The benzene concentrations shown in Figure 2 were calculated using rxs 3) and 4) along with the C_2H_2[19] and C_6H_6[29] mechanisms previously mentioned to fit the SPST data in Figure 3.

Pyridine

LS and TOF profiles have been recently obtained[18] for the thermal decomposition of C_5H_5N over the range 1700-2200 K and 0.13-0.5 atm. The LS profiles displayed local maxima which is a signature for chain acceleration of the net endothermic rate. The main products were identified by TOF to be HCN, C_2H_2, and C_4H_2. A 24 step mechanism was constructed which included the following steps:

$$C_5H_5N + M \text{ -----> } C_5H_4N + H + M \qquad 6)$$
$$H + C_5H_5N \text{ -----> } C_5H_4N + H_2 \qquad 7)$$
$$C_5H_4N + M \text{ -----> } C_4H_3 + HCN \qquad 8)$$

Benzene concentrations were calculated in the manner employed for C_4H_4 and are extremely low which is in accord with the LEX result[6]. The near absence of this key building block inhibits polycylic growth and subsequent soot formation. Intact pyridine rings are not suitable substitutes since polycyclic growth is retarded by the presence of the ring nitrogen.

Temperature Changes

Thermal decompositions are endothermic processes and the system temperature decreases as the reaction progresses. This point is illustrated in Figure 4 in which the soot bell for toluene at 1 ms observation time[4] is shifted markedly when the system temperature at 1 ms is used to plot the sooting tendency instead of the usual practice which employs the no reaction temperature. The temperatures at 1 ms were calculated using a mechanism from recent LS and TOF work on C_7H_8[26] which identifies the major pathway for dissociation as

$$C_7H_8 + M \text{ -----> } C_6H_5 + CH_3 + M \qquad 9)$$

Temperature decreases for the pyrolyses represented in Figures 1 and 2 at 1 ms are listed in Table 1.

Conclusions

There appears to be sufficient evidence to support the correlation of benzene production and soot tendencies. It does not necessarily follow that the key to soot control is limiting solely those reactions and/or species which promote benzene formation. The pyrolyses considered herein were those of "pure" fuels. Synergistic effects have been reported for fuel mixtures; e.g., a 0.75% C_7H_8 - 0.75% C_5H_5N - Ar mixture produced almost as much soot as an equivalent amount of "pure" toluene, 1.5% C_7H_8 - Ar[6]. Nevertheless, the results herein are consistent with the proposal of relatively low concentrations of soot nuclei which subsequently increase in mass due to surface growth by C_2H_2[35].

Acknowledgments

We appreciate the collaboration of Professor Kiefer and his research group and thank the Department of Energy for support under contract DE-FG0585ER/13400.

References

1. Graham, S.C, Homer, J.B. and Rosenfeld, J.L.J., Proc. Roy. Soc. A344(1975) 259.
2. Graham, S.C., Homer, J.B. and Rosenfeld, J.L.J., Proc., 10th Int. Symp. on Shock Tubes and Waves, 1975, p.621.
3. Wang, T.S., Matula, R.A. and Farmer, R.C., 18th Symp. (Int.) on Combustion (1981), 1149.
4. Frenklach, M., Taki, S. and Matula, R.A., Combust. Flame, 49, (1983), 275.
5. Frenklach, M., Taki, S. Durgaprasad, M.B. and Matula, R.A., Combust. Flame, 54, (1983) 81.
6. Rawlins, W.T., Tanzawa, T., Schertzer, S.P., and Kreck, R.H., Final Report submitted to DOE, Contact DEAC2280PC30292, January 1983.
7. Vaughn, S.N., Ph. D. Thesis, Kansas State University, 1980.
8. Vaughn, S.N., Lester, T.W. and Merklin, J.F., Proc., 13th Int. Symp. on Shock Tubes and Waves, 1982, p. 860.
9. Colket, M.B.,Proc., 15th Int. Symp. on Shock Tubes and Waves, 1986, p. 311.

10. Kern, R.D., Singh, H.J., Esslinger, M.A. and Winkeler, P.W., 19th Symp. (Int.) on Combustion, 1982, 1351.
11. Frenklach, M., Clary, D.W., Gardiner, W.C., and Stein, S.E., 20th Symp. (Int.) on Combustion, (1984), 887.
12. Wu, C.H. and Kern, R.D., manuscript submitted to J. Phys. Chem.
13. Singh, H.J. and Kern, R.D., work in progress.
14. Kiefer, J.H., Wei, H.C., Kern, R.D. and Wu, C.H., Int. J. Chem. Kinet., 17, (1985) 225.
15. Kee, R.J., Miller, J.A. and Jefferson, T.H., CHEMKIN: A General Purpose, Problem Independent Transportable, Fortran Chemical Kinetics Code Package, Sandia National Laboratories, SAND 80-8003, 1980.
16. Hindmarsh, A.C., LSODE Livermore Solver for Ordinary Differential Equations, Lawrence Livermore Laboratory, 1980.
17. Kiefer, J.H., Mitchell, K.I., Kern, R.D., and Yong, J.N., manuscript submitted to J. Phys. Chem.
18. Kern, R.D., Yong, J.N., Kiefer, J.H.,and Shah, J.N., paper to be presented at the 16th Int. Symp. on Shock Tubes and Waves, 1987.
19. Wu, C.H. and Kern, R.D., manuscript submitted to Int. J. Chem Kinet.
20. Kakumoto, T., Ushirogouchi, T., Saito, K., Isamura, A., J. Phys. Chem., 91, (1987), 183.
21. Lifshitz, A., Frenklach, M., Burcat, A., J. Phys. Chem., 79, (1975), 1148.
22. Lifshitz, A., Frenklach, M., Burcat, A., J. Phys. Chem., 80, (1976), 2437.
23. Hurd, C.D., Macon, A.R., Simon, J.I., Levetan, R.V., J. Am. Chem. Soc., 84, (1962), 4509.
24. Hurd, C.D., Macon, A.R., J. Am. Chem. Soc., 84, (1962), 4524.
25. Pamidimukkala, K.M. and Kern, R.D., Int. J. Chem. Kinet.,18, (1986), 1341.
26. Pamidimukkala, K.M., Kern, R.D., Patel, M.R., Wei, H.C. and Kiefer, J.H., J. Phys. Chem., 91, (1987), 2148.
27. Singh, H.J. and Kern, R.D., Combust. Flame, 54, (1983), 49.
28. Kern, R.D., Wu, C.H., Skinner, G.B., Rao, V.S., Kiefer, J.H., Towers, J.A., and Mizerka, L.J., 20th Symp. (Int.) on Combustion (1984), 789.
29. Kiefer, J.H., Mizerka, L.J., Patel, M.R., and Wei,H.C., J. Phys. Chem., 89, (1985), 2013.
30. Kiefer, J.H., Mitchell, K.I., Kern, R.D., and Yong, J.N., manuscript submitted to J. Phys. Chem.
31. Tanzawa, T. and Gardiner, W.C., J. Phys. Chem., 84, (1980), 236.
32. Kiefer, J.H., Kapsalis, S.A., Al-Alami, M.Z., and Budach, K.A., Combust. Flame, 51, (1983), 79.
33. Colket, M.B., presented at the 21st Symp. (Int.) on Combustion, 1986, in press.
34. Hidaka, Y., Tanaka, K., and Suga, M., Chem. Phys. Lett., 130, (1986), 195.
35. Harris, S.J., and Weiner, A.M., Ann. Rev. Phys. Chem., 36, (1985), 31.

Table 1.

Temperature Decrease During Pyrolyses of Various Fuels

T_0(K)	$-\Delta T$ (1.0 msec, 2×10^{17} C atoms cm^{-3})						
	C_3H_4	1,2 C_4H_6	1,3 C_4H_6	C_4H_4	C_2H_2	C_5H_5N	C_7H_8
1500	-	57	88	36	<0.5	25	-
1600	-	114	149	95	1	75	93
1700	41	164	211	150	3	155	162
1800	110	206	268	186	6	235	236
1900	168	239	316	205	10	310	311
2000	206	269	354	208	14	375	379
2100	233	300	378	209	18	415	433
2200	249	325	393	210	23	433	462
2300	258	340	400	212	29	433	471
2400	264	349	402	212	33	433	508

Figure 1

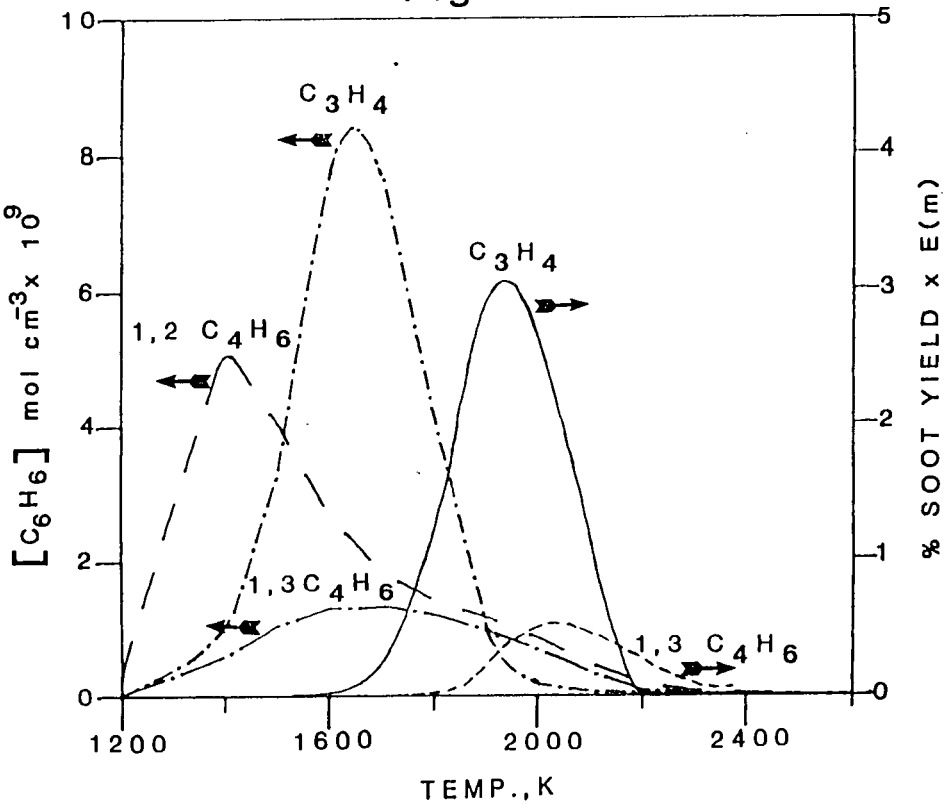
10
8
6
4
2
0
5
4
3
2
1
0
C_3H_4
C_3H_4
1,2 C_4H_6
1,3 C_4H_6
1,3 C_4H_6
$[C_6H_6]$ mol $cm^{-3} \times 10^9$
% SOOT YIELD x E(m)
1200
1600
2000
2400
TEMP., K

Figure 2

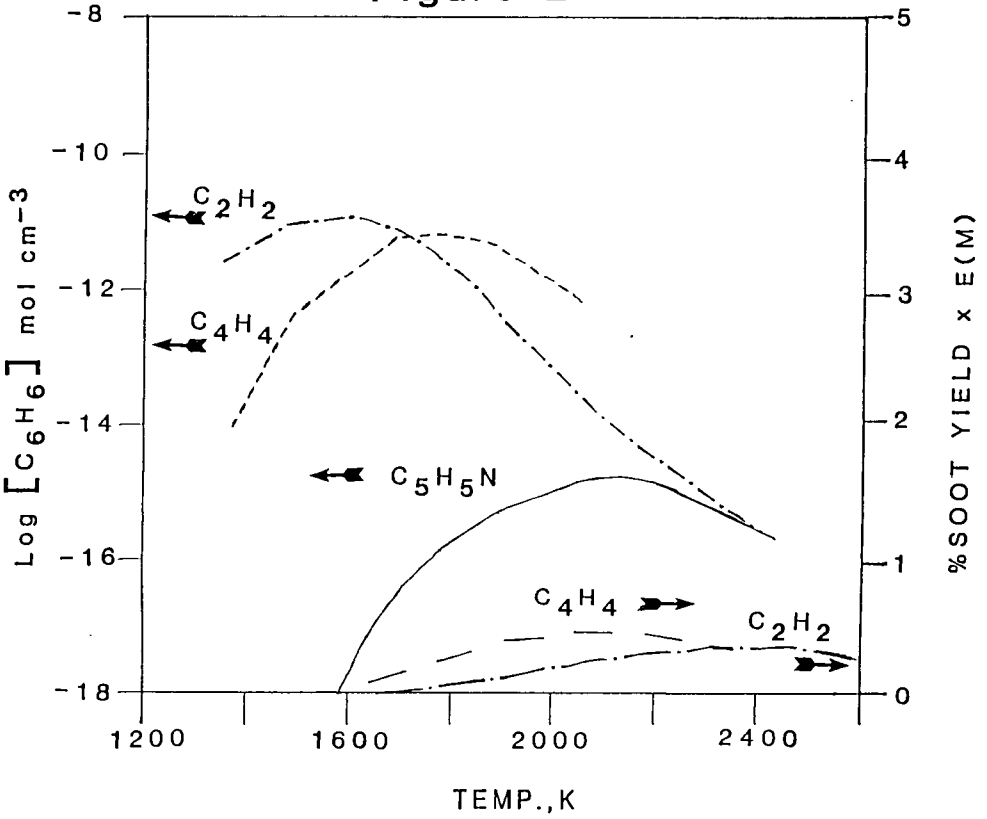
-8
-10
-12
-14
-16
-18
Log [C6H6] mol cm-3
5
4
3
2
1
0
%SOOT YIELD x E(M)
C2H2
C4H4
C5H5N
C4H4
C2H2
1200
1600
2000
2400
TEMP.,K

Figure 3

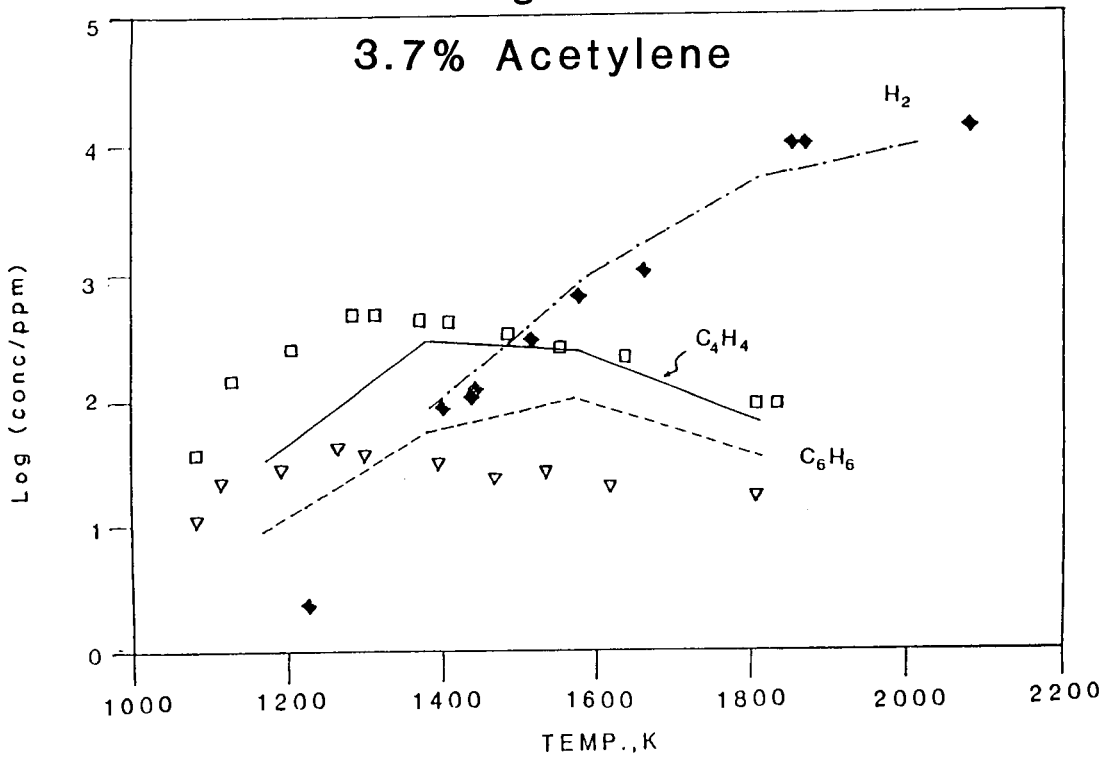
3.7% Acetylene
H2
C4H4
C6H6
Log (conc/ppm)
TEMP.,K
0
1
2
3
4
5
1000
1200
1400
1600
1800
2000
2200

Figure 4

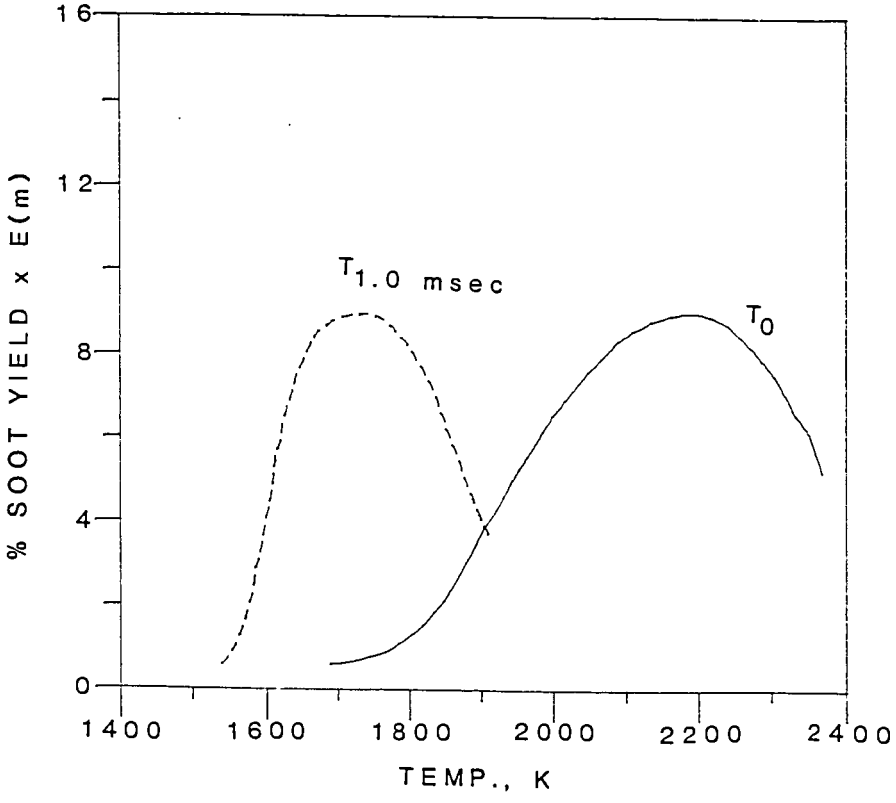
16
12
8
4
0
% SOOT YIELD x E(m)
$T_{1.0\ msec}$
T_0
1400
1600
1800
2000
2200
2400
TEMP., K

SHOCK-TUBE AND MODELING STUDY OF SOOT FORMATION IN MIXTURES OF HYDROCARBONS

M. Frenklach, T. Yuan and M.K. Ramachandra

Fuel Science Program
Department of Materials Science and Engineering
Pennsylvania State University
University Park, PA 16802

INTRODUCTION

Interest in soot formation in binary hydrocarbon mixtures has increased in recent years. Besides the very practical aspects of such knowledge, the subject is of interest from a fundamental point of view: to provide additional information for the elucidation of the soot formation mechanism. There is evidence, both experimental [1–8] and theoretical [9–11], that the key chemical reactions leading to soot formation in hydrocarbon systems are those between aliphatic and aromatic species. The importance of such reactions was suggested as early as 1960 by Stehling *et al.* [12].

This paper presents the results of a shock-tube pyrolysis study on soot formation from a series of binary hydrocarbon mixtures: benzene–additive, where the additives were acetylene, allene, vinylacetylene and 1,3–butadiene; and allene–acetylene, butadiene–acetylene and acetylene–hydrogen.

EXPERIMENTAL

The experiments were conducted behind reflected shock waves in a 7.62 *cm* i.d. shock tube [4–6]. Ten different mixtures were tested during the course of this study. The experimental conditions which were chosen such as to allow comparison with the previous results [5,6]. The experiments were carried out at temperatures from 1500 K to 2490 K, pressures from 1.3 to 3.1 bar, and carbon atom concentrations from 2.0 to 6.8×10^{17} atoms/cm^3. The appearance of soot was monitored by the attenuation of a He–Ne laser beam (632.8 nm) at approximately 10 mm from the end plate of the shock tube. The term soot has been used in our work as a lumped property meaning "species absorbing at a 632.8 nm". For its practical measure, the amount of carbon atoms accumulated in soot is used in this work. The latter property is calculated following the usual Raylegh approximation [13] using the complex refractive index of Dalzell and Sarofim [14].

The experimental results are presented for a reaction time of 1 ms; this time is chosen arbitrary — qualitatively similar results were obtained at all observation times.

RESULTS AND DISCUSSION

Acetylene–Hydrogen

Figure 1 depicts the comparison of soot carbon obtained in a acetylene–hydrogen mixture with those obtained at similar conditions from acetylene alone. As can be seen in this figure, hydrogen strongly suppresses soot formation from acetylene. Wang et al. [15] also observed the suppression effect of hydrogen in toluene–hydrogen mixtures. A chemical kinetic model [9,10] predicts this effect: addition of molecular hydrogen increases the reverse rate of the "reactivation", H–atom abstraction reactions.

Allene–Acetylene and Butadiene–Acetylene

Figures 2 and 3 present the amount of soot formed in mixtures of acetylene with allene and 1,3–butadiene, respectively, and a comparison with the results for the individual fuels. A pronounced synergistic effect is observed for these cases.

A computer simulation for the conditions of a butadiene–acetylene mixture with a mechanism of butadiene pyrolysis [10] qualitatively predicts the experimentally observed synergistic effect (the lack of quantitative agreement, as discussed previously [10,16], is due to insufficient knowledge of thermochemical data). The results of the computer simulation are given in Fig. 4. The analysis of the computational results revealed that the main factor affecting soot formation is the increase in the rate of acetylene–addition reactions. This accelerates cyclization reactions and suppresses decomposition of $n-C_xH_y$ radicals to C_2H_2 and $n-C_{x-2}H_{y-2}$. The reaction pathway to soot is similar to that identified for pyrolysis of butadiene [10], except that cyclization via

$$n-C_4H_5 + C_2H_2 \longrightarrow n-C_6H_7$$
$$n-C_6H_7 \longrightarrow c-C_6H_7$$
$$c-C_6H_7 \longrightarrow \text{benzene} + H,$$

becomes more prominent (yet still slower than the reaction sequence via $n-C_6H_5$ [9],

$$n-C_4H_3 + C_2H_2 \longrightarrow n-C_6H_5$$
$$n-C_6H_5 \longrightarrow \text{phenyl},$$

at the conditions of the soot yield maximum).

Based on the computational analysis of the butadiene–acetylene case, the experimental results obtained for allene–acetylene mixtures (Fig. 2) may indicate the importance of sequential addition of two acetylene molecules to $CH_2{=}C{=}CH\bullet$ radical followed by cyclization to a relatively stable benzyl radical. In other words, we propose that in an allene system the first–ring cyclization is not the formation of phenyl or benzene but rather that of benzyl.

Benzene–Additives

Figures 5 and 6 present the results obtained in mixtures of benzene with aliphatic hydrocarbons. Addition of acetylene (Fig. 5) enhances soot formation. However, the effect is pronounced only at relatively high (2.72 and 1.09 %) initial concentration of acetylene. With smaller amounts (0.54 %) of acetylene added, there is no significant increase in soot production; on the contrary, there is a slight suppression of soot formation at lower temperatures.

The main feature of the dominant reaction pathway to soot identified for benzene pyrolysis [10] is the formation of byphenyl by the addition of phenyl radical to benzene followed by sequential addition of two acetylene molecules to form pyrene. The initial presence of acetylene, as revealed by the results of a computer simulation using a benzene pyrolysis mechanism [10], increases the rate of the ring–growth process and suppresses the rate of phenyl fragmentation, both being promoting factors. However, reaction of acetylene with phenyl forming phenylacetylene removes phenyl radicals from a more efficient ring–forming pathway, addition to benzene molecules, which counteracts the promoting factors.

The experimental results reported in Fig. 6 show that vinylacetylene and 1,3–butadiene are more efficient soot promoters than acetylene. Soot–yield maxima in their mixtures with benzene are shifted to higher temperatures compared to that of benzene alone, which indicates that decomposition of the additives is important. The results of computer simulations, which reproduced (again, qualitatively) the experimental trends, support this conclusion. For instance, in the benzene–vinylacetylene case, decomposition of vinylacetylene via

$$C_4H_4 \longrightarrow C_4H_3 + H$$

initiates the pyrolysis. Reactions of C_4H_4, C_4H_3 and C_2H_3 enhance the growth of aromatics compared to the pyrolysis of benzene alone. For example, reaction sequence

$$\begin{aligned} Ph + C_4H_4 &\longrightarrow PhCHCHCCH + H \\ PhH + n\text{-}C_4H_3 &\longrightarrow PhCHCHCCH + H \\ PhCHCHCCH + H &\longrightarrow \bullet PhCHCHCCH + H_2 \\ \bullet PhCHCHCCH &\longrightarrow 2\text{-naphthyl}, \end{aligned}$$

where •PhCHCHCCH is an *ortho*–substituted phenyl radical, is accelerated with the addition of vinylacetylene to benzene.

The results obtained in a benzene–allene mixture (Fig. 4) indicate a synergistic effect. Thus, not only does allene have a high sooting tendency itself [6], but it appears to be also an efficient soot promoter.

ACKNOWLEDGEMENT

The work was supported by Aerochemistry Branch of NASA–Lewis Research Center, Grants Nos. NAG 3–477 and NAG 3–668.

REFERENCES

1. Bittner, J.D. and Howard, J.B., *Eighteenth Symposium (International) on Combustion*, p. 1105, The Combustion Institute, 1981.
2. Bittner, J.D. and Howard, J.B., in *Soot in Combustion Systems and its Toxic Properties* (J. Lahaye and G. Prado, Eds.), p. 57, Plenum, 1983.
3. Bittner, J.D., Howard, J.B. and Palmer, H.B., *ibid.* p. 95.
4. Cole, J.A., Bittner, J.D., Longwell, J.P. and Howard, J.B., *Combust. Flame* **56**, 51 (1984).
5. Frenklach, M., Taki, S. and Matula, R.A., *Combust. Flame* **49**, 275 (1983).
6. Frenklach, M., Taki, S., Durgaprasad, M.B. and Matula, R.A., *Combust. Flame* **54**, 81 (1983).
7. Frenklach, M., Ramachandra, M.K. and Matula, R.A., *Twentieth Symposium (International) on Combustion*, p. 871, The Combustion Institute, 1985.
8. Bockhorn, H., Fetting, F. and Wenz, H.W., *Ber. Bunsenges. Phys. Chem.* **87**, 1067 (1983).
9. Frenklach, M., Clary, D.W., Gardiner, W.C., Jr. and Stein, S.E., *Twentieth Symposium (International) on Combustion*, p. 887, The Combustion Institute, 1985.
10. Frenklach, M., Clary, D.W., Gardiner, W.C., Jr. and Stein, S.E., *Twenty-First Symposium (International) on Combustion*, in press.
11. Frenklach, M. and Warnatz, J., *Combust. Sci. Technol.* **51**, 265 (1987).
12. Stehling, F.C., Frazee, J.D. and Anderson, R.C., *Eighth Symposium (International) on Combustion*, p. 744, Williams and Wilkins, 1962.
13. Frenklach, M., Taki, S., Li Kwok Cheong, C.K. and Matula, R.A., *Combust. Flame* **51**, 37 (1983).
14. Dalzell, W.H. and Sarofim, A.F., *Trans. ASME* **91**, 100 (1969).
15. Wang, T.S., Matula, R.A. and Farmer, R.C., *Eighteenth Symposium (International) on Combustion*, p. 1149, The Combustion Institute, 1981.
16. Frenklach, M., Clary, D.W., Gardiner, W.C., Jr. and Stein, S.E., *Proc. 15th Int. Symp. Shock Waves and Shock Tubes* (D. Bershader and R. Hanson, Eds.), p. 295, Stanford University, 1986.

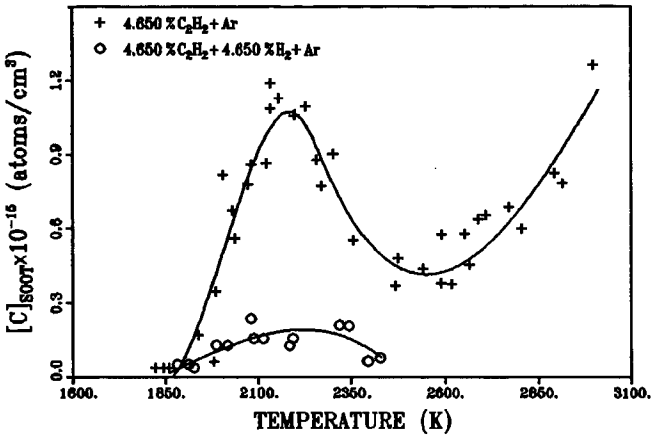

Figure 1. Comparison of soot carbon in pyrolysis of acetylene and acetylene-hydrogen mixture.

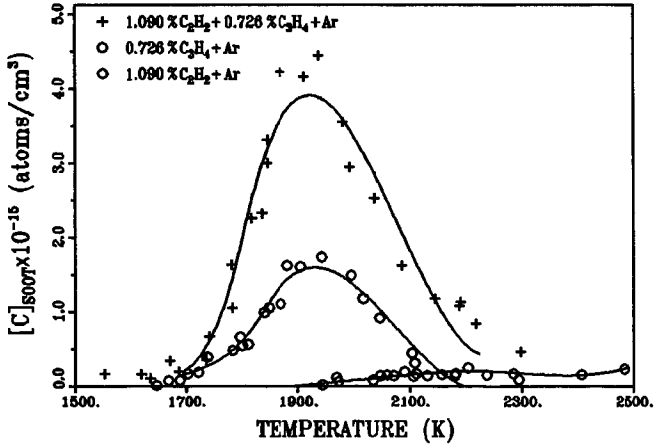

Figure 2. Comparison of soot carbon in pyrolysis of acetylene, allene, and acetylene-allene mixture.

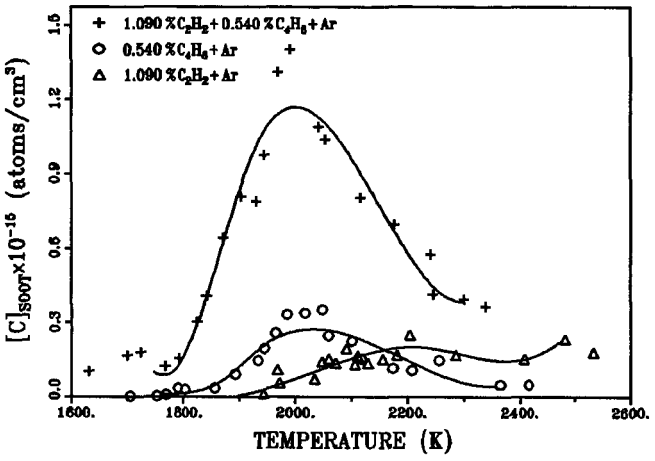

Figure 3. Comparison of soot carbon in pyrolysis of acetylene, 1,3-butadiene, and acetylene-butadiene mixture.

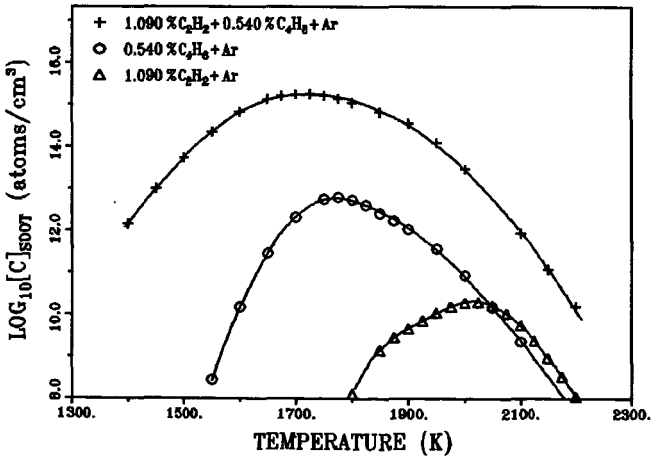

Figure 4. Comparison of computed soot carbon in pyrolysis of acetylene, 1,3-butadiene, and acetylene-butadiene mixture.

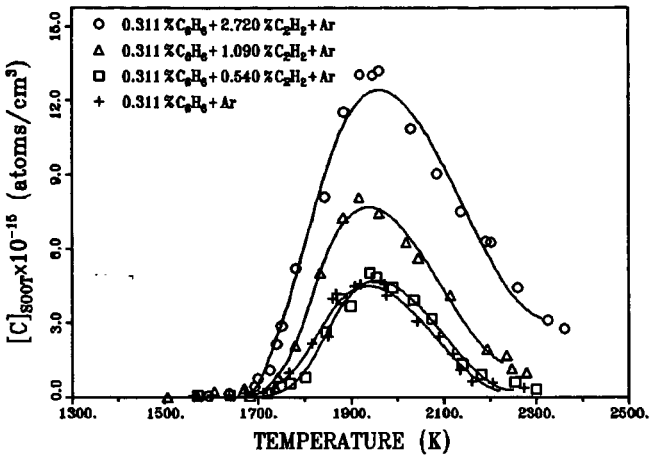

Figure 5. Comparison of soot carbon in pyrolysis of benzene, and benzene-acetylene mixture.

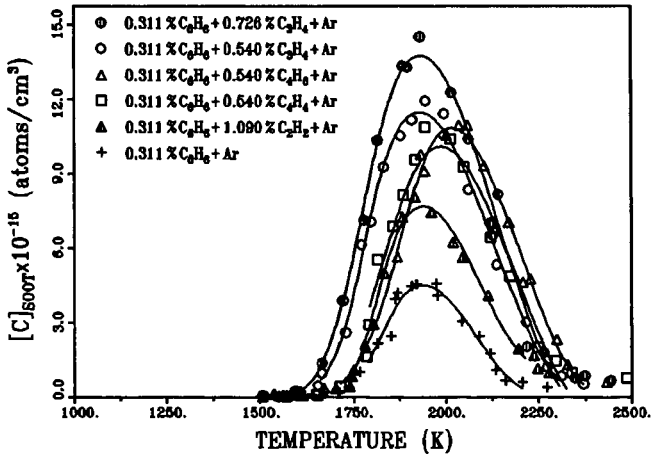

Figure 6. Comparison of soot carbon in pyrolysis of benzene, benzene-acetylene, benzene-allene, benzene-vinylacetylene, and benzene-butadiene mixtures.

THE MOLECULAR DISSOCIATION OF VINYLACETYLENE AND ITS IMPLICATIONS FOR ACETYLENE PYROLYSIS

John H. Kiefer and Kevin I. Mitchell

Department of Chemical Engineering
University of Illinois at Chicago
Chicago, Illinois 60680

Perhaps the most extensively investigated of all fuel pyrolyses is that of acetylene. The reasons are compelling: acetylene is a major product of virtually all hydrocarbon pyrolysis and oxidation, and its reactions usually govern the later states of such processes, in particular the formation of soot. Acetylene is evidently essential to soot formation (1,2), and has also been selected as the prototype fuel in a recent detailed model of the soot formation process (3).

Although C_2H_2 pyrolysis has been observed over an enormous range of temperature (700-3500K) (4-17), and by many different and usually reliable methods, there is little agreement even on its initiation. The process looks much like a single second-order reaction over 700-2500K (5,7) and the early products are commonly dominated by multiples of the C_2H_2 unit. In particular, there is good evidence that vinylacetylene (C_4H_4, 1-buten-3-yne) is the sole initial gaseous product below 1500K (4-8). This all suggests C_2H_2 pyrolysis is largely a molecular polymerization, but the reaction also shows induction periods (11,15), a sensitivity to NO (15), rapid isotopic scrambling in C_2H_2-C_2D_2 mixtures (6), as well as minor products suggestive of radical intermediates (6,9,14). All this of course implies chain reaction, and most recent workers (7,9,10,12,17) have described this pyrolysis as an H-atom chain initiated by

$$2C_2H_2 \rightarrow C_4H_3 + H \qquad 1)$$

There are also some interesting attempts to reconcile the evidence for chain and molecular reaction which postulate an intermediate triplet C_2H_2 (1,2-diradical) (5,7,18).

Given the effort expended on C_2H_2 pyrolysis the lack of consensus is striking. Much of this must simply reflect the complexity of the process. As noted by Palmer and Dormish (7), it is quite unlikely the same mechanism applies for all conditions. Certainly at very high temperatures, above 2500K, the reaction is a degenerate branched chain (10) which is probably initiated by simple dissociation. In the flow and static reactor studies below 1000K there is obviously a large heterogeneous component (5,7). At the lower temperatures impurities could readily compete as a source of chain initiation.

Some of the above complications may be avoided by observing the reverse process, which could well be the dissociation of vinylacetylene. Decomposition of C_4H_4 has recently been studied in the shock tube by Colket (9) and Hidaka et al. (19). They again suggest a radical chain mechanism initiated by

$$C_4H_4 \rightarrow C_4H_3 + H \qquad 2)$$

although they derive activation energies for this of 80-85 kcal/mol, which do seem low. The dominant products are C_4H_2 and C_2H_2 with a very consistent C_2H_2/C_4H_2 ratio of 5-10.

In a collaboration with R. D. Kern (20) we have reinvestigated the C_4H_4 decomposition at very high temperatures (1500-2500K) where the unimolecular dissociation should dominate, using laser-schlieren (LS) and

time-of-flight (TOF) mass spectroscopy techniques on shock waves. Here we present a brief reiteration of the C_4H_4 results together with their implications for the C_2H_2 pyrolysis, implications which have led to the proposal of a new mechanism for this reaction.

EXPERIMENTAL

Both the LS (2 and 4% C_4H_4 - Kr, 1650-2500K, 110-427 torr) and TOF (2% C_4H_4 - Ne, 1500-2200K, 150-300 torr) measurements used apparatus and procedures which have been fully described (21,22). Vinylacetylene was obtained from Wiley Organics, degassed and distilled for purification, finally showing no more than ~0.1% impurities. Thermodynamic properties of C_4H_4 were calculated from molecular properties (23), using an estimated $\Delta H^o_{f,298}$ = 69 kcal/mol (24). A more detailed description of the experiments and calculations will be found in ref. (20).

RESULTS

Example LS semilog density gradient profiles are presented in Figure 1. The important feature here is the upward concave shape. This concavity is consistent throughout the LS experiments and shows there can be no significant chain reaction in C_4H_4 pyrolysis. A chain will accelerate the endothermic decomposition producing a convex profile. For example, in benzene (25) and pyridine (26), which evidently dissociate by C-H scission, this acceleration is so severe it generates a local maximum. The likely consequences of such a chain in C_4H_4 are shown in Figure 2 where we have modeled one LS experiment with a "reasonable" chain mechanism, initiated by reaction 1) (see ref. (20) for details). As expected, the result is a strongly convex profile in complete disagreement with the measurements. In fact, even a small contribution from such a chain is excluded. In Figure 2 we also show the sensitivity to small amounts of chain reaction. Even 1% dissociation through reaction 1) produces noticeable deviation.

The TOF profiles also argue against a chain initiated by reaction 1). They show C_2H_2 and C_4H_2 as major products with C_2H_2/C_4H_2 ~5 independent of temperature (or even time) in essential agreement with the other recent shock tube studies (9,19). The problem is any chain initiated by 1) cannot maintain the required dominance of C_2H_2 at high temperatures where the products mainly arise from dissociation (and abstraction). Such a chain then produces the great excess of C_4H_2 shown in Figure 3.

The product distribution and the absence of discernable chain reaction suggest the main channel for C_4H_4 dissociation must be

$$C_4H_4 \rightarrow 2C_2H_2 \qquad 3)$$

With almost no chain much of the C_4H_2 product must be formed through

$$C_4H_4 \rightarrow C_4H_2 + H_2 \qquad 4)$$

We have modeled the LS and TOF data using just these two reactions with the uniformly excellent results exemplified in Figures 1,2, and 4. Rate constants for the sum of reactions 3) and 4) (both have ΔH^o_{298} very near 40 kcal/mol), derived from the zero-time density gradients, are shown in Figure 5. Here we also show a "routine" RRKM model fit to these data. This model

projects an effective barrier of 79.5 ± 3 kcal/mol and an activation energy for k_∞ of 82.5 kcal/mol, consistent with the results of both Colket (9) and Hidaka et al. (19).

DISCUSSION

A mechanism for the above molecular dissociation channels is suggested by recognizing the vinylacetylene as a substituted ethylene, which like ethylene has no weak bonds. The primary dissociation channel in C_2H_4 is now known to be H_2 elimination (27,28). This evidently involves a 1,1-elimination to singlet vinylidene ($:C=CH_2$) (29) which very rapidly isomerizes to C_2H_2 (30). We now propose that C_4H_4 dissociates analogously - by 2,2-elimination of C_2H_2

$$C_4H_4 \rightarrow :C=CH_2 + C_2H_2 \qquad 3)$$
$$\text{fast} \rightarrow C_2H_2$$

or 1,1-elimination of H_2

$$C_4H_4 \rightarrow :C=CH-C\equiv CH + H_2 \qquad 4)$$
$$\text{fast} \rightarrow C_4H_2$$

We expect similar barriers for these two paths with a lower A-factor for separation of the much lighter H_2. This is then consistent with the predominance of product C_2H_2 and the near constancy of the C_2H_2/C_4H_2 ratios.

The latest value for the heat of formation of singlet vinylidene is 97.7 ± 2 kcal/mol, 43.5 kcal/mol above acetylene (31). Actually this is an upper limit and lower values have been proposed (32). The heat of reaction for $C_4H_4 \rightarrow :C=CH_2 + C_2H_2$ is then $\Delta H^\circ_{293} \leq 54.2 + 97.7 - 69 = 84.9$ kcal/mol, which would drop to below 83 kcal/mol at 0°K. This reaction should have little reverse barrier, so 83 kcal/mol should exceed the forward barrier, and this is quite close enough to the 79.5 ± 3 kcal/mol obtained from the RRKM fit to the LS data.

By detailed balance, observation of the unimolecular dissociation of vinylacetylene to two acetylenes, reaction 3), establishes that a direct dimerization of acetylene to vinylacetylene does indeed occur. The only remaining phenomenological question is whether this can account for the entire second-order rate seen in C_2H_2 pyrolysis. We have calculated equilibrium constants for 3), and second-order rate constants for its reverse, using the k_∞ obtained from the RRKM calculations (this choice is discussed below). The result is compared to a schematic summary of the C_2H_2 dimerization data in Figure 6. Here the agreement with the (homogeneous) shock-tube data (4,6,9,12,17) and with the results of Palmer and Dormish (7) (which were corrected for heterogeneous reaction) is very good. The low temperature data (<1000K) may well have other problems besides heterogeneous reaction (see below), but this detailed balance calculation is anyway much too sensitive to the heat of formation of C_4H_4 at such low temperatures. A reduction of just 2 kcal/mol in this estimated ΔH°_f will actually produce an excellent fit throughout. In any case it is clear that simple dimerization to C_4H_4 is a major part of what goes on in C_2H_2 pyrolysis.

The detailed mechanism of the C_2H_2 dimerization would now be isomerization to vinylidene followed by insertion of this into the C-H bond of acetylene (33)

$$C_2H_2 \rightarrow :C{=}CH_2 \qquad 5)$$

$$:C{=}CH_2 + C_2H_2 \rightarrow C_4H_4 \qquad 6)$$

As long as 5) is equilibrated, the overall forward and reverse rates are still related by the equilibrium constant for 3). However, it is perfectly possible for 5) to be slow enough at low temperatures to generate a detectable induction period.

Although the calculated rates of dimerization to C_4H_4 in Figure 6 seem to account for the entire second-order rate above 1000K, this is rather misleading. Additional reaction paths are probably still necessary at both ends of the temperature range, i.e., outside 1000-1500K. For T>1500K the RRKM calculations show noticeable falloff even for the high pressures (3-10 atm) of the reflected shock experiments in Figure 6 (4,6,12). The use of k_∞ in the detailed balance calculation is then no longer valid, and the rates will begin to fall below the measured second-order data. However, consideration of the following reaction-enthalpy diagram

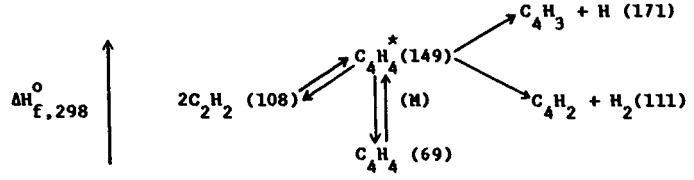

shows that when deactivation to C_4H_4 slows at high temperature (and/or low pressure) it opens the channels

$$2C_2H_2 \rightarrow C_4H_2 + H_2 \qquad 7)$$

$$2C_2H_2 \rightarrow C_4H_3 + H \qquad 8)$$

These will now act to "pull" the dimerization forward, at least partially compensating for the falloff in C_4H_4 formation. The chain initiated by 8) can also convert both C_2H_2 and any residual C_4H_4 to C_4H_2 and higher polyacetylenes, particularly at very high temperatures. Note that here neither 7) nor 8) can proceed till there is falloff of the deactivation, i.e., above about 1500K. The onset of these two channels may provide a reasonable explanation for the crossover from C_4H_4 to C_4H_2 in C_2H_2 pyrolysis which occurs around 1500-1600K (6,7,9). However, a quantitative modeling on this basis may be quite difficult below 1600K, where production of H-atom through reaction 8) must be very slow and could be overwhelmed by impurity generation. We would also suggest the isotopic scrambling in C_2H_2/C_2D_2 mixtures (6), alluded to earlier, probably requires very little H-atom (34) which could be generated by a small contribution from 8) and/or various impurities.

Below 1000K the situation may be even more complex. The pyrolysis now involves polymer, tar, and char formation and has a significant heterogeneous component (5,7,11). Minor products which suggest chain reaction may be generated by polymer carbonization, heterogeneous reaction, or for that matter, impurity initiated chain reaction.

Finally, we offer a highly tentative explanation for the polymer formed at the lowest temperatures. Usually carbenes preferentially insert into multiple bonds (33), so the dominant insertion product should be methylenecyclopropene. This has now been synthesized (35,36) and is quite unstable. For one thing it evidently polymerizes (36); at high temperatures it probably reverts to C_2H_2. This suggestion is closely analogous to the triplet diradical schemes (5, 7, 18) and can deal with the same phenomena. In addition to the right energetics, it also has the advantage of fading out at high temperatures where the methylenecyclopropene reverts to acetylene.

1.) H. B. Palmer and C. F. Cullis, "The Chemistry and Physics of Carbon", (P. L. Walker, Ed., Dekker, New York) 1, 265 (1985).
2.) S. J. Harris and A. M. Weiner, Comb. Sci. and Tech. 31, 155 (1983); 32, 267 (1983).
3.) M. Frenklach, D. W. Clary, W. C. Gardiner, Jr., and S. E. Stein, 20th (Int'l) Symposium on Combustion, The Combustion Institute, Pittsburgh, 1984, p 887.
4.) G. B. Skinner, and E. M. Sokoloski, J. Phys. Chem., 64, 1952 (1960).
5.) C. F. Cullis and N. H. Franklin, Proc. Roy. Soc. (London) A280, 139 (1964).
6.) H. Ogura, Bull. Chem. Soc. Jpn. 50, 1044 (1977).
7.) H. B. Palmer and F. L. Dormish, J. Phys. Chem. 68, 1553 (1964).
8.) C. F. Cullis and I. A. Read, Trans. Fara. Soc. 66, 920 (1970).
9.) M. B. Colket, presented at the 21st (Int'l) Symposium on Combustion, Munich, 1986.
10.) T. Tanzawa and W. C. Gardiner, Jr., 17th (Int'l) Symposium on Combustion, The Combustion Institute, Pittsburgh, 1978, p 563; J. Phys. Chem. 84, 236 (1980).
11.) C. G. Silcocks, Proc. Roy. Soc. (London) A242, 411 (1957).
12.) C. F. Aten and E. F. Greene, Combust. Flame 5, 55 (1961).
13.) G. D. Towell and J. J. Martin, AIChE J. 7, 693 (1961).
14.) M. S. B. Munson and R. C. Anderson, Carbon 1, 51 (1963).
15.) G. J. Minkoff, D. M. Newitt, and P. V. Rutledge, J. Appl. Chem. 7, 406 (1957).
16.) M. A. Nettleton, Ph.D. Thesis, University of London (1960).
17.) I. D. Gay, G. B. Kistiakowsky, J. V. Michael, and H. Niki, J. Chem. Phys. 43, 1729 (1965).
18.) G. J. Minkoff, Can. J. Chem. 36, 131 (1958).
19.) Y. Hidaka, K. Tanaka, and M. Suga, Chem. Phys. Lett. 130, 195 (1986).
20.) J. H. Kiefer, K. I. Mitchell, R. D. Kern, and J. N. Yong, Submitted to J. Phys. Chem.
21.) M. Z. Al-Alami and J. H. Kiefer, J. Phys. Chem. 87, 499 (1983).
22.) M. J. Singh and R. D. Kern, Combust. Flame, 54, 49 (1983).
23.) E. Tørnberg, C. J. Nielsen, P. Klaeboe, H. Hopf, and H. Priebe, Spectrochimica Acta 36A, 975 (1980).
24.) S. W. Benson, "Thermochemical Kinetics", 2nd ed. , Wiley, New York, 1976.
25.) J. H. Kiefer, L. J. Kizerka, M. R. Patel, and H. C. Wei, J. Phys. Chem. 89, 2013 (1985).
26.) R. D. Kern, J. N. Yong, J. H. Kiefer , and J. N. Shah, to be published.
27.) J. H. Kiefer, S. A. Kapsalis, M. Z. Al-Alami, and K. A. Budach, Combust. Flame 51, 79 (1983).
28.) Th. Just, P. Roth, and R. Damm, 16th (Int'l) Symposium on Combustion, The Combustion Institute, Pittsburgh, 1976, p 961, T. Tanzawa and W. C. Gardiner, Jr., Combust. Flame 39, 24 (1980).

29.) K. Raghavachari, M. J. Frisch, J. A. Pople, and P. von R. Schleyer, Chem. Phys. Lett. 85, 145 (1982).
30.) P. S. Skell, F. A. Fagone, and K. J. Klabunde, J. Am. Chem. Soc. 94, 7862 (1972); J. A. Pople, K. Raghavachari, J. H. Frisch, J. S. Brinkley, and P. von R. Schleyer, J. Am. Chem. Soc. 105, 6389 (1983); T. Carrington, Jr., L. M. Hubbard, H. F. Schaefer III, and W. H. Miller, J. Chem. Phys. 80, 4347 (1984).
31.) P. Davidson, H. M. Frey, and R. Walsh, Chem. Phys. Lett. 120, 227 (1985).
32.) J. S. Binkley, J. Am. Chem. Soc. 106, 603 (1984), and references therein.
33.) J. A. Berson, in "Rearrangements in Ground and Excited States", Academic Press, New York, 1980, p 311. See also P. J. Stang, Chem. Rev. 78, 383 (1978).
34.) A. Lifshitz, M. Bidani, and H. F. Carroll, J. Chem. Phys. 79, 2742 (1983).
35.) W. E. Billups, L-J. Lin, and E. W. Casserly, J. Am. Chem. Soc. 106, 3698 (1984)
36.) S. W. Staley and T. D. Norden, J. Am. Chem. Soc. 106, 3699 (1984).

PREDICTION OF KINETICS FOR C_4 SPECIES WHICH FORM BENZENE

Phillip R. Westmoreland

Chemical Engineering Department
University of Massachusetts - Amherst
Amherst, Massachusetts 01003

INTRODUCTION

C_4 species have long been proposed to be critical intermediates in forming aromatics from lighter aliphatics. Recent work (**1**) supports the hypotheses that 1-buten-3-ynyl (1-C_4H_3) and 1,3-butadienyl (1-C_4H_5) are the specific species involved in low-pressure flames of acetylene (C_2H_2) and 1,3-butadiene (1,3-C_4H_6).

1-C_4H_3 and 1-C_4H_5 have been suggested before as the key reactants (**2-6**), but the recent work shows that the earlier, thermal mechanisms are not justified; rather, only chemically activated pathways are feasible. Earlier studies generally assumed addition to C_2H_2, followed by thermal cyclization of the linear adduct to phenyl and cyclohexadienyl, respectively, and by thermal decomposition of the cyclohexadienyl to benzene and H. All reactions were implicitly assumed to be in the high-pressure limit. However, appropriate analysis of falloff indicates that this thermal sequence is too slow, even at 1 atm, while chemically activated intermediates from the same addition reactions lead directly to aromatics with fast enough rate constants.

Identifying the sources of 1-C_4H_3 and 1-C_4H_5 is plainly of interest. Literature analyses (**2-6**) assumed these sources were addition of C_2H and C_2H_3 to C_2H_2, again (implicitly) in the high-pressure limit. Also, the quantitative test in (**1**) was comparison of the measured, net rate of benzene formation to a rate calculated from predicted rate constants and the measured C_2H_2, C_4H_3, and C_4H_5 concentrations. An improved test would use concentrations of the specific isomers 1-C_4H_3 and 1-C_4H_5, which could not be resolved from other C_4H_3 and C_4H_5 isomers experimentally.

Rates are predicted and compared here for the reactions that form and destroy 1-C_4H_3, 1-C_4H_5, and other C_4H_3 and C_4H_5 isomers. Rate constants are estimated by analogy and thermochemical kinetics (**7**) for H-abstraction from 3-butenyne (C_4H_4 or vinylacetylene) and from 1,3-C_4H_6. Using Bimolecular Quantum-RRK (**8-9**), rate constants, branching and pressure dependence are predicted for the association reactions of radical addition ($C_2H+C_2H_2$ and $C_2H_3+C_2H_2$), H-addition (to C_4H_2 and C_4H_4), and H/radical and radical/radical recombination (H+C4 radicals, $C_2H+C_2H_3$ and $C_2H_3+C_2H_3$).

EXPERIMENTAL AND THEORETICAL PROCEDURES

Experimental data. - Profiles of mole fractions were mapped for 38 stable species and free radicals in a lightly sooting flat flame of $C_2H_2/O_2/5\%$ Ar (**10**) using molecular-beam mass spectrometry. The fuel-equivalence ratio was 2.40, burner velocity (298 K) was 0.50 m/s, and pressure was 2.67 kPa (20 torr). Temperatures were measured using a 0.076-mm diameter Pt/Pt-13%Rh thermocouple, coated with a thin BeO/Y_2O_3 glass to eliminate catalytic heating and resistively heated to the flame temperature so as to eliminate convective heat transfer. Mole fractions were shifted 0.11 mm toward the burner (two orifice diameters), compensating for the shift caused by the probe.

Direct and indirect calibrations were used, and the smoothed data curves were used in the present calculations. Major stable species were calibrated directly within 3% except for H_2O (25%). Minor species were calibrated within a factor of two by the method of relative ionization cross-sections (**11**). Because of the correction for ^{13}C isotope effects and the low signals, the shapes of the radical profiles are less well defined than those of the minor stable species.

Complete profiles for all species of interest except C_2H and O were measured. For C_2H and O-atom in the present calculations, mole fractions were predicted (**10**) using a modified Warnatz (**12-13**) reaction mechanism.

Predicted rate constants. - Two types of reactions were considered: abstractions of H and association reactions, which include additions, combinations, and (by microscopic reversibility) unimolecular decompositions. Abstraction rate constants and high-pressure-limit association rate constants may be estimated by simple analogies or by more complex analogies such as thermochemical kinetics. However, as noted above, proper consideration of pressure effects is necessary for association reactions. Even at 1 atm and for relatively large molecules, these effects can be significant at combustion temperatures (**14**).

Bimolecular Quantum-RRK (**8-9**) was used here to predict falloff for addition and combination reactions. The method also predicts rate constants for the chemically activated decomposition paths, which numbered as many as three in the present study. These rate constants are also influenced by pressure but have an inverse falloff behavior (pressure-independent at low pressures (**9**)). Input data needed for the method are high-pressure-limit, Arrhenius pre-exponential factors and activation energies for each association and dissociation step; geometric mean frequency and number of frequencies in each adduct; and collisional properties of adduct and bath molecules.

Arrhenius parameters A and E_{act} were estimated for one direction of reaction, and the parameters for the reverse reaction then were calculated using the equilibrium constant (microscopic reversibility). For example, rate constants

for radical combinations were estimated by an extension (**10**) of a method of Benson (**15**) and were assumed independent of temperature.

ESTIMATION OF THERMODYNAMICS AND OF RATE CONSTANTS

Species involved in the reactions to be analyzed include H, H_2, O, OH, H_2O, C_2H, C_2H_2, C_2H_3, C_2H_4, C_4H_2, C_4H_4 (vinylacetylene), 1,2,3-C_4H_4 (butatriene), 1,3-C_4H_6, and the C_4H_3 and C_4H_5 radicals. Few data are available for the thermodynamics and kinetics of C4 species. The necessary data may be estimated with useful accuracy, but data uncertainties and their effects must be examined.

Thermodynamics. - These properties (Table 1) were estimated using group additivity. The groups of Benson (**7**) were supplemented by the recent groups for unsaturates and rings by Stein and Fahr (**16**). Additional groups for vinyl (ethenyl) and ethynyl radical sites were derived from the heats of formation (298 K) of 70.4 kcal/mol for C_2H_3 (**17**) and 135 kcal/mol for C_2H (inferred from (**18**)). These values appear reliable, but other values as low as 63 and 127 have been suggested.

Structural assignments must be made in order to apply group additivity to the C_4H_3 and C_4H_5 radicals. For 1-C_4H_3 or 1-C_4H_5, the radical site is on a terminal alkene carbon, and properties are inferred by analogy of 1-C_4H_3/C_4H_4 or 1-C_4H_5/1,3-C_4H_6 with C_2H_3/C_2H_4. Similarly, properties of the $CH_2CHCC\cdot$ radical can be estimated from C_4H_4 and C_2H/C_2H_2, and for HCC-CH=CH·, from 1-butyne and C_2H_3/C_2H_4. Even for HCC-CH·-CH_3, the species is easily treated as an allylic radical of 1-butyne.

The remaining two radicals, HCC-C·=CH_2 (2-C_4H_3) and CH_2=CH-C·=CH_2 (2-C_4H_5), are more difficult. No groups are available for vinylic radical sites like these that are created inside conjugated pi-bond systems. Instead, thermodynamics are estimated for equivalent resonance structures for 2-C_4H_3 and 2-C_4H_5, respectively ·CH=C=C=CH_2 and ·CH_2-CH=C=CH_2. The first, allenic radical is assumed to be formed with the 110 kcal/mol bond dissociation energy of C_2H_4, while the second radical is treated as a simple allylic site.

The properties are summarized in Table 1. In addition, necessary geometric-mean frequencies were estimated from frequency assignments and are included in Table 1. Rougher estimates could have been used, as the quantized energy distribution is not affected greatly.

Table 1. Estimated thermodynamic properties and geometric-mean frequencies (enthalpy in kcal/mol; entropy in cal/mol K).

	ΔHf,298	S298	Cp (cal/mol K) at T (K)=								<ω>,
			300K	400	500	600	800	1000	1500	2000	cm-1
C_2H	135.0	49.6	8.9	9.7	10.2	10.7	11.5	12.2	13.3	14.1	
C_2H_3	70.4	54.5	10.9	12.4	13.8	15.1	17.2	18.8	21.3	23.2	
C_4H_2 (HCC-CCH)	105.1	59.8	17.6	20.1	21.9	23.2	25.1	26.6	29.1	30.5	
1-C_4H_3 (HCC-CH=CH.)	126.1	66.5	17.2	20.1	22.4	24.4	27.2	29.2	32.7	34.4	1000
2-C_4H_3 (HCC-C·=CH_2)	138.7	68.3	17.5	20.2	22.5	24.4	27.4	29.6	33.2	34.7	1040
CH_2=CH-CC·	149.2	65.3	15.8	18.8	21.4	23.5	26.9	29.3	33.0	34.4	
C_4H_4 (vinylacetylene)	68.2	65.1	17.5	21.2	24.2	26.6	30.3	33.1	37.6	39.7	1080
123-C_4H_4 (butatriene)	80.9	63.1	18.0	21.5	24.4	26.9	30.7	33.5	37.7	39.5	
1-C_4H_5 (CH_2=CH-CH=CH·)	84.2	68.7	18.6	23.3	26.8	29.5	33.6	36.5	41.4	44.1	1140
2-C_4H_5 (CH_2=CH-C·=CH_2)	72.2	69.9	18.5	22.9	26.5	29.4	34.0	37.4	42.5	44.6	1160
HCC-CH_2-CH_2·	85.6	70.7	19.4	23.3	26.5	29.3	33.5	36.7	42.6	46.2	1450
HCC-CH·-CH_3	96.6	73.1	18.8	22.4	25.5	28.3	32.7	36.1	41.5	43.9	1530
1,3-C_4H_6 (butadiene)	26.3	66.6	19.0	24.3	28.5	31.8	36.9	40.5	46.3	49.9	1190
1-butyne	39.6	69.6	19.5	23.9	27.7	30.9	36.1	40.0	47.1	51.7	
2-butyne	35.0	68.2	18.7	22.7	26.4	29.7	35.2	39.3	45.5	49.2	

Radical additions. - Additions of C_2H and C_2H_3 to acetylene are the routes to 1-C_4H_3 and 1-C_4H_5 that have been assumed in previous analyses (**2-6**). One reason is that such addition leads only to an end radical on the C4 adduct. Less recognized is that the adduct is initially rovibrationally excited (chemically activated) by the depth of the potential well where the ground-state adduct is located. Falloff can occur, and chemically activated decomposition of the hot adduct is possible to form H+C_4H_2 or H+C_4H_4. Thus, 1-C_4H_3 and H+C_4H_2 are not different types of C_2H+C_2H_2 reactions but different product channels from the same addition.

Calculation shows that the decomposition channels dominate over the simple additions for both these reactions over the range of 900 to 2000 K at 2.67 kPa CO. Even at 1 atm N_2, H+C_4H_2 is faster than the 1-C_4H_3 channel by a factor of 3 or more. For C_2H_3+C_2H_2 at 1 atm N_2, the addition/stabilization channel to 1-C_4H_5 is faster than addition/decomposition to H+C_4H_4 up to 1350 K, but the 1-C_4H_5 channel has fallen off to 1% of the high-pressure limit at 2000 K.

H-atom additions. - Addition of H to C_4H_2 or C_4H_4 also can form C_4H_3 and C_4H_5 radicals. In this case, the H can add (in principle) to any carbon, giving different isomers, and some chemically activated decompositions of the adducts may occur.

H-addition to the end carbons of C_4H_2 forms (2-C_4H_3)*, which can only be stabilized if 1,3-H shifts are disallowed. Addition to the internal carbons forms 1-C_4H_3 and C_2H+C_2H_2· in the reverse of the radical addition sequence described above. Calculation shows that falloff makes the 2-C_4H_3 product of H+C_4H_2

negligible, as the rate constants (2.67 kPa, 1500 K) are $2.6 \cdot 10^{11}$, $1.1 \cdot 10^{11}$, and $1.6 \cdot 10^{9}$ $cm^3 mol^{-1} s^{-1}$ for 1-C_4H_3, $C_2H+C_2H_2$, and 2-C_4H_3. $C_2H+C_2H_2$ begins to dominate at 1600 K for 2.67 kPa, but 1-C_4H_3 remains dominant even at 2000 K at 1 atm.

The product spectrum from $H+C_4H_4$ is more complex because addition to each different carbon gives a different adduct. Of the additions forming (1-C_4H_5)* and (2-C_4H_5)*, $C_2H_3+C_2H_2$ dominates at 1500 K and 2.67 kPa ($2.2 \cdot 10^{12}$), followed by 1-C_4H_5 ($7 \cdot 10^{11}$), 2-C_4H_5 ($2.5 \cdot 10^{11}$), and H+butatriene ($6 \cdot 10^{10}$). Addition/stabilization to 1-C_4H_5 is dominant at 1 atm to 1900 K. Here, as for radical addition, C_4H_5 formation is less inhibited by falloff than is C_4H_3 formation.

Radical/radical and H/radical combinations. - Combination reactions have not generally been considered as paths to C_4 radicals. However, chemically activated decompositions to $H+C_4H_x$ are possible from C_2H_3 combinations with C_2H, forming $(C_4H_4)^*$, and with itself, forming $(C_4H_6)^*$. Combinations of H with C_4H_x radicals are also of interest as sinks and as reactive-isomerization reactions for the radicals.

Formation of 1-C_4H_3 +H is dominant at 2.67 kPa for both $C_2H+C_2H_3$ and for 2-C_4H_3 +H reactions. Thermalized C_4H_4 is the only other significant product from 2-C_4H_3 +H, while $C_2H+C_2H_3$ forms minor amounts of C_4H_4 and 2-C_4H_3 +H. From the reaction of 1-C_4H_3 +H, formation of C_4H_4 is strongly favored at both pressures.

In contrast, $C_2H_3+C_2H_3$ leads predominantly to thermalized 1,3-C_4H_6. The 2-C_4H_5 +H and 1-C_4H_5 +H channels are within an order of magnitude of the C_4H_6 channel at 1500 K and 2.67 kPa, but C_4H_6 formation is even more strongly favored at 1 atm. Both C_4H_5+H channels are similarly dominated by C_4H_6 formation.

Thermal decompositions. - Thermal elimination of H by beta-scission can be an important loss mechanism for radicals. Thermal decompositions of molecules require more thermal activation and are usually not important in flames. In both cases, the kinetics may be calculated from unimolecular reaction theory, using the parameters developed for cases above, or from microscopic reversibility, using the rate constants developed above. In summary, elimination of H proved to be the dominant channel for the radicals, while formation of H + 1-C_4H_3 or 1-C_4H_5 was most important for decomposition of the molecules.

Application to flame data. - Only a few reactions prove to be important in determining the totals of formation and destruction rates.. The above rate constants were combined with measured concentrations and temperature profiles to establish the dominant production and destruction channels of 1-

C_4H_3, 2-C_4H_3, 1-C_4H_5, and 2-C_4H_5. Rates were calculated as a function of position and also were integrated over distance.

1-C_4H_3, the apparent precursor of phenyl, is formed two orders of magnitude faster than 2-C_4H_3. This difference would give super-equilibrium concentrations of 1-C_4H_3 because equilibrium levels of 2-C_4H_3 should exceed 1-C_4H_3. Formation of 1-C_4H_3 is primarily by H atom reactions with C_4H_2 (addition) and with C_4H_4 (abstraction), while destruction is dominated by loss of H to form C_4H_2.

One puzzle is that the integrated amount of destruction should be less than or equal to the integrated rate of formation. However, the predicted destruction is greater by a factor of 20. One possible reason is error in the C_4H_3 calibration, as the destruction rate is proportional to C_4H_3 concentration, while formation is independent of it. An alternative is that some formation reaction is not considered. $C_2H_2+C_2H_2$ was examined using a literature rate constant (19) but it was three orders of magnitude too slow to make any difference.

1-C_4H_5 was formed only at 45% of the rate of 2-C_4H_5, in contrast to the C_4H_3 isomers. For both isomers, hydrogen abstraction by H was the principal source, with H+C_4H_4 (addition) and thermal decomposition of 1,3-C_4H_6 making up 1/10 to 1/3 of the total rate. Simple addition to form 1-C_4H_5 was important only very early in the flame. This mix is illustrated in Figure 1. Total destruction was higher then formation for C_4H_5's by a factor of ten. Again, either calibration error or a missing source reaction are suggested as reasons for this difference.

CONCLUSIONS

Formation of 1-C_4H_3 and 1-C_4H_5 radicals is dominated by H-abstraction and H-addition. In contrast, previous workers had assumed that addition of C_2H and C_2H_3 to C_2H_2 were responsible. This conclusion is qualified by the excessive destruction that is predicted, but calibration error may be the cause. Detailed experimental data, combined with careful, comprehensive theoretical predictions of rate constants, account for this new understanding.

This study is continuing, further examining the rate constants and using them in predictive flame mechanisms.

ACKNOWLEDGEMENTS

Support of this C4 study by the University of Massachusetts is gratefully acknowledged. The interest and insights of Professor Jack B. Howard, Professor John P. Longwell, and Dr. Anthony M. Dean are also appreciated.

REFERENCES

1. Westmoreland, P. R., A. M. Dean, J. B. Howard, and J. P. Longwell, submitted for publication.
2. Kinney, R. E., and D. J. Crowley, **Ind. Eng. Chem., 46**, 258 (1954).
3. Stehling, F. C., J. D. Frazee, and R. C. Anderson, **Sixth Symposium (International) on Combustion**, The Combustion Institute, Pittsburgh, 247, 1956.
4. Cole, J. A., J. D. Bittner, J. B. Howard, and J. P. Longwell, **Combustion and Flame, 56**, 51 (1984).
5. Frenklach, M., D. W. Clary, W. C. Gardiner, Jr., and S. E. Stein, **Twentieth Symposium (International) on Combustion**, The Combustion Institute, Pittsburgh, 887, 1984.
6. Frenklach, M., D. W. Clary, T. Yuan, W. C. Gardiner, Jr., and S. E. Stein, **Combust. Sci. and Tech., 50**, 79 (1986).
7. Benson, S. W., **Thermochemical Kinetics, 2nd Ed.**, Wiley, 1976.
8. Dean, A. M., **J. Phys. Chem., 89**, 4600 (1985).
9. Westmoreland, P. R., J. B. Howard, J. P. Longwell, and A. M. Dean, **AIChE J., 32**, 1971 (1986).
10. Westmoreland, P. R., **Experimental and Theoretical Analysis of Oxidation and Growth Chemistry in a Fuel-Rich Acetylene Flame**, Ph. D. thesis, Department of Chemical Engineering, Massachusetts Institute of Technology, 1986.
11. Lazzara, C. P., J. C. Biordi, and J. F. Papp, **Combustion and Flame, 21**, 371 (1973).
12. Warnatz, J., **Combustion Science and Technology, 34**, 177 (1983).
13. Westmoreland, P. R., J. B. Howard, and J. P. Longwell, **Twenty-First Symposium (International) on Combustion**, The Combustion Institute, Pittsburgh, in press.
14. Golden, D. M., and C. W. Larson, **Twentieth Symposium (International) on Combustion**, The Combustion Institute, Pittsburgh, 595, 1984.
15. Benson, S. W., **Can. J. Chem., 61**, 881 (1983).
16. Stein, S. E., and A. Fahr, **J. Phys. Chem., 89**, 3714 (1985).
17. McMillen, D. F., and D. M. Golden, **Ann. Rev. Phys. Chem., 33**, 493 (1982).
18. Wodtke, A. M., and Y. T. Lee, **J. Phys. Chem., 89**, 4722 (1985).
19. Tanzawa, T., and W. C. Gardiner, Jr., **J. Phys. Chem., 84**, 236 (1980).

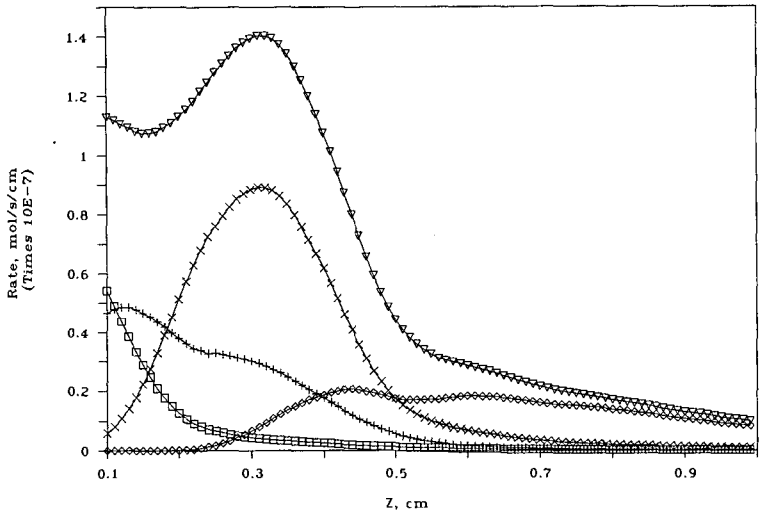

Figure 1. Predicted rates for reactions leading to 1-C_4H_5, using measured concentrations and predicted rate constants for $C_2H_3+C_2H_2$ (□), $H+C_4H_4$ (+), 1,3-C_4H_6 decomposition (◇), 1,3-C_4H_6 + H (×), and total (▽).

Formation of Small Aromatic Molecules in a Sooting Ethylene Flame

Stephen J. Harris
Anita M. Weiner

and

Richard J. Blint
Physical Chemistry Department, General Motors Research Laboratories, Warren, MI 48090-9055

Abstract

Small aromatic species are undoubtedly important precursor molecules in the formation of polycyclic aromatic hydrocarbons and soot, two important pollutants in diesel, direct-injection stratified charge (DISC), and other heterogeneous-combustion engines. Unfortunately, the chemical route to their formation is poorly understood, in part because rate constants for reactions of aromatic species at flame temperatures are largely unknown. In this work we used a quartz sampling probe to measure the concentration profiles of the single-ring aromatics benzene, phenylacetylene, and styrene in a heavily sooting premixed ethylene flame. A detailed chemical kinetics model was then constructed for the purpose of explaining the flame chemistry. The model, which uses estimated rate constants for many of the reactions involving aromatic species, gives good predictions for benzene and styrene and fair predictions for phenylacetylene. A sensitivity analysis has isolated a particular chemical reaction which controls their rate of formation, and it shows that even large errors in the other aromatic rate constants have relatively little effect on the predictions. Our approach will be applied in the future to trying to understand the formation of larger aromatic species and soot.

Introduction

Over the years there has been a considerable effort towards improving our understanding of the detailed chemistry in hydrocarbon combustion[1-3]. Much of the work has concentrated on lean and stoichiometric flame environments, but understanding the processes that take place in rich systems is of great importance since many practical flames are diffusion flames. Unfortunately, rich combustion is a very difficult area for flame modeling because of the involvement of large hydrocarbon molecules and soot, species whose chemistry and thermodynamics are poorly known. In contrast, lean and near-stoichiometric flames involve a smaller number of species, nearly all of which are eventually converted to CO_2 and H_2O.

However, as knowledge of the kinetics and thermodynamics of hydrocarbons has increased, a growing number of studies have considered rich flame environments. These include, for example, the experiments of Homann and Wagner[4], Howard and co-workers[5], Bockhorn[6], and Taylor[7]. In addition, detailed models have recently been constructed specifically to deal with rich flames[8-10]. In most of these cases, however, studies have been limited to non-sooting or lightly sooting flames because the presence of soot can make measurements difficult and because models have tended to avoid systems where pyrolysis chemistry and soot formation played major roles.

In recent work[11] we measured mole fraction profiles of a number of stable and radical species in a heavily sooting ethylene flame, and, building on previous work[2,9,12], we developed a model which predicted the profiles of many of the measured species with good accuracy. It would be very valuable to develop a reliable ethylene combustion model because many fuels such as octane are converted largely to ethylene on their way to being oxidized[1]. Thus, an ethylene oxidation mechanism is an important component for models of more realistic fuels.

Unfortunately, our model severely underestimated the benzene mole fraction, and no other aromatic species was modeled. Since the goal of this research program is to understand the chemistry of soot formation, and since aromatic species undoubtedly play an important role in that process, our inability to model the chemistry of even the simplest aromatics was an important stumbling block. In this paper we describe modifications to our model which allow the successful prediction of the profiles of benzene, styrene, and, to a lesser extent, phenylacetylene. It is our hope that if the chemistry of large aromatics is similar to that of smaller aromatics, then semi-quantitative predictions of soot formation kinetics in well-studied systems such as premixed flat flames[13] may be attainable in the foreseeable future.

Experiment and Model

The experimental conditions employed in this work have been described previously[11]. Briefly, a flat premixed $C_2H_4/O_2/Ar$ flame with C/O ratio of 0.92 ($\phi = 2.76$) was stabilized on a water-cooled porous plug burner surrounded by a shroud of nitrogen. The $Ar : O_2$ mole ratio was 79 : 21. A quartz microprobe withdrew gases from the flame. No measurements could be taken beyond about 3.3 mm above the top of the burner because soot would clog the probe. Species mole fractions, X_i, were measured with a mass spectrometer and signal averaged on a computer. The complete species profiles were measured a number of

times. The resulting statistical uncertainties at the 90% confidence level (estimated from a Student's t distribution) were about $\pm 10\%$ for benzene. For styrene and phenylacetylene the uncertainty was about $\pm 25\%$ near their peaks and $\pm 50\%$ in the pre-flame zone where their concentrations were very low. There was also a potential systematic error of as much as 50% for styrene and phenylacetylene because of uncertainty in the mass spectrometer calibration. The pressure drop across the microprobe orifice was maintained at between 50:1 and 100:1 in order that the stable species chemistry would be adequately quenched. Tests and analysis on several species indicated that the quench was successful[11]. We estimated that the profiles were shifted by approximately 2.5 probe orifice diameters (0.4 mm) from their true location[11]. The figures in this paper have incorporated this shift. Temperatures were determined from measurements with both 3 mil and 5 mil diameter silica-coated, radiation-corrected Pt/Pt-Rh thermocouples. For measurements made in the sooting zone, thermocouple readings were difficult to take because the temperature dropped as soon as the thermocouple became coated with soot. Therefore, measurements were taken continuously with a computer as the flame was ignited. In this way the rise and fall in the thermocouple readings were recorded. We took the highest measured temperature as the true flame temperature, making sure that our results were unaffected by the rate at which the computer took the measurements. The two different thermocouples gave identical temperature profiles. The temperature peaked at 3.1 mm above the top of the burner at about 1640 K.

Concentration profiles were modeled using the Sandia burner code[14] together with a mechanism that we developed for the flame. A number of reactions involving butane, butyl radical, 2-butene, propane, acetaldehyde, and acetaldehyde radical were considered, but they did not contribute to the profiles that we measured under our conditions. Therefore those species were eliminated. A partial mechanism is given in Table 1. (The complete mechanism is available from the authors.) For ease of comparison with previous work of Frenklach *et al.*[10,15], we have used the shorthand nomenclature that they suggested for aromatic species. In this system $A_n(R_m)$ refers to a species with n fused aromatic rings (fused to an m-membered non-aromatic ring). Radicals are indicated by a "•" or a "−". Table 2 shows structures for some of the species which appear in the mechanism. A complete table is given in Frenklach *et al.*[15].

Most of the thermodynamics for small species comes from the Chemkin data base[16], supplemented where necessary by other standard sources[17]. We assumed[11,18a] a 70.5 kcal heat of formation for the vinyl radical (C_2H_3) and a 109 kcal heat of formation for C_4H_2[18b]. For all the aromatic species we used the thermodynamics of Stein and Fahr[19]. (This set of data was called S6[10,19b].) In addition we used Stein and Fahr's thermodynamics for three aliphatic radicals which are closely related in our model to aromatic species, namely n-C_4H_3 ($\Delta H_f^{300} = 124$ kcal/mole), C_8H_5 ($\Delta H_f^{300} = 190$ kcal/mole), and C_6H_5 ($\Delta H_f^{300} = 138$ kcal/mole).

Information on the high temperature kinetics of most aromatic species, especially those larger than benzene, tends to be either too sparse or too tentative for us simply to use literature values for rate constants. In order to make progress we followed the approach of Frenklach, Clary, Gardiner, and Stein[20] (FCGS). These workers considered a very large number of elementary reactions for aromatic formation and growth. The reactions were grouped into classes, and all reactions of a given class were assigned the same rate constant.

For example, based on the measurement by Madronich and Felder[21] for the rate of reaction between OH and benzene, all reactions involving OH abstraction of an aromatic hydrogen were assigned the rate constant $k_{T02} = 2.1 \times 10^{14} e^{-4600/RT}$. For other reaction classes rate constants were not available, and upper limit (nearly gas kinetic) values were assigned to their rate constants. In this way, they were able to identify the major reaction pathways as well as pathways which were not important.

However, use of upper limit values for rate constants entails certain disadvantages. First, because they are in general too large, this approach cannot be expected to yield results that are in quantitative agreement with experiment. Second, the usefulness of sensitivity coefficients cannot be expected to be great if the estimated rate constants are incorrect by very large factors. (However, FCGS[20] identified some pathways to aromatic formation whose relative importance is very small for almost any reasonable choice of rate constants.) Finally, if the rate constants are chosen to be sufficiently high the sensitivity coefficients may be smaller than they otherwise would be (As $k \rightarrow \infty$ its associated sensitivity coefficients will in general approach 0.), and the analysis may conclude that thermodynamics is relatively more important compared to kinetics than it actually is.

In our work we addressed these issues by using experimentally derived rate constants which have recently become available and by testing the effects of some very large changes in the rate constants (see Discussion section). The rate constants for aromatic species were derived as follows:

1. Mallard *et al.*[22] measured the rate for reaction of the phenyl radical with acetylene ($U15$) and ethylene ($U18$). We used the same rate constants for $U16$, $U17$, $U19$, $U20$, and $G10$, which are similar.
2. Kiefer *et al.*[23] obtained the rate constant for abstraction of a benzene hydrogen by H ($T03$) from a model of his shock tube experiments. This rate constant extrapolates at 800 K to a value fairly close to that suggested by Nicovich and Ravishankara[24]. We used the same value for $U02$, $G02$, and $G11$. We assumed that abstraction of an aromatic hydrogen by C_2H and C_2H_3 is five times slower ($G04$, $G05$, $G08$. $G09$, $U04$, $U05$, $U09$, and $U10$).
3. Colket[25] used his shock tube results to obtain the rate constant for the displacement of a benzene hydrogen by C_2H ($U11$). We used the same value for displacement by vinyl ($U12$). The value for k_{T06}, the rate constant for ring formation, is taken from FW[10], which at our temperatures is nearly identical to the value estimated by Colket[25]. k_{U21} and k_{G12} were given the same value.
4. Hsu *et al.*[26] measured the rate constant for decomposition of benzene to phenyl and H ($T01$). We used this value for $U01$, $U06$, $G01$, and $G06$.
5. Cole *et al.*[5b] estimated the rate of formation of benzene from C_4H_5 and C_2H_2 in their low pressure butadiene flame. We used their value for k_{T07}.
6. The rate constant for $U13$ was given an upper limit value taken from Frenklach and Warnatz[10]; the same rate constant was used for $U14$.
7. k_{T08} and k_{U22} are evaluated below.

Reaction Path and Sensitivity Analysis

Principal reaction paths for species up to the C_4's have been presented previously[11].

Graphs of the concentration profiles of many of those species were also presented[11]. Here we discuss profiles and reaction paths for the single-ring aromatic species that we measured.

Benzene (A_1)

The calculated rate of benzene formation peaks between 1.6 and 2.2 mm (from 1450 - 1600 K), compared to peak formation rates of the C_3 and C_4 species between 1 and 1.6 mm. A single reaction path dominates at 1.8 mm, $T08$ followed by $T06$ and $-T01$ or $-T03$. The importance of $T08$ was emphasized originally by Bockhorn *et al.*[6] and FCGS[20]. In the pre-reaction zone $T07$ dominates, reflecting the higher concentration of C_4H_5 compared to *n*- C_4H_3 in the lower temperature environment found there (Figure 1). FW also found that ring formation was dominated by $T07$ in the pre-flame zone. We did not include any oxidation reactions which destroyed the aromatic ring since we have no evidence that such reactions are important in our flame and since the detailed kinetics of the species involved[27] would be entirely speculative.

A sensitivity analysis shows that the calculated benzene concentration in the region of its peak formation rate depends most strongly (sensitivity coefficient $\equiv \left|\frac{\partial \ln X_i}{\partial \ln k_j}\right| > 0.5$) on only three rate constants, k_{F01}, k_{A02}, and k_{T08}; other rate constants to which the benzene concentration is sensitive include k_{H02}, k_{H03}, k_{A08}, k_{V04}, k_{V11}, and k_{F11}. k_{T01} and k_{T06}, with sensitivity coefficients between 0.05 and 0.06 are the only rate constants involving an aromatic ring with a sensitivity coefficient greater than 0.05. In the pre-flame region the above rate constants again have the highest sensitivities. Thus, among all the rate constants involving aromatic formation, many of whose values had to be guessed or extrapolated, only k_{T08} is critical. (This same conclusion was reached by FCGS[20] in their very extensive search for reaction paths leading to the formation of aromatic rings.) The calculated concentration is also sensitive to the thermodynamic values assumed for *n*- C_4H_3, a 5 kcal/mole increase in its heat of formation leading to a 3-fold reduction in the benzene concentration. A similar change in the assumed heat of formation of the aliphatic radical C_6H_5 has only a 10% effect. Assuming, then, that our pathway to form benzene is correct, that oxidation reactions which destroy the ring can be ignored, and that the thermodynamics is correct, we can estimate k_{T08} by comparing predicted and measured benzene concentrations. We chose $k_{T08} = k_{U22} = 1.5 \times 10^{12}$ cm^3/molecule-sec, which is nearly identical to the value found[10] to reproduce best the data of Bockhorn *et al.*[6] (However, considering the differences between our mechanism and the one used in Ref. 10 as well as the differences in the pressure of the flames modeled, the significance of this agreement is not immediately clear.) With this choice, the rate of $T06$ at 1.8 mm is 50% faster than $-T06$, 2.5 times faster than $T08$, and about 10 times faster than $-T08$. Later in the flame, beyond 2.6 mm (1630-1640 K), the experiment shows that net benzene formation nearly comes to a halt. According to the model, in this region benzene is still being formed by $-T01$, but now it is being destroyed by $T03$ at about the same rate. Furthermore, $T06$ and $T08$ briefly run in the reverse (decomposition) directions, with the rate of $-T06$ being 0.6% faster than $T06$ and $-T08$ being 3.6% faster than $T08$. With such a fine balance, it is not surprising that the net directions in which $T06$, and $T08$ run are very sensitive to temperature. For example, our calculations show that if the peak temperature is assumed to be 1600 K, 40 K less than the measured value, these reactions always run in the direction of forming benzene.

A comparison between the experiment and the model is shown in Figure 2. Adjustment of k_{T08} insures agreement at 3 mm, but we note that the model also reproduces fairly well the shape of the rise through the flame zone as well as the sharp leveling out in the profile beyond 2.5 mm.

Phenylacetylene (A_1C_2H) and Styrene ($A_1C_2H_3$)

The predicted phenylacetylene profile (solid curve in Figure 3) differs by a factor of up to 6 from the experimentally measured profile. This discrepancy is more than a factor of two worse than for the C_3 and C_4 species from which phenylacetylene is ultimately formed, and it is much greater than the uncertainty in the measurements. Because all of the aromatic species showed similar first-order sensitivity coefficients to most of the same rate constants, no adjustment of a single rate constant to improve the agreement with phenylacetylene seemed possible without seriously degrading the agreement between the model and experiment for the other aromatic species. It is likely that the discrepancy is due to a combination of errors in more than one rate constant, requiring second- or higher-order sensitivity coefficients to identify them, or to errors in the precursor thermodynamics. However, we considered two alternate explanations for the discrepancy. First, we may not have identified the major pathway forming phenylacetylene. For example, Colket[25] has suggested an overall irreversible pathway to phenylacetylene.

$$C_4H_4 + C_4H_5 \rightarrow A_1C_2H_3 + H. \qquad k_a = 7.9 \times 10^{13} e^{-3000/RT} \tag{a}$$

$$A_1C_2H_3 + H \rightarrow A_1C_2H + H_2 + H \qquad k_b = 4.0 \times 10^{14} e^{-7000/RT}. \tag{b}$$

Addition of these reactions increased the calculated phenylacetylene concentration by less than 10%, while reducing the styrene concentration by nearly an order of magnitude. Such a reduction would seriously degrade the agreement between measured and calculated styrene profiles (see below). (On the other hand, adding a detailed route from styrene to phenylacetylene analogous to the route from ethylene to acetylene—essentially a detailed version of Equation (*b*)—had hardly any effect on any of the aromatic profiles.) Inclusion of other possible routes to phenylacetylene,

$$C_4H_4 + C_4H_3 = A_1C_2H + H$$

or

$$C_4H_2 + C_4H_5 = A_1C_2H + H$$

with $k = 1.0 \times 10^{13}$ had little or no effect. Increasing k_{U22} by a factor of 5 had no effect on the phenylacetylene profile. We found no new reaction pathway which gave a substantial increase in the phenylacetylene concentration. A second possible explanation for the discrepancy between the model and the experiment could be uncertainty in the thermodynamics of phenylacetylene. To test for this possibility we lowered its assumed heat of formation at 300 K from 75 to 71 kcal/mole. The result, shown by the dashed line in Figure 3, is improved overall agreement, although the calculated and experimental profile shapes are still somewhat different. (The same effect could be obtained by changing the assumed entropy or the assumed heat capacity at high temperature.) Among other species, only the benzene and styrene concentrations were affected by this change, being reduced by about 10%.

The peak formation rate for phenylacetylene occurs in the same region as for benzene. Most of the phenylacetylene comes from the direct reaction between phenyl and acetylene ($U15$); a smaller but still substantial amount comes from $U22$ followed by $U21$ and $-U09$. The sensitivity coefficients for phenylacetylene are similar to those for benzene, although sensitivities to k_{F01}, k_{F08}, k_{F11}, k_{A02}, and k_{A08} are somewhat higher, reflecting among other factors a particular sensitivity to the acetylene concentration (which is modeled very well). There is also some sensitivity—about 0.1—to k_{U15}. (But increasing k_{U15} to 1.0×10^{13} increases the phenylacetylene concentration by only about 10%.)

The calculated net styrene formation rate peaks between 1.4-1.7 mm (1300 - 1500 K), somewhat earlier than the other aromatics. This is because the principal reaction forming styrene, $U18$, involves C_2H_4, whose concentration is falling rapidly with height. $-U12$ is the major destruction reaction there. By 2.25 mm the rate of $-U12$ exceeds $U18$ by a factor of 3, causing the stryene mole fraction to fall. Sensitivity coefficients for styrene are very similar to those for phenylacetylene, except for a much lower sensitivity to k_{U15} and some sensitivity to k_{U12} and k_{U18}.

A comparison between calculated and measured styrene mole fractions is shown in Figure 4. The agreement in shape and magnitude is good, although the calculated profile peaks earlier than the experimental one. It is interesting that the experiment showed benzene and phenylacetylene climbing rapidly through the reaction zone and then leveling off, while the styrene concentration peaks and falls. The model reproduces the proper qualitative behavior for all three species. The concentration of styrene falls in part because the mole fractions of ethylene and vinyl drop steeply through the post-flame region (*e.g.*, see Figure 1), increasing the net rate of $-U12$ and decreasing the net rate of $U18$. The most important reactions forming phenylacetylene ($U15$) and benzene ($T08$) run mainly in the forward direction throughout the flame, in part because the acetylene mole fraction does not change substantially in the post-flame region.

Naphthalene (A_2) and Acenaphthalene (A_2R_5)

Although we have no measurements for species larger than styrene, we continued the mechanism up to acenaphthalene in order that profiles of the species that we measured not become artificially high due to a lack of exit channels[28].

The path to larger aromatics funnels through phenylacetylene. Attack by H ($U02$) (or OH ($U03$)) gives phenylacetylene radical, which almost irreversibly adds acetylene ($G13$) and closes to form the naphthalene radical $A_2^{\cdot}X$ ($G12$). This species can give naphthalene ($-G06$ or $-G11$) or react with acetylene ($G10$) to give acenaphthalene.

Our analysis shows that the sensitivity spectra of naphthalene and acenaphthalene are very similar to that of phenylacetylene. In addition both are very sensitive to $U02$ and somewhat sensitive to $G13$, while acenaphthalene is also quite sensitive to $G10$.

Discussion

Comparison with Other Systems

Frenklach and Warnatz[10] have very recently made the first detailed flame calculations to model the profiles of aromatic species in a flame. The flame modeled was a sooting ($\phi = 2.75$) 90 torr premixed acetylene flame studied by Bockhorn *et al.*[6]. Although they

obtained a certain qualitative agreement with Bockhorn's data, the calculated profiles of the aromatics declined precipitously in the post-flame gases, while the measured profiles dropped rather more slowly. The principal reason for this discrepancy[10] comes from an apparent overestimate of the fragmentation rate of aromatic radicals *via* the reverse of reactions such as *T*06. It is possible that this overestimate is due to errors in the thermodynamic parameters, since those parameters determine the reverse reaction rates.

With the chosen value for k_{T08}, the measurements and calculations for benzene and styrene in our flame are in good agreement, both in the profile shapes and in their absolute values. The fact that the experimentally measured benzene and phenylacetylene concentrations do not decline in the post-flame region of our flame as they do in Bockhorn's flame can readily be explained by by the fact that Bockhorn's flame is about 400 K hotter than ours. Graham *et al.*[29] interpreted the fall in the soot yield in their shock tube experiments for temperatures above 1800 K by postulating that at high temperatures the aromatic ring fragments more rapidly than it grows. Other data showing this "bell" have been explained in a similar way[30], and the aromatics in premixed flames may be subject to the same processes.

FCGS[20] have suggested that the driving force behind formation of larger aromatic species and soot is the superequilibrium of *H* atoms. They proposed R/K_{eq} as a measure of this superequilibrium, where $R = [H]^2/[H_2]$ and where $K_{eq} = [H_{eq}]^2/[H_2]$. They attributed the decline in the formation and growth rate of aromatics at long time to the decay of R/K_{eq}. We have plotted this ratio in Figure 2. The precipitous decline in R/K_{eq} to values below about 100 coincides very roughly with the slowdown in the formation of the benzene profile. However, our kinetic analysis and that of FW[10] suggest that it is the increase in temperature through the reaction zone—leading to higher ring fragmentation rates—which is actually responsible for the cessation of net benzene and phenylacetylene formation. From this point of view, the fall in R/K_{eq} is simply a reflection of the fact that the temperature is rising in a region of constant or falling *H*-atom mole fraction. Furthermore, our model predicts that net benzene and phenylacetylene formation accelerates later in the flame where the temperature is lower, even though R/K_{eq} ultimately drops to about 2. (This secondary rise in net aromatic formation has previously been modeled[10] and observed experimentally[31].) The fact that net benzene and phenylacetylene formation is greater when $R/K_{eq} < 10$ than when $R/K_{eq} \sim 100$ suggests that the value of this ratio is not of fundamental significance in aromatic formation.

Robustness of the Model

The model that we have presented relies in many cases on analogies and estimates for rate constants of aromatic species because few of these rate constants are known. When they are measured the new values can replace those used here. Similarly, our knowledge of thermodynamic properties of large aromatic species can be expected to improve. The usefulness of this modeling effort, then, depends on the robustness of the calculations to potentially large changes in the values of the rate constants and to some changes in the thermodynamics. FW[10] have shown the effects of changing certain thermodynamic assumptions, and we have reported above some effects on the calculated phenylacetylene profile. The effects are significant but not drastic for the species modeled here; additional efforts to measure or calculate thermodynamic properties, particularly for larger species,

would be very valuable in order to better understand hydrocarbon growth in flames.

The situation may be somewhat more promising with regard to uncertainty in the rate constants. The analyses done by FCGS[20], FW[10], and ourselves show remarkably small values for most of the sensitivity coefficients. However, as we pointed out above, the model could still be quite sensitive to very large changes in the the rate constants. In order to evaluate this possibility, we ran our flame code using the aromatic mechanism and rate constants of FW, only adding analogous reactions for styrene, which did not appear in their mechanism, and using our value for k_{T08}. This involved many significant changes. For example, FW's value for k_{T03} is about two orders of magnitude greater than that of Kiefer *et al.*[23] The profiles for the single-ring compounds changed by less than 50% compared to those obtained using the mechanism in the Table 1, supporting our conclusion that k_{T08} is the only critical unknown rate constant. (However, the predicted concentrations of 2-ring compounds changed substantially, reflecting their sensitivity to $U02$.)

As a second test of the robustness of our mechanism we asked whether our model is consistent with benzene decomposition measurements made by Kiefer *et al.*[23] According to this proposed mechanism, benzene decomposition at 1 atmosphere follows the route:

$$A_1 = A_1^- + H \qquad k_c = 10^{17} e^{-118000/RT} \tag{c}$$

$$A_1 + H = A_1^- + H_2 \qquad k_d = 2.5 \times 10^{14} e^{-16000/RT} \tag{d}$$

$$A_1^- = C_4H_3 + C_2H_2 \qquad k_e = 1.6 \times 10^{15} e^{-82000/RT} \tag{e}.$$

Our mechanism already includes (*d*); we replaced $T01$ and $T06/T08$ with (*c*) and (*e*). The result is a reduction in the calculated aromatic concentration by 40-45%, with little effect on the qualitative shapes of the profiles. Since we have not used the same thermodynamic assumptions as Kiefer, use of his rate constants in our system is not really warranted. (The reactions are running in the reverse direction.) However, taken together with the fact that Kiefer's results were not highly sensitive to k_e, the modest effect of the change in rate constants suggests that the mechanism of Table 1 is in reasonable agreement with the shock tube results of Kiefer *et al.*

Conclusions

We believe that we have made progress in modeling the pyrolysis processes in our flame up to and including the formation of single-ring aromatic species, even though there is great uncertainty in many of the rate constants. Our sensitivity analysis shows that the basis for this success is that there is a single crucial unmeasured rate constant, k_{T08}, which largely controls the combined single-ring aromatic species concentrations. Our results are in accord with those of FCGS and FW, even though we used experimentally derived rate constants which were not available to them. The robustness of our model to future changes in most of the rate constants used in the aromatic part of our model appears to be high.

We hope in the future to continue our measurements and modeling work to species with more than one aromatic ring. If we are successful in modeling growth from one to two rings, we can have some hope for modeling much larger species if adequate thermodynamics are available.

The ability to model soot formation in a flame, however, requires overcoming several additional hurdles. First, the number of species becomes too large to handle with a code such as that used here. As an alternative we could model the growth to larger species by ignoring diffusion in the post-flame gases and using a much faster code which assumes a homogeneous environment. The burner code, then, would provide estimates for the concentrations of small radicals and hydrocarbons which could be crucial for the hydrocarbon growth. Second, in order to calculate soot particle inception, additional processes such as coagulation and surface growth would have to be included. Recent work[32] suggests that these processes can be considered without significant additional demands on computer resources.

Acknowledgements

We are grateful to Professor Michael Frenklach of Pennsylvania State University for many helpful discussions and for providing us with an advance copy of his paper with Warnatz and with the thermodynamics of Stein and Fahr.

References

1. J. Warnatz, Twentieth Symposium (International) on Combustion, The Combustion Institute, p. 845 (1984).
2. Westbrook, C. K., Dryer, F. L., Schug, K. P., Nineteenth Symposium (International) on Combustion, The Combustion Institute, Pittsburgh, 1982, pg. 153.
3. Miller,J.A., Mitchell, R.E., Smooke, M.D., and Kee, R.J., Nineteenth Symposium (International) on Combustion, The Combustion Institute, p. 181 (1982).
4. Bonne, U., Homann, K.H., and Wagner, H.Gg., Tenth Symposium (International) on Combustion, The Combustion Institute, p. 503 (1965).

5a. Bittner,J.D. and Howard, J.B., Eighteenth Symposium (International) on Combustion, The Combustion Institute, p. 1105 (1982).

b. Cole, J.A., Bittner, J.D., Longwell, J.P., and Howard, J.B. Combustion and Flame **56**, 51 (1984).

6. Bockhorn, H., Fetting, F., and Wenz, H.W., Ber. Bunsenges. Phys. Chem. **87** 1067 (1983).
7. Taylor, B.R., Thesis, Department of Chemical Engineering, MIT, 1984.
8. Warnatz,J., Bockhorn, H., Moser, A., and Wenz, H.W., Nineteenth Symposium (International) on Combustion, The Combustion Institute, Pittsburgh, p. 197 (1982).
9. Levy, J.M., Taylor, B.R., Longwell, J. P., and Sarofim, A. F., Nineteenth Symposium (International) on Combustion, The Combustion Institute, Pittsburgh, p. 167 (1982).
10. M. Frenklach and J. Warnatz, "Detailed Modeling of PAH Profiles in a Sooting Low-Pressure Acetylene Flame," Combustion Science and Technology, in press.
11. Harris, S.J., Weiner, A.M., Blint, R.J., and Goldsmith, J.E.M., Twenty-first Symposium (International) on Combustion, The Combustion Institute, in Press.
12. Cathonnet, M., Gaillard, F., Boettner, J. C., Cambray, P., Karmed, D., Bellet, J.C., "Twentieth Symposium (International) on Combustion", The Combustion Institute, Pittsburgh, 1984, pg. 819.
13. Harris, S.J., Weiner, A.M., Ashcraft, C.C., Comb. and Flame **64**, 65 (1986).

14a. Smooke, M.D., J. Comp. Phys., **48**, 72 (1982).

b. Kee, R.J., Grcar, J.F., Smooke, M.D., and Miller, J.A., "A Fortran Program for Modeling Steady Laminar One-Dimensional Premixed Flames." Sandia Report SAND85-8240, 1985.

15. Frenklach,M., Clary, D.W., Yuan, T., Gardiner, W.C., and Stein, S.E., Combustion Science and Technology **50**, 79 (1986).
16. Kee, R.J., Rupley, F.M., and Miller, J.A., "The Chemkin Thermodynamic Data Base," Sandia Report SAND87-8215, April, 1987.

17a. Stull, D.R., Westrum, E.F., and Sinke, G.C., "The Chemical Thermodynamics of Organic Compounds:" Wiley, New York, 1969.

b. Burcat, A. in "Combustion Chemistry," W.C. Gardiner, ed., Springer-Verlag, New York, 1984, p. 455.

18a. McMillen, D.F. and Golden,D.M., Ann. Rev. Phys. Chem. **33**, 493 (1982).

b. Bittner, J.D., Thesis, MIT, 1981.

19a. Stein, S.E. and Fahr, A. J. Phys. Chem. **94**.3714 (1985).

b. Frenklach, M., Clary, D.W., Gardiner, W.C., and Stein, S.E, 15'th Symposium on Shock Waves and Shock Tubes, Stanford University Press, 1986, p. 295.

20. Frenklach, M., Clary, D.W., Gardiner, W.C., and Stein, S.E, Twentieth Symposium (International) on Combustion, The Combustion Institute, p. 887 (1985).

21. Madronich, S. and Felder, W., J. Phys. Chem. **89**, 3556 (1985).

22. a.Mallard, W.G., Fahr, A.. and Stein, S.E., Chem. Phys. Proc. Combustion, Paper 92, 1984.

b. Mallard, W.G., private communication.

23. Kiefer, J.H., Mizerka, L.J., Patel, M.R. and Wei, H.-C., J. Phys. Chem. **89**, 2013 (1985).

24. Nicovich, J.M. and Ravishankara, A.R., J. Phys. Chem. **88**, 2534 (1984).

25. Colket, M.B., "The Pyrolysis of Acetylene and Vinylacetylene in a Single-Pulse Shock Tube," Twenty-first Symposium (International) on Combustion, The Combustion Institute, in Press.

26. Hsu, D.S.Y., Lin, C.Y., and Lin, M.C., Twentieth Symposium (International) on Combustion, The Combustion Institute, p. 623 (1984).

27. Brezinsky, K., Prog. Energy Combust. Sci. **12**, 1 (1986).

28. Kiefer, J.H., Kapsalis, S.A., Al-Alami, M.S., Budach, K.A., Comb. and Flame **51**, 79 (1983).

29. Graham, S.C., Homer, J.B., and Rosenfeld, J.L., Proc. R. Soc. London **A344**, 259 (1975).

30. Frenklach, M., Ramachandra, M.K. and Matula, R.A., Twentieth Symposium (International) on Combustion, The Combustion Institute, p. 871 (1984).

31. Westmorland, P.R., "Experimental and Theoretical Analysis of Oxidation and Growth Chemistry in a Fuel-Rich Acetylene Flame," Ph. D. Thesis, Department of Mechanical Engineering, Massachusetts Institute of Technology, 1986.

32. Frenklach, M. and Harris, S.J., "Aerosol Dynamics Modeling Using the Method of Moments," J. Colloid and Interface Science, in Press.

33. Gardiner, W. C. and Troe, J., in "Combustion Chemistry," W.C. Gardiner, ed., Springer-Verlag, New York, 1984, p. 173.

34. Frank, Pl, Bhaskaran, K.A., and Just, T., Twenty-First Symposium (International) on Combustion, The Combustion Institute, in press.

Table 1

REACTIONS	A	n	E_a
A02) $C_2H_3 = C_2H_2 + H$	6.6E+19	-2.794	36130.0
A08) $C_2H_2 + OH = CH_2CO + H$	1.0E+14	0.0	11500.0
F01) $C_2H_3 + O_2 = HCO + CH_2O$	4.0E+12	0.0	-250.0
F11) $HCO + O_2 = CO + HO_2$	5.0E+11	0.5	835.0
H02) $H_2 + O = H + OH$	1.5E+07	2.0	7550.0
H03) $H + O_2 = O + OH$	1.2E+17	-.907	16620.0
V04) $C_4H_4 + H = C_4H_3 + H_2$	7.9E+13	0.0	14500.0
V11) $C_2H_2 + C_2H_2 = C_4H_3 + H$	2.0E+12	0.0	45900.0
T01) $A_1 = A_1^- + H$	5.0E+15	0.0	108600.0
T02) $A_1 + OH = A_1^- + H_2O$	2.1E+13	0.0	4600.0
T03) $A_1 + H = A_1^- + H_2$	2.5E+14	0.0	16000.0
T04) $A_1 + C_2H = A_1^- + C_2H_2$	5.0E+13	0.0	16000.0
T05) $A_1 + C_2H_3 = A_1^- + C_2H_4$	5.0E+13	0.0	16000.0
T06) $C_6H_5 = A_1^-$	1.0E+10	0.0	0.0
T07) $C_4H_5 + C_2H_2 = A_1 + H$	3.2E+11	0.0	3700.0
T08) $C_4H_3 + C_2H_2 = C_6H_5$	1.5E+12	0.0	0.0
U01) $A_1C_2H = A_1C_2H^* + H$	5.0E+15	0.0	108600.0
U02) $A_1C_2H + H = A_1C_2H^* + H_2$	2.5E+14	0.0	16000.0
U03) $A_1C_2H + OH = A_1C_2H^* + H_2O$	2.1E+13	0.0	4600.0
U04) $A_1C_2H + C_2H_3 = A_1C_2H^* + C_2H_4$	5.0E+13	0.0	16000.0
U05) $A_1C_2H + C_2H = A_1C_2H^* + C_2H_2$	5.0E+13	0.0	16000.0
U06) $A_1C_2H = A_1C_2H^- + H$	5.0E+15	0.0	108600.0
U07) $A_1C_2H + H = A_1C_2H^- + H_2$	2.5E+14	0.0	16000.0
U08) $A_1C_2H + OH = A_1C_2H^- + H_2O$	2.1E+13	0.0	4600.0
U09) $A_1C_2H + C_2H_3 = A_1C_2H^- + C_2H_4$	5.0E+13	0.0	16000.0
U10) $A_1C_2H + C_2H = A_1C_2H^- + C_2H_2$	5.0E+13	0.0	16000.0
U11) $A_1 + C_2H = A_1C_2H + H$	1.0E+12	0.0	0.0
U12) $A_1 + C_2H_3 = A_1C_2H_3 + H$	1.0E+12	0.0	0.0
U13) $A_1^- + C_2H = A_1C_2H$	1.0E+13	0.0	0.0
U14) $A_1^- + C_2H3 = A_1C_2H_3$	1.0E+13	0.0	0.0
U15) $A_1^- + C_2H_2 = A_1C_2H + H$	3.2E+11	0.0	1350.0
U16) $A_1^- + C_4H_2 = A_1C_2H + C_2H$	3.2E+11	0.0	1350.0
U17) $A_1^- + C_4H_4 = A_1C_2H + C_2H_3$	3.2E+11	0.0	1350.0
U18) $A_1^- + C_2H_4 = A_1C_2H_3 + H$	3.2E+11	0.0	1900.0
U19) $A_1^- + C_4H_4 = A_1C_2H_3 + C_2H$	3.2E+11	0.0	1900.0
U20) $A_1^- + C_4H_6 = A_1C_2H_3 + C_2H_3$	3.2E+11	0.0	1900.0
U21) $C_8H_5 = A_1C_2H^-$	1.0E+10	0.0	0.0
U22) $C_4H_3 + C_4H_2 = C_8H_5$	1.5E+12	0.0	0.0
G01) $A_2R_5 = A_2R_5^- + H$	5.0E+15	0.0	108600.0
G02) $A_2R_5 + H = A_2R_5^- + H_2$	2.5E+14	0.0	16000.0
G03) $A_2R_5 + OH = A_2R_5^- + H_2O$	2.1E+13	0.0	4600.0

G04) $A_2R_5 + C_2H = A_2R_5^- + C_2H_2$	5.0E+13	0.0	16000.0
G05) $A_2R_5 + C_2H_3 = A_2R_5^- + C_2H_4$	5.0E+13	0.0	16000.
G06) $A_2 = A_2^-X + H$	5.0E+15	0.0	108600.0
G07) $A_2 + OH = A_2^-X + H_2O$	2.1E+13	0.0	4600.0
G08) $A_2 + C_2H_3 = A_2^-X + C_2H_4$	5.0E+13	0.0	16000.0
G09) $A_2 + C_2H = A_2^-X + C_2H_2$	5.0E+13	0.0	16000.0
G10) $A_2^-X + C_2H_2 = A_2R_5 + H$	3.2E+11	0.0	1350.0
G11) $A_2 + H = A_2^-X + H_2$	2.5E+14	0.0	16000.0
G12) $A_1C_2HC_2H_2 = A_2^-X$	1.0E+10	0.0	0.0
G13) $A_1C_2H^* + C_2H_2 = A_1C_2HC_2H_2$	1.0E+13	0.0	0.0

Units are cm^3, moles, seconds, calories

Captions

1. Calculated mole fraction profiles for three radical species.
2. Left axis, benzene mole fraction. Symbols are experimental measurements, the curve is the model calculation. Right axis, calculated superequilibrium of H.
3. Phenylacetylene mole fraction. Symbols are experimental measurements, the solid curve is the model calculation, the dashed curve is the model calculation when the assumed heat of formation of phenylacetylene is lowered by 4 kcal/mole.
4. Styrene mole fraction. Symbols are experimental measurements, the solid curve is the model calculation.

Structure	Name
	A_1
	A_1^-
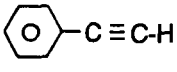	A_1C_2H
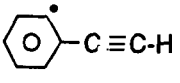	$A_1C_2H^*$
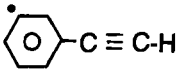	$A_1C_2H^-$
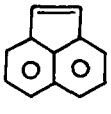	A_2R_5

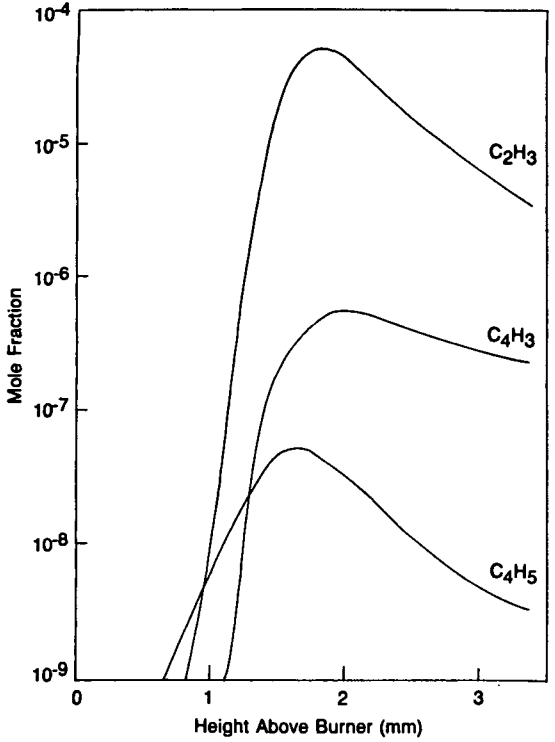
10^{-4}
10^{-5}
10^{-6}
10^{-7}
10^{-8}
10^{-9}
Mole Fraction
C_2H_3
C_4H_3
C_4H_5
0
1
2
3
Height Above Burner (mm)

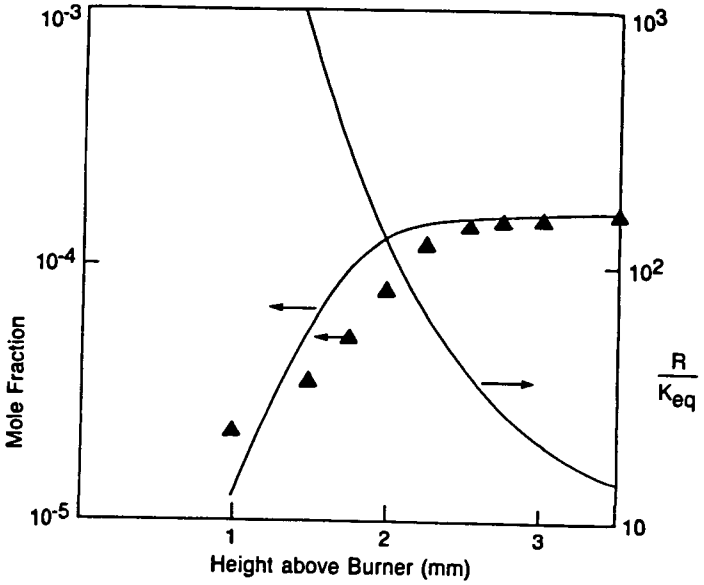
10^{-3}
10^{-4}
10^{-5}
Mole Fraction
10^3
10^2
10
$\frac{R}{K_{eq}}$
1
2
3
Height above Burner (mm)

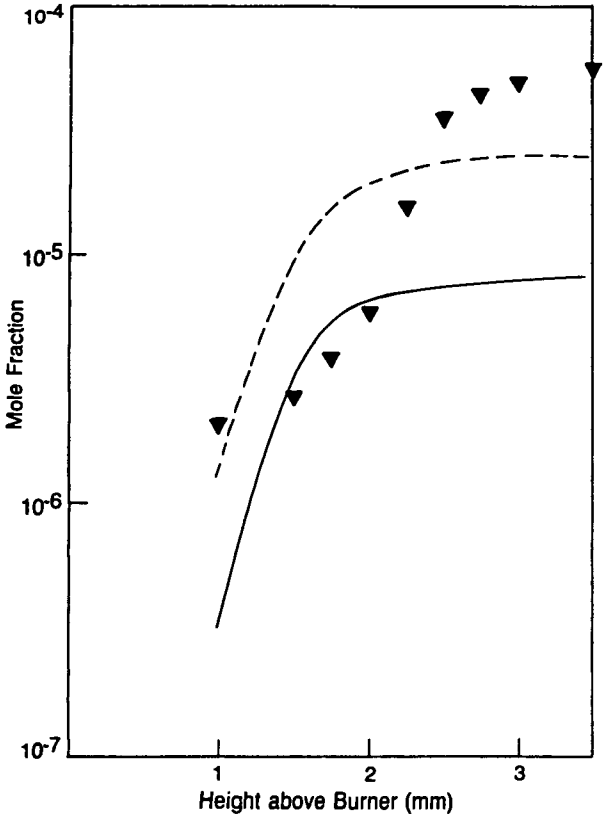
10^{-4}
10^{-5}
10^{-6}
10^{-7}
Mole Fraction
1
2
3
Height above Burner (mm)

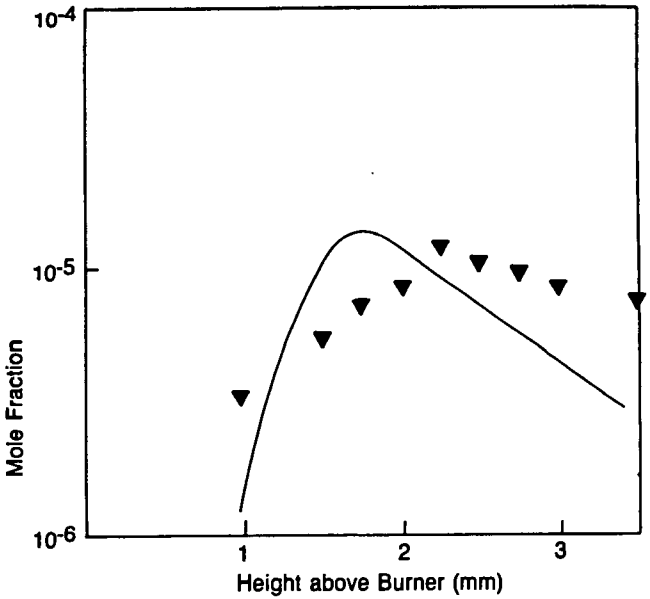
10^{-4}
10^{-5}
10^{-6}
Mole Fraction
1
2
3
Height above Burner (mm)

SOOT FORMATION IN HYDROCARBON DIFFUSION FLAMES

J. Houston Miller, Anthony Hamins, and Trudy A. Kohout

Department of Chemistry
The George Washington University
Washington, DC 20052

Kermit C. Smyth[a] and W. Gary Mallard[b]

[a]Center for Fire Research and [b]Center for Chemical Physics
The National Bureau of Standards
Gaithersburg, MD 20899

INTRODUCTION:

The chemistry of the combustion of simple hydrocarbons to form carbon dioxide and water has been extensively studied and is generally well established [1]. Our level of understanding of the chemistry which leads to the formation of polynuclear aromatic hydrocarbons (PAH) and soot particles is less fully developed. Numerous modelling efforts have been applied to the analysis of concentration data collected in shock tubes and premixed flames [2-6]. Although there are many proposed routes involving specific hydrocarbon free radicals, these models do share some common features. Fuel molecules are converted to relatively high concentrations of acetylene. Two- carbon atom free radicals formed during this pyrolysis process, or by hydrogen atom reactions with acetylene, can react with acetylene to form four carbon atom species.

R1a) $H\cdot + C_2H_2 \rightleftarrows C_2H\cdot + H_2$
R1b) $H\cdot + C_2H_2 \rightarrow C_2H_3\cdot$

R2a) $C_2H\cdot + C_2H_2 \rightleftarrows C_4H_3\cdot \rightleftarrows C_4H_2 + H\cdot$
R2b) $C_2H\cdot + C_2H_4 \rightarrow C_4H_5\cdot \rightarrow C_4H_4 + H\cdot$
R2c) $C_2H_3\cdot + C_2H_2 \rightarrow C_4H_5\cdot \rightarrow C_4H_4 + H\cdot$

Four-carbon atom species can react with either acetylene or two-carbon atom radicals to form six-carbon atom radicals, which may cyclize into aromatic structures. Finally, the cyclic radicals can lose or add hydrogen to form stable aromatic hydrocarbons such as benzene. For example:

R3) $C_4H_4 + C_2H_3\cdot \rightleftarrows n\text{-}C_6H_7\cdot \rightleftarrows cyclic\text{-}C_6H_7\cdot \rightleftarrows C_6H_6 + H\cdot$

Analogous growth processes lead to the formation of larger ring structures and finally soot particles. The aromatic structures are believed to act as "islands of stability" along the reaction pathway [6], in effect providing a measure of irreversibility to the process. Because the thermodynamic stability of the aromatic structures increases with size, these subsequent ring formation steps occur more rapidly than the earlier ones. Our emphasis, therefore, has been on the chemical formation route for the first aromatic ring with the goal of verifying specific mechanisms for this process. A model

must not only account for observed concentrations of intermediate hydrocarbons but also for their net rate of production as a function of flame position.

In our laboratory, specific attention has been given to identifying the important chemistry leading to the formation of the key precursor molecules to soot particle formation in diffusion flames. To achieve this goal measurements of the important intermediate gas phase species, temperature, and velocity fields have been required. The results of these studies provide a comprehensive data base with which to examine the phenomenon of soot particle inception in flames. In this paper, a review of some of the results of these studies will be given along with a discussion of areas of future interest.

Experimental Approach

A study of the structure of laminar diffusion flames has been undertaken in which spatially detailed measurements of the gas phase species, velocity, and temperature fields have been obtained. The majority of the work has been carried out for flames burning methane in air, although some preliminary work has been done for ethylene/air diffusion flames. Only the methane flame results will be described in this paper. The design of the burner has been described elsewhere in detail and will only briefly be summarized here [7]. The fuel flowed through a central slot located between two air slots. The resulting flame sheets are symmetric about the plane through the center of the burner (see Figure 1). The burner assembly was mounted on a two-dimensional computer-controlled, micrometer stage so that movement laterally, through the flame sheets, and vertically was possible. Lateral profiles of temperature, velocity, and species concentrations were collected at relatively high spatial resolution (0.2 mm) at a series of heights (consecutive profiles were taken every 2 mm).

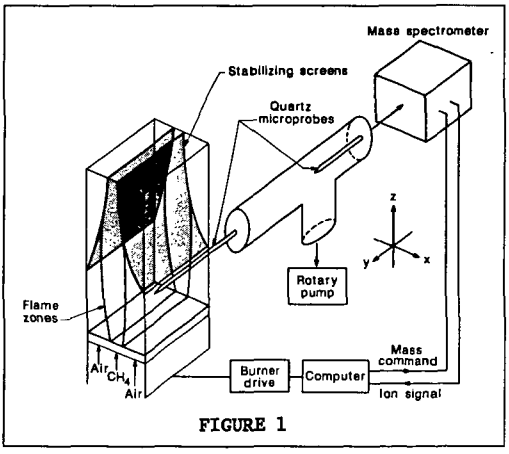

FIGURE 1

Species concentrations were determined by a direct sampling quartz microprobe system with mass spectrometric analysis. A probe following the

design of Fristrom and Westenberg [8] was inserted into the flame parallel to the fuel/air flow separators. Mass spectrometer signals were calibrated against room temperature mixtures, and the resulting calibration factors were corrected for the temperature dependence of the molecular flow through the sampling probe orifice. In a related series of experiments, molecular iodine from a side arm on the probe was mixed with the flame gas sample just inside the orifice [9]. Iodine reacts quantitatively with methyl radicals to form methyl iodide, which could survive the remainder of the sampling train and be detected mass spectrometrically.

Results

Figure 2 illustrates the temperature and velocity fields for the methane/air flame supported on the Wolfhard/Parker slot burner. Shown in solid lines are isothermal contours determined from thermocouple profiles[7]. Also shown are streamlines of convective velocity calculated from the two measured velocity components. The streamlines exhibit trajectories which begin in the lean region of the flame, cross the high temperature reaction zones, and continue into the fuel-rich regions.

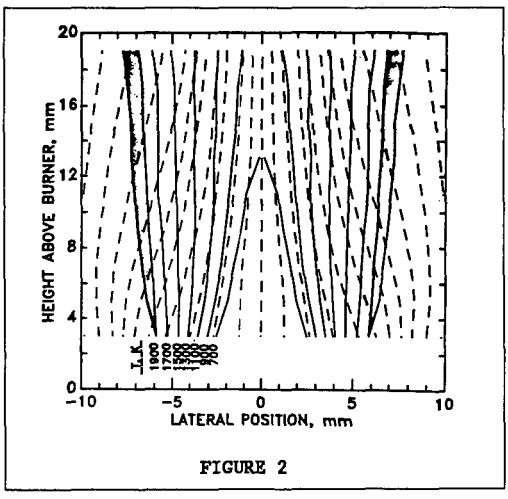

FIGURE 2

Figure 3 shows mass-spectrometric profiles of the concentrations of a variety of stable flame species at a height of 9 mm above the burner. A number of points are noteworthy in comparing Figures 2 and 3. First, the concentrations of oxygen and methane approach zero near the high temperature reaction zone at ± 6 mm from the burner centerline, where the concentration of water is a maximum. Second, the high concentration of nitrogen near the burner centerline reveals that significant entrainment of air (as shown by the velocity measurements in Fig. 1) and diffusion of nitrogen toward the burner centerline occur.

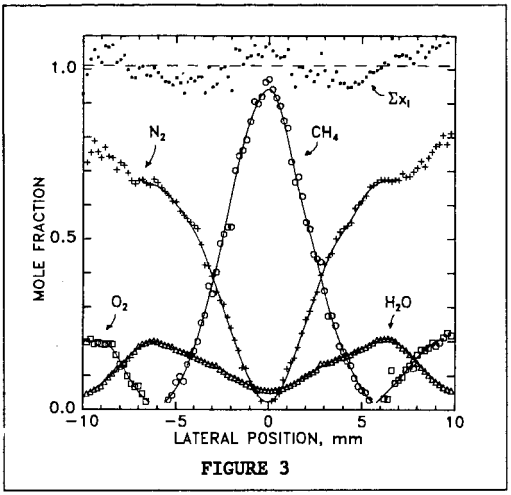

FIGURE 3

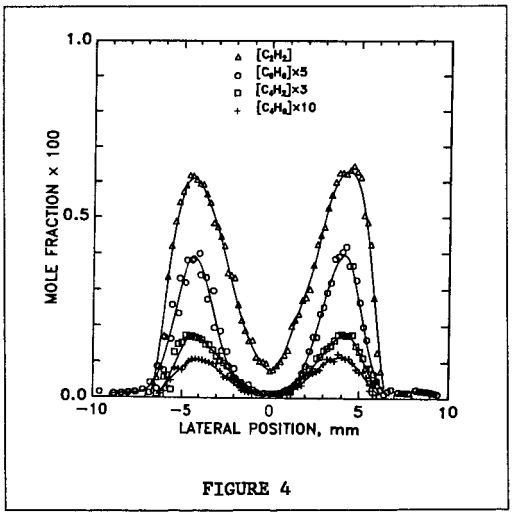

FIGURE 4

Figure 4 illustrates profiles collected at 9 mm above the burner surface for several intermediate hydrocarbons: acetylene, benzene, diacetylene, and butadiene. Peak concentrations at this height for these species are 6200, 800, 570, and 110 parts per million, respectively. Profiles for a large

number of additional intermediate hydrocarbons were obtained, and all have concentration maxima in the same region of the flame.

In addition to the probe studies described above, we have also applied optical diagnostic techniques to the study of the methane/air flame. Figure 5 compares the relative OH concentration profiles at various heights above the burner surface with profiles of C_2 fluorescence. Also shown is the Rayleigh light scattering signal for three flame heights. The absence of distinct peaks in the scattering signal profiles indicates that large soot particles are not detectable below 15 mm in the methane/air flame. The C_2 fluorescence is attributed to laser photolysis of large hydrocarbon molecules. Figure 5 shows that the OH concentration maximum occurs further away from the burner centerline (in more lean regions of the flame) than the area where hydrocarbons such as benzene and soot particles are observed.

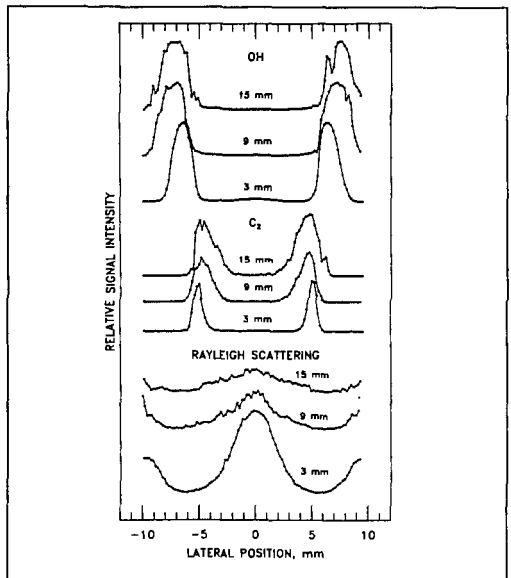

FIGURE 5

Data Analysis and Discussion

A laminar flame is a steady-state system: the value of any macroscopic variable (such as a species concentration) does not change with time at a particular spatial location [10]. Because there is a flow of material into and out of a given volume element due to mass transport, there must be a corresponding change in species' concentrations due to chemical reactions:

$$R_i = \nabla[N_i\ (v + V_i)]. \qquad (1)$$

Here, R_i is the net chemical rate, N_i is the species concentration, v is the mass average (convective) velocity, and V_i is the diffusion velocity of the species into the local mixture. All of the quantities on the right-hand side of Eq. 1 have been experimentally determined (N_i and v) or can be calculated directly from the experimental data (V_i).

Figure 6 illustrates the calculation of the chemical production rate, R_i, for acetylene at heights of 5 and 13 mm above the burner surface. Low in the flame, the rate profile exhibits a maximum destruction value near the high temperature, primary reaction zone, and a formation feature slightly toward the fuel side. This peak in the production rate is located on the lean, higher temperature side of the observed concentration peak (see Figure 4). Higher in the flame, the production rate is diminished by a new destruction feature (see arrow). This new destruction feature spatially overlaps an observed profile maximum for small soot particles, and this feature is believed to be due to acetylene participation in soot surface growth processes [10].

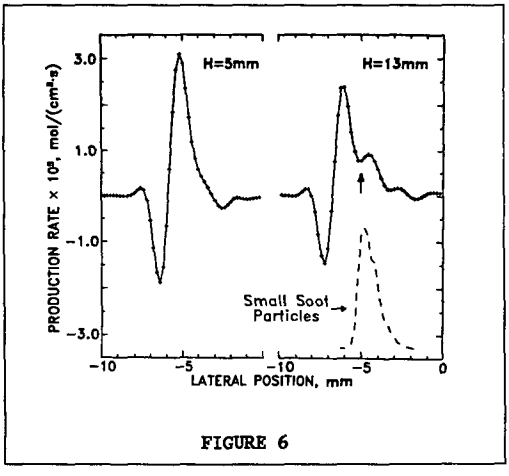

FIGURE 6

The concentration and production rate data have been used to critically evaluate proposed mechanisms for hydrocarbon condensation chemistry in the methane flame. For example, our data allows us to select between competitive reactions during specific growth steps in the formation of benzene. In the Introduction, alternative processes involving two, four, and six carbon-atom free radicals were suggested for the sequence leading from acetylene to benzene. For a given reaction to be important, its maximum forward rate must be faster than the observed production rate of the product benzene. For example, both ethynyl radicals and vinyl radicals can be formed by hydrogen atom reaction with acetylene. For these calculations, the concentration of

hydrogen atoms was determined by assuming equilibrium with methane in the reaction [10]:

$$H\cdot + CH_4 \overset{\leftarrow}{\rightarrow} H_2 + CH_3\cdot$$

In Figure 7, the formation rates of these radicals via reactions 1a and 1b are compared with the observed net benzene formation rate. As this figure indicates, the ethynyl radical, $C_2H\cdot$, is produced too slowly to account for the observed rate of the formation of benzene in the methane flame. In contrast, the vinyl radical, $C_2H_3\cdot$, formed through hydrogen atom addition to acetylene, is formed fast enough to account for our benzene rate data. Another route to vinyl formation is hydrogen abstraction from ethylene:

$$\text{R1c)}\ H\cdot + C_2H_4 \overset{\leftarrow}{\rightarrow} C_2H_3\cdot + H_2.$$

We have recently developed a method for distinguishing the individual contributions to the mass 28 signal from CO, N_2, and C_2H_4. Thus, the importance of reaction 1c) in the formation of benzene can be determined. The forward rate of R1c is plotted in Figure 7. Near the flame reaction zone, the magnitude of vinyl formation through R1c exceeds the observed net forward formation rate of benzene. Thus, in the methane flame, vinyl formation through both acetylene and ethylene can contribute to aromatic ring formation.

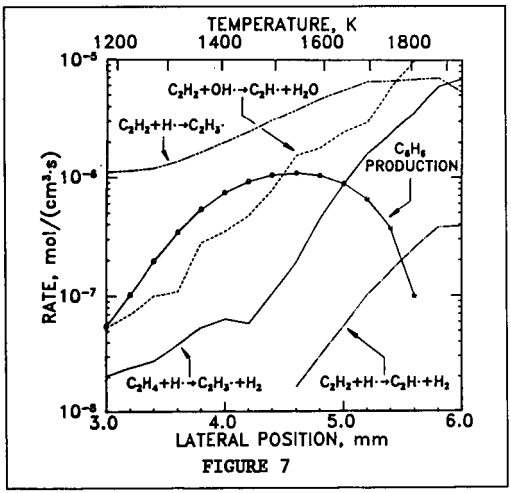

FIGURE 7

In a previous paper on the production rate calculations[10], we concluded that the vinyl radical was the key two-carbon radical in the formation sequence leading to benzene. This result was predicated on the assumption that oxygen containing radicals such as OH were not involved directly in this process. However, OH abstraction of hydrogen from acetylene to form ethynyl is a fast reaction [11] and should be considered in our analysis. We have therefore added reaction 1d)

Rld) $OH\cdot + C_2H_2 \rightleftharpoons C_2H\cdot + H_2O$

to the two-carbon radical formation processes plotted in Figure 7. Because laser induced fluorescence provides a determination of only the relative hydroxyl radical concentration, it is necessary to scale the profile results to a reasonable estimate of the actual OH concentration. To this end, the peak OH concentration was taken to be that predicted by the NASA combustion equilibrium code for methane/air mixtures at the local equivalence ratio, ≈ 0.7, and the temperature, 2030 K, where the fluorescence maximum is observed [12]. This estimate should prove to be conservative: Mitchell et al. have found super-equilibrium concentrations for OH in fuel-rich regions of methane/air diffusion flames [13]. As Figure 7 demonstrates, formation of ethynyl from OH reactions with acetylene is fast enough to account for the observed benzene formation rate.

Further tests of benzene formation mechanisms will focus on competitive routes to four-carbon molecule formation (R2a-R2c). A critical concern will be the relative concentrations of vinyl and ethynyl radicals. If the vinyl radical concentrations far exceed the ethynyl radical concentrations, as has been observed in pre-mixed acetylene flame results [14], then processes such as reaction 2c will be far more important than the ethynyl radical reactions such as 2a or 2b. Reliable estimation or measurement schemes for these radicals remains as one of the great challenges in unravelling diffusion flame chemistry.

References

1. I. Glassman and P. Yaccarino, Eighteenth Symposium (International) on Combustion, The Combustion Institute, 1175 (1981).
2. J. Warnatz, Eighteenth Symposium (International) on Combustion, The Combustion Institute, 69, (1981).
3. T. Tanzawa and W.C. Gardiner, Jr., J. Phys. Chem. 84, 236 (1980).
4. M.B. Colket, III, Chemical and Physical Processes in Combustion, Eastern States Section of the Combustion Institute, Paper 53, November 1985.
5. J.A. Cole, J.D. Bittner, J.P. Longwell, and J.B. Howard, Combustion and Flame 56, 51 (1984).
6. M. Frenklach, J.W. Clary, W.C. Gardiner, and S.E. Stein, Twentieth Symposium (International) on Combustion, The Combustion Institute, 887 (1984).
7. K.C. Smyth, J.H. Miller, R.C. Dorfman, W.G. Mallard, and R.J. Santoro, Combustion and Flame 62, 157 (1985).
8. R.M. Fristrom and A.F. Westenberg, Flame Structure, McGraw-Hill, New York, 1965.
9. J.H. Miller and P.H. Taylor, Combustion Science and Technology, in press.
10. J.H. Miller, W.G. Mallard, and K.C. Smyth, Twenty-first Symposium (International) on Combustion, The Combustion Institute, in press.
11. W. Tsang and R.F. Hampson, Journal of Physical and Chemical Reference Data 15, 1087 (1986).
12. S. Gordon and B.J. McBride, NASA SP-273, 1971.
13. R. Mitchell, A.F. Sarofim, L.A. Clomburg, Combustion and Flame 37, 201 (1980).
14. P.R. Westmoreland, D. Sc. Dissertation, Massachusetts Institute of Technology, 1986.

Soot Particle Formation in Diffusion Flames

Robert J. Santoro

Department of Mechanical Engineering
The Pennsylvania State University
University Park, PA 16802

I. Introduction

Over the past twenty five years a large number of investigations of soot formation, growth and oxidation have been reported. The extensive interest in this problem is a result of the important ramifications that the presence of soot particles have on practical combustion systems. Because of the diversity of these effects, a wide variety of experimental situations have been investigated. These range from small laboratory scale burners to full scale combustion devices. However, insights into the fundamental processes which control the formation and growth of soot particles have largely resulted from studies of simple premixed and diffusion flames. The results of such studies have been periodically reviewed and where applicable related to practical situations [1-4].

Recently a significant amount of attention has been given to the study of laminar and turbulent diffusion flames [5-15]. Many of these studies have utilized optical diagnostics to obtain quantatitive information on soot particle size, concentration and spatial distribution in the flame. These techniques which were first applied to premixed flames [16] have allowed for a significant advance in our quantitative understanding of soot formation processes. In fact, the results of the premixed flames studies established the common sequence of events which is now viewed to govern the formation of soot particles in most combustion situations. These include (1) a chemically kinetically controlled reaction sequence which results in the formation of precursor species needed to form the first particles, (2) a particle inception stage which results in the formation of large numbers of small primary particles, (3) a particle growth period in which surface growth and particle coagulation processes contribute to the increase in particle size and (4) a stage in which material is no longer added to the soot particles and size is controlled by agglomeration or may even be reduced by oxidative attack. Recent work in premixed flames has concentrated on more firmly establishing quantitative measurements of the individual processes which constitute this description. Significant progress has been made in understanding the surface growth and particle coagulation processes which occur in premixed flames [17,18]. Results from these and other studies have emphasized the importance of acetylene (C_2H_2) and available surface area in the particle growth process and have established that soot particle coagulation accounts for the particle number concentration behavior observed in such flames. Presently efforts are focused on the particle inception stage in an effort to link the formation of large intermediate hydrocarbon species which are viewed as precursors to soot

particles and the initial particles observed by light scattering techniques in the flame [19,20]. Such measurements present serious challenges for current diagnostic approaches and progress has been possible only through a combination of experimental measurements and extensive computer modelling of the soot aerosol as it develops in time. In these studies, the effects of particle inception, surface growth and coagulation must be taken into account simultaneously.

Recent studies in laminar diffusion flames have essentially confirmed that the formation and growth of soot particles can be described by a similar series of processes. Using laser-based techniques to measure particle size [6,7], velocity [9,10] and temperature [21], workers have provided a much more detailed understanding of soot particle processes in these flames. Because particle formation is not spatially homogeneous throughout the flame, the high spatial resolution of these techniques have allowed investigation of the structure of the soot particle field and, at least to some degree of accuracy, to follow the time history of the particles as they proceed through the flame [10,11,22]. In particular, attention has been given to the study of effects of temperature [23,24] and pressure [22] on the production of soot particles. Of related interest are studies examining radiative transfer from these flames which indicate that radiation from soot particles represents a significant energy transfer mechanism [15]. This has led several workers to speculate that radiative transfer is important in controlling the emission of soot particles from the flame [7,11,15].

In addition to these studies, which have emphasized the detailed processes involved in soot particle and growth, a large body of work exists concerning the relative sooting tendency of fuels [12,25,26]. These works largely focus on the concept of a "smoke point" or "sooting height" which characterizes an individual fuel. The sooting height is an experimental measurement of the height of a laminar diffusion flame when soot particles are observed to issue from the tip of the flame. Fuels which have a higher tendency to soot are found to have a shorter flame height at this characteristic point. Although a qualitative measure of soot production tendencies, workers investigating soot formation from this approach have made several critical contributions to the phenomenological understanding of soot particle formation [27]. Recently work has appeared to relate the more detailed measurement results in laminar and turbulent flames to these sooting height results with some success [28,29]. This work is particularly significant in that it allows a quantitative relationship to be obtained from the previous relational information on a wide variety of fuels. The fact that information for turbulent flames could be derived from laminar flame measurements is encouraging since it points to the general utility of the laminar diffusion flame results.

It should be mentioned that a good deal of the understanding of the evolution of the soot particle field in diffusion flames draws substantially from the earlier work of Roper [30,31]. In these papers, and recently in an update to that work [32], a simple model of laminar diffusion flames is developed which clearly describes the effects of fuel flowrate, temperature and radiation on the structure of the flame. These works have widely influenced other researchers in this field.

In the above work on diffusion flames, the emphasis has been on the particle aspects of these flames. Studies of the important chemistry have been undertaken for the most part in low pressure and atmospheric laminar premixed flames, although shock tube work has also contributed in some respects [33,34]. These studies have established plausible reaction mechanisms leading to the formation of aromatic compounds with a few rings. There continues to be a debate concerning the role that ions may have in providing the rapid chemical reaction rates needed to form the particles in the reaction times available (~ 1 ms) [35]. However, in the area of diffusion flames a relatively smaller amount of work is available examining the preparticle chemistry [36]. Recently a significant effort has been made to study both the chemistry leading to soot precursors and the subsequent soot particle growth in diffusion flame environments [9]. These results have not yet progressed sufficiently to allow a complete quantitative picture to be drawn, but progress is continuing [37].

The experiments to be described here are an extension of our previous laminar diffusion flame studies of soot particle formation [7,10]. Specifically a detailed examination of the effect of fuel chemical structure has been undertaken. In our previous work, the emphasis has been on examining the effects of fuel flowrate and temperature on the production of soot in diffusion flames [7,10,24]. In addition, specific attention was given to the processes controlling the emission of soot particles from the flame. These results along with the findings of other researchers has established the complex, coupled nature of the processes determining the soot particle evolution in the flame. The individual effects of temperature, flow field (e.g. velocity), pressure and fuel constitutents all must be investigated if a comprehensive understanding of the soot formation process is to be achieved.

II. Experimental Apparatus

For these studies, a coannular laminar diffusion flame has been used in which fuel is burned in air under atmospheric pressure conditions [7]. The burner consists of an 11.1 mm id fuel passage surrounded by 101.6 mm outer air passage. The flame is enclosed in a 405 mm long brass cylinder to shield the flame from laboratory air currents. Slots machined in the chimney provide for optical access while screens and a flow restrictor were placed at the exhaust of the chimney to achieve a stable flame. The burner is mounted on translating stages to provide three-dimensional positioning capability. Radial traversing of the burner is accomplished using a motorized translation stage.

The soot particle measurements were obtained using a laser scattering/extinction technique [16]. Laser extinction and scattering measurements were carried out using a 4 W argon ion laser which was operated at the 514.5 nm laser line. The incident laser power was 0.5 W and was modulated using a mechanical chopper. The transmitted power was measured using a photodiode and the scattered light was detected at 90° with respect to the incident beam using a photomultiplier tube. Signals from each detector were input to a lock-in amplifier and subsequently digitized signals were stored on a computer. The ratio of the measured scattering cross section to the extinction coefficient was used to determine particle size. For these calculations, the particle size

analysis was carried out using a data reduction approach based on Mie theory.

Previously obtained velocity measurements on a similar flame, obtained using a laser velocimeter technique, were used to calculate the particle paths and the residence time in the flame.

III. Results

As has been previously described, the amount of soot formed in a flame is a function of several variables. Temperature, pressure and fuel structure have been shown to be particularly important in determining the amount of soot formed. Thus, it is highly desirable to study soot particle formation under conditions where these variables can be systematically varied. This presents several problems, particularly in the case of fuel structure studies, because the sooting propensity of fuels varies widely [25-27]. This results in important variations in the velocity field and heat losses to the burner for different flames.

To overcome some of these difficulties, a fuel mixture approach has recently been tried for the study of soot particle processes in these flames. In this approach, an ethene/air diffusion flame which has been extensively characterized in terms of the particle, velocity and temperature fields has served as the baseline flame [7]. For the fuel composition studies, different fuel species were added to the baseline fuel (ethene), such that the additional carbon flow rate was the same in each case. Under these conditions, the total carbon flow rate is held constant. In addition, the flame size and shape remains similar for all the flames studied, thus minimizing changes in burner heat loss or particle transport in the flame. An ethene fuel flow rate of 3.85 cc/s (a carbon flow rate of 3.78×10^{-3}gm/s) was selected for the baseline flame since this diffusion flame has been extensively studied [7,10,22]. A second fuel was added to the ethene flow to produce a total carbon flow rate of 4.81×10^{-3}gm/s, an increase of 1.03×10^{-3}gm/s from the baseline case. Results have been obtained for methane, ethane, ethene, acetylene, propene, butene, and toluene. In the case of toluene, the fuel was vaporized using a technique similar to that described by Gomez et al. [12]. The flow conditions for these studies are given in Table 1 along with the calculated adiabatic flame temperatures for the fuel mixtures. Table 1 also includes the measured values for the percent carbon conversion to soot for the fuel increment introduced into the baseline flame. This value is obtained by taking the difference betwen the maximum soot mass flow rate observed in the flame for the fuel mixture case and the baseline flame divided by the carbon mass flow rate increase (1.03×10^{-3}gm/s). The percent conversion is observed to vary strongly as a function of fuel species with the aromatic fuel having the largest conversion percentage.

Using the previously obtained detailed information on the particle paths for the ethene flame, comparisons between the different fuels can be made for different regions of the flame. Two regions of the flame have been selected for illustration using the soot volume fraction (f_v) measurements. Figure 1 shows the time evolution of f_v along the particle path which traverses the annular region of the flame where the maximum f_v

Table 1

Baseline Fuel		Fuel Added	T_{ad}	Carbon Conversion
(cc/s)		(cc/s)	(K)	(%)
C_2H_4(3.85)	+	CH_4 (2.10)	2333	13
"	+	C_2H_6 (1.05)	2344	22
"	+	C_2H_4 (1.05)	2369	18
"	+	C_2H_2 (1.05)	2403	32
"	+	C_3H_6 (0.70	2368	36
"	+	C_4H_8 (0.525)	2359	52
"	+	C_7H_8 (0.30)	2361	98

is observed; Figure 2 shows a similar plot for the center line of the flame. The fuel mixtures shown include three alkenes (ethene, propene and butene) and an aromatic (toluene). As Table 1 indicates, the adiabatic flame temperatures for these fuel mixtures do not vary significantly. Thus, the temperature fields characterizing these flames should be similar, allowing a direct comparison between the flames.

Figures 1 and 2 clearly indicate that differences between the fuels are more pronounced in the annular region of the flame than near the center line. This implies that the higher temperatures and larger radical concentrations present in the annular region of the flame, which lies closer to the flame reaction zone, not only increase the soot formation rates, but also enhance the differences between fuel species. In the annular region (see Fig. 1), all the fuels are observed to reach a maximum in f_v at a similar residence time (≈60 ms). For the alkene fuels, the observed residence time for the first observation of soot particles and the value of f_v at this time are also very similar. However, the different alkene fuels are observed to have measurably different rates of growth in terms of the change in the soot volume fraction with time. For the toluene mixture, although soot particles are first observed at a similar residence time (≈21 ms), the initial concentration is much higher. This implies that soot particle inception occurred at an earlier time or that the inception process is much more vigorous. The particle size and number density measurements, along with the results from nearby particle paths, favor an interpretation indicating an earlier inception time. Thus, these results indicate that the specific nature of the fuel species is observed to affect the initial particle formation process as well as the subsequent growth rates. Comparisons with the data along the center line of the flame (see Figure 2) further support the argument that the aromatic fuel accelerates the inception process. However, the final soot volume fraction values observed in this region show smaller differences as compared to the annular region of the flame for the fuels studied. Thus, the particle growth processes may differ in this fuel rich region which also exhibits lower temperatures than observed in the annular region.

The approach of determining the influence of fuel structure based on fixed increments in the carbon flow rate provides an appropriate framework in which to consider the soot formation process in general. As an example, Fig. 3 shows a plot of the maximum soot mass flow rate as a function of fuel flow rate for a series of ethene/air flames [7,10]. A linear relationship is observed over the flow range studied, indicating that the conversion of fuel carbon to soot is constant beyond some minimum required flow rate to first produce soot particles in the flame. The observed value for the percent conversion for these ethene flames is 18%. Similar experiments for other fuels are presently underway.

IV. Discussion

The results described above, although preliminary nature, have identified several features which are deserving of further investigation. Attention should be focused on differentiating the particle inception and surface growth contributions for the various fuel types. The differences between the alkene and aromatic fuels is, obviously, of most interest in light of the large differences in their sooting tendencies. In addition, the occurence of a constant conversion percentage based on fuel structure needs further investigation. Specifically, this relationship for fuel mixtures needs to be developed over a wider variation of fuel structures and as a function of temperature. Recently, Kent [28] has reported soot conversion percentages for a wide variety of fuels which were directly related to soot volume fraction measurements obtained at the sooting height [28,38]. In this case, the conversion percentages are based on the total amount of conversion of fuel to soot rather than on the incremental change as described above. However, the trends observed in terms of the contrast between the alkene and aromatic fuel species are similar to those observed here. Kent's results indicate the conversion percentage for ethene to be 12% while that for toluene is 38%. The values for acetylene and propene were 23% and 16% respectively which differs in the ordering observed in the present study. However, the present results agree with previous studies of sooting height measurements in terms of the sooting tendency of the studied fuels [12]. These results along with the previous studies mentioned represent the beginning steps to obtaining a quantitative understanding of the effect of fuel molecular structure or soot formation in diffusion flames. Significant progress is likely to continue as experimenters concentrate on specific aspects of the problems such particle inception and surface growth.

Acknowledgement

The support of the Air Force Office of Scientific Research under grant AFOSR-87-0145 is gratefully acknowledged. The author also wishes to acknowledge with great appreciation the contributions of coworkers at the National Bureau of Standards J.J. Horvath, H.G. Semerjian and T.T. Yeh. The U.S. government is authorized to reproduce and distribute reprints for governmental purposes notwithstanding any copyright notation thereon.

References

1. Palmer, H. B. and Cullis, C. F., in The Chemistry and Physics of Carbon, Walker, P. J., Jr. and Thrower, P. A., Marcel Dekker, 1965, Vol. 1, p. 265.

2. Haynes, B. S. and Wagner, H. Gg., Prog. Energy Combust. Sci., 7,22 (1981).

3. Wagner, H. Gg., in Particulate Carbon Formation During Combustion, Siegla, D. C. and Smith G. W., Eds., Plenum, New York, 1981, p. 1.

4. Howard, J. B. and Kausch, W. J. Jr., Prog. Energy Combust. Sci., 6, 263, (1980).

5. Haynes, B. S., and Wagner, H., Gg., Ber. Bunsenges Phys. Chem. 84, 498, (1980).

6. Kent, J. H., Jander, H., and Wagner, H., Gg., Eighteenth Symposium (International) on Combustion, The Combustion Institute, Pittsburgh, 1981, 1117.

7. Santoro, R. J., Semerjian, H. G. and Dobbins, R. A., Combustion and Flame, 51, 203, (1983).

8. Prado, G., Garo, A., Ko, A. and Sarofim, A., Twentieth Symposium (International) on Combustion, The Combustion Institute, Pittsburgh, 1984, p. 989.

9. Smyth, K. C., Miller, J. H., Dorfman, R. C., Mallard, W. G. and Santoro, R. J., Combustion and Flame, 62, 157, (1985).

10. Santoro, R. J., Yeh, T. T., Horvath J. J. and Semerjian, H. G., Combustion Science and Technology, in press (1987).

11. Kent, J. H. and Wagner, H. Gg., Combustion Science and Technology, 41, 245 (1984).

12. Gomez, A., Sidebotham, G. and Glassman, I., Combustion and Flame, 58, 45 (1984).

13. Kent, J. H. and Bastin, S. J., Combustion and Flame, 56, 29 (1984).

14. Kent, J. H., Combustion and Flame, 67, 223 (1987).

15. Markstein, G. H., Twentieth Symposium (International) on Combustion, The Combustion Institute, Pittsburgh, 1985, p. 1055.

16. D'Allessio, A., Di Lorenzo, A., Sarofim, A. F., Berretta, F., Masi, S. and Venitozzi, C., The Fifteenth Symposium (International) on Combustion, The Combustion Institute, Pittsburgh, 1975, p. 1427.

17. Harris, S. J. and Weiner, A. M., Combustion Science and Technology, 32, 155 (1983).

18. Bockhorn, H., Fetting, F., Heddrich, A. and Wannemacher, Twentieth Symposium (International) on Combustion, The Combustion Institute, Pittsburgh, 1985, p. 979.

19. Harris, S. J. and Weiner, A. M., Combustion and Flame, 64, 65 (1986).

20. Kennedy, I. A., Combustion and Flame, 68, 1 (1987).

21. Boedeker, L. and Dobbs, G. M., Combustion Science and Technology, 46, 31 (1986).

22. Flower, W. L. and Bowman, C. T., The Twentieth Symposium (International) on Combustion, The Combustion Institute, Pittsburgh, 1984, p. 1035.

23. Kent, J. H. and Wagner, H. Gg., Twentieth Symposium (International) on Combustion, The Combustion Institute, Pittsburgh, 1984, p. 1007.

24. Santoro, R. J. and Semerjian, H. G., Twentieth Symposium (International) on Combustion, The Combustion Institute, Pittsburgh, 1984, p. 997.

25. Schug, K. P., Manheimer-Timnat, Y., Yaccaino, P. and Glassman, I., Combustion Science and Technology, 22, 235 (1980).

26. Calcote, H. F. and Manos, D. M., Combustion and Flame, 49, 289 (1983).

27. Glassman, I. and Yaccarino, P., Eighteenth Symposium (International) on Combustion, The Combustion Institute, Pittsburgh, 1981, p. 1175.

28. Kent, J. H., Combustion and Flame, 63, 349 (1986).

29. Kent, J. H., Combustion and Flame, 67, 223 (1987).

30. Roper, F. G., Combustion and Flame, 29, 219 (1977)

31. Roper, F. G., Smith, C. and Cunningham, A. C., Combustion and Flame, 29, 227 (1977)

32. Roper, F. G., Combustion Science and Technology, 40, 323 (1984).

33. Bittner, J. D. and Howard, J. B. Eighteenth Symposium (International) on Combustion, The Combustion Institute, Pittsburgh, 1981, p. 1105.

34. Frenklach, M., Clary J., Gardiner, W. C. and Stein, S. E., Twentieth Symposium (International) on Combustion, The Combustion Institute, Pittsburgh, 1984, p. 887.

35. Calcote, H. F., Combustion and Flame, 42, 215 (1981).

36. Flossdorf, J., Jost, W. and Wagner, H. Gg., Ber. Bunsenges. Phys. Chem., 78, 378 (1974).

37. Santoro, R. J. and Miller, H. J., Langmuir, 3, 244 (1987).

38. Olson, D. B., Pickens, J. C. and Gill, R. J., Combustion and Flame [to appear].

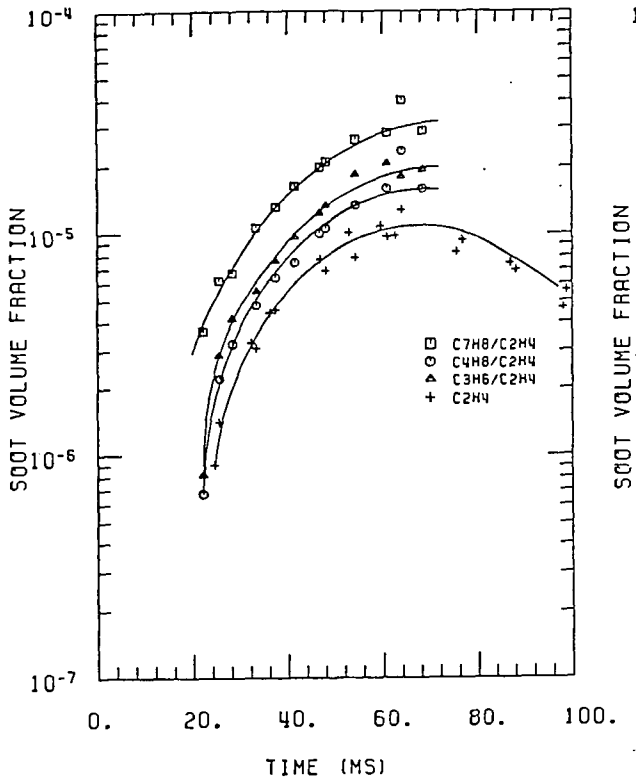

Figure 1. Comparison of the soot volume fraction, along the streak line exhibiting the maximum soot volume fraction for fuel mixtures containing ethene, propene, butene or toluene.

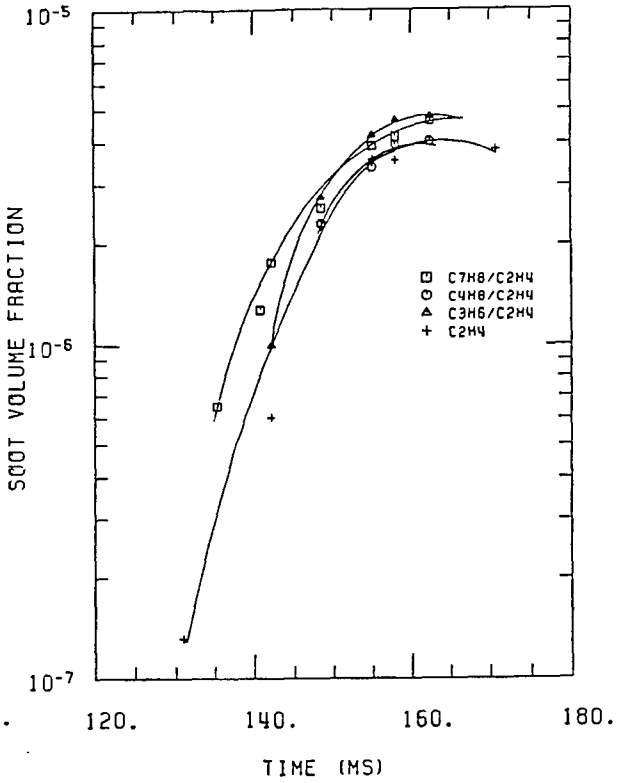

Figure 2. Comparison of the soot volume fraction along the center line of the flame for fuel mixtures containing ethene, propene, butene or toluene.

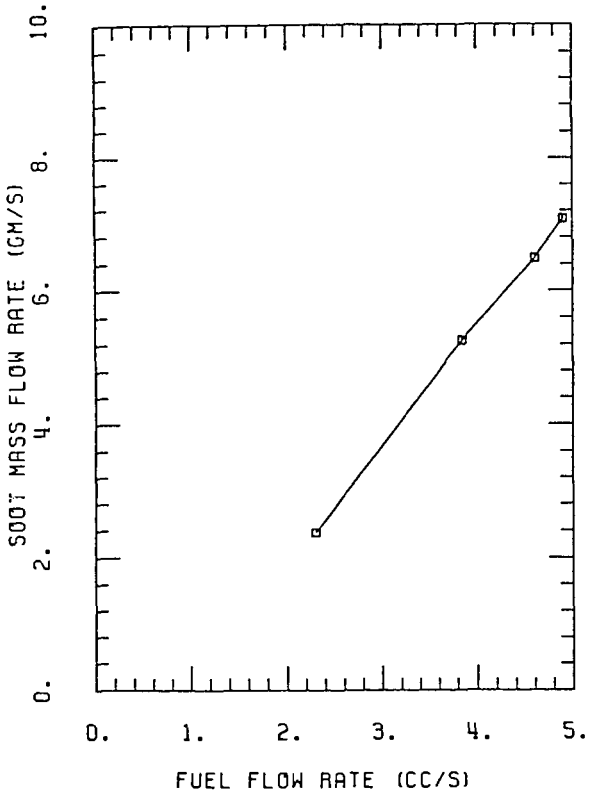

Figure 3. The maximum soot mass flow rate as a function of fuel flow rate for an ethene air diffusion flame.

ARE IONS IMPORTANT IN SOOT FORMATION?

H. F. Calcote, D. B. Olson, and D. G. Keil

AeroChem Research Laboratories, Inc.
P.O. Box 12, Princeton, NJ 08542

I. INTRODUCTION

Many chemical mechanisms have been proposed for the formation of incipient soot in flames. The ionic mechanism has not been widely embraced; it is considered a competitor to free radical mechanisms which have received more attention. It seems timely to review the evidence for the ionic mechanism, which we do here.

The precursor of soot formation is assumed to be the propargyl ion, $C_3H_3^+$ (1-3). The source of this ion is not clear but it is the dominate ion in fuel rich hydrocarbon flames and is generally considered to be a primary chemi-ion, i.e., derived from the reaction of neutral species. There are two isomers of $C_3H_3^+$, a linear structure and a more stable cyclic structure. Measurements of reaction rates for these two isomers at near room temperature demonstrate that reactions of the linear isomer are fast, generally equal to the Langevin rate, while reactions of the cyclic isomer are slower (4-6). Eyler and associates (7) have recently determined that the rate of linear $C_3H_3^+$ reacting with acetylene is small compared to Langevin theory (8,9). The validity of extrapolating these measurements to high temperatures is not clear. The Langevin theory, for ions reacting with non-dipolar molecules, does not predict a temperature dependence. Which isomer of $C_3H_3^+$ is formed initially in flames is also not known, nor is the rate of isomerization.

In the ionic soot formation mechanism, the precursor ion reacts with neutral species, e.g., acetylenes, to produce larger ions. These larger ions continue to react further to produce ever increasingly larger ions.

A major feature of this mechanism is the large rate coefficients for ion-molecule reactions and the ease with which ions isomerize (8). The formation of a cyclic structure does not represent a significant energy barrier as it does for a free radical mechanism. Some of the electrons produced in the chemi-ionization reaction produce negative ions by electron attachment to large molecules; these reactions are favored by low temperature and increasing molecular weight of the neutral reactant. As the ions grow larger their recombination rate coefficient for reaction with electrons or negative ions increases, so positive ions are removed, forming large neutral molecules, the equivalent of small neutral soot particles. The small neutral particles continue to grow and as they become larger their work function approaches that of bulk graphite. At sufficiently high temperature, these particles become thermally ionized; these thermally ionized particles are not of interest for soot nucleation.

In this paper we review the evidence for the sequence of reactions starting with $C_3H_3^+$ and proceeding through large soot ions; this sequence of reactions has been labeled "the ionic mechanism."

II. EVIDENCE

A. Concentration

Concentrations of ions have been measured by AeroChem (2,3,10), Delfau and associates (11,12), and Homann and associates (13,14) in what has been referred to as the "standard flame." This is a premixed, sooting acetylene/oxygen flame on a

flat flame burner at 2.7 kPa, an equivalence ratio of 3.0, and an unburned gas velocity of 50 cm/s. Ion concentrations are shown in Fig. 1 along with neutral soot concentrations, charged soot concentrations, and the flame temperature. The ion concentration in this flame is sufficient to account for the formation of the observed soot.

B. Reaction Rates

Ion-molecule rate coefficients are generally several orders of magnitude greater than for neutral species reactions (8), which, of course, means that the concentration of ions does not have to be as great to react at the same rate.

Figure 1 also contains evidence that the rates of ion-molecule reactions are sufficiently rapid in flames to account for soot formation. As the ion concentration decays by ion recombination, the soot concentration increases. The slopes are comparable within the accuracy of the data. We note, however, that soot particles are identified as those which can be detected using an electron microscope, i.e., their diameter exceeds 1.5 nm.

Several available sets of data on neutral soot particle diameters and positively charged soot particle diameters are presented in Fig. 2 for the standard C_2H_2/O_2 flame. These data have presented a dilemma (15); it appears that neutral particles grow faster than charged particles, but in the early part of the flame the charged particles have a larger diameter. This question seems to relate more to particle growth and thermal ionization than to soot nucleation; nevertheless the location of the phenomena in the flame is at just the distance where the initial ion concentration is falling and the concentrations of neutral particles and charged particles are increasing. In previous calculations (1,16) of thermal ionization of soot particles about 2 cm downstream from the burner, the assumption was made that equilibrium was approached from the side of excess neutral particles. This is difficult to rationalize if the concentration of charged particles exceeds the concentration of neutral particles at small distances where the particle diameters are the smallest.

The fraction of thermally ionized particles and the rate of thermal ionization are both very sensitive to particle diameter. For the small neutral particles the calculated ionization rate is slow compared to the experimental rate. Thus at 2.25 cm above the burner, with the Richardson equation modified for small particles (17), we calculate a rate of ionization of 2×10^{11} charged particles/(cm^3 s) and we measure a rate of 6×10^{11} charged particles/(cm^3 s) from the slope of the "charged soot" curve in Fig. 1. Between 2.5 and 3.0 cm the calculated rate exceeds the observed rate; here and at greater distances equilibrium controls the concentrations. Thus at the first appearance of soot the rate of thermal ionization of neutral particles is too small to account for the observed rate of charged particle appearance; close to the burner equilibrium is approached from the direction of excess charged particles. This is further evidence that charged species are involved in the formation of soot.

The difference in slopes of the neutral and charged particle concentrations in Fig. 2 is probably due to a faster rate of ion-electron recombination for large ions than for small ions. For example, increasing the particle diameter from 5 to 10 nm increases the rate coefficient of recombination from about 1.3×10^{-6} to about 3.8×10^{-6} cm^3/s. Thus the larger charged particles disappear more rapidly than the smaller ones. In the region of the flame where this occurs, the observed charged particles are derived from the chemi-ions produced early in the flame and are not derived from the neutral particles. This is not only further evidence for the ionic mechanism of soot formation, but it makes very awkward any explanation of the source of ions being the thermally ionized particles as some have suggested.

C. Confirmation of Ions

All of the individual ions involved in the postulated mechanism, up to mass 557, have been observed in sooting flames (2,3,11,12). The confirmation that ions larger than these are present in the flame, prior to the appearance of soot, has also been documented (13,14).

D. Location of Ions in Flame

The order of appearance of ions and soot, Fig. 1, in a flame is not in itself evidence that ions are produced before soot in the reaction sequence; the order of appearance would be reversed if the rate of production of soot from ions were fast compared to the rate of production of ions. However, when the species peak at considerable distance apart in the flame it seems safe to assume that the first peak precedes the second in the reaction sequence as well as in order of appearance. This assumption is further warranted when there is no clear means of proceeding from soot to ions (18). With these caveats, the appearance of ions in the flame with respect to the appearance of soot is evidence for ions being the precursors of soot.

Further evidence of a similar nature comes from observations in diffusion flames at one atmosphere. We have made ion concentration measurements (19) in the same methane/air flame on which Smyth et al. (20) made a number of measurements. Our temperature profiles agreed with theirs. The data for this diffusion flame are summarized in Fig. 3 and the rationale for the estimates of concentrations are summarized in the caption. The soot concentration profile was not measured by Smyth et al., but the position of the soot maximum in the flame was determined by laser induced ionization. The relative concentrations of polycyclic aromatic hydrocarbons, PCAH, were estimated from laser induced fluorescence. We confirmed the radial location of the soot maximum by laser extinction measurements at a wavelength of 633 nm somewhat higher in the flame. We estimate from our measurements that the volume fraction of soot is about 5×10^{-8}, which for 20 nm diameter particles would correspond to about 10^{10} particles/cm^3.

The location of soot, Fig. 3, with respect to the possible reactants is evidence for the ionic mechanism as opposed to a mechanism involving only acetylene and a PCAH. For a reaction of acetylene and PCAH to be to be reasonable, it is necessary to assume something else is involved, such as hydrogen atoms (21,22), or that the rate limiting reaction has a very high activation energy. The soot is located between the peak concentrations of acetylenes and ions, just where it would be anticipated if these were the two reactants producing it.

An important question with respect to soot formation is "why does inception stop?" (23). Harris has recently suggested that the falloff in oxygen concentration may be responsible due to its promotion of the formation of high energy species which are important for soot formation and which disappear along with the oxygen. He suggested that the production of excess H-atoms is possibly responsible for the effect. An even more obvious explanation for the termination of soot inception would be the termination of ion formation and the rapid decrease in ion concentration, see e.g., Fig. 1. It is a long established fact that ions show a sharp peak in the flame front of hydrocarbon flames (24,25).

E. Changes With Equivalence Ratio

In premixed flames dramatic changes in ion concentrations occur at the threshold fuel concentration for soot formation as shown in Fig. 4. Small flame ions are replaced by large ions as the equivalence ratio is increased through the threshold soot point. This simple observation would be consistent with an ionic

mechanism of soot formation; there are, however, complications. Why does the total concentration of ions increase at higher equivalence ratios beyond the soot threshold? This observation has, in fact, been used to argue against the ionic mechanism; namely that the occurrence of the increase in ion concentration with equivalence ratio was due to ionization of charged particles (11,15). We have subsequently demonstrated that thermal ionization of soot particles cannot be the explanation for this increase (10) but the phenomenon remains unexplained. Both the maximum flame temperature (26) and the total ion recombination coefficient (10) change at the soot threshold concentration. The temperature drop is probably due to increased radiative losses.

F. Fuel Effects

The occurrence of ions and the appearance of soot in flames of various fuels are consistent with the ionic mechanism of soot formation, i.e., fuels which do not produce ions do not produce soot (1).

Another indication of a correlation between fuel effects on soot formation and ionization can be gleaned from the correlation made by Takahashi and Glassman (27) between the equivalence ratio for soot formation and the number of carbon bonds; the tendency to soot increases with the number of carbon bonds. This is similar to the tendency of compounds to produce ions under various conditions. In flame ionization detectors for gas chromatography the magnitude of the signal produced correlates with the number of carbon atoms in the molecule (28). In premixed fuel/oxygen flames, Bulewicz and Padley (29) found that the electron current increased with the number of carbon atoms in the molecule. Interestingly acetylene differed from their correlation as it does in the Takahashi and Glassman correlation.

G. Chemical Additive Effects

Some of the first evidence quoted for an ionic mechanism of soot formation was from observations of the effect on soot formation of chemical additives with low ionization potentials. Strong correlations are observed between the effectiveness of additives on soot formation and their ionization potentials (30). Alkaline earths are a special case because the level of ionization is greater than anticipated by thermal equilibrium; ions are produced by chemi-ionization (31).

The same additives have been observed to both promote or inhibit (30) the formation of soot, and the results have been interpreted as affecting either the nucleation or the coagulation step. Much of the confusion arises because of the number of possible roles an additive can play and the fact that these roles can vary with the experimental conditions, e.g., the concentration of the additive (32).

The effects of additives on soot nucleation are based on two processes as suggested by Addecutt and Nutt (33): (1) the transfer of charge from a chemi-ion to a metallic atom, A, (34) e.g.:

$$M^+ + A \rightleftharpoons M + A^+ \qquad 1)$$

where M^+ is any hydrocarbon ion, such as $C_3H_3^+$, or (2) by increasing the concentration of electrons due to thermal ionization of easily ionized metals. This would increase the rate of dissociative recombination of chemi-ions:

$$A \rightleftharpoons A^+ + e^- \qquad 2)$$

$$M^+ + e^- \rightarrow \text{Products} \qquad 3)$$

Either one of these mechanisms would remove the precursor chem-ion from the system and thus reduce the number of soot nuclei produced. Reaction 1 will be important under conditions such that the equilibrium concentration of M^+ is lower than that of A^+. In fact, the rate coefficient for Reaction 1 is so much greater than for Reaction 2 that equilibrium concentrations of A^+ may be approached via Reaction 1 rather than Reaction 2. The metal ion, A^+, may also be produced in greater than equilibrium concentrations by Reaction 1 (35). Thus the specific mechanism by which the addition is effective will be determined by the relative equilibrium concentration of A^+ to M^+ and the time available to approach equilibrium.

Miller (36), in a study of additive effects on flame quenching, observed that the addition of carbon tetrachloride to a spherical low pressure diffusion flame transformed a nonsooting flame to a sooting flame and simultaneously completely altered the ionic composition of the flame. The chlorine from the additive forms compounds which attach electrons producing large concentrations of negative ions. These reduce the rate of recombination of positive ions because recombination coefficients with negative ions are about 100 times smaller than with electrons. Thus the positive ion concentration is increased, and this increase, via the ionic mechanism of soot formation, produces observable soot.

Bulewicz et al. (32) have studied the effect of metal additives on soot formation in flames and have given a detailed interpretation of their results which is in complete accord with our current concepts of the mechanism of soot formation via an ionic mechanism. A number of chemical additives were added to the fuel side of an acetylene/oxygen diffusion flame. The soot was collected on a glass fiber filter and weighed. The soot particle size was determined by electron microscopy of samples taken at 2 cm, about 1 ms, above the burner rim, and the total positive ion concentration was determined by Langmuir probe. Flame temperatures were in the range of 1400 to 1800 K.

The same additive acted as a pro-soot or an anti-soot additive, depending upon the total ion concentration due to the additive. With increasing ion concentration, the total quantity of soot increases and then decreases so that at one specific additive concentration, the amount of soot is the same as without the additive. At this additive concentration the particle number density reaches a maximum. Beyond this concentration the number density, total mass of soot, and the soot particle size all decrease so that the dominant effect of the additive is on the nucleation rather than the coagulation step. In other flames the dominant effect of additives is on coagulation, see e.g., Haynes et al. (37).

Bulewicz et al. (32) explain both the pro-soot and the anti-soot effects by means of an ionic mechanism. The reader is referred to their paper for the detailed arguments. Briefly, the anti-soot effect is due to charge transfer from the precursor hydrocarbon ion, M^+, to the metal atom as in Reaction 1. They point out that in their flame, thermal ionization of the metal atom would be too slow to produce electrons above the natural flame level so that Reaction 3 cannot be effective in reducing the concentration of hydrocarbon flame ions. The pro-soot effect is explained by demonstrating that small concentrations of additive may, in fact, maintain the level of M^+ at a higher value throughout the flame than when no additive is present. The potassium level in the range of concentration near the crossover point from pro-sooting to anti-sooting varies from about 10^{10} to 10^{14} atom/cm^3. At about 1600 K, the equilibrium concentration of K^+ varies from about 10^8 to 10^{10} ion/cm^3 (function of solution molarity). The natural flame ionization concentration is about 10^{10} ion/cm^3, several orders of magnitude above equilibrium levels. When the concentration of K is 10^{14} and the concentration of M^+ is 10^{10} it is clear that Reaction 1 can proceed at a significant rate, thus reducing the concentration of M^+. At this high level of additive concentration the equilibrium

concentration of K^+ cannot be exceeded. On the other hand when the K concentration is only 10^{10} atom/cm^3, the M^+ concentration can be only negligibly reduced in the time available. However, the equilibrium level of K^+, which is only about 10^8 ion/cm^3, may be significantly exceeded because the recombination rate is slow compared to the rate of charge transfer from chemi-ions, Reaction 1 (see e.g., Ref. 35). Farther downstream the slow decay of K^+ maintains a higher level of total ionizations and at this point Bulewicz et al. (32) suggest that the reverse of Reaction 1 maintains the concentrations of M^+. In the absence of this reaction, M^+ would have decayed because dissociative recombination of molecular ions is about two orders of magnitude greater than for atomic ions which must decay by a three body process. Thus new ionic nuclei are available at later stages in the combustion process to grow to incipient soot particles.

The pro-soot action of higher ionization elements, e.g., Pb 7.42 eV; Mg 7.64 eV; Cr 6.76 eV; Co 7.86 eV; Mn 7.43 eV; and even Li 5.39 eV, are explained by the above argument. Their equilibrium ionization levels are very low and their ionization potentials are somewhat less than those for hydrocarbon ions, so a concentration above the equilibrium concentration is expected. Clearly this analysis merits more detailed modeling in which all of the simultaneous reactions can be accounted for more quantitatively. It does, however, at this stage of development, support the ionic mechanism of soot formation.

III. SUMMARY

The answer to the question raised in the title seems to be "yes."

ACKNOWLEDGEMENTS

This paper is based on work funded by the Air Force Office of Scientific Research under contract F49620-83-C-0150 and National Science Foundation grant CBT-8502122. The United States Government is authorized to reproduce and distribute reprints for government purposes not withstanding any copyright notation hereon.

REFERENCES

1. Calcote, H.F., Combust. Flame 42, 215 (1981).

2. Olson, D.B. and Calcote, H.F., Eighteenth Symposium (International) on Combustion (The Combustion Institute, Pittsburgh, 1981) p. 453.

3. Calcote, H.F., and Keil, D.G., submitted to Combust. Flame.

4. Smyth, K.C., Lias, S.G., and Ausloos, P., Combust. Sci. Tech. 28, 147 (1982).

5. Eyler, J.R., in The Chemistry of Combustion Processes, T.M. Sloane, Ed., ACS Symposium Series 249 (American Chemical Society, Washington, DC, 1984) p. 49.

6. Baykut, G., Brill, F.W., and Eyler, J.R., Combust. Sci. Tech. 45, 233 (1986).

7. Eyler, J.R., Ozlark, F., Baykut, and Moini, M., to be submitted to J. Phys. Chem.

8. Bowers, M.T., Ed., Gas Phase Ion Chemistry, Vol. 1 and 2, (Academic Press, 1979).

9. Patrick, R. and Golden, D.M., J. Chem. Phys. 82, 75 (1985).

10. Keil, D.G., Gill, R.J., Olson, D.B., and Calcote, H.F., Twentieth Symposium (International) on Combustion (The Combustion Institute, Pittsburgh, 1985) p. 1129.

11. Delfau, J.L., Michaud, P., and Barassin, A., Combust. Sci. Tech. 20, 165 (1979).

12. Michaud, P., Delfau, J.L., and Barassin, A., Eighteenth Symposium (International) on Combustion (The Combustion Institute, Pittsburgh, 1981) p. 443.

13. Homann, K.H., Ber. Bunsenges. Phys. Chem. 83, 738 (1979).

14. Homann, K.H. and Stroefer, E., Soot in Combustion Systems and Its Toxic Properties, J. Lahaye and G. Prado, Eds. (Plenum, New York, 1983) p. 217.

15. Haynes, B.S. and Wagner, H. Gg., Progr. Energy Combust. Sci. 7, 229 (1981).

16. Howard, J.B. and Prado, G.P., Combust. Sci. Tech. 22, 189 (1980).

17. Sodha, M.S. and Guha, S., Adv. Plasma Phys. 4, 219 (1971).

18. Calcote, H.F., in Soot in Combustion Systems and Its Toxic Properties, J. Lahaye and G. Prado, Eds. (Plenum Press, New York, 1983) p. 197.

19. Keil, D.G. and Calcote, H.F., paper in preparation.

20. Smyth, K.C., Miller, J.H., Dorfman, R.C., Mallard, W.G., and Santoro, R.J., Combust. Flame 62, 157 (1985).

21. Frenklach, M, Clary, D.W., Gardiner, W.C., Jr., and Stein, S.E., Twentieth Symposium (International) on Combustion (The Combustion Institute, Pittsburgh, 1985) p. 887.

22. Frenklach, M. and Warnatz, J., accepted for publication in Combust. Sci. Tech.

23. Harris, S.J., Combust. Flame 66, 211 (1986).

24. Calcote, H.F., Combust. Flame 1, 385 (1957).

25. Wilson, H.A., Rev. Mod. Phys. 3, 156 (1931).

26. Calcote, H.F., Olson, D.B., and Keil, D.G., paper in preparation.

27. Takahashi, F. and Glassman, I., Combust. Sci. Tech. 37, 1 (1984).

28. Bulewicz, E.M., Nature 211, 961 (1966).

29. Bulewicz, E.M. and Padley, P.J., Ninth Symposium (International) on Combustion (Academic Press, New York, 1963) p. 638.

30. Howard, J.B. and Kausch, W.J., Jr., Prog. Energy Combust. Sci. 6, 263 (1980).

31. Schofield, K. and Sugden, T.M., Tenth Symposium (International) on Combustion (The Combustion Institute, Pittsburgh, 1965) p. 589.

32. Bulewicz, E.M., Evans, D. G., and Padley, P. J., Fifth Symposium (International) on Combustion (Reinhold Publishing Corp., New York, 1955) p. 1461.

33. Addecutt, K.S.B. and Nutt, C.W., Symposium on Deposit, Wear, and Emission Control, ACS Meeting, September 1969, p. A69.

34. Prado, G.P. and Howard, J.B., in Evaporation - Combustion of Fuels, Advances in Chemistry Series No. 166, J.T. Zung, Ed. (American Chemical Society, Washington, DC, 1978) p. 153.

35. Calcote, H.F., in Ion-Molecule Reactions, Vol. 2, J.L. Franklin, Ed. (Plenum Press, New York, 1972) p. 673.

36. W. J. Miller, Comment following Place and Weinberg paper, Eleventh Symposium (International) on Combustion (The Combustion Institute, Pittsburgh, 1967) p. 252, and unpublished work (AeroChem TP-151, 1967).

37. Haynes, B.S., Jander, H., and Wagner, H.Gg., Seventeenth Symposium (International) on Combustion, (The Combustion Institute, Pittsburgh, 1979), p. 1365.

38. Howard, J.B., Wersborg, B.L., and Williams, G.C., Faraday Soc. Symp. 7, 109 (1973).

39. Bonne, U., Homann, K.H., and Wagner, H. Gg., Tenth Symposium (International) on Combustion (The Combustion Institute, Pittsburgh, 1965), p. 503.

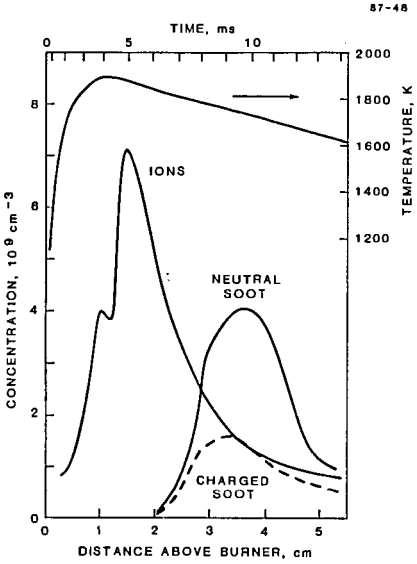

FIGURE 1 COMPARISON OF TOTAL ION CONCENTRATION AND SOOT CONCENTRATION PROFILES IN LOW PRESSURE (2.67 kPa), Ø = 3.0 ACETYLENE/OXYGEN FLAME (50 cm/s UNBURNED GAS VELOCITY)
The temperature, ion profiles, and time axis are from AeroChem (10). The soot profiles are from Howard et al. (38) and have been reduced by 50% so the charged soot and ion concentrations agree at 3.5 cm (10).

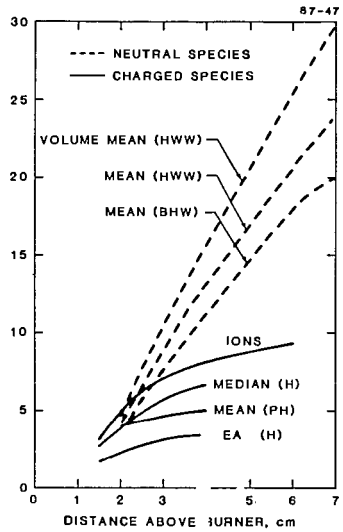

FIGURE 2 NEUTRAL SOOT PARTICLE AND CHARGED SOOT PARTICLE DIAMETERS IN SAME ACETYLENE/OXYGEN FLAME AS FIG. 1
HWW = Ref. 38. BHW = Ref. 39.
(Median) IONS = Refs. 13 and 14.
PH = Ref. 34.

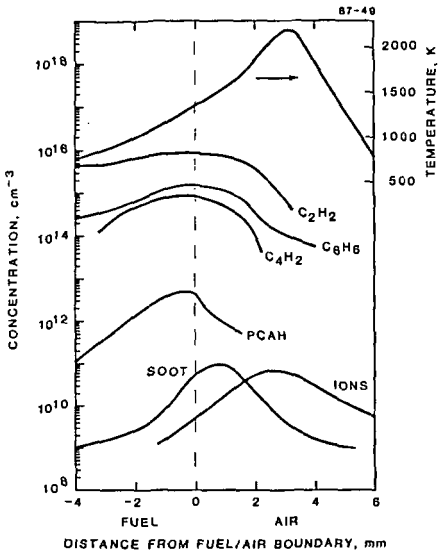

FIGURE 3 PROFILES 15 mm ABOVE A WOLFHARD PARKER SLOT BURNER SUPPORTING AN ATMOSPHERIC PRESSURE METHANE/AIR *DIFFUSION FLAME*

Fuel velocity = 9.7 cm/s. Air velocity = 19.4 cm/s. TEMPERATURE and positive IONS (concentration measured with Langmuir probe, 1000 amu ion mass assumed) profiles measured at AeroChem (19). Other profiles from Smyth et al. (20). Profile for C_4H_2 represents experimental profiles at 9 mm scaled to 15 mm by the acetylene ratio at the two heights. PCAH is visible laser induced fluorescence profile approximately scaled with a constant factor based on the ratio of $C_{14}H_8$ to C_6H_6 concentrations in the low pressure flame of Figs. 1 and 2. SOOT is in arbitrary units and was scaled to maximize at the same concentration as IONS.

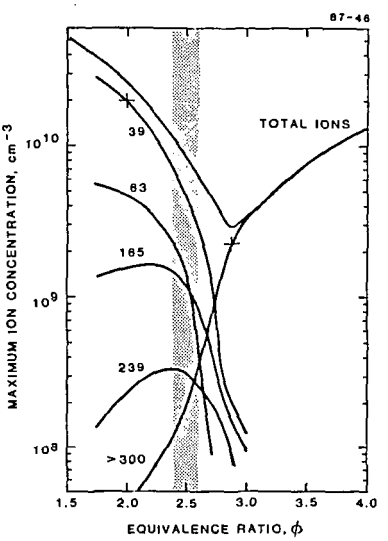

FIGURE 4 VARIATION OF MAXIMUM ION CONCENTRATION WITH EQUIVALENCE RATIO IN LOW PRESSURE ACETYLENE/OXYGEN FLAME

TOTAL IONS are Langmuir probe measurements. Profiles of individual ions indicated by mass in amu were measured with flame ion sampling mass spectrometry. The ratio of TOTAL IONS to the *sum* of the individual currents at $\emptyset = 3$, where mass 39 dominates (+) provided a calibration of the mass spectrometer for lighter masses. Similarly, > 300, representing all heavy masses between 300 amu and the high mass cut-off of the mass spectrometer, was put on an absolute scale at $\emptyset = 2.9$ (+). Shading indicates the threshold for soot formation.

Cluster Size Distribution for Free Molecular Agglomeration

G. W. Mulholland[1], R. J. Samson[2], R. D. Mountain[1], and M. H. Ernst[3]

1. INTRODUCTION

Dobbins and Megaridis (1) have observed soot agglomerates in a diffusion flame via thermophoretic sampling. The agglomerates are made up of spherules with a typical diameter of about 30 nm. A characteristic of the agglomerate is the relatively low density of the structure with much open space as indicated in Fig. 1. This study is concerned with modeling the agglomeration growth process.

Within the flame, the mean free path of the gas is on the order of 300 nm. Under these conditions, the particle continues in a straight path for a distance long compared to the particle size. Such behavior is termed free molecular. Mountain et al. (2) and Sullivan et al. (3) developed a computational technique for simulating particle agglomeration under these conditions, though in these studies the investigators were limited to a total of 500 primary particles in their simulations. The results were very limited in regard to the size distribution function. In this study, we have extended the simulations to 8000 primary particles in order to determine the size distribution function for agglomerates in the free molecular limit.

In addition to the computer simulation results, an expression for the coagulation kernel is developed based on the apparent fractal structure of the agglomerate and the free molecular particle dynamics condition. The size distribution function appropriate to the coagulation kernel is derived in the limit of long time based on the dynamic scaling analysis of van Dongen and Ernst (4). We also directly compute the size distribution function based on a numerical solution of the coagulation equation.

Previous studies of free molecular particle coagulation have been based on spherical particles. Lai et al. (5) have shown that free molecular coagulation with coalescence leads to a so called self-preserving size distribution. Dobbins and Mulholland (6) considered simultaneous particle formation and free molecular growth, but again with the assumption of spherical particle shape. They find that for conditions similar to those existing in a flame, the simultaneous particle formation can lead to a much broader size distribution than the self-preserving distribution obtained by Lai et al.. As indicated above, the soot in the flame exists as an agglomerate. It is of obvious interest to determine the size distribution, structure, and growth kinetics for agglomerates.

Meakin et al. (7) have studied the effect of the cluster diffusivity on the resulting cluster-size distribution. In their study, the diffusion coefficient of a cluster of size k is assumed to be proportional to k^{γ}. Meakin et al. find a critical value of γ, $\gamma_c \approx -1/2$, at which the shape of the cluster-size distribution crosses over from a monotonically decreasing function to a bell-shaped curve. A Monte Carlo simulation is used with the diffusional motion of the clusters represented by random walks on a three-dimensional cubic lattice. In all cases considered, the primary particle size corresponds to one lattice site and the diffusion step is one lattice site. This differs from the free molecular condition that the particle move several particle

[1]National Bureau of Standards, Gaithersburg, Maryland 20899

[2]Vista Chemical Co., 3441 Fairfield Rd., Baltimore, Maryland 21226

[3]Institute for Theoretical Physics, State University, P.O. Box 80.006, 3508 TA Utrecht, The Netherlands.

diameters before changing its trajectory. It is this latter case of free molecular motion that is the focus of this paper.

2. Description of Computer Simulation

The initial condition consists of 8000 spheres of mass m_o and unit diameter σ randomly located in a cube of size L. The initial velocities are obtained using a random number generator which produces normally distributed numbers with unit variance so that the particles are in thermal equilibrium with the background gas through which they diffuse.

The dynamics of a particle are governed by the Langevin equation

$$d(mv_x)/dt=-m\beta v_x + f_x \qquad [1]$$

where v_x is the xth cartesian component of the velocity of the center of mass of the agglomerate of mass m and f_x is a stochastic force satisfying $\langle f_x^2\rangle=2\beta m k_B T$. As can be seen from Eq.[1], β^{-1} represents the relaxation time of the agglomerate. The numerical solution of Eq.[1] to obtain the velocity and coordinates for each particle after a time interval h is described in Mountain et al. (2).

After each time interval h, the system is examined to see if any agglomeration events have occurred. It is assumed that whenever two particles "touch", they stick and the resulting agglomerate diffuses as a rigid assembly. Also, the agglomerates are thermally accommodated after each collision, since thermal accommodation with the host gas may not occur before a second collision at the high particle concentration.

The product $m\beta$ in Eq.[1] is termed the friction coefficient, K. We approximate the friction coefficient of k spheres as k times the friction coefficient of a single sphere. In making this approximation we neglect the shielding effect of the other spheres, but for a tenuous, low density agglomerate this is a reasonable first approximation. Both the mass m and the friction coefficient K are proportional to the number of particles in the agglomerate k; therefore, β is independent of the size of the agglomerate in this independent particle approximation. Dividing both sides of Eq.[1] by m, it is seen that the quantity β is the controlling parameter for the particle dynamics.

The free molecular condition corresponds to the particle relaxation time, β^{-1}, being long compared to the time, $\tau=(m_o\sigma^2/k_BT)^{\frac{1}{2}}$, to free stream a particle diameter; that is,

$$\beta\tau \ll 1. \qquad [2]$$

The following result is derived for $\beta\tau$ in the free molecular limit in Mountain et al. (2):

$$\beta\tau=4P(2m_o m_g)^{\frac{1}{2}}/(\rho_s k_B T), \qquad [3]$$

where m_o is the mass of an individual sphere, ρ_s refers to the density, and m_g is the mass of the gas molecules. The surface accommodation is assumed to have a value of unity. The simulations are carried out for $\beta\tau=0.2$, which corresponds to a 16 nm particle diameter for a 1500 K flame temperature, and for $\beta\tau=0.05$, which corresponds to a 6 nm diameter. The density of the individual particle is taken to be 2.0 g/cm^3 and ambient pressure is assumed.

Another important parameter concerning the simulation is the number density, ρ, defined as the number of particle per volume, where volume is in units of σ^3. Simulations were performed for the following values of ρ: 0.05, 0.0167, and 0.005. Even the lowest of these densities is several orders of magnitude larger than the value of about 10^{-6} observed in flames. The density dependence of the results

provides insight regarding the applicability of the simulations to an actual flame. A value of ρ of 0.005 is the lowest density for which the simulation can be carried out for 8000 particles with 5 runs to obtain adequate statistics using a Cyber 205 computer[4].

3. RESULTS

While the primary focus of this study is the results regarding the size distribution function, it is also of interest to analyze the structure of the agglomerates and the cluster growth rate. The structural information will be used in the next section for deriving an effective collision kernel for the agglomerates. Given the collision kernel, the size distribution can be determined as shown in the next section. The cluster growth rate is of interest in its own right but is also needed for obtaining the scaled size distribution function.

3.1 Structure

The structure of the agglomerates is quite open as indicated in Fig. 1 for a planar projection of the structure. It is also seen that there is a similarity between the actual structure of soot produced by an acetylene diffusion flame and the results of the computer simulation. As has been demonstrated in a number of studies of agglomerate growth including Meakin (8,9) and Mountain et al. (2), the degree of openness can be conveniently characterized in terms of a fractal dimensionality, D_f, which in the case of an agglomerate is conveniently defined by the equation

$$k \propto R_g^{D_f} \qquad [4]$$

where R_g is the radius of gyration of the cluster. In Fig.2, log R_g is plotted versus log k for the case $\beta\tau$=0.05 and ρ=0.005. A linear least square fit of the data over the range 10-500 in k with a uniform weighting on a log scale leads to D_f=1.91±0.06. The choice of the lower bound is determined by onset of power law behavior and the upperbound by condition that agglomerate not extend from one edge of the cell to the other. A indicated in Table I, the mean values of D_f are in the range 1.89 - 2.07. This is to be compared with a value of D_f=1.87±0.04 obtained by Meakin (10) for cluster in the size range 10-500 with ρ=0.005. The model used by Meakin consists of random linear trajectories by both particles and clusters. The model was originally introduced by Sutherland and Goodarz-Nia (11). This model would correspond to the limiting case $\beta\tau$=0 for the free molecular simulation.

3.2 Cluster Growth

The average cluster size, $\bar{k}$, is defined by

$$\bar{k}=N_o/N(t) \ , \qquad [5]$$

where N_o is the number of primary particles and N(t) is the total number of clusters at time t. In Fig.3, $\bar{k}$ is plotted versus number of time steps, t_N, on a log-log plot for all of the simulations. The mean cluster size increases asymptotically as

$$\bar{k} \propto t^z \qquad (t \to \infty) \qquad [6]$$

The exponent z is obtained from a linear least square fit of the log-log plot for the

---

[4]Certain commercial equipment is identified in this paper to specify adequately the calculation method. In no case does such identification imply recommendation or endorsement by the National Bureau of Standards, nor does it imply that the equipment identified is necessarily the best available for the purpose.

range in t over which $20<\bar{k}<100$. As indicated in Table I, there seems to be a decrease in z with decrease in density.

An alternative method for determining the exponent z is suggested by the analysis of van Dongen and Ernst (4). They obtain the following relationship between $\bar{k}$ and t_N:

$$\bar{k} \propto (t_N+t_N^o)^z \qquad [7]$$

The value of t_N^o is obtained as the value for which $\log(\bar{k})$ versus $\log(t_N+ t_N^o)$ has no curvature. The value of the exponent z obtained in this way is also given in Table I.

In Fig. 4, all of the data is reduced to a single curve by plotting $\bar{k}$ vs. τ_1, where

$$\tau_1=(t/\tau)\rho \ . \qquad [8]$$

3.3 Cluster Size Distribution

The cluster-size distribution, N_k, is plotted in Fig. 5 at several times. As a test for the existence of a self-preserving cluster distribution, we also plot the size distribution in terms of the similarity variables, ψ and η, introduced by Friedlander (12),

$$N_k=\bar{k}^2 N_o \psi(\eta) \ , \qquad [9]$$

$$\eta=k/\bar{k} \ . \qquad [10]$$

It is seen from Fig. 6 that the similarity variables do reduce all of the cluster-size distributions to a single curve. The possibility of deriving this universal size distribution is treated in the next section.

Perhaps the size distribution function affording the best comparison with experiment is the number distribution in terms of the radius of gyration, R_g.

$$dN/dR_g=AD_f R^{D_f-1} N_k \qquad [11]$$

Such a size distribution is plotted in Fig. 7. While it may not be practical to evaluate R_g for every cluster by electron microscopy, one might rapidly determine an effective size of the agglomerate based on its length and width.

4. Coagulation Equation

The most widely used tool for studying irreversible clustering phenomena in many fields of science is Smoluchowski's coagulation equation:

$$\dot{n}_k=\tfrac{1}{2}\Sigma\, K(i,j)n_i nj \ - \ n_k \Sigma\, K(k,j)n_j \ , \qquad [12]$$

where n_k is the number concentration of clusters of size k and K(i,j), the coagulation kernel, represents the rate coefficient for a specific clustering mechanism between clusters of sizes i and j. Below an estimate is made for the coagulation kernel for the case of free molecular growth and then Eq. [12] is solved analytically in the asymptotic limit as well as numerically. Finally the results are compared with the results of the computer simulation.

4.1 Coagulation Kernel

For the case of small droplets that coalesce upon contact, the free molecular coagulation kernel is given by

$$K(i,j)=a(i^{1/3} + j^{1/3})^2(1/i+1/j)^{\frac{1}{2}} \qquad [13]$$

$$a=(3v_o/4\pi)^{1/6}(6k_BT/\rho_s)^{1/2} \quad . \qquad [14]$$

The first factor in Eq.[13] corresponds to the size dependence of the collision cross section and the second term to the dependence of the average relative velocity on the reduced cluster mass. The quantity K(i,j) given above is essentially identical to the kinetic theory prediction of the volume swept out per second by colliding molecules.

The collision cross section of two low density agglomerates (fractal objects with Hausdorf dimension D_f=1.9) in free flow (ballistic trajectories) is much larger than for compact spheres, mainly because of their large radii of gyration,

$$R_g \propto k^{1/D_f} .$$

However, there is a subtlety in the argument. Since $D_f<2$, the planar projection of a cluster or cross-sectional area (see Fig. 1) is still a fractal object with Hausdorf dimension D_f=1.9. Therefore, the effective scattering area for two free moving fractal clusters with $D_f<2$ and sizes i and j respectively is:

$$\text{cross-section} \propto (R_g(i)+R_g(j))^{D_f}$$
$$\text{"} \quad \text{"} \propto (i^{1/D_f}+j^{1/D_f})^{D_f} \qquad [15]$$

If however the fractal dimension of the clusters would be $2\leq D_f\leq 3$, then their projections would be compact objects and their collision cross-section would be:

$$\text{cross-section} \propto (R_g(i)+R_g(j))^2$$
$$\text{"} \quad \text{"} \propto (i^{1/D_f}+j^{1/D_f})^2 \qquad [16]$$

Note that the cross-section in both cases [15] and [16] is bounded by const.xj for j>>i. This is a physically obvious requirement. Equation [16] for $D_f<2$ would violate this condition (See Mountain et al.(2)).

The agglomerate speed is not affected by the particle structure based on the equipartition of energy so that the coagulation kernel for the agglomerate in the free molecular limit is given by

$$K(i,j)=a_1(i^{1/D_f}+j^{1/D_f})^{D_f}(1/i+1/j)^{1/2} \quad . \qquad [17]$$

Van Dongen and Ernst (4) have obtained asymptotic solutions to the coagulation equation, Eq.[14], for coagulation kernels classified on the basis of three exponents defined below:

$$K(ai,aj) = a^{\lambda}K(i,j) = a^{\lambda}K(j,i) \quad , \qquad [18]$$

$$K(i,j) \propto i^{\mu}j^{\nu} \quad (j>>i;\ \lambda=\mu+\nu). \qquad [19]$$

For K(i,j) given by Eq.[17], $\lambda = 1/2$, $\mu = -1/2$, and $\nu = 1$. For $\lambda \leq 1$, van Dongen and Ernst (4) show that the exponent z is given by

$$z = 1/(1-\lambda). \qquad [20]$$

So for $\lambda = 1/2$, $z = 2$. The general form of the reduced size distribution for large η is given by van Dongen and Ernst (13).

$$\psi(\eta) \simeq A\eta^{-\theta}\exp(-\alpha\eta) \quad , \ \eta \to \infty \quad . \qquad [21]$$

For coagulation kernels with $\nu<1$, the θ exponent is simply given by $\theta=\lambda$. However, for kernels with $\nu=1$, such as given in Eq.[17], the θ exponent is more complicated. It has been calculated by van Dongen and Ernst (13), and we conclude from their Eqs.[12] through [15] that the exponent θ is determined from the following transendental equation:

$$J(\theta) = 0, \qquad [22]$$

where $J(\theta)$ is defined by

$$J(\theta) = \int_0^{\frac{1}{2}} dx\{K(x,1-x)[x(1-x)]^{-\theta}-x^{\mu-\theta}\} - \int_{\frac{1}{2}}^{\infty} dx\, x^{\mu-\theta} \ . \qquad [23]$$

Since the first integrand diverges at x=0, an asymptotic expansion is made for the integrand to obtain the small x contribution to the integral. For the remainder of the range in x, the integration is obtained numerically. For the case $D_f=1.90$, we obtain $\theta=0.72$.

For large values of D_f the asymptotic solution of Eq.[23] is (14)

$$\theta \simeq 1/2 + 2^{1-D_f}/\pi \quad (D_f \gg 1)$$

This relation gives at $D_f=1.9$ the fair estimate $\theta=0.67$ and at $D_f=1$ is even close to the exact value $\theta=1$.

The size distribution plots given in Fig. 6 suggest a power law region followed by an exponential region. However, one finds a wide range in the value of θ, 0.4 to 0.8, depending on the range in η over which the line is drawn. A better method is to first obtain k from the large η asymptotic slope of $\ln\psi$ vs η and, then obtain θ from the slope of $k\eta+\ln\psi$ vs $\ln\eta$. This approach applied to the case $\beta\tau=0.05$ and $\rho=0.005$ yields $\alpha=0.67$ and $\theta=0.53$ compared to the predicted value of θ of 0.72. There is still some ambiguity in the value of θ, because of the interplay between the value of α and θ. That is, a lower value of α and a larger value of θ will also lead to a good fit to the simulation results.

In the limit of small cluster size and long time, van Dongen and Ernst (4) predict that

$$\psi(\eta) \propto \eta^{-2}\exp(-1/\eta^{\frac{1}{2}}) \quad \text{for} \quad \eta \to 0 \ . \qquad [24]$$

Unlike this predicted exponential behavior, it appears that $\psi(\eta)$ decreases only slightly for small η. Presumably this discrepancy results from the simulations not being carried out to long enough time.

Another approach to comparing the results of the simulations with coagulation theory is to numerically solve for N_k vs k from Eq.[13] based on the kernel given by Eq.[17]. One thousand twenty four coupled rate equations given by Eq.[13] were solved by the Runge Kutta method with fourth order predictor corrector. This is analogous to the technique used by Hidy et al. (15,16) for solving the coagulation equation. Starting from a monodisperse size distribution as in the simulations, it was found that the loss of mass due to particles reaching k=1024 represented a 4% effect when the total number concentration had dropped by a factor of 100. It is seen from Fig. 6 that the reduced size distribution obtained from the numerical solution of the coagulation equation is both self-preserving and agrees very well with the results of the computer simulation. The value of the exponent z characterizing the cluster growth rate is found to be in good agreement with the computer simulation results (1.84 for the coagulation equation vs 1.72 for the simulation).

5. Discussion

The computer simulations of free molecular agglomeration lead to much more rapid growth than is predicted for coalescing droplets in the free molecular limit, which has been the basis for predicting coagulation rates in flames in previous studies (5,6). The agglomeration leads to an exponent z of about 2.0 compared to a value of about 1.2 based on coalescence.

The results of the computer simulations in terms of the fractal structure and the size distribution function seem to vary only slightly with the choice of β (0.2 and 0.05) and ρ (0.05, 0.0167, 0.005). There appears to be a more pronounced affect of the density on the value of the exponent z with the higher density leading to a higher value of z. The value reported by Mountain et al. (2) for a system with 500 primary particles was larger yet with a value of about 2.6 for z. We expect the simulation with the lowest density (ρ=0.005) and lowest value of β (0.05) to give the most appropriate value for physical systems. For the limited range in $\tilde{k}$, Eq.[7] is the most accurate method for determining the exponent z, and this leads to z=2.05 for the simulation.

We do not observe as large a density effect in the free molecular limit as has been observed by Mountain et al. (2) in the continuum limit and by Ziff et al. (17) for agglomerates with diffusion coefficient proportional to the cluster size raised to a power.

We find that a coagulation kernel derived based on the fractal structure of the agglomerate leads to an average growth rate and self-preserving size distribution in good agreement with the computer simulations. The computer simulations have not been run for long enough time to afford a comparison with the predicted small η behavior..

Ziff et al. (17) demonstrated that for a size dependent diffusion coefficient the kinetic rate kernel predicted by taking into account the fractal geometry of the agglomerate is in agreement with the computer simulation results. We have shown that in the free molecular limit that using a kinetic rate kernel based on fractal geometry leads to a size distribution in agreement with the computer simulation. One is encouraged to conjecture that the coagulation equation can be applied to agglomerates provided the agglomerate structure information is included in the kinetic rate.

1. Dobbins, R.A., and Megaridis, C.M., Langmuir accepted for publication.
2. Mountain, R.D., Mulholland, G.W., and Baum H., J. Colloid Interface Sci., **114**, 67 (1986).
3. Sullivan, F.,Mountain, R.D., and O'Connell,J., J. Comput. Phys., in press.
4. van Dongen, P.G.J., and Ernst, M.H., Phys. Rev. Lett., **54**, 1396 (1985).
5. Lai, F.S., Friedlander, S.K., Pich, J., and Hidy, G.M., J. Colloid Interface Sci. **39**, 395 (1972).
6. Dobbins, R.A., and Mulholland, G.W., Comb. Sci. and Tech., **40**, 175 (1984)
7. Meakin, P., Vicsek, T., and Family, F., Phys. Rev. B, **31**, 564 (1985).
8. Meakin, P., J. Colloid Interface Sci., **102**, 491 (1984).
9. Meakin, P., Phys. Review A, **29**, 997 (1984).
10. Meakin, P., J. Colloid Interface Sci., **102**, 505 (1984).
11. Sutherland, D.N.,and Goodarz-Nia, I.,I. Chemical Engineering Sci., **26**, 2071 (1971).
12. Friedlander, S.K., "Smoke, Dust, and Haze", Wiley, New York, 1977.
13. van Dongen, P.G.J.,and Ernst,M.H., "Fractals in Physics",L. Pietronero and E. Tosatti, ed., Elsevier, ,1986.
14. van Dongen, P.G.J., private communication.
15. Hidy, G., and Lilly, D., J. Colloid Sci. **20**, 867 (1965)
16. Hidy, G., J. Colloid Sci. **20**, 123 (1965).
17. Ziff, R.M., McGrady, E.D., and Meakin, P., J. Chem. Phys. **82**, 5269 (1985).

TABLE I. Exponents D_f and z for Free Molecular Simulations

$\beta\tau$	ρ	D_f	z^a	z^b	t_N^o
0.20	0.05	2.05±0.03	1.98±0.05		
0.05	0.05	2.07±0.08	2.40±0.16	4.06±0.19	500
0.05	0.0167	1.89±0.08	1.92±0.07	2.53±0.05	900
0.05	0.005	1.91±0.06	1.72±0.05	2.05±0.03	2000

---

[a] The exponent z is defined by $\bar{k} \propto (t_N)^z$.
[b] Here the exponent z is defined by $\bar{k} \propto (t_N + t_N^o)^z$.

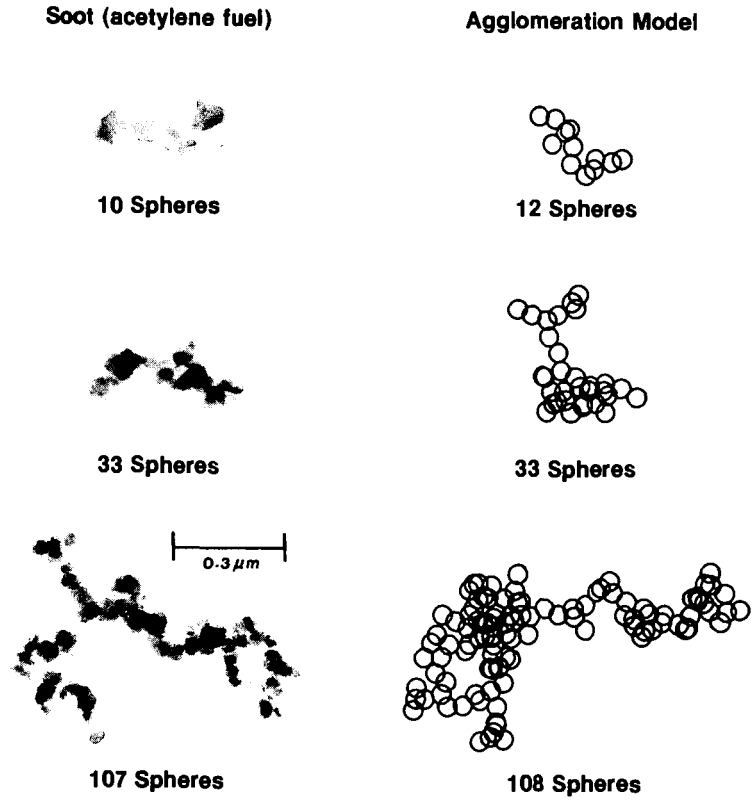

Fig. 1. Qualitative comparison of soot clusters and clusters obtained by computer simulation of free molecular growth.

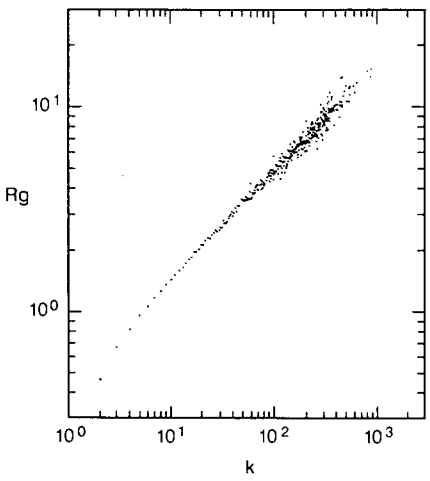

Fig. 2. R_g versus k for $\beta\tau$=0.05 and ρ=0.005.

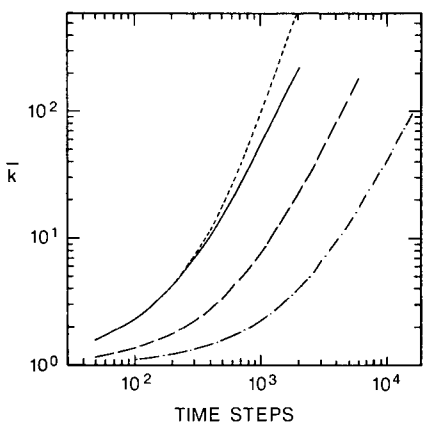

Fig. 3. $\bar{k}$ versus time steps for $\beta\tau$=0.2, ρ=0.05(—); $\beta\tau$=0.05, ρ=0.05(----), ρ=0.0167(— —), ρ=0.005(—·—·).

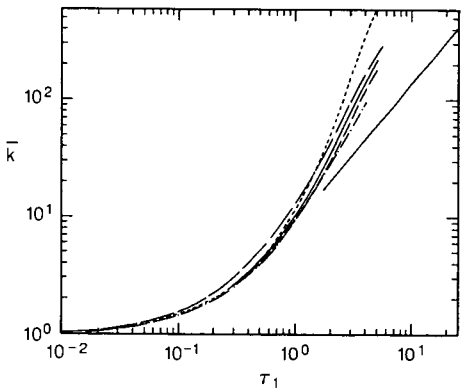

Fig. 4. $\bar{k}$ versus τ_1, for $\beta\tau$=0.2, ρ=0.05(—); $\beta\tau$=0.05, ρ=0.05(----), ρ=0.0167(— —), ρ=0.005(—·—·), fractal coagulation (—— ——), coalescence(——) slope=1.2.

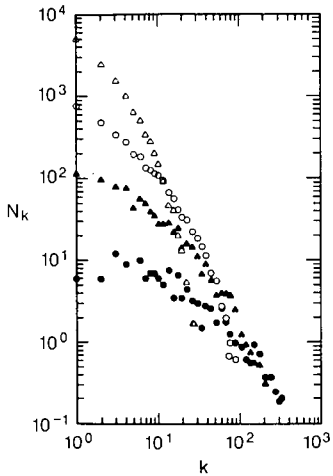

Fig. 5. Size distribution for $\beta\tau$=0.05, ρ=0.005, t_N=1500(Δ), t_N=4200 (o), t_N=8000 (▲), t_N=16,000 (•).

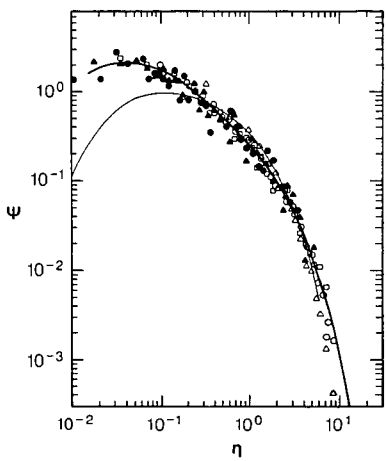

Fig. 6. Self-preserving sized distribution for simulation, fractal coagulation(━), coalescence(—).

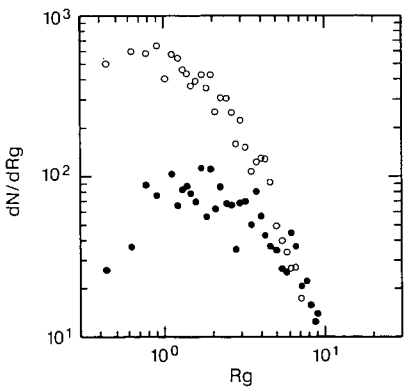

Fig. 7. dN/dR_g versus R_g for t_N=8000(o) and t_N=16,000(•).

A SIMPLE METHOD FOR PREDICTING SOOTING TENDENCIES OF HYDROCARBON FUELS IN PREMIXED FLAMES

Stamoulis Stournas and Euripides Lois

Chemical Engineering Department,National Technical University
42 Patission Street, 106 82 Athens, Greece

ABSTRACT

One of the accepted measures of sooting tendencies of hydrocarbon fuels in premixed flames is the threshold fuel/oxidizer ratio, φ_c,which assumes combustion to CO_2 and H_2O. In this analysis it has been found that this sooting can be accurately predicted by using the group additivity approach based on the nature of the individual carbon atoms that exist in the fuel molecule. The only parameters needed for this prediction are the numbers of sp^3, sp^2, sp, aromatic and benzylic carbons along with the total number of hydrogen atoms in the molecule.

This approach has been used for the calculation of the sooting tendencies of 73 fuels whose measured φ_c has been reported in the literature. Even though the structure of these fuels varied widely and included alkanes, olefins, alkynes and aromatics, the calculated values were always very close to the measured ones. In fact, in 88% of the cases the predicted values lie within 5% of the measured ones, whereas the deviation in the rest never exceeds 10%.

INTRODUCTION

The sooting tendencies of hydrocarbon fuels, either in premixed or diffusion flames, has been studied in the past by a number of investigators (1-12).

A number of parameters have been recognized as important aspects for the sooting tendency of a fuel, such as its molecular structure, fuel/oxygen ratio, flame temperature, etc.

Most of the recent work refers to efforts made to quantify these parameters into a unified approach that will predict the soot threshold of each fuel. More recently, Olson and Pickens (1) investigated a number of probable expressions defining soot thresholds for premixed flames for a large number of hydrocarbons, including alkanes, alkenes, alkynes and aromatics. A few years earlier, Haynes and Wagner (5) discussed soot thresholds for premixed flames, in a comprehensive review of soot formation in terms of critical C/O ratios, $(C/O)_c$.

Olson and Pickens assumed two modified equivalence ratios, one giving combustion products CO_2 and H_2O (φ_c), and the other CO and H_2O (ψ_c); the former was linked eventually with the Threshold Soot Index (TSI) as defined by Calcote and Manos (6).

In the present analysis, we have found that, by using the group additivity principle (13) the sooting tendency of hydrocarbon fuels can be predicted with good accuracy. Group additivity has been successfully used in the past to predict properties such as heat of formation, heat capacity, refractive index, etc.(14); more recently, it has been found useful in the prediction of ignition quality (cetane number) of diesel fuels.(15) Our approach was to divide the carbon atoms that comprise the fuel molecules into groups according

to their chemical nature (sp^3, sp^2, aromatic, etc.) and to assign a different weighting factor to each group. The only other information that is needed for the prediction is the total number of hydrogen atoms in the molecule.

ANALYTICAL APPROACH

Soot threshold is defined by the appearance of the first visible yellow emission as the fuel to air ratio was increased (1,16). This critical fuel to air ratio (F_c), when compared to the stoichiometric fuel to air ratio (F) that is required by the combustion process, gives a measure of the sooting tendency of each particular fuel.

If complete combustion to CO_2 and H_2O is taken as the basis of comparison, then the required stoichiometry for any hydrocarbon fuel C_nH_m is:

$$C_nH_m + \frac{4n+m}{4} O_2 \longrightarrow nCO_2 + \frac{m}{2} H_2O \qquad (1)$$

In this case the stoichiometric fuel/air ratio is given by

$$F = \frac{4}{4n+m} \quad \text{(moles fuel/moles oxygen)} \qquad (2)$$

and the sooting tendency depends on φ_c, defined as

$$\varphi_c = \frac{F}{F_c} = \frac{4}{(4n+m)F_c} \qquad (3)$$

On the other hand, by assuming combustion to CO and H_2O, the stoichiometry is:

$$C_nH_m + \frac{2n+m}{4} O_2 \longrightarrow nCO + \frac{m}{2} H_2O \qquad (4)$$

with

$$F = \frac{4}{2n+m} \quad \text{(moles fuel/moles oxygen)} \qquad (5)$$

The sooting tendency criterion is now ψ_c, defined as:

$$\psi_c = \frac{F}{F_c} = \frac{4}{(2n+m)F_c} \qquad (6)$$

It is clear that φ_c and ψ_c are related by the expression

$$\psi_c = \frac{(4n+m)\varphi_c}{2n+m} \qquad (7)$$

A third criterion, s_c, may be employed as a measure of sooting tendency, if we assume incomplete combustion to elemental carbon and water:

$$C_nH_m + \frac{m}{4} O_2 \longrightarrow nC + \frac{m}{2} H_2O \qquad (8)$$

In this case,

$$F = \frac{4}{m} \quad \text{(moles fuel/moles oxygen)} \qquad (9)$$

and the sooting tendency criterion, s_c, is defined as:

$$s_c = \frac{F}{F_c} = \frac{4}{mF_c} \qquad (10)$$

Also

$$s_c = \frac{(4n+m)\varphi_c}{m} \qquad (11)$$

This last expression permits the computation of the actual s_c for all fuels whose φ_c has been measured experimentally and whose gross structure (i.e. number of carbon and hydrogen atoms in the molecule) is known.

It is recognized that combustion to carbon and water is a rather unrealistic process; as will be shown later, however, s_c is a useful criterion for a unified approach to the prediction of sooting tendencies of hydrocarbon fuels and, by employing relations (7) and (11), it can lead to the better known quantities φ_c and ψ_c.

The relative amounts of carbon and hydrogen in a fuel molecule (in the form of hydrogen content) has been used as a rather intuitive guide to the sooting tendency of hydrocarbon fuels in both premixed and laminar flames, albeit with rather limited success. If, however, the effect of each carbon atom in the fuel molecule is accorded a weighting factor according to its chemical nature, an almost quantitative prediction of sooting tendency can result. We have found that it is sufficient to divide the various types of carbon atoms into five categories:

1. Saturated (sp^3) carbon atoms (C_1)
2. Olefinic (sp^2) carbon atoms (C_2)
3. Acetylenic (sp) carbon atoms (C_3)
4. Aromatic carbon atoms (C_A)
5. Benzylic carbon atoms, i.e. those directly coupled to an aromatic ring (C_B).

For the purpose of this definition, olefinic carbon atoms that belong to conjugated double bonds are counted as aromatic.

Based on the above definitions, the sooting tendency of any hydrocarbon fuel can be accurately predicted in the form of s_c by the relation:

$$s_c = \frac{3.5C_1 + 2.9C_2 + 1.9C_3 + 3.1C_A + 5C_B}{m} \qquad (12)$$

where C_1, C_2, etc. are the numbers of each type of carbon atoms as defined above, and m is the total number of hydrogen atoms in the molecule.

Alternatively, φ_c and ψ_c can be calculated for any fuel by changing the denominator in (12) with (4n+m) and (2n+m) respectively, where n is the total number of carbon atoms in the molecule.

RESULTS AND DISCUSSION

Relation (12) was applied to 73 hydrocarbon fuels whose sooting tendencies have been measured experimentally.(1,2,4,12) The calculated value of φ_c was within ±5% of the experimental value in 64 of the cases, and even in the worst case (1,5-cyclooctadiene) the difference was less than 10%. The linear correlation coefficient (r) between calculated φ_c and experimental φ_c for all the fuels was 0.95; this value can be considered as quite acceptable, given the wide variation in the molecular structure of the fuels (26 paraffins, 20 olefins, 7 alkynes, and 20 aromatics) and the inherent experimental uncertainties in measuring the critical fuel to air ratio. In several cases the values reported by different

investigators for the same fuel differ by more than 10%; the experimental values employed in this work were the averages of the reported values. The results of the calculations are depicted graphically in Figure 1, whereas Table I contains some examples that illustrate the calculation procedure.

Similar results were obtained in the calculation of ψ_c for the same fuels, except that the linear correlation coefficient was somewhat better (r=0.97).

TABLE I
EXAMPLES OF CALCULATED SOOTING TENDENCIES

FUEL	FORMULA	C_1	C_2	C_3	C_A	C_B	EXPERIMENTAL φ_c	EXPERIMENTAL s_c	CALCULATED φ_c	CALCULATED s_c
Propane	C_3H_8	3	0	0	0	0	0.524	1.309	0.525	1.313
iso-Octane	C_8H_{18}	8	0	0	0	0	0.556	1.543	0.560	1.556
Decalin	$C_{10}H_{18}$	10	0	0	0	0	0.613	1.977	0.603	1.944
n-Tetradecane	$C_{14}H_{30}$	14	0	0	0	0	0.575	1.648	0.570	1.633
1-Heptene	C_7H_{14}	5	2	0	0	0	0.552	1.657	0.555	1.664
1-Pentyne	C_5H_8	3	0	2	0	0	0.529	1.852	0.518	1.813
Toluene	C_7H_8	0	0	0	6	1	0.658	2.961	0.656	2.950
Indene	C_9H_8	0	0	0	8	1	0.676	3.716	0.677	3.725
Propylbenzene	C_9H_{12}	2	0	0	6	1	0.633	2.532	0.638	2.550
Tetralin	$C_{10}H_{12}$	2	0	0	6	2	0.676	2.928	0.685	2.967

The best correlation with experimental measurements was obtained in the calculation of s_c for the 73 fuels; in this case the linear correlation coefficient has an excellent value, being equal to 0.994. The results, as depicted in Figure 2, show ancillary advantages of the employment of s_c as a sooting tendency criterion:

a. The values of s_c (approx. 0.9 to 3.8) cover a wider range than those of φ_c (approx. 0.4 to 0.7), thus making it easier to doscern the differences between various fuels.

b. What is more important, s_c tends to divide the sooting tendencies of the fuels into more rational and intuitively acceptable classes. Thus paraffins have s_c values averaging around 1.5, olefins and alkynes average around 1.8, whereas the average for aromatics is close to 3. Such distinctions are difficult to make with φ_c as the sooting tendency criterion.

The above observations, which show a dependence of sooting tendency on molecular structure similar to that observed for diffusion flames,(3) has led us to attempt a correlation of sooting tendencies in diffusion flames with those in premixed flames. Figure 3 shows a plot of s_c vs. the diffusion flame threshold soot index , TSI(3), for 65 fuels. The linear correlation coefficient has an acceptable value of 0.925, which rises to 0.96 if the four points that are circled in Figure 3 are omitted and the correlation employs 61 fuels. When diffusion flame TSI is compared to φ_c, the correlation coefficient has a much less acceptable value of 0.76, whereas the correlation with ψ_c gives results that are only slightly better (r=0.86).

CONCLUSIONS

1. By employing appropriate weighting factors on the carbon atoms that comprise a fuel molecule, its premixed flame sooting tendency in the form of ϕ_c can be predicted with acceptable accuracy. The prediction is even better if the sooting tendency criterion is s_c, which assumes incomplete combustion to elemental carbon and water.

2. A linear correlation exists between sooting tendency in premixed flames as expressed by s_c, and sooting tendency in diffusion flames as expressed by TSI.

REFERENCES

1. Olson, D.B. and Pickens, J.C., Combust. and Flame 57 199 (1984)
2. Wright, F.J., 12th Symposium (International) on Combustion, The Combustion Institute, 1969, p. 867
3. Olson, D.B., Pickens, J.C. and Gill, R.J. Combust. and Flame 62 43 (1985)
4. Blazowski, W.S., Combust. Sci. Technol. 21, 87 (1980)
5. Haynes, B.S. and Wagner, H.G. Prog. Energy and Combust. Sci. 7 229 (1981)
6. Calcote, H.F. and Manos, D.M. Combust. Flame 49 289 (1983)
7. Glassman, I. and Lara, P.V.. Fall Technical Meeting, Eastern Section, The Combustion Institute, 1981
8. Calcote, H.F. and Olson, D.B. Combust. Sci. Technol. 28 315 (1982)
9. Dyer, T.M. and Flower, W.L., in "Particulate Carbon: Formation during Combustion" (D.C. Singh and G.W. Smith, eds.), New York (Plenum), 1981 p. 363
10. Glassman, I. and Yaccarino, P., 18th Symposium (International) on Combustion, The Combustion Institute, 1981, p.1175
11. Siddall, R.G. and McGrath, I.A., 9th Symposium (international) on Combustion, Academic Press, New York, 1963, p.102
12. Street, J.C. and Thomas, A., Fuel 34, 4 (1955)
13. Benson, S.W. and Buss, J.H. J. Chem. Phys. 29, 546 (1958)
14. Benson, S.W. "Thermochemical Kinetics" New York (Wiley) 1976
15. DeFries, T.H., Indritz, D. and Kastrup, R.V. Ind. Eng. Chem. Res. 26, 188 (1987)
16. Burke, S.P. and Schumann, T.E.W., Ind. Eng. Chem. 20, 998 (1928)

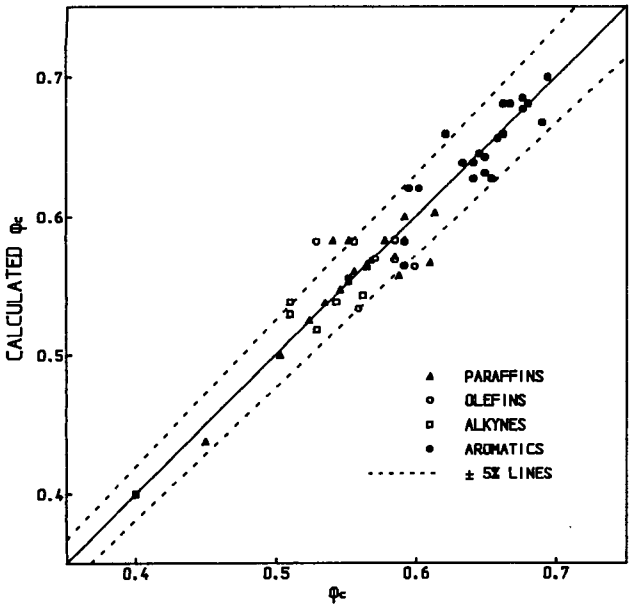

FIGURE 1. CALCULATION RESULTS FOR φ_c

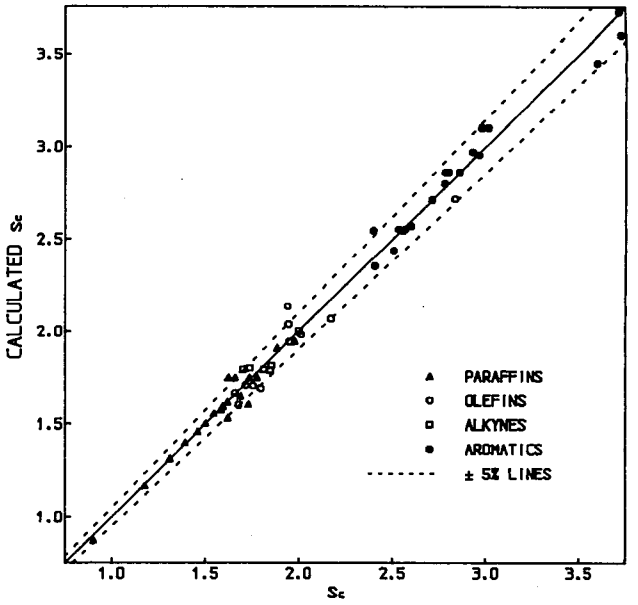

FIGURE 2. CALCULATION RESULTS FOR s_c

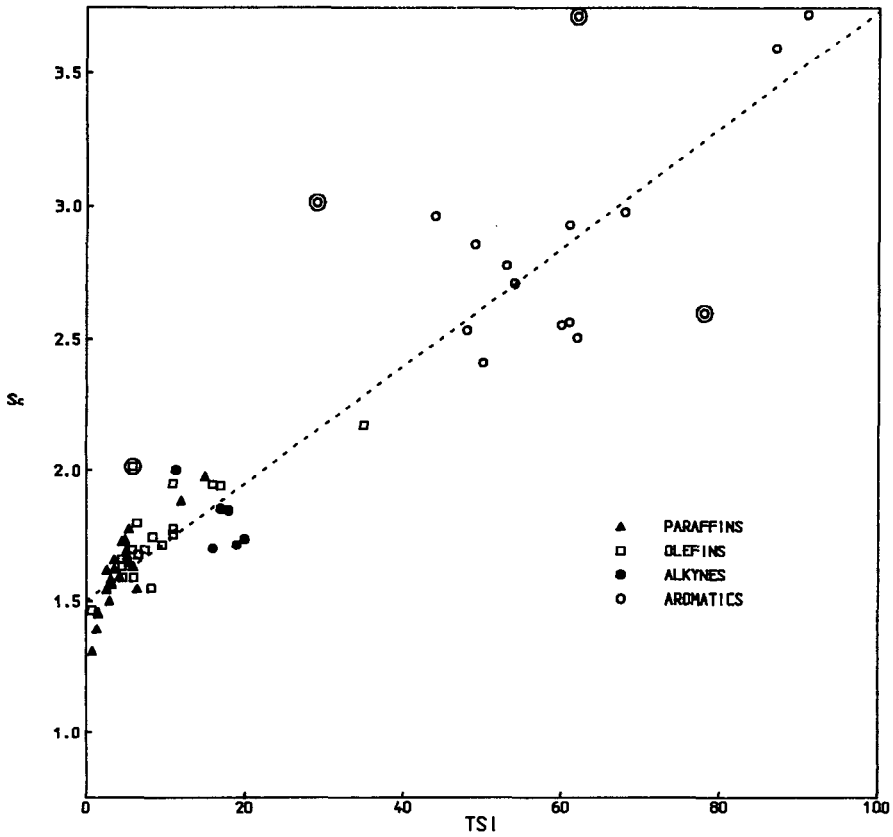

FIGURE 3. CORRELATION OF DIFFUSION FLAME TSI WITH Sc

Oxidation Kinetics of Carbon Blacks over 1300-1700 K*

W. Felder, S. Madronich,† and D. B. Olson

AeroChem Research Laboratories, Inc.
P.O. Box 12, Princeton NJ 08542

I. INTRODUCTION

The oxidation of carbonaceous particulate matter is of wide practical concern in power generation and pollution reduction. Typically, in fuel-rich portions of combustion flames, OH radicals can be the major oxidizing species (1-3). However, in regions of combustors and in the exhaust where soot is present and OH concentrations are essentially negligible (regions in which particles spend the major portion of their lifetimes within a device), oxidation by excess oxygen is important. The work described here utilized an entrained flow reactor (a modified High Temperature Fast Flow Reactor, HTFFR) to determine the reactivity of two carbon blacks with O_2 in the 1300-1700 K range. A wide range of oxygen concentration was investigated while maintaining independent control of total pressure and flow velocity (particle residence time). A method and apparatus were developed for feeding particles to the HTFFR and assuring that particle sizes lie below specified limits.

II. METHODS AND APPARATUS

The primary measurement is the number of moles of carbon converted to CO_x (= CO + CO_2) in a residence time, t. Collected gas samples were analyzed gas chromatographically to determine the amount of CO_x evolved after the particle and oxidizer mixture had traversed the flow tube reactor at a temperature, T, in a time, t. For surface oxidation of monodisperse spherical particles, evolving CO_x at the expense of particle size (4):

$$u(t) = 1 - (1 - (R_e S_0 t/3))^3 \qquad 1)$$

where: $u(t)$ = $(m_0 - m_t)/m_0$, is the burnoff at time t; m_0 and m_t are the mass of carbon input (g/s) and the mass of carbon remaining unoxidized at time t, respectively

R_e = the external surface oxidation reactivity coefficient, g cm^2 s^{-1}, a function of $[O_2]$

S_0 = specific surface area of unoxidized carbon particles, cm^2/g

Equation 1 assumes that the oxidation is chemically controlled (i.e., diffusion is rapid compared to reaction), and that the surface reactivity is a function only of available area. In this work, it was shown that the assumptions of surface reaction and chemical control are valid. The possible change in surface reactivity with oxidation was not addressed; thus the R_e values are referred to the original surface area.

To determine u(t), it is necessary to measure $[CO_x]$ for the experimental condition and $[CO_x(max)]$, the amount of CO_x produced by complete particle oxidation. The $[CO_x(max)]$ gives m_0 in the expression for u(t) and is obtained by replacing the N_2 diluent flow to the HTFFR with an equivalent O_2 flow, thus com-

* This work supported by the U.S. Army Research Office, Contract No. OAAG29-83-C-0023.

† Present address: National Center for Atmospheric Research, Boulder, CO.

pletely converting input carbon to CO_x. Measurement of $[CO_x]$ at other than complete oxidation conditions (replacing part of the N_2 flow with O_2) gives (m_0-m_t). Frequent $[CO_x(max)]$ determinations were interspersed with the $[CO_x]$ measurements.

The HTFFR described by Fontijn and Felder (5) was modified for this work. Optical observation ports in the reaction tube were eliminated, allowing the isothermal zone of the reactor to include between 50 and 70 cm of the overall 90 cm length of the tube, depending on the flow conditions used in the experiments. The reaction tubes (two different diameter tubes were used in the present work, a 4.5 cm i.d. mullite tube, and a 2.5 cm i.d. 998 alumina tube) were resistively heated in three separately controlled zones of ≈ 30 cm each with 0.127 cm diam Pt/40% Rh resistance wire. At the reaction tube exit a HeNe laser beam crossed the particle-laden flow; scattered laser light was detected perpendicular to the beam. A 10 cm diam filter support and filter were mounted in a downstream bypass line so that the entire flow could be routed through it to collect partially oxidized particles for subsequent surface area measurements.

Particle feed was from a 10 cm i.d., 40 cm long tumbling bed supported ≈ 30° from horizontal on two bearings. The particle bed charge consists of 90% (wt.) silica sand and 10% carbon black. A small N_2 flow through the bed formed a carbon black aerosol, some of which entered a particle takeoff tube and flowed to a "settling chamber." Feed rates at the bed outlet of 1-100 mg/min (10^{-6} to 10^{-4} moles C/s) were achieved. In the 15 cm i.d., 75 cm long settling chamber the flow was smoothed with a conically shaped flow straightener and slowed to ≈ 0.5 cm/s so that particle aggregates with aerodynamic diameters ≥ 4 μm settled out of the flow. In some experiments, settling chamber flow speeds up to 2 cm/s were used; under these conditions, particle aggregates up to ≈ 10 μm could have passed through the settling chamber. This range of particle sizes is below the size at which bulk diffusion affects the oxidation rate measurements.

The flow from the settling chamber entered the HTFFR reaction tube, where the major portion of the N_2 diluent and O_2 were added radially to the flow. The mass flow of carbon to the reactor indicated by $[CO_x(max)]$ measurements was 0.05-5.0 mg/ min (10^{-7} to 10^{-5} mol C/s), or about 5% of the output of the particle feeder. The remaining carbon black particles were collected in the settling chamber. The flow of O_2 in the experiments ranged from 5×10^{-5} to 5×10^{-3} mol/s and always exceeded the molar "carbon" flow by a factor of at least 20; for measurements of $[CO_x(max)]$, the oxygen flow was 10^3 to 10^4 times in excess of the "carbon flow."

Laser scattering was also used to obtain kinetic data by measuring the concentration of O_2 required to consume all of the input carbon in exactly the residence time. The O_2 flow to the reactor was progressively incremented while recording the scattered light intensity; a plot was made of relative (to $[O_2] = 0$) scattered light intensity against log $[O_2]$. The intensity decreased linearly on such plots as the particles were consumed; the curve went to zero at the value of $[O_2]$ at which the input carbon was consumed in the burnup time, t_b. The burnup time is simply related to R_e. The R_e values obtained using the scattered light method were identical with those obtained using the gc method.

Partially oxidized particles were collected on the inline filter for surface area measurements which yield information on the physical mechanism of the oxidation process. An adsorption analyzer (Quantachrome MS-8) was used for N_2 adsorption at 77 K, and the results were analyzed using the one point BET method (7). Specific surface area ratios were measured as a function of fractional burnoff, u, from u = 0 (particles that have traversed the reactor with $[O_2] = 0$) to u = 0.7.

The carbon blacks, Raven 16 (R16), a lampblack, and Conductex SC (CSC), a conducting black, were chosen to have a wide difference in initial specific surface area and iron impurity concentration. Both have "high" sulfur concentrations. The materials were donated by Columbian Chemical Corporation, Tulsa, OK, and their properties are summarized in Table I.

III. RESULTS AND DISCUSSION

1. Specific Surface Area Measurements

The interaction between O_2 and the carbon black particles can occur between two extreme modes (4,7,8): (1) reaction on an external non-porous surface; (2) reaction within a completely porous mass. In the first extreme, a particle of constant density, ρ, is oxidized and its radius decreases with burnoff. In the second extreme, a porous particle of constant radius is oxidized internally and its density decreases with burnoff. The ratio of specific surface areas of the unoxidized and partially oxidized particles, $S_0/S(t)$, are given by (9):

$$S_0/S(t) = (1-u)^{0.33} \quad \text{(constant density)}$$
$$S_0/S(t) = (1-u) \quad \text{(constant radius)}$$

Representative data for the two carbon blacks are compared with these functions in Fig. 1; the results indicate that the external surface area available for reaction increases in a manner consistent with a constant density (case 1 above) burning. The present measurements can thus be interpreted as the oxidation of non-porous spherical particles (assumed monodisperse) which react at constant density and with no change in particle number density.

2. Oxidation Rates

Oxidation rates were measured over 1300-1700 K for R16 and 1400-1700 K for CSC, more than three decades of oxygen partial pressure (0.02-60 kPa) and total pressures (O_2 + N_2) from 20 to 60 kPa. Particle residence times were varied from 50-800 ms. The majority of the data were obtained using the gc method; additional data were obtained using the laser scattering method. Representative burnoff data from the gc measurements, plotted against $[O_2]$ are shown in Fig. 2. Figure 3 shows data obtained using the laser scattering diagnostic as discussed above from one experiment on CSC at 1580 K and a total pressure of 27 kPa.

There were no discernible total pressure effect on the measured $[CO_x]$ yields over the approximately factor of two-to-three variation in total pressure covered at each temperature investigated, and no gas velocity effects over a factor of six at any temperature, nor did changing the reaction tube diameter from 2.5 to 4.5 cm have any effect. The measured burnoff depended only on reactor temperature, $[O_2]$ and residence time.

The gc data were analyzed to extract R_ρ by rearranging Eq. 1:

$$R_\rho = (3/S_0 t)\cdot(1 - (1 - u)^{0.33})$$

Representative results are plotted in in Figs. 4 and 5. For the laser scattering measurements, u = 1 when the scattered intensity is zero and

$$R_\rho = 3/S_0 t_*$$

where t_* is the residence time for complete burnoff at the $[O_2]$ determined from plots such as Fig. 3. Values of R_ρ so determined are included in Figs. 4 and 5.

These observed surface reactivities are chemically controlled as can be seen by comparing the calculated diffusion limited and observed reactivities. For diffusion controlled reaction on a spherical particle of radius, r (4):

$$R_{e,D} = (\psi D/r)\cdot(C_0 - C_x) \qquad 2)$$

where $R_{e,D}$ = diffusion controlled reactivity based on external surface area, g cm^{-2} s^{-1}

$\psi = (M_c/M_o\nu)$ where ν is the molar stoichiometric coefficient for the gas and M_c/M_o is the molecular weight ratio of carbon to the reactant gas. For the present studies, $C + 1/2\ O_2 \rightarrow CO$, and $\nu = 1/2$, with $\psi = (12/32)\cdot 2 = 3/4$

D = Binary diffusion coefficient of the oxidant gas, cm^2 s^{-1}.

C = mass density of the gas at the particle surface, C_x, and in the free stream, C_0, g cm^{-3}.

Thus, diffusion control (small values of $R_{e,D}$) is favored by high pressure (low diffusion rates), large particle size, and high temperature (high surface reaction rates). For pure diffusion control, i.e., when the surface reaction rate is infinitely rapid, $C_x \rightarrow 0$. Figure 6 shows the range of $R_{e,D}$ calculated from Eq. 2) with $C_x = 0$ at the temperature and pressure extremes used in the present work (60 kPa and 1700 K) compared to the experimentally measured values. For the nominal particle diameters of the carbon blacks, ≈ 10-100 nm, diffusion controlled rates are large and the reaction rate is controlled by surface chemistry processes. Figure 6 shows that even if aggregates as large as 100 μm were present in the reactor (and the settling chamber ensures that they were not), bulk diffusion rates would still be ≈10 times larger than the observed reaction rates under the present experimental conditions. On this basis, mass transfer to the carbon black particles does not significantly affect the observed measurements.

In the absence of diffusion effects, the slopes of plots like Figs. 4 and 5 give the apparent reaction order in $[O_2]$. The reaction orders, n, lie between 0.6 and 0.8. Table II contains a summary listing of the values of R_e for the present experiments in the form $\log R_e = \log R_0 + n \log [O_2]$. R_0 is a fitting constant with units of g cm^{-2} s^{-1} $[O_2]^{-n}$.

3. Discussion

Figures 2, 4, and 5 show comparisons of the observed u and R_e with the predictions of the Nagle and Strickland-Constable, NSC, formulation (10) which has been successful in describing the reactivity of several carbonaceous materials with O_2, especially at higher temperatures than those used here (10,11). From the plots it is clear that the present results are not well described by two site NSC kinetics (cf. Blyholder, et al. (12)). In particular, the present results show no indication of the change in reaction order in $[O_2]$ suggested by the two site theory (12).

In Fig.7, the R_e values are compared with previous studies of soot and carbon black oxidation at $[O_2] = 3.5 \times 10^{17}$ cm^{-3}. The data are those of NSC (10), Park and Appelton (11), PA, on carbon black oxidation in a shock tube (the PA and NSC results are identical), and of Lee, Thring, and Beér (13), LTB, on soot oxidation in an O_2-rich flame. At this $[O_2]$ and higher, R16 and CSC oxidation are significantly slower than that of previously studied carbon blacks and soot. An "activation energy" of ≈ 170 kJ is consistent with all of the measurements. At lower $[O_2]$ (≈ 2×10^{14}), the present results are compared with those of Rosner and

Allendorf (14), (RA), and NSC in Fig. 8. At this low $[O_2]$, RA's measurements on isotropic and pyrolytic graphite bracket those predicted by NSC and those measured in the present work. The "turnover" in the reactivity coefficient values predicted by NSC and observed by RA may be present for R16, but it is not suggested by the CSC data.

Figures 9 and 10 display the probability of reaction, ξ, per O_2-surface collision calculated using kinetic theory to determine the number of collisions/s per unit surface area and the measured R_t values. The data of RA on pyrolytic graphite over a range of low $[O_2]$ at $\approx$ 1500 K are shown for comparison in Fig. 9. In Fig. 10, ξ for R16 and CSC is shown for most of the wide range of $[O_2]$ covered in this work at the extremes of the temperature ranges investigated. The low reactivity of these carbon blacks translates into collision efficiencies as low as $\approx 1 \times 10^{-6}$ at $[O_2] = 1 \times 10^{18}$ cm^{-3} and as high as $\approx 4 \times 10^{-3}$ at $[O_2] = 1 \times 10^{15}$ cm^{-3}. These values are comparable to those for graphitic carbons.

Thus, the present results indicate low reactivity for R16 and CSC for $[O_2]$ values of practical interest. The complex $[O_2]$-dependence of R_t required by NSC kinetics is not observed over the temperature range studied, despite extremely wide variations in $[O_2]$. The data show no significant differences which can be attributed to metallic content. We speculate that the high sulfur content in these carbon blacks may be the cause of their low reactivity and the failure of the two site model to describe their oxidation kinetics. The sulfur content (mole fraction $\approx$ 40 ppm) may be sufficient to poison potential metallic catalytic sites (on a molar basis, sulfur is $\approx$ 20 times more abundant than metals in R16 and 10 times more in CSC) as well as to interfere with active sites in both carbon blacks. If correct, this speculation suggests that it is important to avoid sulfur contamination where carbonaceous burnout at "low" temperature is desired.

REFERENCES

1. Neoh, K.G., Howard, J.B., and Sarofim, A.F., in Particulate Carbon: Formation During Combustion, D.C. Siegla and G.W. Smith, Eds., Plenum Press, New York, (1981), p. 261.

2. Page, F.M. and Ates, F., in Evaporation and Combustion of Fuels, J.T. Zung, Ed., Advances in Chemistry 166, American Chemical Society, Washington, D.C. (1978), p 190.

3. Fenimore, C.P. and Jones, G.W., J. Phys. Chem. 71, 593 (1967).

4. Laurendeau, N.M., Prog. Energy Combust. Sci. 4, 221 (1978).

5. Fontijn, A. and Felder, W., in Reactive Intermediates in the Gas Phase: Generation and Monitoring, D.W. Setser, Ed., Academic Press, New York, (1979) Chap. 2.

6. Lowell, S. Introduction to Powder Surface Area, Wiley-Interscience, New York (1979).

7. Mulcahy, M.F.R. and Smith, I.W., Pure and Appl. Chem. 19, 81 (1969)

8. Essenhigh, R.H., in Chemistry of Coal Utilization, 2nd Supplementary Volume, M.A. Elliott, Ed., Wiley, New York, (1981) Chap. 19.

9. Smith, I.W., Combust. Flame 17, 303 (1971)

10. Nagle, J. and Strickland-Constable, R.F., Proceedings of the Fifth Conference on Carbon, Volume 1, Macmillan, New York (1962), p. 154.

11. Park, C. and Appelton, J.P., Combust. Flame 20, 369 (1973).

12. Blyholder,G., Binford, J.S., Jr., and Eyring, H., J. Phys. Chem. 62, 263 (1958).

13. Lee, K.B., Thring, M.W., and Beer, J.M., Combust. Flame 6, 137 (1962).

14. Rosner, D.E. and Allendorf, H.D., AIAA J. 6, 650 (1968).

TABLE I. PHYSICAL AND CHEMICAL PROPERTIES OF CARBON BLACKS[a]

Trade Name	Mean Particle Diam.(nm)	BET (N_2) Surface Area(m^2g^{-1})	Volatiles (wt %)	Metal Content (wt %)[c]	Ash (wt %)	Sulfur (wt %)
Raven 16	61	25 (29[b])	0.9	0.1[c]	0.098	1.67
Conductex SC	20	220 (190[b])	1.5	0.08[c]	0.075	0.85

[a] Data supplied by manufacturer.
[b] Measured in this work.
[c] Metallic impurities, wt.%:

	R16	CSC
Σ Mn, Mg, Al, Ti	0.007	0.008
Fe	0.045	0.005
Na	0.021	0.047
Ca	0.025	0.016

TABLE II. EXTERNAL SURFACE REACTIVITY FOR CARBON BLACK OXIDATION BY O_2

$$\log_{10} R_e = \log_{10} R_0 + n \log_{10} [O_2]$$

Carbon Black	T (K)	$\log_{10} R_0$ ($g\ cm^{-2}\ s^{-1}\ [O_2]^{-n}$)	n	$[O_2]$ range ($10^{16}\ cm^{-3}$)
Raven 16	1300	-16.3 ± 0.5[a]	0.62 ± 0.04[a]	0.02 - 158
	1400	-16.5 ± 2.0	0.64 ± 0.12	2.0 - 104
	1470	-16.1 ± 1.3	0.66 ± 0.10	0.02 - 98
	1580	-14.9 ± 1.7	0.59 ± 0.10	0.12 - 177
	1680	-15.1 ± 1.0	0.61 ± 0.07	0.03 - 154
Conductex SC	1410	-18.6 ± 0.5	0.76 ± 0.13	0.03 - 200
	1580	-18.8 ± 1.1	0.82 ± 0.17	0.02 - 130
	1650	-14.2 ± 1.4	0.57 ± 0.09	0.02 - 75

[a] One standard deviation

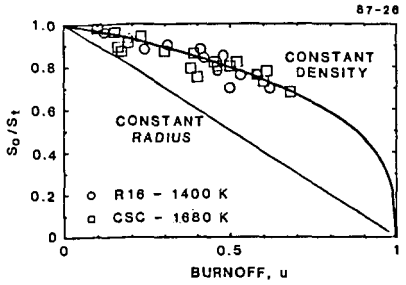

FIGURE 1 VARIATION OF CARBON BLACK SURFACE AREA WITH BURNOFF

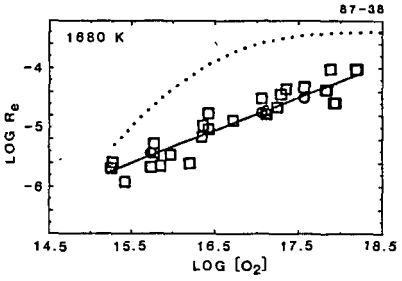

FIGURE 4 R16 OXIDATION BY O_2
□ - gc data; o - scattering data;
··· -NSC (10) prediction

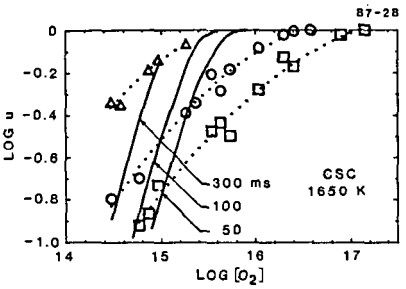

FIGURE 2 BURNOFF OF CSC AT 1650 K
Residence times: □ - 50 ms; o - 100 ms;
Δ - 300 ms. Solid lines are NSC (10) predictions.

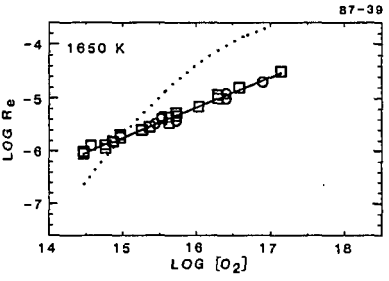

FIGURE 5 CSC OXIDATION BY O_2
□ - gc data; o - scattering data;
··· -NSC (10) prediction

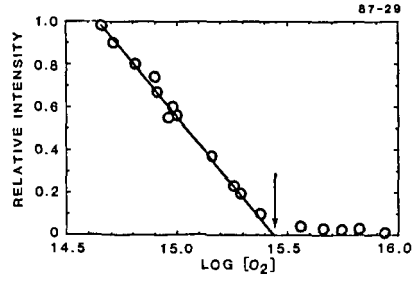

FIGURE 3 LASER SCATTERING MEASUREMENT OF CSC OXIDATION AT 1650 K
$[O_2] = 2.8 \times 10^{15}$ (arrow), t_s = 380 ms

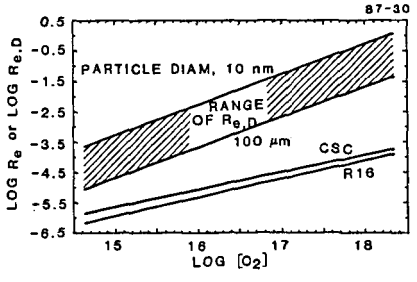

FIGURE 6 COMPARISON OF DIFFUSION-LIMITED REACTIVITY WITH OBSERVED VALUES AT 1700K

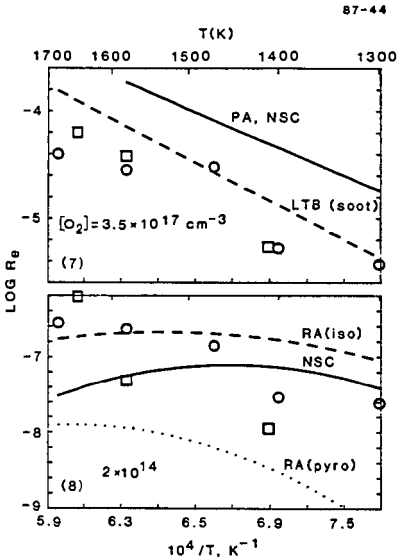

FIGURES 7 and 8 TEMPERATURE DEPENDENCE OF CARBON BLACK OXIDATION
o - R16; ◘ -CSC; NSC - Nagle and Strickland-Constable (10); PA - Park and Appelton (11); LTB -Lee, Thring and Beer (13); RA - Rosner and Allendorf (14) for isotropic (iso) and pyrolytic (pyro) graphite

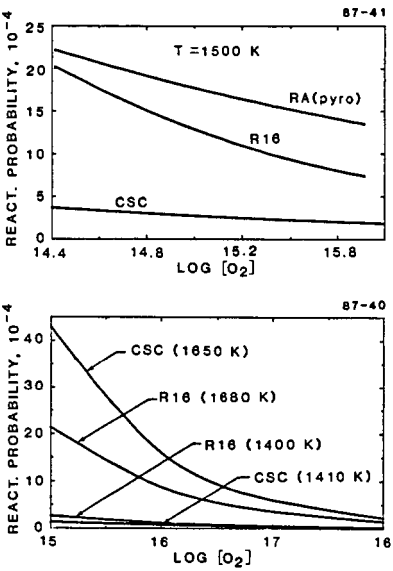

FIGURES 9 and 10 DEPENDENCE OF REACTION PROBABILITY ON $[O_2]$
RA(pyro) - results of Rosner and Allendorf (14) on pyrolytic graphite.